Thermo-mechanical properties of a regolith simulant of the mars insight mission site

Juan-Pablo Castillo Betancourt

To cite this version:

Juan-Pablo Castillo Betancourt. Thermo-mechanical properties of a regolith simulant of the mars insight mission site. Géotechnique. École des Ponts ParisTech; Universidad de los Andes (Bogotá, Colombia ; 1948- ..), 2023. English. ⟨NNT : 2023ENPC0035⟩. ⟨tel-04973392⟩

HAL Id: tel-04973392
https://pastel.hal.science/tel-04973392v1

Submitted on 3 Mar 2025

THÈSE DE DOCTORAT
de l'École des Ponts ParisTech

THERMO-MECHANICAL PROPERTIES OF A REGOLITH SIMULANT OF THE MARS INSIGHT MISSION SITE

École doctorale N° 531, Sciences, Ingénierie et Environnement (SIE)

Spécialité : Géotechnique

Thèse préparée au laboratoire NAVIER

Soutenue le 4 décembre 2023, par
Juan Pablo CASTILLO BETANCOURT

Composition du jury :

Nicolás, ESTRADA MEJÍA Professeur, ENTPE - LTDS, Université de Lyon	*Président*
Hervé, DI BENEDETTO Professeur, ENTPE - LTDS, Université de Lyon	*Rapporteur*
Fernando, LÓPEZ CABALLERO Professeur, Centrale SupElec - Université Paris	*Rapporteur*
Naomi, MURDOCH Docteure, ISAE – SUPAERO, Université de Toulouse	*Examinatrice*
Nadia, BENAHMED Docteure, ISAE – SUPAERO, Université de Toulouse	*Examinatrice*
Juan Carlos, SANTAMARINA Professeur, Georgia Institute of Technology	*Examinateur*
Pierre, DELAGE Professeur, École des Ponts ParisTech	*Directeur de thèse*
Bernardo, CAICEDO Professeur, Universidad de los Andes	*Co-Directeur de thèse*
Philippe, Lognonné Professeur, Institut de Physique du Globe de Paris – Université Paris Cité	*Invité*

A

A

To all family and friends, but specially:

To María Cristina Betancourt, Flavio Humberto Castillo, and Daniel Humberto Castillo

ACKNOWLEDGEMENTS

When beginning to type these pages, the memories of over four years and of all the people who were a part of this process in some way or the other go through my head, as the most important part of all of the great and strongest moments of such a relevant part of my life. I will try my best to focus on my wording and mentioning those that were involved the most (sadly, it may be impossible to mention everyone, when I might not even know some of the people that were involved in some way to make this possible… I offer my deepest apologies in advance if for whatever reason you happen not to be mentioned on these pages, but just in case you happen to be reading this for whatever reason, please know that you will always have my gratitude).

First, I want to dedicate this work to all my family, who were very supporting of this process from the very beginning to the quickly approaching end of it. My parents, Maria Cristina, and Humberto. There are no better parents in the world, and you can rest assured that is confirmed by data taken on Mars. Their support was felt everyday through this journey, and they made this possible and were there during the best moments and the toughest ones. The same can be said for my brother Daniel, who is the greatest inspiration and role model any small brother can ever have. I consider myself infinitely lucky to have been able to learn from you and with you. Daniel’s wife Ángela has also been there to share these years, and their support during the toughest moments of the lockdown was invaluable.

I want to thank both of my thesis advisors, professors Bernardo Caicedo and Pierre Delage. First for trusting my abilities to take on this research project, thus providing me the opportunity to contribute to the InSight mission and work in relation with the field of space exploration. I consider myself fortunate to have had such excellent advisors to guide my work. Now approaching the end of this project, part of me still finds it hard to believe that I got the chance to offer a contribution, as limited as it might be, towards the spatial exploration that has always fascinated me and in which I will always place my hopes for the future of humankind. This gratitude also goes to my undergraduate and master’s advisor Nicolás Estrada, who was the first person to ever grant me the chance of going into the world of research in geotechnics, and without whom I would never have made it into such a fulfilling research project. Their personal and academic support was invaluable through these four years, and I shall never forget that they were always patient, understanding, and willing to help to overcome the numerous and tough challenges that were encountered during this extensive work. I want to extend my gratitude to the other Professors of the GeoSI group, Professors Silvia Caro, Miguel Ángel Cabrera and Mauricio Sánchez for taking me into the GeoSI group and entrusting me with a very active role inside of it. I also thank all of the professors and teachers I ever have had, and I hope to have taken at least a single lesson from every one of you.

My gratitude also goes toward the people and the institutions at Universidad de los Andes and École des Ponts ParisTech, for allowing me to take part in their research, using their excellent laboratories and available resources, and enjoying the invaluable support of their staff. I also thank the institutions that supported our participation in the InSight project and helped finance the necessary experimental equipment and accommodations for the conferences and team meetings, including CNES, CNRS and IPMG at Sorbonne Université. Also, to Fondation de Ponts for supporting me when I needed it during the pandemic to compensate for the delay the sanitary crisis inflicted on the laboratory work.

The laboratory staff at both institutions were some of the most supporting and necessary people for all the work contained in these pages. At Uniandes, Julieth Monroy and José Naranjo supported every experiment and their knowledge in instrumentation, electronics and testing procedure were essential for all the tests. Mauricio Tobar, Manuel Sierra, John Calvo, and Juan Naranjo were also always available to offer their support when possible. At ENPC, the wide expertise of Marine LeMaire, Baptiste Chabot, Xavier Boulay and Loïc Leusuer was always indispensable for the successful completion of experiments. I was also fortunate to be able to rely on Emmanuel de Laure, who helped me assimilate into the group and the environment of the Navier CERMES laboratory, to adapt better to their practices while being extremely patient and accommodating in assisting with any difficulties I may have encountered. I also thank the kind administration staff at both universities, particularly Sabrina Chartier, Dalida Chartrel and Christelle Berol at ENPC, and Luisa Amarillo, Elizabeth and Luz Dary at Uniandes.

I also thank the jury members for their time and collaboration to help the final steps of this work, taking the time to review this document (I hope it is not too long in extension for your comfort).

Last but not least, I consider myself extremely lucky to have had the opportunity to share some unforgettable moments with some exceptional people at both institutions. At ENPC in particular my office colleagues including Quoc-Hung Vu, Sebastián López Retamales, Ahn Kyeung and Catherine Doré Ossipyan and Valerian Guery. The lunches, coffees, football matches and moments shared will be remembered, even if the pandemic significantly limited interactions for most of the time. Also, to Lina Guayacán who was willing to help another Colombian when necessary. I am very proud to have been a part of the Navier CERMES team.

In Uniandes, I am lucky to have shared with so many people through almost nine years, so I want to begin by thanking everyone I shared with whether we are still in contact or not (if the latter if the case, again, my apologies and I hope we may meet again in the future). I thank specially my dear group of friends who shared all those eternal Transmilenio rides (and everything else) back and forth almost daily, so Camilo Sánchez, Diego Noriega and Iván Salazar, who helped make them much more enjoyable and are some of the best friends anyone can ever have. Also, thanks to the excellent friends that were Alejandra Posada, Juan Diego Carvajal and Andrés Salazar for the moments in the classes and the table tennis matches (and to the members of the University table tennis team too). I also thank my dear friend Maria Camila Rubio, with whom I shared most of the nine years at Uniandes, including some of the best and the worst moments as we grew, who helped me become a better person in so many ways, always keeping alive a passion for learning all that can be learned, pushing the limits and maintaining the continuous drive to become a better person every passing day. I want to thank my loved Sofía Sáenz for ten years of friendship, insane table tennis matches, never ending laughter and so many more unforgettable moments. Her continuous support and appreciation helped me to learn to better overcome adversities, to celebrate and appreciate accomplishments, and I thank her for the most special moments, particularly during the final stages of my doctoral studies. Without all of these amazing friends I would never have made it through all these years.

I also want to thank all the students of the GeoSI group, with whom I shared all through the master and doctorate. In this group more than colleagues I found amazing and caring friends to share incredible memories, both on and off the daily work life. Andrés Escobar and Oscar Polanía in particular, who also had their own doctorate stories simultaneously and with whom we shared memorable moments in the office, football and volleyball fields, chess games and plenty of other activities, but also very serious academic discussions over the latest journals. The conversations and moments shared with my close friends and doctoral colleagues Angélica Viana and Maria Juliana Chaparro (one of the most significant collaborators to this work) were also invaluable, concerning both academic, professional and many other topics. I thank them for providing a powerful learning experience as well as a safe space to exchange and discuss ideas and opinions in subjects of every type. Significant learning resulted from similar exchanges with Laura Ibagón and Fausto Molina, who kindly shared their lessons and experiences acquired on their corresponding universities and very impressive academic work.

Also, my gratitude goes to all my dear friends in the group GeoSI through the years, but in particular to Lina León, Johan Perdomo, Luisa Pérez, Diego Borda, Diana Sánchez, Jaime Granados, Nayled Acuña, Carlos Torres, Carlos Benavides, Camila Sánchez, Rafael Romero, Laura Cote, Camila Santos, Santiago Caro, and Juan Pablo Villacreces; thanks to this incredible group of exceptional people for all those coffees, lunches, ice-creams and a plethora of other moments that I will always remember. Also, to the rest of the people in the ML753 office and the everyday work life (Felipe Torres, Camilo, Alejandra, Marta, Yesith, Gabriel and Germán) and the other members of the GeoSI group. All of these remarkable people helped made my time at Uniandes during the last two years of the doctorate some of the best of my life and enabled me to enjoy my work every day.

I also want to thank those friends that stuck with me all the way through school, undergraduate, master and doctorate. To David Pareja, Sebastián and Nicolás Cabrera for all those football matches we won, and the runs in Patios where I did more elevation in a few hours than through the rest of the year.

MOTS CLÉS

MOTS CLÉS: Mission Mars Insight, Analogue de régolithe, sable de Fontainebleau, densité lâche, faibles contraintes, instrument SEIS, pression atmosphérique, bruit sismique, conductivité thermique, préparation d'échantillons, pluviation, bender éléments, propagation des ondes, différences finies, elasticité.

KEYWORDS

KEYWORDS: Mars Insight Mission, Regolith simulant, Fontainebleau Sand, Loose Density, Low Stresses, SEIS instrument, Atmospheric Pressure, Seismic Noise, Thermal Conductivity, Sample Preparation, Pluviation, Bender Elements, Wave Propagation, Finite Differences, Elasticity.

RESUME

La mission Mars InSight de la NASA est une mission Discovery visant à étudier l'intérieur de la planète rouge, et par conséquent à aider à la compréhension de son processus de formation et de celui des autres planètes telluriques. L'un des nombreux fronts d'étude auxquels est confrontée l'équipe scientifique de la mission InSight est l'étude des propriétés du matériau situé en contact direct avec l'atterrisseur et ses instruments, dont certains ont été déployés à la surface de la planète via l'utilisation d'un bras robotique. Cet effort est le but du groupe de travail *Near Surface Working Group* (NSWG), et les travaux et résultats présentés dans ce document est de fournir des informations pour aider cet objectif de recherche. L'atterrisseur utilise trois instruments principaux pour atteindre ses objectifs scientifiques : le premier est le *Seismic Experiment for Interior Structure* (SEIS), un sismomètre de haute précision résultant de plusieurs décennies d'efforts menés par des institutions françaises, dont le Centre National des Études Spatiales CNES et l'Institut de Physique du Globe de Paris IPGP ; cet instrument est le plus pertinent pour ce travail. Le deuxième est le *Heat and Physical Properties Package* (HP^3), une sonde thermique conçue pour forer l'intérieur de la surface martienne jusqu'à des profondeurs allant jusqu'à 5 m. La dernière est l'antenne *Rotation and Interior Structure Experiment* ou RISE, qui étudie la structure intérieure de la planète à l'aide du mouvement de rotation de Mars, en suivant la position de l'atterrisseur et le déplacement du pôle Nord de la planète pour proposer des modèles de son moment d'inertie.

Ce travail consiste en plusieurs activités de recherche dans le domaine de la mécanique des sols, réalisées dans le but de caractériser le matériau situé à la surface de l'atterrisseur Mars InSight de la NASA, installé sur Elysium Planitia depuis novembre 2018. Il s'agit principalement d'essais expérimentaux dans un analogue de régolithe martien et quelques activités complémentaires. Les questions clés abordées étaient l'interaction du SEIS avec le régolithe martien de surface en contact direct avec ses trois pieds, la faible rigidité en déformation de ce matériau (comportement en gamme élastique), ainsi que certaines questions spécifiques telles que la conductivité thermique et l'effet des fluctuations de la pression atmosphérique. Les travaux expérimentaux menés représentent notamment une connaissance précieuse dans le monde peu exploré de la mécanique des sols sous de très faibles contraintes et déformations (le plus souvent inférieures à 50 kPa). La préparation des échantillons est une autre question explorée, puisque les densités les plus faibles possibles de l'analogue du régolithe sont utilisées en cherchant à se rapprocher le plus possible des conditions du matériau sur Mars.

Le travail de thèse a été développé dans le cadre d'une cotutelle entre l'Université des Andes et l'École des Ponts ParisTech. Les travaux expérimentaux ont été menés dans les installations des deux institutions de recherche et ont été rendus possibles grâce à l'expertise du groupe de recherche et de l'équipe technique affiliée à chaque université et ses laboratoires. Ce document contient une synthèse des points clés de chacun de ces travaux. Certaines collaborations avec la

doctorante Maria Juliana Chaparro ont également permis d'évaluer les propriétés dynamiques du matériau analogue du régolithe choisi.

ABSTRACT

The NASA Mars InSight mission is a Discovery mission aiming at to investigating the interior of the red planet to support the understanding of its formation process and that of other rocky planets. One of the many study fronts faced by the InSight Mission Science Team is the study of the properties of the material in direct contact with the lander and its instruments, some of which were deployed on the surface of the planet by using a robotic arm. This endeavour is the key objective of the Near Surface Working Group (NSWG), and the main goal of the different works and results presented in this document is related to this research goal. The lander uses three main instruments: the first one is the Seismic Experiment for Interior Structure (SEIS), a highly accurate seismometer resulting from decades of work by French institutions including Centre National des Études Spatiales CNES and Institut de Physique du Globe de Paris IPGP; this instrument is the most relevant for this work. The second one is the Heat and Physical Properties Package (HP^3), a thermal probe designed to drill inside the Martian surface to depths of up to 5m. The last one is the Rotation and Interior Structure Experiment or RISE antenna, which studies the interior structure of the planet aided by the rotation movement of Mars, tracking the position of the lander and the shifting of the planets north pole to propose models of its moment of inertia.

This work is aimed at characterising the surface regolith properties at the site of the Mars InSight lander, landed on Elysium Planitia since November 2018. This comprises experimental investigations on a Martian Regolith Simulant together with some complementary activities. The key questions addressed were the interaction of the SEIS with the Martian regolith in direct contact with its three feet, its very small strain stiffness (in the elastic range), as well as the thermal conductivity and the mechanical effect of atmospheric pressure fluctuations. The experimental work conducted concerns the poorly explored field of soil mechanics under very low stresses and strains (down to 1.75 kPa). Sample preparation is another question explored, since the loosest possible densities of the regolith analogue are utilised to mimic the Martian regolith.

The thesis was developed within a joint supervision between the Universidad de los Andes (Bogota, Colombia) and the École des Ponts ParisTech (France). Experimental work was conducted at the facilities of both institutions. Collaborations with PhD student Maria Juliana Chaparro (Los Andes) also helped assess the dynamic properties of the regolith simulant.

LISTS OF TABLES AND FIGURES

List Of Figures

Figure 1-1. Mars as seen by the Hubble telescope. (Image credit: https://www.jpl.nasa.gov/spaceimages/details.php?id=PIA01249).. 4
Figure 1-2. Mars Odyssey (2001) and its instruments. (Image credit: https://www.researchgate.net/profile/William-Boynton/publication/226827726/figure/fig2/AS:302384489222149@1449105488554/2001-Mars-Odyssey-Spacecraft-in-Mapping-Configuration-The-Odyssey-spacecraft-as.png).......... 5
Figure 1-3. Artist representation of the Phoenix lander. (https://www.nasa.gov/multimedia/imagegallery/image_feature_857.html) 6
Figure 1-4. The Mars 2020 perseverance Rover (https://mars.nasa.gov/resources/24716/some-differences-between-mars-2020-and-curiosity/)... 6
Figure 1-5. The NASA Opportunity rover mission lasted between 2014 and 2018 and was among the most successful missions on the red planet. (Credit: https://mars.nasa.gov/msl/multimedia/raw-images/?order=sol+desc%2Cinstrument_sort+asc%2Csample_type_sort+asc%2C+date_taken+desc&per_page=50&page=0&mission=msl). 11
Figure 1-6. Shadow of Mars helicopter Ingenuity during its 60th flight, Sol 924. (Image credit: NASA/JPL-Caltech). 12
Figure 1-7. Artist concept of the Mars InSight Lander with its main instruments (https://mars.nasa.gov/insight/spacecraft/instruments/summary/)... 19
Figure 1-8. Coordinates of Elysium Planitia, location of the landing site of Mars InSight (SEIS: Insight’s Seismic Experiment for Internal Structure of Mars (2019)). 20
Figure 1-9. Instrument payload on the landing deck. From left to right, the HP^3 probe, the thermal shield of SEIS and the SEIS instrument (red) 20
Figure 1-10. a) The HP3 instrument and the b) SEIS instrument when deployed as seen by the IDC and ICC cameras respectively. 21
Figure 1-11. The raw SEIS data (deglitched) for the event of Sol 1222 plotted with the obspy python library. 21
Figure 1-12. The plot of the Mars 1222 event after processing (Credit: NASA/JPL, 2022).... 22
Figure 1-13. The geological formations of the Paris region. The Paleogene formations remain among the shallowest in the region (Image credit: Histoire-geologique-du-Bassin-parisien). 25
Figure 1-14. Different proposals for the area occupied by the Stampien sea (Credit: Baut et al., 2003) 26
Figure 1-15. Aspect of Fontainebleau sand a) during an indentation test with a 6 cm diameter plate for reference. Note that grains and groups of grains are distinct to the eye. Some grains observed on b) SEM images. 26
Figure 1-16. Results of spectroscopy on a Fontainebleau sample during SEM microscopy.... 26

Figure 1-17. Size distribution curve for Fontainebleau sand. 27
Figure 1-18. a) A typical grain of Fontainebleau sand, and b) a group of Fontainebleau sand grains seen on SEM microscopy. 28
Figure 1-19. The previously used Martian Simulants. (Karakostas et al., 2013) 28
Figure 1-20. Thermal inertia and the expected properties of the soil at the landing site (Golombek et al., 2017). 29
Figure 2-1. a) Cylindrical container used for the sample, filled with b) the bottom layer of beads. 39
Figure 2-2. Hollow bead with an internal 3 mm diameter used for calibrating the air grey inside the sample. 39
Figure 2-3. Tape used to ensure the central position of the funnel during pluviation. 40
Figure 2-4. After placing the a) upper layer of beads, a new b) conic pile was deposited over the top layer of glass and hollow beads. 40
Figure 2-5. Sample placed into the X-ray tomograph. 40
Figure 2-6. Example of a TIF file of a slice of the scan. The white/light grey circles are the hollow beads, whereas the dark grey circles are the glass beads. 41
Figure 2-7. Images created to facilitate the identification of the beads. The white circles are the hollow beads, whereas the black circles are the glass beads. 42
Figure 2-8. Vertical profiles plotted along the sample. 43
Figure 2-9. Radial profiles of the grey level in main directions at the top and the bottom of the sample. Effect of the Beam Hardening has a radial symmetry. 44
Figure 2-10. Standard deviation of the sample plotted in several directions. The peaks correspond to the beads. 44
Figure 2-11. Graph showing the mean grey value plus and minus the standard deviation. 45
Figure 2-12. Graph showing the mean grey value plus and minus the standard deviation. 45
Figure 2-13. Radial changes in grey level (GL) for sand and bead: a) top level; b) bottom level. 46
Figure 2-14. Density value colormap, shown for the a) upper and b) lower levels. 47
Figure 2-15. Radial density profiles along the upper level of the sample. The top and down peaks corresponds to crossing beads; one silica bead has been crossed at 320° (red curve) and two beads (silica and hollow bead, respectively) have been crossed at 160° (green curve). 47
Figure 2-16. Density profiles along the lower level of the sample. 47
Figure 3-1. Design of the SEIS feet: a) Alternatives investigated and b) Final design of the feet of the SEIS instrument (Karakostas et al., 2013). 52
Figure 3-2. Testing of the SEIS instrument on Earth. (SEIS: Insight’s Seismic Experiment for Internal 52
Figure 3-3. The experimental setup used (Tri scan 50 triaxial press) 54
Figure 3-4. Some of the cycles performed to validate press displacement accuracy. 54

Figure 3-5. Testing process of displacement sensors. The non-contact Eddy sensor is seen in the middle. 55
Figure 3-6. The selected LVDT sensors have a measurement range of a) 4.5mm and b) 25 mm respectively. 55
Figure 3-7. The S-cell force sensor selected. 55
Figure 3-8. Thermal isolation box surrounding the experiment. 56
Figure 3-9. The used data acquisition unit. 56
Figure 3-10. The b) type J thermocouple placed a) inside the setup to monitor temperature during experiments. 56
Figure 3-11. The definitive experimental setup (without the thermal box to see it) 57
Figure 3-12. All system components. 57
Figure 3-13. Sample preparation procedure. 58
Figure 3-14. Simplified schema of the experimental procedure of each test. 59
Figure 3-15. Base model with actual sample dimensions of the container. 60
Figure 3-16. The model built with discretized fine soil layers. 60
Figure 3-17. Several void ratio functions evaluated for Fontainebleau sand. 61
Figure 3-18. Shear moduli for Fontainebleau sand predicted in terms of stress. 61
Figure 3-19 InSight NASA lander concept and main instruments. Image credit JPL/NASA: https://mars.nasa.gov/insight/spacecraft/instruments/summary/ 64
Figure 3-20. IDC photograph showing the scoop of the instrument deployment arm (IDA) compressing the regolith above a hole developed around the self-penetrating mole during hammering. The scoop width is 7·6 cm (image credit JPL-NASA. IDC image acquired on Sol 550, imageD000M0550_645359459EDR_F0000_0800M3) 65
Figure 3-21. Interpretative cross-section of the shallow surface beneath the InSight lander (Golombek et al., 2020, Creative Commons CC BY license) 1, fractured basalt flow; 2, blocky ejecta; 3, fine-grained impact generated regolith; 4, 5, overlapping craters; 6, rockier area; 7, rocks embedded in regolith; 8, pits opened by retro rockets during landing; 9, surface divots; 10, lens of ejecta from other craters. 66
Figure 3-22. The shape of the SEIS foot. The conical spike has a maximum diameter of 10 mm. 66
Figure 3-23. NE 34 Fontainebleau sand: (a) grain size distribution; (b) scanning electron microscope photograph showing the subrounded grains (after Andria-Ntoanina, 2011) 67
Figure 3-24. Experimental set-up, showing more details of the fixation of the mass to the force gauge and the LVDTs providing the vertical displacement. 68
Figure 3-25. Elastic calculations of the vertical and shear stress (presented as percentages of the applied vertical stress) and of the vertical strain below the foot under the SEIS weight, based on the elastic solution by Sneddon (1946) 68
Figure 3-26. (a) Thermal insulation of the device; (b) temperature stabilisation is reached after 10 h for tests DS1, DS2 and DS3 (see Table 3-2) 70

Figure 3-27 Temperature stabilisation in tests DS1, DS2 and DS3 (see Table 3-2) made possible by the thermal insulation of the device, is of the order of 0.1°C. 71
Figure 3-28. Force–penetration curves for the ten tests performed with the disc.................... 73
Figure 3-29 Load–unload cycle performed between 8·98 and 6·37 N in test 10 (disc only). The stiffness coefficient given by the slope is k= 1·47× 106 N/m 73
Figure 3-30. (a) Force–penetration curves for the three tests performed with the foot (disc+ spike). Note that the force significantly increases once the disc contacts the sand surface. The start of the disc/sand contact is taken as 0 for the x-axis, and the curves are started at a point obtained by subtracting the length of the spike (−20 000 μm). (b) Detailed force–penetration curve of the spike alone for test DS1, with a maximum force of 0·14 N reached just before sand/disc contact. Two stick–slips are observed at around 4800 and 8600 μm....................... 75
Figure 3-31 Force–penetration curves for the three tests carried out with the foot (disc + spike) once the spike had fully penetrated the sand and the disc was in contact with the sand. 75
Figure 3-32. Changes in Young's modulus with respect to the average vertical stress at the surface. Data are derived from load cycles tests and from the final unloading step................ 77
Figure 4-1. Strain ranges and associated applications (After Atkinson, 2000) 85
Figure 4-2. Correspondence of moduli by using Bender elements and Resonant column. (Dyvik &Madshus,1985)... 86
Figure 4-3. Void ratio functions for Fontainebleau sand. 87
Figure 4-4. Initial shear moduli estimated for Fontainebleau sand. 88
Figure 4-5. Limited hysteresis of sample wave velocities was observed during the unloading-reloading cycle. 94
Figure 4-6. Compression wave velocity measurements of Fontainebleau sand compared with previous regolith analogues. 96
Figure 4-7. Shear wave velocity measurements of Fontainebleau sand compared with previous regolith analogues. 96
Figure 4-8 Image taken on Sol 1770 (i.e., the 1770th martian day of the mission) by the Instrument Context Camera of the Lander showing the hemispherical Wind and Thermal Shield (WTS, diameter 720 mm) covering the SEIS instrument, with the Instrument Deployment Arm vertically pushing on the soil at the right of the SEIS. A flat footprint made by a former push test by the IDA can also be observed. These push tests were carried out to estimate the surface elastic properties based on the sstrain derived from the SEIS response. The (black) HP3 support system is observed on the left side, close to the place where the self-driving penetrometer has been buried. Some scraps made by the IDA scoop to cover the regolith tether for better thermal insulation can also be seen at the left of the WTS. All instruments are covered by a dust layer progressively brought by the Martian winds (Image Credit: NASA-JPL). 99
Figure 4-9 NE34 Fontainebleau Sand: (a) grain size distribution curve, and (b) SEM image. 102
Figure 4-10. a) Sample preparation (vertical); b) Sample tested (horizontal). 103

Figure 4-11. (a) Setup used for measuring the membrane stiffness; (b) Force/vertical strain elongation curve of the membrane; (c) Schematic drawing for computing the stress on a cylinder. 104
Figure 4-12. FEM (Plaxis 3D) elastic analyses of the sample self-weight to estimate the horizontal stress σ_{gh} on the sample axis. 104
Figure 4-13. P and S waves under 70.75 kPa, with good correspondence between both: the S wave arrival can also be detected in the P wave signal; the arrival of the P wave creates some slight perturbations in the S wave signal (time is in milliseconds). 106
Figure 4-14. P (pink) and S (grey) waves detected under smaller stresses below 10 kPa. 107
Figure 4-15. Measured wave velocities obtained using bender elements compared with those measured by Brinkman et al. (2022) on Mars (red and blue points). 107
Figure 4-16. Changes in Poisson ratio with respect to confining stress determined from bender element measurements (points) and from the fitted curves of Figure 4-15 (curve). 108
Figure 4-17. Change in Poisson ratio of an assembly of identical spheres with respect to the proportion of no-slip contacts ξ. 123
Figure 4-18 Schematic drawing of grains in contact with asperities, with contact radius Rc significantly smaller than Rg. 125
Figure 4-19. Schematic drawing of a sphere resting on a deformable rough surface for the Bahrami et al. (2005) model. 126
Figure 4-20 Ratio between the theoretical stiffness S_n^{Rough}/ S_n^{HM} of rough and smooth quartz spheres as a function of the RMS height of the asperities. The data were computed for particles with R_g=110 μm subjected to isotropic stresses σ_3 (calculated using Eq. 3 and Eq. 4, which relates force to stress) between 1 kPa to 10 MPa, and asperities microhardness H_{mic}=8.2 GPa, as suggested in Yovanovich (2006) for quartz. 128
Figure 4-21. Grain topography measured with the AFM AC tapping mode: a) 3D image; b) Greyscale image. 129
Figure 4-22 AFM investigation of a Fontainebleau sand grain: a) Cross profiles on the AFM measured area; b) Histogram of contact radius along the 6 profiles; c) to h) Roughness plotted along the profiles displayed in a). 131
Figure 4-23. Comparison between measured (Castillo-Betancourt et al. 2023) and theoretical values of wave velocities. 133
Figure 4-24. Comparison between measured and theoretical Poisson ratio. 133
Figure 5-1. Dimensions and model of the experimental setup (units in mm). 139
Figure 5-2 a) original container for clay consolidation, which was extensively modified for this experiment. In b), the bender elements used for the initial stages of the setup. 139
Figure 5-3. Comparison of the composition of Earth’s and Mars’s atmospheres. The terrestrial atmosphere is almost entirely made of Nitrogen and Oxygen, while Carbon Dioxide is the prevalent component for the case of Mars (Image credit: European Space Agency, n.d.). 140

Figure 5-4. Mars InsSight data for atmospheric pressure during three Sols. (Image credit: NASA JPL, n.d.). 141
Figure 5-5. Mars InsSight data for atmospheric pressure for two years. (Image credit: NASA JPL, n.d.). 141
Figure 5-6 The a) VarioSelect pump and its b) digital controller while applying 7 mbar. 142
Figure 5-7. CO2 supply and control system, including two valves and the hose connection to the inside of the sample. 143
Figure 5-8. The results of other tests on thermal conductivity displayed no effect on the measured values for measurements done at room temperature (Nagihara et. al, 2022). 143
Figure 5-9 a) The Cedrat Piezoactuators were used to generate P and S waves by installing them into one of the acrylic covers of the setup. A trench was made into the cover to install the S wave actuator transversally. B) The accelerometers were set directly facing them to register the arriving waves in the opposite wall. 144
Figure 5-10. The TEM TG5011A signal generator was used to generate the signals driving the piezoactuators. It allows work with rectangular and sinusoidal signals in single and burst configurations. 144
Figure 5-11 The data of the accelerometers was collected using a pair of a) Fluke 99 and b) Fluke 99B oscilloscopes, and the sensors were powered with the c) SPD3303X-E power source. 145
Figure 5-12 a) The container, Peltier plates, and b) thermal camera used for the b) preliminary thermal propagation test. 146
Figure 5-13 The more potent Peltier plates of the definitive setup with all their electronic equipment. 147
Figure 5-14. Predominant direction for the envisioned heat conduction experiments. 147
Figure 5-15 Schema displaying the thermocouples' arrangement in the amples' back cover. 147
Figure 5-16. Considerable amount of instrumentation posed a practical challenge. A) ADAM2019+ modules for most thermal sensors alongside the air pressure valve control, and b) data acquisition card for the other thermocouple sensors. 148
Figure 5-17. a) Experimental setup for the calibration of the thermocouple sensors. It was achieved with a well-calibrated b) PT100 probe. 148
Figure 5-18. Calibration test during a test carried out under atmospheric pressure, with T1-T4 measuring consistent values and T5 misfunctioning. 149
Figure 5-19. Test where the Peltier plates are turned off and the temperature is allowed to return to initial values. Notice that all sensors return to the same initial values after 10 hours with minimal fluctuations. 149
Figure 5-20. Linearity and reversibility testing of the temperature sensors. Satisfactory performance was observed during three different tests, although it seems to decrease slightly for the lowest temperatures, particularly for the a) T1 to c) T3 sensors. 150

Figure 5-21. Thermal grease applied to the container’s metallic wall to ensure adequate thermal contact. 150
Figure 5-22. A piston a) with a square plate is used to contact the soil surface and is supported by a b) metallic frame which connects it to the pneumatic jack. The reference plate is used to measure the vertical displacement. 151
Figure 5-23 a) The loading cell and the b) pneumatic actuator. 151
Figure 5-24 a) The loading cell is installed between the piston and the plate contacting the soil. 152
Figure 5-25. The Type 3110 Bellofram transducer was used to control the air pressure acting on the jack. 152
Figure 5-26. The material was dried in an oven for two days before the sample was prepared. 153
Figure 5-27. Vacuum chamber to preserve the soil dry as the material cools down. 153
Figure 5-28. Care must be taken during the pluviation process with the a) funnel so that the b) thermocouple wires remain at the intended horizontal position. 154
Figure 5-29. Seal placed at the top to ensure no leaks beneath the cover. 154
Figure 5-30. The sample ready for testing. Notice the a) vacuum seals and their fixation between the Peltier plates. The container is b) barely visible during testing once it is surrounded by the thermal isolation polystyrene. 155
Figure 5-31. The desired pressure is applied in two steps to avoid disturbing the sample. 156
Figure 5-32 The full setup ready for an experiment. 158
Figure 5-33 Schema of the experimental protocol. 159
Figure 5-34. Side and top views of the model geometry. 160
Figure 5-35. Cross section of the model as the thermal pulse propagates. 162
Figure 5-36. The model was first tested with a considerable cooling step to see the effect of thermal conductivity. 163
Figure 5-37. A very good fit was observed for sensors 1-4 with the numerical model for a test carried out under terrestrial atmospheric conditions (with no vacuum in the chamber). 164
Figure 5-38. A very good fit was observed for sensors 1-4 with the numerical model for a test with 6 mbar atmospheric pressure in the chamber. 164
Figure 5-39. The experimental setup during the definitive experimental program. 165
Figure 5-40. Cooling process for different stresses of sample 1, worked at 4 mbar. 167
Figure 5-41. Cooling process for different stresses of sample 2, worked at 6 mbar. 167
Figure 5-42. Cooling process for different stresses of sample 3, worked at 8 mbar. 168
Figure 5-43. Cooling process for different stresses of sample 4, worked at 10 mbar. 168
Figure 5-44. The first group of numerical results. 169
Figure 5-45 The second group of numerical results. 169
Figure 5-46. All the experimental results presented in the same coordinate space. 170

Figure 5-47. Experimental results of sample 1 (4 mbar) superposed with the curves obtained from the finite differences numerical calculations.. 171
Figure 5-48. Experimental results of sample 2 (6 mbar) superposed with the curves obtained from the finite differences numerical calculations.. 171
Figure 5-49. Experimental results of sample 3 (8 mbar) superposed with the curves obtained from the finite differences numerical calculations.. 172
Figure 5-50. Experimental results of sample 4 (10 mbar) superposed with the curves obtained from the finite differences numerical calculations.. 172
Figure 5-51. All the experimental results presented in the same coordinate space. 173
Figure 5-52. All the experimental results presented in the same coordinate space. 174
Figure 5-53. All the experimental results presented in the same coordinate space. 174
Figure 5-54. The effect of atmospheric pressure and sample stress on thermal conductivity is directly proportional and appears to be rather significant. 175
Figure 5-55. Linear dependency of thermal conductivity from sample stress....................... 175
Figure 5-56. Parameters for the linear models as a function of atmospheric stress............... 176
Figure 5-57. Variations of the height of the sample through the testing program................. 177
Figure 5-58. Void ratio variations in the sample. 178
Figure 5-59. Void ratio variations in the sample. 178
Figure 5-60. Relative density variations in the sample... 179
Figure 5-61. Waves measured in the Sample 1 (4 mbar). The waves produced by the ‘P’ actuator are shown in violet, and the ones of the ‘S’ actuator are shown in grey. The input signal is displayed in blue. 180
Figure 5-62. Waves measured in the Sample 2 (6 mbar). The waves produced by the ‘P’ actuator are shown in violet, and the ones of the ‘S’ actuator are shown in grey. The input signal is displayed in blue. 181
Figure 5-63. Waves measured in the Sample 3 (8 mbar). The waves produced by the ‘P’ actuator are shown in violet, and the ones of the ‘S’ actuator are shown in grey. The input signal is displayed in blue. 181
Figure 5-64. Waves measured in the Sample 4 (10 mbar). The waves produced by the ‘P’ actuator are shown in violet, and the ones of the ‘S’ actuator are shown in grey. The input signal is displayed in blue... 182
Figure 5-65. Waves measured in the Sample 1 (4 mbar). The waves produced by the ‘P’ actuator are shown in violet, and the ones of the ‘S’ actuator are shown in grey. The input signal is displayed in blue. 182
Figure 5-66. Waves measured in the Sample 2 (6 mbar). The waves produced by the ‘P’ actuator are shown in violet, and the ones of the ‘S’ actuator are shown in grey. The input signal is displayed in blue. 183

Figure 5-67. Waves measured in the Sample 3 (8 mbar). The waves produced by the ‘P’ actuator are shown in violet, and the ones of the ‘S’ actuator are shown in grey. The input signal is displayed in blue. 183
Figure 5-68. Waves measured in the Sample 4 (10 mbar). The waves produced by the ‘P’ actuator are shown in violet, and the ones of the ‘S’ actuator are shown in grey. The input signal is displayed in blue........ 184
Figure 5-69. Zoom in of the waves measured in the sample 1 (4 mbar). The waves produced by the ‘P’ actuator are shown in violet, and the ones of the ‘S’ actuator are shown in grey. The input signal is displayed in blue........ 185
Figure 5-70. Frequency content of an acquired P-wave. The frequency content shows only P-waves are involved........ 187
Figure 5-71. Frequency content of an acquired P-wave. The frequency content shows both P and S-waves are involved. 187
Figure 5-72. The waves recorded included not only a) the waves recorded by the corresponding accelerometer but also b) the ones recorded in the accelerometer intended to record the other type of wave........ 188
Figure 5-73. Frequency content of an acquired S-wave on the p-plane. S-wave excluded.... 189
Figure 5-74. Frequency content of an acquired S-wave on the p-plane. P-wave excluded.... 189
Figure 5-75. Interpretation of arrival times for sample 1........ 190
Figure 5-76. The use of the chosen interpretation criterion for both waves........ 190
Figure 5-77. The use of the chosen interpretation criterion for both waves........ 191
Figure 5-78. The use of the chosen interpretation criterion for both waves........ 191
Figure 5-79. The use of the chosen interpretation criterion for both waves........ 192
Figure 5-80. The use of the chosen interpretation criterion for both waves........ 192
Figure 5-81. The use of the chosen interpretation criterion for both waves........ 193
Figure 6-1. Atmospheric pressure of Mars after Viking descent data. 197
Figure 6-2. Atmospheric temperature of Mars after Viking descent data. 197
Figure 6-3. Atmospheric density of Mars after Viking descent data........ 198
Figure 6-4. Atmospheric viscosity of Mars after Viking descent data. 198
Figure 6-5 Vertical stress below the ground surface due to a pressure wave........ 201
Figure 6-6 Layout of the Boussinesq solution for the stress increment induced by a strip load (Braja, 2011). 202
Figure 6-7. Values of intrinsic permeability for several materials (data from Berhane, 2006). 204
Figure 6-8. Mars InsSight data for atmospheric pressure for two years. (Image credit: NASA JPL, n.d.). 205
Figure 6-9. Kinematic Viscosity dependence on Temperature after Sutherland law. 205
Figure 6-10. Conditions for the Sorrells scenario, under the passage of a periodic wave...... 206
Figure 6-11 Increments of the total stress for the evaluated values of T. 208

Figure 6-12 The pressure penetrates up to around 60 meters into the soil under the considered conditions and the highest utilised permeability value. 208
Figure 6-13. The pressure penetrates up to around 8 meters into the soil under the considered conditions and an intermediate selected permeability value. 209
Figure 6-14. The pressure penetrates up to around 2 meters into the soil under the considered conditions and the lowest utilised permeability value. 209
Figure 6-15. Effect of the permeability on material pore pressure for the lowest period of 10 seconds. 210
Figure 6-16. Effect of the permeability on material pore pressure for the highest period of 200 seconds. 210
Figure 6-17. Effective stress profiles for the lowest period case presented for the evaluated intrinsic permeability, for the lowest period value of 10 seconds. 211
Figure 6-18. Effective stress profiles for the lowest period case presented for the evaluated intrinsic permeability, for the lowest period value of 10 seconds. 211
Figure 6-19. Vertical strain profiles for the lowest period case presented for the evaluated intrinsic permeability, for the lowest period value of 10 seconds. 212
Figure 6-20. Vertical strain profiles for the lowest period case presented for the evaluated intrinsic permeability, for the highest period value of 200 seconds. 212
Figure 6-21. Compliance cycles for the lowest and highest values of permeability evaluated. 213
Figure 6-22. Compliance cycles for the lowest and highest values of period evaluated. 213
Figure 6-23. Global summary of the terrestrial scenario for the compliance model. 214
Figure 6-24. Comparison of the results with Sorrells data. 214
Figure 6-25. Model parameters used for the preliminary evaluation of the Mars scenario. 215
Figure 6-26. Pore pressure in the material for different permeabilities with the simplified Mars scenario. 216
Figure 6-27. Compliance results for the Mars scenario. 216
Figure 6-28. Compliance results for the Mars scenario as a percentage of a total stress calculation. 217
Figure 6-29: Schematic description of the space discretisation for gas flow. 223
Figure A-1. Interface of the originally developed GUIDE tool for single wave data analysis. E
Figure A-2. Aspect of the second iteration of the result interpretation program. F
Figure A-3. Simultaneous visualization of the P and S waves using the result software. G
Figure A-4 Waves acquired during the 23/09 experimental program. Depart an arrival times are signaled both for P and S waves. G
Figure B-1. Reference system for finite differences. I

List Of Tables

Table 1-1. History of Missions to Mars outside the United States 6
Table 1-2. Planned missions to Mars for the current decade. 10
Table 1-3. History of NASA missions to Mars........ 12
Table 1-4. Past, active, and future Discovery missions summarized........ 16
Table 1-5. Past, active, and future Discovery missions summarized........ 17
Table 1-6. Main Planetary Regolith Simulants used. 24
Table 1-7. Sedimentary cycles of the Paris Basin during the Paleogene 25
Table 1-8. Results of weight composition by element........ 27
Table 1-9. Characteristics of Fontainebleau sand in different studies. 27
Table 3-1. Module values for each model layer. 62
Table 3-2. Experimental program carried out. 72
Table 4-1 Sample densities of the 4 samples tested. 105
Table 5-1. Model parameters used for the materials. 161
Table 5-2. Experimental program 165
Table 6-1. Parameters involved in the model. 203
Table 6-2. Material parameters adapted for the model. 206

CONTENTS

ACKNOWLEDGEMENTS C

MOTS CLÉS .... F

KEYWORDS .... F

RESUME .... G

ABSTRACT I

LISTS OF TABLES AND FIGURES .... J

- List Of Figures .... J
- List Of Tables .... T

CONTENTS .... U

INTRODUCTION 1

1. SOIL MECHANICS IN SPACE EXPLORATION 4
   - 1.1. The exploration of Mars 4
   - 1.2. The NASA exploration of Mars 11
   - 1.3. The NASA Discovery program 16
   - 1.4. The Mars InSight Lander 18
   - 1.5. Soil mechanics outside of earth 22
   - 1.6. Martian Regolith Simulants 23
   - 1.7. Fontainebleau sand 24
     - Geological origin 25
     - Material description 26
   - 1.8. Fontainebleau sand as a Martian regolith simulant 28
   - 1.9. Lessons learned from the Mars InSight mission 30
   - 1.10. References 32
2. SAMPLE PREPARATION AND HOMOGENEITY 37
   - 2.1. X-ray micro-tomography investigation of the effects of funnel pluvation on sample homogeneity (Article 1: Manuscript in process) 38
     - Abstract 38
     - Introduction 38

Sample preparation 39
X-Ray tomography 40
Preparation and processing of the data 41
Discussion 48
Conclusions 49
References 49
3. THE INTERACTION BETWEEN THE FOOT OF SEIS AND THE MARTIAN REGOLITH 52
3.1. The feet of the SEIS instrument 52
3.2. Experimental setup 54
3.3. The experimental procedure 58
3.4. Experimental program results, analysis, and interpretation 59
3.5. Finite element verification 59
3.6. Conclusions 62
3.7. The interaction between the SEIS seismometer of the InSight Martian mission and a regolith simulant (Article 2: Published) 63
Introduction 63
Materials and methods 66
Experimental results 72
Interpretations and discussion 75
Conclusions 79
Acknowledgements 80
Appendix 80
Notation 81
References 81
4. WAVE VELOCITY MEASUREMENTS ON THE REGOLITH SIMULANT 85
4.1. Characterization of soil behaviour at very low strains 85
4.2. Bender Elements and soils: an ongoing story 88
Interpretation of the Bender Element Test 90
Study with Bender Elements on different soil types 92

4.3. Work on bender elements (and wave velocity to determine stiffness or Poisson ratio) 93

4.4. Wave Velocities and Poisson Ratio in a Loose Sandy Martian regolith Simulant under Low Stresses. Part 1: Laboratory Investigation (Article 3: Published, JGR-Planets) 97

Key Points 97

Abstract 97

Plain Language Summary 98

Keywords 98

Introduction 98

Wave velocity and Poisson ratio in sands 100

Materials and Methods 101

Experimental results 105

Discussion 108

Conclusions 109

Acknowledgments 110

References 111

Open Research 114

Appendix A: Methodology for travel time determination 114

4.5. Wave velocities and Poisson Ratio in a loose sandy Martian regolith simulant under low stresses. Published, JGR-Planets) 120

Abstract 120

Plain Language Summary 120

Introduction 121

Theoretical background 121

Slippage between particles 123

Effect of particle's roughness on the elastic properties 124

AFM roughness assessment of the Fontainebleau sand as a Martian Regolith Simulant 129

Discussion 131

Conclusions 134

References 135

Acknowledgements 136
Open Research 137
5. THERMAL CONDUCTIVITY AND WAVE VELOCITY MEASUREMENTS 138
5.1. Basic concept for the experimental setup 138
5.2. Vacuum pump and CO_2 supplying 140
5.3. Experimental setup for wave velocity measurements 144
5.4. Experimental setup for thermal conductivity measurements 145
5.5. Stress control in the sample and height variation monitoring 150
5.6. Experimental protocol 152
Previous drying of the sample material 153
Preparation of the sample in the container 153
Thermal conductivity test 155
Wave velocity measurement procedure 157
5.7. Interpretation of the experimental results 159
Formulation of the finite differences for the heat conduction 160
5.8. Experimental program 165
5.9. Thermal conductivity measurements 166
5.10. Wave velocity measurements 180
5.11. Conclusion 193
5.12. References 195
6. ATMOSPHERIC PRESSURE AND GROUND COMPLIANCE 196
6.1. The atmosphere of Mars 196
6.2. Assessment of the compressibility of sand deposits by coupling seismic and meteorological measurements. (Article 5: Manuscript in process) 199
Introduction 199
Part A: Ground compliance model in effective stress 200
Part B: Analysis of compliance, effective and total stress. Case of Earth. 206
Part C: Application of the ground compliance model to Mars Insight landing site 215
Conclusions 217
References 218
Appendix A: Demonstration of the compliance model 220

LESSONS LEARNED FROM INSIGHT 227
GENERAL CONCLUSIONS 229
PERSPECTIVES 232
LIST OF PUBLICATIONS 234
REFERENCES 236
A. Appendix A: Wave velocity software .... A
  1.1. General concept and purpose of the tool .... A
  1.2. Versions of the tool .... A
    Version 1.0 .... A
    Version 2.0 .... B
    Version 3.0 .... B
  1.3. Software architecture of the tool .... B
  1.4. User interface of the tool .... B
  1.5. Utilization of the tool C
  1.6. The future of the tool .... D
B. Appendix B: Original expressions for the boundary condition I

INTRODUCTION

Tt he NASA InSight Lander reached the surface of Mars on November 26th, 2018. It is part of the Discovery program (launched in 1996) for planetary operation and aims to widen the existing knowledge concerning the formation and evolution history of the terrestrial planets (ScienceNASA, 2020). Shortly after its landing, the lander has succeeded in deploying the Seismic Experiment for Interior Structure (SEIS), the first ever seismometer to ever be deployed on direct contact with the surface of the red planet (Lognonné et al., 2019). The payload of the spacecraft includes SEIS (regarded as the main instrument), along other two instruments, namely the Heat Flow and Physical Properties Package (HP3) (Spohn et al., 2018), and finally the Rotation and Interior Structure Experiment (RISE) antenna (Folkner et al., 2018). The lander used a robotic arm to safely descend the SEIS and HP3 devices from its deck to the surface once a safe and adequate location was selected for them (Trebi-Ollennu et al., 2018).

The landing site is in the Elysium Planitia region (Banerdt et al., 2018). A landing ellipse was chosen after several proposals were considered to meet both the operational and scientific requirements (Morgan et al., 2018). This region is located near the equatorial zone and the dichotomy that separates in the Martian topography the flat north hemisphere and the mountainous south hemisphere. The geology of the landing site has been studied by Golombek et al., 2020.

SEIS is the first seismometer placed in direct contact with the Martian regolith. In 1976, the Viking 1 lander made use of a three-axis seismometer that was placed in the lander and the measurements were heavily affected by the wind (Mimoun et al., 2018). It was deemed necessary to protect SEIS from both the atmospheric noise and the considerable temperature changes that take place every sol (Martian day, around 90°C). Consequently, a thermal shield was designed and built to isolate the instrument from its environment. This shield is a white dome-shaped structure, mechanically isolated from SEIS (Lognonné et al., 2019).

The Very Broad Band sensors (VBB) of SEIS have been developed and made through a cooperation between the Centre National des Études Spatiales (CNES) and the Institut de Physique du Globe de Paris (IPGP). The German Max Planck Institute designed the LVL levelling system, the British Imperial College London provided the Short Period (SP) sensors, and JPL developed in the US the tether that provides energy and transmits data to the lander. As a result of this joint effort and after nearly 20 years of work, the SEIS instrument boasts very accurate levels of measurement; it is capable of detecting movements smaller than a hydrogen atom (SEIS - InSight, 2017).

As part of the Science Team analysing the data from the mission, the Near Surface Working Group (NSWG) is dedicated to investigating the properties and structure of the surface layer, providing data useful for the rest of the team to process SEIS signals or any other data from the mission, as well as serving for future work with Martian and other extra-terrestrial materials.

Since no Martian regolith is available on Earth, experimental work is carried out on Martian regolith simulants. Several simulants have been utilised by NASA and other institutions for testing some responses of the SEIS instrument. For instance, three different sands were considered when designing the supports for the LVL levelling system. A real-size testing bed has been installed at JPL to previously test some activities to be done on Mars. In this work, a new simulant was chosen for experimental activities carried out both in ENPC and in Universidad de los Andes.

This thesis report is structured in several chapters dealing with the different activities carried out to investigate the regolith properties at Mars InSight landing site.

The first chapter presents the general context surrounding the exploration of Mars, clarifying the main objectives of different Martian missions. After presenting the Mars InSight mission, the focus shifts to an overview of the study of extra-terrestrial soils, with particular emphasis on Mars and the use of regolith simulants. The chapter ends by presenting the selected sandy simulant, comparing it with other simulants of other works to justify its choice and assess its possibilities and limitations.

The second chapter concerns the key question of preparing homogeneous sand samples, evaluating its homogeneity with the help of X-ray microtomography.

After reviewing some of the key characteristics relevant to the soil mechanics activities of the InSight mission, the third chapter contains a published paper (Géotechnique) devoted to the measurement of the stiffness governing the interaction between the SEIS foot and the soil. To do so, a significantly improved version of the experimental setup used at the ENPC when designing the SEIS foot (Karakostas et al. 2013) is used.

Chapter four presents experimental investigation of the dynamic low stiffness - low strain response of the regolith, based on the use of an original setup utilising bender elements in low stress conditions to determine wave velocities, with particular attention devoted to accurately calculate the stress applied in the axis to of a horizontal triaxial sample submitted to various levels of vacuum. The obtained data are analysed through a theoretical approach based on the micro-scale analysis of the inter-grain contacts. This work has been presented in two companions papers submitted to the Journal of Geophysical Research: planets (already accepted for publication).

Chapter five presents the concept, setup and results obtained in a new device built at the laboratory of Universidad de los Andes for the simultaneous investigation of wave velocities and thermal conductivity on a sand simulant under Mars atmospheric conditions. This work is related with the surface thermal conduction measurements carried out by using the HP^3 device

(Grott et al., 2023). The idea evolved as challenges were met and solved, and this section presents this process as well as the results obtained once the setup was fully operational.

The sixth and final chapter deals with numerical modelling activities done to link atmospheric pressure variations to surface displacements, a work concerning Mars and other rocky planets including the Earth. Calculations, based on the Finite Differences method, provide an estimation of the ground compliance under changes in atmospheric pressure due to wind and dust devils. Compared to common calculations that are carried out in total stress conditions, these calculations, carried out in effective stress, account for the effects of gas penetration within the regolith.

Finally, some general conclusions are presented and some potential prospects for future work are stated.

1. SOIL MECHANICS IN SPACE EXPLORATION

"To boldly go, where no one has gone before".
Star trek Intro, 1966

This chapter serves the purpose of explaining the relevance of applying soil mechanics knowledge to the questions encountered during space exploration, in particular for the case of the planet Mars. To begin, the basic information and history of Mars exploration context is presented; the purpose and relevance of this exploration is emphasized. The initiatives of the different countries having attempted and or succeeded at undertaking Mars exploration missions are mentioned, in hope of clarifying the gargantuan complexity and considerable difficulty of such endeavours. Given the emphasis on the InSight mission for the scope of this work, the NASA Mars exploration history, and the Discovery Program for the exploration of the solar system are given the main focus. The concepts for future missions are also mentioned. Then, the main relevant information about the InSight mission is summarized, including the instrument payload, the scientific goals and the characteristics of the landing area. The context is then connected to the use of soil mechanics activities to help in the study of the surface material at the landing site, departing from presenting the potential contributions and emphasizing the use of regolith simulants for experimental activities to obtain or estimate key parameters. The chapter finishes presenting the choice of regolith simulant for this work.

Figure 1-1. Mars as seen by the Hubble telescope. (Image credit: https://www.jpl.nasa.gov/spaceimages/details.php?id=PIA01249)

1.1. The exploration of Mars

After the Moon, Mars is the most accessible planet for humankind in the solar system. While the interest in studying the red planet dates to ancient times, it is only since the early 1960s that missions have been sent to Mars by different space agencies around the world. Since then, the exploration of the system formed by Mars and its two satellites Deimos and Phobos has acquired key relevance to several Space Agencies around the globe. In addition to its relative proximity, the remarkable similarities of the history of Mars with that of the Earth have contributed to the increase of this interest (since both are rocky planets, like Mercury and Venus). This means that a better comprehension of the history of the red planet may provide valuable insights into the understanding of the interior structure and the key questions still surrounding the formation history of the Earth.

The extensive US NASA Mars Exploration Program will be detailed separately in the next section, but the most relevant missions of spatial agencies from other countries span over several decades and are summarised in Table 1-1. During the XXth century, the main participants were the Soviet Union (and after 1991 the Russian Federation) and the United States, with only Japan sending an orbiter with the failed Nozomi mission in the late 1990s.

The XXIst century has seen further efforts from NASA, while several other countries and their space agencies launch towards Mars. The first new participant was the European Space Agency (ESA), with Mars Express sending an orbiter and the Beagle 2 lander. While Russia did not launch for Mars during the first decade of the century, while the failed Fobos-Grunt 2011 mission included what was to be the first Chinese probe. India and the United Arab Emirates also sent their first missions to the red planet in the late 2010s and early 2020s, while China obtained its first success in 2022 with Tianwen-1.

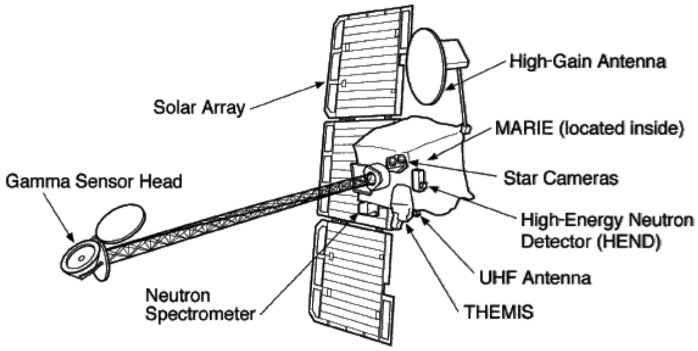

Figure 1-2. Mars Odyssey (2001) and its instruments. (Image credit: https://www.researchgate.net/profile/William-Boynton/publication/226827726/figure/fig2/AS:302384489222149@1449105488554/2001-Mars-Odyssey-Spacecraft-in-Mapping-Configuration-The-Odyssey-spacecraft-as.png)

The vehicles sent are varied in type and instrument payload. They range from orbiters which do not land but provide valuable information on a planetary scale, such as Mars Odyssey seen in Figure 1-2; they can also act as information transmitting relays. They allowed great advances in the exploration of Mars such as mapping and landing site selection for other missions. Other vehicles do land and may be split on two different categories: stationary landers such as Phoenix, seen in Figure 1-3, and moving rovers, such as Perseverance (see Figure 1-4). Some missions use a combination of landing vehicles and permanent orbiters.

Figure 1-3. Artist representation of the Phoenix lander.
(https://www.nasa.gov/multimedia/imagegallery/image_feature_857.html)

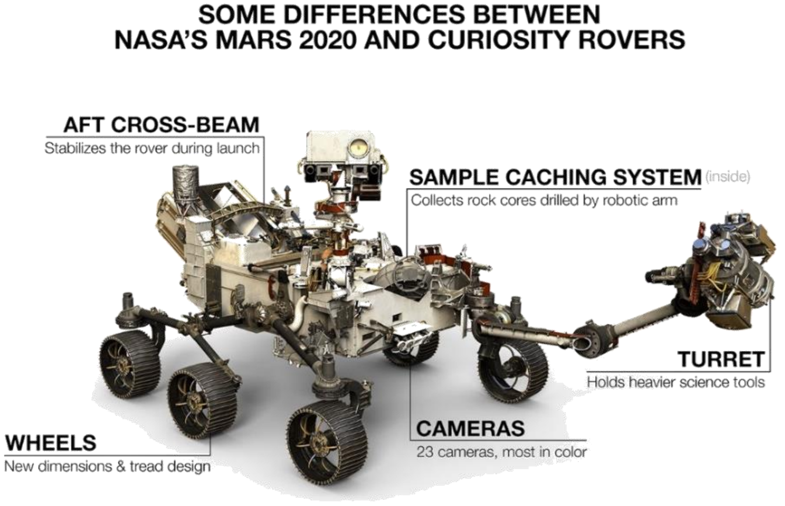

Figure 1-4. The Mars 2020 perseverance Rover (https://mars.nasa.gov/resources/24716/some-differences-between-mars-2020-and-curiosity/).

Table 1-1. History of Missions to Mars outside the United States

Period	Mission and Country	Type	Purpose	Status
1960-1960	URSS-Marsnik 1 (Mars 1960A)	Flyby	First flyby of Mars, study space in travel to Mars, return images.	Lost before achieving Earth orbit.
1960-1960	URSS-Marsnik 2 (Mars 1960B)	Flyby	First flyby of Mars, study space in travel to Mars, return images.	Lost before achieving Earth orbit.

Period	Mission and Country	Type	Purpose	Status
1962-1962	URSS-Mars 1	Orbiter	Designed to image the surface and send back data on cosmic radiation, micrometeoroid impacts and Mars' magnetic field, radiation environment, atmospheric structure, and possible organic compounds.	Failure
1971-1972	URSS-Mars 2	Orbiter + Lander	The orbiter's primary scientific objectives were to provide images of the Martian surface and clouds, to determine the temperature on Mars, to study the topography, composition and physical properties of the surface, to measure properties of the atmosphere, to monitor the solar wind and the interplanetary and Martian magnetic fields, and to act as a communications relay for the lander. The lander was equipped with two television cameras with a 360° view of the surface, a mass spectrometer to study atmospheric composition, temperature, pressure, and wind sensors and devices to measure mechanical and chemical properties of the surface, including a mechanical scoop to search for organic materials and signs of life.	Partial success
1972-1972	URSS-Mars 3	Orbiter + Lander	The primary scientific objective of the Mars 3 descent module was to perform a soft landing on Mars, return images from the surface, and return data on meteorological conditions, atmospheric composition, and mechanical and chemical properties of the soil.	Partial success
1973-1974	URSS-Mars 4	Orbiter	Mars 4 was equipped with a television imaging system consisting of two cameras. The spacecraft was also equipped with a Lyman-Alpha photometer to search for hydrogen in the upper atmosphere, a magnetometer, plasma ion traps and a narrow angle electrostatic plasma sensor to study the solar wind, an infrared radiometer (8-40 microns) to measure surface temperature, a radio telescope polarimeter (3.5 cm) to probe the subsurface dielectric constant, two polarimeters (0.32-0.70 microns) to characterize surface texture, and a spectrometer (0.3 - 0.8 microns) to study emissions in the upper atmosphere.	Failure
1973-1974	URSS-Mars 5	Orbiter	The Mars 5 automatic station was designed to orbit Mars and return information on the composition, structure, and properties of the Martian atmosphere and surface.	Partial success

Period	Mission and Country	Type	Purpose	Status
1973-1974	URSS-Mars 6	Lander	There were four photometers on board: one for 2 carbon dioxide bands to obtain altitude profiles, one at 0.35 - 0.7 microns for albedo and colour studies, one in the water vapor band (1.38 microns) to study water in the atmosphere, and a UV photometer (0.26 and 0.28 microns) to measure ozone. The probe was equipped with a radio-occultation experiment to profile atmospheric density and a dual-frequency radio occultation experiment to profile ionospheric density. The spacecraft also carried French experiments, one called Zhemo to study the distribution and intensity of fluxes of solar protons and electrons and one known as Stereo-2 to study solar radio emissions.	Partial success
1973-1974	URSS-Mars 7	Lander	The flyby module contained a telephotometer to image Mars, a Lyman alpha sensor to search for hydrogen in the upper atmosphere, a magnetometer, an ion trap and narrow angle electrostatic plasma sensor to study the solar wind and its interaction with Mars, solar cosmic ray sensors, micrometeorite sensors, and a French-supplied solar radiometer to measure solar long-wavelength radio emissions. It was also equipped to perform a radio occultation experiment to profile the atmosphere and ionosphere. The lander carried a panoramic telephotometer to image the Martian surface around the lander, atmospheric temperature, pressure, density, and wind sensors, an accelerometer to measure atmospheric density during the descent, a mass spectrometer to estimate atmospheric composition, a radio altimeter, an activation analysis experiment to study soil composition, and mechanical properties soil sensors.	Partial success
1988-1988	URSS-Phobos 1	Orbiter	The objectives of the Phobos missions were to: (1) conduct studies of the interplanetary environment; (2) perform observations of the Sun; (3) characterize the plasma environment in the Martian vicinity; (4) conduct surface and atmospheric studies of Mars; and, (5) study the surface composition of the Martian satellite Phobos.	Partial success
1988-1989	URSS-Phobos 2	Orbiter + 2 Landers	The objectives of the Phobos missions were to: (1) conduct studies of the interplanetary environment; (2) perform observations of the Sun; (3) characterize the plasma environment in the Martian vicinity; (4) conduct surface and atmospheric studies of Mars; and, (5) study the surface composition of the Martian satellite Phobos.	Partial success
1996-1996	Russian Federation-Mars 96		The Russian Mars 96 mission was designed to send an orbiter, two small autonomous stations, and two surface penetrators to Mars to investigate the evolution and contemporary physics of the planet by studying the physical and chemical processes which	Failure

Period	Mission and Country	Type	Purpose	Status
			took place in the past and which currently take place.	
1998-2003	Japan-Nozomi	Orbiter	was planned as a Mars orbiting aeronomy mission designed to study the Martian upper atmosphere and its interaction with the solar wind and to develop technologies for use in future planetary missions. Specifically, instruments on the spacecraft were to measure the structure, composition and dynamics of the ionosphere, aeronomy effects of the solar wind, the escape of atmospheric constituents, the intrinsic magnetic field, the penetration of the solar-wind magnetic field, the structure of the magnetosphere, and dust in the upper atmosphere and in orbit around Mars.	Failure
2011-2011	Russian Federation-Fobos - Grunt	Lander	Landing on Phobos	Failure
2011-2011	China-Yinghuo-1	Orbiter	The primary scientific objectives of the mission are to study Martian space environmental structure, plasma distribution and other characteristics; the solar wind-atmosphere coupling and energy deposition processes, Martian ion escape processes and mechanisms, the regional gravity field of Mars, and to perform Martian and Phobos surface imaging.	Failure
2003-Active	EU-Mars Express	Orbiter + Lander	The scientific objectives of the Mars Express Orbiter are to obtain global high-resolution photo-geology (10 m resolution), mineralogical mapping (100 m resolution) and mapping of the atmospheric composition, study the subsurface structure, the global atmospheric circulation, and the interaction between the atmosphere and the subsurface, and the atmosphere and the interplanetary medium. The Beagle 2 lander objectives were to characterize the landing site geology, mineralogy, and geochemistry, the physical properties of the atmosphere and surface layers, collect data on Martian meteorology and climatology, and search for possible signatures of life.	Active
2013-2022	India-Mangalyaan	Orbiter	The science payload has a total mass of 15 kg and comprises five instruments. The Mars Color Camera, the Lyman Alpha Photometer, the Thermal Imaging Spectrometer, the Mars Exospheric Neutral Composition Analyzer, and the Methane Sensor for Mars.	Success
2016-Active	EU-ExoMars 2016. TraceGasOrbiter.	Orbiter + Lander	The Trace Gas Orbiter contains a 112 kg science payload to characterize and study the behaviour of trace gases on Mars. The three primary objectives of	Active

Period	Mission and Country	Type	Purpose	Status
			the orbiter are to conduct investigations into the biological or geological origin of trace gases on Mars with a scientific payload of 4 instruments; deliver Schiaparelli and support part of the data transmission during its descent and surface operations; and serve as a data relay to support communications for the ExoMars 2018 rover and the surface science platform. Its trace gas investigations will include monitoring seasonal changes in atmospheric composition and temperature and mapping subsurface hydrogen.	
2020-Active	United Arab Emirates-HOPE	Orbiter	It carries three scientific instruments mounted on one side of the spacecraft. The Emirates eXploration Imager (EXI) is a high resolution multiband (visible and UV) camera, the Emirates Mars Ultraviolet Spectrometer (EMUS), a far-UV imaging spectrograph, and the Emirates Mars InfraRed Spectrometer (EMIRS), and FTIR scanning spectrometer.	Active
2020-Active	China-Tianwen 1	Orbiter, lander and rover	The scientific objectives of the mission are to study Martian topography and geology, characterize the soil and its water-ice content, determine the composition of the surface material, profile the Martian ionosphere, climate, and environment, and constrain the gravity and magnetic fields and the interior structure.	Active

The future looks promising for the exploration of Mars with Spatial Agencies from several new countries getting involved and being capable of cooperating with each other and building upon the lessons learned through the successes and failures of every mission that has already taken place. The most promising projected missions for the immediate future are summarized in Table 1-2. It can be noticed that the focus is for the return of samples to the Earth, which should be attained by the early 2030s.

Long term proposals also aim towards human crewed missions on Mars, and cooperation with the private sector such as the envisioned for the operation model of the NASA Artemis program adds further support towards this ambitious goal.

Table 1-2. Planned missions to Mars for the current decade.

Launch planned	Mission and Country	Type	Purpose	Planned duration
2024	Japan-MMX	Orbiter + Lander	Determine origin of Phobos. Sample return mission to the satellite.	Planned, 5 years
2024	India-Mangalyaan 2	Orbiter	The mission will include a hyperspectral camera, a high-resolution panchromatic camera and a radar to understand early Martian crust, recent basalts and boulder falls.	Planned, 1 year

Launch planned	Mission and Country	Type	Purpose	Planned duration
2025	Tianwen 2 China	Orbiter + Lander	Asteroid sample return with a flyby of Mars	Planned, 10 years
2028	Tianwen 3 China	Orbiter + Lander + rover	Sample return mission, consisting of the vehicles necessary to prepare and return the sample to Earth.	Planned, 3 years
2023	ESCAPADE COUNTRY	2 orbiters	The Escape and Plasma Acceleration and Dynamics Explorers (EscaPADE) are a dual-spacecraft mission to study ion and sputtered escape from Mars. The two identical spacecraft were scheduled for launch as secondary satellites on the Psyche mission in August 2022, but were removed due to problems with the required trajectory.	Planned, 1.5 years
2028	Rosalind Franklin Rover US	Rover	It will collect samples with a drill down to a depth of 2 m and analyse them with next-generation instruments in an onboard laboratory. Underground samples are more likely to include biomarkers, since the tenuous Martian atmosphere offers little protection from radiation and photochemistry at the surface. The primary objective is to land the rover at a site with high potential for finding well-preserved organic material, particularly from the very early history of the planet.	Planned 1 year

1.2. The NASA exploration of Mars

The general idea of the Mars Exploration Program is presented in its mission statement:

“The goal of the Mars Exploration Program is to explore Mars and to provide a continuous flow of scientific information and discovery through a carefully selected series of robotic orbiters, landers and mobile laboratories interconnected by a high-bandwidth Mars/Earth communications network”. (NASA, n.d.)

Figure 1-5. The NASA Opportunity rover mission lasted between 2014 and 2018 and was among the most successful missions on the red planet. (Credit: https://mars.nasa.gov/msl/multimedia/raw-

images/?order=sol+desc%2Cinstrument_sort+asc%2Csample_type_sort+asc%2C+date_taken+desc&per_page=50&page=0&mission=msl).

To guide the key aspects of the exploration program, NASA has established four main scientific goals for its Mars exploration program (*NASA, n.d.*). These are:

- Life: To determine if there ever was life on Mars.
- Climate: To properly understand the Processes and History of Climate on Mars.
- Geology: To study the planet seeking to understand its origin and evolution through time as a geological system.
- Humans: To prepare for the future human exploration of Mars.

NASA missions to Mars have been quite successful including the landing of numerous and increasingly complex rovers such as the Curiosity – Opportunity duo (see Figure 1-5), which considerably outlasted their expected mission lengths and made key findings such as clay materials supporting the ideas about the history of water in the planet. One of the most recent achievements was the successful completion of the first controlled flight outside of Earth, achieved by the small helicopter deployed by Mars 2020, called Ingenuity (see Figure 1-6); as of September 2023, this helicopter has completed 60 flights (flights last about 120 – 180 seconds).

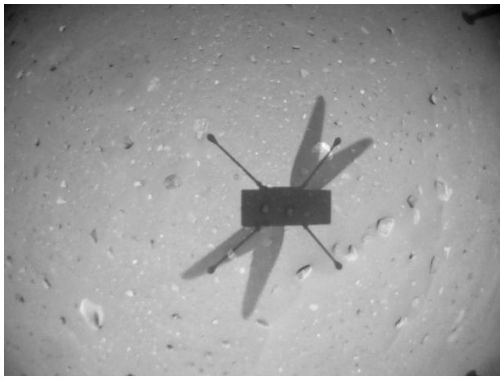

Figure 1-6. Shadow of Mars helicopter Ingenuity during its 60th flight, Sol 924. (Image credit: NASA/JPL-Caltech).

The history of the NASA missions launched to Mars is summarized on Table 1-3.

Table 1-3. History of NASA missions to Mars

Launch date	Mission name	Type	Purpose	Status
August 4, 2007, UTC	Mars Phoenix	Stationary Lander	to study the history of water in the Martian arctic, search for evidence of a habitable zone and assess the biological potential of the ice-soil boundary.	Success

Launch date	Mission name	Type	Purpose	Status
June 10, 2003, UTC	Mars Exploration Rovers - Spirit	Rover	Spirit landed in a region called Gusev Crater, to explore the crater because they thought it could have held water long ago. From pictures taken by satellites, it looked like several large rivers flowed into Gusev Crater.	Success
July 8, 2003, UTC	Mars Exploration Rovers - Opportunity	Rover	Opportunity was the second of the two rovers launched in 2003 to land on Mars and begin traversing the Red Planet in search of signs of ancient water	Success
January 3, 1999, UTC	Mars Polar Lander/Deep Space 2	Lander	Mars Polar Lander was an ambitious mission to set a spacecraft down on the frigid terrain near the edge of Mars' south polar cap and dig for water ice with a robotic arm.	Failure
December 11, 1998, UTC	Mars Climate Orbiter	Orbiter	Mars Climate Orbiter was designed to function as an interplanetary weather satellite and a communications relay for Mars Polar Lander. The orbiter carried two science instruments: a copy of an atmospheric sounder on the Mars Observer spacecraft lost in 1993, and a new, lightweight colour imager combining wide- and medium-angle cameras.	Failure
November 7, 1996, UTC	Mars Global Surveyor	Orbiter	The mission has studied the entire Martian surface, atmosphere, and interior. One of the most exciting observations of the spacecraft's wide-angle camera system, known as the Mars Orbital Camera, is that the red planet has very repeatable weather patterns. Each day the camera operates, it collects images that are used to build up a daily global map. These maps provide a record of changing meteorological conditions on Mars. Weather patterns observed by the spacecraft include some dust storms that repeat in the same location within a week or two of the time they occurred in the previous year. In addition, local disturbances and dust devils may start up at any time after the first day of spring and continue until Martian autumn	Success
December 4, 1996, UTC	Mars Pathfinder	Lander	It was designed as a technology demonstration of a new way to deliver an instrumented lander and the first-ever robotic rover to the surface of the red planet. Pathfinder not only accomplished this goal but also returned an unprecedented amount of data and outlived its primary design life.	Success
September 25, 1992, UTC	Mars Observer	Orbiter	The payload of science instruments was designed to study the geology, geophysics and climate of Mars.	Failure

Launch date	Mission name	Type	Purpose	Status
August 20, 1975, UTC	Viking 1 Orbiter & Lander	Lander	NASA's Viking Project found a place in history when it became the first U.S. mission to land a spacecraft safely on the surface of Mars and return images of the surface. Two identical spacecraft, each consisting of a lander and an orbiter, were built. Each orbiter-lander pair flew together and entered Mars orbit; the landers then separated and descended to the planet's surface.	Success
September 9, 1975, UTC	Viking 2 Orbiter & Lander	Lander	Besides taking photographs and collecting other science data on the Martian surface, the two landers conducted three biology experiments designed to look for possible signs of life. These experiments discovered unexpected and enigmatic chemical activity in the Martian soil but provided no clear evidence for the presence of living microorganisms in soil near the landing sites. According to scientists, Mars is self-sterilizing. They believe the combination of solar ultraviolet radiation that saturates the surface, the extreme dryness of the soil and the oxidizing nature of the soil chemistry prevent the formation of living organisms in the Martian soil.	Success
May 8, 1971	Mariner 8	Orbiter	Both were designed to be the first Mars orbiters, marking a transition in our exploration of the red planet from flying by the planet to spending time in orbit around it.	Failure
May 30, 1971, UTC	Mariner 9	Orbiter	Both were designed to be the first Mars orbiters, marking a transition in our exploration of the red planet from flying by the planet to spending time in orbit around it.	Success
February 24, 1969, UTC	Mariner 6	Flyby	Mariner 6 and 7 were the second pair of Mars missions in NASA's Mariner series of solar system exploration in the 1960s and early 1970s.	Success
March 27, 1969, UTC	Mariner 7	Flyby	As with the other Mariners, each launched on an Atlas rocket with either an Agena or Centaur upper-stage booster and weighed less than half a ton (without onboard rocket propellant).	Success
November 5, 1964, UTC	Mariner 3	Flyby	Between 1962 and 1973, NASA's Jet Propulsion Laboratory designed and built 10 spacecraft named Mariner to explore the inner solar system -- visiting the planets Venus, Mars and Mercury for the first time, and returning to Venus and Mars for additional close observations. The Mariners were all relatively small robotic explorers, each launched on an Atlas rocket with either an Agena or Centaur upper-stage booster, and weighing less than half a ton (without onboard rocket propellant).	Failure

Launch date	Mission name	Type	Purpose	Status
November 28, 1964, UTC	Mariner 4	Flyby	Mariner 3 and 4 were identical spacecraft designed to carry out the first flybys of Mars. Mariner 3 was launched on November 5, 1964, but the shroud encasing the spacecraft atop its rocket failed to open properly, and Mariner 3 did not get to Mars. Three weeks later, on November 28, 1964, Mariner 4 was launched successfully on an eight-month voyage to the red planet.	Success
April 7, 2001, UTC	2001 Mars Odyssey	Orbiter	Its mission includes making the first global map of the amount and distribution of many chemical elements and minerals that make up the Martian surface. Measurements by Odyssey have enabled scientists to create maps of minerals and chemical elements and identify regions with buried water ice. Images that measure the surface temperature have provided spectacular views of Martian topography. Early in the mission, Odyssey determined that radiation in low-Mars orbit -- an essential piece of information for eventual human exploration because of its potential health effects -- is twice that in low-Earth orbit.	Active
June 2, 2003, UTC	Mars Express (ESA)	Orbiter	The mission's main objective is to search for sub-surface water from orbit. Seven scientific instruments on the orbiting spacecraft have conducted rigorous investigations to help answer fundamental questions about the geology, atmosphere, surface environment, history of water, and potential for life on Mars.	Active
November 26, 2011, UTC	Mars Science Laboratory	Rover	Curiosity set out to answer the question: Did Mars ever have the right environmental conditions to support small life forms called microbes? Early in its mission, Curiosity's scientific tools found chemical and mineral evidence of past habitable environments on Mars. It continues to explore the rock record from a time when Mars could have been home to microbial life.Curiosity explores Gale Crater and acquires rock, soil, and air samples for onboard analysis. The car-size rover is about as tall as a basketball player and uses a 7-foot-long arm to place tools close to rocks selected for study. Curiosity's large size allows it to carry an advanced kit of 10 science instruments. It has tools including 17 cameras, a laser to vaporize and study small pinpoint spots of rocks at a distance, and a drill to collect powdered rock samples. It hunts for special rocks that formed in water and/or have signs of organics.	Active

Launch date	Mission name	Type	Purpose	Status
August 12, 2005, UTC	Mars Reconnaissance Orbiter	Orbiter	Carries the most powerful camera ever flown on a planetary exploration mission for homing in on details of Martian terrain with extraordinary clarity. While previous cameras on other Mars orbiters were able to identify objects no smaller than a dinner table, this camera is able to spot something as small as a dinner plate. This capability provides not only an astoundingly detailed view of the geology and structure of Mars but helps identify obstacles that could jeopardize the safety of future landers and rovers.	Active
November 18, 2013	Mars Atmospheric and Volatile EvolutioN	Orbiter	MAVEN is obtaining critical measurements of the Martian atmosphere to help understand dramatic climate change on the red planet over its history.	Active
March 14, 2016	ExoMars 2016 Mission	Orbiter/Lander Pair	The European Space Agency's (ESA) ExoMars program (Exobiology on Mars) is a series of missions designed to understand if life ever existed on Mars. ESA's Trace Gas Orbiter studies the Martian atmosphere for the presence of methane and other gases that may be present in small concentrations.	Active
May 5, 2018	Interior Exploration using Seismic Investigations, Geodesy and Heat Transport	Lander	By using sophisticated geophysical instruments, InSight will delve deep beneath the surface of Mars, detecting the fingerprints of the processes of terrestrial planet formation, as well as measuring the planet's "vital signs": Its "pulse" (seismology), "temperature" (heat flow probe), and "reflexes" (precision tracking).	Active
July 30, 2020	Mars 2020 Perseverance Rover Helicopter	Rover	Seek signs of ancient life (Jezero Crater) and collect samples of rock and regolith (broken rock and soil) for possible return to Earth. Also carries Mars Ingenuity helicopter.	Active

1.3. The NASA Discovery program

Following the success of the Apollo program on the Moon and other scientific endeavours throughout the 20th century, NASA launched the Discovery program in 1992, radically reforming space exploration. The program seeks to explore the solar system at what could be considered a “low-cost” scale for spatial exploration, to explore planets, their moons and smaller bodies such as comets and asteroids.

The main missions of the NASA Discovery program are summarized in Table 1-5.

Table 1-4. Past, active, and future Discovery missions summarized.

Table 1-5. Past, active, and future Discovery missions summarized.

Launch date:	Short Name	Mission name	Objective	Goal	Status
February 17, 1996	NEAR	Near-Earth Asteroid Rendezvous	433 EROS	first spacecraft to orbit and land on an asteroid, 433 EROS	Success
December 4, 1996	Pathfinder	Mars Pathfinder	Mars	lander + rover, paving the way for future NASA Mars rovers	Success
January 6, 1998		Lunar Prospector	Moon	low polar orbit investigation of the Moon, including mapping of surface composition and possible polar ice deposits, measurements of magnetic and gravity fields, and study of lunar outgassing events	Success
February 7, 1999	Stardust	Stardust	comet Wild-2	first spacecraft to make a close encounter with comet Wild-2 and return samples to Earth.	Success
August 8, 2001	Genesis	Genesis orbiter spacecraft		collecting solar wind samples and return them to Earth for study.	Success
July 3, 2002	CONTOUR	Comet Nucleus TOUR		Intended to visit and study two comets	Failure
August 3, 2004	MESSENGER	Mercury Surface, Space Environment, Geochemistry and Ranging	Mercury	orbited Mercury for more than four years, but not before doing two flybys of Venus and three flybys of Mercury as well	Success
January 12, 2005		Deep Impact	Comet Tempel	to send an “impactor” probe which would collide with Comet Tempel 1 on July 3, 2005	Success
September 27, 2007		Dawn		Ceres and Vesta--the two largest objects in the main asteroid belt between Mars and Jupiter	Success
March 7, 2009		Kepler	star field in the Cygnus-Lyra region	To explore the structure and diversity of planetary systems	Success
September 10, 2011	GRAIL	Gravity Recovery and Interior Laboratory,	Moon	To map lunar gravity and use that information to increase understanding of the Moon's interior and thermal history	Success
Active					
June 18, 2009	LRO	Lunar Reconnaissance Orbiter	Moon	set out to map the lunar surface	Success

Launch date:	Short Name	Mission name	Objective	Goal	Status
May 5, 2018	InSight	Interior Exploration using Seismic Investigations, Geodesy and Heat Transport	Mars	first outer space robotic explorer to study in-depth the "inner space" of Mars: its crust, mantle and core.	Success
October, 2021	Lucy	Lucy	A unique family of asteroids that orbit the Sun in front of and behind Jupiter	These asteroids are very different from one another. Understanding the causes of the differences will provide unique and critical knowledge on planetary origins, the source of volatiles and organics on the terrestrial planets, and the evolution of the planetary system.	
Future					
August, 2022		Psyche	a giant metal-rich asteroid, known as 16 Psyche	Unlike most other asteroids that are rocky or icy bodies, it appears to be the exposed nickel-iron core of a protoplanet.	
September, 2024	MEGAN E		Phobos	ability to "see" the elemental composition of the Martian moon Phobos by measuring gamma rays and neutrons.	
2028-2030	DAVINCI +	Deep Atmosphere Venus Investigation of Noble gases, Chemistry, and Imaging	Venus	To measure the composition of Venus' atmosphere to understand how it formed and evolved, as well as determine whether the planet ever had an ocean	
2028-2030	VERITAS	Venus Emissivity, Radio Science, InSAR, Topography, and Spectroscopy	Venus	To determine the planet's geologic history and understand why it developed so differently than Earth	

1.4. The Mars InSight Lander

The NASA InSight Lander (see Figure 1-7) reached the surface of Mars on November 26th, 2018. It is part of the Discovery program (launched in 1996) for planetary operation and aims to widen the existing knowledge about the formation and evolution history of the rocky planets (NASA Science, 2017). Shortly after landing (November 2018), the lander succeeded in deploying the Seismic Experiment for Interior Structure (SEIS), the first seismometer ever deployed in direct contact with the surface of the red planet (Lognonné et al., 2019). The payload of the spacecraft includes SEIS (the main instrument) along with other two instruments, namely the Heat Flow and Physical Properties Package (HP^3) (Spohn et al., 2018) and the Rotation and Interior Structure Experiment (RISE) antenna (Folkner et al., 2018).

The lander used a robotic arm to safely move the SEIS and HP3 devices from its deck to the surface once a safe and adequate location has been selected (Trebi-Ollennu et al., 2018).

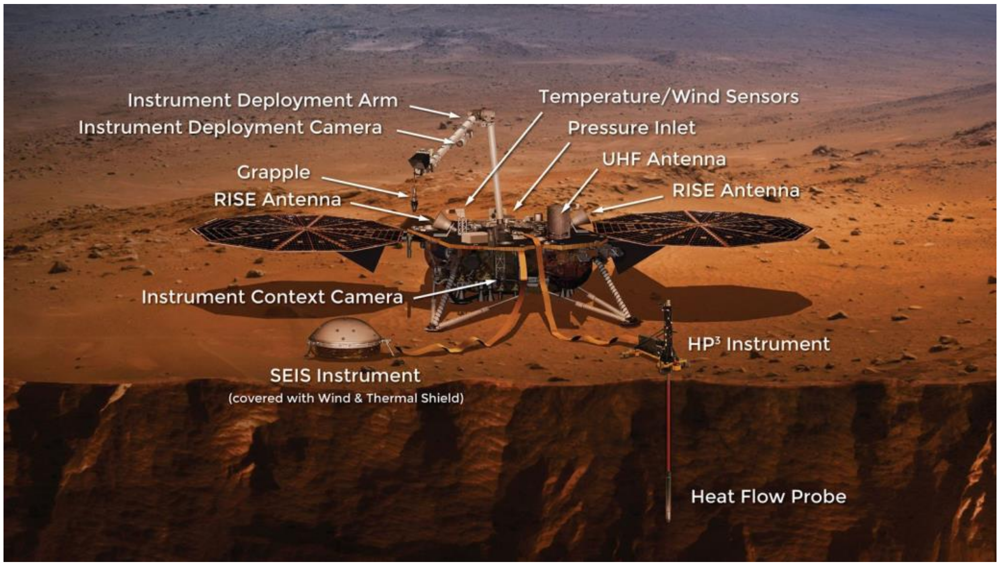

Figure 1-7. Artist concept of the Mars InSight Lander with its main instruments (https://mars.nasa.gov/insight/spacecraft/instruments/summary/).

The landing site is in the Elysium Planitia region (Golombek et al. 2018, Banerdt et al., 2018). This location has been selected after several proposals having to meet both the operational and scientific requirements (Morgan et al., 2018). This region is located near the equatorial zone (see Figure 1-8) and near the discontinuity that characterises the dichotomy in the Martian topography, between the flat lower north hemisphere and the mountainous higher south hemisphere. The geology of the landing site has been studied by Golombek et al. (2020).

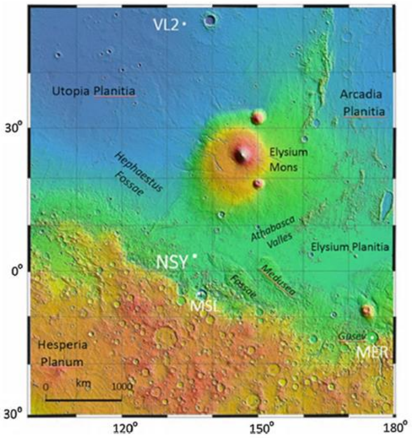

Figure 1-8. Coordinates of Elysium Planitia, location of the landing site of Mars InSight (SEIS: Insight’s Seismic Experiment for Internal Structure of Mars (2019)).

Although SEIS is not the first seismometer placed on Mars, it is the first one placed in direct contact with the surface regolith. In 1976, the Viking 1 lander made use of a three-axis seismometer to study the seismic activity of the planet; but the instrument was mounted on the top of the landing vehicle, and the measurements were heavily affected by the wind (Mimoun et al., 2017).

Figure 1-9. Instrument payload on the landing deck. From left to right, the HP^3 probe, the thermal shield of SEIS and the SEIS instrument (red)

These lessons were taken into consideration during the design of SEIS. It was deemed necessary to protect the instrument from both the atmospheric noise the considerable temperature changes between day and night (around 90°C). Consequently, a thermal shield was designed and built to insulate the instrument from its environment. This shield (Figure 1-9) is a white dome-shaped structure, mechanically isolated from the instrument (Lognonné et al., 2019).

SEIS is the result of several decades worth of work and international cooperation. In France, the Centre National des Études Spatiales (CNES) and the Institute de Physique du Globe de Paris (IPGP) lead the development of the Very Broad Band sensors (VBB). The German Max Planck Institute contributed with the LVL levelling system, the British Imperial College London with the Short Period sensors, and the JPL developed in the US the scientific tether that provides energy and transmits data to the lander (CNES, 2018). The SEIS instrument boasts very accurate levels of measurement; it is capable of detecting movements smaller than a hydrogen atom (SEIS - InSight, 2017).

The results of the mission have been multiple and include detailed observations based on the sources of the seismicity on Mars (Giardini et al. 2020), the geologic history of the area (Golombek et al. 2020) and the interior structure of the planet based on seismic data (Lognonné et al., 2020), even from the earliest stages (Banerdt et al. 2020). The accurate size of the core was also determined (Witze et al. 2021). Models have been obtained for the surface structure properties (Kenda et al. 2020), based on the utilisation of single station methods (Panning et al. 2015).

The lander has two cameras: the Instrument Deployment Camera (IDC) fixed on the robotic arm to help in deployment of the instrument, and the Instrument Context Camera placed on the lander, with a fish lens to monitor a wide area close to the lander. Views of the deployed instruments can be seen in Figure 1-10.

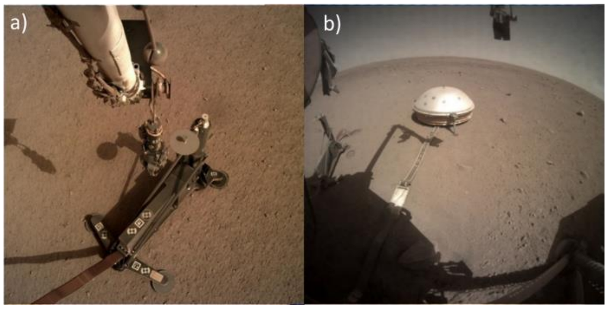

Figure 1-10. a) The HP3 instrument and the b) SEIS instrument when deployed as seen by the IDC and ICC cameras respectively.

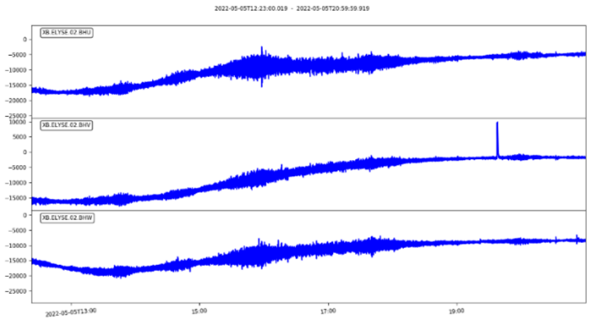

Figure 1-11. The raw SEIS data (deglitched) for the event of Sol 1222 plotted with the obspy python library.

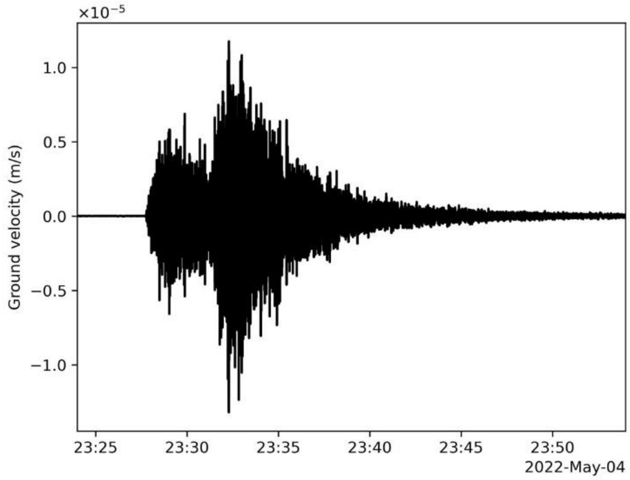

Figure 1-12. The plot of the Mars 1222 event after processing (Credit: NASA/JPL, 2022).

While on Mars, the SEIS instrument detected a total of 1319 seismic events or Marsquakes during the 1440 sols (Martian days) of the mission. These events where classified in four types based on data quality and the ability to locate their origin (Banerdt et al., 2020). Most of the biggest Marsquakes were located close to a geological structure known as Cerberus Fossae (Stähler et al., 2022). Some level of tectonic activity exists in the region, including landslides. The magnitude of these events is relatively small, with the biggest one detected on May 5th, 2020 (Sol 1222). The raw data for this event from the SEIS VBB sensors (after the deglitching process done by the science team) is seen in the Figure 1-11. After considerable processing, the seismogram for this biggest Masquake was obtained by NASA/JPL, which can be seen in Figure 1-12.

While initially planned to last 709 sols (equivalent to 728 Earth days), an Extended Mission proposal was approved, and the mission remained active until December 20th, 2022. Due to dust accumulation on the solar panels, an excessive decrease in power resulted in the closure of the mission. The system completed 1445 sols (4 years and 18 terrestrial days) on the red planet, far beyond the initial planned duration.

1.5. Soil mechanics outside of earth

The soils or rocks planets (or other extra-terrestrial bodies) that have been visited by either unmanned or manned missions have been investigated in various manners. Adequate knowledge of the soil is necessary for the selection of landing sites (Golombek et al. 2016) and considerable effort has been devoted to predicting surface properties from orbital measurements (Fernando et al. 2015, 2016).

Examples of mechanical investigation on simulants include triaxial compression tests and cone penetration tests performed on a lunar regolith simulant in low gravity fields (Mo et al. 2019).

Effects of reduced gravity on stiffness and shear resistance were assessed. Some limited changes were observed, and novel similitude testing methods were conceived.

The angle of repose of loose granular materials under varying levels of gravity has also been studied (Kleinhans et al., 2011) to check whether it was dependent on the gravity value. Rotating drums in parabolic flights were used in both dry and wet conditions. The angle of repose was observed to vary at low gravity values, decreasing both for dry and wet scenarios in materials with grain sizes between 0.2 mm to 2.4 mm (sand, glass beads and gravels).

Mimicking extra-terrestrial conditions implies the use of instrumentations in extreme conditions, such as very low temperatures which may affect the performance of displacement sensors such as potentiometers. Strain gauge displacement sensors are less affected by temperature while being more vulnerable to the effect of strong magnetic fields (Milushev et al., 2004).

Another soil mechanics problem is related to the cratering produced by rocket exhaust during landing. Lane et al. (2010) investigated shearing mechanisms and particle ejection by using Computational Fluid Dynamics simulations and checked their calculations with tests on dry cohesionless sand. Observations of gas propagation in porous soils has shown that soil removal from the crater was due to variations in gas pressure, reinforcing the need for proper studies of the effect of transient gas flow in such materials (Scott & Ko, 1968, Wu et al., 1998). Other examples include the cone penetration problem, that can be studied with DEM (Arroyo et al. 2011) and applied for lunar regolith (Mo et al. 2019).

1.6. Martian Regolith Simulants

Since no samples have been returned from Mars to Earth, Martian regoliths simulants have to be used. Simulant have also been utilized for works on the Moon, even though some – small – amount of Moon regolith have been available from the Apollo missions). So far, a considerable number of simulants have been utilized to study the surface properties of Mars and the Moon (see https://ares.jsc.nasa.gov/projects/simulants/. A few additional materials have been used as simulants for asteroids since 2017.

The first documented simulant is the MSL-1, aimed to mimick the mineralogy and texture of the Lunar Maria (or Mare), the youngest geologic units of the Lunar surface (Hill et al., 2007). For Mars, the earliest simulant is the JSC - Mars-1 based on the spectral similarity with the bright regions of Mars and developed by NASA in 1997 upon the findings of the Pathfinder and Viking missions. Other data on simulants may be found in Seiferlein et al. (2008). A summary of the main planetary regolith simulants is presented in Table 1-6. Several of these simulants including Mojave and Martian Dust Simulant (JMDS-1) were utilised for studying the thermal conductivity at the surface of the InSight landing site and other missions (Nagihara et al. 2022 and Yu et al. 2022). Work on simpler material including glass beads and crushed quartz particules have also been used to measure thermal conductivity (Presley & Christensen, 1997). Note that the websites "the Martian Garden" and "the Planetary Simulant database" contain detailed information for each simulant (some of them can be obtained through the Martian Garden).

Table 1-6. Main Planetary Regolith Simulants used.

Simulant used	Year	Reference	D50	Type
MLS-1	1988	Weiblen & Gordon, 1988	0.1 mm	Lunar
JSC-1	1991	Mc Kay et al., 1994	0.2 mm	Lunar
JSC Mars-1	1998	Allen et al., 1998	0.15 mm	Martian
MMS-1 Mojave	2007	Peters et al., 2008	0.05 mm	Martian

For this work, the Fontainebleau sand was selected as simulant. Its characteristics are further detailed below.

1.7. Fontainebleau sand

Fontainebleau sand is often utilised as a common reference sand and several theses have been completed studying in detail most aspects of the mechanical behaviour of this sand, (Andria-Ntoanina, 2011, Benahmed, 2001) while other works have used it to explore more specific aspects of its mechanics. These studies range from relatively simple matters as the bearing capacity of the material for surface foundations (Combarieu, 1999) to the measurement of the material's dynamic properties in medium dense and very dense arrangements (Dano& Hicher, 2002) and its interaction as a fine matrix on coarser soils (El Dine et al., 2010).

These works characterize the material in detail with the use of numerous triaxial tests (Latini & Zania, 2017), consolidation tests, and even some dynamic testing such as cyclic triaxial tests and resonant column tests. An example of these works studied the effects of grouting Fontainebleau sand (Delfosse-Ribay et al., 2004) on the shear modulus and damping ratio of the material; since the results include the pure sand as a benchmark, these results are a useful comparison for those obtained with dynamic testing on the material. Recent more specific work includes assessment of liquefaction with dynamic penetrometers such as Panda 3 (López, 2022) and the study of hydro-thermal behaviour of sandy soils subjected to freezing conditions (Hung, 2022).

It is worth noting that the subject of this work is not to focus on characterizing an already well studied sand, but rather to use it in experimental setups conceived to simulate the behaviour of a (considered to be) mechanically similar Martian regolith. Consequently, only the key aspects of the materials are now summarized; the reader may nevertheless consult the works mentioned above for further details on the material.

Geological origin

As part of the Bassin Parisien, the Île-de-France region contains numerous maritime deposits from the early Paleogene (34-66 Million years ago) when it was recurrently subjected to several cycles of transgressions and regressions of the sea. The main cycles at the Bassin during this period are summarized on Table 1-7 in chronological order.

Table 1-7. Sedimentary cycles of the Paris Basin during the Paleogene

Cycle	***Millions of years ago***	***Paleogene epoch***	***Deposit type***
Dano-Montien	65.5-59	Paleocene	Calcareous limestone
Thanétien	59-56	Paleocene	Bracheux sands
Ypresian/Sparnacian	56-51	Eocene	Soissonnais clays
Ypresian/Cuisian	51-48	Eocene	Cuise fine sands
Lower, middle and upper Lutetian	48-40	Eocene	Calcareous limestone
Bartonian / Auversien, Marinesian	40-37	Eocene	Auverss and Bauchamp sands
Bartonian / Ludian	37-34	Eocene	Gypsum deposit
Stampien/ Sannoisien, Stampien and Aquitanian	34-28	Oligocene	**Fontainebleau sand**

The deposits of these relatively recent formations remain shallow for the mostpart as can be seen in Figure 1-13; consequently, the material deposits have been used in numerous practical applications. The Lutetian calcarean limestone was used for construction materials during the 19th and 20th centuries; the gypsum from the Bartonian for plaster, and the Stampian deposits of silica sands (Fontainebleau sand is composed almost purely of silica) were used for optical lenses.

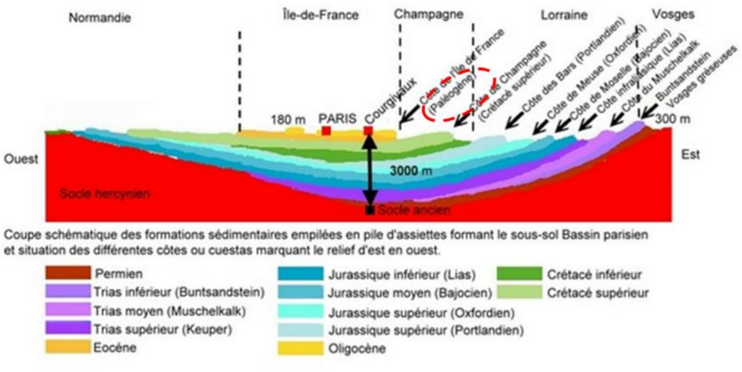

Figure 1-13. The geological formations of the Paris region. The Paleogene formations remain among the shallowest in the region (Image credit: Histoire-geologique-du-Bassin-parisien).

Fontainebleau sand in particular results from the regression of the Stampien sea from about 30 million years ago, during the late Paleogene (Oligocene). As seen in Figure 1-14, the different hypotheses for the area occupied by this ancient sea includes what today is the Île-de-France region. This was the final sea incursion of the sea into the region.

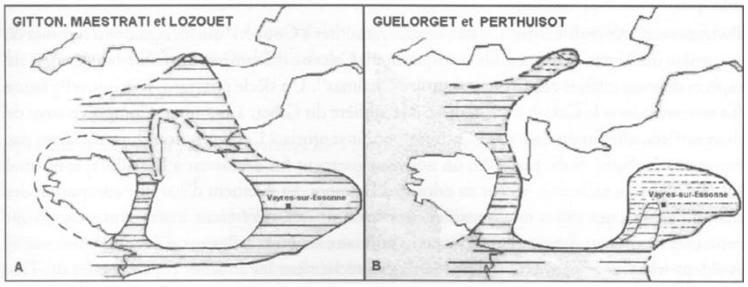

Figure 1-14. Different proposals for the area occupied by the Stampien sea (Credit: Baut et al., 2003)

Material description

The Fontainebleau sand is a uniform fine sand of a beige colour, which can be seen in Figure 1-15. Its grains composed almost entirely of silica, which can be seen to be the prevalent element in the spectroscopy in Figure 1-16 and Table 1-8 (the other elements are a result of sample manipulation, the presence of air and the gold plating required for SEM microscopy).

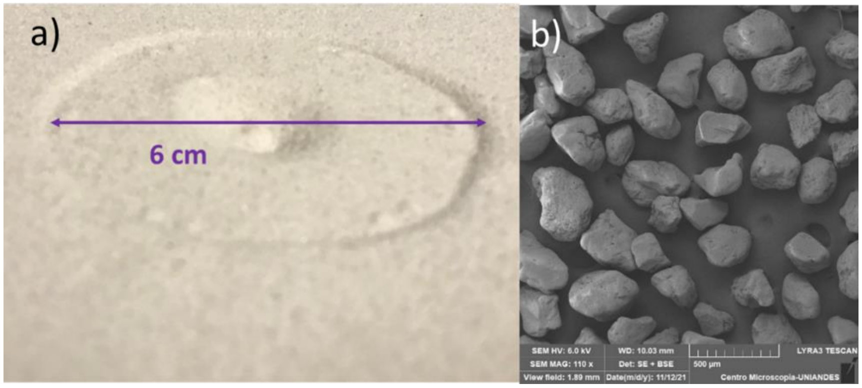

Figure 1-15. Aspect of Fontainebleau sand a) during an indentation test with a 6 cm diameter plate for reference. Note that grains and groups of grains are distinct to the eye. Some grains observed on b) SEM images.

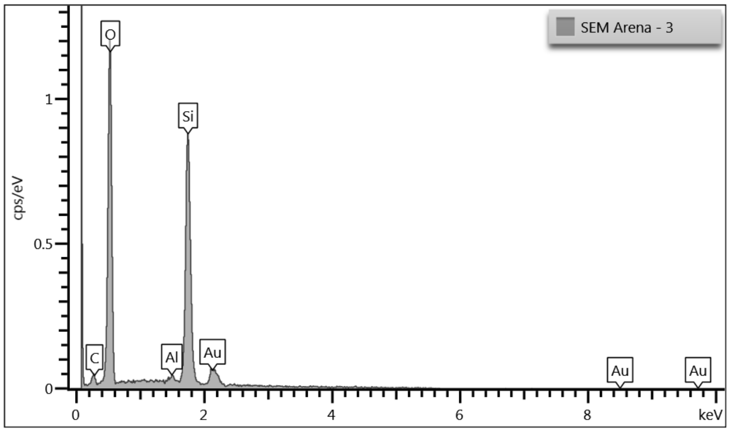

Figure 1-16. Results of spectroscopy on a Fontainebleau sample during SEM microscopy.

Table 1-8. Results of weight composition by element.

Element	Wt%
C	4.65
O	52.82
Al	0.73
Si	41.80
Total:	100.00

The D_{50} for the material is 220 μm, and the material can be considered uniform due to its coefficient of uniformity being $C_u = 1.52$. The key characteristics for the material as indicated in different studies are presented in Table 1-9, and the granulometric curves available are presented in Figure 1-17.

Table 1-9. Characteristics of Fontainebleau sand in different studies.

Source	$D_{50}(mm)$	C_u	e_{min}	e_{max}	$\rho_s(g/cm^3)$
Andria-Ntoanina, 2011	0.223	1.48	0.545	0.866	2.65
Georgiannou et al., 2008	0.220	1.48	0.540	0.865	2.64
López, 2022	0.21	1.52	0.55	0.85	2.65
Benahmed, 2001	0.21	1.52	0.54	0.94	2.65

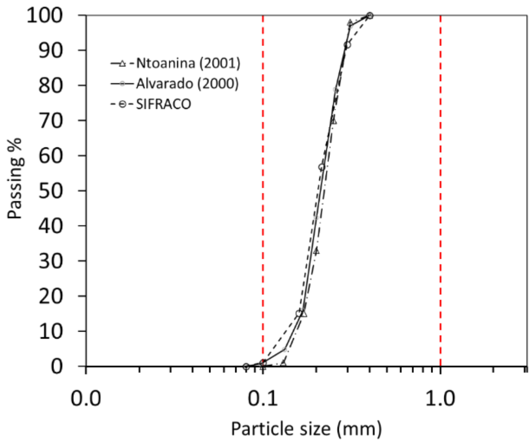

Figure 1-17. Size distribution curve for Fontainebleau sand.

The rounded shape of an individual typical grain can be appreciated in Figure 1-18a. Notice the 100 μm spans slightly less than the grain diameter. A group of grains is seen through SEM microscopy in Figure 1-18b, where some variability in the shapes of the grains can be observed.

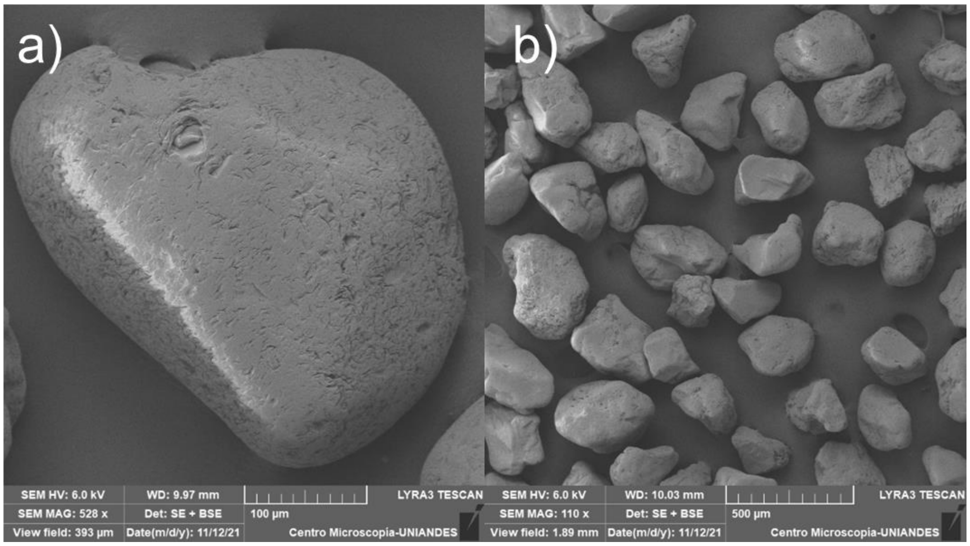

Figure 1-18. a) A typical grain of Fontainebleau sand, and b) a group of Fontainebleau sand grains seen on SEM microscopy.

1.8. Fontainebleau sand as a Martian regolith simulant

Much of the work carried out in this contribution comprises experimental activities in a new regolith simulant, chosen to recreate the soil present at Elysium Planitia. The material in question is the Fontainebleau sand. This material is presented in some detail now, and with some more detail at the beginning of the next sections.

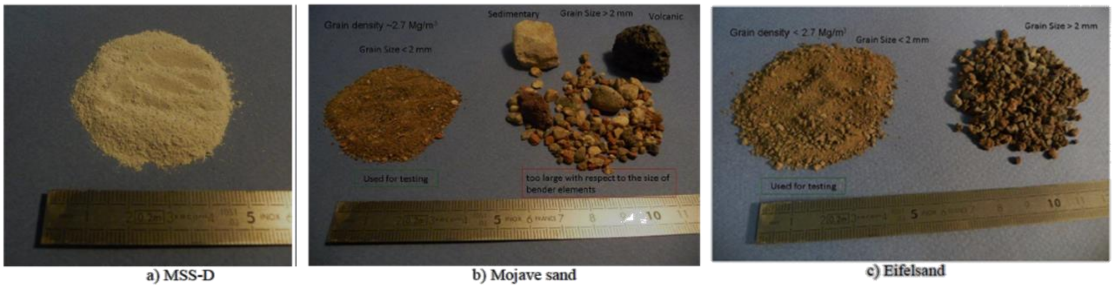

a) MSS-D
b) Mojave sand
c) Eifelsand

Figure 1-19. The previously used Martian Simulants. (Karakostas et al., 2013)

When designing the feet for SEIS (Karakostas et al., 2013), work was done making use of the simulants chosen with the best information available at the time. These feet were designed by the Navier laboratory at the École des Ponts et Chaussées, after performing tests on the best available Martian regolith simulant materials at the time. Since information in the pre-landing was limited to relatively low-resolution orbital data, further redundancy was achieved by working on three different simulants. These materials can be appreciated in Figure 1-19 and were good enough choices, since thanks to this design, the SEIS instrument stands on three feet on the surface of Mars. They intended to guarantee that the instrument would be well supported by penetrating the surface layer. Therefore, these three feet have the form of a sharp cone in the middle of a 60 mm disk. The cone has 20 mm in height and 10 mm of diameter (Delage et al., 2017). Learning from the serious disruptions that the winds of the red planet posed to the Viking seismometer, the SEIS instrument was also deployed below a thermal shield, topped by a white hemisphere with 70 cm of diameter (Lognonné et al., 2019).

However, since InSight landed in late 2018, the choice for adequate regolith simulant could now be based on proper knowledge of the material encountered at the site. For the case of Mars InSight, this material had been the objective of dedicated study from before the arrival of the lander (Morgan et al, 2018, Golombek et al, 2009). Microscopic observations such as those from Phoenix also play a key role (Goetz et al, 2010a).

The most relevant factor in this regard is the choice of grain size based on thermal inertia (denoted as *I*), which has been studied with high detail for the landing site both before and after the landing (Piqueux & Christensen, 2009). This property is a measure of the resistance that the surface layer of a material poses for temperature to propagate inside of it, and its definition is as follows:

$$I = \sqrt{k\rho c} \qquad (1)$$

Where k is the thermal conductivity, ρ is the density and c is the specific heat capacity of the material.

As seen in Figure 1-20, for the expected value of $160 - 230Jm^{-1}2K^{-2}s^{-1/2}$, a proper choice is a clean sand with little to no cohesion and packed in as loose as density as possible, since the values of expected density are all but unknown for natural sand deposits on Earth.

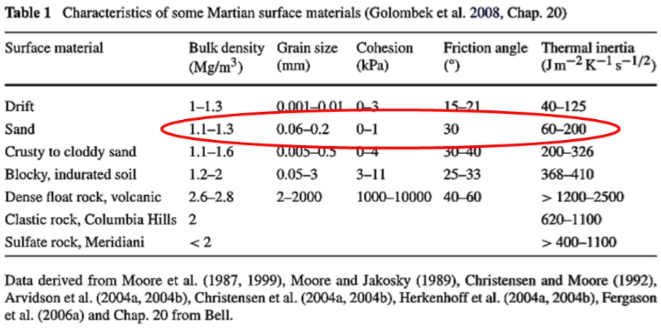

Table 1 Characteristics of some Martian surface materials (Golombek et al. 2008, Chap. 20)

Surface material	Bulk density (Mg/m^3)	Grain size (mm)	Cohesion (kPa)	Friction angle (°)	Thermal inertia ($J\,m^{-2}\,K^{-1}\,s^{-1/2}$)
Drift	1–1.3	0.001–0.01	0–3	15–21	40–125
Sand	1.1–1.3	0.06–0.2	0–1	30	60–200
Crusty to cloddy sand	1.1–1.6	0.005–0.5	0–4	30–40	200–326
Blocky, indurated soil	1.2–2	0.05–3	3–11	25–33	368–410
Dense float rock, volcanic	2.6–2.8	2–2000	1000–10000	40–60	> 1200–2500
Clastic rock, Columbia Hills	2				620–1100
Sulfate rock, Meridiani	< 2				> 400–1100

Data derived from Moore et al. (1987, 1999), Moore and Jakosky (1989), Christensen and Moore (1992), Arvidson et al. (2004a, 2004b), Christensen et al. (2004a, 2004b), Herkenhoff et al. (2004a, 2004b), Fergason et al. (2006a) and Chap. 20 from Bell.

Figure 1-20. Thermal inertia and the expected properties of the soil at the landing site (Golombek et al., 2017).

After these works, and by using the available measurements of the thermal inertia at the landing site, a better simulant has been chosen. Thermal inertia values were available for the site being obtained both from orbit and directly on the planet.

As a result, since the reported value of I at the landing site was verified to be consistent with the expected 160–230 $Jm^{-1}2K^{-2}s^{-1/2}$ (Golombek et al., 2020), a material particle size close to 170 μm can be expected to be the case for the material encountered at the site. The

Fontainebleau sand, which is natural from deposits close to Paris and thus easily available at the ENPC, presents a good choice for a simulant.

The utilisation of Fontainebleau sand also poses several practical advantages. It is a well characterized sand that has been employed for numerous studies already. Some of the most important aspects of its behaviour have been meticulously studied. For instance, it is well known that the behaviour of the soil is highly dependent on its void ratio, and so the evolution of strains at the materials compresses is also relevant. This aspect of the material studied by the oedometric tests has also been done for Fontainebleau sand (Schanz & Vermeer, 1999). Dynamic behaviour concerning this moduli degradation, but also the increase of the material dampening as it strains have also been researched to some extent (Delfosse-Ribay et al., 2004). Dynamic testing including the utilisation of bender elements has also taken place using the material (Dano & Hicher, 2002).

1.9. Lessons learned from the Mars InSight mission

The Mars InSight mission was successful, acquiring and processing over 4 years of data, far surpassing the projected 1-year lifespan. It provided quite unique geological insights into the red planet, concerning its interior structure and formation history. The SEIS instrument, as the first of its type to be deployed outside of Earth, was key to achieve this. Along the important SEIS contribution, significant results were obtained from the other two main instruments RISE and HP3, as well as from the auxiliary instruments and cameras.

SEIS accomplished significant milestones for the study of Mars seismicity. The seismic activity recorded included numerous events (over 1300 events were registered processed and catalogued), particularly the 12 class A events with large and proper enough signals to trace their origin back to the formation known as Cerberus fossae (Stähler et al., 2022), where marginal activity of magma remains at depths of 30-50 km. The detected activity included a very large event (magnitude 5) on May the 4th, 2022, and another very large one (magnitude 4.2) on August 25, 2021. Impacts were also detected, particularly a very large impact on Amazonis Planitia that took place in December 24th of 2021, melting ice layers on the surface near the equator. This was a remarkable achievement, given how unlikely it was to have such a large impact during the relatively limited timespan of the mission. This impact generated surface waves transmitted through the planetary crust, helping its characterisation. Additionally, some of the seismic activity detected by SEIS resulted from smaller meteor impacts, such as the one that took place on 5 September 2021, which was the first event to be confirmed as an impact (Garcia et al., 2022).

The high sensibility of SEIS not only enabled to acquire signals from impacts on the planet, but also to record effects as subtle as the passage of the Phobos moon above Elysium Planitia. This effect (known as the Phobos tide), which was slightly delayed but visible on the SEIS data, also provided relevant scientific results (Pou et al., 2022a and 2022b). Studying this phenomena was also key to assess the size and state of the planet's core, resulting in a planet core size estimated to 1820+/-80 km (Pou et al., 2022b), similar to the liquid core size estimated from radio tracking of 1835+/-55 km obtained from the RISE instrument (Le Maistre et al., 2023). These contributions also suggested an entirely liquid core, in contrast to previous ideas, another key contribution of the mission.

SEIS data showed periodical spikes, known as glitches, that were not anticipated from pre-mission testing. Glitches are attributed to step-like dilations inside the instrument components due to thermal variations (Scholz et al., 2022). Some tilt also had a mechanical origin, such as that induced by the passage of dust devils, that could be observed on both VBB and SP data (Murdoch et al., 2017).

Besides the successful geophysical results gained on the structure of the planet, the InSight mission on Mars also provided rich output in the field of meteorology (Spiga et al., 2018), spatial imagery, and even on the evolution of the magnetic field from the onboard magnetometer (Johnson et al., 2020, Mittelholz et al., 2023a, 2023b). The magnetometer founded the remnants of an ancient magnetic field larger than expected, and monitored continuous fluctuations attributed to solar wind interaction with the thin atmosphere of Mars.

The effects of dust devils on the seismometer data (Kenda et al., 2020, Murdoch et al., 2017) were analysed in details, together with the seismic noise resulting from changes in atmospheric conditions. This was repeatedly observed through the contrast between quiet nights, with little seismic noise, in contrast to very active days, with convective vortices, noise generated by the interactions between the wind and the lander, and the large thermal cooling-heating cycle and other vortices that induced ground deformation at surface (Stutzmann et al., 2021).

The HP3 hammering to penetrate the Martian soil did not attain the desired 5 m depth (Spohn et al., 2022a). Nevertheless, the HP3 provided valuable lessons, since it became clear that despite its penetration power, it was too light to penetrate the surface of a too stiff material (Spohn et al., 2022b). The hammering process resulted in small seismic signals that were detected by SEIS and analysed to determine the wave velocities of the surface layer (Brinkman et al. 2022). The HP3 also provided interesting data on the thermal conductivity at the surface (Grott et al. 2022, Spohn et al., 2022a). These data were coherent with lab estimation provided by Nagihara et al. (2022), and also with the results presented in this work.

The properties of the surface material at the landing site were better known (Delage et al, 2022a). Interesting data were also obtained from the arm activities, including digging trenches, pushing down on the surface and measuring the SEIS tilt (Golombek et al., 2023, Marteau et al., 2023). The grain size distribution of the surface regolith was also better assessed by observing the effect of wind transportation during the pouring carried out with the robotic arm to cover the SEIS tether (Verdier et al, 2023).

1.10. References

Allen, C. C., Jager, K. M., Morris, R. V., Lindstrom, D. J., Lindstrom, M. M., & Lockwood, J. P. (1998). JSC MARS-1: A Martian Soil Simulant. Space and Robotics.

Andria-Ntoanina, I. (2011). Caractérisation dynamique de sables de référence en laboratoire - Application à la réponse sismique de massifs sableux en centrifugeuse. [Thesis]. ENPC.

Banerdt, W. B., Folkner, W. M., Dehant, V., Le Maistre, S., Yseboodt, M., Rivoldini, A., Van Hoolst, T., Asmar, S. W., & Golombek, M. P. (2018). The InSight mission. Space Science Reviews, 214(5).

Banerdt, W. B., Smrekar, S. E., Banfield, D., Giardini, D., Golombek, M., Johnson, C. L., Lognonné, P., Spiga, A., Spohn, T., Perrin, C., Stähler, S. C., Antonangeli, D., Asmar, S., Fillingim, M., Folkner, W., Garcia, R. F., Garvin, J., Grant, J., Grott, M., … Mclennan, S. M. (2020). Initial results from the InSight mission on Mars.

Baut, J., Researcher, I., Merle, D., & Hervet, S. (2003). Le gisement à vertébrés fossiles de Vayres-sur-Essonne une découverte importante pour l'histoire de la mer stampienne. Cossmanniana, Hors-série(April 2015), 37–38.

Benahmed, N. (2001). Comportement mécanique d'un sable sous cisaillement monotone et cyclique : application aux phénomènes de liquéfaction et de mobilité y clique [Thesis]. ENPC.

Brinkman, N., Schmelzbach, C., Sollberger, D., Pierick, J. ten, Edme, P., Haag, T., Kedar, S., Hudson, T., Andersson, F., van Driel, M., Stähler, S., Nicollier, T., Robertsson, J., Giardini, D., Spohn, T., Krause, C., Grott, M., Knollenberg, J., Hurst, K., … Banerdt, W. B. (2022). In Situ Regolith Seismic Velocity Measurement at the InSight Landing Site on Mars. Journal of Geophysical Research: Planets, 127(10). https://doi.org/10.1029/2022JE007229

CNES. (2018). INSIGHT. November 27. https://insight.cnes.fr/en/INSIGHT/index.htm

Combarieu, O. (1999). Caractérisation mécanique d 'un massif de sable compacté Cohérence des essais réalisés. Bulletin des Laboratoires des Ponts Et Chaussées, mm, 69–73.

Dano, C., & Hicher, P.-Y. (2002). Mesure du module de cisaillement de differents materiaux par la technique des bender elements. Paramètres de Calcul Géotechnique.

Delage, P., Karakostas, F., Dhemaied, A., Belmokhtar, M., Lognonné, P., Golombek, M., de Laure, E., Hurst, K., Dupla, J. C., Kedar, S., Cui, Y. J., & Banerdt, B. (2017). An Investigation of the Mechanical Properties of Some Martian Regolith Simulants with Respect to the Surface Properties at the InSight Mission Landing Site. Space Science Reviews, 211(1–4), 191–213. https://doi.org/10.1007/s11214-017-0339-7

Delfosse-Ribay, E., Djeran-Maigre, I., Cabrillac, R., & Gouvenot, D. (2004). Shear modulus and damping ratio of grouted sand. Soil Dynamics and Earthquake Engineering, 24(6), 461–471. https://doi.org/10.1016/j.soildyn.2004.02.004

El Dine, B. S., Dupla, J. C., Frank, R., Canou, J., & Kazan, Y. (2010). Mechanical characterization of matrix coarse-grained soils with a large-sized triaxial device. Canadian Geotechnical Journal, 47(4), 425–438. https://doi.org/10.1139/T09-113

Fernando, J., Schmidt, F., & Douté, S. (2016). Martian surface microtexture from orbital CRISM multi-angular observations: A new perspective for the characterization of the geological processes. Planetary and Space Science, 128, 30–51. https://doi.org/10.1016/j.pss.2016.05.005

Fernando, J., Schmidt, F., Pilorget, C., Pinet, P., Ceamanos, X., Douté, S., Daydou, Y., & Costard, F. (2015). Characterization and mapping of surface physical properties of Mars from CRISM multi-angular data: Application to Gusev Crater and Meridiani Planum. Icarus, 253, 271–295. https://doi.org/10.1016/j.icarus.2015.03.012

Folkner, W. M., Dehant, V., Le Maistre, S., Yseboodt, M., Rivoldini, A., Van Hoolst, T., Asmar, S. W., & Golombek, M. P. (2018). The Rotation and Interior Structure Experiment on the InSight Mission to Mars. Space Science Reviews, 214(5), 1–16. https://doi.org/10.1007/s11214-018-0530-5

Garcia, R., Daubar, I., Beucler, É., Posiolova, L., Collins, G., Lognonné, P., Rolland, L., Xu, Z., Wójcicka, N., Garcia, R., Daubar, I., Beucler, É., Posiolova, L., & Collins, G. (2022). Newly formed craters on Mars located using seismic and acoustic wave data from InSight To cite this version : HAL Id : hal-03945839. Nature Geoscience, 15, 774–780.

Georgiannou, V. N., Tsomokos, A., & Stavrou, K. (2008). Monotonie and cyclic behaviour of sand under torsional loading. Geotechnique, 58(2), 113–124. https://doi.org/10.1680/geot.2008.58.2.113

Giardini, D., Lognonné, P., Banerdt, W. B., Pike, W. T., Christensen, U., Ceylan, S., Clinton, J. F., van Driel, M., Stähler, S. C., Böse, M., Garcia, R. F., Khan, A., Panning, M., Perrin, C., Banfield, D., Beucler, E., Charalambous, C., Euchner, F., Horleston, A., … Yana, C. (2020). The seismicity of Mars. Nature Geoscience, 13(3), 205–212. https://doi.org/10.1038/s41561-020-0539-8

Goetz, W., Pike, W. T., Hviid, S. F., Madsen, M. B., Morris, R. V., Hecht, M. H., Staufer, U., Leer, K., Sykulska, H., Hemmig, E., Marshall, J., Morookian, J. M., Parrat, D., Vijendran, S., Bos, B. J., El Maarry, M. R., Keller, H. U., Kramm, R., Markiewicz, W. J., … Tanner, R. (2010a). Microscopy analysis of soils at the Phoenix landing site, Mars: Classification of soil particles and description of their optical and magnetic properties. Journal of Geophysical Research E: Planets, 115(8), 1–23. https://doi.org/10.1029/2009JE003437

Golombek, M., Grott, M., Kargl, G., Andrade, J., Marshall, J., Warner, N., Teanby, N. A., Ansan, V., Hauber, E., Voigt, J., Lichtenheldt, R., Knapmeyer-Endrun, B., Daubar, I. J., Kipp, D., Muller, N., Lognonné, P., Schmelzbach, C., Banfield, D., Trebi-Ollennu, A., … Banerdt, W. B. (2018). Geology and Physical Properties Investigations by the InSight Lander. In Space Science Reviews (Vol. 214, Issue 5). Springer Netherlands. https://doi.org/10.1007/s11214-018-0512-7

Golombek, M., Kipp, D., Warner, N., Daubar, I. J., Fergason, R., Kirk, R. L., Beyer, R., Huertas, A., Piqueux, S., Putzig, N. E., Campbell, B. A., Morgan, G. A., Charalambous, C., Pike, W. T., Gwinner, K., Calef, F., Kass, D., Mischna, M., Ashley, J., … Banerdt, W. B. (2017). Selection of the InSight Landing Site. Space Science Reviews, 211(1–4), 5–95. https://doi.org/10.1007/s11214-016-0321-9

Golombek, M. P., Huertas, A., Marlow, J., McGrane, B., Klein, C., Martinez, M., Arvidson, R. E., Heet, T., Barry, L., Seelos, K., Adams, D., Li, W., Matijevic, J. R., Parker, T., Sizemore, H. G., Mellon, M., McEwen, A. S., Tamppari, L. K., & Cheng, Y. (2009). Size-frequency distributions of rocks on the northern plains of Mars with special reference to Phoenix landing surfaces. Journal of Geophysical Research: Planets, 114(3). https://doi.org/10.1029/2007JE003065

Golombek, M., Warner, N. H., Grant, J. A., Hauber, E., Ansan, V., Weitz, C. M., Williams, N., Charalambous, C., Wilson, S. A., DeMott, A., Kopp, M., Lethcoe-Wilson, H., Berger, L., Hausmann, R., Marteau, E., Vrettos, C., Trussell, A., Folkner, W., Le Maistre, S., … Banerdt, W. B. (2020). Geology of the InSight landing site on Mars. Nature Communications, 11(1), 1–11. https://doi.org/10.1038/s41467-020-14679-1

Hill, E., Mellin, M. J., Deane, B., Liu, Y., & Taylor, L. A. (2007). Apollo sample 70051 and high- and low-Ti lunar soil simulants MLS-1A and JSC-1A: Implications for future lunar exploration. Journal of Geophysical Research: Planets, 112(2). https://doi.org/10.1029/2006JE002767

Hung Vu, Q. (2022). Effect of fines content on hydro-thermal behaviour of sandy soil in the context of artificial ground freezing.

Johnson, C. L., Mittelholz, A., Langlais, B., Russell, C. T., Ansan, V., Banfield, D., Chi, P. J., Fillingim, M. O., Forget, F., & Haviland, H. F. (n.d.). Crustal and time-varying magnetic fields at the InSight landing site on Mars. Nature Geoscience, 2020(3), 199–204. https://doi.org/10.1038/s41561-020-0537-xï

Karakostas, F., Delage, P., Laure, E. De, Dhemaied, A., Dupla, J. C., Tang, A. M., & Cui, Y. J. (2013). The geotechnical properties of some Mars regoliths simulants (Issue November).

Kenda, B., Drilleau, M., Garcia, R. F., Kawamura, T., Murdoch, N., Compaire, N., Lognonné, P., Spiga, A., Widmer-Schnidrig, R., Delage, P., Ansan, V., Vrettos, C., Rodriguez, S., Banerdt, W. B., Banfield, D., Antonangeli, D., Christensen, U., Mimoun, D., Mocquet, A., & Spohn, T. (2020). Subsurface Structure at the InSight Landing Site From Compliance Measurements by Seismic and Meteorological Experiments. Journal of Geophysical Research: Planets, 125(6), 1–30. https://doi.org/10.1029/2020JE006387

Kleinhans, M. G., Markies, H., De Vet, S. J., In't Veld, A. C., & Postema, F. N. (2011). Static and dynamic angles of repose in loose granular materials under reduced gravity. Journal of Geophysical Research: Planets, 116(11). https://doi.org/10.1029/2011JE003865

Lane, J. E., Metzger, P., & Carlson, J. (2010). Lunar Dust Particles Blown By Lander Engine Exhaust in Rarefied and Compressible Flow.

Le Maistre, S., Rivoldini, A., Caldiero, A., Yseboodt, M., Baland, R.-M., Beuthe, M., Van Hoolst, T., Dehant, V., Folkner, W. M., & Buccino, D. (2023). Spin state and deep interior structure of Mars from InSight radio tracking. Nature, 619, 733–737. https://doi.org/10.1038/s41586-023-06150-0ï

Latini, C., & Zania, V. (2017). Triaxial Tests in Fontainebleau Sand (Vol. 20).

Lognonné, P., Banerdt, W. B., Giardini, D., Pike, W. T., Christensen, U., Laudet, P., de Raucourt, S., Zweifel, P., Calcutt, S., Bierwirth, M., Hurst, K. J., Ijpelaan, F., Umland, J. W., Llorca-Cejudo, R., Larson, S. A., Garcia, R. F., Kedar, S., Knapmeyer-Endrun, B., Mimoun, D., … Wookey, J. (2019). SEIS: Insight's Seismic Experiment for Internal Structure of Mars. In Space Science Reviews (Vol. 215, Issue 1). The Author(s). https://doi.org/10.1007/s11214-018-0574-6

Lognonné, P., Banerdt, W. B., Pike, W. T., Giardini, D., Christensen, U., Garcia, R. F., Kawamura, T., Kedar, S., Knapmeyer-Endrun, B., Margerin, L., Nimmo, F., Panning, M., Tauzin, B., Scholz, J. R., Antonangeli, D., Barkaoui, S., Beucler, E., Bissig, F., Brinkman, N., … Zweifel, P. (2020). Constraints on the shallow elastic and anelastic structure of Mars from InSight seismic data. Nature Geoscience, 13(3), 213–220. https://doi.org/10.1038/s41561-020-0536-y

López-Retamales, S. (2022). Development of a method to evaluate the risk of liquefaction of sands from a dynamic penetrometer test. ENPC.

Mckay, D. S., Carter, J. L., Boles, W. W., Allen, C. C., & Allton, J. H. (1994). JSC-1: A NEW LUNAR SOIL SIMULANT. Engineering, Construction, and Operations in Space, 4, 857–866. http://ares.jsc.nasa.gov/HumanExplore/Exploration/EXLibrary/DOCS/EIC050.HTML

Milushev, M., Süßer, M., & Wüchner, F. (2004). Investigation of two different types of displacement transducers in the cryogenic environment. Cryogenics, 44(3), 197–201. https://doi.org/10.1016/j.cryogenics.2003.11.004

Mimoun, D., Murdoch, N., Lognonné, P., Hurst, K., Pike, W. T., Hurley, J., Nébut, T., & Banerdt, W. B. (2017). The Noise Model of the SEIS Seismometer of the InSight Mission to Mars. Space Science Reviews, 211(1–4), 383–428. https://doi.org/10.1007/s11214-017-0409-x

Mittelholz, A., Johnson, C. L., Fillingim, M., Grimm, R. E., Joy, S., Thorne, S. N., & Banerdt, W. B. (2023). Mars' External Magnetic Field as Seen From the Surface With InSight. Journal of Geophysical Research: Planets, 128(1). https://doi.org/10.1029/2022JE007616

Mo, P. Q., Gao, F., Zhou, G., Li, R., Yan, K., & Chen, J. (2019). An experimental study on triaxial compression tests and cone penetration tests in planetary regolith simulant under low gravity fields. Journal of Testing and Evaluation, 47(3). https://doi.org/10.1520/JTE20180005

Morgan, P., Grott, M., Knapmeyer-Endrun, B., Golombek, M., Delage, P., Lognonné, P., Piqueux, S., Daubar, I., Murdoch, N., Charalambous, C., Pike, W. T., Müller, N., Hagermann, A., Siegler, M., Lichtenheldt, R., Teanby, N., & Kedar, S. (2018). A Pre-Landing Assessment of Regolith Properties at the InSight Landing Site. In Space Science Reviews (Vol. 214, Issue 6). https://doi.org/10.1007/s11214-018-0537-y

Murdoch, N., Kenda, B., Kawamura, T., Spiga, A., Lognonné, P., Mimoun, D., & Banerdt, W. B. (2017). Estimations of the Seismic Pressure Noise on Mars Determined from Large Eddy Simulations and Demonstration of Pressure Decorrelation Techniques for the Insight Mission. In Space Science Reviews (Vol. 211, Issues 1–4, pp. 457–483). Springer Netherlands. https://doi.org/10.1007/s11214-017-0343-y

Nagihara, S., Ngo, P., & Grott, M. (2022). Thermal Properties of the Mojave Mars Regolith Simulant in Mars-Like Atmospheric Conditions. International Journal of Thermophysics, 43(7). https://doi.org/10.1007/s10765-022-03023-y

NASA/JPL. (2022). InSight's Seismogram of Big Martian Quake. May 09, 2022. https://mars.nasa.gov/resources/26731/insights-seismogram-of-big-martian-quake/

Panning, M. P., Beucler, É., Drilleau, M., Mocquet, A., Lognonné, P., & Banerdt, W. B. (2015). Verifying single-station seismic approaches using Earth-based data: Preparation for data return from the InSight mission to Mars. Icarus, 248, 230–242. https://doi.org/10.1016/j.icarus.2014.10.035

Peters, G. H., Abbey, W., Bearman, G. H., Mungas, G. S., Smith, J. A., Anderson, R. C., Douglas, S., & Beegle, L. W. (2008). Mojave Mars simulant-Characterization of a new geologic Mars analog. Icarus, 197(2), 470–479. https://doi.org/10.1016/j.icarus.2008.05.004

Piqueux, S., & Christensen, P. R. (2009). A model of thermal conductivity for planetary soils: 2. Theory for cemented soils. Journal of Geophysical Research: Planets, 114(9). https://doi.org/10.1029/2008JE003309

Pou, L., Nimmo, F., Lognonné, P., Mimoun, D., Garcia, R. F., Pinot, B., Rivoldini, A., Banfield, D., & Banerdt, W. B. (2021). Forward Modeling of the Phobos Tides and Applications to the First Martian Year of the InSight Mission. Earth and Space Science, 8(7). https://doi.org/10.1029/2021EA001669

Pou, L., Nimmo, F., Rivoldini, A., Khan, A., Bagheri, A., Gray, T., Samuel, H., Lognonné, P., Plesa, A.-C., & Gudkova, T. (2022). Tidal Constraints on the Martian Interior. Journal of Geophysical Research. Planets, 2022(11), 10. https://doi.org/10.1029/2022JE007291ï

Presley, M. A., & Christensen, P. R. (1997). Thermal conductivity measurements of particulate materials 2. Results. Journal of Geophysical Research: Planets, 102(E3), 6551–6566. https://doi.org/10.1029/96JE03303

Schanz, T., & Vermeer, P. A. (1999). Pre-failure Deformation Behaviour of Geomaterials.

Scholz, J.-R., Widmer-Schnidrig, R., Davis, P., Lognonné, P., Pinot, B., Garcia, R. F., Hurst, K., Pou, L., Nimmo, F., Barkaoui, S., De Raucourt, S., Knapmeyer-Endrun, B., Knapmeyer, M., Orhand-Mainsant, G., Compaire, N., Cuvier, A., Beucler, É., Bonnin, M., Joshi, R., … Banerdt, W. B. (2022). Detection, Analysis, and Removal of Glitches From InSight's Seismic Data From Mars Detection, Analysis, and Removal of Glitches From InSight's Seismic Data From Mars Detection, Analysis, and Removal of Glitches From InSight's Seismic Data From Mars. Earth and Space Science, 2020(11), 10. https://doi.org/10.1029/2020ea001317ï

ScienceNASA. (2017). Discovery program. Discovery Program. https://www.nasa.gov/planetarymissions/discovery-program/

Scott, R. F., & Ko, H. Y. (1968). Transient rocket-engine gas flow in soil. AIAA Journal, 6(2), 258–264. https://doi.org/10.2514/3.4487

Seiferlin, K., Ehrenfreund, P., Garry, J., Gunderson, K., Hütter, E., Kargl, G., Maturilli, A., & Merrison, J. P. (2008). Simulating Martian regolith in the laboratory. Planetary and Space Science, 56(15), 2009–2025. https://doi.org/10.1016/j.pss.2008.09.017

SEIS-InSight. (2017). SEIS Instrument. Instruments. https://mars.nasa.gov/insight/spacecraft/instruments/seis/

Spiga, A., Banfield, D., Teanby, N.A. *et al.* Atmospheric Science with InSight. *Space Sci Rev* **214**, 109 (2018). https://doi.org/10.1007/s11214-018-0543-0

Spohn, T., Grott, M., Smrekar, S. E., Knollenberg, J., Hudson, T. L., Krause, C., Müller, N., Jänchen, J., Börner, A., Wippermann, T., Krömer, O., Lichtenheldt, R., Wisniewski, L., Grygorczuk, J., Fittock, M., Rheershemius, S., Spröwitz, T., Kopp, E., Walter, I., … Banerdt, W. B. (2018). The Heat Flow and Physical Properties Package (HP3) for the InSight Mission. In Space Science Reviews (Vol. 214, Issue 5). The Author(s). https://doi.org/10.1007/s11214-018-0531-4

Stähler, S. C., Mittelholz, A., Perrin, C., Kawamura, T., Kim, D., Knapmeyer, M., Zenhäusern, G., Clinton, J., Giardini, D., Lognonné, P., & Banerdt, W. B. (2022). Tectonics of Cerberus Fossae unveiled by marsquakes. Nature Astronomy, 6(12), 1376–1386. https://doi.org/10.1038/s41550-022-01803-y

Stutzmann, E., Schimmel, M., Lognonné, P., Horleston, A., Ceylan, S., van Driel, M., Stahler, S., Banerdt, B., Calvet, M., Charalambous, C., Clinton, J., Drilleau, M., Fayon, L., Garcia, R. F., Giardini, D., Hurst, K., Jacob, A., Kawamura, T., Kenda, B., … Spiga, A. (2021). The Polarization of Ambient Noise on Mars. Journal of Geophysical Research: Planets, 126(1). https://doi.org/10.1029/2020JE006545

Trebi-Ollennu, A., Kim, W., Ali, K., Khan, O., Sorice, C., Bailey, P., Umland, J., Bonitz, R., Ciarleglio, C., Knight, J., Haddad, N., Klein, K., Nowak, S., Klein, D., Onufer, N., Glazebrook, K., Kobeissi, B., Baez, E., Sarkissian, F., … Lin, J. (2018). InSight Mars Lander Robotics Instrument Deployment System. Space Science Reviews, 214(5). https://doi.org/10.1007/s11214-018-0520-7

Weiblen PW, & Gordon, K. (1988). Characteristics of a Simulant for Lunar Surface Materials. Symposium on Lunar Bases and Space Activities in the 21st Century, Paper No. LBS-88-213.

Witze, A. (2021). Mars’s core has been measured - and it’s surprisingly large. Nature, 591(7851), 514–515. https://doi.org/10.1038/d41586-021-00696-7

Wu, Y. S., Pruess, K., & Persoff, P. (1998). Gas Flow in Porous Media with Klinkenberg Effects. Transport in Porous Media, 32(1), 117–137. https://doi.org/10.1023/A:1006535211684

Verdier, N., Ansan, V., Delage, P., Ali, K. S., Beucler, E., Charalambous, C., Constant, E., Spiga, A., Golombek, M., Marteau, E., Lapeyre, R., Gaudin, E., Yana, C., Hurst, K., Lognonné, P., & Banerdt, B. W. (2023). Using Wind Dispersion Effects During the InSight Tether Burial Activities to Better Constrain the Regolith Grain Size Distribution. Journal of Geophysical Research: Planets, 128(5). https://doi.org/10.1029/2022JE007707

Yu, W., Zeng, X., Li, X., Wei, G., & Fang, J. (2022). New Martian Dust Simulant JMDS-1 and Applications to Laboratory Thermal Conductivity Measurements. Earth and Space Science, 9(1), 1–15. https://doi.org/10.1029/2020EA001347.

2. SAMPLE PREPARATION AND HOMOGENEITY

Plus ça change, plus c’est la même chose.”.
“The more things change, the more they stay the same*”.*
Jean-Baptiste Alphonse Karr, 1849

Homogeneity and density are key components for the mechanical behaviour of sands. Given the loose density of the regolith at the InSight landing site (Grott et al. 2010), it was necessary to obtain very loose sand assembly for the specimens to be tested. Consequently, special care was devoted to preparing loose sand samples and particular attention was devoted to homogeneity issues. To achieve this, X-ray tomography tests (Thiery 2013) were performed on the samples. This chapter contains a brief explanation of the use of tomography to study soil density and also details the sample reparation technique.

Since the original works about sand pluviation (Kolbuszewski, 1984), several developments to get controlled and homogeneous density in sand samples have been carried out. The pluviation technique has also been addressed by Cresswell et al. 1999, Taboroei et al. 2017, Gade & Dasaka, 2017, and Flitti et al., 2021.

Some other investigations assess the effect of pluviation on the response of the sand (Miura 1982, Vaid et al., 1999, Wanatowski & Chu, 2008, Jafri et al., 2018), on the influence under triaxial and torsional strength (Tatsuoka et al., 1986) and on damping (Tatsuoka et al., 1979). The effects of fabric and its degradation under stress cycles has been studied by Oda (1972, 1972b). More complex materials such as combined sand and silt mixtures have also been addressed (Yamamuro & Wood, 2004).

Specimen reconstitution in the laboratory with the pluviation technique compared to other methods has also been addressed (Vaid et al., 1999, Kodicherla et al., 2018) as has been its effect on static response of sand (Miura & Toki, 1982) as has been the effect it has on complex anisotropy considerations (Oda 1972a, Oda 1972b). Anisotropy aspects have been investigated by Siddiquee et al., 2018. Effects on other complex aspects of soil behaviour due to specimen preparation such as non-plastic behaviour and modulus degradation have been studied too (Zlatovic & Ishihara, 1997, Oda 1972b).

Some works studying sample preparation homogeneity with X-ray tomography already exist (Al-Shibli 1996, Alshibli & Hasan, 2008, Chao-Fa et al., 2017, Chen et al., 2017). Shear band thickness has also been studied with the use of this technique (Borja et al., 2012).

The preliminary draft of an article further addressing sample homogeneity due to sample preparation with X-ray tomography is presented below.

2.1. X-ray micro-tomography investigation of the effects of funnel pluvation on sample homogeneity (Article 1: Manuscript in process)

Abstract

Adequate sample preparation is a key aspect to ensure useful and correct results for numerous experimental testing procedures in geotechnics. For the case of sands in particular, mechanical behaviour is dictated significantly by the density of the sample and the associated void ratio present in the sample. Consequently, sand samples are prepared at a desired density level by using several procedures, including several variations of the pluviation or rain deposition technique. In this work, the effect of sample preparation technique on the homogeneity of the obtained density level is evaluated with the aid of X-ray microtomography. Spatial variation of the density in the vertical and radial direction of a cylindrical specimen is analysed based on several scans, and the data is analysed to account for perturbations due to beam-hardening; this phenomenon was addressed with careful sample preparation and calibration with a novel technique. It is observed that negligible small-scale variations occur along the vertical direction of the sample, as well as the middle section of the radial direction; more variation was observed near the walls of the sample. Thus, for experiments conducted in the top central section of the sample, assuming the density value as constant through the sample is a valid supposition.

Introduction

Density is a key feature in the mechanical behaviour of sands, that must be carefully considered during sample preparation. Most often, density measurements are determined at a global level, with less attention paid to homogeneity and to the spatial variability of density within the sample. In this context, X-ray tomography, that enables in sands a detailed 3D image identification of samples, is particularly adapted. In this work, X-ray based tomography was utilised on a sample of Fontainebleau sand used as a simulant of the Martian regolith at the InSight landing site (Delage et al., 2022).

Various X-ray scans were conducted on a sample used to investigate the interaction between the foot of the Mars InSight SEIS seismometer and the surface soil (Delage et al., 2022). In these tests, the sand was deposited in a container made up of a 240 mm diameter and 120 mm high transparent cylinder filled with sand in an as loose as possible state. To do so, the sand was deposited by using a funnel placed in the cylinder axis and slowly elevated while ensuring a zero-fall height between the funnel and the top of the sand pile. The homogeneity in density was investigated both vertically and radially by X-Ray microtomography.

Due to the different lengths crossed within the cylindrical sand sample scanned by the X-rays, the grey values of the tomograph images must be corrected to account for beam-hardening effects (Brooks & Di Chiro, 1976). To do so, a series of 5 mm diameter silica glass beads were placed in the sand at a given level to use them for calibration. The glass beads have a density of 2460.39 ± 16 kg/m^3 and are used as a reference for the almost pure silica Fontainebleau sand, with a density of 2640 kg/m^3 (Saadi et al., 2017). 5 mm diameter 3D printed hollow plastic beads with an internal cavity of 3 mm in diameter were used as a reference for the grey value of the air inside of the sample.

Sample preparation

The 120 mm height and 240 mm diameter cylindrical container is shown in Figure 2-1a. The container was placed on a scale prior to deposit the sand, done with the funnel at almost zero fall height to place an initial thin layer. Then, 20 glass beads with 5 mm diameter and 10 hollow beads (as the one in Figure 2-2) of the same size were placed at random positions (both radius and angle) around the sample (see Figure 2-1b). They were covered with sand carefully placed with a spoon, so that they keep their position. Then, the sand was deposited with the funnel, centred by using tape stripes fixed to the container as seen in Figure 2-3, guaranteeing that the funnel rises in a true vertical trajectory over the middle of the sample, with the conic pile of deposited sand rising homogenously.

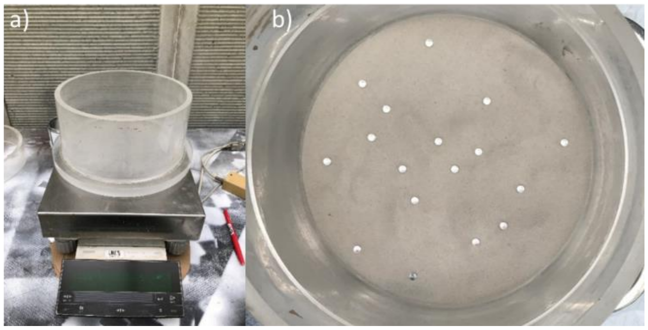

Figure 2-1. a) Cylindrical container used for the sample, filled with b) the bottom layer of beads.

Once the base of the sand cone reached the top of the container, the cone was removed so that the clean surface of the container was visible, and a new layer of glass and hollow beads was placed, as seen in Figure 2-4a. After covering these beads, a secondary ring with 40 mm height was placed on top of the container, and pluviation resumed to cover the second bead layer with another cone as seen in seen in Figure 2-4b.

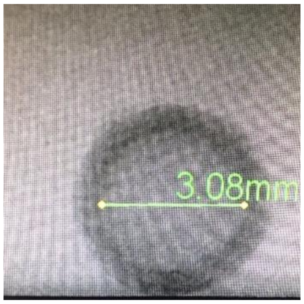

Figure 2-2. Hollow bead with an internal 3 mm diameter used for calibrating the air grey inside the sample.

Once the sample was ready for testing, it was weighted to determine the global density of the sample, prior to carefully placing it in the tomograph without any disturbance of the loose state.

Figure 2-3. Tape used to ensure the central position of the funnel during pluviation.

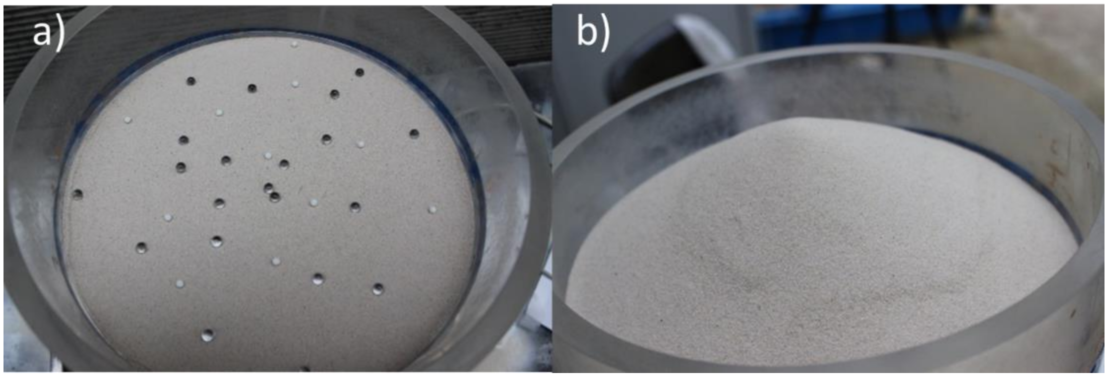

Figure 2-4. After placing the a) upper layer of beads, a new b) conic pile was deposited over the top layer of glass and hollow beads.

X-Ray tomography

The equipment used was the RX Solutions Ultratom (Ultra High-Performance 3D CT System) available at the Navier laboratory (see Figure 2-5). To get adequate and sufficient data, three full scans were carried out. Two of them were made with the sensor aligned with the vertical plane of each glass bead layer (top and bottom) and the third one was performed with the sensor placed at the sample middle height, scanning a plane only made up of sand particles and air voids. The voxel size for the scans was of 85 μm, smaller than the D_{50} of the Fontainebleau sand.

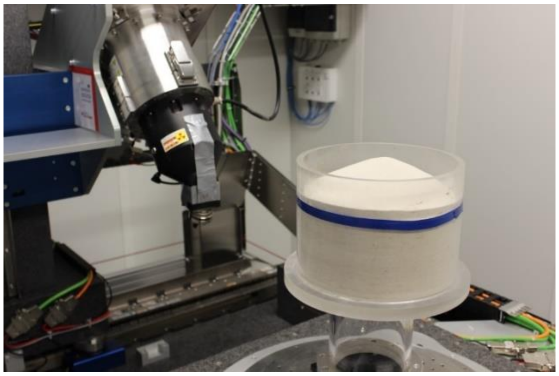

Figure 2-5. Sample placed into the X-ray tomograph.

Preparation and processing of the data

Preparing the data for processing

Once the X-ray microtomograph data was acquired, the first stage of data analysis was to reconstruct the sample using the various functionalities of the X-Act software. Of particular importance were the ring filters used as an initial correction to account for the circular rings that appear in the data.

The result obtained was a group of two-dimensional slices, stored as very high resolution TIF image files., as the one seen in Figure 2-6. Each pixel of these slices contains the grayscale value associated to the corresponding voxel. In order to work with these data, stacks comprising several slices at each level with glass beads were created, utilising the data of the scan performed with the sensor located at the same vertical height. These images were cropped as a square (taking good care not to lose any information) around the cylindrical container to remove unnecessary data.

With a voxel size of 85 µm, a void ratio of around 0.82 and the D_{50} of 220 µm, the number of slices to be used to make up each slice was computed as: $\frac{220\mu\text{m}*10*0.82}{85\mu\text{m}} = 25.88$ slices/stack. Consequently, the results obtained would be representative of a layer spanning some 20 grains vertically stacked, which was considered big enough for a real representative volume of the thin layer investigated.

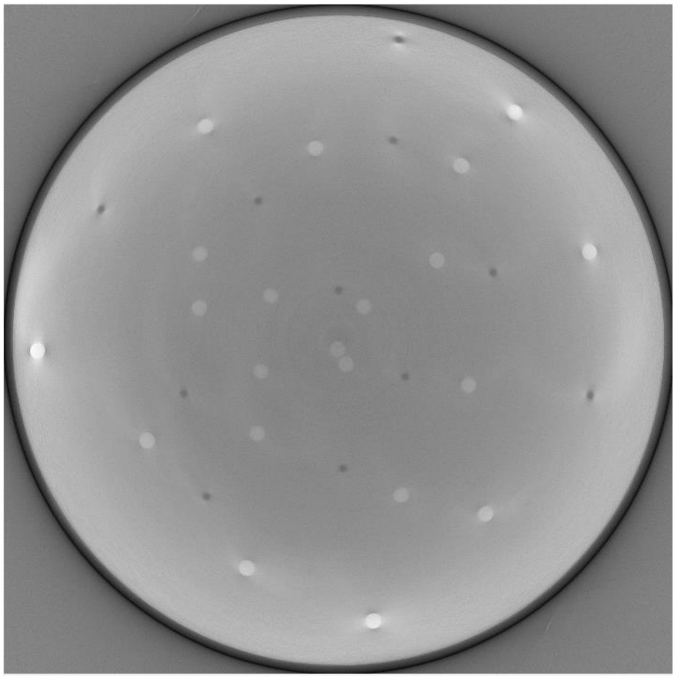

Figure 2-6. Example of a TIF file of a slice of the scan. The white/light grey circles are the hollow beads, whereas the dark grey circles are the glass beads.

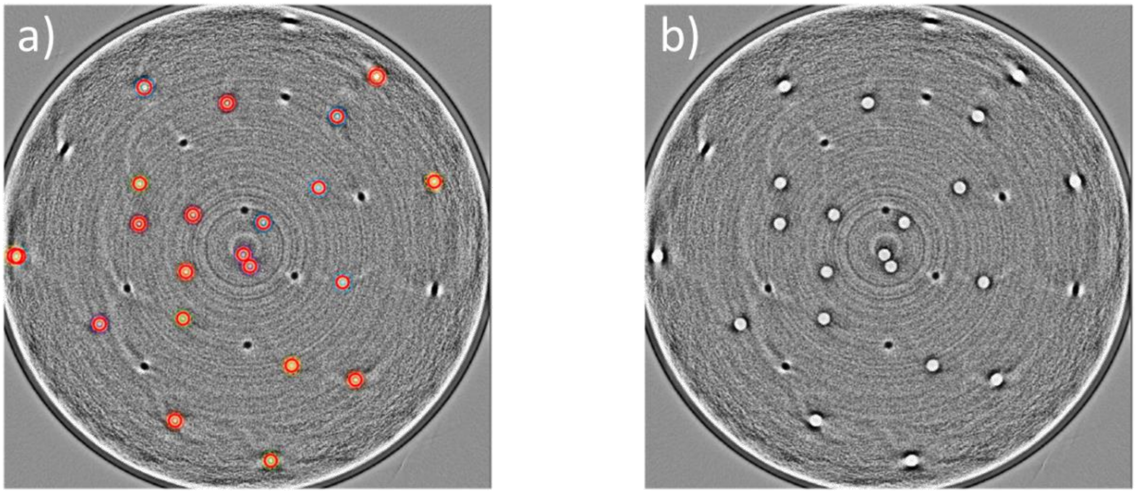

Figure 2-7. Images created to facilitate the identification of the beads. The white circles are the hollow beads, whereas the black circles are the glass beads.

These stacks were now reduced to a single TIF image obtained by averaging each pixel vertically along the stack. This average image was then subjected to some transformations aimed at exaggerating the contrast between the glass beads and the hollow beads, and the sand surrounding them. The transformations include enhancing the local contrast (Zuiderveld, 1994) making use of Contrast Limited Adaptive Histogram Equalization (CLAHE), a properly calibrated bandpass filter, and an image smoothing process. As observed in Figure 2-7, the resulting image clearly highlights both the hollow and the glass beads, which significant helps when subjecting the image to an automated circle detection method, as needed for the next step of the data treatment. Note that the grey level on this altered image is different from that in the original data; this image was only used to obtain and coordinates the position of the beads and as a general geometrical reference, while the actual data for the grey value is taken from the unaltered image. All these transformations were done by using the Fiji distribution for Ubuntu of the ImageJ software. Work was done on stacks of 30-40 slices.

Data processing

Some profiles extracted at various points of the section of the sample along the vertical direction of the sample are presented in Figure 2-8, using the data from the scan done with the sensors placed at the height of the middle of the sample. One observes that the change in grey value along the sample height is reasonably tiny. It was then concluded that the effects of beam hardening along the vertical direction are negligible. Beam hardening was then treated as a two-dimensional problem along each stack.

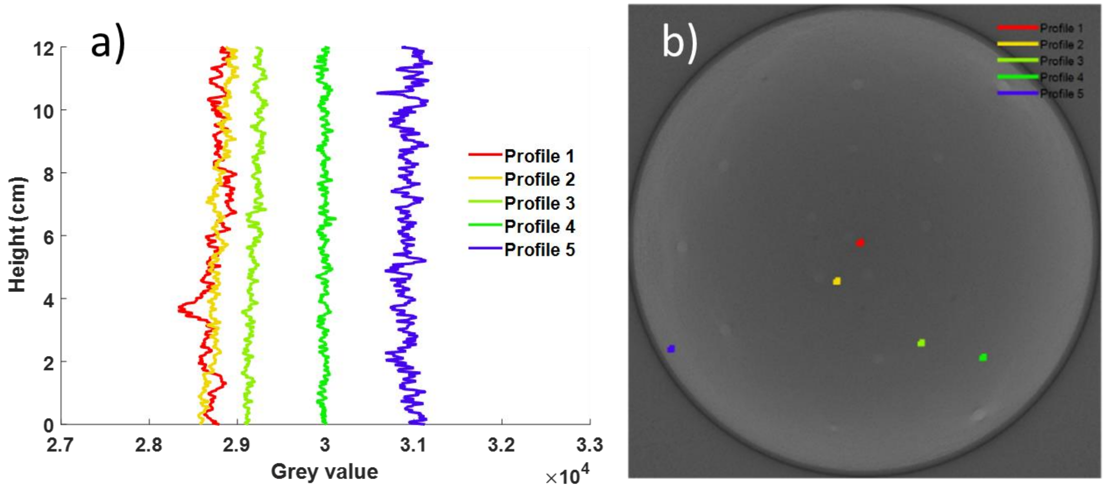

Figure 2-8. Vertical profiles plotted along the sample.

As already mentioned, the purpose of including silica and hollow beads in the sand sample was to correct the measured grey level with respect to the beam hardening effects. The beam hardening effect corresponds to the increase in grey level along a radius observed in Figure 2-9, with an increase independent of the direction and larger grey level at the sample periphery.

The *imfindcircles* function of the MATLAB computational environment, based on the Circular Hough Transform (CHT) was used to detect the position and radius of the beads in each plane. This was done separately for the glass and the hollow beads. It was then possible to construct a plot of the grey level as a function of the radii.

Seeking to verify the independence of this with the radial direction of measurement, an image was reconstructed mapping every bead to the positive horizontal axes, and the results of this procedure can be observed in the Figure 2-9. This data is plotted from the scan done with the sensor aligned with each layer, to exclude the effects from beam-hardening in the vertical direction (even though it was already established that they would be limited at worst). It is observed that the raw data is roughly homogeneous in the radial direction.

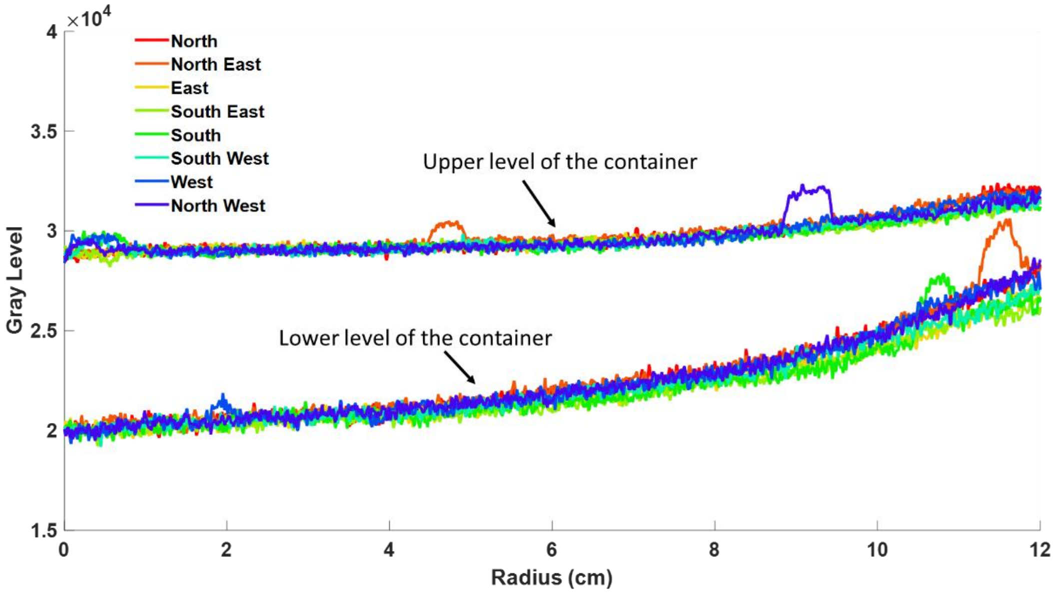

Figure 2-9. Radial profiles of the grey level in main directions at the top and the bottom of the sample. Effect of the Beam Hardening has a radial symmetry.

The same plot was constructed for standard deviation of the grey level (considering a small circle of 30 pixels for each point, except near the sample borders). These curves, shown in Figure 2-10 showed that the variation of the grey level remains mostly constant across the radius of the sample and in all directions; it can also be seen that the deviation corresponds to 1ess than 1.5% of the measured grey level.

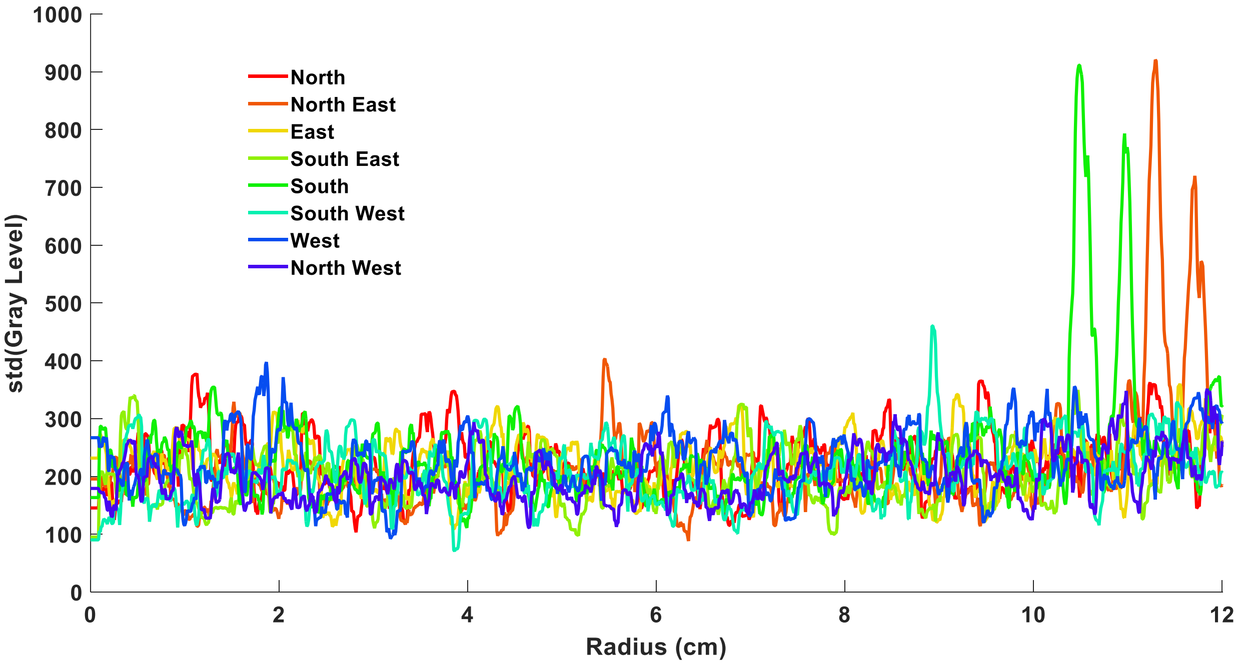

Figure 2-10. Standard deviation of the sample plotted in several directions. The peaks correspond to the beads.

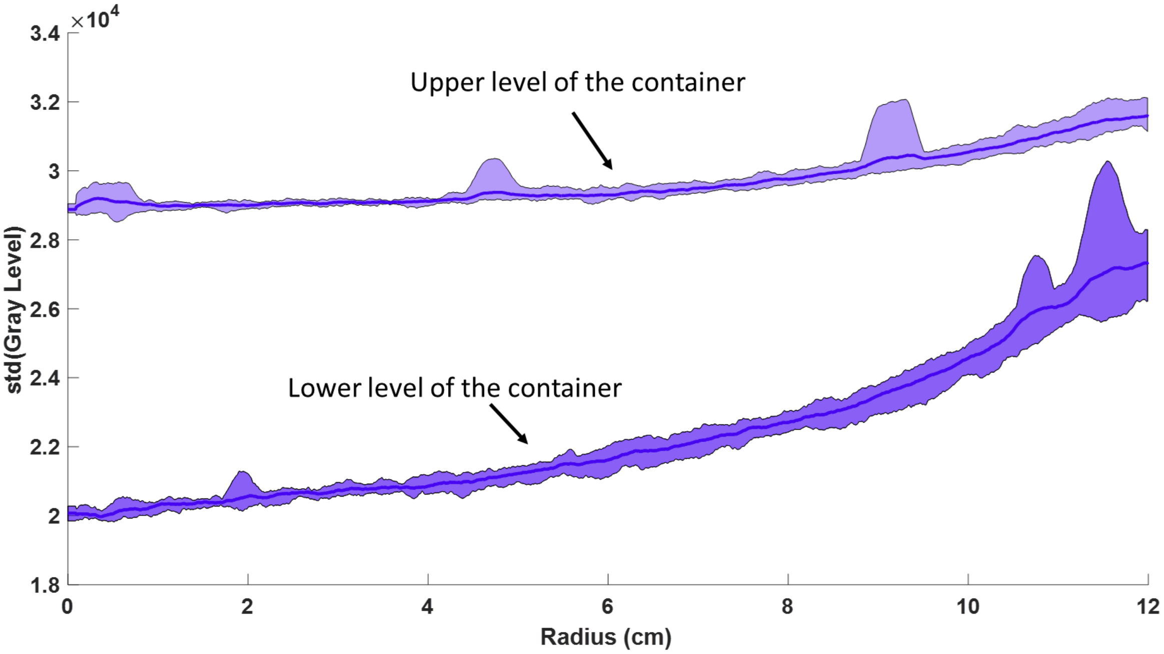

Figure 2-11. Graph showing the mean grey value plus and minus the standard deviation.

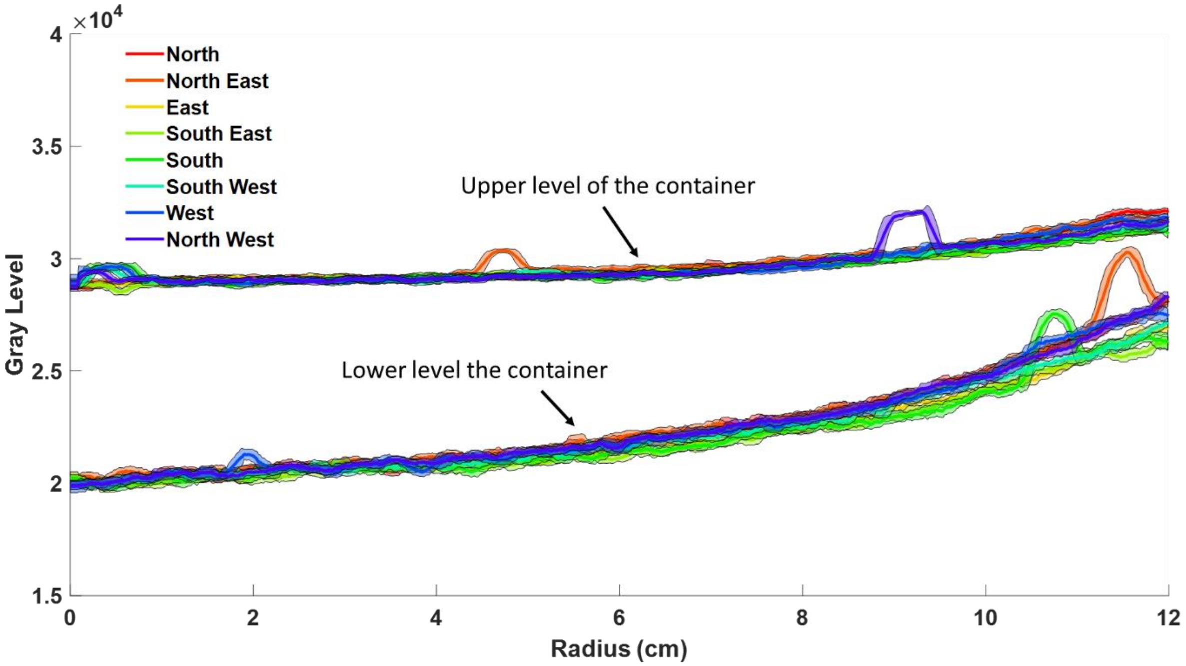

Figure 2-12. Graph showing the mean grey value plus and minus the standard deviation.

These two results where combined to observe the areas of greatest variation in sample Grey Level, resulting in the curves as the one shown in Figure 2-11. Apart from the beads, grey level standard deviation remains through most of the sample, but clearly increases towards the edges of the sample. It is also clear that the lower level of the sample is much less homogeneous than the top.

The same result is shown in all the main radial directions in Figure 2-12. While the upper level remains homogeneous, the lower level shows not only radial but also directional inhomogeneity, which can be appreciated in how the curves for each direction further deviate from each other as radius increases.

The radial changes in grey level of the hollow beads, the glass beads and the sand are presented in Figure 2-13. For the beads, discrete data are fitted by using a cubic polynomial extrapolation. Note that more bead data are available for the top layer (a) compared to the bottom one (b). During sample preparation, it was easier to place beads at exactly the same height at the sample top by using the top of the container as a reference, whereas this was more difficult at the bottom level, when mounting the sample.

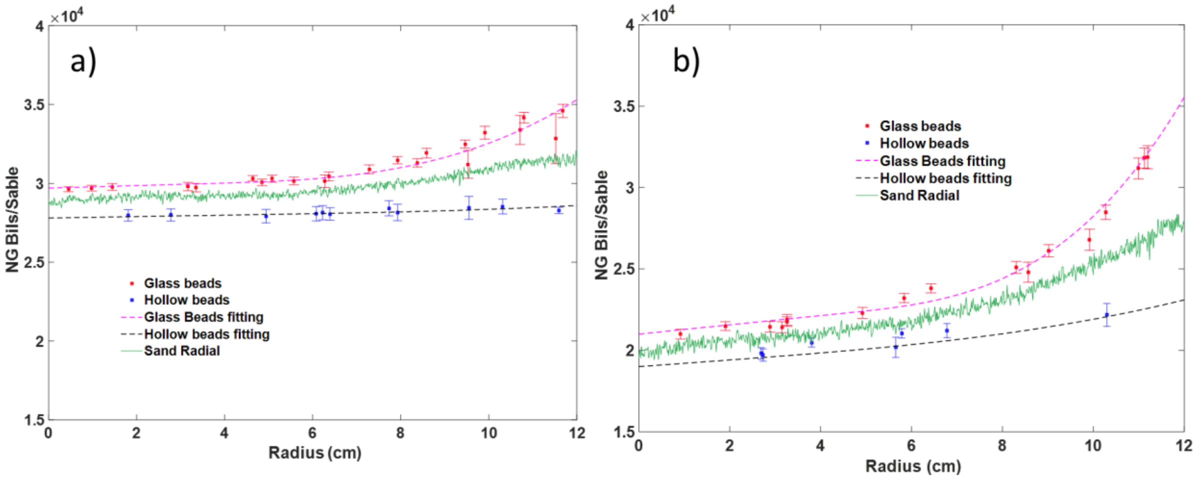

Figure 2-13. Radial changes in grey level (GL) for sand and bead: a) top level; b) bottom level.

These corrected data can be used to compute the density related to each pixel of the image. Assuming a nearly linear relation between the density *ρ(r)* at radius *r* and the grey level (GL), with a grey level GL1 for beads (silica) and GL0 for hollow beads (corresponding to the air in the pores), the following relation can be easily established:

$$\rho_r(r) = \frac{1}{\left(GL_1(r) - GL_0(r)\right)} GL(r) - \frac{GL_0(r)}{GL_1(r) - GL_0(r)}$$

where $GL(r)$ is the grey level from experimental data, $GL_1(r)$ is the grey level at radius *r* based on the cubic polynomial model for glass beads data and $GL_0(r)$ is the grey level of hollow beads. The density results are presented in colour map in Figure 2-14 for the upper and lower sections. Some profiles along several directions are also presented for the top level in Figure 2-15 and for the bottom level in Figure 2-16.

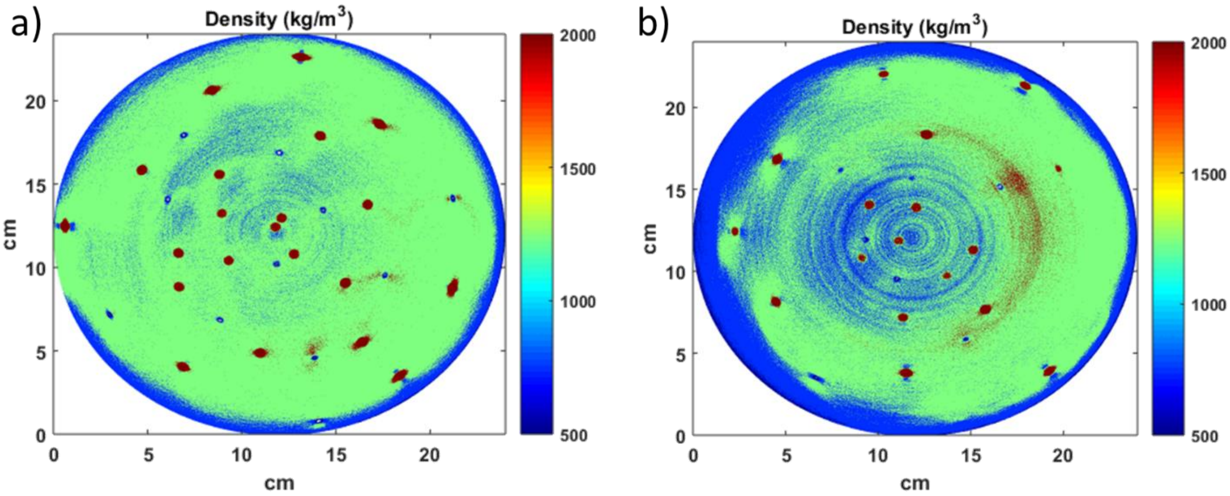

Figure 2-14. Density value colormap, shown for the a) upper and b) lower levels.

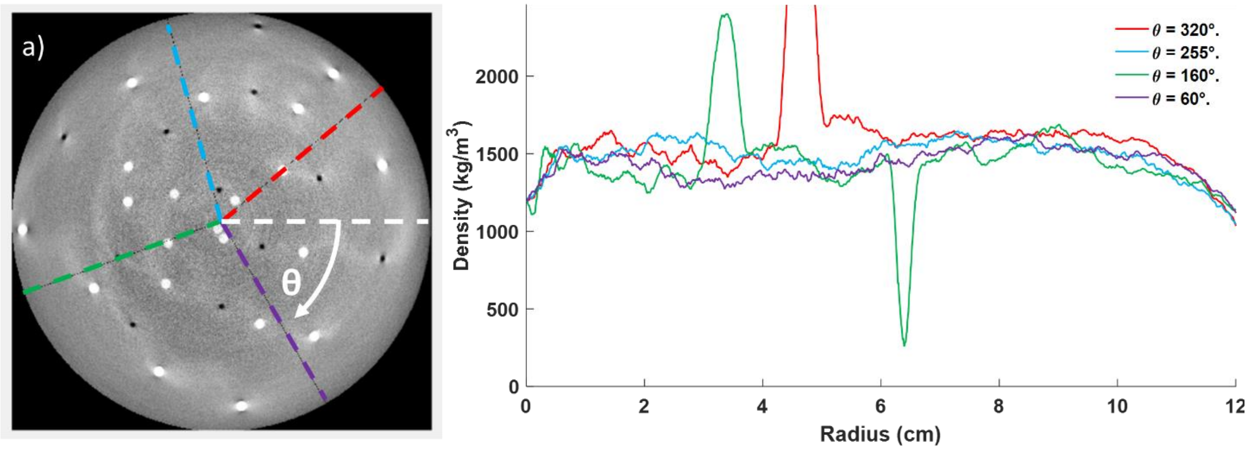

Figure 2-15. Radial density profiles along the upper level of the sample. The top and down peaks corresponds to crossing beads; one silica bead has been crossed at 320° (red curve) and two beads (silica and hollow bead, respectively) have been crossed at 160° (green curve).

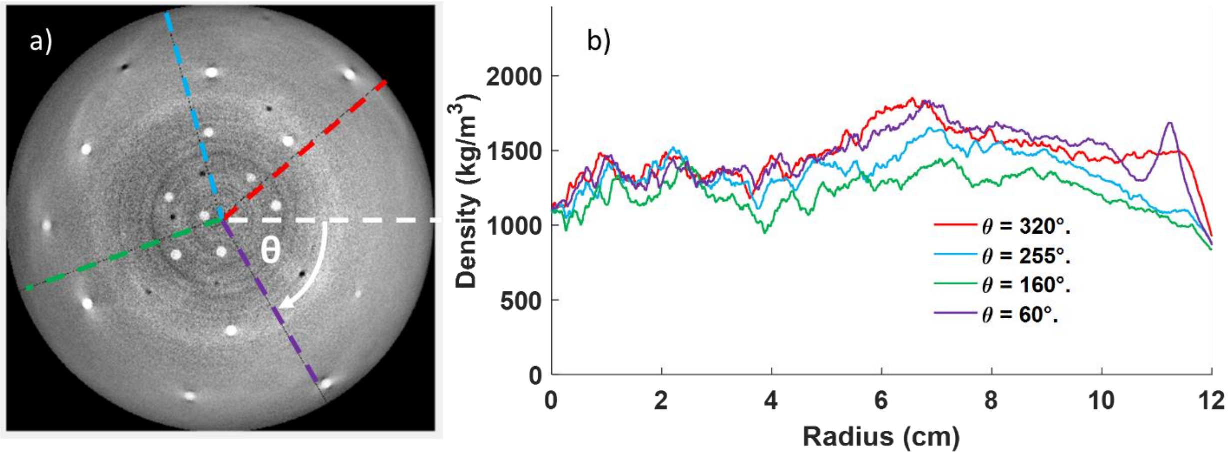

Figure 2-16. Density profiles along the lower level of the sample.

Discussion

The changes in grey value with respect to the radius presented in Figure 2-13 for both top and bottom layers of beads show that, as expected, the average greyscale values of the tested material (a mix of sand and air) are between the highest values of the glass beads, that corresponds to the silica that constitute the sand grains (curve on top) and the smallest values of the hollow beads that correspond to air. All three curves are significantly affected by the beam hardening effect.

Inspection of the corrected density values presented in colour map in Figure 2-14 and of the density profiles along various angles (60, 160, 255 and 320°) in Figure 2-15 and Figure 2-16 on the top and bottom sections, respectively, shows a better homogeneity on the top section. Along the directions investigated, density values are between 1300 and 1600 kg/m^3 (not including the value of the beads) are obtained on the top section, where the peaks of a silica bead is observed at 60° with also two peaks of silica and hollow beads, respectively, at 320°. Data are less good on the bottom section, with density between 1000 and 1600 kg/m^3. Note however that the dominant green colour observed in the colour map of Figure 2-14 on the top section (density around 1100-1400kg/m^3) indicate a rather satisfactory global homogeneity. The worse homogeneity of the bottom section is also clear in the Figure 2-14, with various blue spots indicating looser areas.

It is also observed that, for both sections, loose areas with density values below 1000 kg/m^3 appear at the periphery of the cylinder in contact with the container wall, indicating that the grains coming in this area, with a higher velocity after rolling over the whole slope of the pile on the top of which they have been poured, are arranged in a significantly looser arrangement. Note that this is also true at the centre of the samples, as seen in the density profiles of Figure 2-15 and Figure 2-16, with densities of 1250 and 1100 kg/m^3, respectively. The path followed by these grains is significantly different from that of the former ones along the periphery, given that they are not supposed to have rolled over the slope of the pile, but to have stayed in the place where they have flowed from the funnel at zero height. For comparison, sample global density was estimated at 1423.37 kg/m^3.

It is also observed that for both sections the highest levels of deviation for sample density appear towards the vicinity of the container walls, where density drops significantly compared to the values near the middle, as seen in Figure 2-15; the lowest values of density of each cross sections are found here, diverging as much as 18% from the significantly more uniform values found at the middle of the sample. It is possible that this elevated density is due to the lower kinetic energy level of the particles reaching the wall of the sample container after a brief slide, in contrast to the denser deposition at the middle of the sample, deposed directly with high energy impacting from a fall. This is consistent to what is observed at the energic layer proposed by Emam (Emam et. Al, 2005), in which the still falling particles contact the sand surface and result in denser deposition at the surface as the particle media accumulates, and lesser as it slides away.

In contrast, less satisfactory results were obtained for the measurements taken at the lower level of the sample, as seen in Figure 2-16. The lesser number of hollow beads available for model calibration at this level might also be partially related to the observed variation level. Nevertheless, it appears that even this rather simple variation of the pluviation technique can be used to obtain sufficiently homogeneous large samples, at least for work done in the middle of the surface of the material.

Conclusions

Density uniformity measurements were performed on loose arrangements of Fontainebleau Sand. The material is currently being utilised as a Martian regolith analogue for the study of the mechanical properties of the soil existing at the InSight mission landing site.

A series of three x-ray microtomograph scans were performed on a cylindrical sample to determine whether simple pluviation with a funnel was sufficient to obtain a uniform value of density throughout the sample. A system of glass and hollow beads were successfully utilised to correct the data from the directly measured values to account for the effect of beam-hardening on the acquired 3D imaging. These effects were to be observed to be of relevance only on the horizontal direction. Beam hardening effects on the value of the grey level was observed to be independent of the direction thanks to the sample being scanned from all the directions all 360° around. The variation through the radius was properly fitted with a cubic polynomial, and it is considered that this key phenomenon was properly accounted for in the results interpretation of this work.

Reduced density variation was observed near the middle of the sample, which confirms that as expected this area is suitable for testing. In contrast, a moderate significant of values appears to take place near the walls of the sample. Material at the top of the sample appears to be significantly more homogeneous than the one located at the bottom of the sample. Nevertheless, it appears that this simplified version of the pluviation technique is adequate enough to produce homogeneous samples as long as the testing is limited to the middle of the sample, without too many worries in depth other than the ones associated to eventual boundary effects.

References

Alshibli, K. A., & Hasan, A. (2008). Spatial variation of void ratio and shear band thickness in sand using X-ray computed tomography. Geotechnique, 58(4), 249–257. https://doi.org/10.1680/geot.2008.58.4.249

Borja, R. I., Song, X., Rechenmacher, A. L., Abedi, S., & Wu, W. (2013). Shear band in sand with spatially varying density. Journal of the Mechanics and Physics of Solids, 61(1), 219–234. https://doi.org/10.1016/j.jmps.2012.07.008

Brooks, R. A., & Di Chiro, G. (1976). Beam hardening in X-ray reconstructive tomography. Physics in Medicine and Biology, 21(3), 390–398. https://doi.org/10.1088/0031-9155/21/3/004

Chao-Fa, Z., Pinzón, G., Wiebicke, M., Andò, E., Niels, P. K., & Viggiani, G. (2017). Chao-Fa, Zhao Gustavo Pinzón. Computers and Geotechnics.

Chen, Y., Gélébart, L., Chateau, C., Bornert, M., King, A., Aimedieu, P., Sauder, C., Chen, Y., Gélébart, L., Chateau, C., Bornert, M., & King, A. (2017). Caractérisation des mécanismes d ' endommagement des tubes CVI-SiC / SiC par tomographie X To cite this version : HAL Id : hal-01598516 Caractérisation des mécanismes d ' endommagement des tubes CVI -SiC / SiC par tomographie X Characterization of damage .

Delage, P., Betancourt, J. C., Hormaza, B. C., Karakostas, F., Laure, E. D. E., Lognonné, P., Antonangeli, D., & Banerdt, B. (2020). The interaction between the SEIS seismometer of the InSight Martian mission and a regolith simulant. Géotechnique.

Emam, S., Roux, J.-N., Canou, J., Corfdir, A., & Dupla, J.-C. (2005). Granular packings assembled by rain deposition: an experimental and numerical study. In T. & Francis (Ed.), Powders and Grains 2005, Two Volume Set (p. 4). CRC Press.

Flitti, A., Della, N., De Kock, T., Cnudde, V., & Verástegui-Flores, R. D. (2021). Effect of initial fabric on the undrained response of clean Chlef sand. European Journal of Environmental and Civil Engineering, 25(13), 2441–2456. https://doi.org/10.1080/19648189.2019.1631217

Gade, V. K., & Dasaka, S. M. (2017). Assessment of Air Pluviation Using Stationary and Movable Pluviators. Journal of Materials in Civil Engineering, 29(5). https://doi.org/10.1061/(asce)mt.1943-5533.0001798

Grott, M., Piqueux, S., Spohn, T., Knollenberg, J., Krause, C., Marteau, E., Hudson, T. L., Forget, F., Lange, L., Müller, N., Golombek, M., Nagihara, S., Morgan, P., Murphy, J. P., Siegler, M., King, S. D., Banfield, D., Smrekar, S. E., & Banerdt, W. B. (2023). Seasonal Variations of Soil Thermal Conductivity at the InSight Landing Site. Geophysical Research Letters, 50(7). https://doi.org/10.1029/2023GL102975

Jafri, N. J. S., Rahim, M. A. A., Bawadi, N. F., Zahid, M. Z. A. M., Ahmad, M. M., & Mansor, A. F. (2018). Determination of dry density ratio of compacted soils using sand replacement method. AIP Conference Proceedings, 2013(October). https://doi.org/10.1063/1.5054213

Kodicherla, S. P. K., Gong, G., Fan, L., Moy, C. K. S., & He, J. (2018). Effects of preparation methods on inherent fabric anisotropy and packing density of reconstituted sand. Cogent Engineering, 5(1), 1–14. https://doi.org/10.1080/23311916.2018.1533363

Kolbuszewski, J. . (1984). International society for soil mechanics and foundation engineering. Geotextiles and Geomembranes, 1(2), 161–162. https://doi.org/10.1016/0266-1144(84)90012-8

Miura, S., & Toki, S. (1982). A sample preparation method and its effec on static and cyclic deformation-strength properties of the sand. Japanese Society of Soil Mechanics and Foundation EngineeringJapanese Society of Soil Mechanics and Foundation Engineering, 22(1), 61–77. http://www.mendeley.com/research/geology-volcanic-history-eruptive-style-yakedake-volcano-group-central-japan/

Oda, M. (1972a). Initial fabrics and their relations to mechanical properties of granular material. Japanese Society of Soil Mechanics and Foundation Engineering, 12(1), 17–36. http://www.mendeley.com/research/geology-volcanic-history-eruptive-style-yakedake-volcano-group-central-japan/

Oda, M. (1972b). The mechanism of fabric changes during compressional deformation of sand. Japanese Society of Soil Mechanics and Foundation Engineering, 2(1), 17–36. http://www.mendeley.com/research/geology-volcanic-history-eruptive-style-yakedake-volcano-group-central-japan/

Saadi, F. Al, Wolf, K.-H., & Kruijsdijk, C. van. (2017). Characterization of Fontainebleau Sandstone: Quartz Overgrowth and its Impact on Pore-Throat Framework. Journal of Petroleum & Environmental Biotechnology, 08(03). https://doi.org/10.4172/2157-7463.1000328

Siddiquee, M. S. A., Islam, M. S., Tatsuoka, F., & Islam, M. K. (2018). An Anisotropic Model for Granular Material Based on Experiments. Geotechnical and Geological Engineering, 36(3), 1447–1462. https://doi.org/10.1007/s10706-017-0400-z

Tabaroei, A., Abrishami, S., & Hosseininia, E. S. (2017). Comparison between Two Different Pluviation Setups of Sand Specimens. Journal of Materials in Civil Engineering, 29(10), 1–11. https://doi.org/10.1061/(asce)mt.1943-5533.0001985

Tatsuoka, F., Iwasaki, T., Fukushima, S., & Sudo, H. (1979). Cyclic undrained triaxial and torsional shear strength of sands for different sample preparation methods. Japanese Society of Soil Mechanics and Foundation Engineering, 19(1), 39–54. https://www.jstage.jst.go.jp/article/bpb1993/17/11/17_11_1460/_pdf/-char/ja

Tatsuoka, F., Ochi, K., Funjii, S., & Okamoto, M. (1986). Cyclic undrained triaxial and torsional shear strength of sands for different sample preparation methods. Japanese Society of Soil Mechanics and Foundation Engineering, 26(3), 23–41. http://www.mendeley.com/research/geology-volcanic-history-eruptive-style-yakedake-volcano-group-central-japan/

Thiery, C. (2013). Tomographie à rayons X Tomographie à rayons X. Techniques de l'ingénieur. P950 V3 (2013) 1–30. https://doi.org/10.51257/a-v1-p950

Vaid, Y. P., Sivathayalan, S., & Stedman, D. (1999). Influence of Specimen-Reconstituting Method on the Undrained Response of Sand. Geotechnical Testing Journal, 22(3), 187–195. https://doi.org/10.1520/gtj11110j

Wanatowski, D., & Chu, J. (2008). Effect of specimen preparation method on the stress-strain behavior of sand in plane-strain compression tests. Geotechnical Testing Journal, 31(4), 308–320. https://doi.org/10.1520/gtj101307

Yamamuro, J. A., & Wood, F. M. (2004). Effect of depositional method on the undrained behavior and microstructure of sand with silt. Soil Dynamics and Earthquake Engineering, 24(9–10), 751–760. https://doi.org/10.1016/j.soildyn.2004.06.004

Zlatovic, S., & Ishihara, K. (1997). Normalized behavior of very loose non-plastic soils: effect of fabric. Soils and Foundations, 37(4), 47–56. http://www.mendeley.com/research/geology-volcanic-history-eruptive-style-yakedake-volcano-group-central-japan/

Zuiderveld, K. (1994). Contrast Limited Adaptive Histogram Equalization (CLAHE). In Academic Press. https://la.mathworks.com/matlabcentral/fileexchange/22182-contrast-limited-adaptive-histogram-equalization-clahe?s_tid=FX_rc2_behav.

3. THE INTERACTION BETWEEN THE FOOT OF SEIS AND THE MARTIAN REGOLITH

> *"If I have seen further, it is by standing on the shoulders of giants".*
>
> *Isaac Newton, 1676.*

The goal of the experimental activity of this chapter is to investigate the interaction between the foot of the SEIS seismometer and a simulant of the Martian regolith at the InSight landing site. The seismometer foot was designed at the CERMES group at École des Ponts ParisTech by performing experiments carried out on three regolith simulants (Delage et al., 2017). This investigation was updated by improving the experimental device to achieve higher precision with tests carried out on Fontainebleau sand as a simulant and has been published in a paper that is presented in this chapter.

3.1. The feet of the SEIS instrument

The SEIS instrument stands on three feet on the surface of Mars. These feet were designed at CERMES, the geotechnical group of the Navier laboratory at École des Ponts ParisTech. Tests were intended to guarantee that the instrument would be correctly supported by a satisfactory penetration into the surface layer.

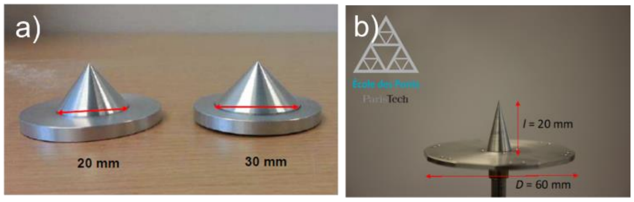

Figure 3-1. Design of the SEIS feet: a) Alternatives investigated and b) Final design of the feet of the SEIS instrument (Karakostas et al., 2013).

Several foot shapes have been tested (see Figure 3-1a) and the performance of the final design was checked on tests on a sand bed on Earth (Figure 3-2). The final form consists of a 60 mm disk with a conical spike in its axis, where the cone has 20 mm in height and 10 mm in diameter, as seen in the Figure 3-1b (Delage et al., 2017).

Figure 3-2. Testing of the SEIS instrument on Earth. (SEIS: Insight's Seismic Experiment for Internal Structure of Mars (2019))

THE INTERACTION BETWEEN THE FOOT OF SEIS AND THE MARTIAN REGOLITH

Although the landing site was selected to be as flat as possible, it was necessary to compensate for some possible inclination, which was achieved through the development of the mechanical levelling system (LVL), capable to accomodate inclinations up to 15° (Morgan et al., 2018). To correctly process the SEIS signals, it was necessary to know the transfer function of the LVL. An analytical model was developed in this regard. Based on a sensitivity analysis performed by Fayon et al., (2018), it was established that the key inputs for the model are the mechanical response of the foot – soil interaction. The most important parameters of the model are the spring constants characterising the force-displacement response between the seismometer foot and the Martian regolith. These variables are the horizontal stiffness k_h^g and the torque C_h^g , respectively, defined as follows:

$$k_h^g = \frac{16(1-\nu)Ea}{(7-8\nu)(1+\nu)} \qquad (1)$$

where k_h^g is the horizontal spring constant, ν is the Poisson ratio, E is the Youngs modulus and a is the radius of the seismometer foot, and

$$C_h^g = \frac{4Ea^3}{3(1-\nu)^2} \quad (2)$$

where C_h^g is the torque induced on the ground by the seismometer feet.

To determine parameter k_h^g, penetration tests of the foot in a regolith simulant, that are described later on, were carried out.

The model of the seismometer foot consists of a 1 kg mass on top of the designed foot, that correspond on Mars to that supported by a foot.

Given that the mass of SEIS is 7467 g in total.

$$m_{SEIS} = 7467g$$

With $g_{Mars} = 3.711m/s^2,$ the weight of SEIS on Mars is:

$$W_{SEIS}^{Mars} = 7467 * g_{Mars} = 27.71N$$

Resulting in each of the three feet on SEIS having to support $W_{SEIS_{foot}}^{Mars} = 9.2367N$

To apply the same force on Earth, the mass needed would then be:

$$m_{SEIS}^{eq} = \frac{9.2367N * s^2}{9.81m} = 0.94\ kg$$

Leading to the use of a 1 kg mass.

3.2. Experimental setup

The first concept of the test can be seen in Figure 3-3 (Karakostas et al. 2013). The soil is placed in a container (240 mm diameter and 120 mm height) put on the plateau of a triaxial press. The foot model is held by a spring used as force sensor. LVDT displacement sensors are used to measure the displacement of the press. By raising the press plateau, the foot contacts the soil and penetrates the surface.

The need of more accurate measurements resulted in substantial modifications with respect to the original setup. Most of the sensors were replaced and several components were added to strengthen the device.

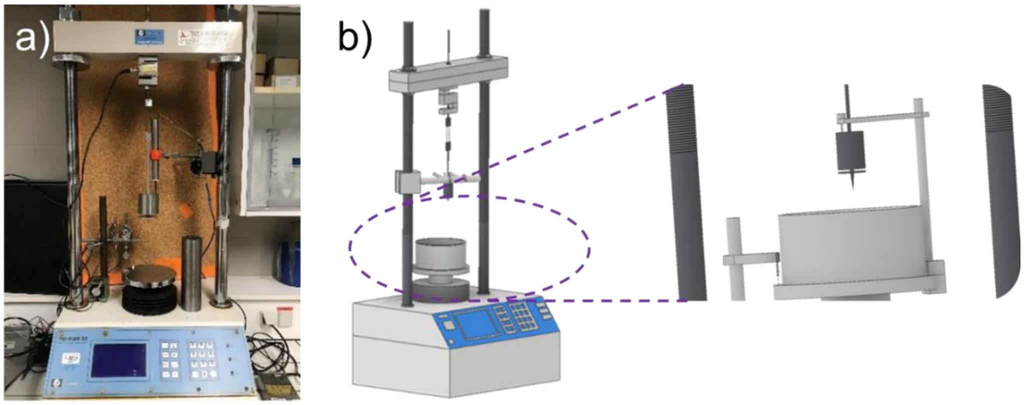

Figure 3-3. The experimental setup used (Tri scan 50 triaxial press)

The triaxial press has a high accuracy in velocity (0.01 µm/min, as seen in Figure 3-4) and displacement. One of the first modifications was to change the displacement sensor for a more accurate alternative.

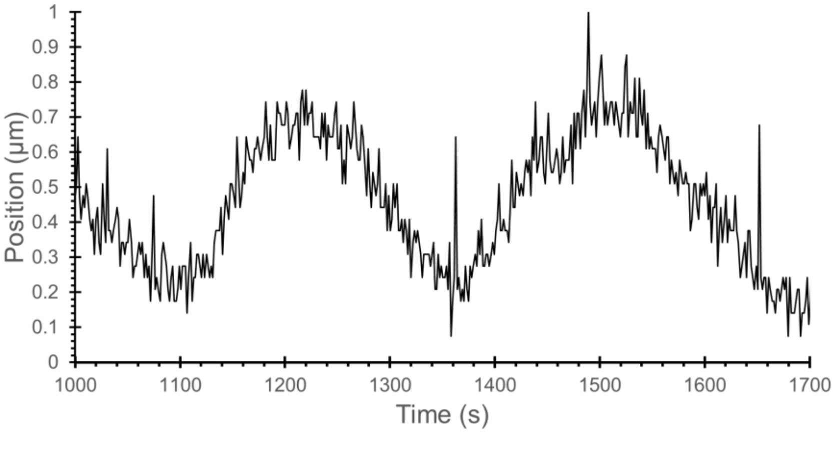

Figure 3-4. Some of the cycles performed to validate press displacement accuracy.

Extensive testing was carried out to evaluate the accuracy of different available displacement sensors. One considered a no-contact Eddy current displacement sensor (see Figure 3-5), that featured acceptable accuracy but only along a too small measurement range (1.5 mm). A better alternative was found with available LVDT sensors.

Using two LVDTs makes it possible to determine penetration of the foot in the soil sample. All sensors were connected to a LabVIEW developed interface.

Figure 3-5. Testing process of displacement sensors. The non-contact Eddy sensor is seen in the middle.

A recent work at CERMES (Belmokhtar et al., 2018) demonstrated an accuracy of LVDT about 0.1 µm. Two LVDTs were selected, with measurement ranges of 4.5 and 25 mm, respectively to monitor the soil penetration into the soil.

Two LVDT sensors were thus selected, which had range measurements of 4.5mm and 25 mm respectively. These could now be used to monitor the soil penetration into the soil once the setup was adapted for the purpose, all while maintaining sufficient accuracy well below 0.1 µm.

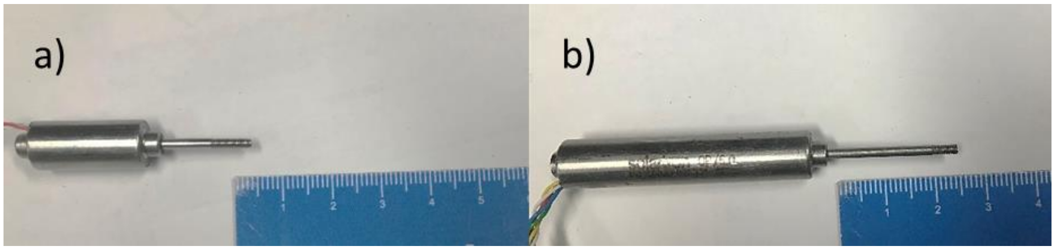

Figure 3-6. The selected LVDT sensors have a measurement range of a) 4.5mm and b) 25 mm respectively.

The force sensor was upgraded to accurately measure a force below 10 N and the S-cell seen in Figure 3-7 was selected, with a range of 25 kN and a +/-0.05 N accuracy.

Figure 3-7. The S-cell force sensor selected.

To achieve satisfactory accuracy with no effects of thermal dilation of the system (press and sensors) on the displacement measurements, a thermal insulation box made up of polystyrene and cork (Figure 3-8) was placed around the whole device.

Figure 3-8. Thermal isolation box surrounding the experiment.

The thermal performance of the insulating box was verified by several day/night temperature measurements (up to 36h), showing that temperature changes were reduced to 0.5°C (see data in the paper below). Data acquisition of the various sensors was made by a Keysight 34970A data acquisition unit (Figure 3-9).

Figure 3-9. The used data acquisition unit.

The temperature inside the device was monitored by using type J thermocouples (Figure 3-10), with a precision of 0.015 °C.

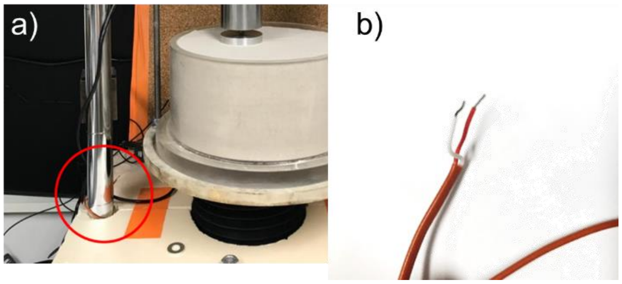

Figure 3-10. The b) type J thermocouple placed a) inside the setup to monitor temperature during experiments.

The final setup can be seen in Figure 3-11. Note that the sensors have been fixed to a stiff metallic structure to improve accuracy; Both thermal and mechanical insulations have been placed below the container, with a polystyrene and a thick aluminium plate.

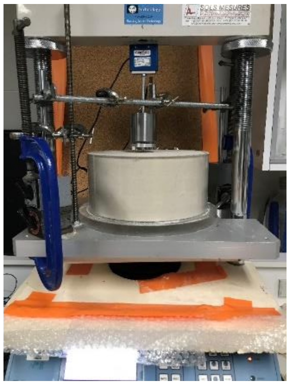

Figure 3-11. The definitive experimental setup (without the thermal box to see it)

All components can be seen in Figure 3-12, including the sensors, the data acquisition card and also 3 data track tracker 200 units for calibrating the different sensors and the 2 Solartron OD5 signal conditioners for the sensors.

Figure 3-12. All system components.

The experimental procedure for the test is presented next.

3.3. The experimental procedure

The sample is prepared, close to the triaxial press, by using a funnel to deposit the Fontainebleau sand in the container (see Figure 3-13), as described in the previous chapter. The sample is weighed to determine its density. This deposition technique made it possible to obtain density between 1400-1500 kg/m^3, corresponding to a density index I_D of 6-8%. The container is then placed on the plateau of the triaxial press with great care to avoid any change of the loose arrangement of sand grains.

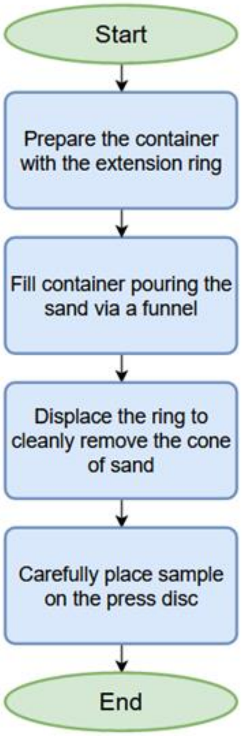

Figure 3-13. Sample preparation procedure.

The three sensors are placed, and the data acquisition system is activated. The LVDT sensors are placed only once the foot model is placed close enough to the sample surface, due to their reduced range.

Test procedure is summarized in Figure 3-14. Before starting the test, temperature stabilization must be attained, which takes about 14 hours. The sample has hence to be prepared the day before the test within the thermal insulation box to stabilize temperature during the night. The next morning, the change in temperature is checked and the test is started when temperature remains stable within +/-0.1°C. Temperature was monitored during all the test duration.

A slow displacement rate of 0.01 mm/min is applied to move upwards the plateau. The rate was chosen after some testing confirming that the response did not depend on it. Various loading and unloading cycles are then applied by changing the displacement direction of the press. The detailed test program for these tests can be seen in the article in Table 3-2.

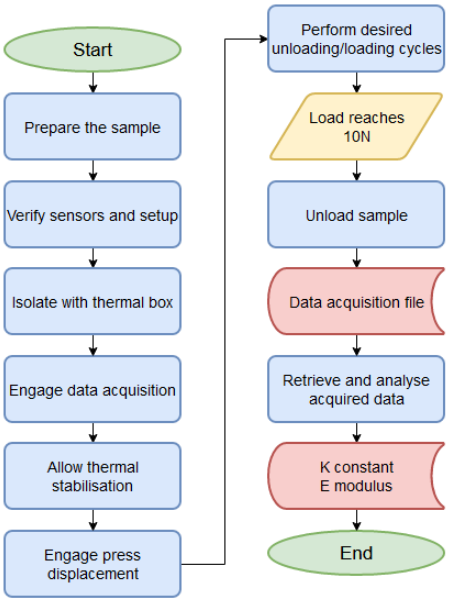

Figure 3-14. Simplified schema of the experimental procedure of each test.

The first tests were conducted using a flat disk that was replaced by the actual SEIS foot with a spike in its axis.

3.4. Experimental program results, analysis, and interpretation

Several series of tests were conducted to reach the final configuration, with many modifications resulting from successive problems resolved thanks to the help of the technical team. A definitive program comprising 10 tests with the disc setup, and 3 with the seismometer foot setup were performed. From each test, a load-displacement curve is plotted. The initial segment of the curve is the consequence of both plastic and elastic strains of the soil; on the unloading/reloading cycle, elastic behaviour is observed, and the slope K of the cycle can be calculated that can be converted into the desired Young modulus *E* by considering the stress field taking place around the seismometer feet. The results obtained during these experiments are presented in the article at the end of this chapter.

The results obtained during these experiments are presented in the article at the end of this chapter.

3.5. Finite element verification

Several Finite Element Method calculations were made by using the commercially available PLAXIS code, taking advantage of the cylindrical symmetry of the experimental setup. Particular interest was devoted to check the boundary conditions imposed by the container to check whether the infinite half-space assumption adopted in some calculations was valid.

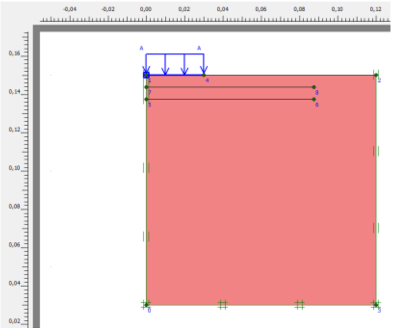

Figure 3-15. Base model with actual sample dimensions of the container.

Several scenarios were evaluated; to achieve this, a base departure model with 20 MPa material module and the actual inner dimensions of the container was prepared, as seen in Figure 3-15. The metallic plate was modelled as being infinitely rigid. It was then modified to a model with double the size to evaluate the difference in the wall settlement, but only a marginal difference of 5.8 x 10^{-4} μm/N vertical displacement at the wall (0.01 μm being the base result) was observed under the 10N loading condition, and 0.04 μm/N difference at the middle (2.6 μm being the result). Another condition taken into consideration after the suggestion of the article reviewers was the consideration of different layer *E* modules with depth (see Figure 3-16). To achieve this, the model was discretized in depth using a series of fine layers (modules are detailed in Table 3-1) with each one being 1 cm thick.

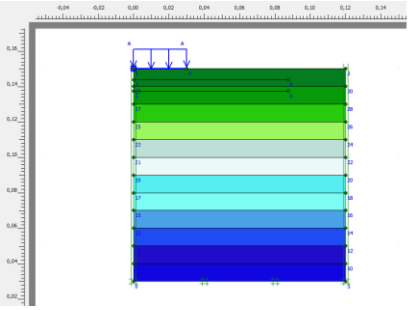

Figure 3-16. The model built with discretized fine soil layers.

It is necessary to remark that the level of stress being considered is extremely low. This can be appreciated when considering the existing relations of the *E* modulus with stress, which were determined with the use of the following expression. The expected range of values for different void ratios of the material can be estimated in terms of stress. Various relationships of the following form are usually considered:

$$E = K_E \cdot f(e) \left(\frac{p}{p_a}\right)^n \cdot p_a \qquad (3)$$

Here, E is the Youngs modulus, $f(e)$ is a function of the void ratio (several choices are available), p is the confinement stress, p_a is the atmospheric pressure, and n is a power usually chosen to be 0.45-0.5 depending on the void ratio function of choice. The values of several of these void ratio functions for the material in consideration are presented in Figure 3-17.

As can be appreciated in Figure 3-18, the usual order of magnitude is at least in the hundreds of kPa, whereas in the performed measurements these values barely reach 4 kPa. In this segment, the effect of the Density Index I_D variation is unclear, since as it is seen in the figure the lines almost superpose each other. The currently existing relationships are thus inadequate at this level. The obtained results therefore provide valuable insight into this mostly unexplored range of stresses and strains.

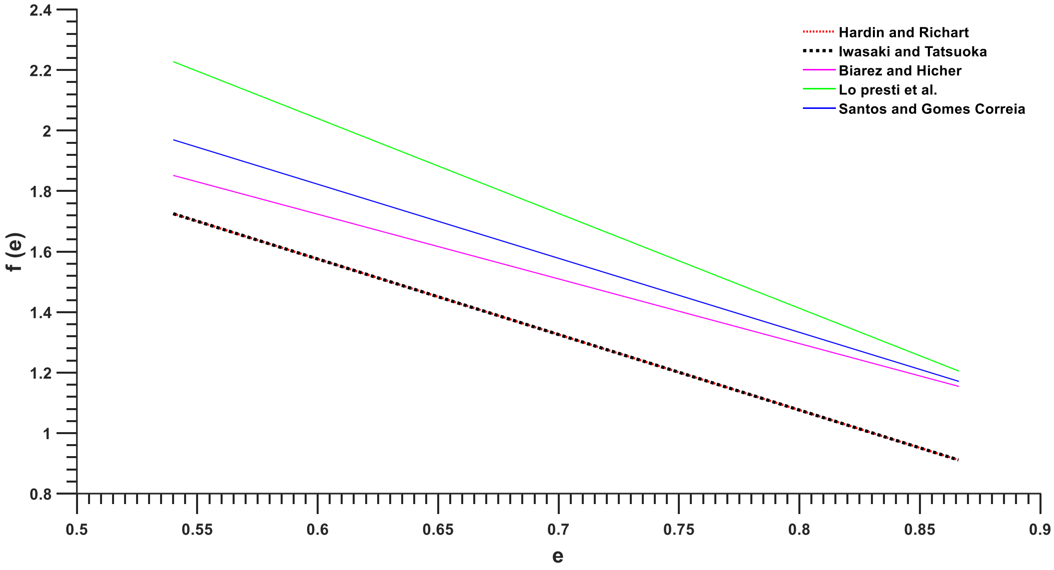

Figure 3-17. Several void ratio functions evaluated for Fontainebleau sand.

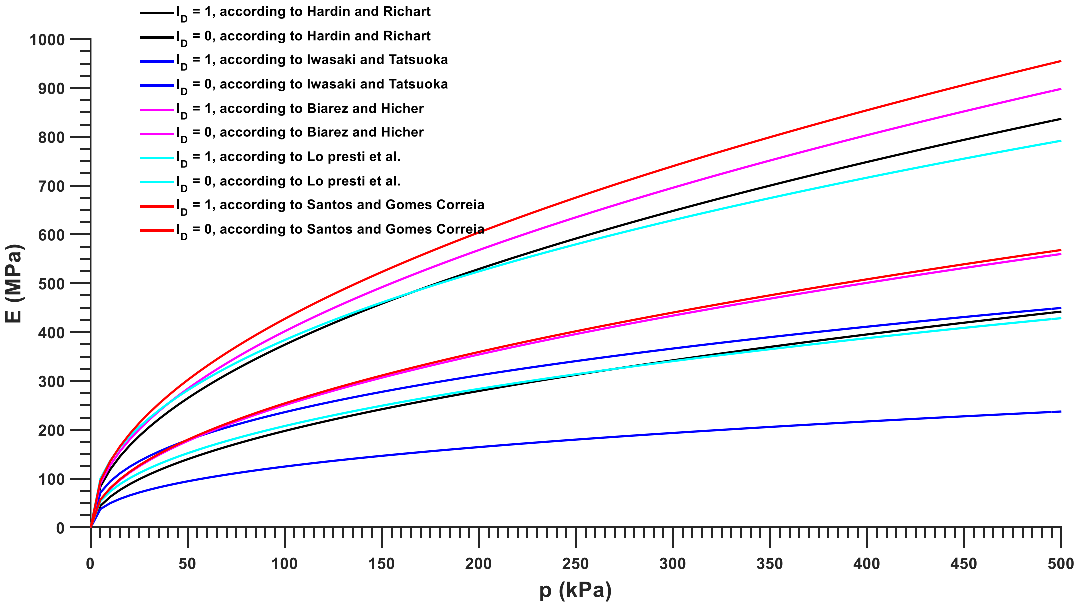

Figure 3-18. Shear moduli for Fontainebleau sand predicted in terms of stress.

However, the differences again turned negligible due to the difference in stresses from the bottom layer to the top layer being less than 1.75 kPa (2.6 μm displacement at the middle being the result). With these scenarios analysed, it was concluded that the boundary condition has negligible effect, and the assumptions are valid.

It is worth noting that modelling the soil behaviour during the penetration process (outside the loading-reloading cycles) with conventional constitutive models available such as Linear Elastic or Hardening soil may not be possible as the existing models are not well suited to the early but very small plastic strains that occur at these very low stresses. Consequently, these results only intend to send as a validation of what happens in the very small unloading-reloading cycles done on the sample and are limited to the verification of the boundary conditions effects.

Table 3-1. Module values for each model layer.

Layer	E (MPa)
1	9.68
2	13.68
3	16.76
4	19.35
5	21.64
6	23.70
7	25.60
8	27.37
9	29.03
10	30.60
11	32.09
12	33.52

3.6. Conclusions

Refer to conclusions in the article below.

3.7. The interaction between the SEIS seismometer of the InSight Martian mission and a regolith simulant (Article 2: Published)

PIERRE DELAGE, JUAN-PABLO CASTILLO BETANCOURT, BERNARDO CAICEDO HORMAZA, FOIVOS KARAKOSTAS, EMMANUEL DE LAURE, PHILIPPE LOGNONNÉ, DANIELE ANTONANGELI and BRUCE BANERDT

A detailed investigation has been conducted of the interaction between a Martian regolith simulant and the foot of a seismometer (SEIS) recently deployed on the surface of Mars within the NASA InSight mission. A specific device used to investigate the SEIS/ground interaction was improved to provide accurate measurements of low forces and displacements, with a higher system stiffness and appropriate thermal insulation. A series of tests was carried out with a 60 mm diameter disc and the SEIS foot (disc with a spike at its centre). The maximum disc penetration in the loose sand used as simulant under the SEIS weight (10 N) was between 400 and 600 μm, with a tiny effect of the spike. Load cycles under various forces were performed to investigate the elastic interaction, with good reversibility and a linear change of the Young's modulus with respect to the average vertical stress. The tests provided comparable values, showing that the Young's modulus was around 20 MPa – which is compatible with that of loose terrestrial sands – and agreed well with the seismic wave velocities at the surface (from laboratory experiments and from measuring on the surface of Mars the travel times of waves received by the SEIS seismometer).

KEYWORDS: laboratory tests; sands; soil–structure interaction

Introduction

The 'Seismic experiment for interior structure' (SEIS) (Lognonné et al., 2019, 2020) of the National Aeronautics and Space Administration (NASA) InSight mission on Mars (interior exploration using seismic investigations, geodesy and heat transport (Banerdt et al., 2020)) is the first seismometer ever deployed in direct contact with the surface of the planet Mars, in the footsteps of the Apollo lunar surface experiments package on the moon (e.g. Latham et al., 1969, 1970; Bates et al., 1979) and 44 years after the landing of the two Viking seismometers in 1976 (these seismometers, placed on the landers with no direct contact with the ground, did not provide any exploitable data). The InSight mission is a geophysical mission aimed at further understanding the structure of Mars and the other terrestrial planets of the solar system. The main geophysical instruments deployed on Mars are a very high-sensitivity seismometer (SEIS) funded by the French space agency (Centre National d'Etudes Spatiales (CNES)) and the HP^3 instrument (heat flow and physical properties package), a self-penetrating dynamic probe (called the mole, 39.6 cm long and 2.7 cm diameter) funded by the German Institute for Planetary Research (Deutsches Zentrum für Luft- und Raumfahrt (DLR)). The HP^3 instrument is designed to perform thermal conductivity measurements along the first 3–5 m below the surface. The InSight lander that landed on Mars on 26 November 2018, is represented in an artist’s view in Figure 3-19, with both the SEIS (covered by a wind and thermal shield) and the HP3 instruments deployed. Both are linked to the lander by tethers that transmit energy and data.

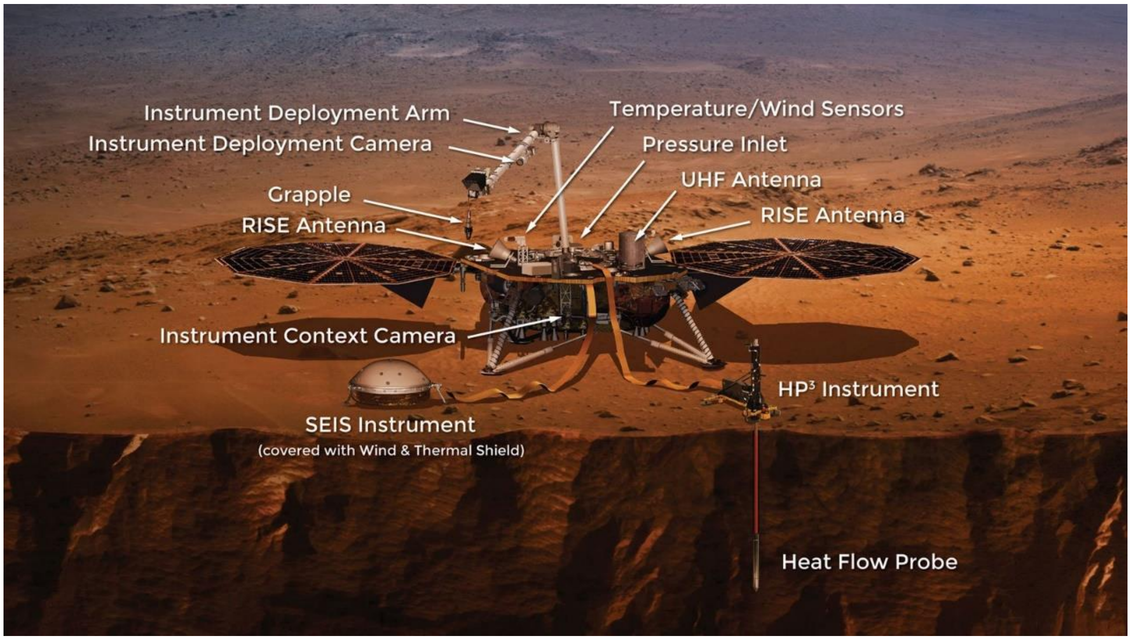

Figure 3-19 InSight NASA lander concept and main instruments. Image credit JPL/NASA: https://mars.nasa.gov/insight/spacecraft/instruments/summary/

The Figure 3-19 also shows the 2 m long instrument deployment arm (IDA) and its grapple that deployed both SEIS and HP^3 on the ground. The IDA also carries a high-resolution instrument deployment (colour) camera (IDC). The lander is also equipped with an instrument context camera (ICC), a meteorological station including temperature, windspeed and pressure sensors, two ‘rotation and interior structure experiment’ (RISE) antennas providing a precise location of the lander to accurately monitor the movements of the planet from the Earth and an ultra-high-frequency antenna for data transmission. Energy is provided by twin 1.8 m diameter solar panels with a power of 700 W each, on clear days.

The average size of the regolith particles on Mars was determined from thermal inertia measurements by the Viking lander and the Themis orbiter (Arvidson et al., 1989). The microscopic imagers of the Mars exploration rovers (MER – Spirit and Opportunity, 2004), Mars science laboratory (MSL – Curiosity, 2012) and Phoenix lander (2008) provided evidence of sorted dark grey basaltic sub-rounded to rounded fine sand particles (due to wind saltation under a 750 Pa atmospheric pressure), with diameter between 80 and 200 μm. This range is compatible with the average diameter (170 μm) derived from thermal inertia measured at the InSight landing site (160–230 $J/(m^{é}\ K\ s^{1/2})$ (Golombek et al., 2020)). Bright red dust particles (2–5 μm) of slightly chemically altered basalt are also observed (Arvidson et al., 2004a, 2004b, Golombek et al., 2006a, 2006b and Goetz et al., 2010b). Orbiter observations indicated that dust has been expelled by the rockets during landing at an average distance of 20 m around the InSight lander (Golombek et al., 2020).

Figure 3-20shows a high-definition IDC photo of the Martian surface in the InSight landing site, showing the sand-like appearance of the regolith, with also some pebbles on the surface around.

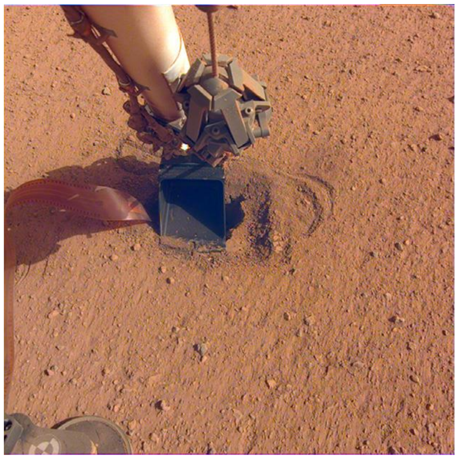

Figure 3-20. IDC photograph showing the scoop of the instrument deployment arm (IDA) compressing the regolith above a hole developed around the self-penetrating mole during hammering. The scoop width is 7·6 cm (image credit JPL-NASA. IDC image acquired on Sol 550, imageD000M0550_645359459EDR_F0000_0800M3)

A detailed geological description of the so-called ‘homestead hollow’ where the lander is located was presented by Golombek et al. (2020), from which the interpretative cross-section of the landing site of Figure 3-21 has been extracted. It shows a typical regolith profile, with a layer around 3 m thick of relatively fine-grained impact-generated regolith (labelled number 3 in the Figure 3-21) that is likely to grade with depth into coarse, blocky ejecta (labelled 2), which overlies fractured basalt flows (labelled 1), with an estimated 10 m thick layer of blocky ejecta.

This paper is devoted to investigating further the elastic interaction between the SEIS foot and a Martian regolith simulant, by using a specific device working at very low stresses and strains. In a first approach, the investigation was carried out under terrestrial gravity (9.81 m/s^2), higher than Mars’ gravity (3.72 m/s^2). The aim of the programme is to provide an estimation of the value of the axial elastic spring constant of the regolith simulant to allow for theoretical modelling of the elastic interaction between the SEIS and the Martian regolith (see Fayon et al., 2018). From a seismology point of view, the elastic parameters of the surface regolith that can be derived from this experiment are also interesting to estimate the wave velocity in the near surface.

Materials and methods

Introduction

The shape of the SEIS foot was designed based on a first series of tests carried out in a device developed at École des Ponts ParisTech (Karakostas et al., 2013) is presented in Figure 3-22. The foot consists of a disc with 60 mm diameter and a 20 mm long conic spike (10 mm diameter at its base) in its centre. As further detailed in the later subsection entitled ‘Experimental set-up’, the device was improved to obtain better accuracy in terms of displacement and force measurements.

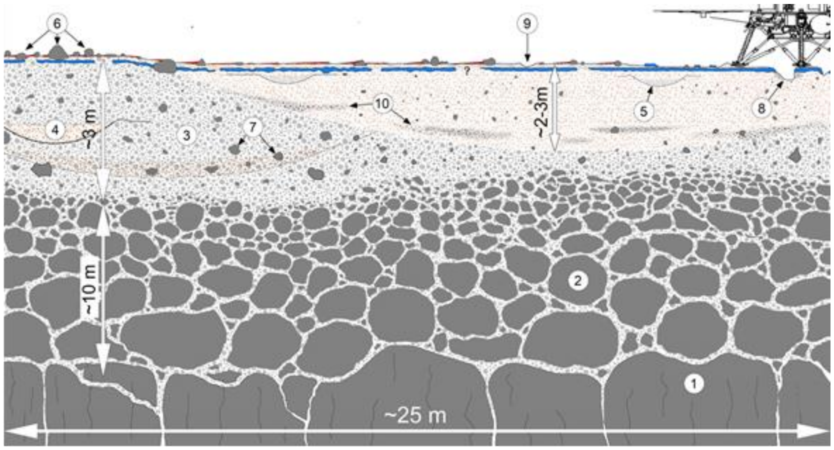

Figure 3-21. Interpretative cross-section of the shallow surface beneath the InSight lander (Golombek et al., 2020, Creative Commons CC BY license) 1, fractured basalt flow; 2, blocky ejecta; 3, fine-grained impact generated regolith; 4, 5, overlapping craters; 6, rockier area; 7, rocks embedded in regolith; 8, pits opened by retro rockets during landing; 9, surface divots; 10, lens of ejecta from other craters.

Figure 3-22. The shape of the SEIS foot. The conical spike has a maximum diameter of 10 mm.

Martian simulant

The selection of a relevant Martian regolith simulant is a difficult task (Seiferlin et al., 2008). Given the data providedby the MER, MSL and Phoenix missions and by thermal inertia measurement (see above), it was decided to adopt the Fontainebleau sand (NE34), awell-sorted rounded sand with an average grain diameter D_{50} =220 μm (a little bit larger than the 170 μm estimated value at the InSight site) and a uniformity coefficient C_u = 1.57 (the maximum and minimum void ratios are e_{min}= 0.54 and e_{max} = 0.86, respectively (Andria-Ntoanina, 2011)). The grain size distribution curve and a scanning electron microscopy (SEM) photo showing the rounded shape of the grains are presented in Figure 3-23. As observed in Figure 3-20, it is possible that the InSight regolith could be less well sorted with more fine particles, but it is currently difficult to obtain further precision about the exact in situ grain size distribution. Observations from previous missions also indicated a loose state of the regolith (Golombek et al., 2008), which was recently confirmed by local thermal measurements conducted at the surface by the HP^3 mole (Grott et al., 2021).

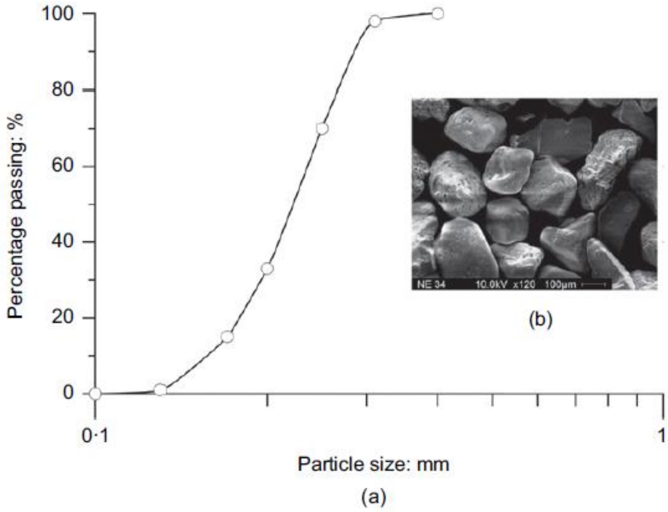

Figure 3-23. NE 34 Fontainebleau sand: (a) grain size distribution; (b) scanning electron microscope photograph showing the subrounded grains (after Andria-Ntoanina, 2011)

Experimental set-up

The precision of the experimental device used by Karakostas et al. (2013) was significantly improved by adopting high-precision sensors for the measurements of both force and displacement (0.1 μm), together with a stiff device designed to support the displacement transducer and a thermal insulation device of the whole system. The device (Figure 3-24) consists of a sand container of 240 mm diameter and 120 mm high, placed on the platform of a standard 100 kN triaxial press, allowing for upwards displacement at constant speed at 0.080 mm/min. The diameter of the container was constrained by the space available between the two rods of the triaxial press.

The relevance of the container dimensions with respect to boundary conditions was examined through elastic calculations based on the solution by Sneddon (1946) of a rigid circular plate on a semi-infinite elastic homogeneous space (see Appendix), with the following expression of the vertical displacement Δz.

$$\Delta z = \frac{\pi}{2}(1-\nu^2)\frac{\sigma_V R}{E} = \frac{F}{2RE}(1-\nu^2) \qquad (1)$$

where R is the disc radius; F is the applied force; $\sigma_v = F/\pi R^2$ is the average applied vertical stress; E is the Young's modulus; and ν is the Poisson's coefficient. AYoung's modulus typical of loose sands (E =20 MPa (Massarsch, 2015)) was adopted and ν was taken as equal to 0.22 (Delage et al., 2017). Equation (1) allows the stresses on the boundaries of the mould to be analysed, as shown in Figure 3-25. This analysis reveals slight changes in stress at the bottom (5% for σ_z and 2% for τ_{zx} of the vertical stress applied on the surface) and at the periphery, leading to a vertical strain $\varepsilon_z = 0.001\%$ at the bottom (compared to 0.018% below the disc).

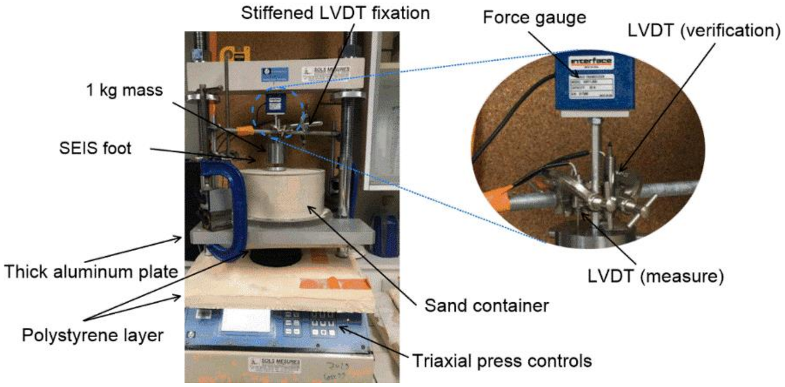

Figure 3-24. Experimental set-up, showing more details of the fixation of the mass to the force gauge and the LVDTs providing the vertical displacement.

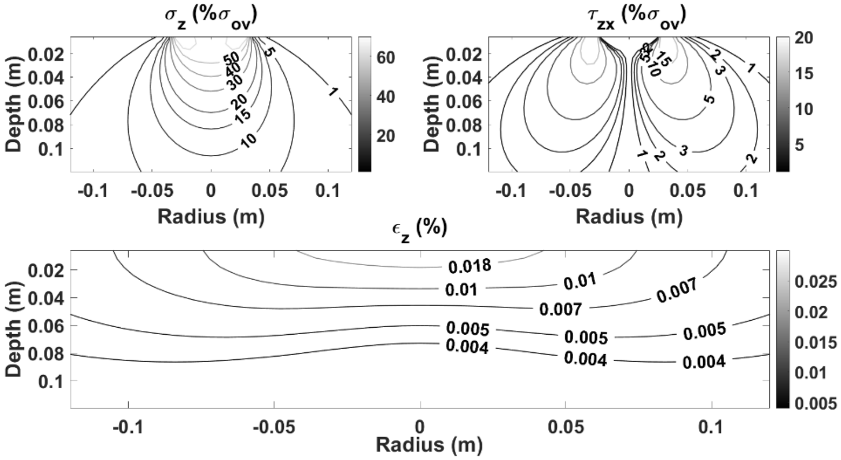

Figure 3-25. Elastic calculations of the vertical and shear stress (presented as percentages of the applied vertical stress) and of the vertical strain below the foot under the SEIS weight, based on the elastic solution by Sneddon (1946)

Finite-element elastic calculations were also carried out with the Plaxis code to account for possible effects that could be attributed to the dimensions of the mould. Calculations made with the mould (240 mm diameter and 120 mm high) were compared to those with a much larger container comparable to a semi-infinite space (600 mm diameter and 550 mm deep). The differences obtained between the vertical displacements were 5.8 x 10^{-4} μm/N on the lateral boundary and 0.04 μm/N in the middle axis. They were considered small enough to conclude that the semi-infinite hypothesis used in Sneddon's approach was satisfactory for the mould used. Compared to the 220 μm average diameter of the sand grains, the small displacements calculated would result in a tiny movement of the grains at the interface with the container, with no significant effect on the disc penetration in the centre.

The option adopted in the work was to keep the real (Martian) foot dimensions by reusing the foot model used during the SEIS foot design (Karakostas et al., 2013), by putting it in contact with a simulant with grain size and shape comparable to (albeit slightly larger than) those of the InSight regolith, and by loading it up to the force supported by each foot on Mars. The length scale used is 1 (e.g. L_m/L_p = 1, where L_m is the length of the model and L_p is the prototype's length), leading to a disagreement in the similitude scale for stresses, which can be analysed by splitting stresses into those due to the seismometer weight σs (with a scale relationship of 1, e.g. $\sigma_s^m/\sigma_s^p = 1$) and those due to the self-weight of the soil σ_g, which is 2.64 times greater than on Mars. The match is not perfect along the earlier part of penetration, where the stresses due to soil self-weight predominate. However, once the load grows, the issue with similitude on stresses decreases because the induced stresses beneath the foot dominate over the self-weight stresses.

The SEIS foot is fixed at the bottom of a cylindrical mass of 1 kg, corresponding to the load supported by one SEIS foot under the gravity of Mars, fixed to the horizontal rigid top beam of the press through a force gauge. The experiment is carried out by putting the spike of the foot in contact with the surface of the sand, prior to activating the upwards movement of the press. This allows for the progressive penetration, at a constant displacement rate, of the foot within the sand mass, until reaching the contact between the disc and the sample surface. The spike penetration is monitored through the displacement rate of the press, which has been carefully calibrated. Once the disc contacts the sand, a high accuracy in displacement monitoring is achieved by using a linear variable differential transducer (LVDT) of 4.5 mm range with 0.1μm resolution.

The force measurement was improved by using a 25 N range force gauge (Interface SMT1-25N). To reduce the noise in displacement measurements, a stiffer fixation system for the LVDT was adopted. As seen in Figure 3-24, the system is made up of two vertical rods strongly fixed on a thick aluminium plate placed on the plateau of the press along a diameter of the container, and a horizontal rod strongly fixed to the two vertical ones. The 4.5 mm LVDT was fixed on this system, with its stem in contact with the upper side of the 1 kg mass. Another LVDT with a larger range of 20 mm, shown in Figure 3-24, has also been used for tilt verification. With the same aim, a system of insulation from temperature changes and air movements has been set up, with particular attention paid to thermally insulate the two vertical rods of the triaxial press, because of the possible perturbations on the displacement measurements through their thermal expansion/contraction. The insulation system consisted of a light prismatic box made up of a 5 cm thick expanded polystyrene and cork layer, placed around the device, as seen in Figure 3-26(a), with a small access made through the box for the control system.

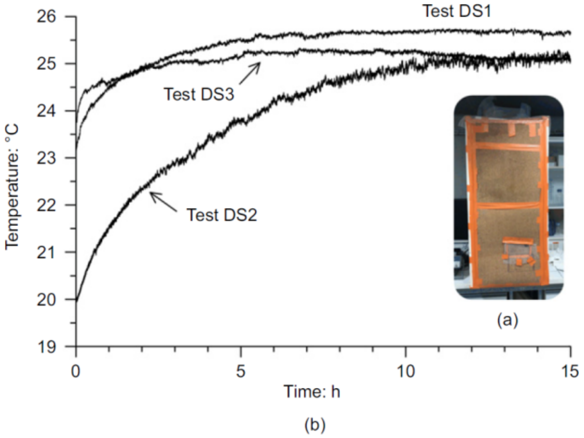

Figure 3-26. (a) Thermal insulation of the device; (b) temperature stabilisation is reached after 10 h for tests DS1, DS2 and DS3 (see Table 3-2)

The performance of the insulating system was verified by taking several day/night temperature measurements by means of a thermocouple (able to detect changes in temperature smaller than 0.1°C, see Figure 3-27 inside the box for up to 3 days. As shown in Figure 3-26(b), thermal stabilisation was attained around 10 h after the box was placed around the device. Also, the sand container was insulated from possible thermal perturbations from the press by placing a thick polystyrene plate between the plateau and the thick plate. As observed in Figs 8(b) and 9, the resulting stabilisation after 14 h reduces temperature variations to the order of 0.1°C, which is found to be quite satisfactory.

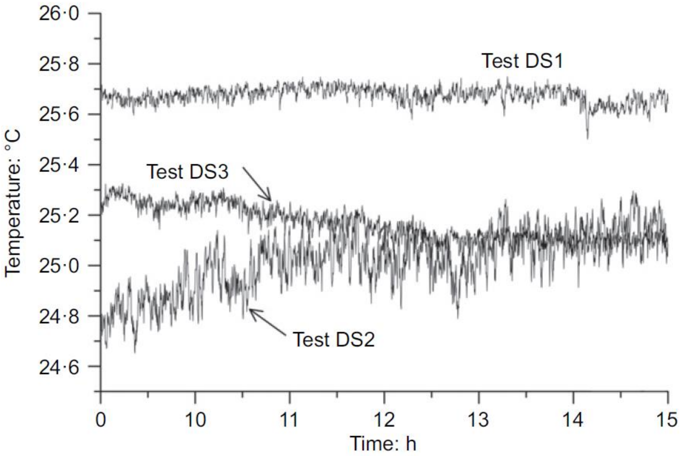

Figure 3-27 Temperature stabilisation in tests DS1, DS2 and DS3 (see Table 3-2) made possible by the thermal insulation of the device, is of the order of 0.1°C.

Setting up the low-density simulant specimen

Given the low unit mass of the regolith (1400 kg/m^3 or even less; Golombek et al., 2008; Delage et al., 2017; Morgan et al., 2018; Grott et al., 2021), a dry funnel deposition procedure, as already used by various authors (including Tatsuoka et al., 1979; Lade & Yamamuro, 1997; Zlatovic & Ishihara, 1997; Yamamuro & Wood, 2004; Flitti et al., 2021) was adopted. To do so, the sand was gently poured at the centre of a container by using a funnel, keeping a zero falling height between the bottom end of the funnel and the top of the cone. The funnel was gently lifted by hand as the pile rose. An upper plexiglass ring (8 cm high) with the same diameter was placed on top of the container. Once the sand pile had reached the right height, the ring was removed and the excess sand was carefully erased to obtain a smooth horizontal upper plane surface. To minimise any disturbance, the sample was prepared close to the press and to a scale, on a mechanically insulating polystyrene layer. Once prepared, it was very carefully placed (no walking) on the scale for weighing, prior to being placed on the platen of the press. Once on the platen, the erased top surface of the sand was inspected to make sure that it stayed at the top of the container, which was the case. The unit mass of the deposited sand samples was found to be between 1389 and 1436 kg/m^3 (see Table 3-2). This corresponds to an average density index, I_d =6%, indicating a very loose state of the specimen.

Starting the test

Once the sample had been placed on the platen of the press, the thermal insulation box was placed, and data acquisition started. As already mentioned, almost 1 day was necessary to reach temperature stabilisation, a mandatory condition for proper displacement measurements. The plateau was moved at a low velocity of 0.08 mm/min to adequately monitor all relevant parameters. Various loading and unloading cycles were applied at different forces to investigate the dependence of the elastic response with respect to stress (see Table 3-2).

Experimental results

Most preliminary tests were aimed at establishing the validity of the device and checking repeatability. To do so, it was found to be simpler to carry out tests with the 60 mm diameter disc (without spike), because it allowed for easier detection of the first sand/disc contact. As can be seen in Table 3-2, ten tests were conducted with the disc. Once the performance of the system had been assessed, it was found that only three tests with the foot (disc +spike) were enough. The data obtained are presented in Table 3-2, including the values of the spring coefficient K_c determined from load cycles under various forces, and K_f from the final unloading and the Young's moduli (E_c and E_f). The latter was derived under the hypothesis of elastic semi-infinite homogeneous half-space, as mentioned later in the paper.

Table 3-2. Experimental program carried out.

N°	Unit mass kg/m^3	Max. p_t^* µm (± 0.1)	Max. force N (± 0.01)	Load cycles min – max N (± 0.01)	Slope K_c cycle MN/m (± 0.07)	Slope K_{fu} final unload MN/m (± 0.07)	Young modulus E_c cycle MPa (± 1.1)	Young modulus E_{fu} final unload MPa (± 1.1)
Disk only								
D1	1421	412.6	10.48	8.14 - 9.63	1.32	1.19	20.89	18.8
D2	1432	534.1	10.39	2.72 - 1.57 7.51 - 5.53	0.28 1.31	1.47	4.46 20.76	23.31
D3	1413	419.6	10.47	9.30 - 8.06	1.33	1.09	21.11	17.21
D4	1389	605.9	10.15	4.00 - 2.83	0.37	1.43	5.84	22.68
D5	1421	485.5	10.27	3.01 - 2.07 5.67 - 3.32	0.27 0.82	1.36	4.23 12.94	21.57
D6	1436	438.2	10.	9.46 - 7.87	1.23	1.47	19.53	23.31
D7	1423	392.5	10.01	6.92 - 5.62	1.03	0.93	16.38	14.71
D8	1409	605.4	10.97	3.12 - 1.77 5.53 - 3.02	0.63 1.15	0.76	10.03 18.17	11.97
D9	1428	348.6	9.80	8.77 - 7.44	1.16	1.53	18.37	24.27
D10	1435	408.3	10.31	8.98 - 6.37	1.47	1.37	23.25	21.73
Disk + spike								
DS1	1428	607.4	10.6	8.55 6.49	1.11	1.087	17.59	17.24
DS2	1403	598.4	9.91	8.81 - 6.77	1.26	0.825	20.02	13.09
DS3	1418	611.3	10.56	- 7.40	1.18	0.936	18.65	14.85

* *p_t: penetration*

Penetration tests with the disc

Ten tests were carried out with the disc up to a maximum force of 10 N – that is, the force applied on the ground by each SEIS foot on Mars. Half of them were performed to determine, through a load cycle, the elastic response under 10 N. Five others were performed under smaller stresses to characterise the variation of the elastic response with stress. All final unloading sequences were also used to determine the K_f coefficients and the E_f Young's moduli, as designated in Table 3-2.

Figure 3-28 shows the penetration curves of the ten tests in terms of force (N) with respect to the penetration distance (μm) monitored by the 4.5 mm range LVDT. The Figure 3-28 shows some variability in the maximum penetration observed, which ranges between around 400 μm for seven tests and around 600 μm for the other three tests. The responses at the beginning of the series of seven tests show a stronger increase in force with respect to the displacement. A comparable slope is reached, however, for the three other tests after a penetration of 300 μm.

All curves show many spikes corresponding to sudden decreases in force, followed by a force recovery along several micrometres, which brings the curve back along the initial one as is typical of slip and stick phenomena (Cain et al., 2001).

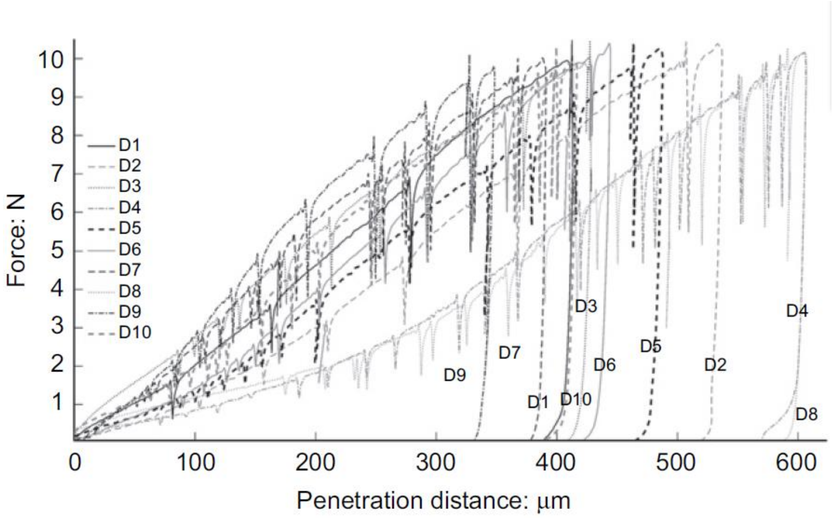

Figure 3-28. Force–penetration curves for the ten tests performed with the disc.

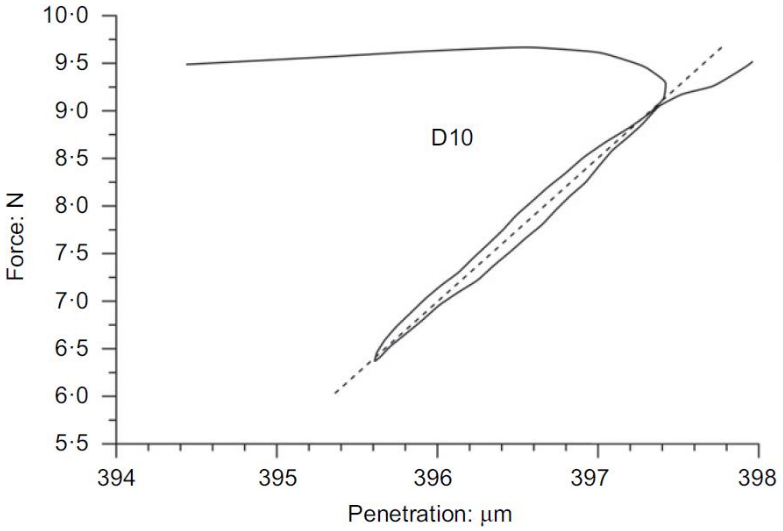

Figure 3-29 Load–unload cycle performed between 8·98 and 6·37 N in test 10 (disc only). The stiffness coefficient given by the slope is k= 1·47× 106 N/m

As indicated in Table 3-2, the elastic response under the SEIS weight (10 N) and thus very small stresses was investigated through cycles of force. Figure 3-29 shows a cycle performed during test D10 between 8.98 and 6.37 N (force amplitude of 2.61 N), with a resulting penetration response between 395.65 and 397.4 μm (amplitude of 1.75 μm). The curve shows that the decrease in force, resulting from stopping and reversing the direction of the movement of the plateau, is not instantaneous, with a progressive decrease in force between 9.67 and 9.29 N occurring along 0.8 μm, followed by a frank linear decrease in both force and displacement. A very slight hysteresis is observed, with a difference of 0.2 μm between the two points at 8 N, showing quite a good reversibility and linearity of the response. A value of an elastic spring constant $\Delta F = \Delta d$ of 1.47106 N/m is derived from the graph.

Penetration tests with the foot (disc + spike)

The difficulty was to determine accurately the first contact between the spike and the sand, an impossible task if based on force measurement. Since it was easier to detect the contact between the disc and the sand, it was decided to set this point at zero and to plot back the penetration of the spike, as shown in Figure 3-30(a). The curve shows that the penetration of the spike along the first 17 mm (17 000 μm to compare to the 400–600 μm of disc penetration) provides no significant added effect of the spike in the loose sand (added contribution between 0.14 and 0.54 N). The force–penetration curve of test DS1 is presented in Figure 3-30(a) and Figure 3-30(b), showing no significant force mobilisation below 3 mm and a maximum force of 0.14 N obtained just before the sand/disc contact is reached. The monitored forces also give an idea of the force gauge accuracy, which can be estimated ± 0.01 N. The sudden drops in force previously observed with the disc and typical of stick and slip are also seen with the cone (at 5200 and 9100 μm).

The curves illustrating the interaction between the foot and the sand (Figure 3-31) are similar to those obtained without the spike, confirming the tiny effect of the spike. A maximum penetration of 600 μm was obtained in these tests, as in three of the tests with the disc only (Figure 3-28). Reversible load cycles similar to that presented in Figure 3-29 were also observed, confirming little effect of the spike on the elastic response.

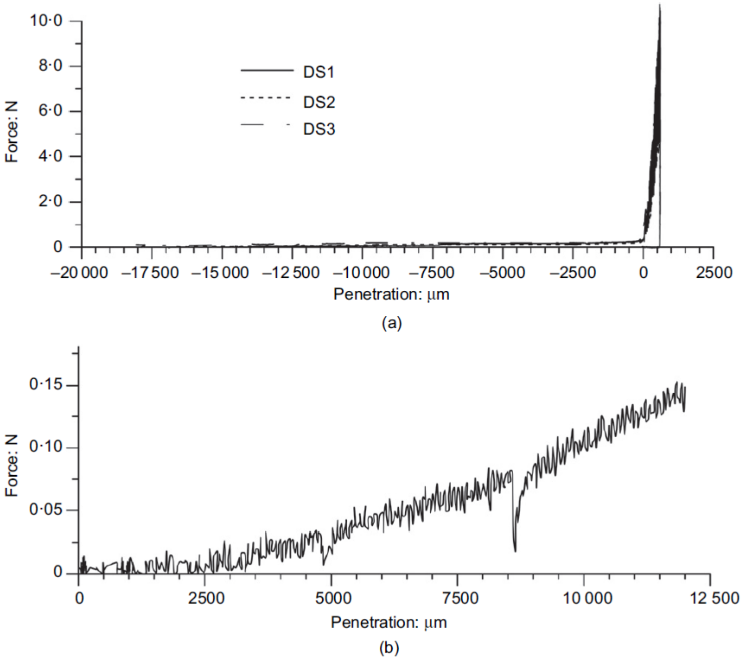

Figure 3-30. (a) Force–penetration curves for the three tests performed with the foot (disc+ spike). Note that the force significantly increases once the disc contacts the sand surface. The start of the disc/sand contact is taken as 0 for the x-axis, and the curves are started at a point obtained by subtracting the length of the spike (−20 000 μm). (b) Detailed force–penetration curve of the spike alone for test DS1, with a maximum force of 0·14 N reached just before sand/disc contact. Two stick–slips are observed at around 4800 and 8600 μm

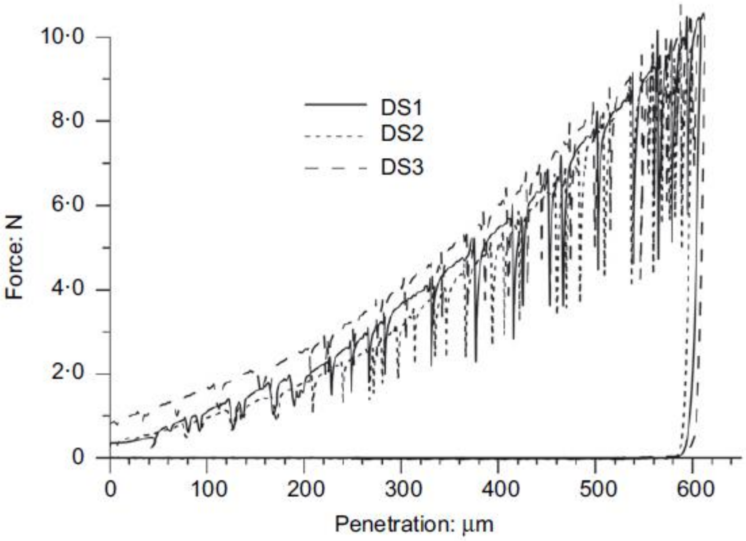

Figure 3-31 Force–penetration curves for the three tests carried out with the foot (disc + spike) once the spike had fully penetrated the sand and the disc was in contact with the sand.

Interpretations and discussion

General considerations

The challenge of setting up an experimental device able to deal with very low stress and strain has been met, thanks to special care devoted to the thermal insulation and to the stiffness of the device, resulting in a precision of around 0.1 μm in displacements. The maximum disc penetration obtained with the authors' device under the weight of the SEIS (under the gravity of Mars– around 10 N) is between 400 and 600 μm, whereas the average grain diameter of the Fontainebleau sand, 220 μm, is around two to three times smaller. The low stress in the area affected by the disc penetration hence results in quite small plastic strains that correspond to the displacement of a limited number of grains below the sample surface, illustrated by the slope of the curves of Figure 3-28. The data of Figure 3-28 and Figure 3-31 show that the force reached at a displacement corresponding to the average grain diameter is between 2 and 7.5 N. This shows that the beginning of the curve is influenced by the roughness of the surface, which is controlled by the arrangement of the grains. Besides possible effects of local changes in density, this may be the explanation for the less pronounced start of the curves reaching 600 μm. Conversely, the reversible load cycles illustrate a small elastic response of 1.3–2 μm in vertical displacement, to be compared to the 220 μm average diameter of the grains, indicating a limited reorganisation of the grain assembly. The elastic response should mainly be governed by the reversible stress release/recompression at grain contacts, following the Hertz–Mindlin contact theory (Hertz, 1882; Mindlin, 1949).

When comparing the penetration curves and the close values of the elastic spring constants of the foot and the disc only (Table 3-2), no significant added effect of the spike was observed, showing that there is space enough in the loose contracting sand to accommodate the thin spike without any added strength. This probably also holds for the InSight regolith, the low density of which has been confirmed by both the development of a pit around the mole at the start of the penetration of the HP3 instrument (Golombek et al., 2020) and by some in situ thermal conductivity measurements that provided estimated unit mass values around 1200 kg/m^3 (Grott et al., 2021). Some pebbles, like those observed in Figure 3-20, have also been observed in the excavations created by the rockets during landing and in the mole pit. The possibility of not having full penetration of one of the SEIS feet due to blocking by a pebble cannot be completely eliminated. However, the thin shape of the spike is the optimum in this regard, allowing easier deviation of the spike along a small enough pebble, and full penetration in the loose regolith.

Elastic interpretation of the response

Based on the measurements of elastic spring constants K_v presented in Table 3-2and on the simplifying assumption of homogeneous linear and isotropic behaviour of the sand, the Young's moduli for all the cycles performed (see Table 3-2) were derived based on the following expression derived from Sneddon's equation (1)

$$E = \frac{k_v(1-\nu^2)}{2R} \quad (2)$$

The elastic strain increment corresponding to the force cycle of Figure 3-29 is equal to 6 x 10^{-5}, showing that the Young's moduli are determined at small deformations, not far from the range of those derived from bender element measurements (10^{-5} - 10^{-6}), as done in Delage et al. (2017). The changes in Young's modulus with respect to the average vertical stress at the surface are presented in Figure 3-32 (given the negligible effect of the spike, the calculations for the foot have also been made by using Sneddon's solution).

In the area corresponding to the SEIS weight (around 3.5 kPa), some dispersion is observed, with *E* values derived from load cycles between 17.59 and 23.25 MPa. This is an indication of possible changes in local density of the sample at the contact area with the disc/spike, probably enhanced by the small number of grains mobilised by the low applied stress, or for other reasons that are not yet clear, including possible hysteretic material behaviour of the sand. Averaging the values between 3 and 3.5 kPa yields an average *E* value of 20.07 MPa (note that, for some reason, some of the monotonic unloading coefficients at maximum force stay well below the line, with values as small as 11.97–14.85 MPa). The possible effects of changes in Young's modulus with depth, suggested by the data of Figure 3-32, were investigated by carrying out finite-element calculations with a linear change of *E* with depth, in a model composed of 12 layers of 1 cm thickness. The difference in settlement at the surface was found to be equal to 0.0468 μm/m, indicating negligible effects of changes in Young's modulus with depth.

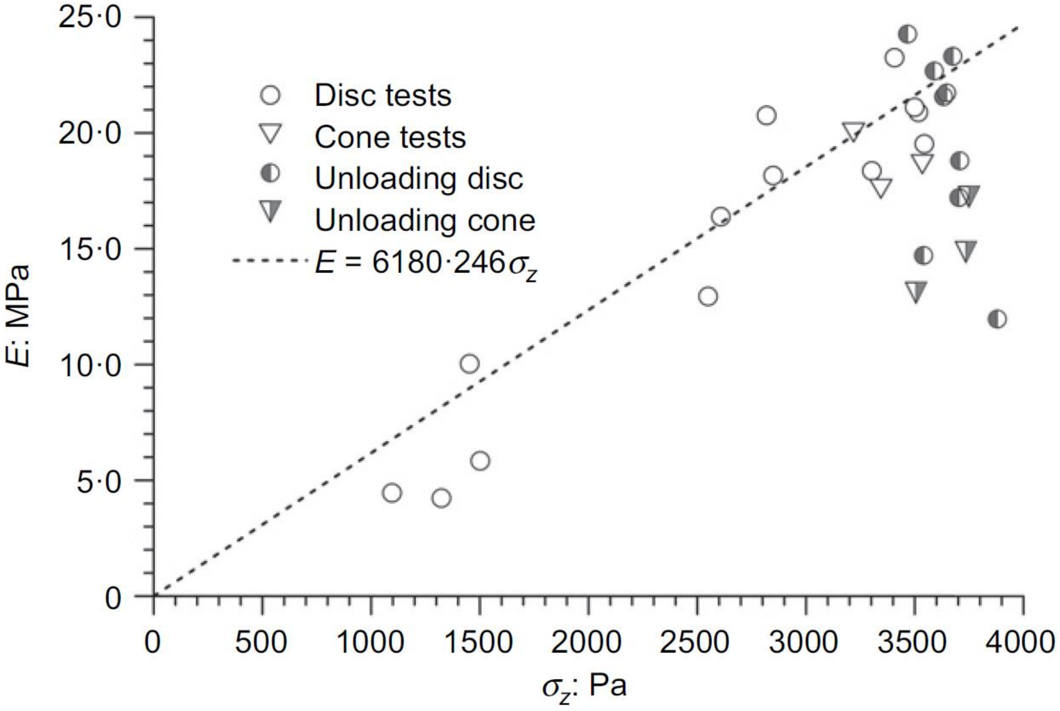

Figure 3-32. Changes in Young's modulus with respect to the average vertical stress at the surface. Data are derived from load cycles tests and from the final unloading step.

The linear changes in Young's modulus with respect to changes in average vertical stress (a value easy to calculate under a rigid plate) observed in Figure 3-32 are distinct from the well-known power law that relates the Young's modulus with the confining stress, defined by the two following equations (e.g. Santamarina et al., 2001)

$$V_p = \alpha \left(\frac{p}{1\,kPa}\right)^{\beta} \qquad (3)$$

And

$$E = \rho {V_p}^2 \left(\frac{3 - \frac{4}{l^2}}{l^2 - 1} \right) \qquad (4)$$

With

$$l = \sqrt{\frac{2(1-\nu)}{1-2\nu}}$$

where p is the mean stress, and α (m/s) and β are two fitted parameters. Delage et al. (2017) obtained β = 0.3 and ν= 0.22 on three different (more angular) Martian simulants. Following Santamarina et al. (2011), it was found more relevant to adopt, for sub-rounded grains, a slightly smaller value of 0.28, which results in a power law with β =0.56, slightly larger than the 0.5 value commonly adopted for sands (e.g. Hardin & Black, 1966; Oztoprak & Bolton, 2013).

The significant difference with the linear changes observed in Figure 3-32 is related to the use of average vertical stress σ_z instead of mean stress ((σ_z + 2 σ_x /3, since $\sigma_x = \sigma_y$). Inspection of the Sneddon's expressions of σ_z, σ_x and σ_y (see Appendix) shows that the relation between σ_z and p is far from simple, with the added difficulty of properly estimating the relevant layer thickness needed to estimate p under the disc.

Knowing E allows for the calculation of the other parameters governing the SEIS/ground interaction used in Fayon et al. (2018) in their modelling of the SEIS ground interaction – that is, the horizontal spring coefficient k_h and the torque C_h (Poulos & Davis, 1974)

$$k_h = \frac{16\ \mathrm{ER}(1-\nu)}{(7-8\nu)(1+\nu)} = 1.17\ \times 10^6 N/M \qquad (5)$$

$$C_h = \frac{4\ \mathrm{ER}^3}{3(1-\nu^2)} = 756.6\ N.m \qquad (6)$$

Given that the Young's modulus has been derived at a strain of 6 x 10^{-5}, another interesting seismic parameter that can be derived is the compression wave velocity at the surface, according to the following equation:

$$V_p = \sqrt{\frac{\mathrm{E}(1-\nu)}{\rho(1+\nu)(1-2\nu)}} \qquad (7)$$

in which ρ is the regolith unit mass. Adopting E=20 MPa, ρ= 1400 kg/m3 and ν= 0.22 yields a value of compression wave velocity of 128 m/s, in the expected range for sands under low confinement. Interestingly, this is also in good agreement with the in-situ velocities at the surface of Mars derived from analysing the seismic signals received by SEIS from HP^3 hammering at around 0.3 m depth, and 1.1 m away, equal to 118± 34 m/s for a surface layer approximately 30 cm thick (Lognonné et al., 2020).

Note, however, that these satisfactory agreements do not necessarily prove that the current experiment exactly reproduces the situation on Mars. Some limitations have been discussed above in this regard, both in terms of simulant and scale effects. The calculations here are also made based on a simplifying assumption of an equivalent homogeneous isotropic semi-infinite medium, whereas it is known that there is an increase of the elastic modulus of granular media with increased mean stress, as shown in Figure 3-32. Alongside the detailed geological examination of the surface (Golombek et al., 2020), further investigations are presently being carried out in this regard within the Near Surface Working Group of the InSight Science Team, based on visual and geological analyses, on the local measurements of thermal inertia, the seismic signals received by SEIS and the thermal data provided by HP^3. Based on thermal inertia measurement, one possibility is to have a finer material with some cohesion, which would also be compatible with the very low density suspected.

Conclusions

Some improvements were made to the specific device that allowed to design the final shape of the SEIS foot to be designed (Lognonné et al., 2019) and to provide the first estimation of the elastic parameters governing the interaction between a Martian simulant and the SEIS foot, as analysed in Fayon et al. (2018). To successfully carry out accurate tests in conditions of very low stresses (<4 kPa) and displacements (<600 μm), particular care was taken to optimise measurements by using a stiff system to support the container and the LVDT gauges, by using an adapted force gauge and a complete thermal insulation device, which made it possible to eliminate any perturbation that could result from the thermal expansion/contraction of the loading system, provided a waiting time period of 24 h was allowed to ensure a constant temperature with variations smaller than 0.5°C. This high-precision device allowed interaction tests to be successfully carried out between a disc and the foot. The tests showed that, under the weight of the SEIS, the maximum penetration in the simulant adopted was around 600 μm – in other words, less that the thickness of a layer made up of three grains of Fontainebleau sand, a well graded rounded sand with an average grain diameter of 220 μm. As a consequence, the start of the penetration curves was affected by the roughness of the specimen surface, which resulted in having maximum penetration between 400 and 600 μm – that is, around twice the diameter of a grain. The large number of tests conducted on loose specimens with dry unit mass around 1400 kg/m^3 (density index of 6%) showed reasonable repeatability, but with some dispersion in measured modulus related to possible changes in local density. The elastic response was investigated by conducting stress cycles at various force levels that provided fairly reversible responses with small hysteresis. A simplified analysis considering a homogeneous elastic isotropic semi-infinite medium was carried out to determine the dependency of the Young's modulus with respect to the average vertical stress. The linearity seen was distinct to the power law observed with respect to the mean stress, a value difficult to estimate in the present case. It was also shown that the effect of the spike in a loose regolith was not significant.

The order of magnitude of the Young's modulus under the SEIS foot is 20 MPa, a reasonable value for loose sand on Earth. This value was found to be compatible with previous laboratory estimations of the surface compression wave velocity and with in situ seismic measurements carried out on the InSight landing site by SEIS, from the hammering sessions of HP^3. The data obtained from this improved system will allow for better determination of the SEIS–regolith interaction and the resulting resonance frequencies (Fayon et al., 2018). They of course could be improved in the future, once better knowledge regarding the regolith simulant is obtained. They can also be used for the resonance frequencies of the lander itself, which appeared also to have significant effects on the SEIS measurements.

Acknowledgements

The work presented in this paper is part of the first author's PhD thesis, funded by a joint support from both Ecole des Ponts ParisTech (France) and Universidad de los Andes (Bogota, Colombia). The work was also supported by CNES (Centre National d'Etudes Spatiales), the French Spatial Agency and Institut de Physique du Globe (Université de Paris). The authors want to acknowledge the help provided by the CERMES technical team, with the contributions of Loic Lesueur for the setting up of the experiment and Xavier Boulay for the sensor installation, calibration and data acquisition. The suggestions made by Baptiste Chabot and Julieth Monroy (from Universidad de los Andes, Bogota) for improving the experimental set-up and analysiswere also key to the success of this work. This paper is InSight contribution 209.

Appendix

The normal and stress fields presented in Figure 3-25 are based on Sneddon's solution for a cylindrical indenter. The expressions are presented in more detail below.

Sneddon (1946) provided, from an elastic analysis based on Boussinesq's solution, the following expressions for the stress and strain field under a rigid loaded plate

$$\sigma_z = \frac{3F}{2\pi} \cdot \frac{z^3}{R^5}$$

$$\sigma_x = \frac{3F}{2\pi} \cdot \frac{x^2 z}{R^5} - \frac{m-2}{3m}\left[-\frac{1}{R \cdot (R+z)} + \frac{(2R+z)x^2}{(R+z)^2 R^3} + \frac{z}{R^3}\right]$$

$$\sigma_y = \frac{3F}{2\pi} \cdot \frac{y^2 z}{R^5} - \frac{m-2}{3m}\left[-\frac{1}{R \cdot (R+z)} + \frac{(2R+z)y^2}{(R+z)^2 R^3} + \frac{z}{R^3}\right]$$

$$\tau_{xy} = \frac{3F}{2\pi} \cdot \frac{xyz}{R^5} - \frac{m-2}{3m}\left[\frac{(2R+z)xy}{(R+z)^2 \cdot R^3}\right]$$

$$\tau_{xz} = \frac{3F}{2\pi} \cdot \frac{xz^2}{R^5}$$

$$\epsilon_z = \sigma_z/E$$

$$p_t = \frac{1+\nu}{2\pi E} \cdot \left[\frac{z^2}{R^3} - \frac{(1-2\nu)x}{R}\right] \cdot F$$

in which F is the force applied on the disc; z is the depth; x and y are the horizontal distance from the axis; $R = \sqrt{x^2 + y^2 + z^2}$; p_t is the penetration; and $m = 1/\nu$.

Notation

C_h torque spring coefficient
C_u uniformity coefficient (grain size distribution)
D_{50} median particle diameter
E Young’s modulus
E_c Young’s modulus derived from stress cycle
$E_f u$ Young’s modulus derived from final unloading
e, e_{max}, e_{min} void ratio, maximum void ratio, minimum void ratio
F applied surface force
k_c axial soil–foot stiffness, derived from stress cycle
k_{fu} axial soil–foot stiffness, derived from final unloading
k_h horizontal elastic spring coefficient
k_v vertical elastic spring constant
L length dimension
p mean stress
p_t penetration distance
R disc radius
V_p compressive wave velocity
z depth
α fitting multiplier coefficient for the compression wave equation
β fitting exponent coefficient for the compression waveequation
ε, ε_z strain, vertical strain
ν Poisson’s ratio
ρ unit mass
σ_v average surface vertical normal stress
σ_z, σ_x, σ_y normal vertical stress, horizontal stresses along x and y
τ shear stress

References

Andria-Ntoanina, I. (2011). Caractérisation dynamique de sables de référence en laboratoire – application à la réponse sismique de massifs sableux en centrifugeuse. PhD thesis, Université Paris-Est, Ecole des Ponts ParisTech, Paris, France (in French).

Arvidson, R. E., Guinness, E. A., Dale-Bannister, M., Adams, J., Smith, M., Christensen, P. R. & Singer, N. B. (1989). Nature and distribution of surficial deposits in Chryse Planitia and vicinity, Mars. J. Geophys. Res. 94, No. b2, 1573–1587.

Arvidson, R. E., Anderson, R. C., Bartlett, P., Bell, J. F., Blaney, D., Christensen, P. R., Chu, P., Crumpler, L., Davis, K., Ehlmann, B. L., Fergason, R., Golombek, M. P., Gorevan, S., Grant, J. A., Greeley, R., Guinness, E. A., Haldemann, A. F. C., Herkenhoff, K., Johnson, J., Landis, G., Li, R., Lindemann, R., McSween, H., Ming,D.W., Myrick, T., Richter, L., Seelos, F. P., Squyres, S. W., Sullivan, R. J., Wang, A. & Wilson, J. (2004a). Localization and physical properties experiments conducted by spirit at Gusev crater. Science 305, No. 5685, 821–824.

Arvidson, R. E., Anderson, R. C., Bartlett, P., Bell, J. F. III, Christensen, P. R., Chu, P., Davis, K., Ehlmann, B. L., Golombek, M. P., Gorevan, S., Guinness, E. A., Haldemann, A. F. C., Herkenhoff, K. E., Landis, G., Li, R., Lindemann, R., Ming, D.W., Myrick, T., Parker, T., Richter, L., Seelas IV, F. B., Soderblom, L. A., Squyres, S.W., Sullivan, R. J. & Wilson, J. (2004b). Localization and physical properties experiments conducted by opportunity at Meridiani Planum. Science 306, No. 5702, 1730–1733.

Banerdt, W. B., Smrekar, S. E., Banfield, D., Giardini, D., Golombek, M., Johnson, C. L., Lognonné, P., Spiga, A., Spohn, T., Perrin, C., Stähler, S. C., Antonangeli, D., Asmar, S., Beghein, C., Bowles, N., Bozdag, E., Chi, P., Christensen, U., Clinton, J., Collins, G. S., Daubar, I., Dehant, V., Drilleau, M., Fillingim, M., Folkner, W., Garcia, R. F., Garvin, J., Grant, J., Grott, M., Grygorczuk, J., Hudson, T., Irving, J. C. E., Kawamura, T., Kedar, S., King, S., Knapmeyer-Endrun, B., Knapmeyer, M., Lemmon, M., Lorenz, R., Maki, J., Margerin, L., McLennan, S. M., Michaut, C., Mimoun, D., Mittelholz, A., Mocquet, A., Morgan, P., Mueller, N. T., Murdoch, N., Nagihara, S., Newman, C., Nimmo, F., Panning, M., Pike,W. T., Plesa, A. C., Rodriguez, S., Rodriguez-Manfredi, J. A., Russell, C. T., Schmerr, N., Siegler, M., Stanley, S., Stutzmann, E., Teanby, N., Tromp, J., van Driel, M., Warner, N., Weber, R. & Wieczorek, M. (2020). Initial results from the InSight mission on Mars. Nat. Geosci. 13, No. 3, 183–189.

Bates, J. R., Lauderdale, W. W. & Kernaghan, H. (1979). ALSEP termination report, NASA reference publication series, NASA-RP-1036, p. 162, S-480, 914-40-73-01-72. Washington, DC, USA: National Aeronautics and Space Administration (NASA).

Cain, R., Page, N. & Biggs, S. (2001). Microscopic and macroscopic aspects of stick–slip motion in granular shear. Phys. Rev. E 64, No. 1 Pt 2, 1–8, https://doi.org/10.1103/physreve.64.016413. Delage, P., Karakostas, F., Dhemaied, A., Belmokhtar, M., Lognonné, P., Golombek, M., De Laure, E., Hurst, K., Dupla, J. C., Kedar, S., Cui, Y. J. & Banerdt, B. (2017). An investigation of the mechanical properties of some Martian regolith simulants with respect to the surface properties at the InSight mission landing site. Space Sci. Rev. 211, No. 1–4, 191–213, https://doi.org/10.1007/s11214-017-0339-7.

Fayon, L., Knapmeyer-Endrun, B., Lognonné, P., Bierwirth, M., Kramer, A., Delage, P., Karakostas, F., Kedar, S., Murdoch, N., Garcia, R. F., Verdier, N., Tillier, S., Pike, W. T., Hurst, K., Schmelzbach, C. & Banerdt,W. B. (2018). A numerical model of the SEIS leveling system transfer matrix and resonances: application to SEIS rotational seismology and dynamic ground interaction. Space Sci. Rev. 214, No. 8, article 119, https://doi.org/10.1007/s11214-018-0555-9.Flitti, A., Della, N., De Kock, T., Cnudde, V. & Verástegui-Flores, R. D. (2021). Effect of initial fabric on the undrained response of clean Chlef sand. Eur. J. Environ. Civ. Engng 25, No. 13, 2441–2456.

Goetz, W., Pike, W. T., Hviid, S. F., Madsen, M. B., Morris, R. V., Hecht, M. H., Staufer, U., Leer, K., Sykulska, H., Hemmig, E., Marshall, J., Morookian, J. M., Parrat, D., Vijendran, S., Bos, B. J., El Maarry,M. R., Keller, H. U., Kramm, R., Markiewicz,W. J., Drube, L., Blaney, D., Arvidson, R. E., Bell, J. F. III, Reynolds, R., Smith, P. H., Woida, P., Woida, R. & Tanner, R. (2010b). Microscopy analysis of soils at the Phoenix landing site, Mars: classification of soil particles and description of their optical and magnetic properties. J. Geophys. Res. E: Planets 115, No. 8, E00E22, https://doi.org/10.1029/2009JE003437.

Golombek, M. P., Grant, J. A., Crumpler, L. S., Greeley, R., Arvidson, R. E., Bell, J. F. III, Weitz, C. M., Sullivan, R., Christensen, P. R., Soderblom, L. A. & Squyres, S. W. (2006a). Erosion rates at the Mars exploration rover landing sites and long-term climate change on Mars. J. Geophys. Res. 111, No. 12, E12S10, https://doi.org/10.1029/2006JE002754.

Golombek, M. P., Crumpler, L. S., Grant, J. A., Greeley, R., Cabrol, N. A., Parker, T. J., Rice Jr., J. W., Ward, J. G., Arvidson, R. E., Moersch, J. E., Fergason, R. L., Christensen, P. R., Castano, A., Castano, R., Haldemann, A. F. C., Li, R., Bell, J. F. III & Squyres, S.W. (2006b). Geology of the Gusev cratered plains from the spirit rover transverse. J. Geophys. Res. 111, No. E2, E02S07, https://doi.org/10.1029/2005je002503.

Golombek, M. P., Haldemann, A. F. C., Simpson, R. A., Fergason, R. L., Putzig, N. E., Arvidson, R. E., Bell, J. F. III & Mellon, M. T. (2008). Martian surface properties from joint analysis of orbital, earth-based, and surface observations. In The Martian surface: composition, mineralogy and physical properties (ed. J. F. Bell III), ch. 21, pp. 468–497. Cambridge, UK: Cambridge University Press.

Golombek, M., Warner, N. H., Grant, J. A., Hauber, E., Ansan, V., Weitz, C. M., Williams, N., Charalambous, C., Wilson, S. A., DeMott, A., Kopp, M., Lethcoe-Wilson, H., Berger, L., Hausmann, R., Marteau, E., Vrettos, C., Trussell, A., Folkner, W., Le Maistre, S., Mueller, N., Grott, M., Spohn, T., Piqueux, S., Millour, E., Forget, F., Daubar, I., Murdoch, N., Lognonné, P., Perrin, C., Rodriguez, S., Pike, W. T., Parker, T., Maki, J., Abarca, H., Deen, R., Hall, J., Andres, P., Ruoff, N., Calef, F., Smrekar, S., Baker, M. M., Banks, M., Spiga, A., Banfield, D., Garvin, J., Newman, C. E. & Banerdt,W. B. (2020). Geology of the InSight landing site on Mars. Nat. Communs 11,No. 1, 1–11, https://doi.org/10.1038/s41467-020-14679-1.

Grott, M., Spohn, T., Knollenberg, J., Krause, C., Hudson, T. L., Piqueux, S., Müller, N., Golombek, M., Vrettos, C., Marteau, E., Nagihara, S., Morgan, P., Murphy, J. P., Siegler, M., King, S. D., Smrekar, S. E. & Banerdt, W. B. (2021). Thermal conductivity of the Martian soil at the InSight landing site from HP3 active heating experiments. J. Geophys. Res.: Planets 126, No. 7, e2021JE006861, https://doi.org/10.1029/2021JE006861.

Hardin, B. O. & Black, W. L. (1966). Sand stiffness under various triaxial stresses. J. Soil Mech. Found. Div 92, No. SM2, 667–692.

Hertz, H. (1882). Ueber die Berührung fester elastischer Körper (On the fixed elastic body contact). J. für Reine Angew. Math. (Crelle) 92, 156–171 (in German).

Karakostas, F., Delage, P., De Laure, E., Dhemaied, A., Dupla, J. C., Tang, A. M. & Cui, Y. J. (2013). The geotechnical properties of some Mars regoliths simulants and their interaction with the SEIS foot. In-house research report prepared for Institut de Physique du Globe de Paris. Paris, France: Ecole des PontsParisTech.

Lade, P. V. & Yamamuro, J. A. (1997). Effects of non-plastic fines on static liquefaction of sands. Can. Geotech. J. 34, No. 6, 918–928.Latham,G.V.,Ewing,M.,Press,F.,Sutton,G.,Dorman, J.,Toksoz,N., Wiggins, R., Nakamura, Y., Derr, J. & Duennebier, F. (1969). Passive seismic experiment. InApollo 11 preliminary science report, vol. SP-214, pp. 143–161. Washington, DC, USA: National Aeronautics and Space Administration (NASA).

Latham, G. V., Ewing, M., Press, F., Sutton, G., Dorman, J., Nakamura, Y., Toksoz, N., Wiggins, R., Derr, J. & Duennebier, F. (1970). Passive seismic experiment. Science 167, No. 3918, 455–457, https://doi.org/10.1126/science.167.3918.455.

Lognonné, P., Banerdt, W. B., Giardini, D., Pike, W. T., Christensen, U., Laudet, P., de Raucourt, S., Zweifel, P., Calcutt, S., Bierwirth, M., Hurst, K. J., Ijpelaan, F., Umland, J.W., Llorca-Cejudo, R., Larson, S. A., Garcia, R. F., Kedar, S., Knapmeyer-Endrun, B., Mimoun, D., Mocquet, A., Panning, M. P., Weber, R. C., Sylvestre-Baron, A., Pont, G., Verdier, N., Kerjean, L., Facto, L. J., Gharakanian, V., Feldman, J. E., Hoffman, T. L., Klein, D. B. Klein, K., Onufer, N. P., Paredes- Garcia, J., Petkov, M. P., Willis, J. R., Smrekar, S. E., Drilleau, M., Gabsi, T., Nebut, T., Robert, O., Tillier, S., Moreau, C., Parise, M., Aveni, G., Ben Charef, S., Bennour, Y., Camus, T., Dandonneau, P. A., Desfoux, C., Lecomte, B., Pot, O., Revuz, P., Mance, D., tenPierick, J., Bowles, N. E., Charalambous, C., Delahunty, A. K., Hurley, J., Irshad, R., Liu, H., Mukherjee, A. G., Standley, I. M., Stott, A. E., Temple, J., Warren, T., Eberhardt, M., Kramer, A., Kühne, W., Miettine, E.-P., Monecke, M., Aicardi, C., André, M., Baroukh, J., Borrien, A., Bouisset, A., Boutte, P., Brethomé, K., Brysbaert, C., Carlier, T., Deleuze, M., Desmarres, J. M., Dilhan, D., Doucet, C. Faye, D., Faye-Refalo, N., Gonzalez, R., Imbert, C., Larigauderie, C., Locatelli, E., Luno, L., Meyer, J.-R., Mialhe, F., Mouret, J. M., Nonon, M., Pahn, Y., Paillet, A., Pasquier, P., Perez, G., Perez, R., Perrin, L., Pouilloux, B., Rosak, A., Savin de Larclause, I., Sicre, J., Sodki, M., Toulemont, N., Vella, B., Yan, C., Alibay, F., Avalos, O. M., Balzer, M. A., Bhandari, P., Blanco, E., Bon, B. D., Bousman, J. C., Bruneau, P., Calef, F. J., Calvet, R. J., D'Agostino, S. A., de los Santos, G., Deen, R. G., Denise, R.W., Ervin, J., Ferraro, N. W., Gengl, H. E., Grinblat, F., Hernandez, D., Hetzel, M., Johnson, M. E., Khachikyan, L., Lin, J. Y., Madzunkov, S. M., Marshall, S. L., Mikellides, I. G., Miller, E. A., Raff,W., Singer, J. E., Sunday, C. M., Villalvazo, J. F., Wallace, M. C., Banfield, D., Rodriguez-Manfredi, J. A., Russell, C. T., Trebi-Ollennu, A., Maki, J. N., Beucler, E., Böse, M., Bonjour, C. Berenguer, J. L., Ceylan, S., Clinton, J., Conejero, V., Daubar, I., Dehant, V., Delage, P., Euchner, F., Estève, I., Fayon, L., Ferraioli, L., Johnson, C. L., Gagnepain-Beyneix, J., Golombek, M., Khan, A., Kawamura, T., Kenda, B., Labrot, P., Murdoch, N., Pardo, C., Perrin, C., Pou, L., Sauron, A., Savoie, D., Stähler, S., Stutzmann, E., Teanby, N. A., Tromp, J., van Driel, M., Wieczorek, M., Widmer-Schnidrig, R. & Wookey, J. (2019). SEIS: insight's seismic experiment for internal structure of Mars. Space Sci. Rev. 215, No. 1, 12–182, https://doi.org/10.1007/s11214-018-0574-6.

Lognonné, P., Banerdt,W. B., Pike,W. T., Giardini, D., Christensen, U., Garcia, R. F., Kawamura, T., Kedar, S., Knapmeyer-Endrun,B.,Margerin,L.,Nimmo,F.,Pa Panning,M.,Tauzin, B., Scholz, J.-R., Antonangeli, D., Barkaoui, S., Beucler, E., Bissig, F., Brinkman, N., Calvet, M., Ceylan, S., Charalambous, C., Davis, P., van Driel, M., Drilleau, M., Fayon, L., Joshi, R., Kenda, B., Khan, A., Knapmeyer, M., Lekic, V., McClean, J., Mimoun, D., Murdoch, N., Pan, L., Perrin, C., Pinot, B., Pou, L., Menina, S., Rodriguez, S., Schmelzbach, C., Schmerr, N., Sollberger, D., Spiga, A., Stähler, S., Stott, A., Stutzmann, E., Tharimena, S., Widmer-Schnidrig, R., Andersson, F., Ansan, V., Beghein, C., Böse, M., Bozdag, E., Clinton, J., Daubar, I., Delage, P., Fuji, N., Golombek, M., Grott, M., Horleston, A., Hurst, K., Irving, J., Jacob, A., Knollenberg, J., Krasner, S., Krause, C., Lorenz, R., Michaut, C., Myhill., R., Nissen-Meyer, T., ten Pierick, J., Plesa, A.-C., Quantin-Nataf, C., Robertsson, J., Rochas, L., Schimmel, M., Smrekar, S., Spohn, T., Teanby, N., Tromp, J., Vallade, J., Verdier, N., Vrettos, C., Weber, R., Banfield, D., Barrett, E., Bierwirth, M., Calcutt, S., Compaire, N., Johnson, C. L., Mance, D., Euchner, F., Kerjean, L., Mainsant, G., Laudet, P., Nebut, T., de Raucourt, S.,Warren, T.,Wieczorek, M., Yana, C., Mocquet, A., Rodriguez Manfredi, J. A., Pont, G., Robert, O., Russell, C. T., Sylvestre-Baron, A., Tillier, S. & Zweifel, P. (2020). Constraints on the shallow elastic and anelastic structure of Mars from InSight seismic data. Nat. Geosci. 13, No. 3, 213–220, https://doi.org/10.1038/s41561-020-0536-y.

Massarsch, K. R. (2015). Determination of shear modulus of soil from static and seismic penetration testing. In Jubilee volume. Proceedings in honour of Prof. A. Anagnostopoulos, Technical University of Athens (ed. M. Kavvadas), pp. 335–352. Athens, Greece: Tsotras.

Mindlin, R. (1949). Compliance of elastic bodies in contact. Trans. ASME, J. Appl. Mech. 16, No. 3, 259–268.

Morgan, P., Grott, M., Knapmeyer-Endrun, B.,Golombek, M., Delage, P., Lognonné, P., Piqueux, S., Daubar, I., Murdoch, N., Charalambous, C., Pike, Q. T., Müller, N., Hagermann, A., Siegler, M., Lichtenheldt, R., Teanby, N. & Kedar, S. (2018). A pre-landing assessment of regolith properties at the InSight landing site. Space Sci. Rev. 214, 104–151, https://doi.org/10.1007/s11214-018-0537-y.

Oztoprak, S. & Bolton, M. D. (2013). Stiffness of sands through a laboratory test database. Géotechnique 63, No. 1, 54–70, https://doi.org/10.1680/geot.10.P.078.

Poulos, H. G. & Davis, E. H. (1974). Elastic solutions for soil. Series in soil engineering. New York, NY, USA: Wiley.

Santamarina, J. C., Klein, K. A. & Fam, M. A. (2001). Soils and waves. New York, NY, USA: Wiley.

Seiferlin, K., Ehrenfreund, P., Garry, J., Gunderson, K., Hütter, E., Kargl, G., Maturilli, A. & Merrison, J. P. (2008). Simulating Martian regolith in the laboratory. Planet. Space Sci. 56, No. 15, 2009–2025.

Sneddon, I. N. (1946). Boussinesq's problem for a flat-ended cylinder. Math. Proc. Cambridge Phil. Soc. 42, No. 1, 29–39, https://doi.org/10.1017/S0305004100022702.

Tatsuoka, F., Iwasaki, T., Yoshida, S., Fukushima, S. & Sudo, H. (1979). Shear modulus and damping by drained tests on clean sand specimens reconstituted by various methods. Soils Found. 19, No. 1, 39–54, https://doi.org/10.3208/sandf1972.19.39.

Yamamuro, J. A. & Wood, F. M. (2004). Effect of depositional method on the undrained behavior and microstructure of sand with silt. Soil Dyn. Earthq. Engng 24, No. 9–10, 751–760.

Zlatovic, S. & Ishihara, K. (1997). Normalized behavior of very loose non-plastic soils: effects of fabric. Soils Found. 37, No. 4, 47–56, https://doi.org/10.3208/sandf.37.4_47.

4. WAVE VELOCITY MEASUREMENTS ON THE REGOLITH SIMULANT

"Not all treasure is silver and gold mate".
Captain Jack Sparrow, (2003).

This chapter concerns the study of wave velocities in the Martian regolith simulant under low stresses and strains. Since low density is key to mimic the behaviour of the regolith at the InSight landing site, particular attention has been paid to the procedure used to achieve loose density states. Then, the bender elements technique of measuring wave velocities in sands is presented, with some emphasis put on the travel time determination. The approach adopted to achieve low stress conditions is described prior to presenting the results of wave velocities and Poisson ratio, based on the use of software tools developed to assist in data interpretation. The results are then analysed based on a micro-mechanical contact theory supported by SEM and AFM observations. This work is presented in two companion papers already accepted in the Journal of Geophysical Research: Planets.

4.1. Characterization of soil behaviour at very low strains

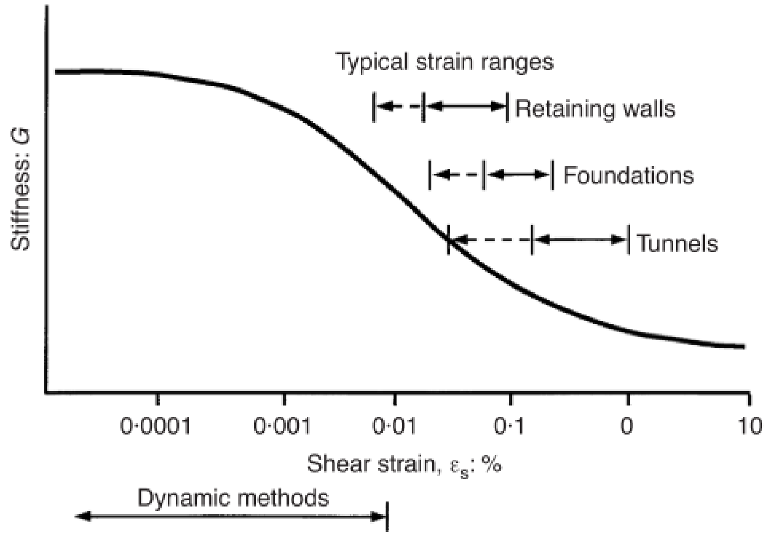

Figure 4-1. Strain ranges and associated applications (After Atkinson, 2000)

The determination of the change in shear modulus of soils with strain is relevant for geotechnical applications, especially under cyclic or dynamic conditions (Atkinson, 2000), particularly in offshore pile analysis and design (Sim et al., 2013). The maximum initial modulus of different soils in terms of void ratio and the degradation with strain has been investigated (e.g. Viggiani & Atkinson 1995, Oztoprak & Bolton 2013). Novel devices have been developed for determining elastic modulus at very low stress range and small strains (e.g. Cabrera et al. 2015, Caicedo et al. 2020, Villacreces et al. 2020) and at larger strains (e.g. Cagliero et al., 2015).

The ranges of stiffnesses considered for geotechnical applications are displayed in Figure 4-1. The elastic or very strain range is defined below $1x10^{-6}$ or $1x10^{-5}$, with intermediary strains up to $5x10^{-3}$ (Oztoprak & Bolton, 2013) and large strains above. The cyclic triaxial test (Bishop & Wesley, 1975) is used for larger strains, whereas medium strains are measured with the Resonant Column test (RC). Besides the shear modulus, these tests also provide the damping ratio of the soils, that are derived from the hysteretic cycles recorded under stress cycles.

The Bender Element (BE) testing method was developed in the late 1970s in the very low strain range (10^{-6}) to measure in a simplified way the initial shear modulus (denoted G_o or $G_{m\acute{a}x}$). The strain range of each test is summarized as follows, for the particular case of sands (Khiatine et al., 2019):

Bender elements	$\gamma < 10^{-5}$	Very small to small deformations
Resonant columns	$10^{-6} < \gamma < 10^{-4}$	Medium to large deformations
Cyclic triaxial	$\gamma > 10^{-3}$	Large deformations

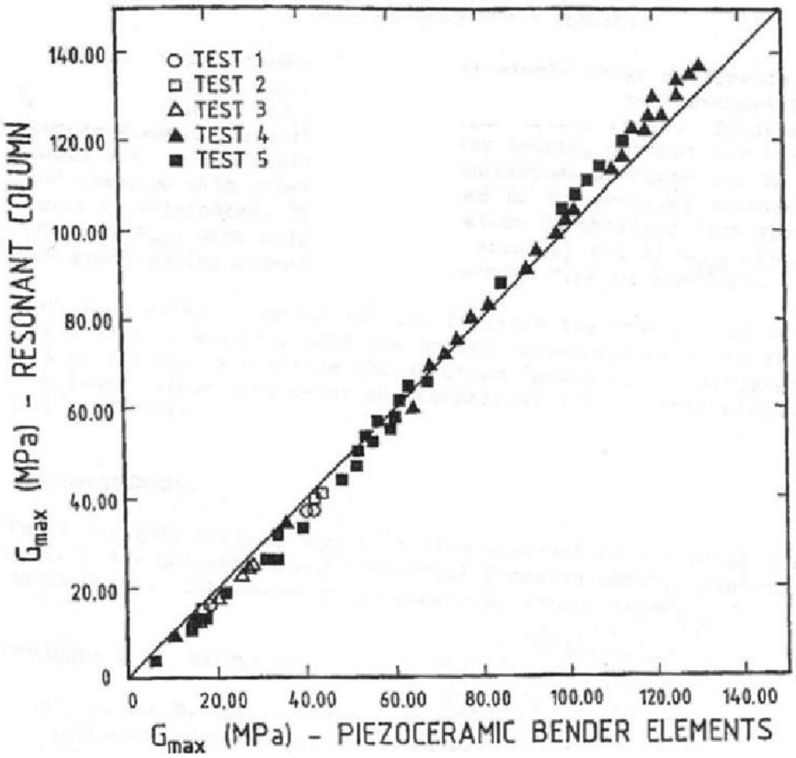

Figure 4-2. Correspondence of moduli by using Bender elements and Resonant column. (Dyvik &Madshus,1985)

Ideally, a single continuous degradation curve (showing the evolution of the value of G as shear strain γ increases) could be constructed combining the results of the three tests, as successfully done by Dyvik & Madshus, 1985 in the case of BE and resonant column (Figure 4-2).

Many models of the degradation curve have been proposed, starting with the hyperbolic expression of Hardin & Drnevich (1972). Oztoprak & Bolton (2013) considered a very large soil database to propose relevant expressions and parameters.

$$\frac{G}{G_o} = \frac{1}{1+\left(\frac{\gamma-\gamma_e}{\gamma_r}\right)^a} \qquad (1)$$

where G is the shear modulus at a strain γ, γ_r is a reference strain for 50% degradation and a is a curvature parameter. Most often, the following expression is adopted for G_0 (Hardin, 1972):

$$G_0 = A \cdot f(e) \cdot p'^m \qquad (2)$$

A and m are material constants and $f(e)$ is a void ratio function, for which many different expressions have been proposed. The results for these calculations based on available literature data for Fontainebleau sand in the literature is presented below, with the void ratio in Figure 4-3 and the maximum shear modulus on Figure 4-4.

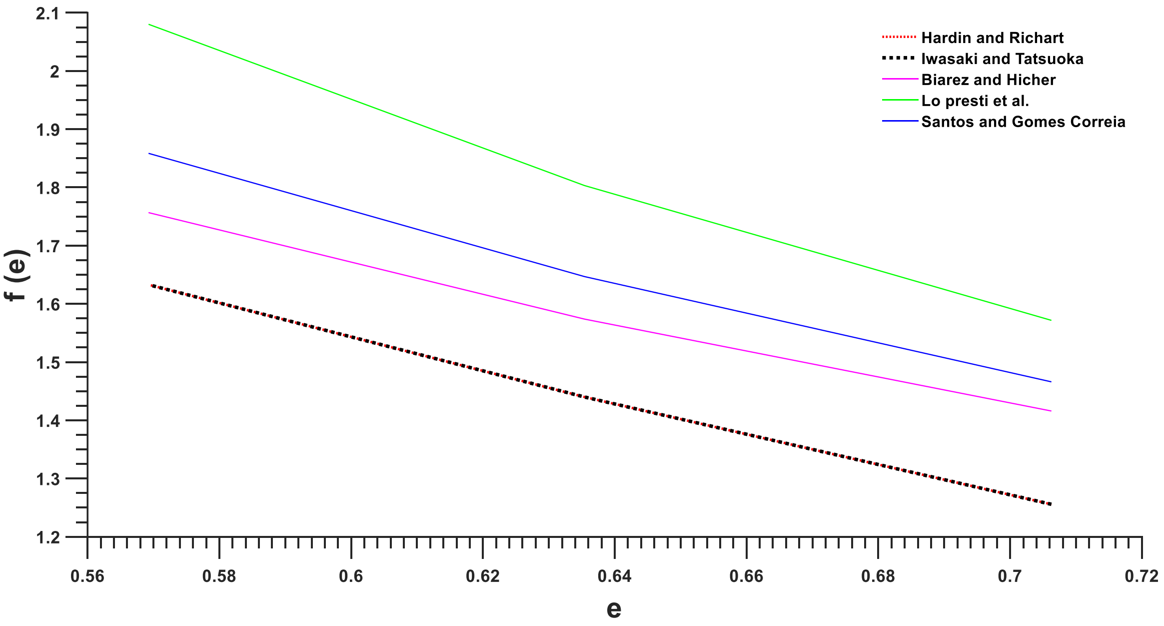

Figure 4-3. Void ratio functions for Fontainebleau sand.

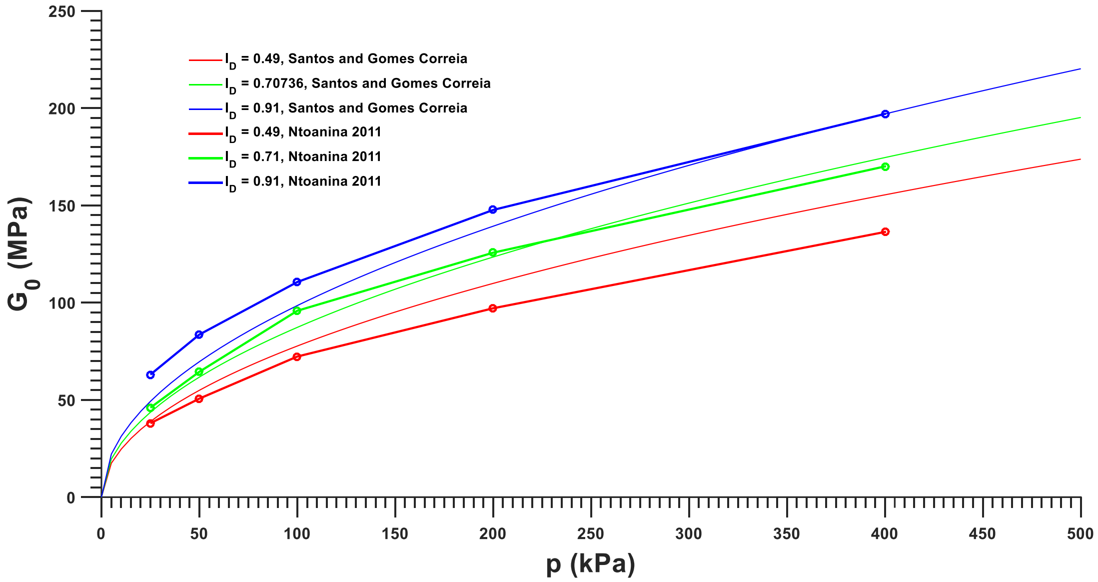

Figure 4-4. Initial shear moduli estimated for Fontainebleau sand.

The figure shows that reasonable estimates are obtained. Above 50 kPa, these reference values are useful, even if a direct test is to be preferred. However, data and fittings are limited below 50 kPa. Consequently, the work done with Bender Elements in this chapter (chosen instead of the resonant column to focus in the elastic range at these very low stresses and strains) can help for further calibration of these curves, especially in the low stress section.

The history of development of the Bender Element test and, particularly, the interpretation of the results it yields is now presented.

4.2. Bender Elements and soils: an ongoing story

The first works with bender elements started in the late 1970s. An array of ceramic benders was used to study the propagation of S waves in porous laboratory kaolinite sediments, determining both moduli and attenuation (Shirley & Hampton, 1978). The size of these early bender elements (3cm x 0.5 cm) were similar to modern versions. It is worth noting that initial work with Bender Elements was limited to S waves, due to the use of actuators limited to cantilever flexural displacements. The simultaneous propagation of P waves could not be correctly determined because of near-field effects.

The elastic expression for the calculation of the parameters were already established at the time, with the following expression of shear (V_s) and compression waves (V_p):

$$V_s^2 = G/\rho \qquad (3)$$

$$V_p^2 = K + \frac{4}{3}\frac{G}{\rho} \qquad (4)$$

where G is the shear modulus, K the bulk modulus, and ρ the density.

New experimental setups able to send, receive and interpret *P* wave signals for wave velocity determination were carried out, among others, by Schultheiss (1981), Bates (1989), Nakagawa et al., 1996 and Brignoli et al., (1996). A significant contribution concerned the development of actual piezoelectric actuators capable of generating and receiving both P and S waves directly, known as *bender extender* elements (Lings & Greening, 2001). The result of these advancements was substantial, since it meant that the same equipment with a simple change in connection could be used to simultaneously assess both wave velocities in the same sample, avoiding the need for different samples or indirect estimations. The change in connection modifies the actuator and receiver movement from cantilever flexion to a longitudinal extension and contraction. This was validated acquiring the received signal in two different flipped configurations. Since no change in polarity was observed, added to the fact that the measured velocity was too high for a shear wave, it was realized that the nature of the pulse was that of a compression wave. High quality signals were observed and recorded after filtering, which excluded considerable low frequency noise from the recorded signal. The signal arrival time can be attributed to the first depart from the zero axis, since there is no other wavefront faster that the emitted P wave, thus facilitating the interpretation of the results in comparison to the S wave signals which are obscured by faster P components (Santamarina et al, 2001).

Thanks to these progresses, anisotropic materials have been studied (Pennington 1999), along wide stress ranges and by using different setups with numerous bender actuator and receiver groups placed in complex geometrical configurations. This is usually done placing bender elements or similar piezo actuators as part of the experimental setup of other tests, such as triaxials (Dutta et al., 2020) or even more sophisticated equipment. An example of such a study is Duttine et al. (2007), where the anisotropy of reference sands mixed with kaolinite clay was addressed; in this work, benders were placed in testing equipment to accurately determine small strain moduli. This was combined with hollow cylinder and triaxial tests to compare an elastic isotropic model with a hypo-elastic anisotropic model. One of the same reference sands was studied under dynamic and static solicitations with rotated principal axes (Blanc et al. 2011), in the same equipment equipped with piezoelectric actuators. The results of these works can be used to calibrate complex model that account for the anisotropy at small strains with a few additional parameters (Yimsiri & Soga, 2003). As described further below, this problem has been studied with success in both frozen materials and viscoelastic materials such as bitumen. Another problem often addressed is that of reconstituted specimens, to assess the effect that sample preparation has on low strain anisotropy of the stiffness (Masanobu Oda, 1972a, 1972b). The particular case for clean sands after pluviation has been studied, observing that while the degree of saturation has only a negligible slight effect on the moduli, the preparation sample can result in 3-15% differences in measured dynamic properties due to the resulting different degrees of anisotropy resulting from sample preparation (Tatsuoka et al., 1979, 1986).

Other questions that remain relevant are those of the proper method of interpretation of the waveform signals, the effects of signal frequency and the response under low pressures, highly relevant for planetary investigations under low gravity. In this regard, novel experimental devices have been developed with glass bead samples subjected to very low confining stresses in microgravity conditions (Tell et al., 2020). Measurements at very low stresses range are defined as a normalization parameter (shear velocity at 1 kPa) for some of the exponential models describing the dependence of rigidity with effective stress (Cha et al., 2014). The parameters for these models are related to the soil compressibility coefficient C_c. Granular media subjected to extremely low stresses has also been studied (S. Van Den Wildenberg et al., 2013a), showing that wave velocity becomes hard to measure at stresses lower than 1 kPa as the linearity of the wave degrades. This was also related to a loss of evolution of the granular packing beyond what continuum theories may adequately describe (S. Van Den Wildenberg et al., 2013b). Since the lowest stress in this study is 3 kPa, the lowest datapoints are acquired near this limit, constituting a challenging zone for adequate measurements.

Wave velocities measured at very low strains have been used to assess the Poisson ratio of loose unconsolidated sands near the surface (Bachrach et. al, 2000, Spencer et al., 1994). This seldom addressed question of the Poisson ratio has been treated by Suwal & Kuwano (2013) from triaxial tests. The effect of the relative density has been investigated by (Kumar & Madhusudhan, 2010). Initial stiffness G_{max} has been determined from benders by V. Jovičić et al., (1996), Viggiani & Atkinson (1995b), Youn et al. (2008), with interest in the low strain domain paid by Jovičić & Vilhar, 2009). Anisotropy was also investigated by Suwal & Kuwano, (2013) and Siddiquee et al., (2018) and the evolution of the moduli near kinematic yielding was investigated by Kuwano & Jardine (2007).

Interpretation of the Bender Element Test

The proper interpretation of Bender element tests should properly address i) the determination of the travel distance and ii) the travel time of the waves. The travel distance is separation between the tips of the bender elements and is easy to determine (Brignoli et al. 1996, Dyvik & Madshus 1985, Simonelli & Vinale, 1989). The determination of travel time has been addressed in detail by Viggiani & Atkinson (1995a), who addressed the different sources for uncertainty, showing that a 16% error on the shear moduli may be due to the travel distance determination. They also shown that travel time uncertainty mainly due to the choice of the arrival time. The wave arrival is often related to the first deflection from the axis in pure S wave signals and the polarity of the first deflected peak is used to back this choice (Abiss 1981).

However, other studies (Sanchez-Salinero et al., 1986) associate the first peak observed in S waves to a near field component, corresponding to a wave with compression wave velocity, also evidenced in Brignoli et al. (1996). These parasites waves are the usual criterion to choose a sample size that allows for a travel distance of at least four wavelengths.

$$\lambda = V_s / f \qquad (5)$$

Where λ is the wavelength, V_S is the sample wave velocity and f is the wave frequency. As a result of using this criterion, the uncertainty may be significant since the arrival time uncertainty can result in a 60% error in the determination of G_0. This work also uses both sinusoidal and square waves as emission signals (10 V at 50 Hz square, 1kHz-10kHz sinusoidal). Larger arrival times were observed, similar to those obtained with the different available frequential domain methods.

Flat plate ceramics and resonant column were also successfully used for results validation when exploring the question of signal interpretation (Brignoli et al., 1996), further reinforcing the idea that adequate sample size in terms of sufficient wavelengths is needed for obtaining quality signals. In this work, P and S waves were measured in two clays and a saturated sand. While P wave is treated as trivial with the first axis depart, multiple arrival waveforms are suggested for the choice of the S wave arrival time for different scenarios, depending on the frequency choice for the transmitted signals, while always considering the polarity of the wave as positive. Interpretation is facilitated by using proper frequency for the sinusoidal wave, resulting in the near-field components becoming less relevant and facilitating the choice of the arrival time.

In Brignoli's work, though considering the frequency-domain based methods as the most accurate, the use of the final point of the received signal (both square and sinusoidal) was deemed most adequate for its proximity to the frequency values. For simplicity, this point may be referred to as the *first major reversal of the polarity*. Use of inadequate methods may result in overestimating the result in up to 14%. This is the case for pure S wave signals.

Further work on the proper arrival time determination question was addressed in the following decades. An "objective criterion" was proposed (Jovičić et al., 1996) for improving this criterion. While acknowledging the ability of using sinusoidal waves as being able to reduce the uncertainty to about 7%, based on Sanchez-Salinero et al (1986), the first deflection in a bender S wave signal was attributed to the near field effect and thus discarded. It is also stated that based on this solution that when using a square wave, "*a near field effect will necessarily always be present since it carries a whole spectrum of frequencies".* It was also noted that *"The precise shape of the near field effect is a little different to that given by the analytical solution or the test data".*

Performance and interpretation continued to be heavily focused (Lee & Santamarina, 2006), incorporating more complex considerations into the analysis such as crosstalk, resonance, and further insights into the near-field effect. Recommendations are given to avoid crosstalk, considering the possible connection configurations (series and parallel), mainly through grounding. A point is also made that although the travel time is unaffected regardless of the used frequency, working in the vicinity of the resonant frequency of the bender-soil system can significantly help the interpretation of the measured signals (and poses the alternative of using a square wave to include a range of frequencies). Finally, the utilisation of the cross-correlation approach is encouraged to account for the multiple reflections of the wave in the walls of the container.

The problem of overshooting is also presented in this Salinero et al. (Sanchez-Salinero et al., 1986), where the ideal sinusoidal waves may not be used at the desired high frequencies for very stiff materials, resulting in the necessity of measures at lower frequency (thus not making it possible to avoid the near field effect merely by using only very high frequency sinusoidal waves). While also providing two possible solutions to avoid the overshooting problem, this work also confirmed the use of the reverse arrival point for the sinusoidal waves.

Numerical solutions for the motion at the arrival point were proposed by Sanchez-Salinero et al. (1986), showing that 3 components (two propagating at V_s speed and one at V_p velocity) are present in the S wave received. A distance Ratio Rd was defined, a key parameter for bender element as it relates distance with wavelength and is thus useful for assessing eventual near field effects. These near field effects seem to be more drastic for stiffer materials. This Rd parameter can be used to select adequate frequency values with or without a more drastic field effect.

Work on the bender element interpretation continued during the 2010s, with more methodologies for interpretation of increasing complexity, including complex reconstructions of the signal waveforms elaborated on the cross-correlation methods (Ogino et al., 2010).

Despite all these efforts, accurate interpretation remains a challenging task and the manufacturing companies tend to provide their own detailed interpretation guides indicating what works best for their equipment.

Study with Bender Elements on different soil types

The initial works using bender elements were mainly conducted on clays (including Shirley & Hampton, 1978). However, since then, both dry and saturated sand have also been studied to evaluate the performance of the different interpretation criteria, including time domain methods, cross-correlation and frequency-based methods to evaluate sinusoidal pulses.

Tests on a silty sand (Jovičić & Vilhar, 2009) confirmed the significant difference between time and frequency domain methods, with a tendency to yield lower *G* for the frequency domain methods. The case for both dry and saturated Toyoura sand (Gu et al., 2015) was addressed to further improve the criteria in a wide range of experimental conditions, while comparing with the resonant column and torsional shear test for further validation. The comparison established that the use of these dynamic methods enabled to observe a slight reduction in the values observed for the initial shear modulus under saturated conditions, in contrast to those obtained for dry ones, which can be attributed to the wetting of the grain at contacts, an effect already been observed by Nakagawa et al. (1997). Sand anisotropy whas also studied with multiple bender elements on uniform Kenya ($D_{50} = 0.12\,mm$) and Ticino sands $D_{50} = 0.6\,mm$ (Fioravante, 2000).

Many clays have also been studied successfully with bender elements, including the work of (Jamiolkowski et al.,1995) on six clays, allowing for the proposition and calibration of early models. The initial shear modulus was observed to depend on the void ratio and principal effective stresses, and not the over consolidation ratio (OCR). The setup also benefited from the relative simplicity of bender elements to explore material anisotropy by measuring wave velocities in three different directions. Another important result was the comparison with field measurements, observing considerable differences with other methods used for the estimation of G_0 (with bender elements, velocities are from slightly lower to around half those measured in the field, and 20-25% higher than data from resonant column). This suggests that the true elastic threshold for deformation of these clays may be lower than usually considered.

Another work including measurements of anisotropy was part of a doctoral thesis (Pennington 1999) on a clay with significant kaolinite content. Accuracy was estimated to be around 1.5-2.5% for the velocity measurement, and 2-6% for the modulus values. The use of bender elements allowed to characterize the highly anisotropic Cambridge clay as intended, supported again by considering the polarity of the received S waves for arrival time identification. This anisotropy was observed to be highly dependent on the void ratio.

Frozen soils have also been studied to assess anisotropy of the small-strain modulus with piezoelectrics, since icing cycles can induce freezing (J. Wang et al., 2019). Linear viscoelastic materials have also been studied using wave propagation with piezo actuators (Sauzeat & Di Benedetto, 2015), analysing the waves with both frequential and time domain methods and enabling to study the anisotropy of the complex modulus and even the Poisson ratio of the material (Benedetto et al., 2007, 2009).

The main problem is the choice of interpretation methods. Extensive works have already been made which compile existing methods and detail the choice of departure or arrival times, while also explaining the cross-correlation and the frequency-based methods (Murillo 2006, Asslan 2009, Boulanger et al., 1997). The main interest has been recently paid on methods using parallel interpretation, in which simultaneous measurements of both P and S waves are used to interpret the signals under an established set of criteria (Wang et al., 2017).

4.3. Work on bender elements (and wave velocity to determine stiffness or Poisson ratio)

The two papers detailing the work and interpretation done with bender elements used in sandy simulant under low stress are now presented.

For reference (additionally to the article results), some additional information is provided here concerning the results of these two works.

As seen in Figure 4 5, limited hysteresis was observed during the testing results, starting from 10 kPa where the metallic container was removed. It can be seen that for all the four samples evaluated during the work presented in the article the unloading process was reversible. This is the result of carefully choosing the starting stress of the stress trajectory, since it was found that the sample could be turned to a horizontal position at 10 kPa without disturbing it too much.

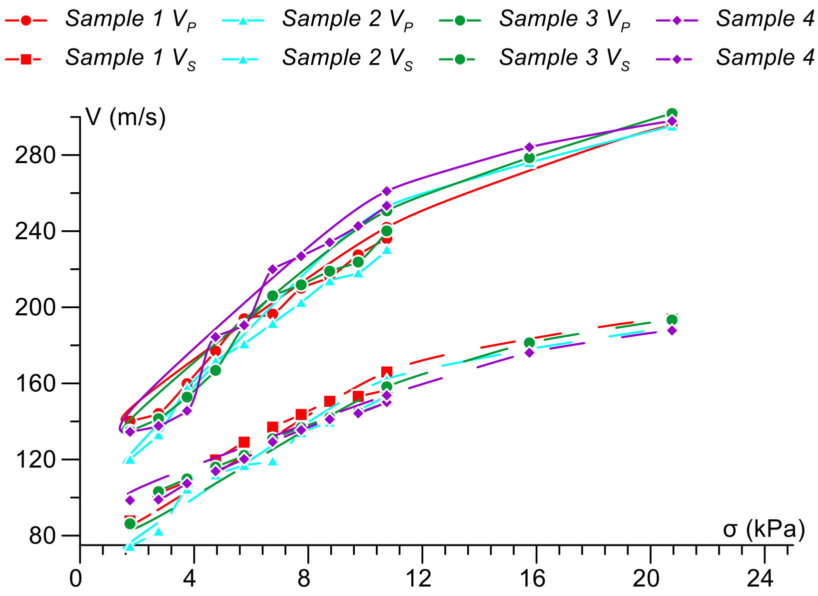

Figure 4-5. Limited hysteresis of sample wave velocities was observed during the unloading-reloading cycle.

Figure 4-6 and Figure 4-7 shows a comparison of the obtained results for compression and shear wave velocity in the new simulant (Fontainebleau sand) in contrast to the previously used regolith simulants. It can be seen how low the stress range measurement used is, with several points in the new tests being measured below the lowest stress measured in previous works (Karakostas et al., 2013).

The stress values presented on the measurement results were determined combining the imposed vacuum with the effect of sample self-weight and the stress imposed by the membrane holding the sample together, as described in the article. The sample was unloaded from the initial 10 kPa value where it was dismounted without observing significant height variations (less than 1 mm height variation through the entire testing), and only then unloaded to the lowest stress values. It was then reloaded up to the highest values of stress of 80kPa; this procedure ensured that the very loose assembly was not disturbed by the application of the higher stress values.

A measurement datapoint results from averaging three to five of the waveform signals acquired by the oscilloscope. Each of these waveforms results from continuous operation of the bender elements, averaging 256 rapidly recorded signals until a stable waveform is attained. Several measurements are thus obtained, in identical conditions to ensure repeatability and as a first assessment of variability; three were deemed sufficient for higher stresses were almost no difference existed (The typical variability was observed to be of a few m/s above 15 kPa, thus well below 1%), while five were considered necessary to further reduce the incertitude present on the measurements done at lower stress levels (with variations staying below 5%). In addition to measurement incertitude, it was necessary to quantify the effects of making use of different samples, and thus of a slightly different density value and particle arrangement. Preliminary tests showed that only limited variation in the results was present, but it was nevertheless to perform four experimental programs in different samples to discard the effect of sample preparation on the results. The results of all the samples as seen in the article show great correspondence and thus it can be considered that the presented results are easily reproducible.

Since no hysteresis was observed, even at the lowest stresses, and considering that no important sample dimension variation was observed during the complete testing procedure, it can be considered that no relevant irreversible grain rearrangement took place during the tests.

High frequency content was observed in the acquired signals in contrast to the frequency of the emitted wave; since a single pulse is being used instead of a continuous sinusoidal signal, which theoretically would have a single frequency content. Instead, the single pulse implies that both higher (and lower) frequencies are present in the transmitted signal pulse, which then appear on the received waveform signal as higher frequency components. While the velocity results are considered to be independent from the actuator excitation frequency, it was decided to work at a fixed 10 kHz frequency for the sinusoidal pulse, which considered was adequate to not introduce additional variability of different frequency values (Youn et al., 2008, Santamarina et al., 2005). This frequency content may be somewhat limited in comparison to the use of a square wave, which would carry all frequencies. But the bender element assembly in use is well known and working at 10 kHz enables for the use of clear signals which can be interpreted (the frequency of the sinusoidal does not affect the true arrival time, but proper choice of frequency can help data interpretation), and as mentioned previously some higher frequency energy is transmitted due to the utilisation of a single sinusoidal pulse.

The most adequate method to determine this stress was to determine the stress level present after placing the sample in horizontal position, and accounting for the effect of the membrane stiffness in a FEM calculation (considered adequate since the sample is relatively large in dimensions and mostly undisturbed) once this static configuration has been attained. Further detail on this methodology can be found in the first article below. Further complexity to account for factors such as sample anisotropy resulting from the preparation procedure were not considered necessary. The sampling frequency used was 500kHz, so the signal waveforms were obtained consistently with a very high quality.

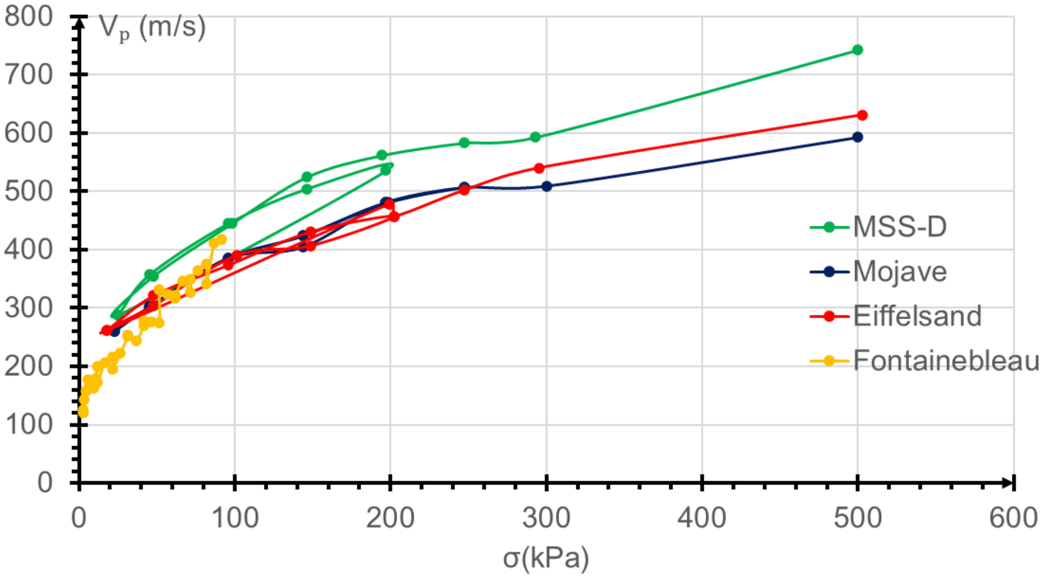

Figure 4-6. Compression wave velocity measurements of Fontainebleau sand compared with previous regolith analogues.

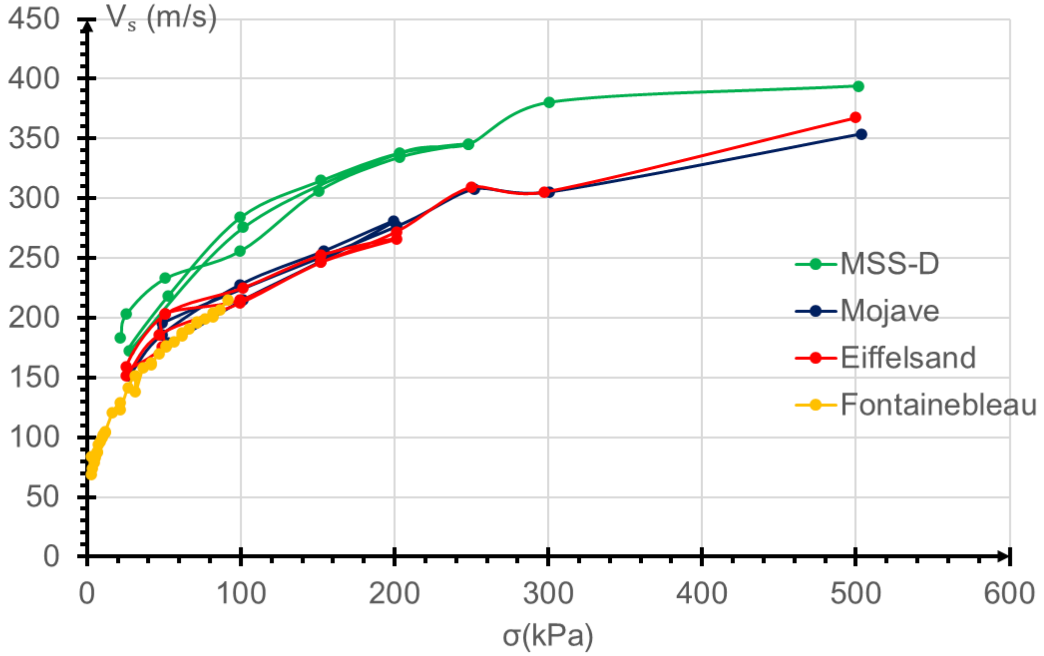

Figure 4-7. Shear wave velocity measurements of Fontainebleau sand compared with previous regolith analogues.

4.4. Wave Velocities and Poisson Ratio in a Loose Sandy Martian regolith Simulant under Low Stresses. Part 1: Laboratory Investigation (Article 3: Published, JGR-Planets)

J. P. Castillo Betancourt[1,2], P. Delage[1], B. Caicedo[2], Ph. Lognonné[3], B. Banerdt[4]

[1] Ecole des Ponts ParisTech, lab. Navier-CERMES, CNRS, UGE, Marne la Vallée, France.

[2] Universidad de los Andes, Bogota, Colombia.

[3] Université Paris-Cité, Institut de Physique du Globe, CNRS, Paris, France.

[4] Jet Propulsion Laboratory, California Institute of Technology, Pasadena, California, USA.

Key Points

Bender Element measurements of V_p and V_s carried out on a novel device on loose Fontainebleau sand samples used as a Mars regolith simulant.

Study carried out within a so far unexplored low stress range, below 10 kPa and as low as 1.75 kPa.

Poisson ratio observed to remain mostly constant at low stress, with a possible decrease in the zone below 5 kPa.

Abstract

Wave velocity measurements were performed on Fontainebleau sand samples used as Martian regolith simulant to investigate the elastic properties of the surface material at the InSight landing site on Mars (Elysium Planitia). Loose samples (density 1.4 Mg/m3, density index 6%) were prepared by using the pluviation method, to adequately represent the low regolith density at the InSight landing site. A novel device derived from triaxial testing was designed to to measure wave velocities at low stresses along a horizontal cylindrical specimen. Four tests were made, in which the confining stress was applied by applying vacuum between 1 and 80 kPa. Wave velocities were measured by using bender elements under stresses as low as 1.75 kPa, a very low value compared to the standard stress ranges generally considered in terrestrial geotechnics (> 10 kPa). The changes in compression and shear wave velocities obey a standard power law, with however two slightly different exponents for V_p and V_s, indicating a not perfectly elastic behavior. Data showed greater variability below 5 kPa, indicating some limitations of the bender elements technique in this range. A slight decrease in Poisson ratio was detected below 5 kPa, which certainly deserves more investigation. This investigation is useful to better analyze the data of the InSight mission, both in terms of wave propagation at surface and to interpret some in-situ elastic tests carried out with the scoop. These data are interpreted in the light of a granular contact mechanics theory in a companion paper.

Plain Language Summary

The InSight mission lander placed on Mars a highly sensitive seismometer to detect seismic waves from Marsquakes and meteorite impacts. To help analysing the seismic waves, a special laboratory device was developed to measure wave velocities on a loose sandy simulant mimicking the surface regolith, with wave emitting/receiving transducers placed on both sides of a cylindrical sand sample submitted to external stress. Due to reduced gravity, stresses, that control wave velocity (larger stress, faster waves) are very low at the Mars surface. To impose low stresses (down to 1.75 kPa), we used a horizontal sample with a careful stress calculation along the sample axis, along which waves propagate. We determined the changes in wave velocity with stress (governed by a power law) and observed greater variability under 5 kPa, showing the limit of our transducers at low stresses. Based on elasticity theory, derived from wave velocities parameters governing sample deformations under strain changes. We suspect a slight decrease of Poisson ratio (that characterises radial elastic strain of a cylindrical sample under axial loading) below 5 kPa. Data is useful to better constrain the response of Mars sandy surface materials, at the InSight site and other areas for future Mars missions.

Keywords

Wave velocities, Martian regolith, Bender element test, InSight mission.

Introduction

Recent interest into the elastic behavior at small strain of sands under low stresses has been gained through the investigation of the mechanical properties of the surface layer at the InSight landing site on Mars, submitted to reduced gravity (g = 3.721 m/s2). Briefly, the NASA InSight mission is a geophysical mission landed on Mars (Elysium Planitia) in November 2018. The InSight lander installed on Mars' surface a highly sensitive seismometer, funded by CNES (Centre National d'Etudes Spatiales, the French Space Agency) aimed at investigating both the seismic activity and the meteorite impact activity on Mars. The lander also installed the so-called HP3 thermal device funded by DLR (Deutsches Zentrum für Luft- und Raumfahrt, the German Aerospace Center) that comprised a self-driving penetrometer aimed at measuring the thermal flow emitted by Mars and at characterising the surface thermal properties (Spohn et al., 2018). The seismometer (Lognonné et al., 2019, 2020) provided valuable information about the seismic activity on Mars (e.g. Banerdt et al., 2018, Giardini et al. 2020, Hobiger et al., 2021) and about meteorite impacts (e.g. Garcia et al., 2022; Posiolova et al., 2022). Unfortunately, the selfdriving penetrometer could not penetrate more than 40 cm deep, due to a lack of friction along its shaft (Spohn et al., 2022a and b). It provided however the surface thermal conductivity (0.039 ± 0.002 W m-1 K-1), in agreement with orbital and in-situ thermal inertia estimates. Thermal data also allowed to derive a quite low surface density of 1.2 Mg/m3 (Grott et al., 2021).

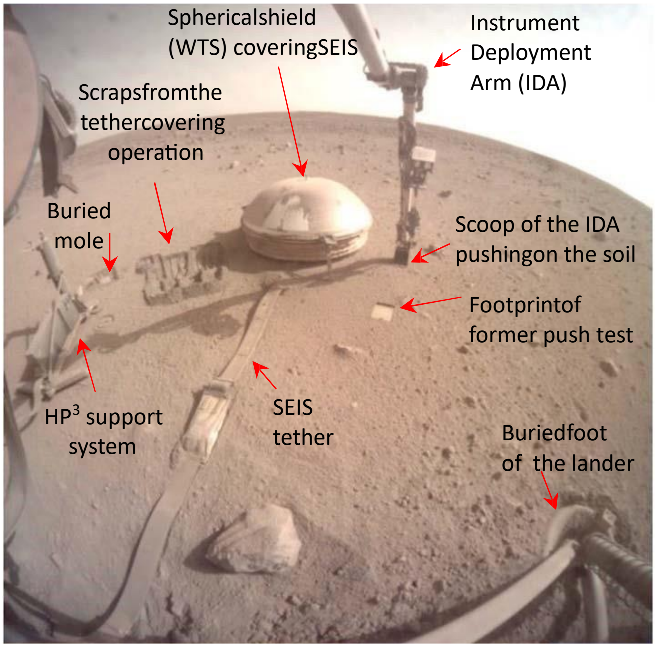

Figure 4-8 Image taken on Sol 1770 (i.e., the 1770th martian day of the mission) by the Instrument Context Camera of the Lander showing the hemispherical Wind and Thermal Shield (WTS, diameter 720 mm) covering the SEIS instrument, with the Instrument Deployment Arm vertically pushing on the soil at the right of the SEIS. A flat footprint made by a former push test by the IDA can also be observed. These push tests were carried out to estimate the surface elastic properties based on the sstrain derived from the SEIS response. The (black) HP3 support system is observed on the left side, close to the place where the self-driving penetrometer has been buried. Some scraps made by the IDA scoop to cover the regolith tether for better thermal insulation can also be seen at the left of the WTS. All instruments are covered by a dust layer progressively brought by the Martian winds (Image Credit: NASA-JPL).

The InSight mission provided much information on the mechanical properties of the surface (Morgan et al., 2018, Spohn et al., 2021, Delage et al. 2022a, 2022b, 2023, Marteau et al. 2021, 2022, 2023, Verdier et al. 2023). Significant input in this regard was gained by using the Instrument Deployment Arm (IDA). The IDA, designed to place the instruments on the surface of the planet, was also used in various scrapping and piling activities carried out with the scoop at its edge (Golombek et al., 2023). Figure 4-8 shows a photo taken by the Instrument Context Camera of the lander on sol 1771, close to the end of the mission, illustrating these activities. The photo shows that the landing site is flat and characterised by a sandy deposit with little rock abundance, as planned from orbiter data during the landing site selection (Golombek et al., 2017). The photo also shows the hemispherical Wind and Thermal Shield (WTS) placed above the SEIS seismometer and the scraps made by the Instrument Deployment Arm (IDA) placed with its scoop in contact with the soil on the right hand side of SEIS). One also observes, left of SEIS, the scraps made by the IDA scoop during the operation of covering the SEIS tether to improve thermal insulation and reduce glitches in the seismic signals (Golombek et al. 2023). The support system of the self penetrating thermal probe is observed on the left hand side, close to the place where the probe has been penetrated. One can observe that all devices are covered by a dust layer that finally hampered the functioning of the solar arrays, resulting in a too weak power supply to keep the instruments working. This led to the end of the mission on 18 December 2022.

The surface layer properties are not fully understood. Due to long term wind saltation, Mars regolith particles at surface are sub-rounded to rounded (Goetz et al. 2010b). Direct visual observations of the pits excavated by the rocket exhausts during landing evidenced a layer of cohesive sandy matrix containing some pebbles, called duricrust (see Warner et al. 2022, Delage et al. 2022a). It is suspected that the surface low density is made possible by inter-grains cemented bonds within a loose arrangement of regolith particles. The inter-grains cement is suspected to be due to salts deposited by thin films of water via interactions of atmospheric water vapor and soils, as suggested by chemical measurements by Viking and Mars Exploration Rover spacecraft (Banin et al. 1992, Haskin et al. 2005, Hurowitz et al. 2005).

The in-situ determination of the surface regolith elastic properties could be made by recording with the seismometer the waves emitted during the hammering sessions of the penetrometer (Brinkman et al., 2022). The mean values of compression and shear wave velocities were Vp = 119 m/s and Vs= 63 m/s, respectively, in reasonable agreement with previous lab estimations on loose sands used as regolith simulants (Delage et al., 2017).

In spite of the difference between the sandy simulants used in terrestrial lab testing (Seiferlin et al. 2008, Delage et al. 2017, Delage et al. 2022b) and the regolith at the InSight landing site, it was found interesting to further investigate the elastic properties of sandy simulants under stresses lower than those currently considered in terrestrial Soil mechanics to better analyse the properties of surface sandy regolith on Mars, that are submitted to very low stresses. To do so, a specific device was developed in the laboratory to measure wave velocities in loose sand with bender elements under low stresses. This paper presents the device and the results obtained in terms of wave velocities and Poisson ratio. In a companion paper (Caicedo et al. 2023), the data are analysed through a theory of contact mechanics accounting for the roughness of particles (Bachrach et al. 2000, Bahrami et al. 2005, Bachrach and Avseth 2008, Butt et al. 2015).

Wave velocity and Poisson ratio in sands

The Poisson ratio ν of sands has been determined through wave velocity measurements by using bender elements by various authors, including Bates (1989), Nakagawa et al. (1996), Prasad (2002), Kumar & Madhusudhan (2010) and Suwal & Kuwano (2013). The expression of ν with respect to V_p and V_s is as follows, assuming an isotropic elastic medium:

$$\nu = 0.5\frac{\left(\frac{V_p}{V_s}\right)^2-2}{\left(\frac{V_p}{V_s}\right)^2-1} \tag{1}$$

where V_p and V_s are the compression and shear wave velocities, respectively, given by the following expressions:

$$V_P = \sqrt{\left(K + \frac{4}{3}G\right)/\rho_b} \text{ and } V_s = \sqrt{\frac{G}{\rho_b}} \quad (2)$$

where K and G are the bulk and shear elastic moduli, respectively, and ρb the bulk unit mass of the sample.

In the stress ranges considered by these authors, the Poisson ratio decreased under increased stress. Under high stresses, Prasad (2002) observed a decrease from 0.38 to 0.30 between 1 and 10.2 MPa, with ν = 0.30 up to 20 MPa. For Toyoura sand (D_{50} = 0.19 mm, I_D = 0.68), Suwal and Kuwano (2013) showed that ν decreased from 0.175 down to 0.15 between 50 and 400 kPa. Kumar and Madhusudhan (2010) investigated the effects of stress (between 100 and 500 kPa), density index I_D between 0.4 and 0.8 ($I_D = \frac{e - e_{min}}{e_{max} - e_{min}}$, where e_{max} and e_{min} are the sand maximum and minimum void ratios, respectively) and and decreased with increased density index. Some data under lower stresses in a dense random pack of identical glass beads were presented by Bachrach et al. (2000), with ranging between 0.130 and 0.151 for stresses between 5 and 40 kPa. They also conducted in-situ wave measurements in Moss Landing beach (California, dry angular sand) using a seismic line parallel to the shoreline of 20 geophones distant of 30 cm, and a hammer (about 50 kg) applied on a metal block as source. The Poisson ratio derived from the velocity profile between 0 and 5 m (vertical stress between 0 and 78.5 kPa with a dry unit mass of 1.7 Mg/m3) was equal to 0.15, with no increase with depth. The Poisson ratios that they determined in the lab were between 0.13 and 0.26, with a tendency to decrease i) under increased stress - more significantly for fine-grained sand - and ii) under increased density index, whereas the in-situ determination by Bachrach et al. (2000) evidenced a constant ν with respect to stress.

Materials and Methods

3.1 Fontainebleau sand as a Martian Regolith simulant

To account for the rounded shape of regolith grains on Mars (Goetz et al. 2010b), we adopted the NE34 Fontainebleau sand (see Delage et al. 2022b). It is a well-sorted silica sand (grain density ρs = 2.651 Mg/m3) from the Paris Basin with a median diameter D50 of 220 µm (see Figure 4-9, Benahmed 2001), to compare with the 175 µm diameter derived from thermal inertia measurements in the InSight landing site (Golombek et al. 2017). The uniformity coefficient Cu is equal to 1.65. The grain size distribution is presented in Figure 4-9a, together with a scanning electron microscope photo (b) that shows that grains are sub-rounded to rounded. The minimum and maximum void ratios are emin = 0.54 and emax = 0.86, respectively (Andria-Ntoanina 2011).

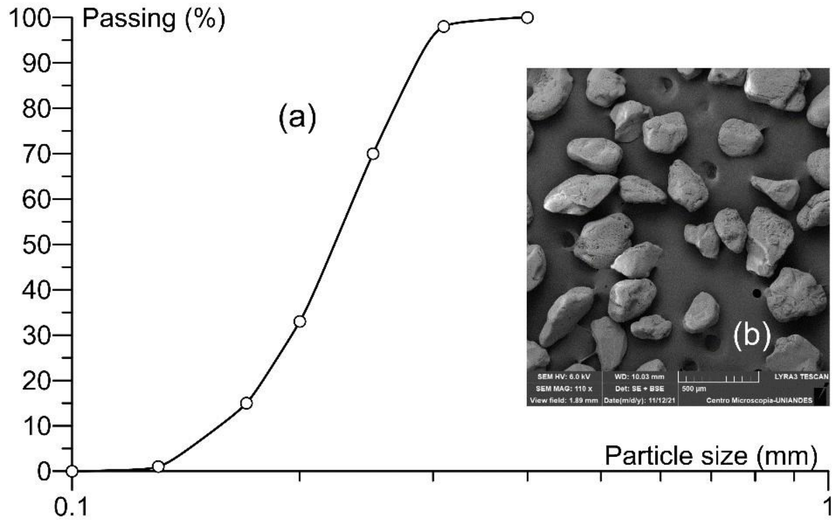

Figure 4-9 NE34 Fontainebleau Sand: (a) grain size distribution curve, and (b) SEM image.

3.2 Sample preparation

The sample was prepared, as for standard triaxial testing, by using a 170 mm high mould of internal diameter 100 mm into which a neoprene membrane, fixed to the base of the triaxial cell and the external face of the mould at the top by using two O-rings, was maintained by applying vacuum (80 kPa). The pluviation technique (Kolbuszewski, 1948; Cresswell et al., 1999, Benahmed, 2001, Hariprasad et al. 2016) was used to prepare a low density sample, adopting an almost null fall height (resulting in an upward speed of the sieve of 3 cm/s) and a small sand flow.

The final dimensions of the sample are 100 mm in diameter and 150 mm in height, with a density around 1.4 Mg/m3 (void ratio $e = 0.84 - 0.82$, density index I_d = 6 - 10%). After pluviation, the sand in excess was carefully removed, the top cap was carefully placed on the flattened sand surface and the membrane was wrapped around it and fixed by an O-ring. Before dismounting the mould, the vacuum was decreased to 10 kPa, a pressure that appeared to be high enough to maintain the cylindrical shape of the sample.

3.3 Experimental setup at low stress

The wave velocity measurements were carried out by using 3 mm height bender elements (GDS brand, able to send and receive both compression P and shear S waves) inserted into the top and bottom ends of the sample. They were controlled via a signal generator producing sinusoidal waves at a fixed frequency of 10 kHz and 14 V amplitude. An amplifier was used to increase the magnitude of the received signal. Data acquisition was made through an oscilloscope, using two channels spatially located the furthest from each other, thus reducing as much as possible the crosstalk effect between bender elements (Lee & Santamarina, 2005).

In a vertical position, with a density of 1.4 Mg/m3, the vertical stress σv at the base is around 2.21 kPa (the weight of the soil column). Given the low-stress range considered (below 10 kPa), the stress difference between the top and bottom of the sample was not acceptable. It was then decided to place the sample in a horizontal position (Figure 4-10).

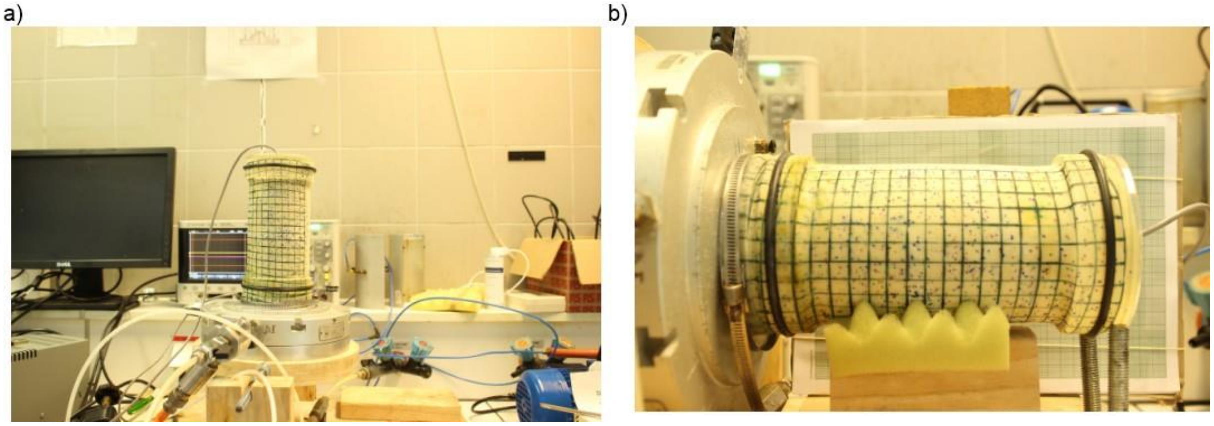

Figure 4-10. a) Sample preparation (vertical); b) Sample tested (horizontal).

The wave travel path along the axis of the horizontal cylindrical sample is submitted a total stress σ equal to the sum of three components:

(3)

where σ_{gh} is the gravity-induced stress within the horizontal sample, σ_m the membrane isotropic confining stress and σ_{vac} the vacuum-induced isotropic stress.

The stress produced by the membrane was evaluated using the solution for a small wall cylinder under pressure as follows:

- The stiffness of the membrane was measured by imposing different forces on a membrane, as shown in Figure 4-11a. From the linear response obtained (Figure 4-11b), one can derive the spring coefficient k of the membrane as the ratio between the half of the applied unit load and the axial strain of the membrane. The data of the Figure 4-11 provides k = 1613.85 N/m.

- The force Fm applied by the membrane around the sample (Figure 4-11c) is given by F_m=k Δr/r, where k is the membrane spring coefficient, Δr the increase in the radius of the membrane between the free state and the stressed state around the sample and r the sample radius. Δr was obtained by subtracting the sample perimeter from the length of the extended membrane, Lm, divided by 2π ($\Delta r = r - L_m/2\pi$).

- Using the solution for a small wall cylinder under pressure, as shown in Figure 4-11c, the radial stress σm applied by the membrane per unit length on the sample is $\sigma_m = F/r$.

With k = 1613.85 N/m, Δr = 2.5 mm and r = 50 mm (a significant initial 5% variation), the confining stress due to the membrane is σm = 1.6 kPa, a result similar to that obtained by Henkel & Gilbert (1952) and Newland & Allely (1959).

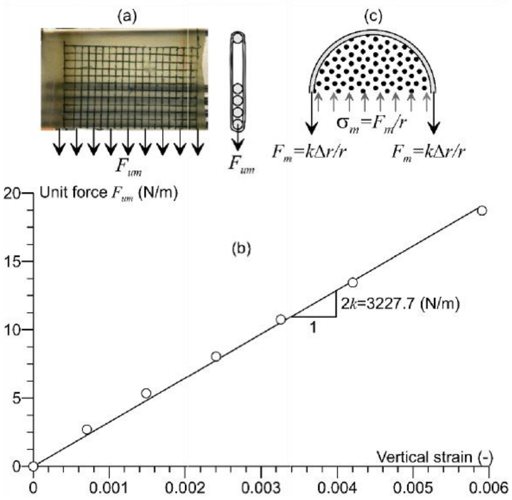

Figure 4-11. (a) Setup used for measuring the membrane stiffness; (b) Force/vertical strain elongation curve of the membrane; (c) Schematic drawing for computing the stress on a cylinder.

The gravity-induced stress was computed in elastic conditions (accepting the limitations of assuming the material as isotropic) by using the Plaxis 3D finite element code (see Figure 4-12), applying the membrane stress as a boundary condition, providing σ_{gh} = 0.75 kPa at a density of 1.4 Mg/m3.

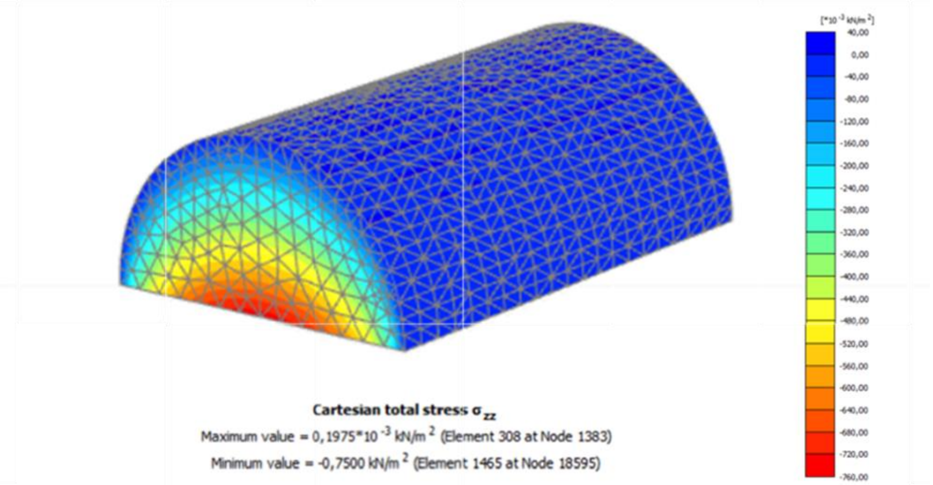

Figure 4-12. FEM (Plaxis 3D) elastic analyses of the sample self-weight to estimate the horizontal stress σ_{gh} on the sample axis.

The constant stress due to the combined effect of both gravity and the membrane is $\sigma_m + \sigma_{gh}$ = 0.75 kPa. The total stress applied to the sample was changed by changing the vacuum applied within the sample. Once the (vertical) sample pluviated and the membrane fixed around it, a 10 kPa vacuum was applied before removing the mould and rotating the sample in the horizontal position, with no change observed in its size. The total horizontal stress applied on the sample axis was obtained by adding 0.75 kPa to the applied vacuum. Then, the loading path was applied by changing vacuum as follows:

- A step unloading path from 10 kPa to 1 kPa, (10 - 9 - 8 - 7 - 6 - 5 - 4 - 3 - 2 - 1 kPa) followed by reloading back to 10 kPa.
- A step loading path from 10 kPa up to 80 kPa, (10 - 20 - 30 - 40 - 50 - 60 - 70 - 80 kPa). Moreover, some tests were performed at 5 and 15 kPa to investigate eventual hysteresis effects.

Various wave measurements were carried out at each stress to assess variability and repeatability. Five waves were recorded for stresses below 10 kPa, as a higher variability was observed in this stress range. In contrast, three measurements were deemed sufficient at 15 kPa and above (the number of repetitions was chosen after interpreting the results of the initial tests).

Experimental results

The tests were carried out on 4 pluviated samples (EP 1 to 4), with densities given in Table 4-1.

Table 4-1 Sample densities of the 4 samples tested.

Sample	***Density (Mg/m^3)***
EP1	1.443
EP2	1.443
EP3	1.447
EP4	1.452

Determining the accurate travel time of the waves is crucial in bender element tests, and various methods have been used in the literature. They include the first inversion of the output signal and the first zero value immediately after the signal inversion (Shirley & Hampton, 1978; Dyvik & Madshus, 1985; Jamiolkowski et al., 1995; Jovičić et al., 1996; Jovičić & Vilhar, 2009), the peak-to-peak-method (Viggiani & Atkinson, 1995a), the cross-correlation frequency-domain method (Viggiani & Atkinson, 1995b; Arulnathan et al., 1998; Boulanger et al., 1998; Mohsin & Airey, 2003; Murillo et al., 2009; Murillo et al., 2011) and some methods simultaneously analysing the travel time of both P and S waves (Lee & Santamarina, 2005; Wang et al., 2017).

As seen in Figure 4-13, which presents the data for 70.75 kPa, an accurate determination of the travel time could be made by considering, for both P and S waves, the starting point of the sinusoidal emitted signal and that of the received P and S signals. Interestingly, there is a clear coupling between the reception of both waves. The S wave arrival could be detected in the received P wave signal (at 0.57 ms), as commented by Wang et al. (2017). Note also that some slight oscillations due to the P wave arrival (after 0.4 ms) are detected in the S wave signal, whereas a clear increase in amplitude in the P wave signal is observed when the S wave arrives after 0.57 ms.

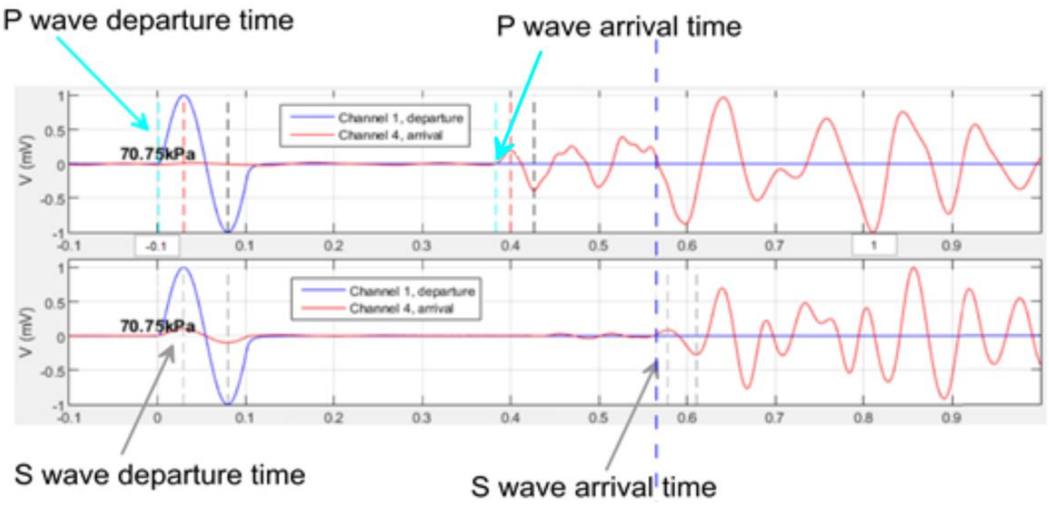

Figure 4-13. P and S waves under 70.75 kPa, with good correspondence between both: the S wave arrival can also be detected in the P wave signal; the arrival of the P wave creates some slight perturbations in the S wave signal (time is in milliseconds).

As seen in Figure 4-14, that presents both P (pink) and S (grey) signals under lower stresses (< 10 kPa), the signals become less clear at small stresses, particularly below 2.75 kPa. Besides carefully examining both signals and their coupling, the arrival time was also determined by extrapolating the trend resulting from larger stresses. The data show that bender elements can be used in (loose) sands, even under low stresses, smaller than those currently investigated in terrestrial geotechnical engineering.

Good agreement was also found with peak-to-peak data (calculating velocity with the tiptip distance between bender elements, Lee & Santamarina 2005). A software (Appendix A) was implemented to interpret arrival times, visualise all P/S waves of each experimental program in a group and suggest the departing and arriving points.

Figure 4-13 shows the change in wave velocities with stress in the tests on samples EP1 to EP4. The shape of the curves is comparable to other data on sands (e.g. Bachrach et al. 2000, Zimmer et al. 2002, Delage et al. 2017). As indicated in the Figure 4-13, the stress path followed first decreases from 10.75 kPa to 0.75 kPa, before increasing to 10.75 kPa up to 80.75 kPa.

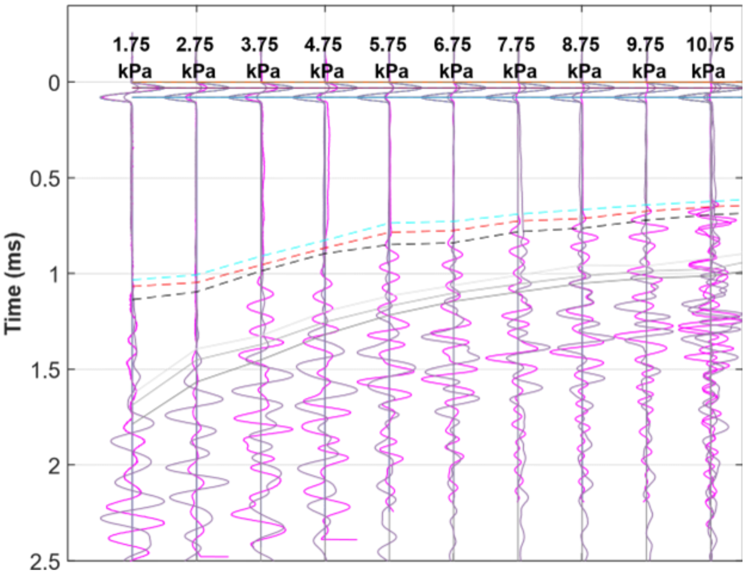

Figure 4-14. P (pink) and S (grey) waves detected under smaller stresses below 10 kPa.

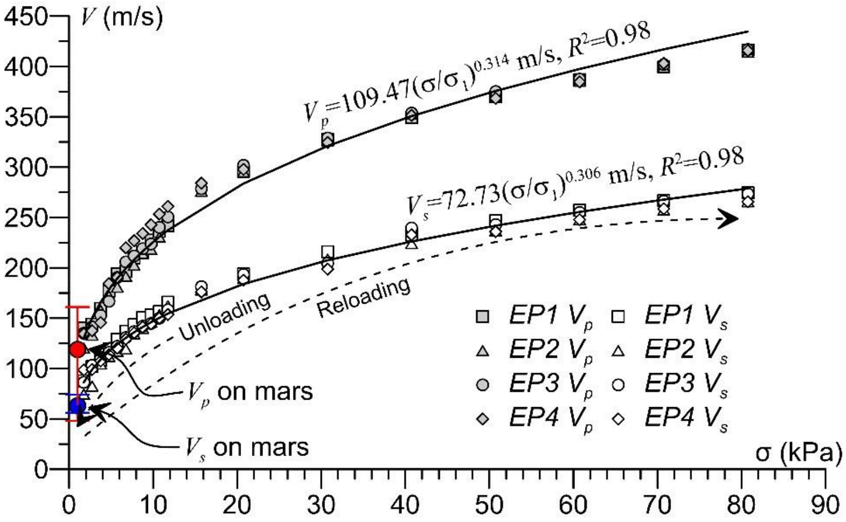

Figure 4-15. Measured wave velocities obtained using bender elements compared with those measured by Brinkman et al. (2022) on Mars (red and blue points).

Inspection of data along the unloading-reloading path indicates no significant hysteresis effect in both V_p and V_s curves, showing satisfactory reversibility in the response, in conjunction with slight changes in the grain assembly. Also, the variability of the measured wave velocities between the different samples is low, demonstrating good repeatability and providing confidence in the results.

As expected, the velocities decrease with decreased applied stress, according to the following equations:

$$V_{\mathrm{p}} = 109.47\left(\frac{\sigma}{\sigma_1}\right)^{0.314} \qquad R^2=0.98 \qquad (4)$$

$$V_s = 72.73\left(\frac{\sigma}{\sigma_1}\right)^{0.306} \qquad R^2=0.98 \qquad (5)$$

where σ1 =1 kPa is a reference stress.

Discussion

The exponents derived from Figure 4-15 (Eqs 4 and 5) are slightly different for V_p and V_s, showing that our experimental data are not fully in agreement with the elasticity theory. When trying to fit V_p and V_s with the same exponent, one gets a value of 0.31, with no dependency of the Poisson ratio with respect to the confining stress. This leads however to a Poisson ratio of 0.105, in disagreement with our experimental results. The exponents values derived from Figure 4-15 are higher than those measured (0.22) at higher stresses between 25 and 450 kPa by Delage et al. (2017) on three other Martian simulants (Mojave Mars simulant, MSS-D and Eifel sand).

Interestingly, these data agree reasonably well with the in-situ measurements performed on Mars during the hammering campaign of the HP3 self-penetrating dynamic probe (see Figure 4-8), during which emitted waves were detected by SEIS. The V_p/V_s values determined by Brinkman et al. (2022) are reported in the Figure 4-15, considering that they correspond to a vertical stress of 0.9 kPa, resulting from an average depth of 0.2 m at a density of 1.2 Mg/m^3 (Grott et al. 2022) under a gravity of 3.721 m/s^2.

Figure 4-16, that presents the Poisson ratios computed using Eq. 1 from V_p - V_s measurements at each point, exhibits more variability below 5 kPa. This is probably related to the difficulty of properly measuring travel times at low stresses (see Figure 4-19), in a stress range for which the use of bender elements becomes trickier.

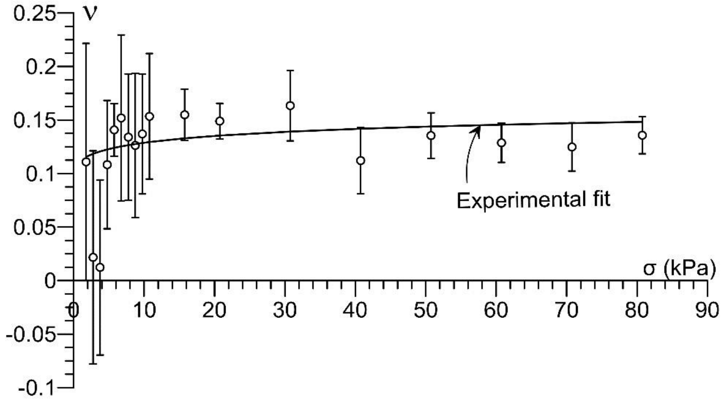

Figure 4-16. Changes in Poisson ratio with respect to confining stress determined from bender element measurements (points) and from the fitted curves of Figure 4-15 (curve).

Since the values of the exponents of Eqs 4 and 5 are close, the relationship V_p/V_s is slightly dependent on stress, with $V_p / V_s = (\sigma/\sigma_1)$. Therefore, from Eq. 1, the fitting equation for the Poisson ratio becomes:

$$\nu = 0.5\frac{2.265\left(\frac{\sigma}{\sigma_1}\right)^{0.016}-2}{2.265\left(\frac{\sigma}{\sigma_1}\right)^{0.016}-1} \tag{6}$$

This low dependency of the Poisson ratio with respect to stress is illustrated in the curve of Figure 4-16 that indicates a slight decreasing trend below 10kPa, derived from both individual points and fitted curves.

The larger dispersion of our experimental data below 5 kPa indicates that bender elements are less efficient in this area. Inspection of the data of Figure 4-16 also shows that the changes in V_p/V_s with stress seems to somewhat differ below 10 kPa, with a less regular curvature of the data. The changes in Poisson ratio below 5 kPa would certainly deserve more investigation, in an area where the efficiency of bender elements is perhaps limited.

The velocities may be used to calculate the elastic shear modulus G (from Eq. 2) and the Young modulus $E = 2G(1 + \nu)$. The results, presented in Figure 4-17, show how the moduli decrease with decreased stress. Interestingly, the data at low stress are not far from the measured value of E from interaction tests carried out with the SEIS foot on Fontainebleau sand (20 MPa at 3.5 kPa, Delage et. al 2022b).

Conclusions

Wave measurements were performed under low stresses by using bender elements on loose samples of Fontainebleau sand used as a Martian regolith simulant. This was made to better constrain the elastic properties of the regolith at the surface of the InSight landing site and to help interpreting in-situ elastic data obtained at surface through wave measurements (Brinkman et al. 2022) of indentation experiment carried out with the IDA (Golombek et al.2023). Current knowledge on wave transfer in sands was extended to low stresses (< 10 kPa) by using a horizontal cylindrical sample submitted to changes in vacuum (between 2 and 80 kPa). Additional stresses due to gravity and to the confining membrane were carefully calibrated and accounted for. Uncertainty in wave velocity determination was reduced by performing 3 to 5 measurements at each stress, and tests were carried out on 4 different samples. Bender elements were able to provide wave velocity measurements at stresses as low as 1.75 kPa, with however greater variability below 5 kPa. The change in V_p and V_s with respect to stress followed a power law, with however two slightly different exponent values, indicating that elastic hypotheses were not fully respected within the sand sample. The calculation of the Poisson ratio ν from wave velocities measurements confirmed that ν was reasonably constant above 10 kPa. Conclusions are less clear below 5 kPa, where the bender elements measurements are less accurate. The possibility of having a decreasing Poisson ratio in this area seems still worth of investigation, to be conducted through other experimental techniques.

This study enlarged the knowledge of the elastic behaviour of sands under low-stress and low strain, a novel topic in wave velocities investigations, that was useful to interpret local wave velocitiy measurement carried out at the InSight landing site (Brinkman et al. 2022). Further information was also gained about the Poisson ratio under low stress, another important parameter to estimate the surface elastic response of the surface.

However, the comparison of our laboratory data on a Martian simulant with what could be the response of a true Martian regolith is not straightforward. First, one has to consider possible differences in the grain package, that is known to have significant effects on seismic wave travel. It is very probable that the packing resulting from our pluviation method on a vertical sample, that has been put horizontally afterwards, differs from the packing of surface regolith grains on Mars, that results from very long-term wind saltation (through many repetitive small lateral jumps of sand grains along the wind direction). It could be that the post convenient way to mimic the resulting packing would be by trying to reproduce the saltation process on a (subrounded) sand field submitted to constant wind. Then, the best would probably to run in situ wave determination by using a line of geophones aimed at detecting an impact made on the ground, as done by Bachrach et al. 2000 on a beach in California.

Note also that direct observations and measurements made on the InSight landing site showed that the soil profile was not only made up of a sandy material. The soil profile is composed of a surface 1 cm thick sand/dust layer, overlaying an around 20 cm thick loose duricrust made up of a cohesive matrix containing some pebbles, located above a 12 cm layer of sand overlaying a gravel/sand deposit (Golombek et a. 2020, Warner et al. 2022, Delage et al. 2022, Spohn et al. 2022). However, in-situ wave velocity measurements carried out during the hammering session of the HP3 self-penetrating gauge (Brinkman et al. 2022) provided values of velocity and Poisson ratio close to those found in this work. Also, our investigation may be useful, as a first step, for other areas of Mars, where thicker deposits of sand, with dunes and ripples, have been observed (e.g., Ehlmann et al. 2017).

This can also be the case for future Mars missions.

Some of the questions raised in this experimental investigation are further considered in a companion paper (Caicedo et al. 2023) in which data at small stress are analysed through a contact mechanics theory derived from Bachrach et al. (2000).

Acknowledgments

These results are part of the PhD thesis of Juan-Pablo Castillo Betancourt, financially supported by Universidad de los Andes (Colombia) and École des Ponts ParisTech (France). The authors are also grateful to NASA, CNES, their partner agencies and Institutions (UKSA, SSO, DLR, JPL, IPGP-CNRS, ETHZ, IC, MPS-MPG). The authors want to thank the contributions made by the Ecole des Ponts ParisTech Navier-CERMES technical team for setting up the experimental device, especially Loic Lesueur, Marine Lemaire, Emmanuel De Laure, Baptiste Chabot and Xavier Boulay. This paper is Insight contribution N° ICN 327.

References

Andria-Ntoanina, I. (2011). Caractérisation dynamique de sables de référence en laboratoire - Application à la réponse sismique de massifs sableux en centrifugeuse. PhD thesis, Ecole des Ponts ParisTech (in French).

Arulnathan, R., Boulanger, R. W. and Riemer, M. F. (1998). Analysis of Bender Element Tests. In Geotechnical Testing Journal, GTJODJ, 21(2).

Bachrach, R., Dvorkin, J. and Nur, A. M. (2000). Seismic velocities and Poisson's ratio of shallow unconsolidated sands. Geophysics, 65(2), 559–564. https://doi.org/10.1190/1.1444751.

Bachrach, R., and Avseth, P. (2008). Rock physics modeling of unconsolidated sands: Accounting for nonuniform contacts and heterogeneous stress fields in the effective media approximation with applications to hydrocarbon exploration. Geophysics, 73(6). https://doi.org/10.1190/1.2985821

Bahrami, M., Yovanovich, M. M. and Culham, J. R. (2005). A compact model for spherical rough contacts. J. Tribol. Oct 2005, 127(4): 884-889, https://doi.org/10.1115/1.2000982

Banin, A. et al. 1992. in MARS (eds Kieffer, H. H., Jakosky, B. M., Snyder,C. W. & Matthews, M. S.) 594–625 (University of Arizona Press, Tucson, 1992).

Banerdt, W. B., Smrekar, S. E., Banfield, D., Giardini, D., Golombek, M., Johnson et al. (2018). Initial results from the InSight mission on Mars. Nature Geosciences (13) 183 – 189.

Bates, C. R. (1989). Dynamic soil property measurements during triaxial testing. Géotechnique, 39(4), 721-726.

Benahmed, N. (2001). Comportement mécanique d'un sable sous cisaillement monotone et cyclique : application aux phénomènes de liquéfaction et de mobilité cyclique. PhD thesis, Ecole des Ponts ParisTech (in French).

Boulanger, RW, Arulnathan, R., Harder, LF, Torres, R., and Driller, M. (1998): Dynamic Properties of Sherman Island Peat, Journal of Geotechnical and Geoenviromental Engineering, ASCE, 124, (1), 12-23.

Brinkman, N., Schmelzbach, C., Sollberger, D., Pierick, J. T., Edme, P., Haag, T. et al. (2022). In situ regolith seismic velocity measurement at the InSight landing site on Mars. Journal of Geophysical Research: Planets, 127(10), e2022JE007229.

Butt, S. U., Antoine, J. F. and Martin, P. (2015). Simplified stiffness model for spherical rough contacts. Tribology-Materials, Surfaces & Interfaces 9(2), 63-70.

Caicedo B., Castillo Betancourt J. P., Delage P., Lognonné Ph., Banerdt W.B. (2023). Waves velocities and Poisson ratio in a loose sandy martian regolith simulant under low stresses. Part 2: theoretical analysis

Castillo-Betancourt Juan Pablo. (2023a). juan9715/MRA-Bender-Element-data: Bender data public repository release (Release) [Data set]. Zenodo. https://doi.org/10.5281/zenodo.8161970

Castillo- Betancourt Juan Pablo. (2023b). juan9715/WaveVelocitiesSoftwareAndSpreadsheet: Wave Velocities Data Release (v) [Data set]. Zenodo. https://doi.org/10.5281/zenodo.8415384 Cresswell, A., Barton, M. E. and Brown, R. (1999). Determining the maximum density of sands by pluviation. Geotechnical Testing Journal, 22(4), 324–328. https://doi.org/10.1520/gtj11245j

Delage, P., Karakostas, F., Dhemaied, A., Belmokhtar, M., Lognonné, P., Golombek, M. et al. (2017). An Investigation of the Mechanical Properties of Some Martian Regolith Simulants with Respect to the Surface Properties at the InSight Mission Landing Site. Space Science Reviews, 211(1–4), 191–213. https://doi.org/10.1007/s11214-017-0339-7

Delage, P., Marteau, E., Vrettos, C., Golombek, M., Ansan, V., Banerdt, W. B. et al. (2022a). The mechanical properties of the Martian soil at the InSight landing site. In Proceeedings 20th International Conference on Soil Mechanics and Geotechnical Engineering, Sydney. https://hal.science/hal-03706564.

Delage, P., Castillo-Betancourt, J. P., Caicedo Hormaza, B., Karakostas, F., De Laure, E., Lognonné, P.et al. (2022b). The interaction between the SEIS seismometer of the InSight Martian mission and a regolith simulant. Géotechnique, 1-12.

Delage P., B. Caicedo, M. P. Golombek, T. Spohn, C. Schmelzbach, N. Brinkman, et al. (2023). Investigating the Martian soil at the InSight landing site. Keynote Lecture, International Symposium IS Porto 2023, submitted to Soils and Rocks.

Dyvik, R. and Madshus, C. (1985): Laboratory measurement of Gmax using bender elements, Proc. ASCE Annual Convention, Advances in the art of testing soils under cyclic conditions, Detroit, 186196.

Ehlmann B.L. et al. 2017. Chemistry, mineralogy, and grain properties at Namib and High dunes, Bagnold dune field, Gale crater, Mars: a synthesis of Curiosity rover observations. Journal of Geophysical Research, Planets 122: 2510–2543. https://doi.org/10.1002/2017JE005267

Garcia, R. F., Daubar, I. J., Beucler, É., Posiolova, L. V., Collins, G. S., Lognonné, P. et al. (2022). Newly formed craters on Mars located using seismic and acoustic wave data from InSight. Nature Geoscience, 15(10), 774-780.

Giardini D., Lognonné P., Banerdt W.P., Pike W.T., Christensen U., Ceylan S. et al. (2020). The seismicity of Mars. Nature Geosciences 13: 205 – 212.

Goetz, W., Pike, W. T., Hviid, S. F., Madsen, M. B., Morris, R. V., Hecht, M. H. et al., (2010b). Microscopy analysis of soils at the Phoenix landing site, Mars: Classification of soil particles and description of their optical and magnetic properties. Journal of Geophysical Research E: Planets, 115(8), 1–23. https://doi.org/10.1029/2009JE003437

Golombek, M., Kipp D., Warner I.J., Daubar I.J., Fergason R.L., Kirk R.L. et al. (2017). Selection of the InSight landing site. Space Science Review 211, 5–95.

Golombek M, Warner NH, Grant JA, Hauber E, Ansan V, Weitz CM et al (2020). Geology of the InSight landing site on Mars. Nat Commun 11(1):1014. https://doi.org/10.1038/s41467-020-14679-1

Golombek M., T. Hudson, P. Bailey, N. Balabanska, E. Marteau, C. Charalambous et al. (2023). Results from InSight Robotic Arm Activities. Space Science Review, 219:20 doi:10.1007/s11214-023-00964-0

Grott M., T. Spohn, J. Knollenberg, C. Krause, T.L. Hudson, S. Piqueux et al., (2021). Thermal Conductivity of the Martian Soil at the InSight Landing site from HP3 Active Heating Experiments. Journal of Geophysical Research - Planets, doi 10.1002/essoar.10506340.1.

Hariprasad, C., Rajashekhar, M. & Umashankar, B. Preparation of Uniform Sand Specimens Using Stationary Pluviation and Vibratory Methods (2016). Geotechnical and Geological Engineering 34, 1909–1922. https://doi.org/10.1007/s10706-016-0064-0

Haskin, L. A. et al. Water alteration of rocks and soils from the Spirit rover site, Gusev crater, Mars. Nature 436, 66–69 (2005).

Henkel, D. J. and Gilbert, G. D. (1952). The effect measured of the rubber membrane on the triaxial compression strength of clay samples. Géotechnique, 3(1), 20–29.

Hobiger, M., Hallo, M., Schmelzbach, C., Stähler, S. C., Fäh, D., Giardini, D. et al. (2021). The shallow structure of Mars at the InSight landing site from inversion of ambient vibrations. Nature communications, 12(1), 1-13.

Hurowitz, J. A. et al. In situ and experimental evidence for acidic weathering of rocks and soils on Mars. J. Geophys. Res. 111, E02S19 (2006).

Jamiolkowski, M., Lancellotta, R. and Lo Presti D.C.F. (1995). Remarks on the stiffness at small strains of six Italian clays. Proc. Symposium on Pre-failure Deformation Behaviour of Geomaterials, 817 – 836, Balkema. https://www.researchgate.net/publication/306157192

Jovičić, V., Coop, M. and. Simic. M. (1996): Objective criteria for determining Gmax from bender element tests, Géotechnique, 46(2), 357-362. juan9715. (2023). juan9715/MRA-Bender-Element-data: Bender data public repository release (Release). Zenodo. https://doi.org/10.5281/zenodo.8161970

Kolbuszewski J.J. (1948). An empirical study of maximum and minimum porosities of sand. In: Proceedings of Second International Conference on Soil Mechanics and Foundation Engineering, Rotterdam, Netherland: ISSMGE, vol 1, pp 158–165

Kumar, J. and Madhusudhan, B. N. (2010). Effect of relative density and confining pressure on Poisson ratio from bender and extender elements tests. Géotechnique, 60(7), 561-567.

Lee, J.-S. and Santamarina, J. C. (2005). Bender Elements: Performance and Signal Interpretation. Journal of geotechnical and geoenvironmental engineering. 131(9), 1063-1070. https://doi.org/10.1061/ASCE1090-02412005131:91063

Lognonné, P., Banerdt, W. B., Giardini, D., Pike, W. T., Christensen, U., Laudet, P. et al. (2019). SEIS: Insight's seismic experiment for internal structure of Mars. Space Science Reviews, 215(1), 1-170.

Lognonné P., Banerdt W. B., Pike W. T., Giardini D., Christensen U., Garcia R. F. et al., (2020). Constraints on the shallow elastic and anelastic structure of Mars from InSight seismic data. Nature Geoscience, https://doi.org/10.1038/s41561-020-0536-y.

Marteau E, Golombek M, Vrettos C, Garvin JB, Williams NR (2021). Soil mechanical properties at the InSight landing site, Mars. In: 52nd Lunar and Planetary Science Conference, abstract #2067, Houston.

Marteau E, Golombek M, Vrettos C, Delage P, Williams NR, Ansan V (2022). Soil strength properties derived from scraping and dumping activities at the InSight landing site on Mars. In: 53rd Lunar and Planetary Science Conference. Abstract #1523, Houston.

Marteau E, Golombek M, Delage P, Vrettos C, Hurst K, Gomez A et al. (2023). Initial results from the Insight lander robotic arm soil mechanics experiments on Mars. 54th Lunar and Planetary Science Conference. Abstract #1597, Houston.

Morgan, P., Grott, M., Knapmeyer-Endrun, B., Golombek, M., Delage, P., Lognonné, P. et al. (2018). A pre-landing assessment of regolith properties at the InSight landing site. Space Science Reviews, 214(6), 1-47.

Mohsin, A. K. M. and Airey D. W. (2003): Automating Gmax measurement in triaxial test. Deformation characteristics of Geomaterials, Proceedings 3rd International Symposium IS Lyon. Balkema, Lyon, 73-80.

Murillo, C. A., Thorel, L. and Caicedo, B. (2009). Spectral analysis of surface waves method to assess shear wave velocity within centrifuge models. Journal of Applied Geophysics, 68(2), 135–145. https://doi.org/10.1016/j.jappgeo.2008.10.007

Murillo, C., Sharifipour, M., Caicedo, B., Thorel, L. and Dano, C. (2011). Elastic parameters of intermediate soils based on bender-extender elements pulse tests. Soils and Foundations, 51(4), 637649.

Nakagawa, K., Soga, K. & Mitchell, J. K. (1996). Pulse transmission system for measuring wave propagation in soils. J. Geotech. Engng Div., ASCE 122(4), 302–308.

Newland, P. L. and Allely, B. H. (1959). Volume changes during undrained triaxial tests on saturated dilatant granular materials. Géotechnique, 9(4), 174–182.

Prasad, M. (2002). Acoustic measurements in unconsolidated sands at low effective pressure and overpressure detection. Geophysics, 67(2), 405–412. https://doi.org/10.1190/1.1468600

Posiolova, L. V., Lognonné, P., Banerdt, W. B., Clinton, J., Collins, G. S., Kawamura, T. et al. (2022). Largest recent impact craters on Mars: Orbital imaging and surface seismic co-investigation. Science, 378(6618), 412-417.

Seiferlin K., Ehrenfreund P., Garry J., Gunderson K., Hütter E., Karg G. et al. (2008). Simulating Martian regolith in the laboratory. Planetary and Space Science 56: 2009 – 2025

Shirley, D. J. and Hampton, L. D. (1978). Shear-wave measurements in laboratory sediments. The Journal of the Acoustical Society of America, 63(2), 607-613. http://acousticalsociety.org/content/terms.

Spohn, T., Grott, M., Smrekar, S. E., Knollenberg, J., Hudson, T. L., Krause, C. et al. (2018). The Heat Flow and Physical Properties Package (HP3) for the InSight Mission. In Space Science Reviews (Vol. 214, Issue 5). The Author(s). https://doi.org/10.1007/s11214-018-0531-4

Spohn, T., Hudson, T. L., Marteau, E., Golombek, M., Grott, M., Wippermann, T. et al. (2022a). The InSight HP3 Penetrator (Mole) on Mars: Soil Properties Derived From the Penetration Attempts and Related Activities. Space Science Reviews (2022) 218:72, https://doi.org/10.1007/s11214-022-00941z

Spohn, T., Hudson, T. L., Witte, L., Wippermann, T., Wisniewski, L., Kedziora, B. et al. (2022b). The InSight-HP3 mole on Mars: Lessons learned from attempts to penetrate to depth in the Martian soil. Advances in Space Research, 69(8), 3140-3163, doi :10.1007/s11214-022-00941-z.

Suwal, L. P. and Kuwano, R. (2013). Statically and dynamically measured Poisson's ratio of granular soils on triaxial laboratory specimens. Geotechnical Testing Journal, 36(4), 493-505.

Verdier, N., Ansan, V., Delage, P., Ali, K. S., Beucler, E., Charalambous, C., Constant, E., Spiga, A., Golombek, M., Marteau, E., Lapeyre, R., Gaudin, E., Yana, C., Hurst, K., Lognonné, P., & Banerdt, B. W. (2023). Using Wind Dispersion Effects During the InSight Tether Burial Activities to Better Constrain the Regolith Grain Size Distribution. Journal of Geophysical Research: Planets, 128(5). https://doi.org/10.1029/2022JE007707

Viggiani, G. and Atkinson, J. H. (1995a). Stiffness of fine-grained soil at very small strains. Géotechnique, 45(2), 249–265.

Viggiani, G. and Atkinson, J. H. (1995b). Interpretation of bender element tests. Géotechnique, 45(1), 149–154.

Vilhar, G. & Jovičić, V., (2009). Measurement And Interpretation Of The Small Strain Stiffness Of Boštanj Silty San. Acta Geotechnica Slovenica. 6(2), 57-75

Wang, Y., Benahmed, N., Cui, Y. J. and Tang, A. M. (2017). A novel method for determining the smallstrain shear modulus of soil using the bender elements technique. Canadian Geotechnical Journal, 54(2), 280–289. https://doi.org/10.1139/cgj-2016-0341

Warner N. H., M. P. Golombek , V. Ansan, E. Marteau , N. Williams , J. A. Grant et al. (2022). In Situ and Orbital Stratigraphic Characterization of the InSight Landing Site—A Type Example of a Regolith-Covered Lava Plain on Mars. Journal of Geophysical Research – Planets, doi 10.1029/2022JE007232s

Zimmer, M., Prasad, M., & Mavko, G. (2002). Pressure and porosity influences on VP-VS ratio in unconsolidated sands. The Leading Edge, 21(2):178-183, https://doi.org/10.1190/1.1452609.

Open Research

All the Waveform data csv files from the Bender Element measurements performed on the four samples, used for wave velocity calculations in the study are available at the public MRA-Bender-element-repository repository (Castillo-Betancourt Juan Pablo. (2023)). Instructions may be found on the “README” file of the repository.

Appendix A: Methodology for travel time determination

A Matlab script was developed to enable accurate and quick identification of the departing and arrival times on a considerable amount of data within a reasonable timeframe (about 150 waves were acquired in each of the four experimental programs, with a total of 1200 wave measures to analyse).

The MATLAB script allows to simultaneously consider up to three methodologies for identifying the departing and arrival times. The procedure identifies local maximum, minimum and zero values, that make up the potential points of interest of the signal (shown in Figure A1). This identification is an automatic initialisation method of suggested arrival and departure points. To achieve this, the following procedure was implemented.

1. Initially, a set of candidates for local maximums and minimums is established after evaluating the sign function of numerically calculated derivatives between every point in the signal and its surrounding neighbours. This procedure is a recursive method based on a parameter selected to determine an adequate number of points (seeking to not saturate the visual interface with too many choices of potential candidate points).

2. After that, the search is widened from each candidate point by following the curve up to the previous existing inflection point (or the beginning of the signal, should it be the case). A new candidate point is then proposed.

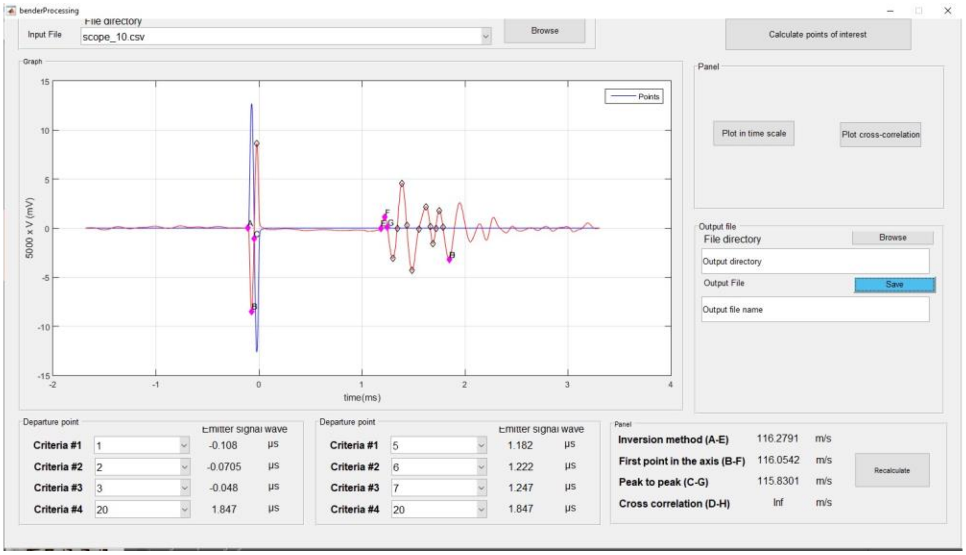

Input File: scope_10.csv

Departure point		Emitter signal wave	
Criteria #1	1	-0.108	μs
Criteria #2	2	-0.0705	μs
Criteria #3	3	-0.048	μs
Criteria #4	20	1.847	μs

Departure point		Emitter signal wave	
Criteria #1	5	1.182	μs
Criteria #2	6	1.222	μs
Criteria #3	7	1.247	μs
Criteria #4	20	1.847	μs

Panel		
Inversion method (A-E)	116.2791	m/s
First point in the axis (B-F)	116.0542	m/s
Peak to peak (C-G)	115.8301	m/s
Cross correlation (D-H)	Inf	m/s

Figure A1. The interface of the Matlab script for single wave data analysis.

The script also allows simultaneous visualisation of the waves under various confining stresses, as seen in Figure A2. All the signals acquired at the same stress value are averaged to account for variability and repeatability. By observing all the available choices, the user can easily choose the time arrival points for the method of choice by clicking on a visual interface.

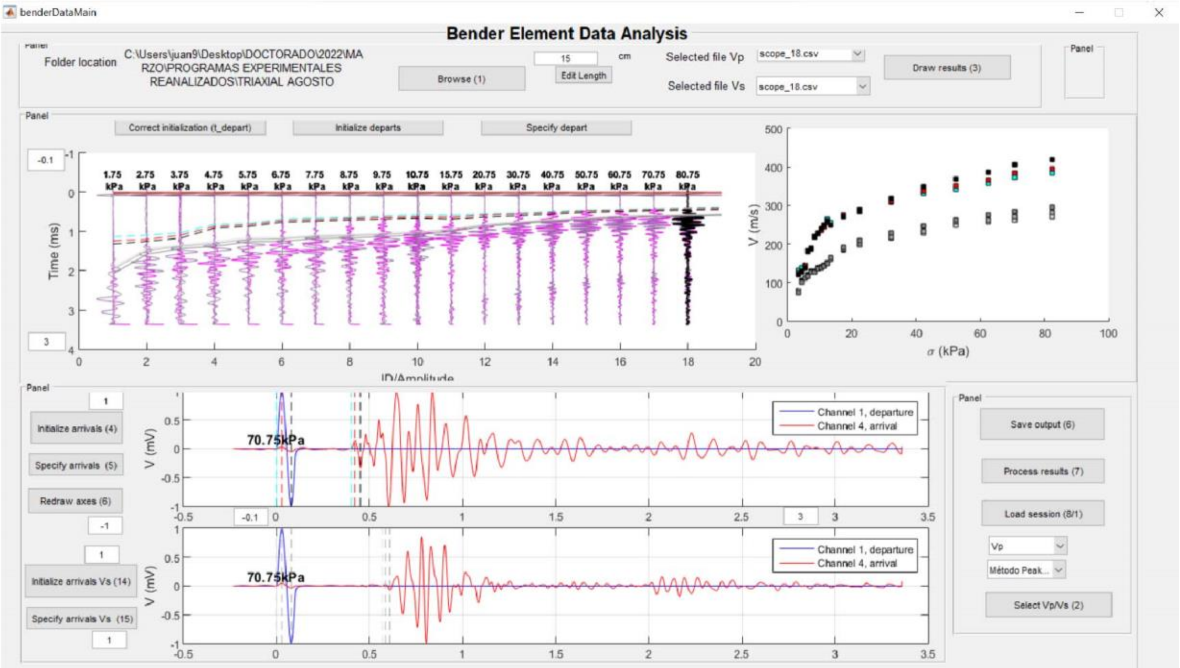

benderDataMain

Bender Element Data Analysis

Folder location C:\Users\juan9\Desktop\DOCTORADO\2022\MARZO\PROGRAMAS EXPERIMENTALES REANALIZADOS\TRIAXIAL AGOSTO

15 cm

Selected file Vp scope_18.csv

Selected file Vs scope_18.csv

Vp

Método Peak...

Figure A2. Interpretation script showing all waves measured at different stresses.

Proper signal visualisation is critical when using Wang’s arrival time approach, because it requires viewing P and S waves simultaneously on the same timescale, as seen in Figure A2. In contrast to usual methods like peak-to-peak or arrival-to-arrival, a matching of P and S wave signals are compared. While determining the P wave arrival time is relatively simple (the choice is given by the first departure of the signal from the zero axis in the P signal), Wang’s criterion indicates that the location of the S wave arrival time correspond to the peak of the “initial main excursion in the opposite direction of movement compared to that of the S-wave received signal”. This means that the first sizeable negative peak in P wave will correspond to the S wave arrival time. Choosing this ‘first significant’ peak making use of the S wave alone can often be a challenge and the associated P wave hence allows an objective and repeatable measurement. The chosen point for the S wave arrival time is to be found at the exact location when the first negative peak with significant amplitude appears in the P wave signal, indicating the arrival of the S components produced by this P wave signal. This also implies that the motion registered in the S wave signal before the chosen time of arrival corresponds to the faster P wave produced by the action of the bender that emitted the S wave and its rebounds on the sample walls.

Figure A3 shows an example of the waveforms acquired during one of the four experimental programs, along with lines marking the identified locations of the departure and arrival of the waves for the three utilised criteria.

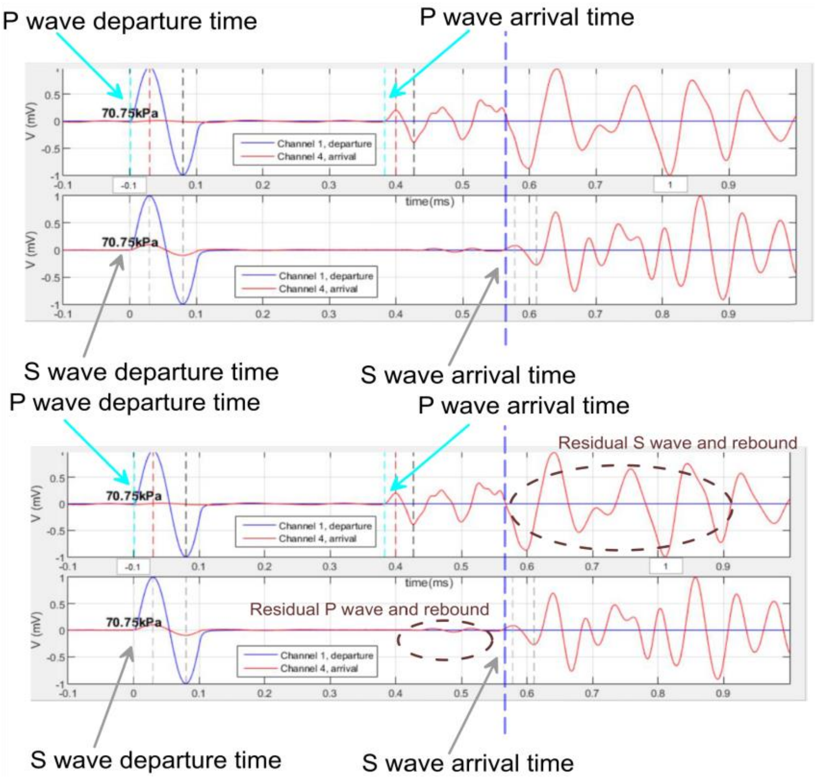

Figure A3. Simultaneous visualisation of the P and S waves following Wang's method.

The following figures present the waves acquired during the other three experimental programs, along with the lines identifying the departure and arrival times for both P and S waves. The figures are shown as generated in the data processing tool built for data interpretation.

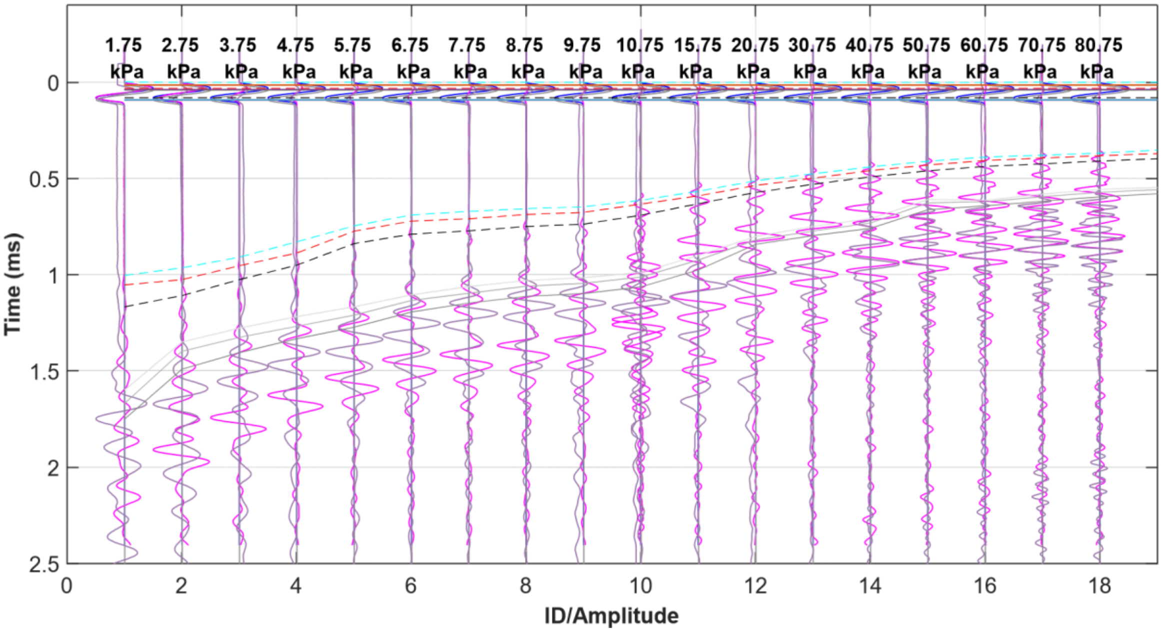

Figure A4. Waves acquired on sample EP1. Depart and arrival times are indicated both for P and S waves.

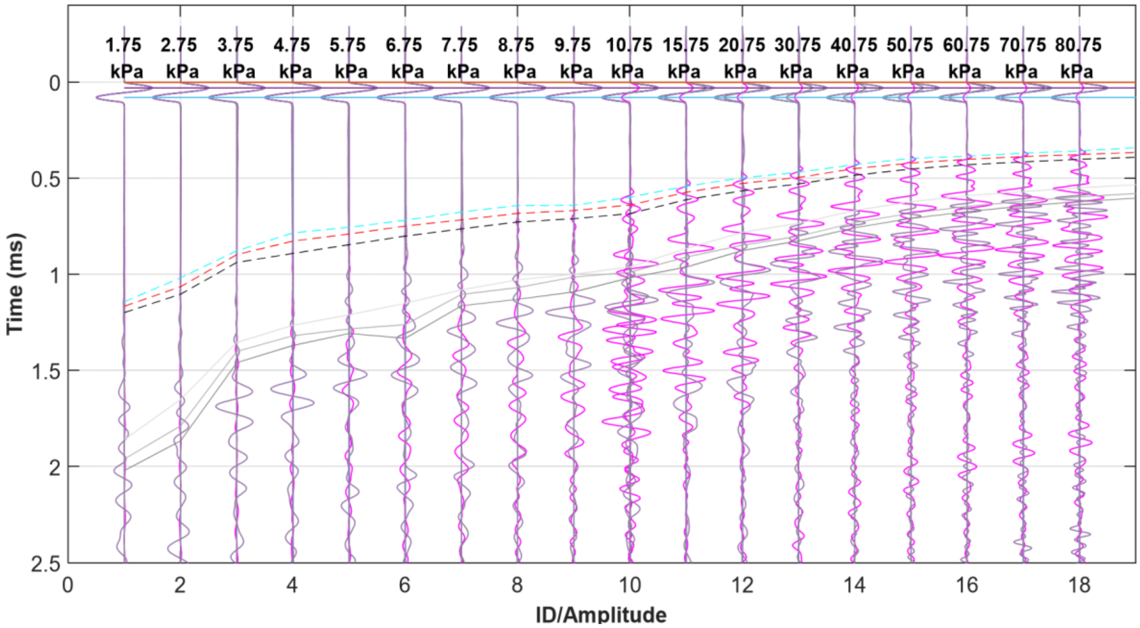

Figure A5. Waves acquired on sample EP2. Depart and arrival times are indicated both for P and S waves.

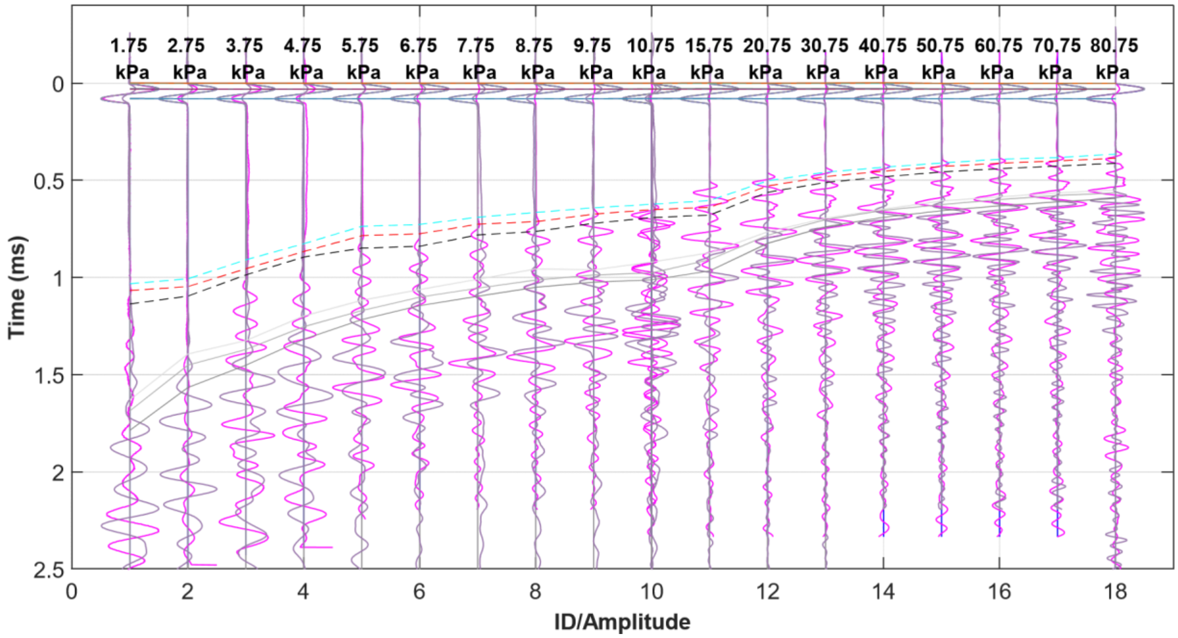

Figure A6. Waves acquired on sample EP3. Depart and arrival times are indicated both for P and S waves.

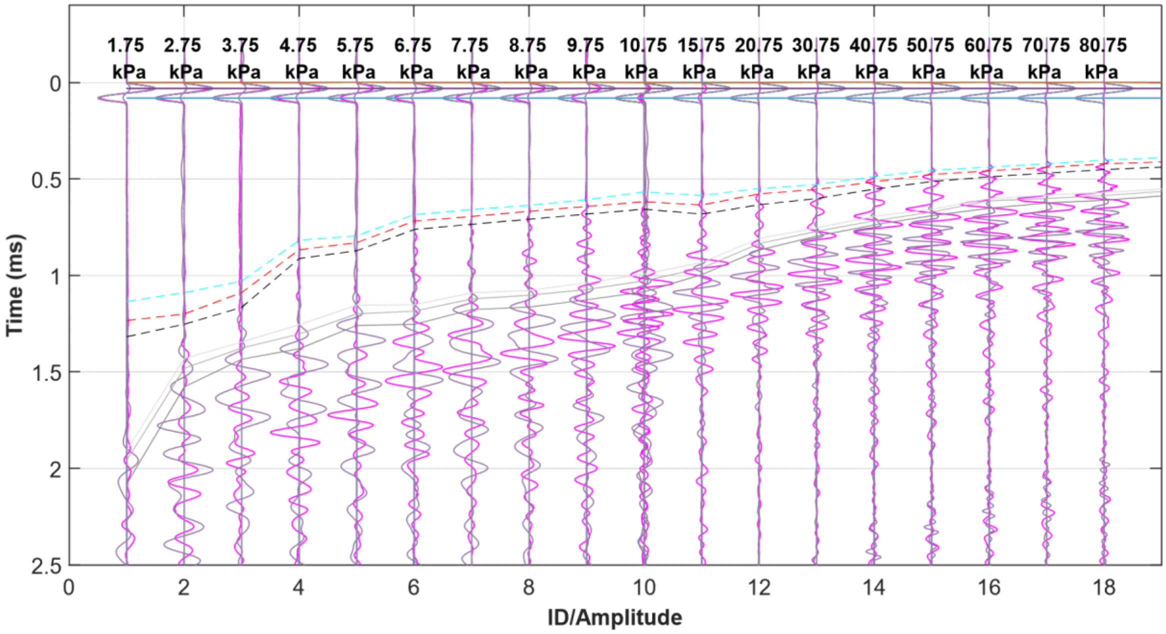

Figure A7. Waves acquired during on sample EP4. Depart and arrival times are indicated both for P and S waves.

4.5. Wave velocities and Poisson Ratio in a loose sandy Martian regolith simulant under low stresses. Published, JGR-Planets)

B. Caicedo1, J. P. Castillo Betancourt1,2, P. Delage2, Ph. Lognonné3, B. Banerdt4

1 Ecole des Ponts ParisTech, lab. Navier-CERMES, CNRS, UGE, Marne la Vallée, France.

2 Universidad de los Andes, Bogota, Colombia.

3 Université Paris-Cité, Institut de Physique du Globe, CNRS, Paris, France.

4 Jet Propulsion Laboratory, California Institute of Technology, Pasadena, California, USA.

Key points:

- A novel theory based on contact mechanics was proposed to calculate Vp and Vs of uniform granular materials.
- The theory considers the roughness of the particles, the stress, the porosity of the granular assembly and the properties of the grains.
- Theoretical results agree with experimental measurements on loose samples of Fontainebleau sand used as a Mars regolith simulant.

Abstract

This paper presents a theoretical analysis of the data on wave velocities measurements at small stresses presented in a companion paper on a Martian regolith loose sandy simulant (Fontainebleau sand) of the soil at the InSight landing site on Mars (Elyseum Planitia). Experimental data of wave velocities and Poisson's ratio are interpreted in the light of a granular contact mechanics theory and completed accounting for rugosity effects, that are suspected to have stronger effects in sands under low stresses. The asperities of a grain of Fontainebleau sand were investigated through Atomic Force Microscopy, but larger asperities had to be adopted so as to better fit the model prediction with experimental data. A good agreement between the experimental data and the model predictions is obtained for stress above 10 kPa. Below 5 kPa, an area in which asperities are suspected to have a stronger influence, the model is not fully satisfactory, showing that further experimental and theoretical investigation are necessary in a stress zone particularly relevant to surface soils in planets, with probably enhanced effects of asperities on the intergrains contact mechanics.

Plain Language Summary

To better understand seismic wave propagation at the surface of the InSight landing site on Mars, this paper presents a theoretical interpretation of the seismic wave velocities at low stress measured in a sand sample used as Martian regolith simulant, presented in a companion paper. The theory is based on both a theoretical elastic model of a pack of smooth spheres of same

diameter and an approach accounting for the effects of local rugosity at the contact between sand grains (rugosity is supposed to have a stronger influence at the low stresses resulting from the smaller gravity on Mars). The sphere pack model shows that some slippage between grains is necessary to properly account for the radial deformation of a cylindrical sample submitted to an increase in axial stress (as described by an elastic parameter called the Poisson ratio). Accounting for rugosity effects allows a better prediction of the changes in wave velocity with respect to stress. The decrease in velocity under decreased stress is confirmed, but the rugosity parameter measured by using an Atomic Force Microscope was under-estimated, probably due to the 5over-simplistic hypothesis of considering spheres. Proper prediction was obtained by fitting this parameter at a twice larger value.

Introduction

The elastic behaviour of sands under low stresses and small strains, poorly investigated in standard terrestrial geotechnics, presents a particular interest in planetary geotechnics due to reduced gravity. This is the case of the surface layer at the InSight landing site on Mars, with a gravity of g = 3.721 m/s^2. In this context, an experimental investigation on wave velocities at low stresses carried out on a sandy regolith simulant by using a specific novel device has been presented in a companion paper (Castillo-Betancourt et al. 2023), in which some details about the InSight mission are also provided. This paper is devoted to analysing the experimental data of this paper through a theory of contact mechanics accounting for the roughness of particles (Richart et al., 1970; Dobry et al., 1991; Bachrach et al., 2000; Bahrami et al., 2005; Butt et al., 2015). This analysis is carried out to better understand the micro-mechanisms governing wave transfers in loose sands under low stress, a domain where particle roughness plays an important role. Conclusions about the changes in Poisson ratio at low stress and strain are also derived from the analysis.

Theoretical background

The results of Bachrach et al. (2000) are among the few available data in the domain of the in-situ investigation of the elastic behaviour of sands under low stresses and small strains. They conducted in-situ wave measurements in the Moss Landing beach (California, dry angular sand) by using a seismic line parallel to the shoreline with 20 geophones distant 30 cm and a hammer (about 50 kg) applied on a metal block as source. The Poisson ratio derived from the velocity profile between 0 and 5 m (vertical stress between 0 and 78.5 kPa with a dry unit mass of 1.7 Mg/m^3) was equal to 0.15, with no increase with depth. Bachrach et al. (2000) also presented some experimental data under lower stresses in a dense random pack of identical glass beads, and they observed that the Poisson ratioν increased from 0.130 to 0.151 between 5 and 40 kPa.

Bachrach et al. (2000) also provided a theoretical analysis of the physics of the contacts in loose unconsolidated sands using the Hertz-Mindlin theory (HM). Mindlin (1949) provided the following expressions of the normal and shear stiffness (S_n and S_t, respectively) of two similar elastic smooth spheres in contact (see also Mavko et al., 1998):

$$S_n = \frac{4 \cdot a \cdot G_g}{1 - \nu_g} \tag{1}$$

$$S_t = \frac{8 \cdot a \cdot G_g}{2 - \nu_g} \tag{2}$$

where G_g and ν_g are the shear modulus and Poisson ratio of the sphere, respectively. *a* is the radius of the contact area between the spheres.

According to Hertz, *a* is given by:

$$a = \left[\frac{3 \cdot F \cdot R_g (1 - \nu_g)}{8 \cdot G_g}\right]^{1/3} \tag{3}$$

where R_g is the grain radius and *F* the compressive force between them, given by Bachrach et al., (2000) in an assembly of spheres of same radius:

$$F = \frac{4 \cdot \pi \cdot R_g^2 \cdot \sigma_3}{n(1 - \phi)} \tag{4}$$

where σ_3 is the mean stress, *n* is the coordination number (average number of contacts per sphere) and ϕ the porosity of the assembly.

Through statistical averaging, Digby (1981) and Walton (1987) provided the following expressions of the bulk (K_{HM}) and shear (G_{HM}) moduli of a pack of identical elastic spheres of radius R_g with mutual contact obeying the Hertz-Mindlin theory:

$$K_{HM} = \frac{n\,(1 - \phi)}{12 \cdot \pi \cdot R_g} S_n \tag{5}$$

$$G_{HM} = \frac{n\,(1 - \phi)}{20 \cdot \pi \cdot R_g} (S_n + 1.5\, S_t) \tag{6}$$

The Poisson ratio of the pack can hence be expressed as follows:

$$\nu_{HM} = \frac{3K_{HM} - 2G_{HM}}{2(3K_{HM} + G_{HM})} = \frac{S_n - S_t}{4S_n + S_t} = \frac{\nu_g}{10 - 6\nu_g} \tag{7}$$

Eq. 7 shows that the Poisson ratio of a pack of identical smooth spheres governed by the Hertz-Mindlin model (i.e., with no slippage between spheres) only depends on that of the constituent, with no dependence on the sphere radius R_g. For quartz, $\nu_g = 0.08$, yielding $\nu_{HM} = 0.0084$. This too low value indicates that, with no slippage, the radial strain of a vertically stressed cylindrical sample is very small compared to its axial one. Such very low values are not met in sand behaviour, showing the limits of the Hertz-Mindlin approach with no slippage between particles.

Slippage between particles

By considering a zero tangential stiffness (S_t = 0) allowing slipping between all the grains, Bachrach et al. (2000) showed from Eq. 7 that $\nu_{HMB} = 0.25$ (where HMB stands for Hertz-Mindlin-Bachrach). This indicates that grains free to slip logically result in a larger radial expansion of a vertically stressed cylindrical sample. Bachrach et al. (2000) obtained a continuous variation of ν_{HMB} by assuming a mixture with a proportion ξ of no slipping contacts and by applying the Hashin Shtrikman bounds (Hashin and Shtrikman, 1963). From this theory, the tangential stiffness of the mixture S_t^{mix} is given by Eq. 8 and the Poisson ratio by Eq. 9. As a result, ν_{HMB} decreases from 0.25 down to 0.0084 when the fraction of no-slip contacts increases from 0 to 1, as shown in Figure 4-17 (with ν_{HMB} = 0.159 for half grain contacts slipping - ξ = 0.5).

$$S_t^{mix} = S_t + \frac{1-\xi}{-\frac{1}{S_t} + \frac{2\xi(S_n+2S_t)}{5S_t(S_n+4/3S_t)}} \tag{8}$$

$$\nu_{HMB} = \frac{S_n - S_t^{mix}}{4S_n + S_t^{mix}} \tag{9}$$

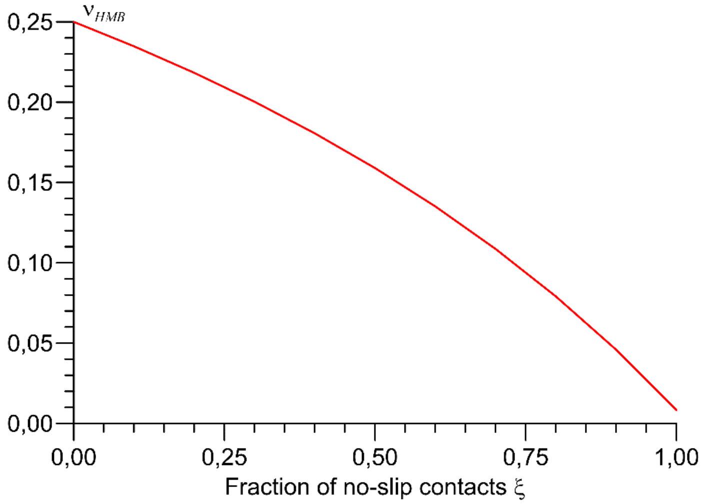

Figure 4-17. Change in Poisson ratio of an assembly of identical spheres with respect to the proportion of no-slip contacts ξ.

The range of magnitude of the Poisson ratio from this theory agrees well with most common measurements on sands. However, it is derived from some simplistic assumptions of perfect smooth spheres of the same radius interacting together. Rather than fully describing physical phenomena in sands (with grains of different sizes, shapes and angularity, for which ν may be larger than 0.25), it provides further insight into the macroscopic effects of some micromechanical processes. Another limitation is that ν_{HMB} (Eq. 9) is not dependent on the sphere radius R_g (unique in the case of identical spheres). As shown by Kumar and Madhasuda (2010), there is a dependency of ν on the grain size distribution.

Effect of particle's roughness on the elastic properties

Bachrach et al. (2000) observed that the Hertz-Mindlin theory overestimated by two the wave velocities for sands under low-stress, an issue that they relate to roughness effects at inter-particles contacts. Persson (2006) confirmed this, recalling that, for smooth contact surfaces, the Hertzian theory leads to a circular contact area $A_H = \pi a^2$ proportional to the force to a power of 2/3 (Eq. 3, $A_H \propto F^{2/3}$). Conversely, they showed that experimental data on randomly rough surfaces evidenced a contact area linearly proportional to the force ($A_H \propto F$).

According to Hertz-Mindlin's theory, compressive and shear inter-grains stiffness (S_n and S_t, respectively) are proportional with interparticle force to a power of 1/3 (Eqs. 1, 2, 3, 4). Also, from Eqs. 5, 6, and 10, the wave velocities V_p and V_s are related to the interparticle forces through the bulk (K_{HM}) and shear (G_{HM}) moduli.

$$V_P = \sqrt{\left(K_{HM} + \frac{4}{3} G_{HM}\right) / \rho_b} \quad \text{and} \quad V_S = \sqrt{\frac{G_{HM}}{\rho_b}} \qquad (10)$$

Then, assuming that force and stress are linearly related through Eq. 4, wave velocities are also related to stress, with a power of 1/6.

In contrast, in the case of rough surfaces (Persson 2006), the linear relationship between interparticle forces or stress and the contact area results in having compressive stiffnesses proportional to a power of 0.5, and wave velocities to a power of 0.25. These exponents have been mentioned by Santamarina et al. (2001), i.e., 0.25 for cone-to-plane contacts (typical of rough or angular particles) and 0.25 for spherical particles with yield at contact.

To consider the effect of roughness on sands undergoing low stresses, Bachrach et al. (2000) assume that the contact radius R_c is significantly smaller than the grain radius R_g, as shown in Figure 4-18.

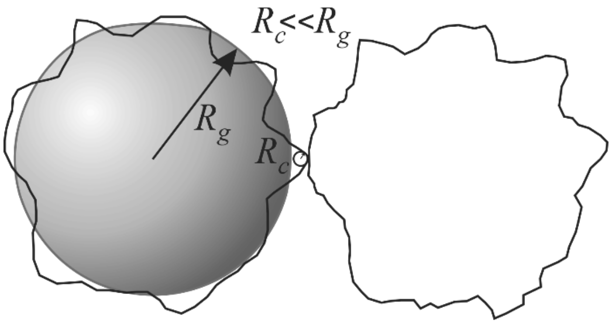

Figure 4-18 Schematic drawing of grains in contact with asperities, with contact radius Rc significantly smaller than Rg.

Bachrach et al. (2000) hence suggest replacing the grain radius R_g by the contact radius R_c in Eq. 3. The radius of the contact area, a_B, hence becomes:

$$a_B = \left[\frac{3 \cdot F \cdot R_c (1 - \nu_g)}{8 \cdot G_g}\right]^{1/3} \quad (11)$$

Eq. 11 shows that the radius of the contact area *a* given by Hertz has to be corrected by a correction factor $(R_c/R_g)^{1/3}$, as follows:

$$a_B = a \left(\frac{R_c}{R_g}\right)^{1/3} \quad (12)$$

This change decreases the normal and shear stiffness S_n and S_t and the bulk and shear moduli K_{HM} and G_{HM} by a factor $(R_c/R_g)^{1/3}$ (Eqs. 5, 6), hence reducing the wave velocities V_p and V_s by a factor $(R_c/R_g)^{1/6}$ (Eq. 10).

For the Moss Landing beach sand, Bachrach et al. (2000) suggested using a constant ratio R_c/R_g=0.086. However, this value indirectly resulted from fitting in-situ measurements, without any physical link with the true particle's roughness. A more rigorous analysis is possible using theories dealing with roughness effects on bodies in contact, where contact only occurs at some discrete microcontacts points. This analysis is based on the pioneering work of Archard (1957), who demonstrated a linear proportionality between the inter-particles force and the contact area. A contact model for rough surfaces developed by Greenwood and Williamson (1966) was used by Greenwood and Trip (1967) to provide the first theory for rough elastic spherical bodies. Majumdar and Bhushan (1991) concluded that smaller asperities are more likely to undergo small plastic deformation under increased load, and to merge together to form elastic contact points. This is in agreement with Persson (2006), who concluded that all microcontacts deform plastically, except for polished surfaces.

Most theoretical models involve complex integral equations requiring intensive iterative numerical calculations. Few analytical models dealing with rough spherical surfaces are available, except that proposed by Bahrami et al. (2005), who splitted the deformation of rough spheres under compression into two components: (i) the bulk compression of the sphere and (ii) the deformation of the asperities. In this model, asperities are described by their RMS asperity height, σ_{rms} (defined as the square root of the average of the squares of all wave heights) and the microhardness of the asperities H_{mic}. Butt et al. (2015) modified Bahrami's model by directly calculating the relationship between the contact stiffnesses of rough spheres and those obtained with the Hertz-Mindlin model for smooth spheres.

The Bahrami-Butt model assumes the following hypotheses to compute the contact behaviour between rough spheres:

(i) The deformation mode of asperities is plastic.

(ii) The bulk deformation of the contact is elastic and occur at elastic half-space with an effective modulus of elasticity E' given by $1/E' = (1 - \nu^2)/E$. Note that the method was developed for a rigid sphere on a deformable flat surface (Figure 4-19). Still, the same solution is obtained for a deformable sphere on a rigid flat surface.

(iii) The pressure at microcontacts is limited by the microhardness of the softer material in contact.

(iv) Surface roughness behaves like a plastic layer in the sense that the pressure distribution can be considered as continuous pressure $P(r)$ given by the sum of pressures at all microcontacts.

(v) The microhardness is constant throughout all the contact area.

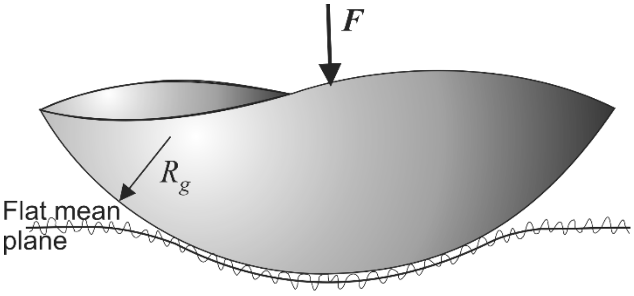

Figure 4-19. Schematic drawing of a sphere resting on a deformable rough surface for the Bahrami et al. (2005) model.

Bahrami-Butt's method starts by computing the Hertzian radius of the contact area given by Eq 3. Then, the method uses two non-dimensional parameters α and τ that depend on the RMS surface roughness σ_{rms} and the microhardness of the contacts H_{mic} as follows:

$$\alpha = \sigma_{\mathrm{rms}} R_g / a^2 \tag{13}$$

$$\tau = \frac{E'}{H_{\mathrm{mic}}} \left(\frac{R_g}{\sigma_{\mathrm{rms}}} \right)^{1/2} \tag{14}$$

These parameters allow computing three non-dimensional values: the non-dimensional pressure distribution P_0', the non-dimensional contact radius a_R', and the generalised pressure distribution exponent, γ, given by, respectively:

$$P_0' = \frac{1}{1+1.22\alpha\tau^{-0.16}} \tag{15}$$

$$a_R' = 1.631 P_0'^{-0.496} - 0.631 P_0'^{3.358} \tag{16}$$

$$\gamma = 1.5 P_0' a_R'^2 - 1 \tag{17}$$

These non-dimensional variables allow computing the radius of the rough contact area a_R, the maximum contact stress P_0 and the stress distribution on the contact area $P(r)$ as follows:

$$a_R = a_R' a \tag{18}$$

$$P_0 = (1-\gamma)\frac{F}{\pi(a_R)^2} \tag{19}$$

$$P(\zeta) = \gamma P_0 (1-\zeta^2) \quad \text{where} \quad \zeta = r/a_R \tag{20}$$

The maximum displacement at the centre of the rough contact area, δ_R, is given by:

$$\delta_R = \frac{P_0 a_R}{E'} B(0.5, \gamma+1) \tag{21}$$

Where the beta function B(0.5,γ+1) is obtained based on a function Γ, as follows:

$$B(0.5, \gamma+1) = \frac{\Gamma(1/2)\Gamma(\gamma+1)}{\Gamma(\gamma+1.5)} \tag{22}$$

The following closed type expression for function Γ was proposed by Butt et al. (2015):

$$\Gamma(x+1) = a_1 (x+a_2)^{x+a_2} \left(1 + \frac{a_3}{a_4 + x^{a_5}} + \frac{a_6}{x^{a_7} + a_8}\right) e^{-x^{a_9}} (2\pi)^{1/2} \tag{23}$$

The values of the constants $a_{1..9}$ of function Γ were obtained by Butt et al. (2015) by least square parameter optimisation, leading to: a_1=0.5641886354, a_2=0.500007096, a_3=0.1091637999, a_4=1.621840565, a_5=0.992925298, a_6=0.0115834573, a_7=1.271839956, a_8=1.505508639, a_9=1. It is important to note that the purpose of Eq. 23 is to fit function Γ in a closed form rather than in its integral form; therefore, the values $a_{1..9}$ are constants, unrelated to the physics of the contact problem.

The ratio between the stiffness of the rough surface and the ideal hertzian stiffness (S_n^{Rough}/S_n^{HM}) depends on the ratio between displacements at the centre of the contact area for rough and smooth spheres δ_R/δ_H, as follows:

$$\frac{S_n^{Rough}}{S_n^{HM}} = \left(\frac{\delta_R}{\delta_H}\right)^{1/2} \qquad \text{with } \delta_H = a^2/R_g \tag{24}$$

Finally, the Bahrami - Butt model provides the radius of the contact area of rough spheres, a_R, as follows:

$$a_R = a\frac{S_n{}^{Rough}}{S_n{}^{HM}} \tag{25}$$

Note that the reduction of the contact stiffness by the ratio S_n^{Rough}/S_n^{HM} in Eq. 25 is similar to that of Bachrach et al. (2000)'s approach, in which the stiffness in Eq. 12 was reduced by the ratio $\left(\frac{R_c}{R_g}\right)^{1/3}$. However, Bachrach et al. (2000)'s approach resulted from fitting experimental results, while the Bahrami – Butt approach rests on the physics of the contact, and the relationship $\frac{S_n^{Rough}}{S_n^{HM}}$ depends on stress and the size and strength of the asperities.

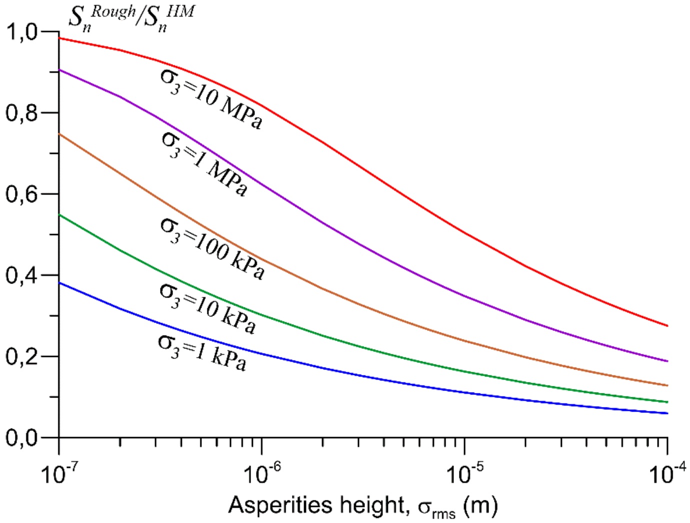

Figure 4-20 Ratio between the theoretical stiffness S_n^{Rough}/S_n^{HM} of rough and smooth quartz spheres as a function of the RMS height of the asperities. The data were computed for particles with R_g=110 μm subjected to isotropic stresses σ_3 (calculated using Eq. 3 and Eq. 4, which relates force to stress) between 1 kPa to 10 MPa, and asperities microhardness H_{mic}=8.2 GPa, as suggested in Yovanovich (2006) for quartz.

Figure 4-20 shows the relationship $\frac{S_n^{Rough}}{S_n^{HM}}$ for different asperities height with respect to σ_{rms} at different stresses. The Figure 4-20 illustrates how, when the contact stress increases, more asperities come into contact and contact stiffness increases. Unsurprisingly, the effect of roughness on stiffness is more significant at low stresses and decreases as stress increases. This is an essential conclusion for our investigation regarding wave velocities at low stresses.

The effect of particle roughness on wave velocities is obtained by introducing the reduced expression of a_R in Eqs 1…6 and then into Eq. 10, leading to the expression of V_p and V_s of an assembly of identical rough spheres. In summary, the model uses the following parameters: for the assembly: ϕ, n, ξ; for the grains, R_g, G_g, ν_g, σ_{rms}, and H_{mic}.

AFM roughness assessment of the Fontainebleau sand as a Martian Regolith Simulant

To account for the rounded-subrounded shape of regolith grains on Mars (e.g. Goetz et al., 2010b), we adopted in our experimental investigation (see Castillo-Betancourt et al. 2023) the NE34 Fontainebleau sand (see Delage et al. 2022a, b). It is a well-sorted silica sand (grain density ρ_s = 2.651 Mg/m^3) from the Paris Basin with a D_{50} of 220 μm (Benahmed, 2001) to compare with the 175 μm diameter derived from thermal inertia measurements in the InSight landing site (Golombek et al., 2017, 2020). Its uniformity coefficient C_u is equal to 1.65.

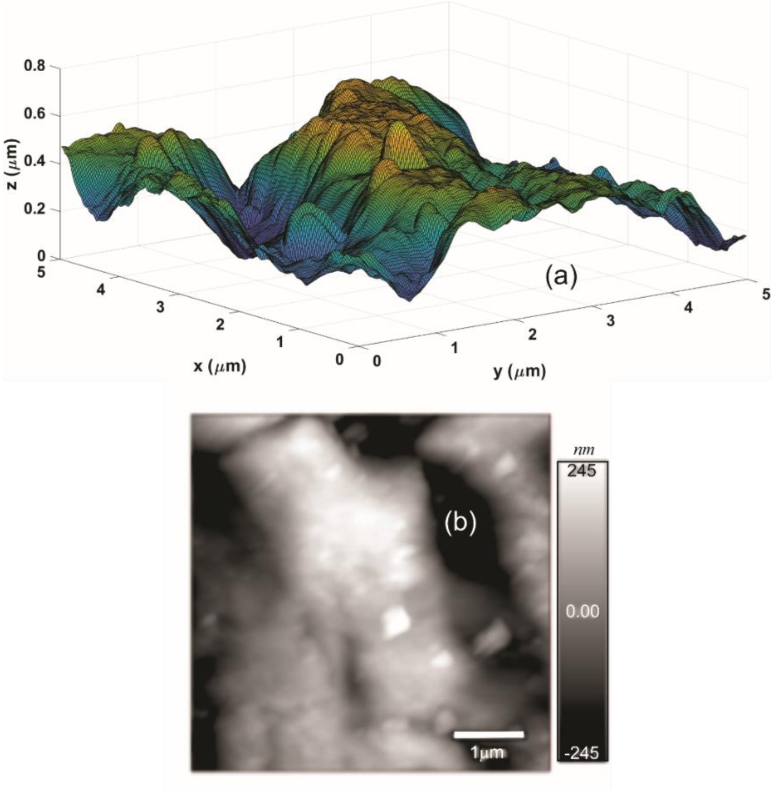

Figure 4-21. Grain topography measured with the AFM AC tapping mode: a) 3D image; b) Greyscale image.

Given the importance of the surface roughness at inter-grain contacts at small stresses, an investigation of the roughness of the Fontainebleau sand grains was conducted by using an

Atomic Force Microscope (AFM - Cypher ES) to obtain a highly detailed surface topography using the Height Tapping Method (Binnig et al., 1986). Figure 4-21a displays the AFM data, with a 256 x 256 resolution in an area of 5 x 5 µm of a grain (average grain diameter is 220 µm). Compared to the (apparently) smooth grain surfaces observed in SEM, high-resolution AFM images evidence significant asperities on the surface. The greyscale image of Figure 4-21b shows that the rugosities height spread along in a wide span, between -245 nm (black) and + 245 nm (white). The AFM measurements give an RMS height σ_{rms} = 0.123 µm.

The cross profiles of Figure 4-22c to Figure 4-22h along various directions in the grey-scale image of Figure 4-21a provide an order of magnitude of the asperity radii. Figure 4-22b shows the radius histogram of the 30 circles that reasonably coincide with the asperities, providing an average radius R_c = 0.35 µm. This analysis is only a first estimate that provides approximate information about the roughness. In fact, this methodology has the following limitations:

- Only a small portion of a grain was measured with the AFM,
- Choosing 30 radios across 6 profiles does not consider the entire radius spectrum,
- The radius histogram, shown in Figure 6b, is not symmetrical and, considering that it only involves a small portion of a grain, does not include radii that have a curvature greater than the portion of the grain analysed.
- A 2D analysis is not the most appropriate methodology to evaluate 3D asperities. It is only correct for spherical contacts. On the other hand, in the case of ellipsoidal contacts with two radii of curvature R_1 and R_2, the contact area must be evaluated using the Gaussian radius of curvature defined as $\tilde{R}=\sqrt{R_1 R_2}$, Caicedo (2018).

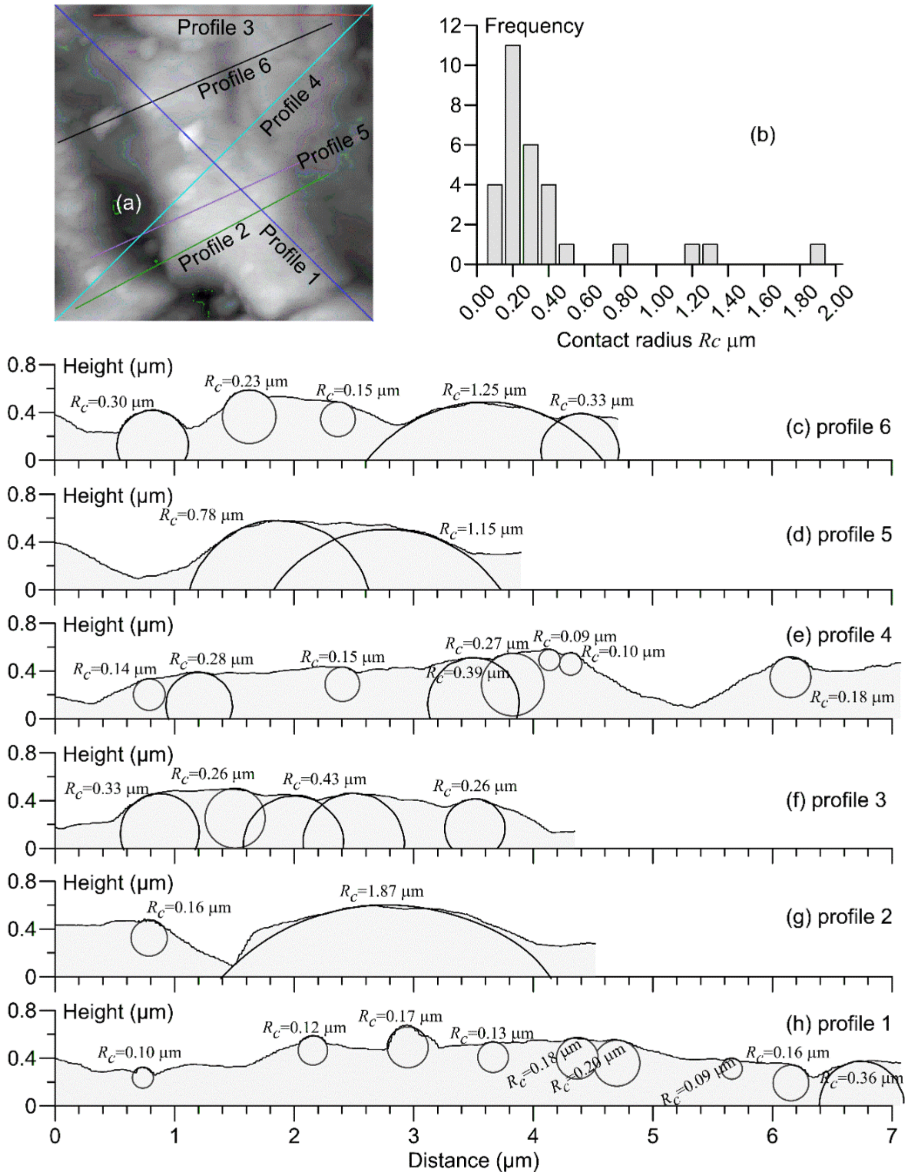

Figure 4-22 AFM investigation of a Fontainebleau sand grain: a) Cross profiles on the AFM measured area; b) Histogram of contact radius along the 6 profiles; c) to h) Roughness plotted along the profiles displayed in a).

Discussion

This section presents the performance of the proposed theoretical model applied to the experimental data published in the companion paper (Castillo-Betancourt 2023). All calculations are available Castillo-Betancourt (2023).

The model parameters are:

- Porosity ϕ: the average porosity of the four samples tested is $\phi = 45.5\%$.

- Coordination number n: a proper value for a loose arrangement of uniform spheres is $n = 6$ (see Mavko et al. 1989 and Caicedo 2018).
- Non-slipping fraction ξ: in sands, Bachrach et al. (2000) recommend for ξ a constant value of 0.5. However, for our experimental results, a better agreement was found with $\xi = 0.6$. This difference probably results from the different origin of the Fontainbleau sand compared to the Moss Landing beach sand.
- Grain size R_g: as in Bachrach et al. (2000)'s model, our (simplified) model considers a pack of identical spheres. The Fontainebleau sand has however a well-sorted grain size distribution with a D_{50} = 220µm and a uniformity coefficient C_u = 1.65, providing $R_g = D_{50}/2$ = 110 µm. The similarity with a pack of identical spheres is then reasonably acceptable.
- Grain's shear modulus G_g: for silica grains, $G_g = 44$ GPa (Bachrach et al., 2000).
- Grain's Poisson ratio ν_g: for silica grains, $\nu_g = 0.08$ (Bachrach et al. 2000).
- Microhardness of the asperities: H_{mic} = 8.2 GPa, according to Yovanovich (2006) for silica grains.
- Asperities height σ_{rms}: the asperities characteristics derived from the AFM data (i.e., σ_{rms} = 0.123 µm from Figure 4-22a and mean contact radius R_c = 0.35 µm in Figure 4-22b) do not result in a good agreement between our data and the model. Actually, good fitting was obtained for larger values (0.6 µm < σ_{rms} < 0.8 µm), as shown in Figure 4-23. This discrepancy probably comes from the imperfect evaluation of roughness that results from the 2D evaluation of only six profiles of the same grain, as described in the previous section. On the other hand, the mean value is not the most appropriate descriptor for a radius distribution shown in Figure 4-23b that is clearly asymmetric. The Figure 4-23 also shows how sensitive the model is to asperities. Logically, smaller velocities are obtained for larger asperities, under the same stress.

There are various possible reasons for this discrepancy in asperities data. The first one is perhaps the approximation made between our sand and an assembly of spheres of the same diameter, like in Bachrach et al. (2000). Also, a better estimation of the asperities parameters should probably be gained from an area larger than the 5 x 5 µm one observed in our case on a single grain. However, the shape of the observed fitted curve in Figure 4-23 pretty well matches the data, at least above 10 kPa. For smaller stresses, the fitting is not as good, with a tendency for the points to be aligned along straight segments, exhibiting a linear change of velocities with respect to stress. This shows that something else may occur at very low stresses below 10 kPa, a trend already suspected in the experimental investigation (Castillo-Betancourt et al. 2023).

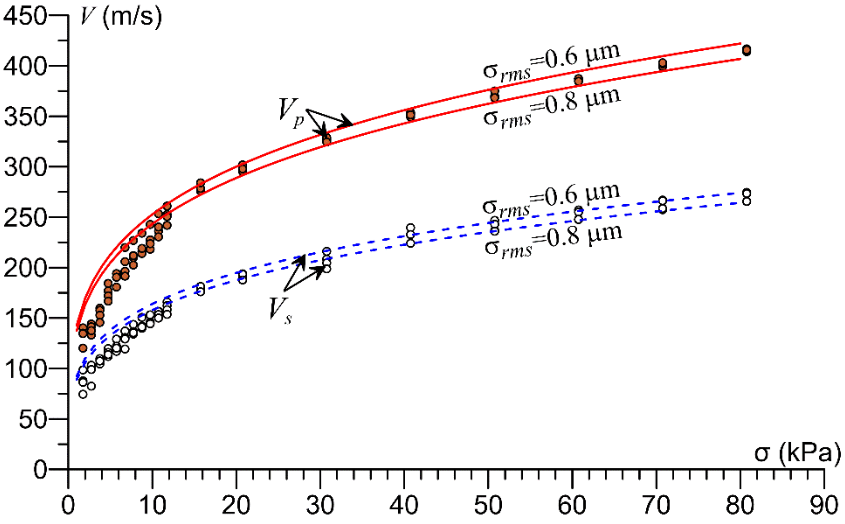

Figure 4-23. Comparison between measured (Castillo-Betancourt et al. 2023) and theoretical values of wave velocities.

Figure 4-24 shows the theoretical Poisson ratio computed from Eq. 9 for different non-slipping fractions. The Figure 4-24 evidences good agreement between our experimental data and the theory for 0.55 < ξ < 0.65. The results are close to the Poisson ratio ν = 0.15 ± 0.03 reported for rounded silica grains in Bachrach et al. (2000).

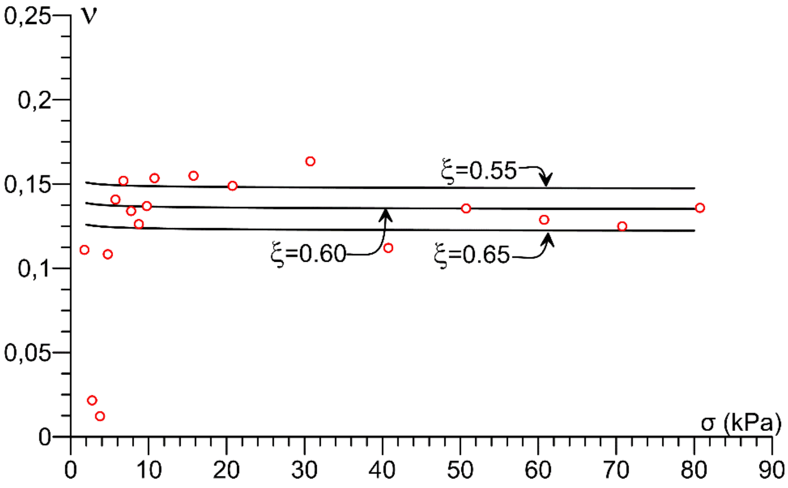

Figure 4-24. Comparison between measured and theoretical Poisson ratio.

Despite the good agreement of the predicted Poisson ratio, some discrepancy appears at low stresses (< 10kPa). As commented in Castillo-Betancourt et al. (2023), the larger dispersion observed below 5 kPa indicates that the performance of the experimental device is perhaps limited at very low stress, an area that certainly needs further investigation. A more accurate device would be necessary in an area where the efficiency of standard bender elements for measuring wave velocities is perhaps limited.

Based on the (dispersed) experimental points below 5 kPa, it is not fully guaranteed that the Poisson ratio remains constant at very low stress. According to Bachrach's approach (Figure 4-18), a decrease in the proportion of slipping grains significantly reduces the Poisson ratio. This could be physically explained by an enhanced effect of asperities in reducing inter-grains slippage at very low stresses.

Conclusions

This paper presents a theoretical model for assessing wave velocities in loose sands subjected to low stresses. The experimental data were obtained from a companion paper (Castillo-Betancourt et al. 2023) in which a loose sample of Fontainebleau sand was used as Martian regolith simulant of the InSight landing site, and wave velocities were measured atlow stresses by using bender elements.

Based on the works of Bachrach et al. (2000), Bahrami et al. (2005) and Butt et al. (2015), a contact theory model was developed, with particular attention paid to both the proportion of inter-grains slippage occurring in a loose assembly of identical spheres, and to the effects of grains asperities, that become stronger at low stress. Bachrach et al (2000)'s approach showed that, to correctly model the elastic response of an assembly of identical spheres and to obtain a reasonable response in Poisson ratio, one has to consider some (irreversible) slippage between spheres, that are by essence not an elastic process. The values of Poisson ratio obtained in this work (and others works on sands, generally conducted at higher stresses) confirm that some slippage may occur, even in the "elastic" response of sands at very low stress (around 10^{-6} for wave transfers).

Good agreement with experimental data was obtained by the model, but we had to adopt asperities characteristics larger than those obtained by the AFM measurements carried out. This probably results from the strong assumption of assimilating our sand to an assembly of identical spheres. The AFM estimation of asperities were also carried out on a limited area (5 x 5 µm) on a single grain (average diameter 220 µm), providing an approximate determination of the asperities. The correspondence of the model with experimental data is less satisfactory below 5 kPa, an area where the velocity change are more difficult to detect and with, perhaps, stronger effects of asperities.

The calculation of the Poisson ratio ν from wave velocities measurements confirmed the constantness of ν with stress, at least above 5 kPa. Conclusions are less clear below 5 kPa, in an area that certainly deserves more investigation. Due to possible enhanced effects of asperities and to the consequences on the proportion of sliping grains, the changes in Poisson ratio at very low stresses is to be further investigated with a more adapted device.

This study offers the possibility of assessing theoretically the elastic behaviour of sands under low stress and low strain based on the properties of the granular assembly. The proposed theory can be useful for assessing the elastic properties of other areas of Mars or the Moon. Further work being carried out by the authors includes the study of the effect of shear stresses on the mechanical response of the regolith simulant, Chaparro-López et al. (2023).

References

Archard, J. F. (1957). Elastic deformation and the laws of friction. Proceedings of the Royal Society of London. Series A. Mathematical and physical sciences, 243(1233), 190-205.

Bachrach, R., Dvorkin, J. and Nur, A. M. (2000). Seismic velocities and Poisson's ratio of shallow unconsolidated sands. Geophysics, 65(2), 559–564. https://doi.org/10.1190/1.1444751.

Bahrami, M., Yovanovich, M. M. and Culham, J. R. (2005). A compact model for spherical rough contacts. J. Tribol. Oct 2005, 127(4): 884-889, https://doi.org/10.1115/1.2000982

Benahmed, N. (2001). Comportement mécanique d'un sable sous cisaillement monotone et cyclique : application aux phénomènes de liquéfaction et de mobilité cyclique. PhD thesis, Ecole desPonts ParisTech (in French).

Binnig, G., Quate, C. F. and Gerber, C. (1986). Atomic Force Microscope. Physical Review Letters, 56(9), 1930–1934.

Butt, S. U., Antoine, J. F. and Martin, P. (2015). Simplified stiffness model for spherical rough contacts. Tribology-Materials, Surfaces and Interfaces, 9(2), 63-70.

Caicedo, B. (2018). Geotechnics of roads: Fundamentals. CRC Press.

Castillo Betancourt, J. P., Delage, P., Caicedo B., Lognonné, P. and Banerdt B.W. (2023). Waves Velocity and Poisson Ratio in Loose Sandy Martian Regolith under Low Stresses. Part 1: Experimental Investigation. Submitted to Journal of Geophysical Research: Planets.

Castillo-Betancourt Juan Pablo. (2023a). juan9715/MRA-Bender-Element-data: Bender data public repository release (Release) [Data set]. Zenodo. https://doi.org/10.5281/zenodo.8161970

Castillo- Betancourt Juan Pablo. (2023b). juan9715/WaveVelocitiesSoftwareAndSpreadsheet: Wave Velocities Data Release (v) [Data set]. Zenodo. https://doi.org/10.5281/zenodo.8415384 Chaparro-López M.J., Castillo-Betancourt J.P., Cabrera M., Caicedo B., Delage P., Lognonné P., and Banerdt B. (2023) "Dynamic Mechanical Analysis Test for Evaluating Loose Sands on a Wide Strain Range—Application to the InSight Mission on Mars," Geotechnical Testing Journal https://doi.org/10.1520/GTJ20230381.

Delage, P., Marteau, E., Vrettos, C., Golombek, M., Ansan, V., Banerdt, W. B. et al. (2022a). The mechanical properties of the Martian soil at the InSight landing site. In Proceeedings 20th International Conference on Soil Mechanics and Geotechnical Engineering, Sydney.

Delage, P., Betancourt, J. P. C., Caicedo Hormaza, B., Karakostas, F., De Laure, E., Lognonné, P. et al. (2022b). The interaction between the SEIS seismometer of the InSight Martian mission and a regolith simulant. Géotechnique, 1-12.

Digby, P. J. (1981). The effective elastic moduli of porous granular rocks. J. Appl. Mech. 48(4): 803-808.

Dobry, R., Ng, T. T., Petrakis, E., & Seridi, A. (1991). General model for contact law between two rough spheres. Journal of engineering Mechanics, 117(6), 1365-1381.

Goetz, W., Pike, W. T., Hviid, S. F., Madsen, M. B., Morris, R. V., Hecht, et al., (2010b). Microscopy analysis of soils at the Phoenix landing site, Mars: Classification of soil particles and description of their optical and magnetic properties. Journal of Geophysical Research E: Planets, 115(8), 1–23. https://doi.org/10.1029/2009JE003437

Golombek, M., Kipp D., Warner I.J., Daubar I.J., Fergason R.L., Kirk R.L. et al. (2017). Selection of the InSight landing site. Space Science Review 211, 5–95.

Golombek, M., Warner, N. H., Grant, J. A., Hauber, E., Ansan, V., Weitz et al. (2020). Geology of the InSight landing site on Mars. Nature Communications, 11(1), 1–11. https://doi.org/10.1038/s41467-020-14679-1.

Greenwood, J. A. and Williamson, B. P., 1966, "Contact of Nominally Flat Surfaces," Proc. Phys. Soc., London, Sect. A, 295, pp. 300–319.

Greenwood, J. A. and Tripp, J. H., 1967, "The Elastic Contact of Rough Spheres," ASME J. Appl. Mech., 89, pp. 153–159.

Hashin, S. and Shtrikman, S., 1963, A variational approach to the elastic behavior of multiphase materials: J. Mech. Phys. Solids, 11, 127–140.

Kumar, J. and Madhusudhan, B. N. (2010). Effect of relative density and confining pressure on Poisson ratio from bender and extender elements tests. Géotechnique, 60(7), 561-567.

Majumdar, A. and Bhushan, B., 1991, "Fractal Model of Elastic-Plastic Contact Between Rough Surfaces," ASME J. Tribol., 113, pp. 1–11.

Mavko, G., Mukerji, T. and Dvorkin, J., 1998, The rock physics handbook: Cambridge Univ. Press.

Mindlin, R. D., 1949, Compliance of elastic bodies in contact: J. Appl. Mech., 16, 259–268.

Persson, B. N. (2006). Contact mechanics for randomly rough surfaces. Surface science reports, 61(4), 201-227.

Richart,Jr.,F.E.,Hall,J.R.,andWoods,R.D.(1970).Vibrationofsoilsandfoundations.PrenticeHall,Inc.,EnglewoodCliffs,N.J.

Santamarina, J. C., Klein, K. A. and Fam, M. A. (2001). Soils and waves. New York: J. Wiley and Sons.

Walton, K. (1987). The effective elastic moduli of a random packing of spheres. Journal of the Mechanics and Physics of Solids, 35(2), 213-226.

Yovanovich, M. (2006). Micro and macro hardness measurements, correlations, and contact models. In 44th AIAA Aerospace Sciences Meeting and Exhibit (p. 979).

Acknowledgements

This work is part of the PhD thesis of Juan-Pablo Castillo Betancourt, financially supported by Universidad de los Andes (Colombia) and École des Ponts ParisTech (France). The authors are also grateful to NASA, CNES, their partner agencies and Institutions (UKSA, SSO, DLR, JPL, IPGP-CNRS, ETHZ, IC, MPS-MPG). This paper is InSight contribution N° ICN 328.

Open Research

All the Waveform data csv files from the Bender Element measurements performed on the four samples, used for wave velocity calculations in the study and presented in the companion paper Castillo Betancourt et al. (2023) are available at the public MRA-Bender-element-repository Castillo-Betancourt (2023b), and all software and Excel spreadsheets used are available on another repository at Castillo-Betancourt (2023a). Instructions may be found on the "README" file of the repository.

5. THERMAL CONDUCTIVITY AND WAVE VELOCITY MEASUREMENTS

> *"Honestly, if you were any slower, you would go backwards".*
> *Draco Malfoy, on soil thermal conductivity (probably).*

Thermal conductivity of the surface material is one of the properties that the InSight Science Team studies for the regolith encountered at the landing site. The main resource to accomplish this is the different measurements performed by the Heat flow and Physical Properties Package (HP^3) instrument. An experimental setup was conceived and constructed at Universidad de los Andes to aid in this task for coupled wave velocity and thermal conductivity measurements on a regolith simulant. This chapter details the work that led to the setting up of the experimental device, allowing to carry out experiments in a CO_2 environment under controlled temperature and pressure conditions, which mimic the atmosphere of Mars. Since the complete experimental device is somewhat complex, the setup's wave velocity, thermal, CO2, and vacuum components are explained separately, followed by a detailed explanation of the experimental protocol for the device's utilisation. The initial results obtained with this setup are also presented to illustrate its development process. After presenting the experimental program performed, the definitive results are presented and interpreted; the chapter then concludes with some remarks concerning lessons learned for these kinds of measurements and presents some general conclusions.

5.1. Basic concept for the experimental setup

The main goal of this work component was to construct an experimental setup that allowed for simultaneous measurements of wave velocity and thermal conductivity on soil. For this purpose, adequately sized dismountable containers, which could sustain a vacuum inside, were used. These containers have an internal square base of 80x80mm and 200 mm in height, of which 160 mm are filled with soil, as seen in Figure 5-1. Two sides are acrylic walls, while the two others are thick aluminium plates that act as a metallic heat-conducting boundary. Acrylic walls were modified with several holes to host wave-emitting actuators (initially Bender Elements) and receiver devices to register the wave arrival. The container and the Bender elements can be seen in Figure 5-2.

However, after some testing, it was appreciated that the wave produced by the bender elements could not cross the loose material under very low stresses (below 10 kPa). Consequently, much more powerful piezo actuators were adapted into the wall of the sample container to generate the pulses capable of crossing the sample and connected to a signal generator and amplifier to generate the pulse. Meanwhile, uniaxial accelerometers were placed (correctly oriented) on the opposite wall to register the arrival of the waves.

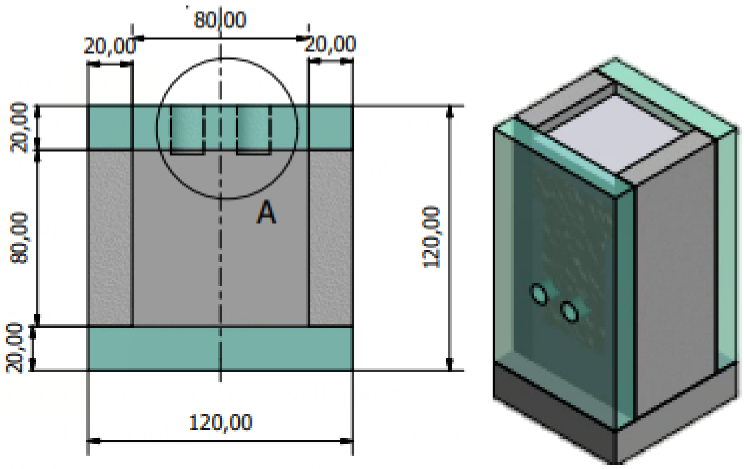

Figure 5-1. Dimensions and model of the experimental setup (units in mm).

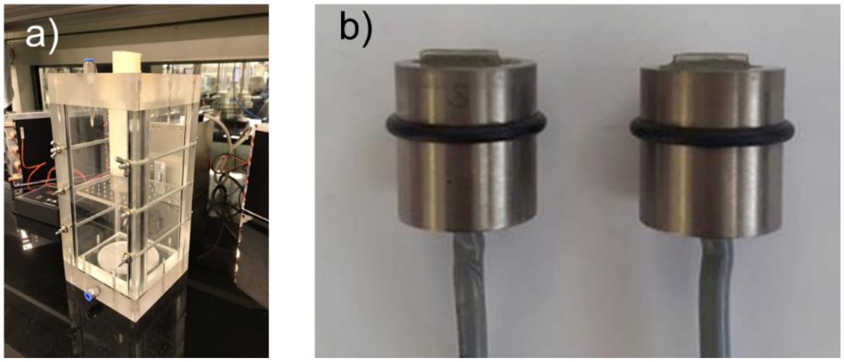

Figure 5-2 a) original container for clay consolidation, which was extensively modified for this experiment. In b), the bender elements used for the initial stages of the setup.

Peltier plates were placed in contact with each metallic wall of the sample container for the thermal conductivity measurements. After testing some Peltier plates with the regolith simulant and observing on a measurement that propagation took too long, it was decided to utilise more powerful TeTech Peltiers to propagate the heat. Type K Thermocouples were observed to be adequate to keep the propagation of heat inside the sample, and tests were conducted to determine the number of thermocouples to be placed along the axis of the sample container.

A regulated vacuum was to be imposed inside the sample container using a pump to reproduce the conditions of the Martian Atmosphere. Since the Martian atmosphere is so light, the pressure to attain inside the sample container was about 6-7 millibars, so a special pump was required. After some inquiry, Vacuubrand VarioSelect equipment capable of imposing vacuums as low as 0.3 mbar was selected and tested before being adopted. Several modifications to the testing device had to be implemented to accommodate the consequences of this extremely low vacuum pressure, as will be noted in the following sections. The following sections describe the components separately.

5.2. Vacuum pump and CO_2 supplying

The Mars gas composition and pressure must be recreated to perform the measurements in conditions as similar as possible to those encountered at Mars. To accomplish this, the air inside the sample must be replaced by the CO_2, which makes up 96% of the air of Mars (as is seen in Figure 5-3); notice that Earth's air is 78.1% Oxygen and 20.9% oxygen, with other gasses accounting for the additional 1% of the composition.

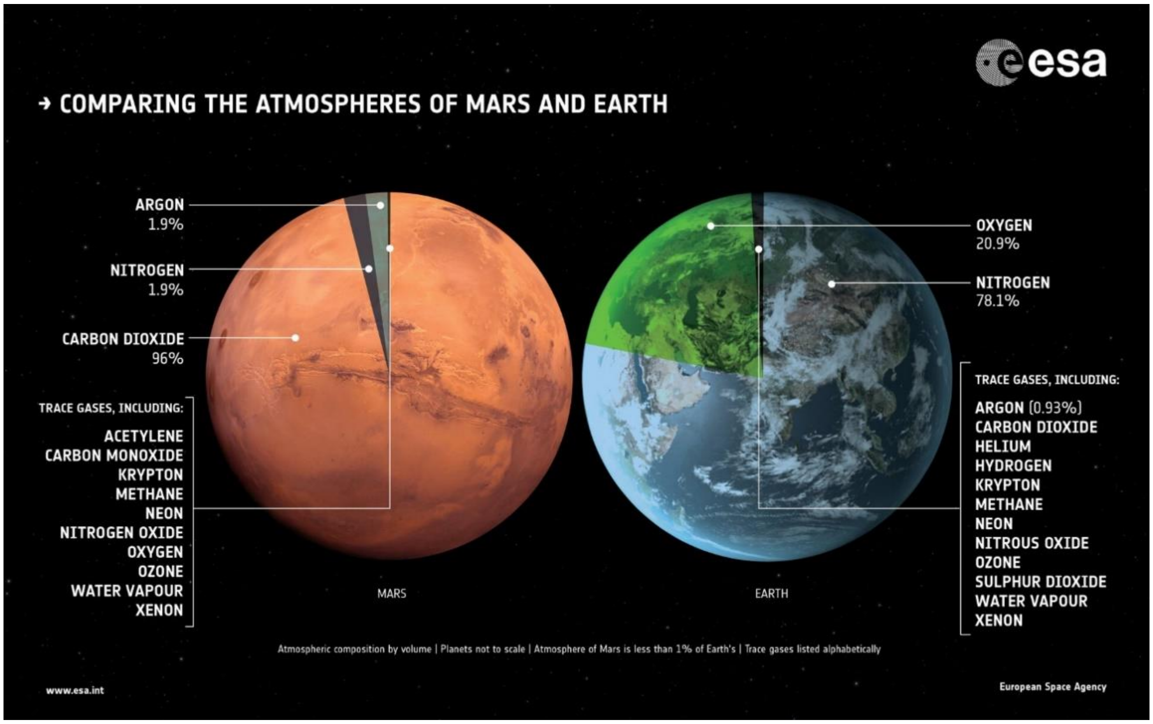

Figure 5-3. Comparison of the composition of Earth’s and Mars’s atmospheres. The terrestrial atmosphere is almost entirely made of Nitrogen and Oxygen, while Carbon Dioxide is the prevalent component for the case of Mars (Image credit: European Space Agency, n.d.).

As seen in Figure 5-4, the atmospheric pressure at the Mars InSight landing site is in the order of 750 Pa, with low-frequency fluctuations of about +/-18 Pa during one Sol. However, when dealing with seasonal variations, atmospheric pressure can be as low as 620 Pa or as high as 800 Pa, as can be seen in Figure 5-5; consequently, the pressure levels to be applied in the sample container are in the range of 600 – 800 Pa.

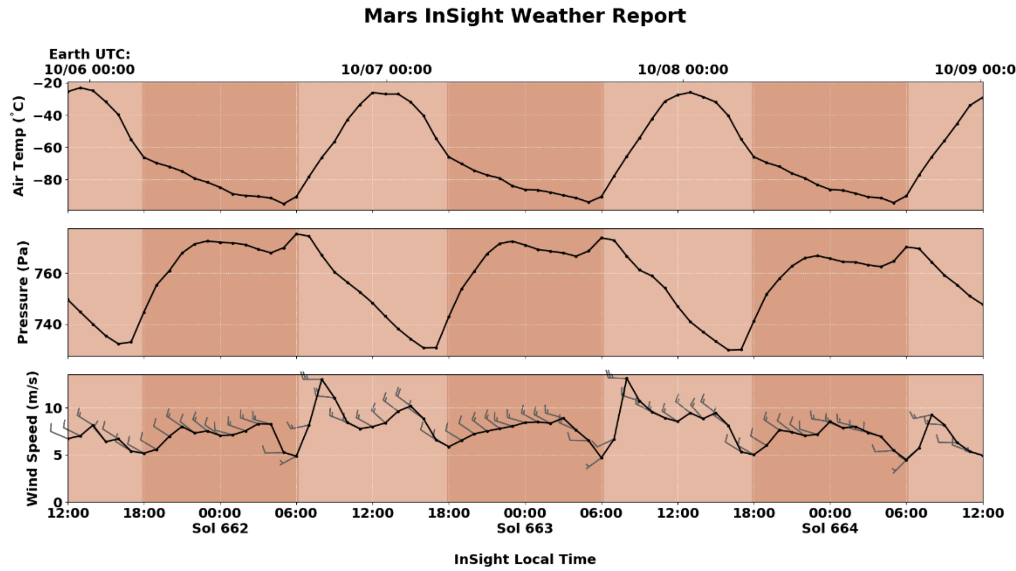

Figure 5-4. Mars InsSight data for atmospheric pressure during three Sols. (Image credit: NASA JPL, n.d.).

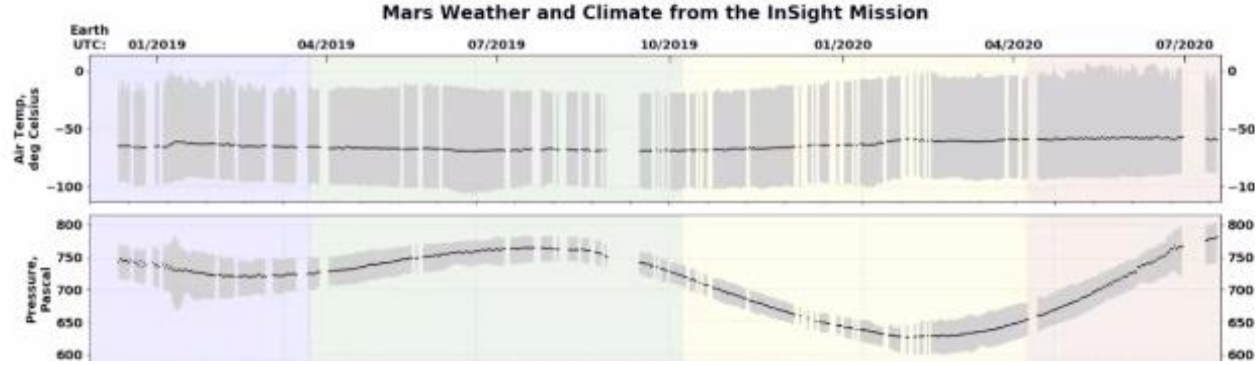

Figure 5-5. Mars InsSight data for atmospheric pressure for two years. (Image credit: NASA JPL, n.d.).

The very low 6-8 mbar vacuum (equivalent to 600 – 800Pa) is applied using the Vacuubrand VarioSelect MV2 pump, capable of producing vacuums as low as 0.3 mbar with 0.1 mbar accuracy (see Figure 5-6). The controller can reach these vacuum values within a few minutes and hold it for several hours, which is key for adequate thermal conductivity measurements.

Several steps were followed to check whether the sample container was vacuum proof, testing it with water and air pressure to fix any potential leaks. The absence of leaks was verified by using soap and water at the locations of possible leaks in the sample and checking for air scape through the fluid (observed as growing air bubbles).

The safety of the pump equipment was guaranteed by deploying a sand trap, a secondary container connected between the sample container and the vacuum pump. It is worth mentioning that since an almost absolute vacuum was induced into the container (and consequently into the sand trap), the container utilised needed to be stiff and strong enough. A triaxial chamber, which was guaranteed to withstand the significant solicitation of the atmospheric pressure surrounding the container, was thus used for this purpose.

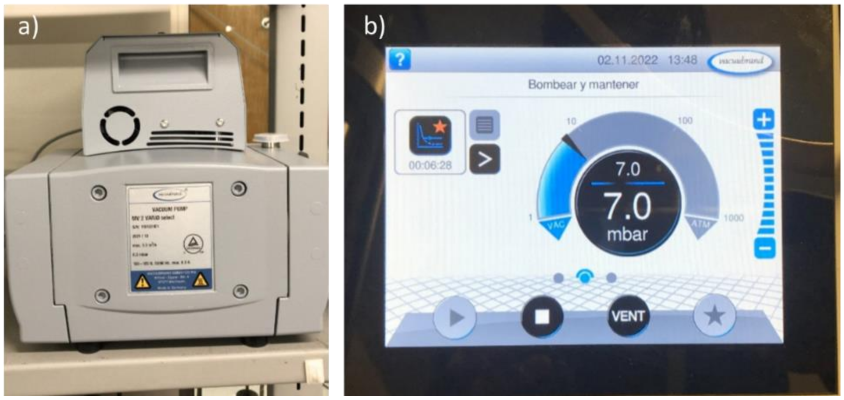

Figure 5-6 The a) VarioSelect pump and its b) digital controller while applying 7 mbar.

The sample container was impermeabilised by outfitting it with seals spanning all the joints between the plates spanning the side of the container, as well as between the top and bottom of the sample. Small holes for wires and in the cover were closed with silicon. All joints of the rectangular shape were closed with seals and toric joints (o-rings and similar). A rubber seal was made to ensure no escapes between the sample container and its cover, which was the face most often removed since that was necessary for sample replacement.

The next step was to connect the laboratory's CO2 supply to the container sample. This system can be seen in Figure 5-7, and it has two valves: the first one, seen furthest to the right, is fully opened to begin or end the gas flow, while the second one has a valve to control the flow magnitude. This flow needs to be as slow as possible so that it will not disturb particle arrangement, and after some measurements, it was observed that the lowest flow that the valve could control was 60-80mL/min. Given that 16 of the 20 cm of the height of the container volume is already occupied by the soil, and knowing that it is necessary to fill not only the sample container but also the sand trap, this volume can be estimated as:

$$\frac{\pi * {d_t}^2}{4} * h_t + {b_c}^2 * h_c = \frac{\pi * (0{,}12m)^2}{4} * 0{,}28m + (0{,}08m)^2 * (0{,}16 * 0{,}5 + 0{,}04)m = 3.94L$$

Where b_c and h_c are the base and height of the container, and h_t and d_t are height and diameter of the triaxial chamber acting as a sand trap. Since it was necessary to fill a combined volume of about 4L (a small volume of the sample of hoses), the worst-case scenario was that a 65.6-minute fill time would be enough to fill both containers. To account for the significant incertitude in the gas flow control, it was decided that 80 minutes would be used to ensure the complete filling.

Next, the sample container was adapted to accommodate the entry of the necessary CO_2 to recreate the conditions of the Mars atmosphere. A valve located at the bottom of the container (also seen in Figure 5-7) regulated the access of the CO_2 into the sample container. Since carbon dioxide is about 1.5 times heavier than air, the continuous injection of the gas allowed the air to leave the sand trap chamber and escape via another valve to the outside, thus ensuring saturation of the gas media inside the sample with CO_2.

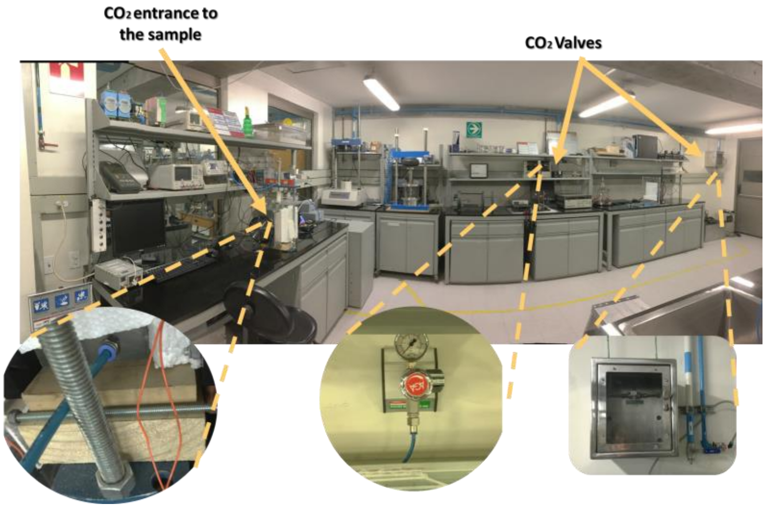

Figure 5-7. CO2 supply and control system, including two valves and the hose connection to the inside of the sample.

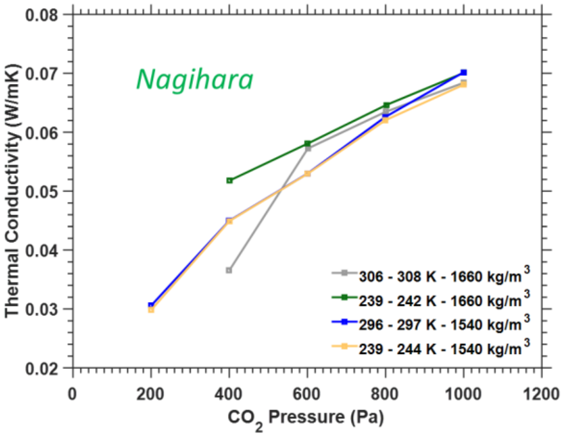

Figure 5-8. The results of other tests on thermal conductivity displayed no effect on the measured values for measurements done at room temperature (Nagihara et. al, 2022).

The other variable that could potentially be replicated in the experiment is the temperature of the Martian atmosphere. Figure 5-5 and Figure 5-6 show this can be estimated at -50°C. However, as seen in measurements in Figure 5-8, work on other regolith analogues showed no difference for thermal conductivity tests conducted at room temperature from those conducted at very low temperatures (Nagihara et al., 2022), especially compared to sample density. Consequently, considering the considerable practical complications of cooling the whole experiment down to these temperatures (particularly in terms of instrumentation), it was decided not to incorporate this effect.

5.3. Experimental setup for wave velocity measurements

After observing that the Bender elements could not measure the wave velocity under the very low stresses being studied, a pair of Cedrat Technologies PPA 40M piezo actuators were adopted to transmit the waves. These actuators produce a powerful strike, sending a pulse that traversed the sample when subjected to a voltage of positive 5V that then passes through an amplifier. It is essential to mention that this was not the case for the bender at any voltage or frequency combination. To use these elements, the container had to be modified to allow them to be placed in a manner that could generate P and S waves on demand. As can be appreciated in Figure 5-9a, the frontal acrylic cover was modified with a hole and a trench to accommodate both actuators, oriented in such ways that one strike was directed in a direction normal to the soil (thus generating P waves). The second one was placed in a small ditch into the cover to enable the actuator to strike transversally to the soil mass, producing primarily S waves. The actuators were fixed in place and surrounded by an acrylic box impermeabilised with several sealing silicone layers before it became truly hermetic.

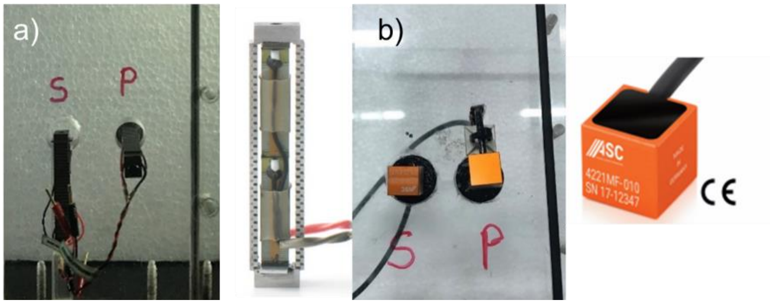

Figure 5-9 a) The Cedrat Piezoactuators were used to generate P and S waves by installing them into one of the acrylic covers of the setup. A trench was made into the cover to install the S wave actuator transversally. B) The accelerometers were set directly facing them to register the arriving waves in the opposite wall.

Meanwhile, the other acrylic cover of the sample container (Figure 5-9b) was modified to fit two uniaxial accelerometers aligned in the proper directions to register the arriving waves. These sensors and their associated electronics will be described in detail below.

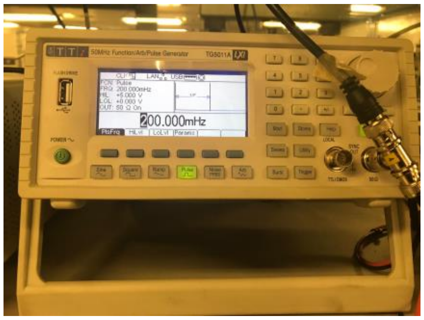

Figure 5-10. The TEM TG5011A signal generator was used to generate the signals driving the piezoactuators. It allows work with rectangular and sinusoidal signals in single and burst configurations.

A TEM TG5011A signal generator was used to generate the waves (Figure 5-10), capable of producing periodical sinusoidal and square waves while set up to a particular burst configuration. This versatile device enabled a high control of both sinusoidal and rectangular signals. The generator was plugged into a Cedrat LA75C amplifier, capable of amplifying the generated waves by a factor of x20. Then, an AlphaWire bifurcation cable was adapted to enable simple switching of the amplifier connection to the active piezo actuator (for either P or S wave as desired).

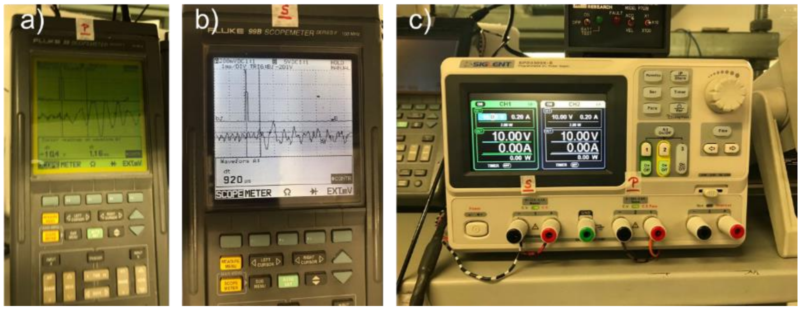

Figure 5-11 The data of the accelerometers was collected using a pair of a) Fluke 99 and b) Fluke 99B oscilloscopes, and the sensors were powered with the c) SPD3303X-E power source.

The signal acquisition was done using a pair of ASC4221MF-005-6A uniaxial accelerometers from PM Instrumentation, each one being oriented in the appropriate direction to register the arriving P and S wave from the actuator directly facing it (see Figure 5-9). The accelerometer signal was read using a pair of independent two-channel Fluke 99 oscilloscopes labelled for each wave (see Figure 5-11), eliminating any potential undesired crosstalk effect. The accelerometers were set to the specified parameters of 10 V and a 2-mA current supplied by the SPD3303X-E power source.

5.4. Experimental setup for thermal conductivity measurements

The next step was to conceive and implement a setup that could be used to generate, regulate, and receive thermal impulses through a material sample. The depart concept for the experiment was to impose the desired boundary conditions in terms of a controlled temperature and to measure the temperature inside of the sample, potentially at several locations in the longitudinal direction, to observe the passing of the temperature rises and drops.

A preliminary activity was carried out to validate the concept for the study of heat propagation in the studied material, which was to utilise a thermal camera to visualise the propagation of a heat wave on the material's surface. A basic setup (seen in Figure 5-12) consisting of a small prismatic box filled with the Fontainebleau sand was implemented to do this. One Peltier plate was placed at each end of the box to heat up to a fixed temperature, and two type K thermocouples were installed into the material. Then, an infrared thermal camera was fixed, surveying the setup's surface to observe the temperature pulse's passage. The plates were then connected to a power source to heat the sample. After a few hours, this observation was possible, and a video was recorded. With this simple activity, it was decided that although the concept was valid, more powerful Peltier elements and a considerable number of temperature sensors would be necessary for the definitive setup.

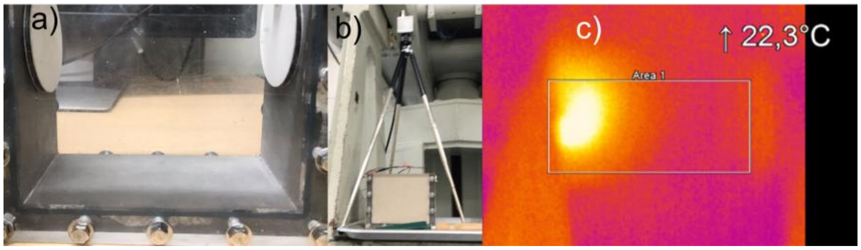

Figure 5-12 a) The container, Peltier plates, and b) thermal camera used for the b) preliminary thermal propagation test.

Consequently, for the definitive setup, the chosen equipment was a pair of the TeTech LC 200 Peltier plates, along with their TC-48-20 controllers and power sources (all elements seen in Figure 5-13). This equipment incorporates a cooling fan and is powerful enough to keep the test going during numerous continuous hours, as required for some thermal conductivity measurements. They can also impose cooling instead of heating with the proper connections.

The desired boundary conditions in terms of temperature were controlled in the metallic walls of the container utilising the Peltier plates, with a predominant unidirectional heat conduction direction seen in Figure 5-14. To register the evolution of the temperature through time in the sample and alongside the plates, seven type K thermocouples were placed into the experimental device, using silicone to seal the holes in which they were installed not to affect the vacuum sealing of the container. They can be seen before being placed in Figure 5-15b. The heat propagation through the soil is monitored using the five thermocouples installed in the soil, as seen in the arrangement presented in Figure 5-15. At the same time, the other two serve to monitor the Peltier actuators and verify that the reading provided by the controller equipment agrees with the measurements.

With seven thermocouples to monitor the experiment, data acquisition for all these sensors was becoming a considerable challenge, requiring the installation of an ADAM 2019+ with 8 channels for this type of sensor, but also of a NI 9172 data acquisition card, which is seen in Figure 5-16. Also, since the heat would be conducted to some extent through the plexiglass walls of the sample, all of the container walls were surrounded by thick polystyrene layers.

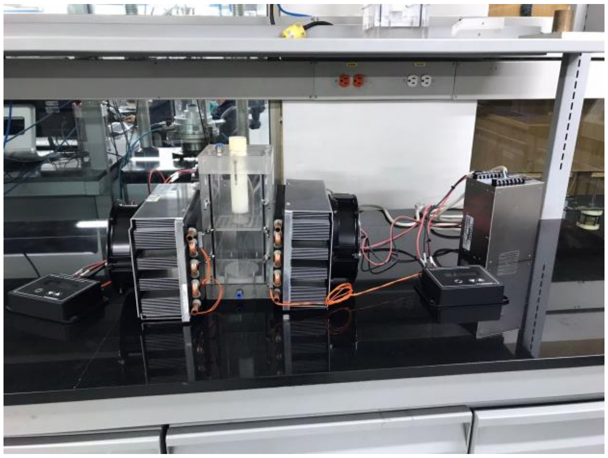

Figure 5-13 The more potent Peltier plates of the definitive setup with all their electronic equipment.

Once all these elements were in place, it was decided that before proceeding with the definitive testing program, it was necessary to conduct a rigorous calibration of the thermocouples to ensure accurate and repeatable measurements. To do this, it was decided that a well-calibrated PT100 probe would be introduced in the sample, and all thermocouples' calibration constants were evaluated per the PT100 probe measurements. The setup for this work can be seen in Figure 5-17.

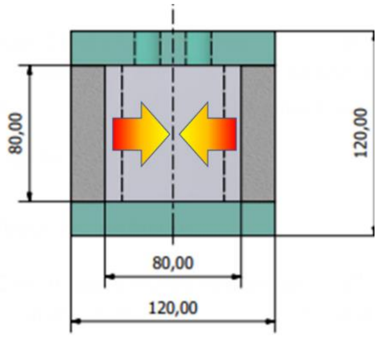

Figure 5-14. Predominant direction for the envisioned heat conduction experiments.

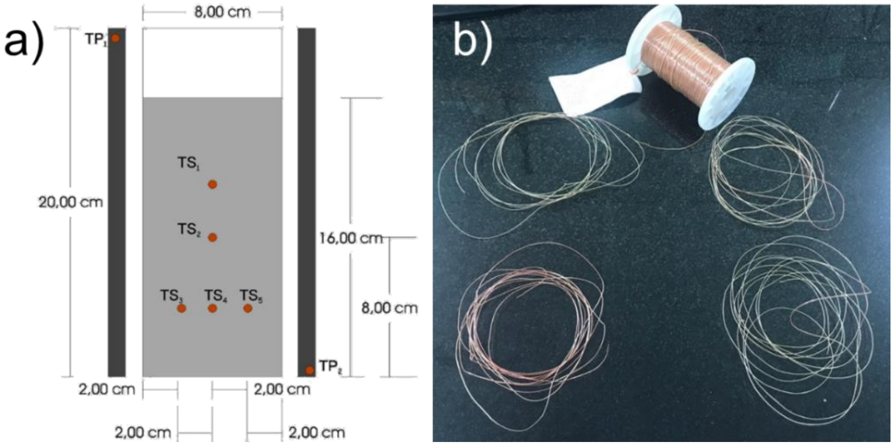

Figure 5-15 Schema displaying the thermocouples’ arrangement in the amples’ back cover.

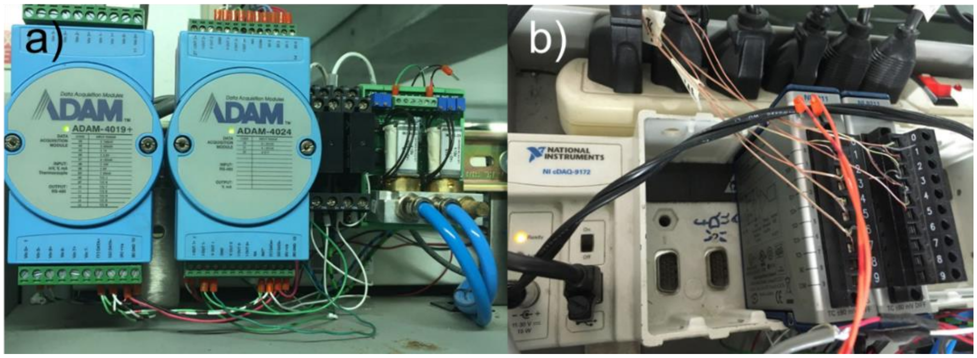

Figure 5-16. Considerable amount of instrumentation posed a practical challenge. A) ADAM2019+ modules for most thermal sensors alongside the air pressure valve control, and b) data acquisition card for the other thermocouple sensors.

After several tests conducted under atmospheric pressure and 6mbar pressure, satisfactory performance for most of the sensors (TS1, TS2, TS3, TS4) was obtained, as seen in the test seen in Figure 5-18, where the empty container was cooled to 14°C. It is observed that the measurements reported by all the sensors continue in the same line throughout testing, and their calibration is considered satisfactory. However, despite several attempts, T5 yielded inconsistent results most of the time, and it was decided to exclude this sensor from the analysis. The same behaviour is observed in the test of Figure 5-19, in which the temperature stabilised after the Peltier plates were turned off. In this case, the measurements of T5 are less inconsistent. This test of return to initial conditions also gives information for a practical aspect since it can be noticed that 10 hours of delay between tests are enough to allow all the temperatures to return to their initial values, and a new test can begin without encountering complications due to different initial readings on the sensors.

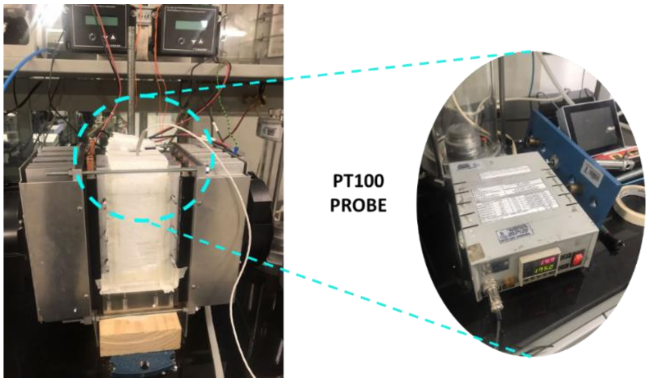

Figure 5-17. a) Experimental setup for the calibration of the thermocouple sensors. It was achieved with a well-calibrated b) PT100 probe.

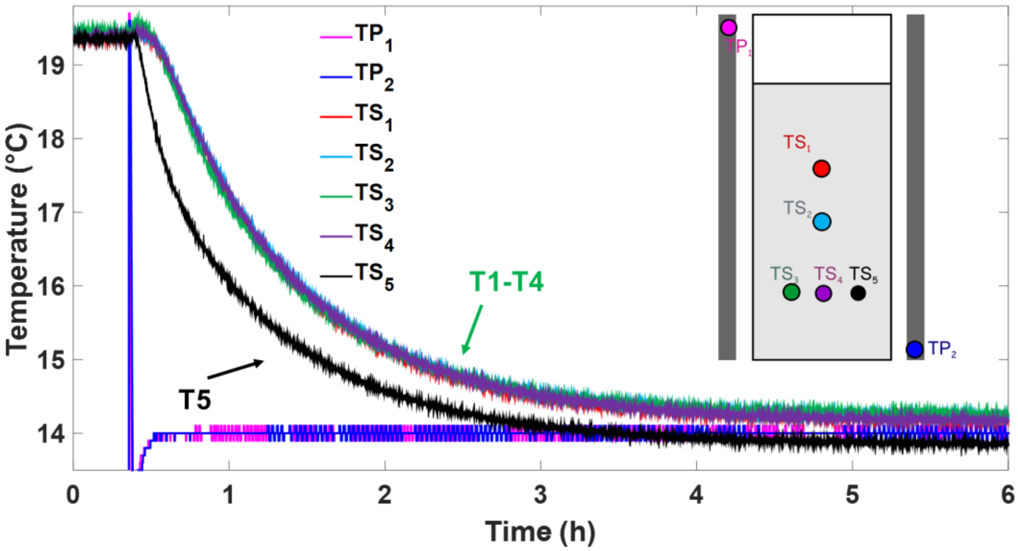

Figure 5-18. Calibration test during a test carried out under atmospheric pressure, with T1-T4 measuring consistent values and T5 misfunctioning.

The reversibility of these measurements was also verified by three tests in Figure 5-20, where all the sensors show good linearity during a prolonged cooling-reheating cycle. However, it is also observed that the best results are obtained if the measurements are restricted to a smaller range (variations of about 3°C) since the use of greater temperature steps (variations greater than 5°C) may produce some deviation, as observed in the figure Figure 5-20a-c. Consequently, it was decided that the temperature change for the definitive test program would be limited to 3°C of cooling to ensure that the temperature measurements would be as accurate as possible.

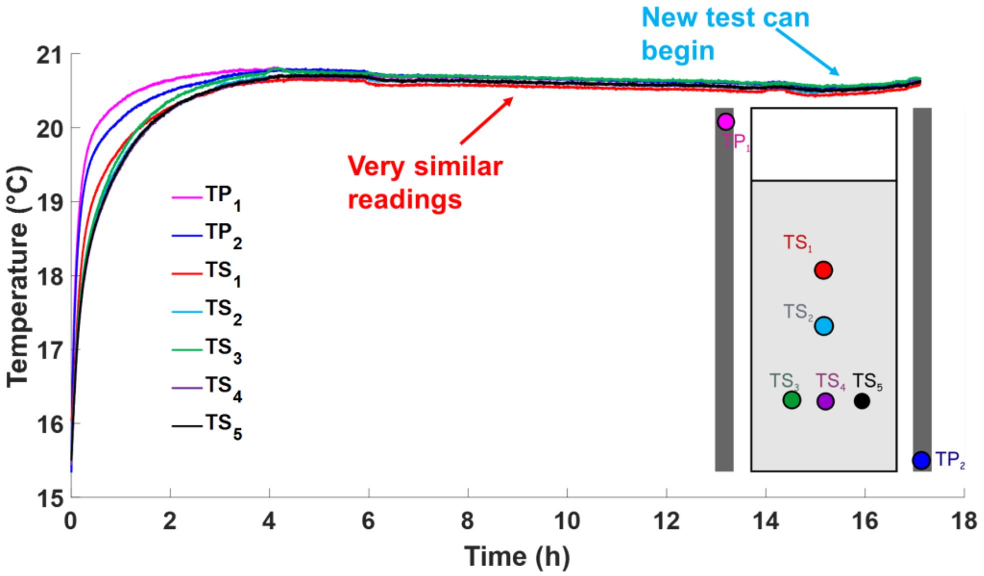

Figure 5-19. Test where the Peltier plates are turned off and the temperature is allowed to return to initial values. Notice that all sensors return to the same initial values after 10 hours with minimal fluctuations.

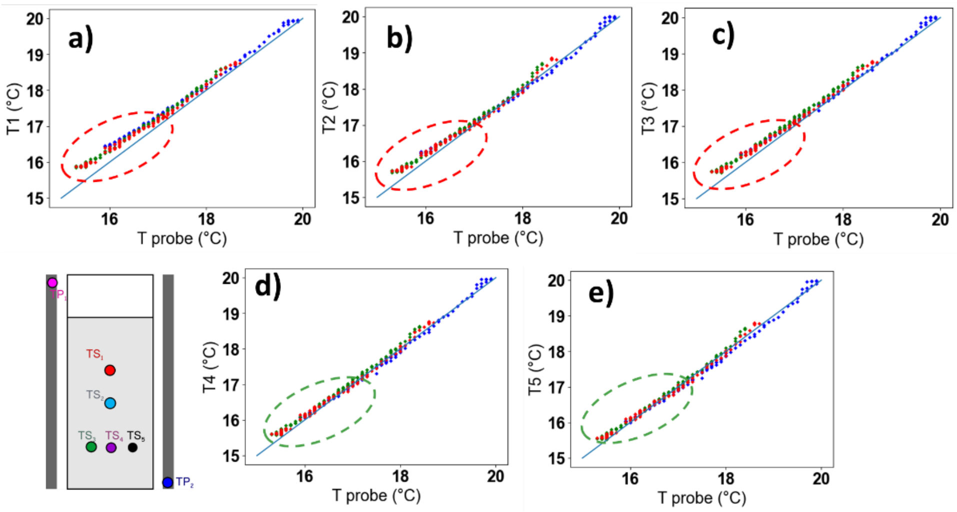

Figure 5-20. Linearity and reversibility testing of the temperature sensors. Satisfactory performance was observed during three different tests, although it seems to decrease slightly for the lowest temperatures, particularly for the a) T1 to c) T3 sensors.

Given the relevance of adequate boundary conditions for the experiments, it was necessary to ensure adequate contact between Peltier plates and the metallic walls of the container. To do this, HY510 thermal grease was applied to the contact surface of the metal wall as seen in Figure 5-21 to ensure continuous thermal contact. Several nuts and screws further ensure this contact.

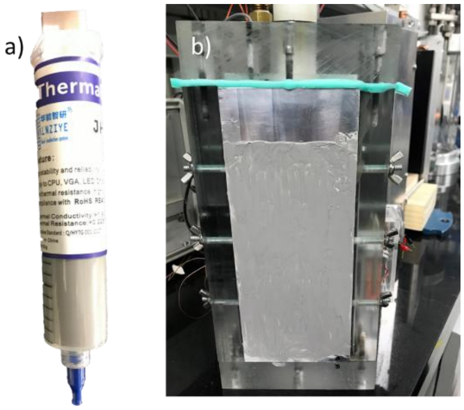

Figure 5-21. Thermal grease applied to the container's metallic wall to ensure adequate thermal contact.

5.5. Stress control in the sample and height variation monitoring

A key component of the experimental setup was the system used to control the stresses acting on the sample. The vertical stress acting on the sample at the height where the measurements are conducted (80 mm from the bottom, the middle point of the sample height) results from the sample self-weight plus the stress applied on the soil's surface.

As seen in Figure 5-22a, the container has a piston holding a square plastic plate that contacts the soil's surface. The plate has rounded corners and slightly smaller dimensions than the container to avoid contacting the walls when it moves. To know the stress acting on the sample, it is necessary to control and measure the force with which this plate contacts the soil.

To control the force actuating on the surface of the soil, the piston holding the plate is fixed to a metallic frame (shown in Figure 5-22b) and is controlled with a pneumatic actuator seen above the blue hose of the jack air pressure. This double-acting actuator (seen on Figure 5-23b) can pull and push the piston with a controlled force, and the direction of this force can be changed simply by connecting the hose to the desired orifice. This ability to pull the piston is relevant since it enables testing to be performed without actuating loads acting on the soil surface, as is explained further below. The force was measured with an accurate load cell (seen in Figure 5-23a) installed inside the sample container between the piston and the plate contacting the soil, as seen in Figure 5-24. This installation was chosen because any variation of the actuators' compression force (due to fluctuations in the air pressure, or the friction of the piston with the box and the vacuum seals surrounding it) is accounted for in the load cell force measurement.

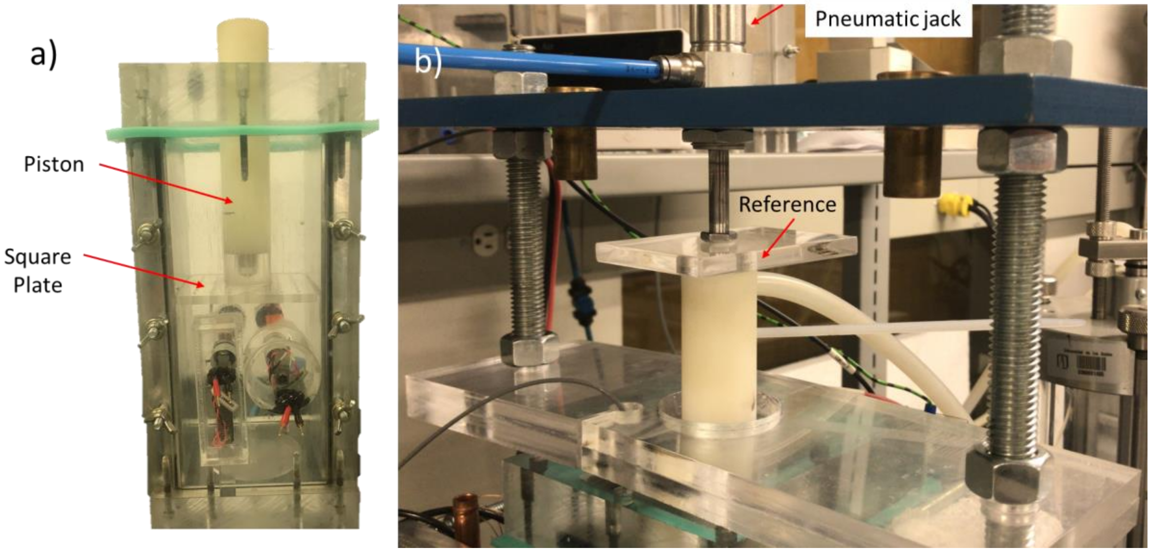

Figure 5-22. A piston a) with a square plate is used to contact the soil surface and is supported by a b) metallic frame which connects it to the pneumatic jack. The reference plate is used to measure the vertical displacement.

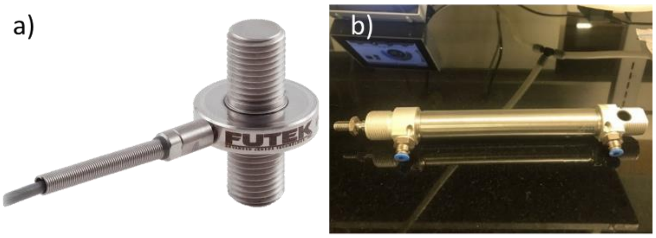

Figure 5-23 a) The loading cell and the b) pneumatic actuator.

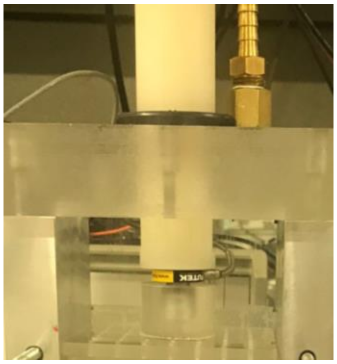

Figure 5-24 a) The loading cell is installed between the piston and the plate contacting the soil.

When the vacuum pump is engaged, the piston is sucked into the sample and will strongly contact the soil. This force must then be compensated with the pneumatic actuator pulling against it, since if the piston is allowed to contact the sample surface the soil will be densified, and the sample will have to be prepared again to restart the experimental program. Not contacting the soil also allows the experimental setup to impose very low near-zero stress values on the soil sample. After some testing, it was observed that 100kPa of air pressure on the jack is sufficient to avoid contact with the soil sample. The reading of the loading cell can be monitored to reveal that undesired contact of the plate with the soil took place.

From the moment the plate contacts the soil, variations in the height of the soil sample were monitored by measuring the relative displacement of the reference plate (seen in Figure 5-22b) with respect to the metallic frame with a calliper. For testing at higher stresses, the actuator can push the piston and exert a force on the sample, up to the maximum 1 MPa capacity of the pneumatic actuator. The air pressure controlling the jack can be specified through a LabVIEW interface with the help of a type 3110 Bellofram electro-pneumatic transducer, as seen in Figure 5-25b. Such a valve converts a voltage signal into a pressure signal.

Figure 5-25. The Type 3110 Bellofram transducer was used to control the air pressure acting on the jack.

5.6. Experimental protocol

Once the setup was completed with all the previously described components, an experimental protocol was devised to carry out the experiments of the projected measurement program.

The testing procedure can be split into the following stages:

- Previous drying of the sample material.
- Placing the sample in container.
- Thermal conductivity test.
- Wave velocity measurements.

The following sections describe in detail each stage.

Previous drying of the sample material

The procedure for a test begins with a preliminary drying of the sample material. Previous work in regolith simulants to study thermal conductivity (Nagihara et al., 2022) emphasised the importance of the material samples being as dry as possible. Thus, before an experiment began, 1600 g of the soil was left in an oven (Figure 5-26) for two days prior to the sample preparation at 120°C, given that 24 hours at 110°C are typically considered enough for clean sands such as the one in use, this drying process was adequate.

Figure 5-26. The material was dried in an oven for two days before the sample was prepared.

Figure 5-27. Vacuum chamber to preserve the soil dry as the material cools down.

Afterwards, the material is extracted from the oven and placed inside a vacuum chamber (seen in seen in Figure 5-27) to preserve it dry as it cools down for three hours since it cannot be pluviated into the container yet as it may damage the accelerometers and the piezo actuators.

Preparation of the sample in the container

Placing the sample into the container is achieved through the following steps:

- *Material pluviation*: This step involves loosely placing the dry sand into the sample container. First, a double-layer filter paper is placed on the bottom of the container; then, the material (previouslyweighed) is pluviated into the sample container using a funnel (adapted with a hose given the significant height of the sample container). This process needs to be careful, not to upset the position of the thermocouple wires, as seen in Figure 5-28b. Pluviation continues, placing the material as loosely as possible till a 160 cm height This sample size guarantees that the middle row of sensors is aligned with the middle height of the soil sample. Finally, a double-layer filter paper is placed on top of the sample.

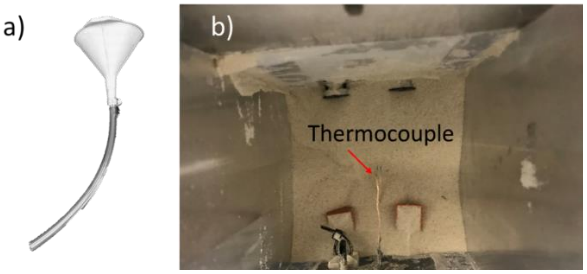

Figure 5-28. Care must be taken during the pluviation process with the a) funnel so that the b) thermocouple wires remain at the intended horizontal position.

- *Close and seal the vacuum container*: Once pluviation has been achieved, the cover with the piston and the force sensor is placed on top and the sample container is closed carefully to ensure it is completely sealed (including the cover seal seen in Figure 5-29). To do this, all the eight screws of the top cover must be tightened firmly. Several layers of polystyrene are also placed around the sample to ensure proper insulation.

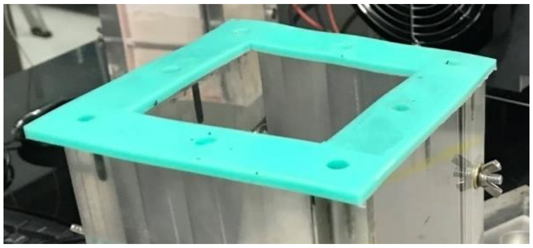

Figure 5-29. Seal placed at the top to ensure no leaks beneath the cover.

- *Place and fix the sample container in the experimental assembly*: The sample container is placed into the experimental setup by carefully placing it between the Peltier plates and fixing the nuts holding them in place. The thermal grease of the contact is replaced if necessary. The metallic frame and the pneumatic actuator are then installed while taking care not to push the piston into contact with the soil.
- *Connecting CO_2 and vacuum*: Finally, the hoses for the vacuum pump are connected to the sample container in the top and back covers respectively. Several cable ties are used at every hose connection to avoid leaks through these connections.

TheT he following checklist is verified before starting a testing program:

1. Verify that the box is correctly accommodated, guaranteeing that the Peltier plates are well in contact with the metallic plates.
2. Verify that the vacuum pump, passing through the safety of the sand trap to protect the equipment, is connected to the top cap to enable vacuum application in the sample and that the corresponding valves of the sand trap are closed or open as necessary.
3. Verify that the top cover is secured with all the screws and that the retainer seal is secured around the piston. If desired, a vacuum test can be conducted to discard the presence of any potential leaks.

After such verifications, the sample can be considered ready for an experimental program, which can start the next day. The sample ready for testing can be seen in Figure 5-30, and once the thermal isolation is placed it is mainly hidden behind it as seen on side b of the same figure.

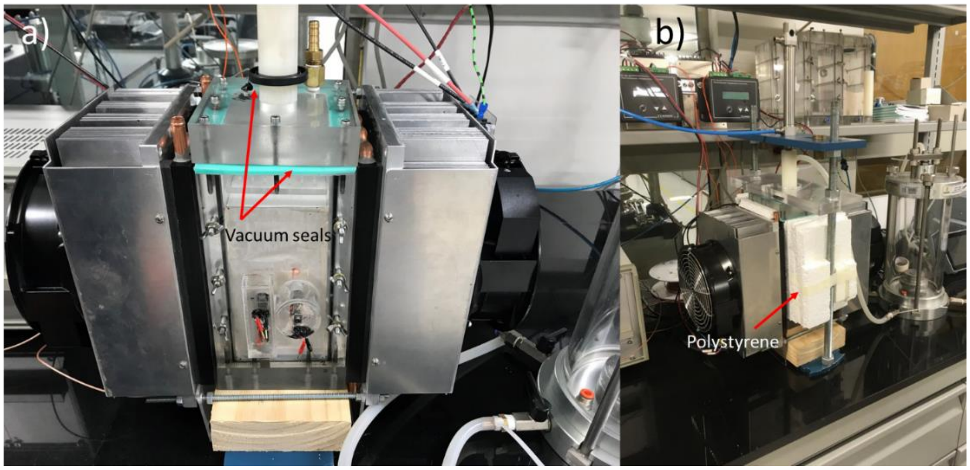

Figure 5-30. The sample ready for testing. Notice the a) vacuum seals and their fixation between the Peltier plates. The container is b) barely visible during testing once it is surrounded by the thermal isolation polystyrene.

Each test was carried out at the constant same vacuum pressure inside the sample, increasing vertical stress to ensure Normally Consolidated soil conditions. Consequently, a stress value is selected for each of the testing days. In this work, four cycles (4 atmospheric pressure) were performed, with five stress values selected for the thermal conductivity measurements in each sample. Since each of these tests lasts a day, each cycle lasts six days. Measurements of the vertical position of the piston with respect to the metallic frame were performed at the beginning and end of each test day to monitor the sample height for eventual density variation, using the plate seen in Figure 5-22b.

Thermal conductivity test

Once the sample is tested, thermal conductivity measurements can be taken. These tests were done at a rate of one per day since the whole process lasted over nine hours. The steps for each of these tests are the following:

- *Turn on instruments*: This includes the control computer, the power source for the Peltiers (set at 5V and activated output), and the vacuum pump and its digital controller. All these instruments are verified to be turned on before starting the testing process, and the data acquisition for the load cell and the temperature sensors is engaged, after naming the storage file that will be used for the data setting. The load cell measurement is set to zero.
- *CO_2 saturation of the sample*: The CO_2 is then applied to the chamber at a very slow rate, seeking to displace the entirety of the air residing in the soil container box as was previously described, and the valves are closed after 80 minutes.
- *Application of stress*: The thermal conductivity measurements are taken at a specified stress value. For the lowest possible value, the pneumatic jack actuator can be engaged to pull at over 100 kPa so that the piston will not exert any force on the soil surface. For all the other values, the jack is connected to pull on the sample The actuator is connected to pull on the sample for all the other values by connecting the air hose on to the other orifice (see Figure 5-23b). The piston is then smoothly in contact with the soil surface to apply the required stress (from 100kPa to 800kPa).
- *Application of the vacuum*: Then, the pump is activated so that the controlled vacuum is applied to the inside of the container until the desired pressure is attained. The pump controller enables the application of this suction in several steps, and a two-echelon process was utilised to avoid excessively rapid vacuum application that may disturb the loosely deposited sample. As seen in Figure 5-31, the first step lowers the pressure to 70 mbar, and after a minute of stabilisation, a second action of the pump attains the desired value, in this case, 6 mbar (600 Pa).

Figure 5-31. The desired pressure is applied in two steps to avoid disturbing the sample.

- *Starting the thermal conductivity test:* Ten minutes of stabilisation are allowed once the vacuum is reached, and the temperature indicated by the thermocouples is recorded. After the work described in the precedent sections, it was decided that a standardised ΔT of -3°C would be used for all the tests to enable comparison between them.
- *Attaining temperature stabilisation*: The temperature of the sample decreases and is monitored with the different thermocouples included in the setup. It is monitored until a

stabilisation is observed. After some testing, a standardised duration of 7 hours was established since it is enough to allow for acceptable temperature stabilisation in all sensors.

- *Finishing the test*: Once the temperature has stabilised, the Peltier plates are turned off, and the sample can return to its initial temperature for the next following text. It takes about 14 hours from when Peltier plates are turned on for the temperature to be uniform and return to its initial value in all sensors. The recovery time is used to perform wave velocity measurements on more stable conditions; it is not recommended to do these measurements while the Peltiers are working since there will be considerable vibrations due to the cooling fan unit of each plate.

Wave velocity measurement procedure

The wave velocity measurements can occur once a thermal conductivity measurement has been completed (the temperature has stabilised, and the Peltier plates have been turned off). The steps for these measurements are as follows:

- *Turn on all instruments:* To begin, the instruments are turned on. This includes the signal generator, amplifier, oscilloscopes, power source for the accelerometers, and the computer used for waveform data storage. The voltage on the power source is verified to be set at 10 mV, and both channels are activated. For the moment, the output switches on both the signal generator and the amplifier remain turned off.
- *Recall preset wave function:* A previously stored setup is now recalled in the signal generator. This must be done since **great care must be taken not to apply a negative voltage to the piezo actuators** since they only have a very limited negative voltage range. This setup corresponds to a positive 5V square pulse with a duration of 6 ms. This function results in two strikes, one in each direction. The function uses the burst feature of the generator so that one of these rapid oscillation pairs takes place every five seconds, allowing time to store the wave data since data acquisition is, in part, manual.
- *Connect the desired actuator*: The setup was conceived to switch between the generation of P or S waves easily. To achieve this, the two cables connected to the amplifier (coloured black and red) are connected to the desired piezoelectric device.
- *Start wave recording:* The output of the signal generator is turned on, and so are the switches on the amplifier. A wave of the type selected in the previous step will now be emitted every five seconds and can be recorded on each oscilloscope. Note that the signals received at both oscilloscopes can be interesting, not just the one facing the actuator in use. Each Fluke 99 can store 10 waveforms on two channels (one for the input signal and the other for the recorded wave on the accelerometer), so 10 repetitions were stored for each wave in this work.

- *Finish wave recording:* To stop emitting waves, the output of the signal generator is turned off, and so are the switches on the amplifier. The cables of the piezo actuator can now be switched to the other emitter to record the other type of waves (S or P) at the same stress.
- *Switch stress value:* Once the previous steps have been completed, a complete data set has been acquired for the specified stress, and the procedure can be repeated for the subsequent stress.
- *End test:* To end the test, the first step is to turn off the vacuum, allow the sample to ventilate, and slowly return to atmospheric conditions. The pressure on the pneumatic jack is set to zero, and the data acquisition is turned off. All the instruments and computers can now be turned off, and the piezo actuators are disconnected from the signal generator.

The full setup and experimental procedure can be seen in Figure 5-32 and Figure 5-33 respectively.

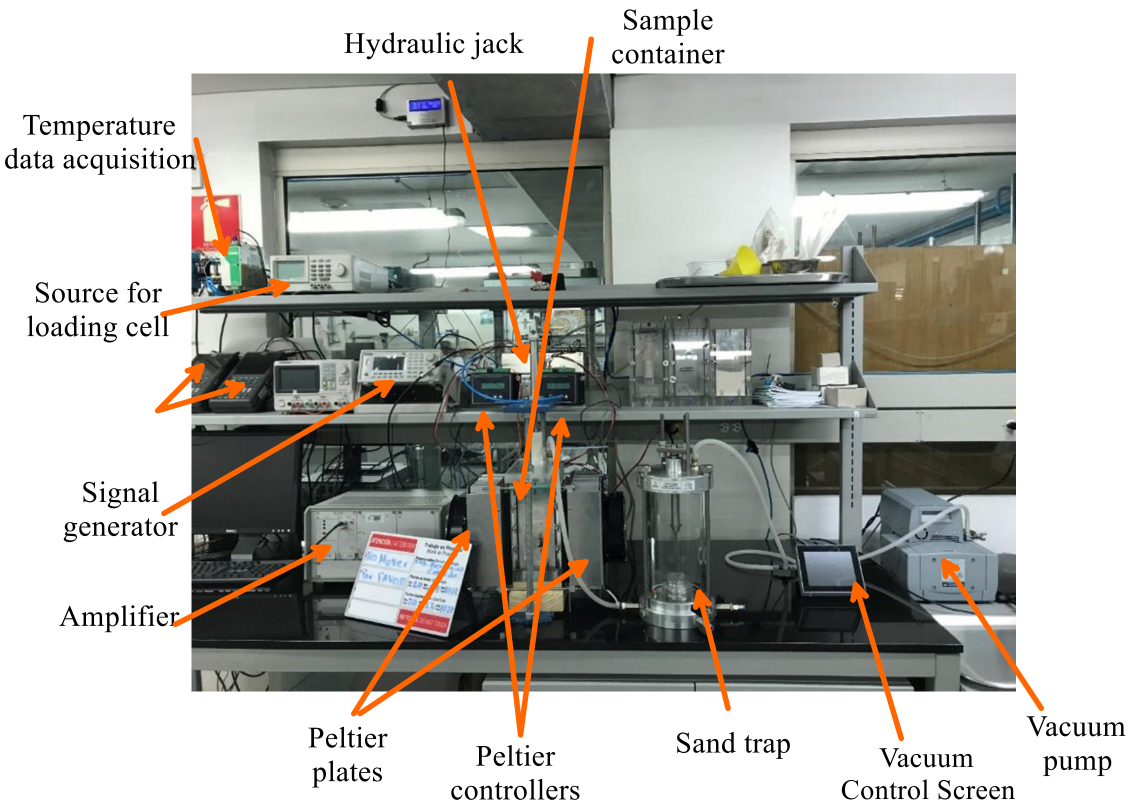

Figure 5-32 The full setup ready for an experiment.

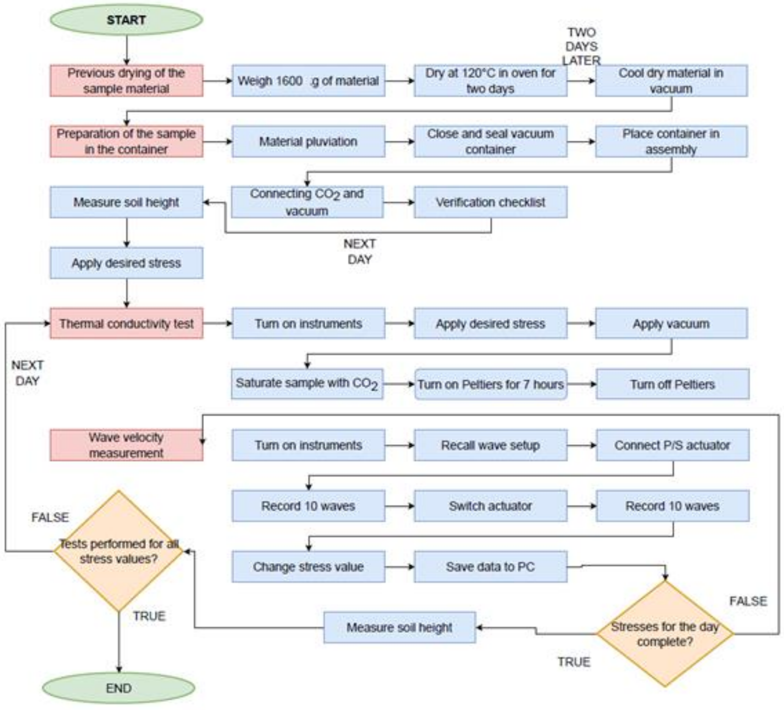

Figure 5-33 Schema of the experimental protocol.

5.7. Interpretation of the experimental results

Although heat and mechanical waves have unidirectional propagation in the experimental setup, they are affected by the walls. Indeed, due to the low thermal conductivity of the dry sand, heat propagating through the plexiglass walls could affect the unidirectional heat propagation through the sand. On the other hand, considering the sample is confined to rigid walls, wave propagation could be affected by wave reflections.

Numerical tools were developed to help interpret the results, considering such difficulties. Given the prismatic shape of the sample, the differential equation describing both phenomena was solved with a transient 3D finite difference model.

The thermal model includes different materials of the sample container and the interfaces connecting them. Then, the thermal model includes the propagation throughout the metallic and plexiglass walls.

Regarding mechanical wave propagation, particular emphasis was given to the key question of the rigid boundaries. The numerical model is based on the model proposed by Dong-Joo et al., 2004, and it is described in Appendix B: Original expressions for the boundary condition.

Formulation of the finite differences for the heat conduction

A finite difference model to was formulated for a solution of the heat conduction in three-dimensional space. In this case, the equation to solve is:

$$c\rho\frac{\delta T}{\delta t} = \nabla(k\nabla \cdot \mathrm{T}) \qquad (1)$$

A MATLAB script was prepared to solve this transient equation. The following paragraphs describe the main characteristics of this model.

Model geometry

The model is 3D, as seen in Figure 5-34; the cross-section of the model is a square box with 120 mm sides. All the walls are 20 mm thick, and the aluminium sides are smaller (80 mm) than the plexiglass ones (120 mm). While the sample container is 200 mm tall, it was not filled during the experiment as described previously. Consequently, only the 160 mm of height filled with soil is included in the model.

Notice that the lower plate, with a height of 30 mm, is made of plexiglass.

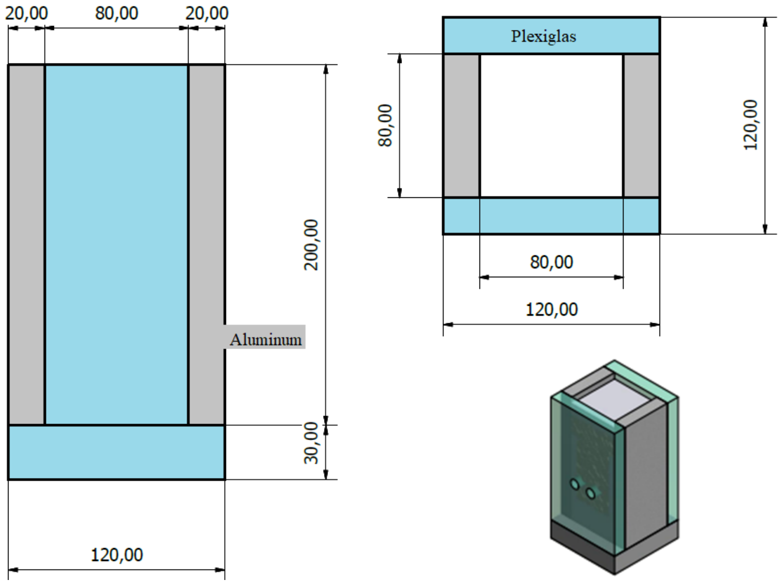

Figure 5-34. Side and top views of the model geometry.

Model materials

Materials involved in this model are the soil sample and the container walls made of aluminium and plexiglass. Including these three materials allows for accounting for heat conduction through the plexiglass walls. However, since the container is isolated from the environment with polystyrene, which has a conductivity of 0.034-0.038 W/mK comparable to that of the simulant, the experiment is not perfectly isolated. This is a difficulty that affects the measurements mainly for the long duration of the experiment.

Table 5-1. Model parameters used for the materials.

Material	Density (g/cm^3)	Thermal conductivy (W/mK)	Specific heat (J/gK)
Plexiglass	1.18	0.18	1.47
Aluminum	2.7	205	0.5
Fontainebleau sand	1.47	Evaluated	0.733

The thermal conductivity involved the use of three materials, which are summarised in Table 5-1.

Boundary conditions

The initial conditions for the model are set at a constant temperature of 19°C, corresponding to the values measured at the beginning of a test. The exact temperature can vary by a few tenths of a degree. However, the measure of interest is the variation of this initial temperature, not the temperature's value itself.

The thermal conductivity test applies a constant temperature to the aluminium walls. Since the aluminium's conductivity is very high compared to the other materials involved (see Table 5-1), all the nodes associated with aluminium are set to 16°C to recreate the conditions of 3°C cooling. Boundary conditions outside the container are zero heat flux. This implies that no exchange occurs with the environment, which is not entirely accurate given that, as mentioned above, the system's thermal insulation is imperfect.

The expressions used for imposing a continuity condition are now presented:

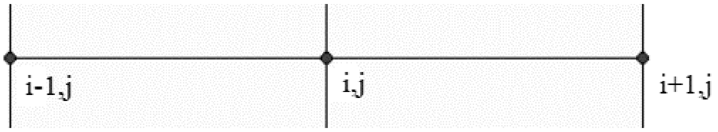

The flux at the neighbour nodes is:

$$Q_H^{i-1} = k \frac{T_{i-1}^t - T_i^t}{\Delta y} \Delta y \qquad (2)$$

$$Q_H^{i+1} = k \frac{T_i^t - T_{i+1}^t}{\Delta x} \Delta y \qquad (3)$$

Replacing in the right side of the equation:

$$\frac{Q_H^{i-1} - Q_H^{i+1}}{\Delta x \Delta y} = k_1 \frac{T_{i-1}^t}{\Delta x^2} - k_1 \frac{T_i^t}{\Delta x^2} - k_2 \frac{T_i^t}{\Delta x^2} - k_2 \frac{T_{i+1}^t}{\Delta x^2} \qquad (4)$$

So, the whole equation becomes:

$$c\rho\frac{T_i^{t+\Delta t}-T_i^t}{\delta t}=k_1\frac{T_{i-1}^t}{\Delta x^2}+k_2\frac{T_{i+1}^t}{\Delta x^2}-\left(k_1\frac{T_i^t}{\Delta x^2}+k_2\frac{T_i^t}{\Delta x^2}\right)$$

$$T_i^{t+\Delta t}=\frac{\Delta t}{c\rho}\left[k_1\frac{T_{i-1}}{\Delta x^2}+k_2\frac{T_{i+1}}{\Delta x^2}-\left(k_1\frac{T_i^t}{\Delta x^2}+k_2\frac{T_i^t}{\Delta x^2}\right)\right]+T_i^t \qquad (5)$$

Where Q is the flux, k is the thermal conductivity, c is the specific heat, and T is the temperature.

Experimental and numerical results during validation

The cross-section of the model with the associated dimensions can be seen in Figure 5-35 as the pulse propagates through the material. It can be seen how the Plexiglass (more conductive than the soil) is colder and is already at a lower temperature compared to the soil, where an elliptic symmetry in the temperature occurs and where the heat still flows radially. At the same time, the aluminium with a thermal conductivity two orders of magnitude higher has long ago stabilised at a uniform temperature.

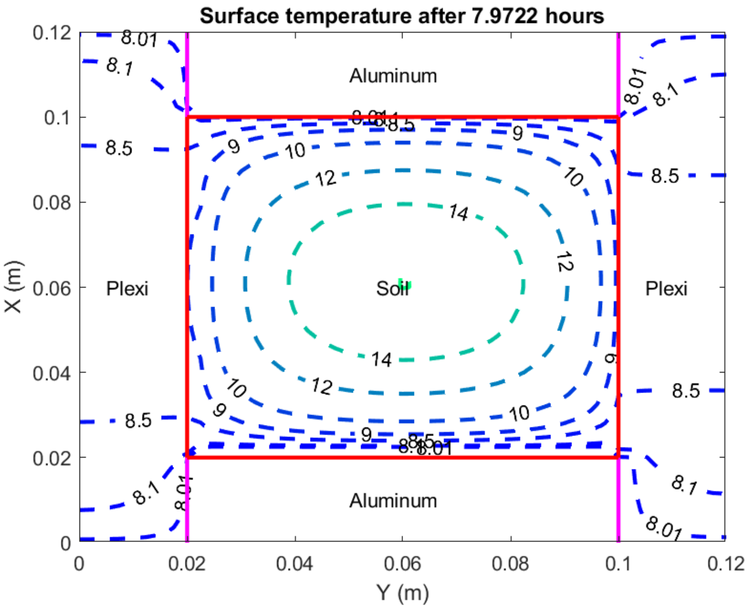

Figure 5-35. Cross section of the model as the thermal pulse propagates.

To ensure comparability of the model with the experimental results, the nodes corresponding to the location of all the thermocouples were identified. The temperature in these nodes at the time of interest was then stored to make it possible to obtain a curve of the temperature evolution in time that could be compared with those obtained in the experimental data.

An initial validation test was done comparing cooling tests. A large temperature difference was used to do this, bringing the sample from an initial temperature of 19°C down to 8°C. The parameters for the model were fixed to the values mentioned above, and the thermal conductivity of the soil sample (k) varied.

Numerical computations, seen in Figure 5-36, varying *k* with a 0.01 W/mK resolution between 0.05 W/mK and 0.12 W/mK, a range of thermal conductivities agreeing with expected Mars conditions. An additional calculation at 0.5 W/mK is included to show model sensitivity. These preliminary calculations showed the drastic effect of *k* on the model results and that if working in a standardised range of temperatures, a moderate number of calculations would suffice to determine the sample's thermal conductivity accurately.

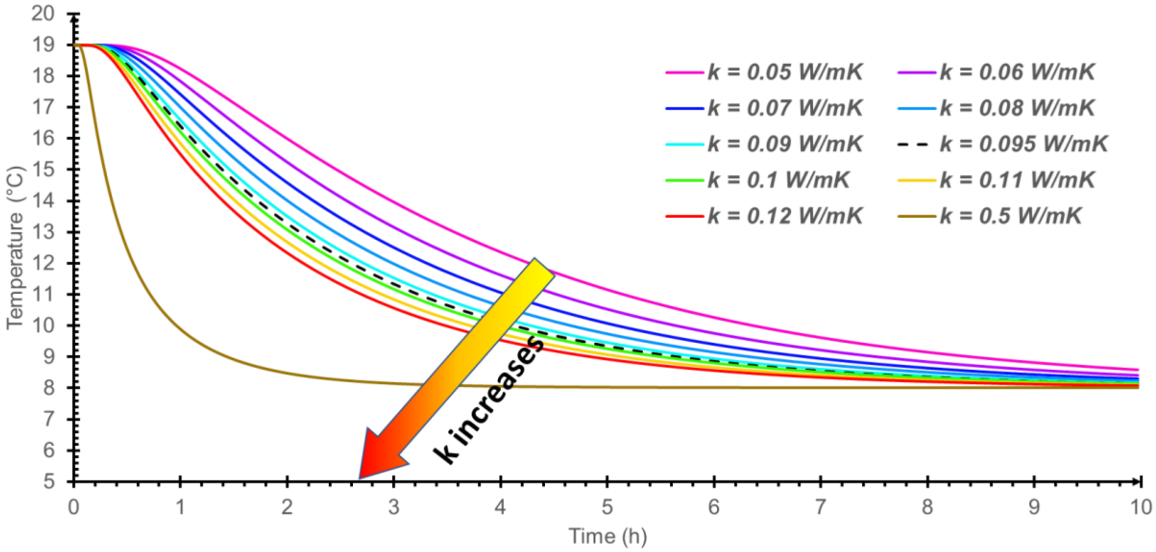

Figure 5-36. The model was first tested with a considerable cooling step to see the effect of thermal conductivity.

Figure 5-37 compares the results of a test done at atmospheric conditions with the numerical results. The figure shows good similarity of the curves, and the conductivity can be estimated to be between 0.2 and 0.3 W/mK, thus with a slightly better than 0.1 W/mK accuracy. However, the sample was not cooled to exactly 14°C, showing a thermal leak in the system.

The same was done for tests done at the conditions of the Mars atmosphere, where a sample was cooled from 19.4°C down to 14°C. The test can be seen in Figure 5-38, compared to values of k near 0.1W/mK. Good correspondence is seen again in this scenario since the test curve overlaps with the green curve corresponding to 0.1 W/mK. In this case, the value of k was determined with a much better accuracy of 0.01W/mK compared to the previous scenario.

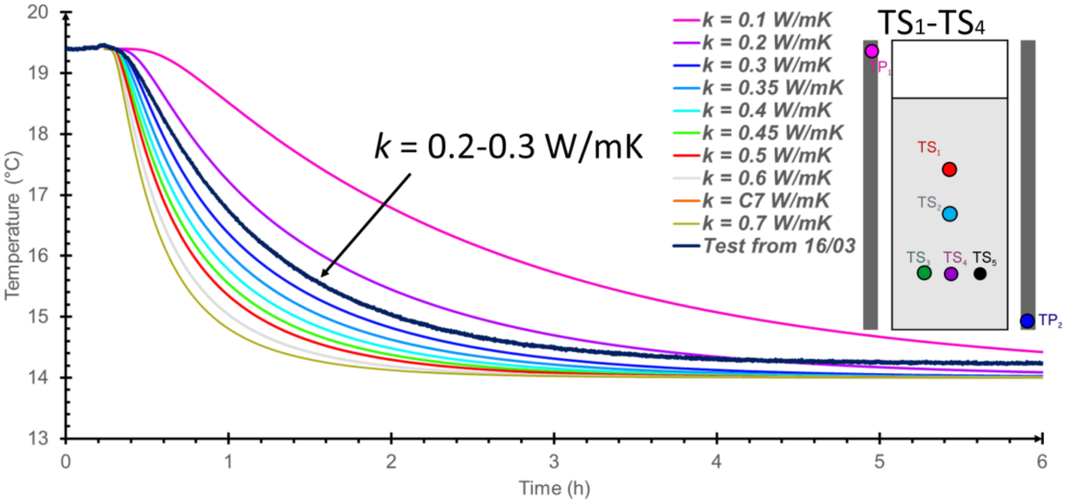

Figure 5-37. A very good fit was observed for sensors 1-4 with the numerical model for a test carried out under terrestrial atmospheric conditions (with no vacuum in the chamber).

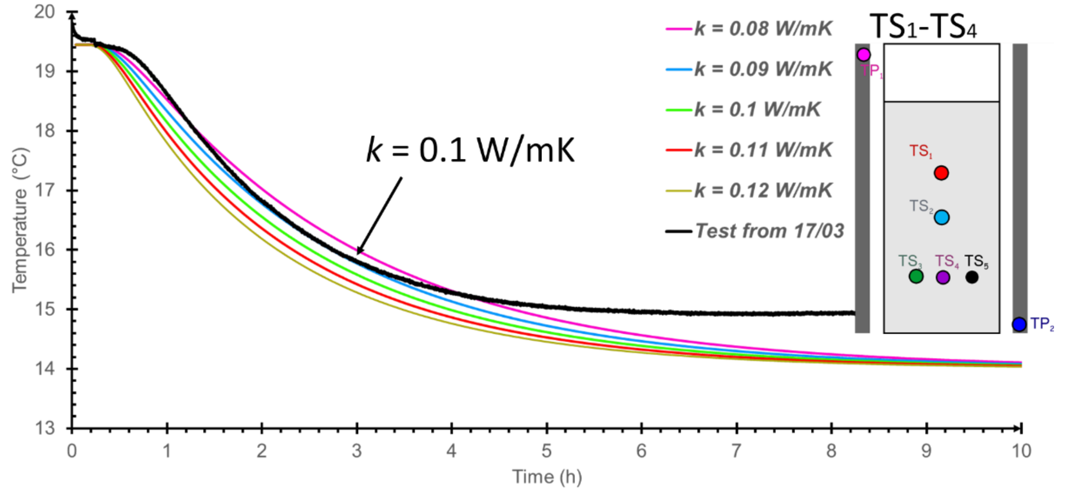

Figure 5-38. A very good fit was observed for sensors 1-4 with the numerical model for a test with 6 mbar atmospheric pressure in the chamber.

Figure 5-38 shows again that a thermal leak exists since the sample does not cool down to the imposed 14°C at the border of the experiment. For this reason, when comparing the analysis, it was decided to limit the interpretation to the first two hours since the numerical and experimental results do not deviate from each other during the initial stages.

The model displayed a good capacity for reproducing the test results in both cases since the test data curve is coherent with the numerical curves. For simplicity, the measurement of thermocouple 2, located in the middle of the sample, was decided to be used for the work done in the experimental program. This allows to measure at a soil layer subjected to the same stress value as the wave velocity measurements (allowing for better eventual comparison).

5.8. Experimental program

A thermal conductivity and wave velocity measurement program was conceived to explore the effect of atmospheric pressure and sample stress on the variables of interest.

The different stresses resulted from 2.5 kPa increments in the acting stress on the material sample; 1.12 kPa is added from the vertical stress of the soil above the middle where the measurements occur. The experimental program is summarised in Table 5-2.

Table 5-2. Experimental program

Pressure/stress	Density	0 kPa	2.5 kPa	5 kPa	7.5 kPa	10 kPa
Stress+Self weight		1.12 kPa	3.62 kPa	6.12 kPa	8.62 kPa	11.12 kPa
Sample 1: 4 mbar	1425.869 kg/m^3	Test 1-1	Test 1-2	Test 1-3	Test 1-4	Test 1-5
Sample 2: 6 mbar	1425.498 kg/m^3	Test 2-1	Test 2-2	Test 2-3	Test 2-4	Test 2-5
Sample 3: 8 mbar	1422.324 kg/m^3	Test 3-1	Test 3-2	Test 3-3	Test 3-4	Test 3-5
Sample 4: 10 mbar	1421.455 kg/m^3	Test 4-1	Test 4-2	Test 4-3	Test 4-4	Test 4-5

Figure 5-39. The experimental setup during the definitive experimental program.

5.9. Thermal conductivity measurements

The results from the experimental program are presented in this section. The thermal conductivity results are then obtained by comparing the measured data's initial segment (first two hours) with the finite differences in numerical results, as explained further below. When performing this comparison, only the initial portion of the curve (0-2 hours) is considered. As can be appreciated in Figure 5-46, the final temperature attained during the tests is not the same imposed on the Peltier plates. This is because some thermal leaks persist in the setup (despite the measures adopted to mitigate this effect, including isolation with thick polystyrene plates), resulting in significant differences between the numeric model and the experimental results, mainly because the temperature variation does not reach the imposed 3°C of cooling. Nevertheless, this effect is less significant in the early portion of the cooling, as was observed in the initial testing described in the previous sections, it is considered, and the first two hours can be used to obtain the thermal conductivity result.

Temperature measurements for each test include 7 hours of data recorded. The segment of interest begins when both Peltier plates are turned on. The curves constructed with this data represent how the middle point of the sample cooled during seven hours under a $-3°C$ temperature difference imposed at the wall borders. For easier visualisation, the data corresponding to each sample is assigned a family of colours.

- Sample 1, worked at 4 mbar is red.
- Sample 2, worked at 6 mbar is blue.
- Sample 3, worked at 8 mbar is green.
- Sample 4, worked at 10 mbar is black.

Experimental data
The raw data for each sample is presented in the following figures.

Sample 1:

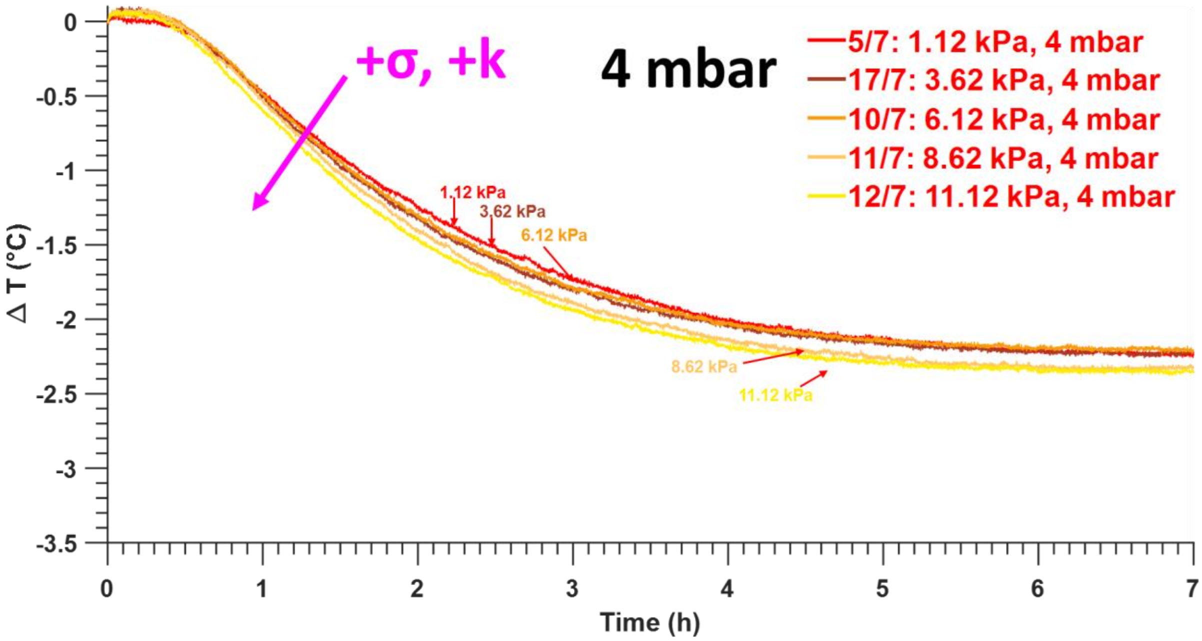

Figure 5-40. Cooling process for different stresses of sample 1, worked at 4 mbar.

Sample 2:

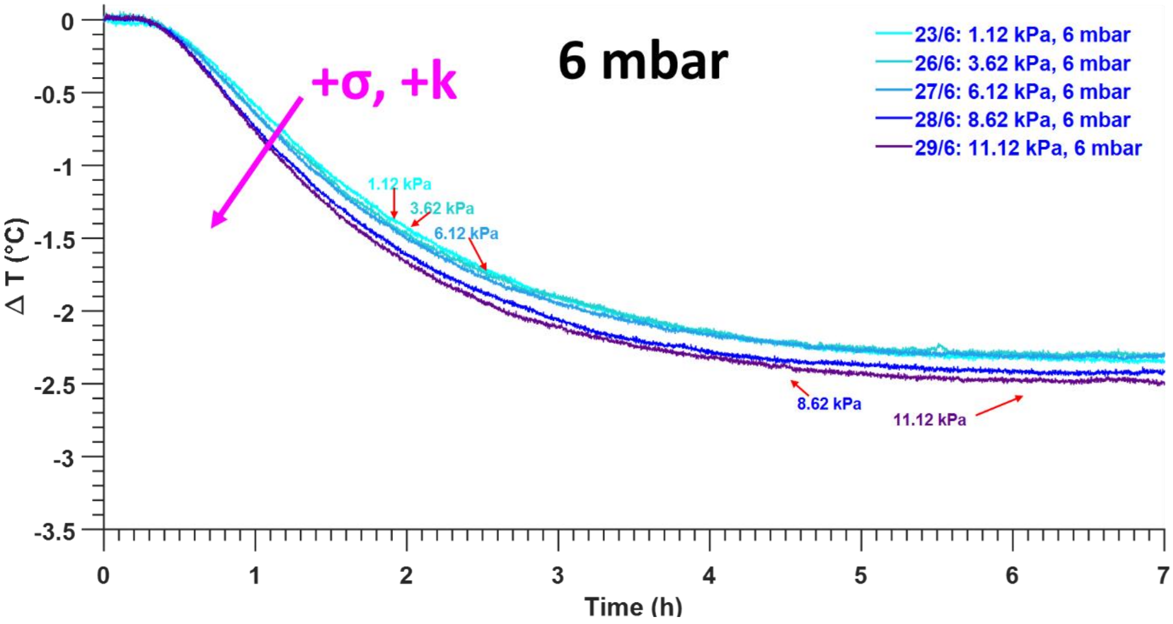

Figure 5-41. Cooling process for different stresses of sample 2, worked at 6 mbar.

Sample 3:

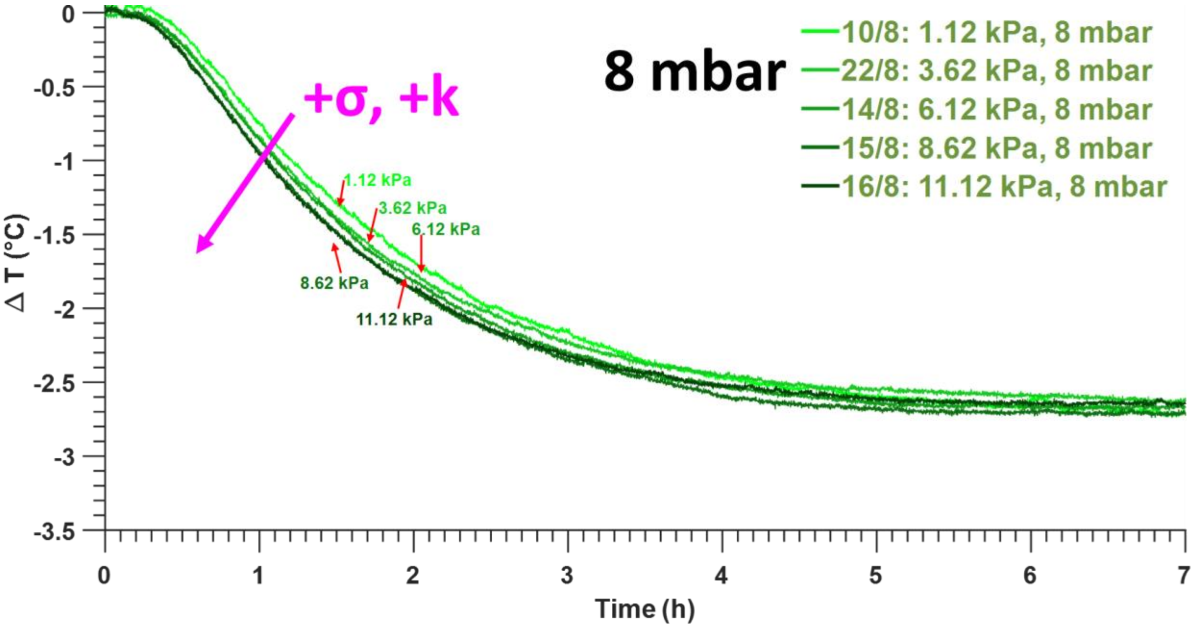

Figure 5-42. Cooling process for different stresses of sample 3, worked at 8 mbar.

Sample 4:

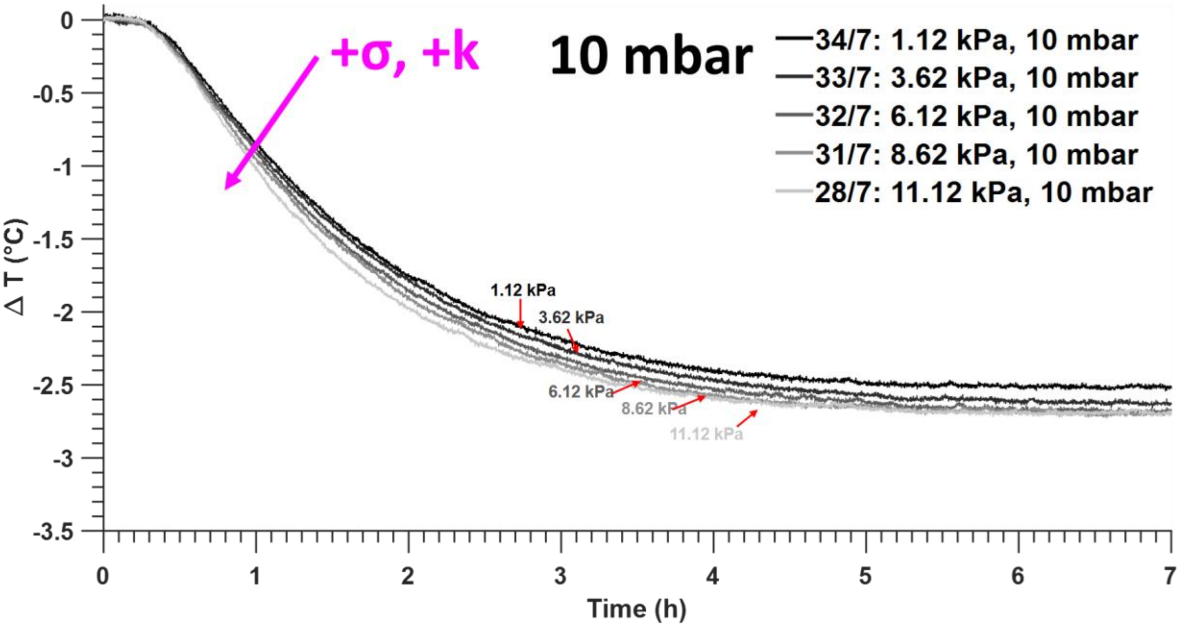

Figure 5-43. Cooling process for different stresses of sample 4, worked at 10 mbar.

Analysis of the results

An extensive program of numerical calculations with the numerical code was launched to analyse these results based on the preliminary test described in the previous sections. Initially, the values between 0.05 and 0.45 W/mK were evaluated, obtaining the results shown in Figure 5-44.

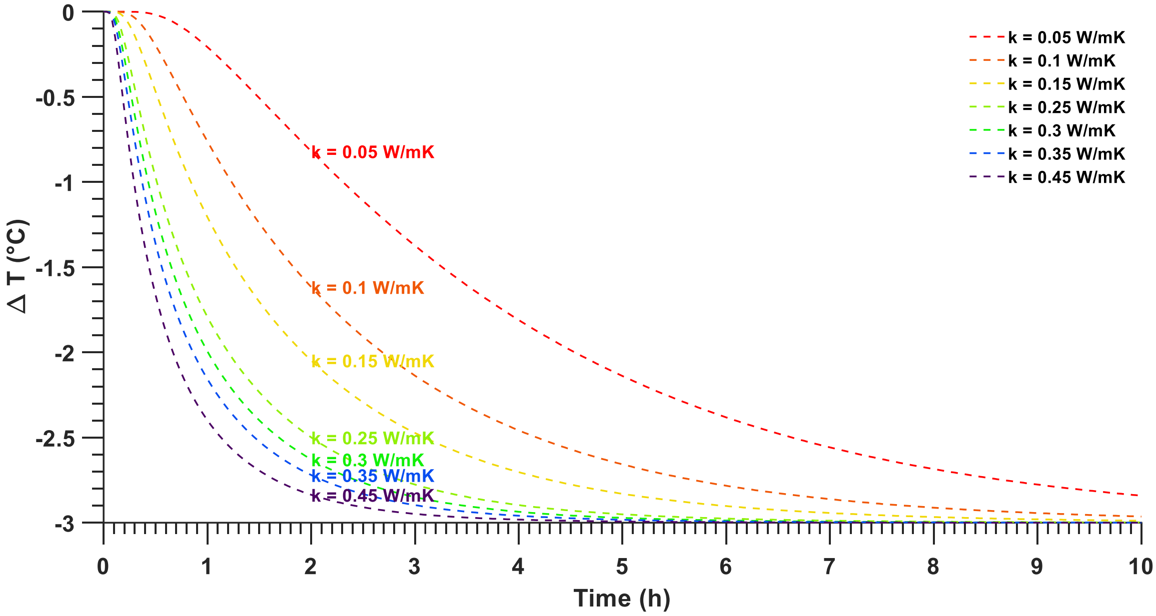

Figure 5-44. The first group of numerical results.

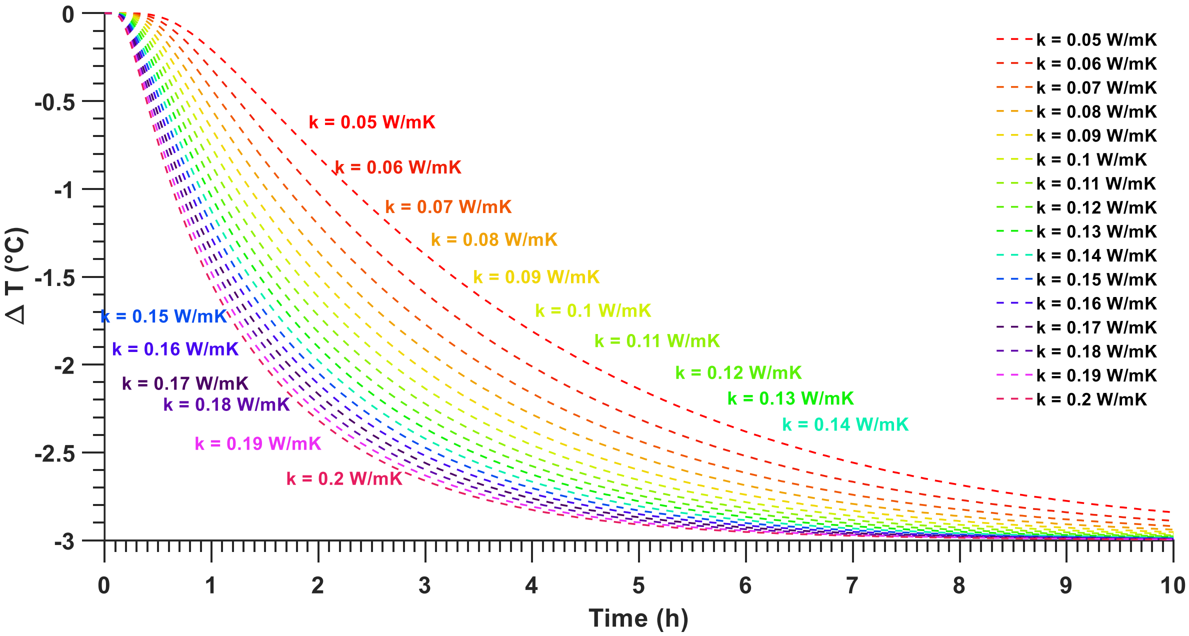

Figure 5-45 The second group of numerical results.

However, it was seen that these values were not adequate since the curves for values of *above* 0.25 W/mK had slopes far too steep compared to the test. Consequently, it was decided to limit the range to 0.05-0.2 W/mK, but now all the values with a 0.01 interval were included. The result for this is seen in Figure 5-45.

A general summary of the curves of the experimental results of the thermal conductivity is presented in Figure 5-46. It can be appreciated that the thermal conductivity relates to the gas pressure as expected since the temperature drops faster for the highest atmospheric pressure (10 mbar, shown in black) and slower for the lower atmospheric pressure (4 mbar, shown in red). Results show that the thermal conductivity k increases with both atmospheric pressure and stress, as the figure shows that the higher pressures (black) descend in temperature faster, and the lower pressure (red) descends. Figure 5-40 to Figure 5-43 show the trend in terms of stress. Finally, these results can be superposed with the numerical results to determine the thermal conductivity for each scenario.

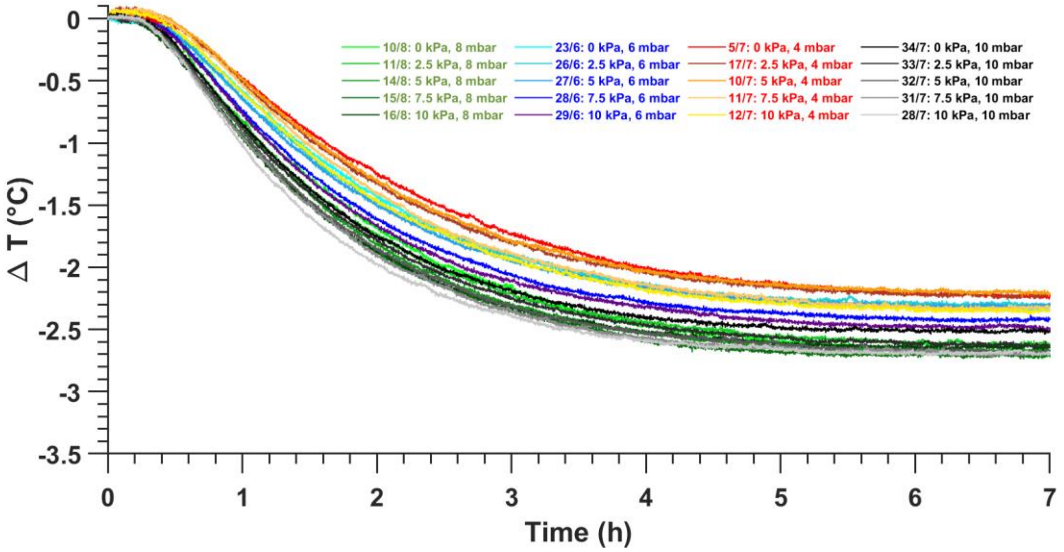

Figure 5-46. All the experimental results presented in the same coordinate space.

The experimental results are initially compared to those of the numerical calculation in the figure, where it was observed that the thermal conductivity value for all the tests can be located in the 0.05 W/mk – 0.2 W/mK. Consequently, the decision was made to compute all of the centesimal values between 0.1 and 0.2 and between 0.05 and 0.1.

When performing this comparison, only the initial portion of the curve (0-2 hours) is considered. As it can be appreciated in Figure 5-46, the final temperature attained during the tests is not the same imposed on the Peltier plates. This is because some thermal leaks still persist in the setup (despite the measures adopted to mitigate this effect including isolation with thick polystyrene plates), resulting in significant differences between the numeric model and the experimental results, mainly that the temperature variation does not reach the imposed 3°C of cooling. Nevertheless, this effect is less significant in the early portion of the cooling as was observed in the initial testing described in the previous sections, it is considered, and the first two hours can be used to obtain the thermal conductivity result.

Sample 1:

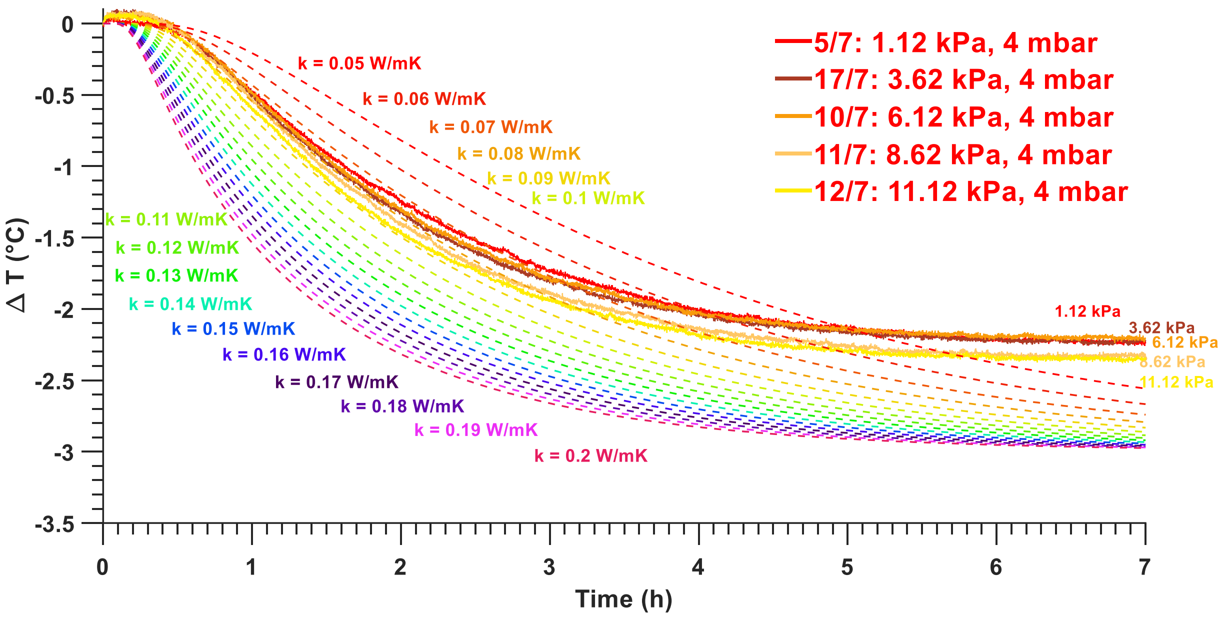

Figure 5-47. Experimental results of sample 1 (4 mbar) superposed with the curves obtained from the finite differences numerical calculations.

Sample 2:

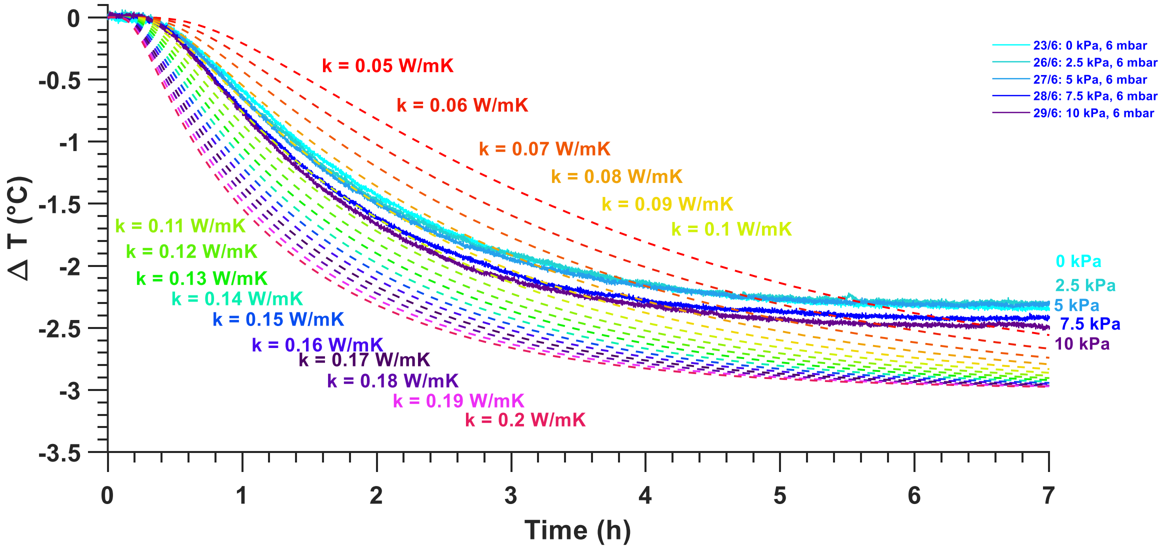

Figure 5-48. Experimental results of sample 2 (6 mbar) superposed with the curves obtained from the finite differences numerical calculations.

Sample 3:

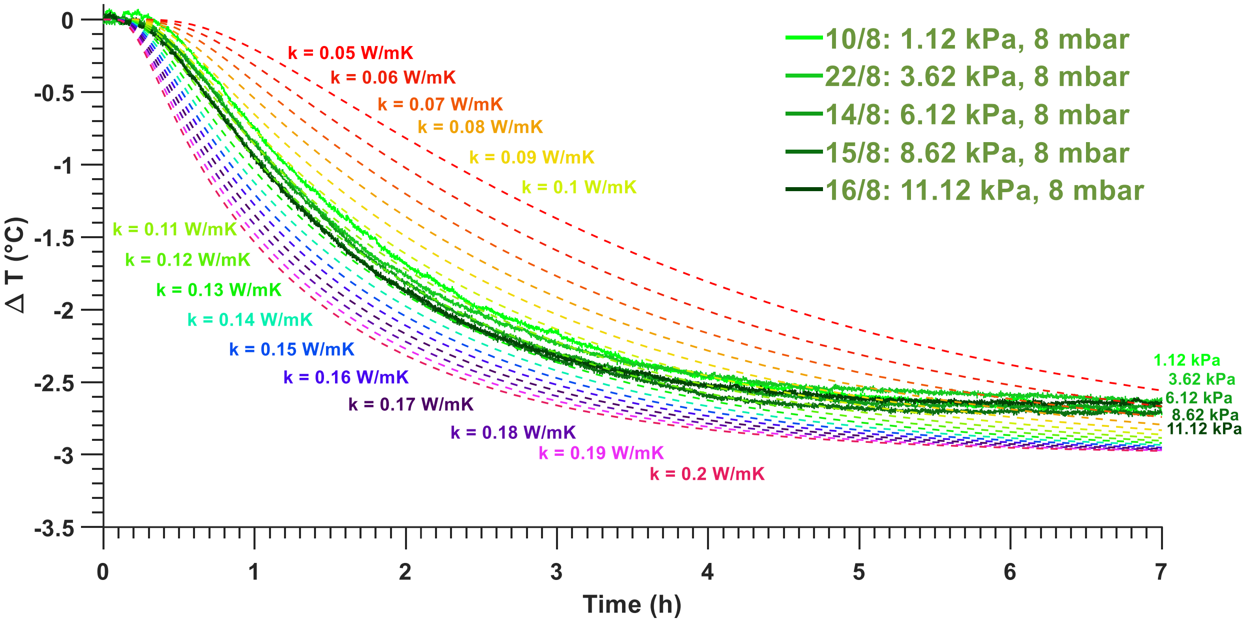

Figure 5-49. Experimental results of sample 3 (8 mbar) superposed with the curves obtained from the finite differences numerical calculations.

Sample 4:

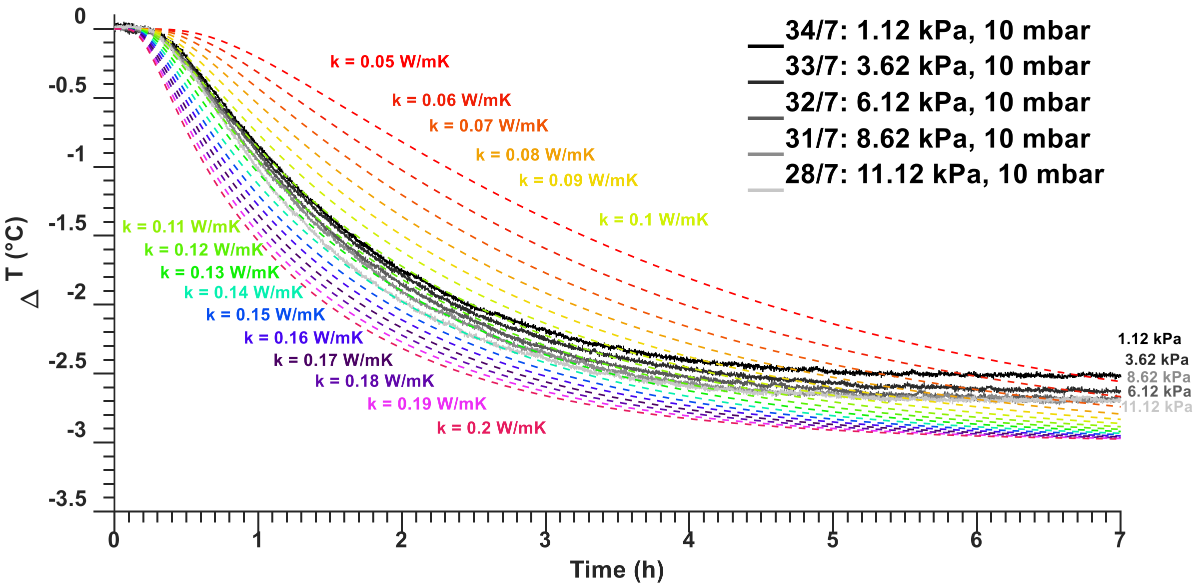

Figure 5-50. Experimental results of sample 4 (10 mbar) superposed with the curves obtained from the finite differences numerical calculations.

The results of the programs for each sample were presented in different figures to allow for better visualisation; however, they can also be grouped in the same coordinate space as seen in Figure 5-51 to see the overall range of *k* values measured.

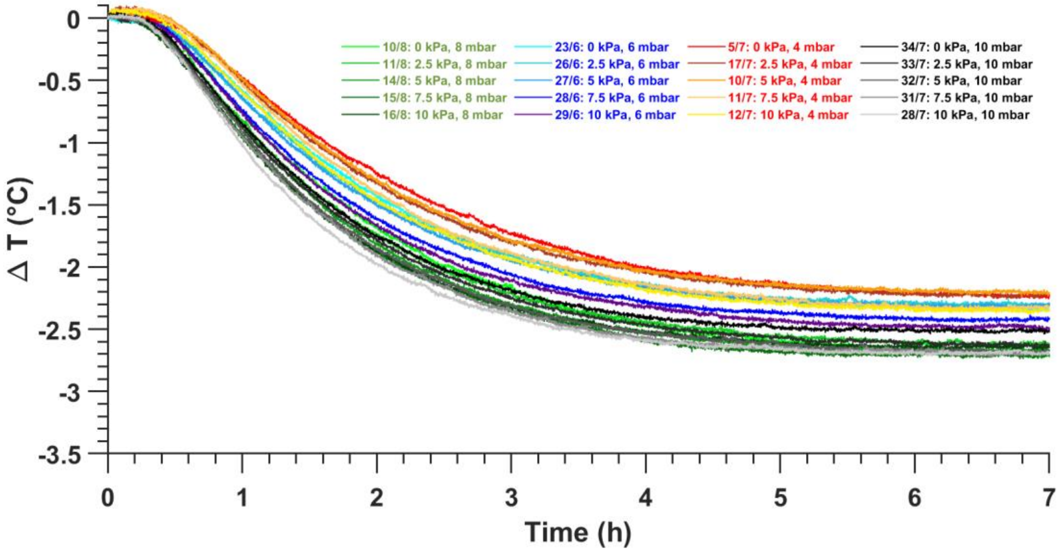

Figure 5-51. All the experimental results presented in the same coordinate space.

Using these figures, the thermal conductivity values for each test can be derived from the initial segment of the curve, with an accuracy of +/- 0.01 W/mK. The results are presented in Figure 5-52

Based on these results, it can be stated that the range for thermal conductivity for the material is in the order of 0.07 – 0.14 W/mK at these very low stresses, and that it can be measured with just sufficient accuracy in the devised setup to observe the dependency of this magnitude with respect to the variables of gas pressure and sample stress. It is appreciated that the value of thermal conductivity increases along with that of the gas pressure; the same is the case for sample stress, although the effect over the analysed pressure range seems more subtle than that of the one due to atmospheric pressure.

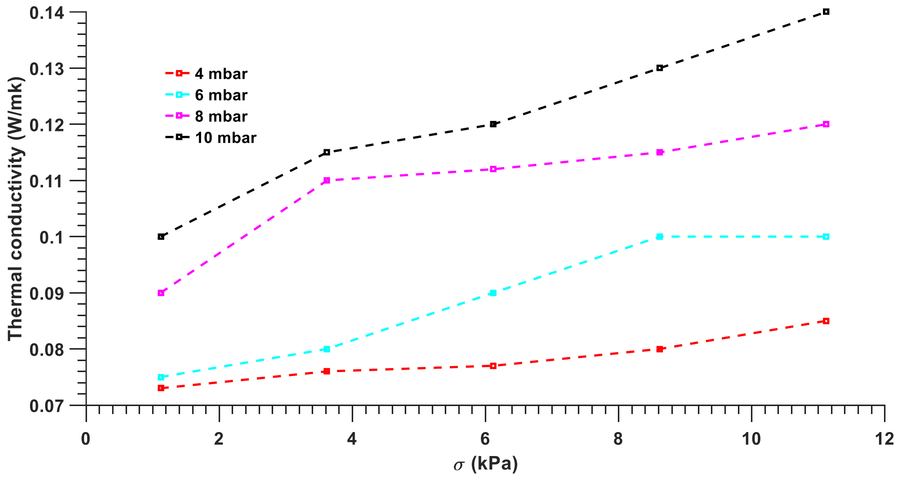

Figure 5-52. All the experimental results presented in the same coordinate space.

For the case of Mars, the atmospheric pressure is near 6 mbar, and thus, the conductivity at the surface can be considered lower than 0.1 W/mK, as indicated by the blue line of Figure 5-52. Over the first cm, the stress value can be as low as 3 kPa, and consequently, the value corresponding to the conditions present at the Mars InSight landing site is 0.08+/-0.01 W/mK.

Compared with the results reported in thermal conductivity studies with other regolith analogues (Nagihara et al., 2022), this is somewhat higher by about 0.02 W/mK. The comparison of the results of this work with these reference values is presented in Figure 5-53.

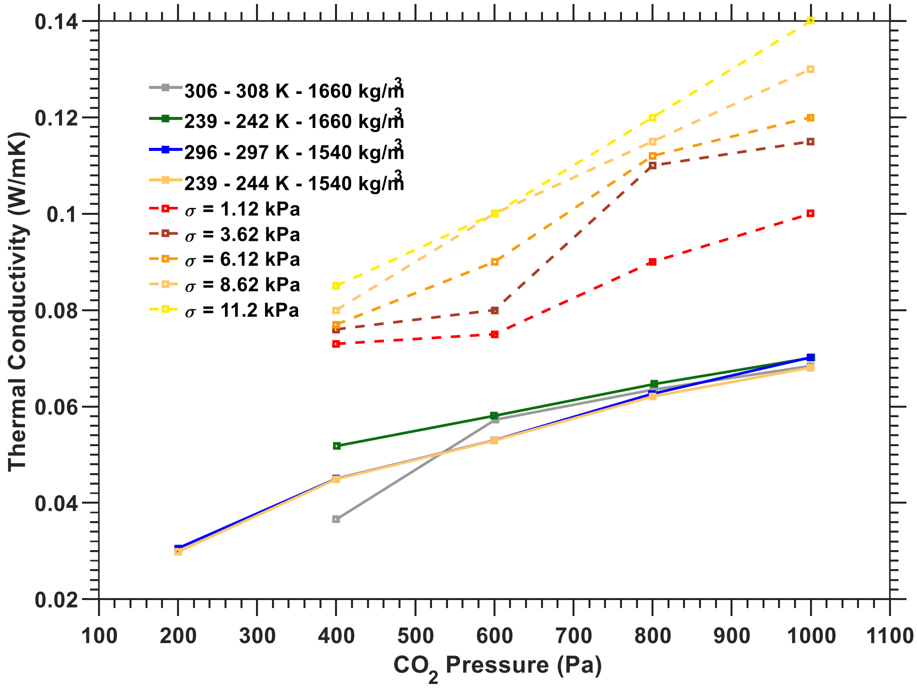

Figure 5-53. All the experimental results presented in the same coordinate space.

The most probable explanation for this difference is the significant mineralogical composition and particle shape difference between Fontainebleau sand and the regolith simulants used for that study. This is not too surprising since the simulants used by Nagihara (mainly the Mojave Mars Simulant or MMS) are mainly based on basalt, which has a relatively low thermal conductivity of 2.5W/mK at 20°C (Halbert & Parnell, 2022), in contrast to Fontainebleau sand composed almost entirely by quartz (7.7-8.4 W/mK), one of the highest thermal conductivities among soil minerals (De Vries, 1963; Zhang et al., 2015). It is also possible that part of this difference is due to the more angular particles of Mojave and the other simulants used by Nagihara, which have grains with pointy edges and, in consequence, a lower contact area between the particles, thus reducing the flow of heat between the material grains.

As a final note, it can be seen in Figure 5-54 that the results of Nagihara show little effect of sample density on the thermal conductivity result at the pressures reported for the InSight landing site (600 – 800 Pa). These effects also appear to become more relevant at pressures below 400 Pa, which should not be encountered at the InSight site.

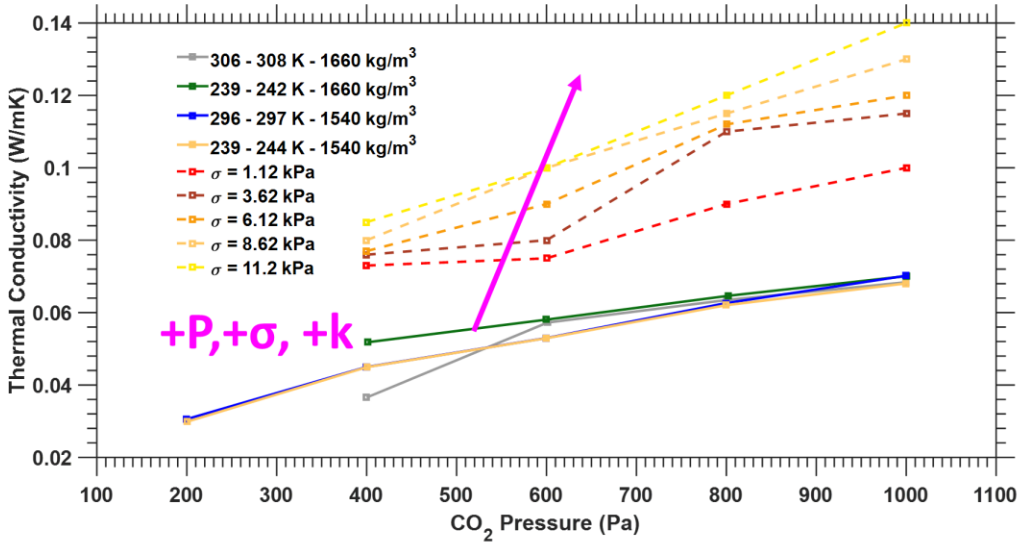

Figure 5-54. The effect of atmospheric pressure and sample stress on thermal conductivity is directly proportional and appears to be rather significant.

Finally, it must be emphasized that the must substantial contribution of the present study was the ability to observe effect of sample stress on material thermal conductivity. Consequently, linear models are proposed for the relationship of conductivity *k* as a function of σ stress, as seen in Figure 5-55.

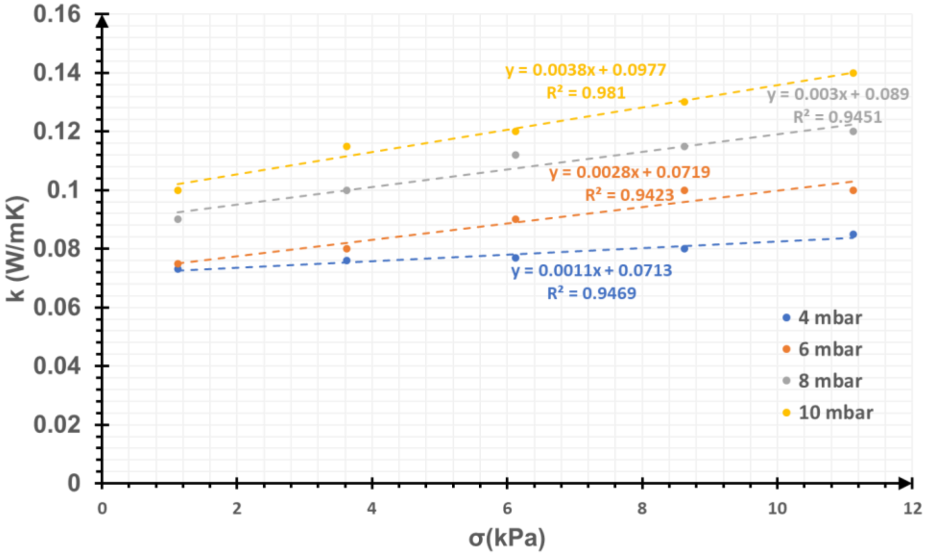

Figure 5-55. Linear dependency of thermal conductivity from sample stress.

The R^2 values for all these fits are above 0.90. The expressions for this dependency are:

$$k = 0.0011\sigma + 0.0713 \qquad (4\ \text{mbar})$$

$$k = 0.0028\sigma + 0.0719 \qquad \text{(6 mbar)}$$

$$k = 0.0030\sigma + 0.089 \qquad \text{(8 mbar)}$$

$$k = 0.0038\sigma + 0.0977 \qquad \text{(10 mbar)}$$

The parameters for these expressions are now presented as functions of atmospheric pressure, using linear relationships in Figure 5-56.

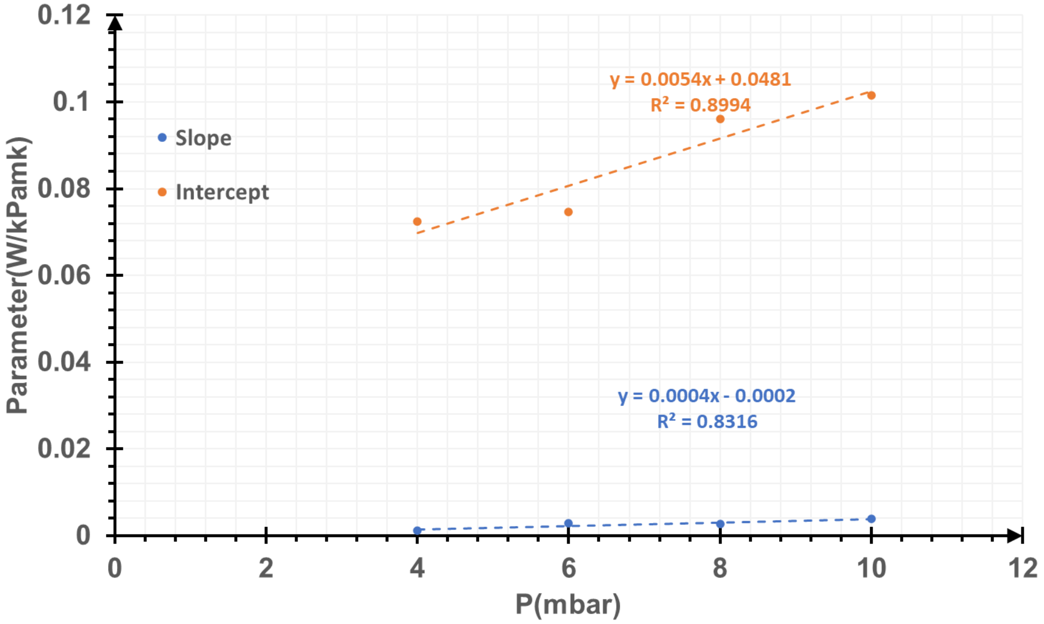

Figure 5-56. Parameters for the linear models as a function of atmospheric stress.

Resulting in the following expressions for the parameters:

$$Intercept = 0.0054\text{P} + 0.0481$$

$$Slope = 0.0004\text{P} - 0.0002$$

Where P is the pressure in mbar, this concludes the presentation and analysis of the results obtained for the thermal conductivity part of the experiment.

Volume variation during testing

The sample height was monitored through the development of each experimental program to observe eventual density variations. These measurements are presented in Figure 5-57, showing that the sample is compressed some 2 mm in total by the 6kPa stress increment.

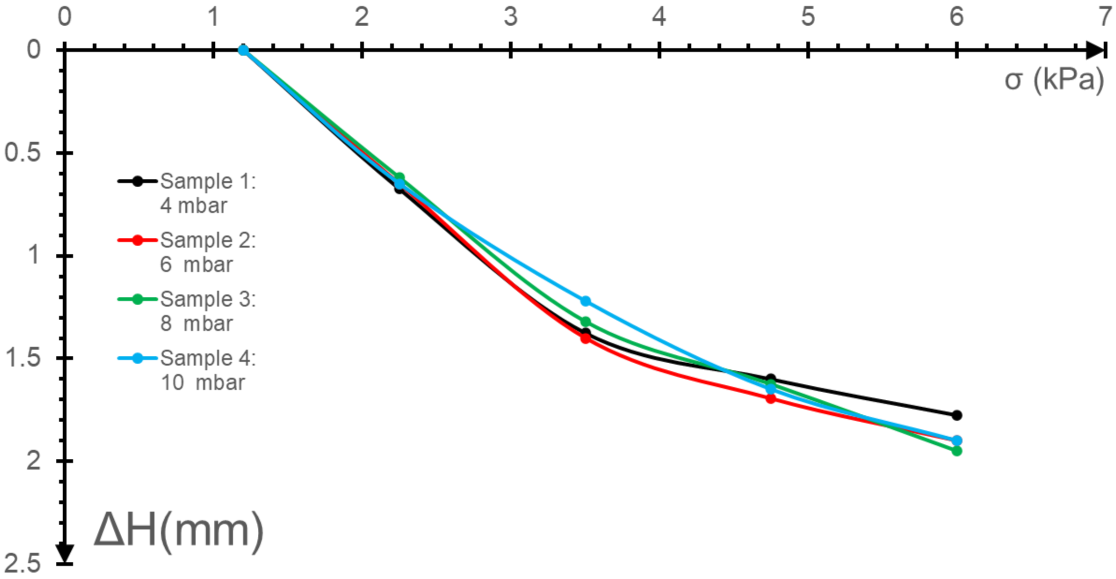

Figure 5-57. Variations of the height of the sample through the testing program.

The sample volume is a prism with a square base with 80 mm side and an initial height of 160 mm. Knowing this and the specific gravity of the Fontainebleau sand, the volume changes can be computed and expressed in terms of the void ratio. The results of these calculations are presented in Figure 5-58 showing that from the initial value of 0.85-.86, it drops down to 0.83-0.84. Given the values for the maximum and minimum void ratio ($e_{max} = 0.866$ and $e_{max} = 0.545$), Roughly, this translates to a variation from the initial mean density of 1425 kg/m^3 to a final mean density of 1443 kg/m^3 for all the samples, a density variation of around 1%. Alternatively, the same result is seen Figure 5-59 in terms of porosity, $\eta = e/(1 + e)$.

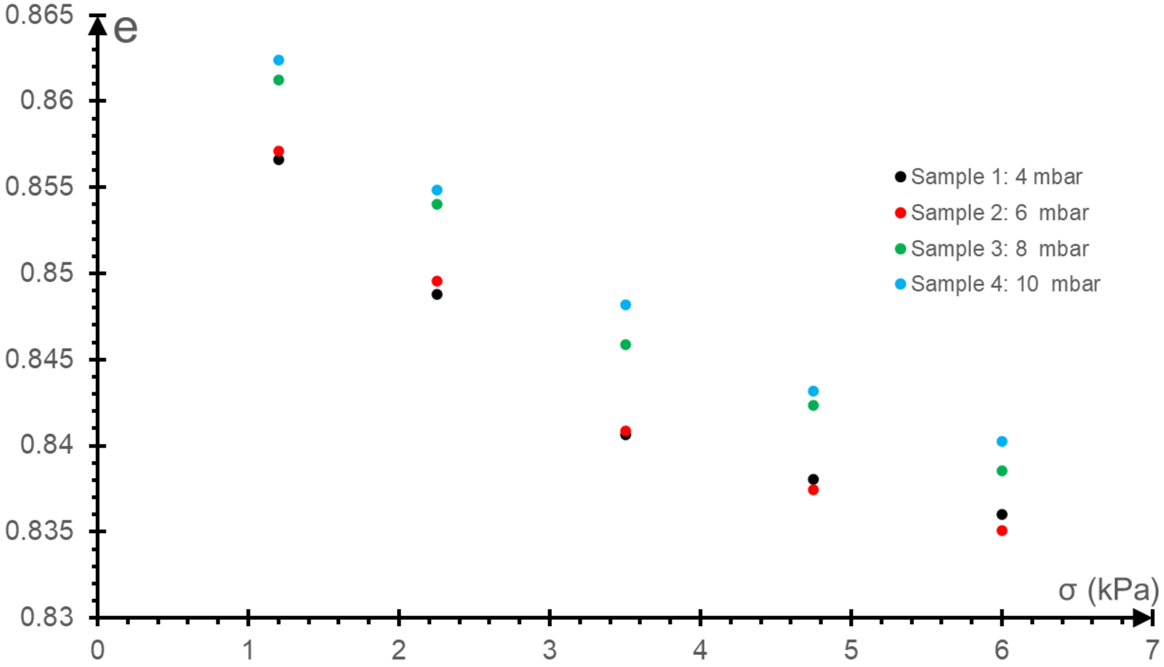

Figure 5-58. Void ratio variations in the sample.

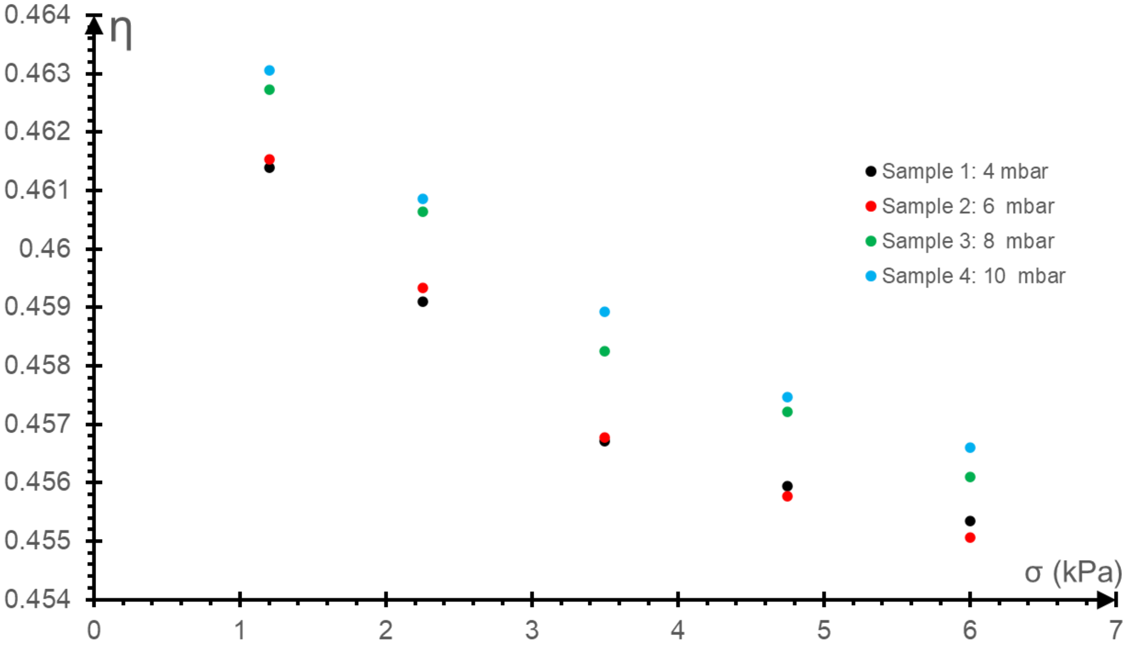

Figure 5-59. Void ratio variations in the sample.

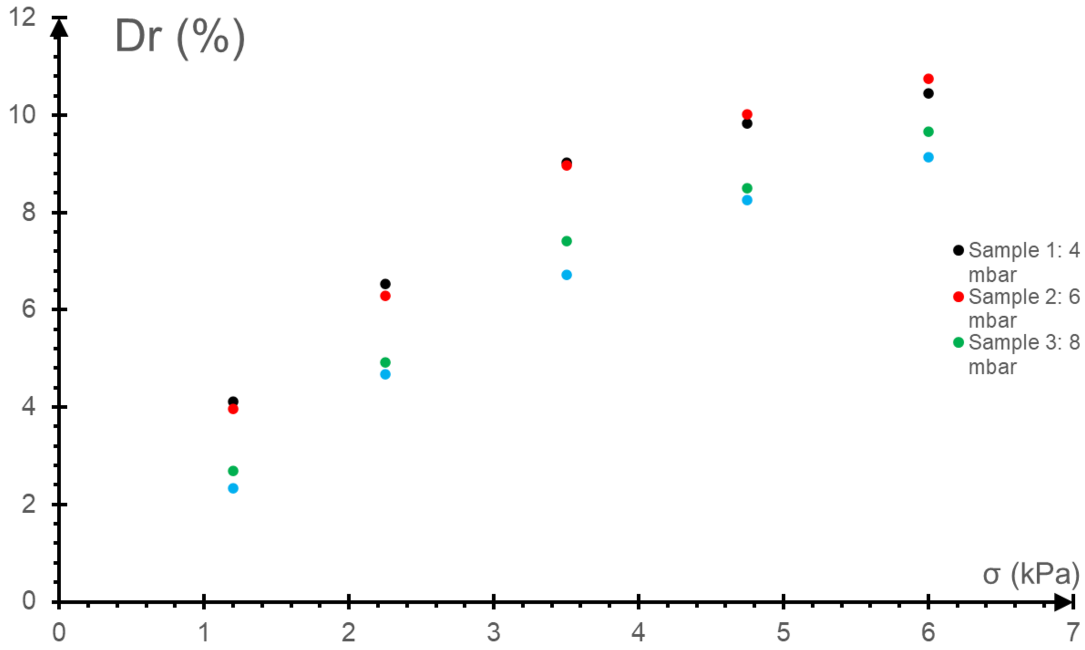

Figure 5-60. Relative density variations in the sample.

5.10. Wave velocity measurements

Experimental data

Waveforms acquired for the four samples. P waves are shown in violet, the S in grey, and the input signal in blue.

The first group of data obtained was for the normally consolidated samples. The sample has not been subjected to any higher stresses than those applied when the measurement is taken. Additionally, intermediate values were taken between each point measured in the thermal conductivity test, resulting in a total of 10 stress values measured. The signals are presented in a normalised scale for better visualisation. During the experimental program described in Table 5-2, wave measurements were taken for each sample at the defined stresses. At the end of the program for each sample, the measurements were repeated, obtaining results corresponding to the material's over-consolidated state.

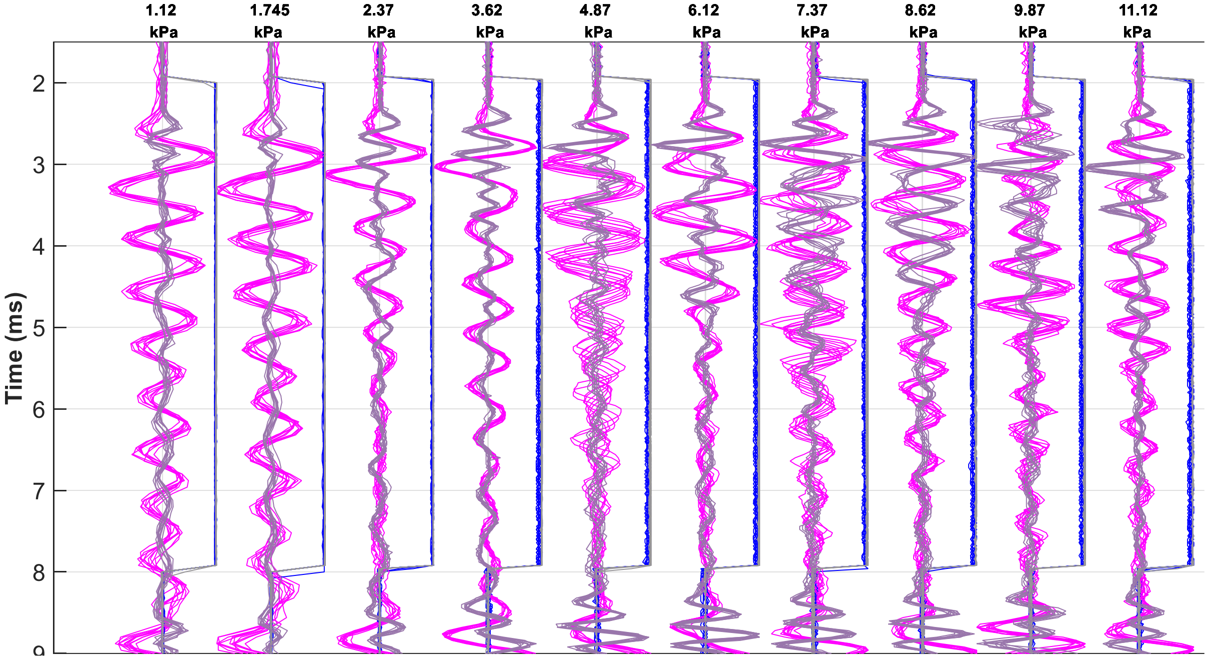

Figure 5-61. Waves measured in the Sample 1 (4 mbar). The waves produced by the 'P' actuator are shown in violet, and the ones of the 'S' actuator are shown in grey. The input signal is displayed in blue.

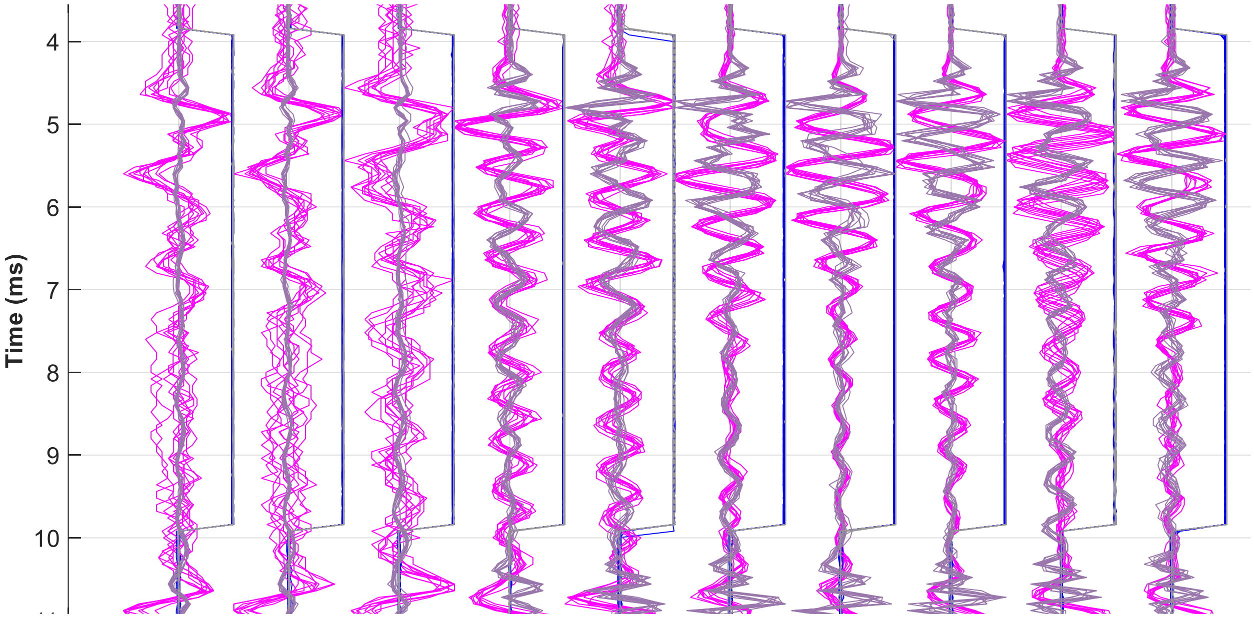

Figure 5-62. Waves measured in the Sample 2 (6 mbar). The waves produced by the 'P' actuator are shown in violet, and the ones of the 'S' actuator are shown in grey. The input signal is displayed in blue.

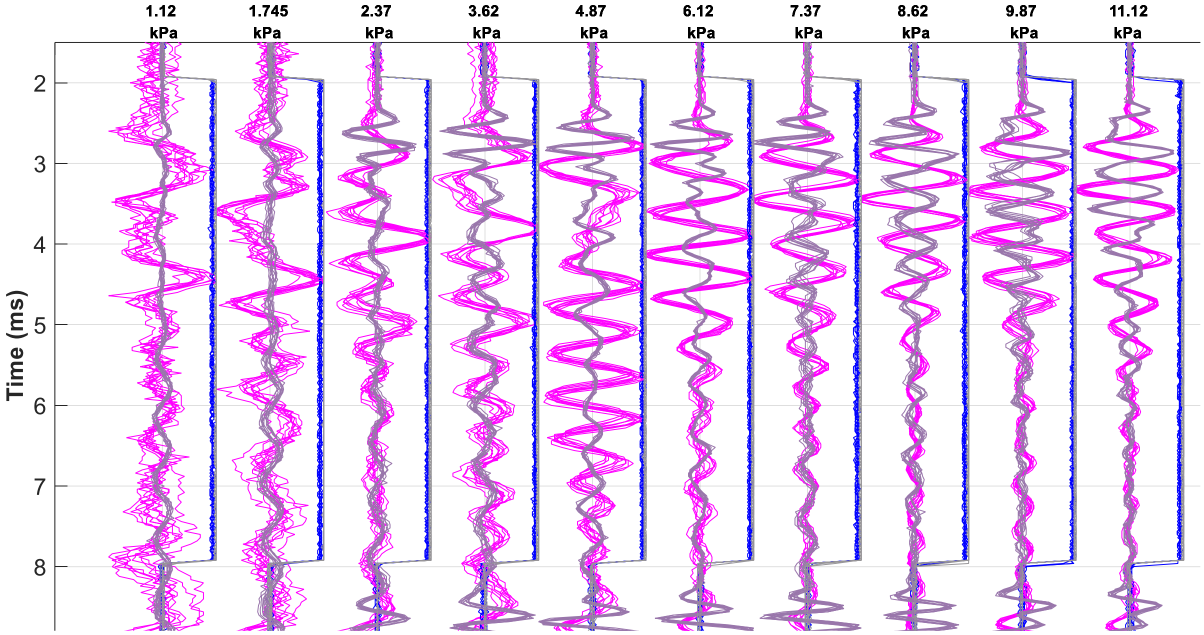

Figure 5-63. Waves measured in the Sample 3 (8 mbar). The waves produced by the 'P' actuator are shown in violet, and the ones of the 'S' actuator are shown in grey. The input signal is displayed in blue.

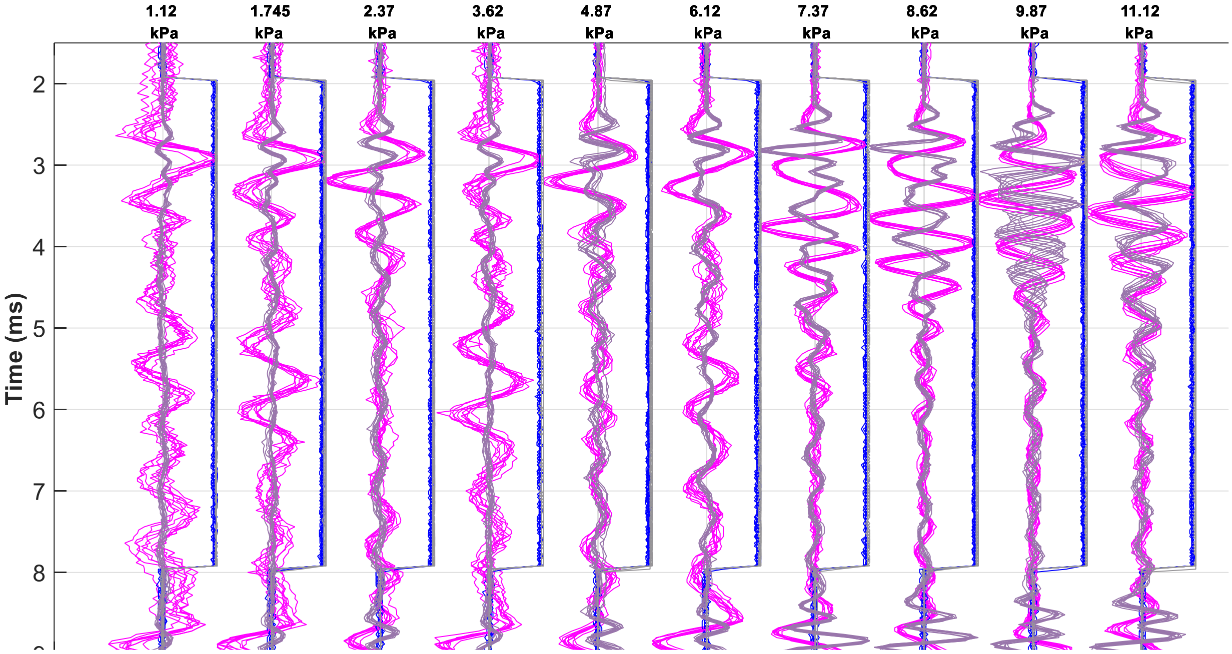

Figure 5-64. Waves measured in the Sample 4 (10 mbar). The waves produced by the 'P' actuator are shown in violet, and the ones of the 'S' actuator are shown in grey. The input signal is displayed in blue.

The signals obtained using the overconsolidated sample (once the full set of thermal conductivity measurements was concluded) are presented now, from Figure 5-65 to Figure 5-68.

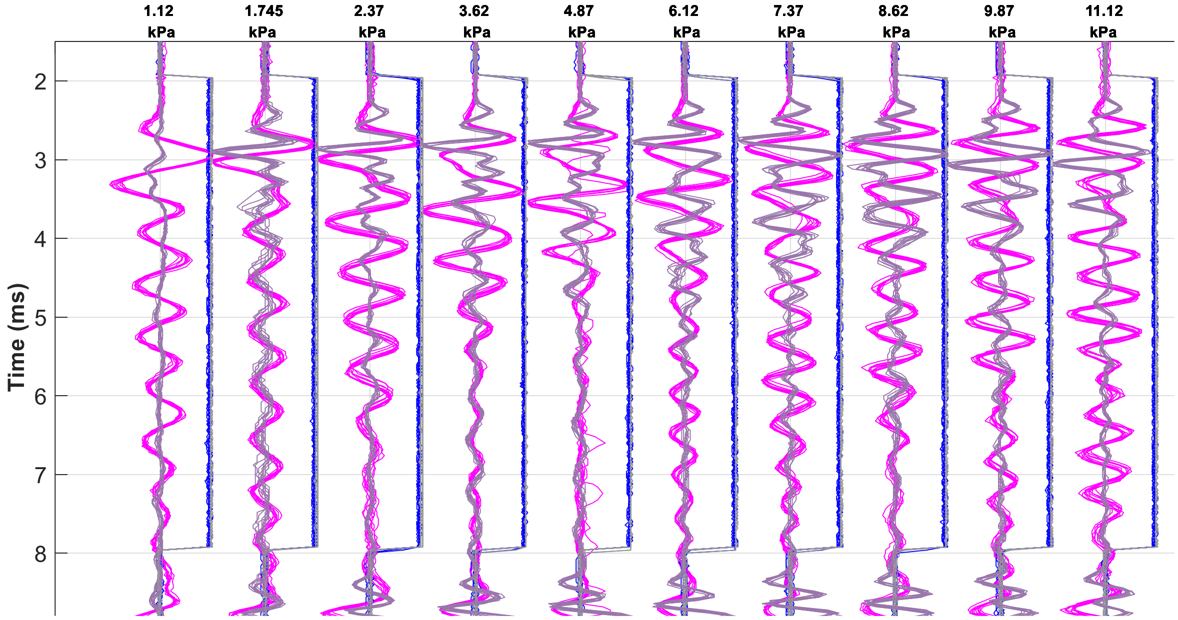

Figure 5-65. Waves measured in the Sample 1 (4 mbar). The waves produced by the 'P' actuator are shown in violet, and the ones of the 'S' actuator are shown in grey. The input signal is displayed in blue.

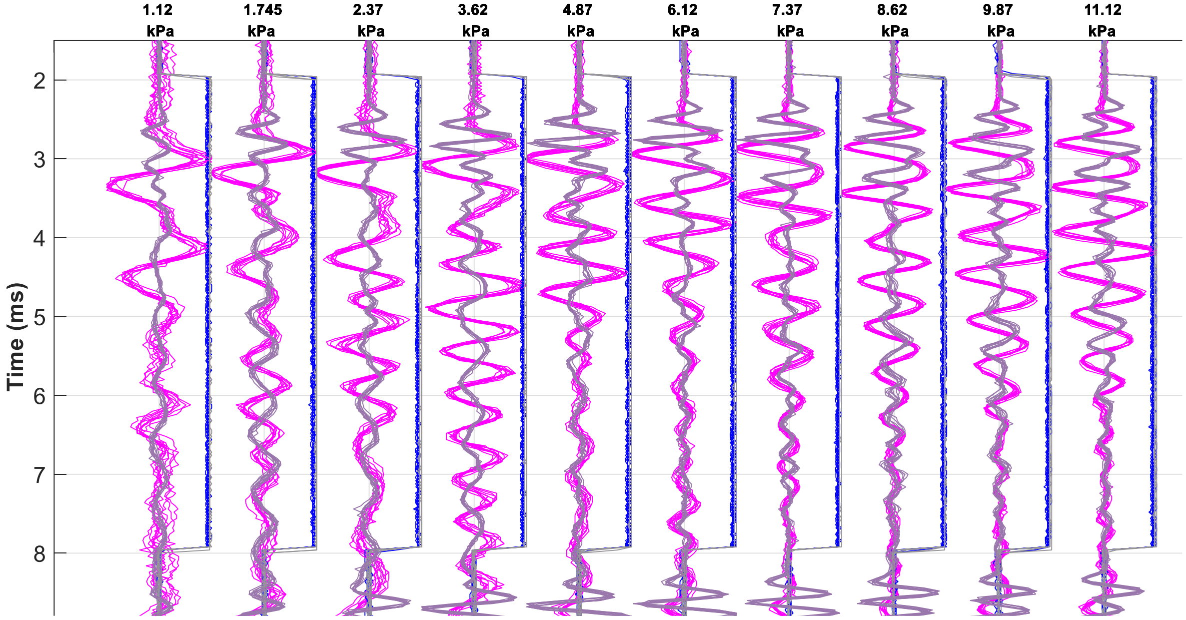

Figure 5-66. Waves measured in the Sample 2 (6 mbar). The waves produced by the 'P' actuator are shown in violet, and the ones of the 'S' actuator are shown in grey. The input signal is displayed in blue.

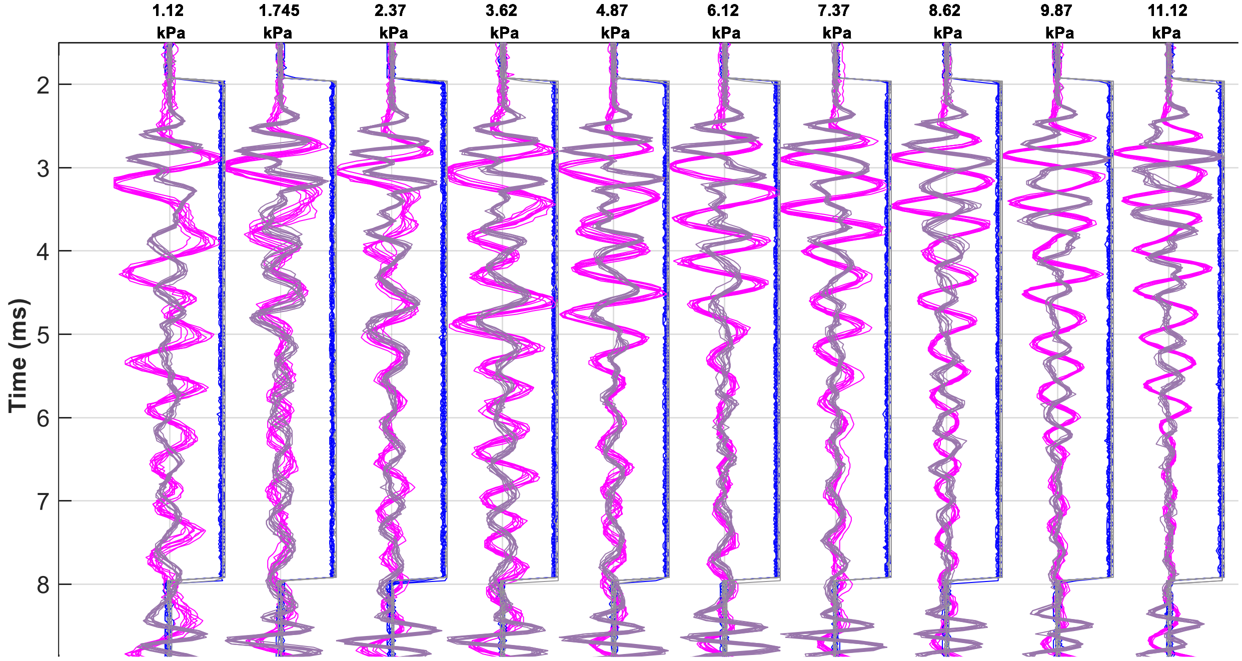

Figure 5-67. Waves measured in the Sample 3 (8 mbar). The waves produced by the 'P' actuator are shown in violet, and the ones of the 'S' actuator are shown in grey. The input signal is displayed in blue.

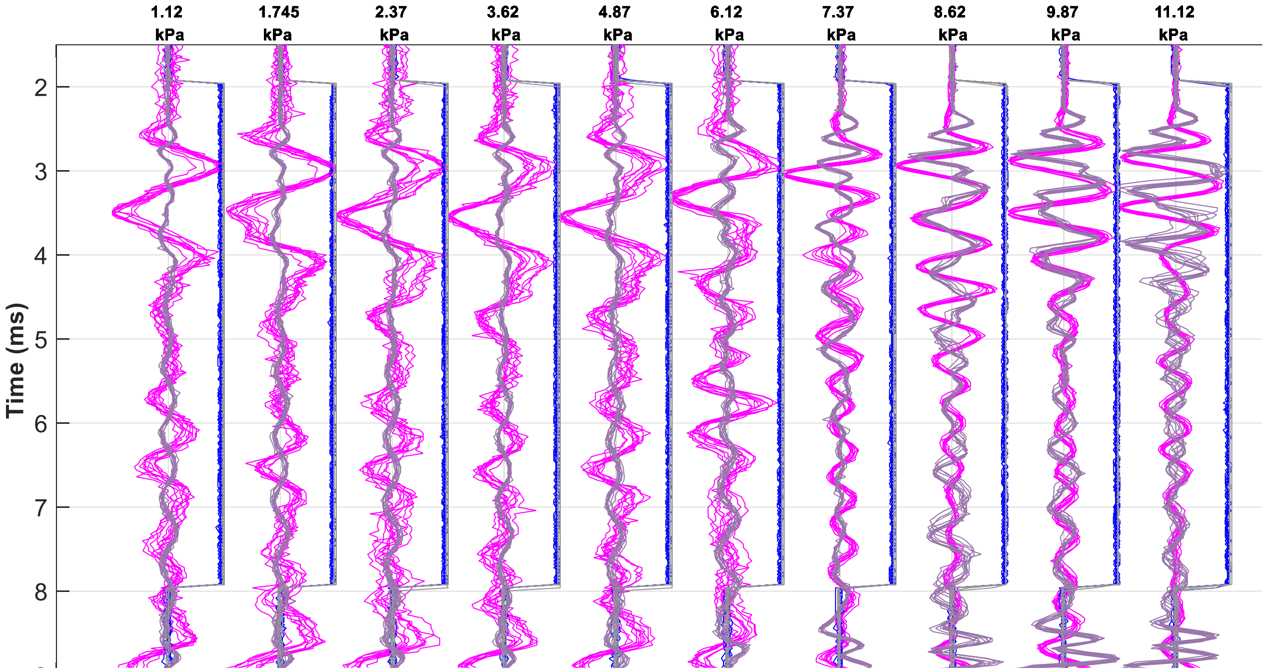

Figure 5-68. Waves measured in the Sample 4 (10 mbar). The waves produced by the 'P' actuator are shown in violet, and the ones of the 'S' actuator are shown in grey. The input signal is displayed in blue.

Analysis of the results

The waveform signals presented in the precedent section show that the apparatus can transmit and receive waves through the soil. Figure 5-61 to Figure 5-68 show that the measures are repeatable since for every datapoint (each column plotted), the data acquired for separate 10 waves superpose from perfectly in some scenarios as is the case of Figure 5-65 to Figure 5-67, to small variations as the ones seen in the Figure 5-63. It can also be observed that more variability is present for the measurements done on the normally consolidated samples (from Figure 5-61 to Figure 5-64). In contrast, very clean signals superposing almost perfectly are observed for the over-consolidated samples present in Figure 5-65 to Figure 5-68.

The violet P wave signals show a clean dampening motion after a few oscillations, generally seen more clearly at higher stresses and less at the lowest ones. On the other hand, the grey S waves exhibit a first group of 1-3 large peaks and then highly variable irregular shapes. Consequently, the possibility that mixed P wave components affect the proper interpretation of these waves must be considered.

Due to the expected dependency of soil wave velocity with the applied stress, in all the figures, the first big peak arrives faster for the bigger stress values, which can be observed mainly in the violet P waves. Nevertheless, the increase is quite subtle and proper determination requires detailing signals at a bigger scale; for this purpose, the results corresponding to sample 1 in an overconsolidated state are detailed in Figure 5-69. It can be seen in this figure that the peaks of both types of waves (located at around 2.7ms) progressively arrive earlier for the higher stress, and even if the difference is very subtle at this scale, it is visible. For the case of the S wave (grey), it is also observed that above 8.75 kPa, one of the S wave's peaks reduces its amplitude and even disappears. In contrast, the violet P wave signals show no apparent variation in this range, so it is not clear if the variation of the S wave is due to interference with earlier arriving P wave components or a noise arriving faster than the S waves.

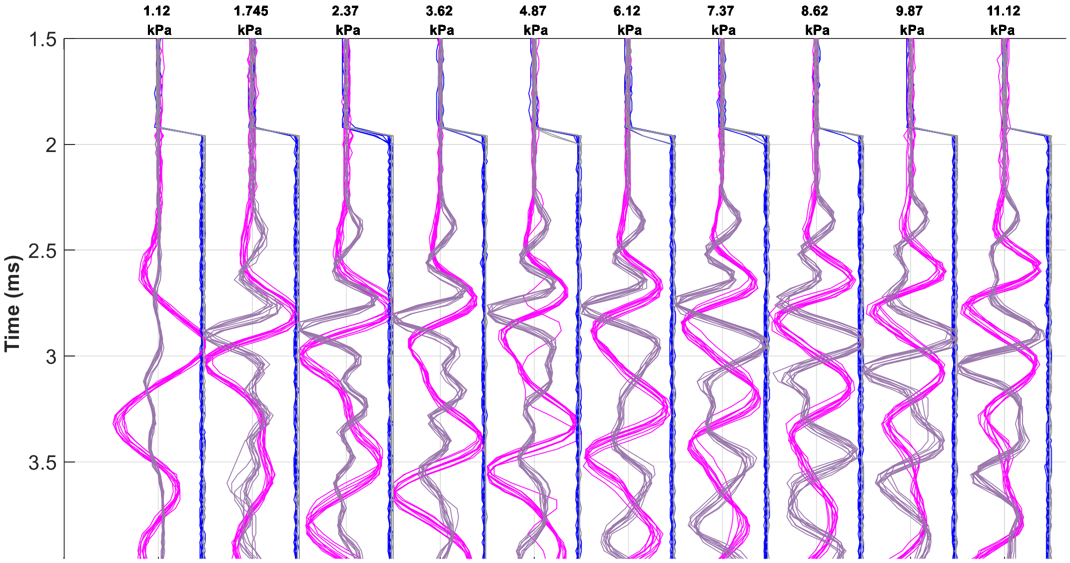

Figure 5-69. Zoom in of the waves measured in the sample 1 (4 mbar). The waves produced by the ‘P’ actuator are shown in violet, and the ones of the ‘S’ actuator are shown in grey. The input signal is displayed in blue.

Concerning the case for determining the P wave travel time, as explained in the previous chapter, it is helpful to use a simultaneous visualisation of P and S wave signals, as presented in Figure 5-69. In these curves, it can be observed that the first departure from the axis is roughly the same for P waves and S waves alike, in Figure 5-58 and all the precedent figures. In all the figures, the violet and grey waves depart from the axis almost simultaneously in opposite directions, which can be observed in the zoom-in provided by Figure 5-69. This first arrival can then be used to determine the arrival time of the P wave and should be considered consistent with the existing criteria for bender element testing.

Much like in Bender element testing, these observations are more apparent at the higher stress values and less evident at the smaller stress values, particularly for the minimum 1.12 kPa point. Consequently, assisting the interpretation of each wave with its neighbour stress values could be a valuable resource.

It is becoming clear that interpreting these waveform signals might not be trivial. Nevertheless, the similarity with the bender element test can be a reasonable basis for approaching the problem. As it was mentioned in the previous chapter explaining bender element interpretation (see section 4-2), when looking at the arrival of the S waves, it may be problematic to distinguish the arrival point of the actual shear pulse from the misguiding P wave components that arrive at a higher velocity. This probably is happening here since, as described in the previous paragraph, the effect of sample constraint on travel time is present in the result. Thus, discarding the worrisome possibility that the wave will propagate through the container walls instead of through the soil. Hence, it was decided that looking into the frequency content of the signals in question would be desirable since it might help identify the different components of the signals and possibly even filter them to isolate the specific waves of interest.

Figure 5-66 shows the Fast Fourier Transform for one of the acquired P-wave signals. The figure shows that most of the frequency content is focused on the 0-4000 Hz, with a peak around 3000 Hz. The red signal shows the obtained waveform when frequencies outside this range are excluded; since it is almost identical to the original signal it can be concluded that this signal is a P-wave, and no significant S-waves are involved in this frequency range. Notice that this waveform consists of a few big peaks followed by a rather complex waveform that does not appear too indicative. In contrast, Figure 5-71 displays one of the acquired S wave signals. In this case, a small peak appears at about 4000 Hz.

The used input signals were square pulses with a duration of 6 ms, thus providing a wide range of frequencies in the emitted wave, which has some advantages for travel time interpretation. The output signals were filtered in the frequential domain making use of lowpass filters cutting frequencies at 2.5 kHz with a lowpass to aid determination of wave travel time, but also a bandpass Butterworth type filter was used allowing passage of frequencies between 2.5kHz and 3.5 kHz. This filtering made use of the sampling frequency of the data, which was fixed at 500 kHz in the oscilloscopes to ensure high quality signals.

When filtering the signal, allowing to pass only the frequencies around 4 kHz, it can be observed that the amplitude is substantially reduced; furthermore, a decaying waveform that appears to be coherent with a dampening phenomenon can be distinguished in the red signal, which was not evident in the original unfiltered cyan curve. The spectra show that considerable frequency in the frequencies 0-2000 Hz has been excluded, corresponding to the range of the P wave observed in the P-wave signal. It can thus be hypothesised that P-wave components in the low-frequency range are affecting the interpretation of the S-wave signals.

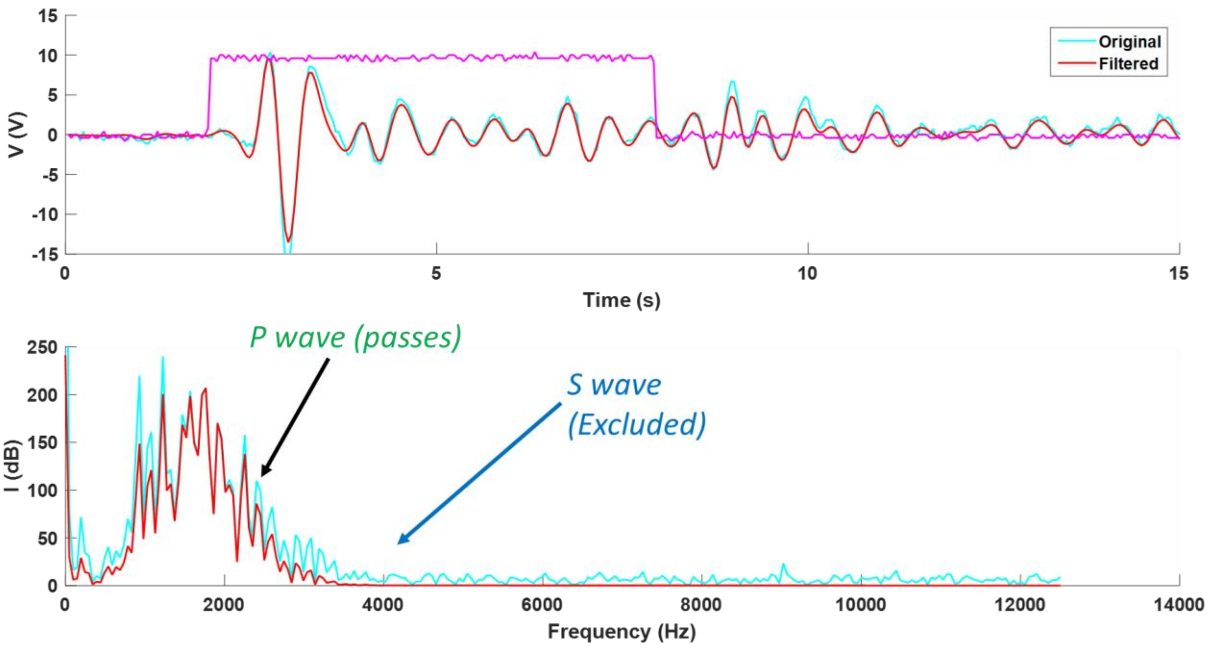

Figure 5-70. Frequency content of an acquired P-wave. The frequency content shows only P-waves are involved.

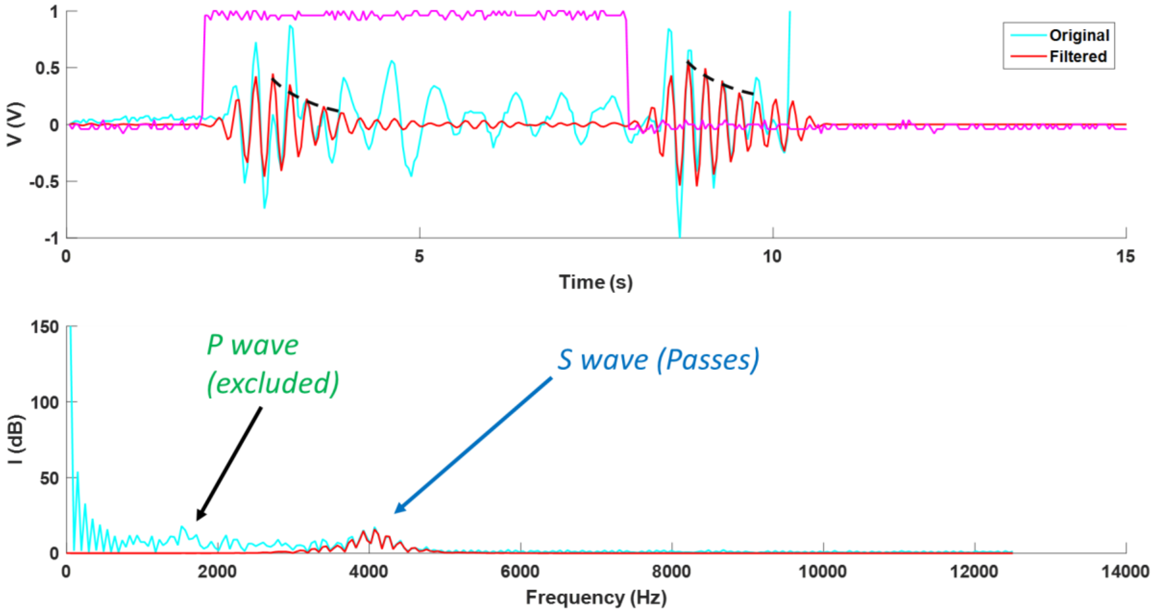

Figure 5-71. Frequency content of an acquired P-wave. The frequency content shows both P and S-waves are involved.

To investigate this hypothesis further, the signals registered by the accelerometer facing the P-wave emitter (which records horizontal motion only) when wave perturbations were induced can also be considered (as seen in Figure 5-72b). The spectrum for this wave is shown in Figure 5-75, where the suspected P-wave of frequencies is allowed to pass, and in Figure 5-74, where only the S-wave range of frequencies is allowed to pass. This time, the wave carries considerable content in both frequency ranges since it is expected as it is an S wave in nature that generates P wave motion in the plane transversal to the movement of the actuator. The filtered P signal exhibits similar behaviour to the pure P signal shown previously, with a prevalent peak subsisting after both strikes (at around 3ms and 9ms, respectively); meanwhile, the S wave component shows a dampening movement section preceded by a few peaks of residual P-motion, much like in the near-field complications encountered on bender element signal interpretation.

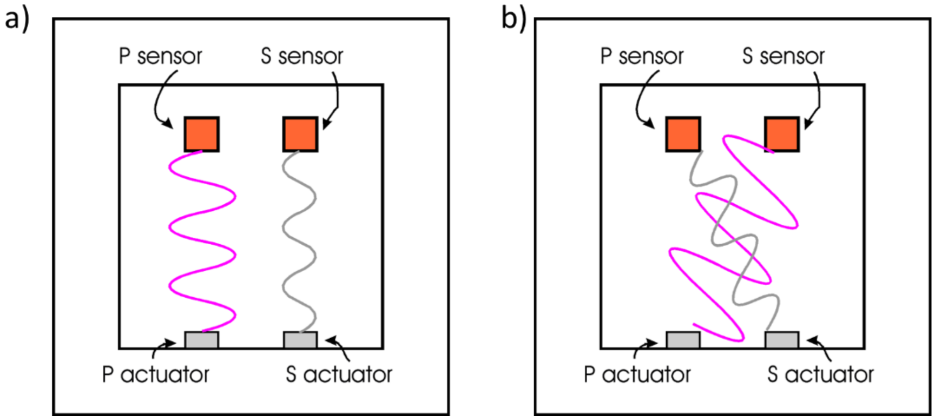

Figure 5-72. The waves recorded included not only a) the waves recorded by the corresponding accelerometer but also b) the ones recorded in the accelerometer intended to record the other type of wave.

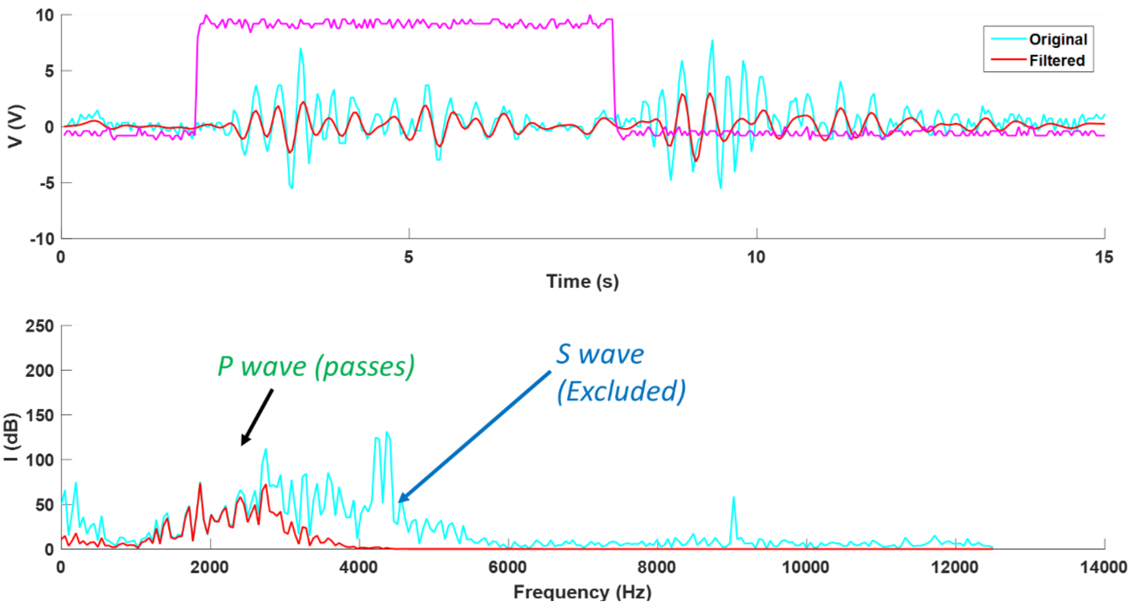

Figure 5-73. Frequency content of an acquired S-wave on the p-plane. S-wave excluded.

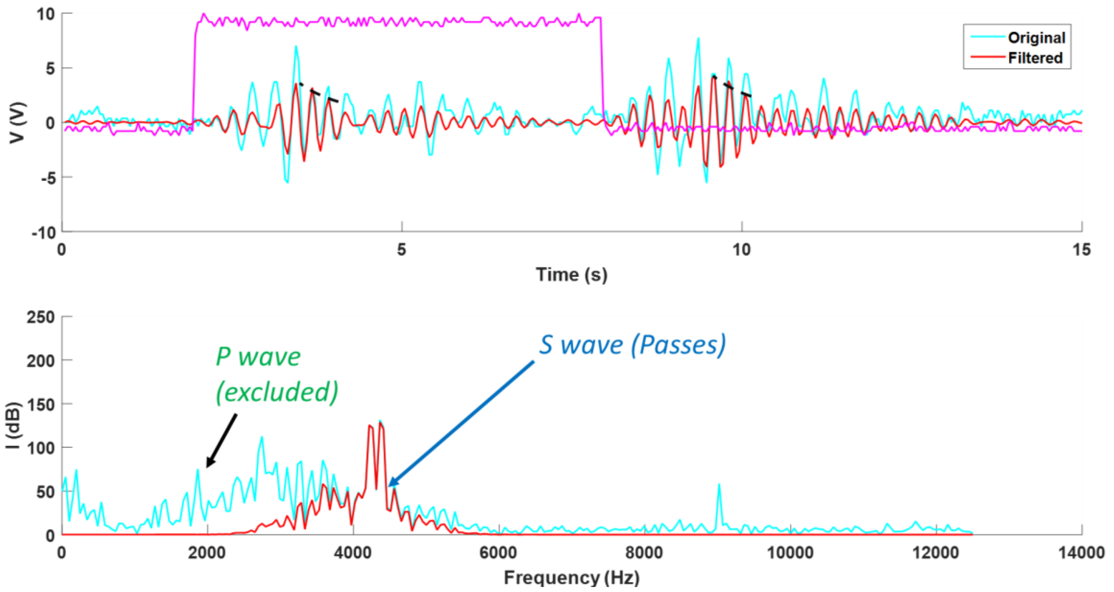

Figure 5-74. Frequency content of an acquired S-wave on the p-plane. P-wave excluded.

Considering these observations were consistent for several signals, it seems that this analysis could be reliable and that potentially calibrating an adequate filter to allow the S-waves through exclusively is the path towards adequate interpretation of S-wave travel time.

Based on this, a preliminary interpretation can be proposed for the experimental program of unconsolidated waves completed for sample 1. The selection of arrival times is displayed in Figure 5-75. Note that the P-wave arrival time is selected at the first departure time from the axes (coherent for both waves), whereas the S-wave arrival time is selected at the second departure time from the axes, which also coincides in both waves. The utilisation of this criterion can be visualised in Figure 5-76.

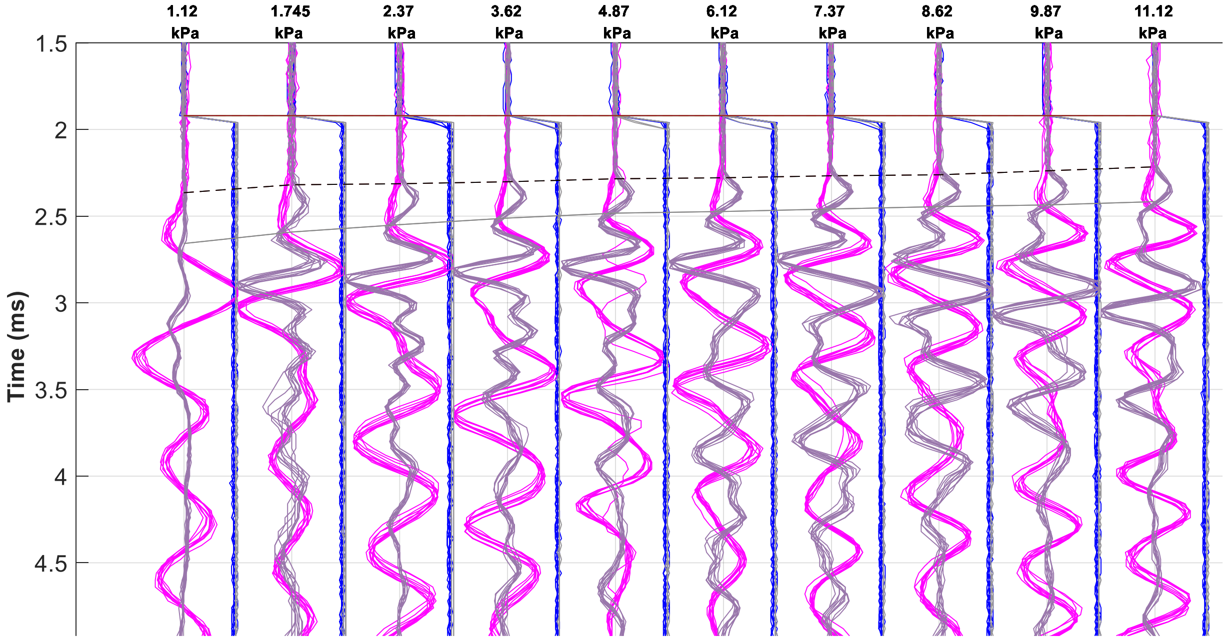

Figure 5-75. Interpretation of arrival times for sample 1.

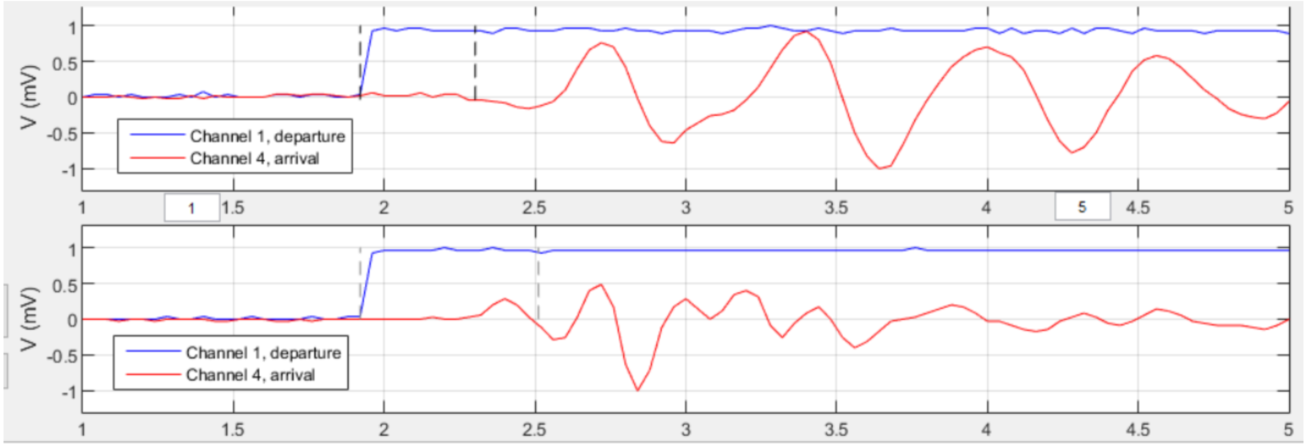

Figure 5-76. The use of the chosen interpretation criterion for both waves.

The results for this experimental program on sample 1 are visualised in Figure 5-77, fitted with a potential expression which provides reasonable fits. An alternative expression in terms of a power law for the logarithm of the velocity is presented in Figure 5-78. Finally, the computed Poisson’s ratio is presented in Figure 5-79.

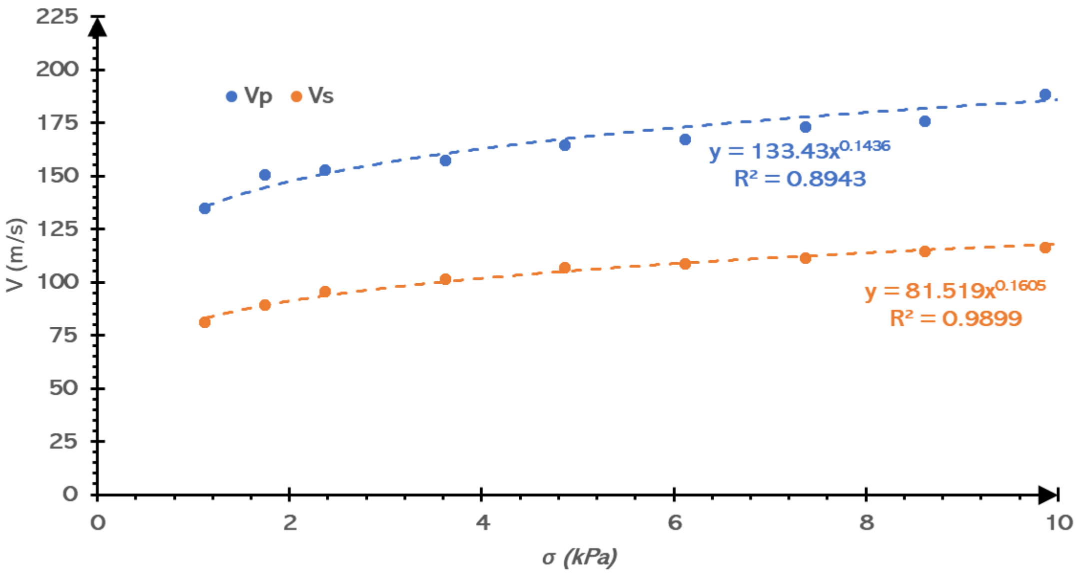

Figure 5-77. The use of the chosen interpretation criterion for both waves.

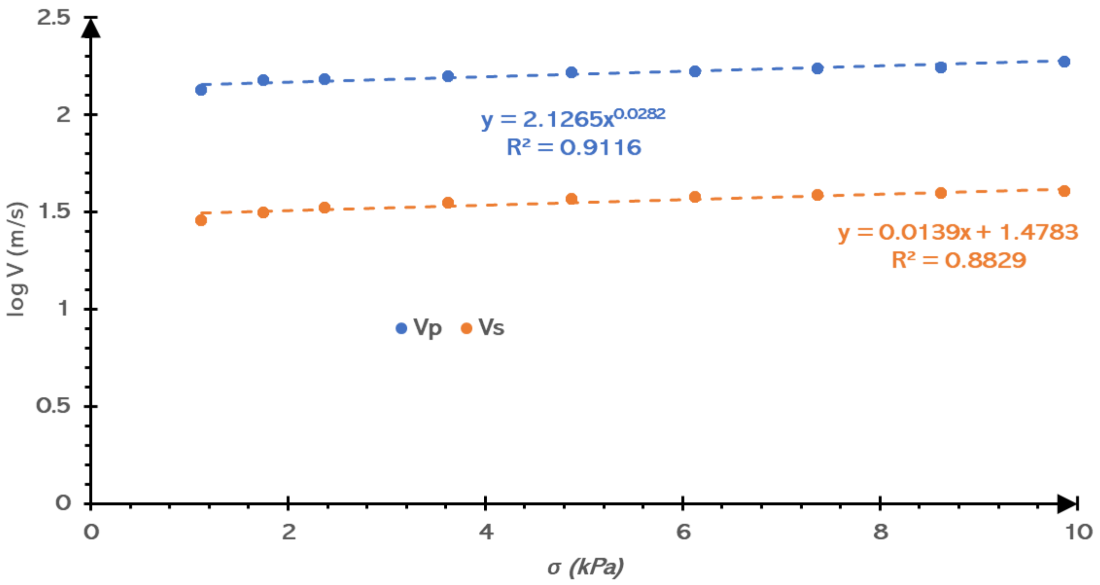

Figure 5-78. The use of the chosen interpretation criterion for both waves.

Notice that the middle ν value of this result is about 0.15, coherent with the results obtained with the bender element measurements. This could mean that the interpretation criterion presented here has some value. Nevertheless, it must be noted that this criterion must be further supported with the result of the numerical calculations, which is still a work in progress that should be completed during the following months before applying it to the considerable amounts of data registered.

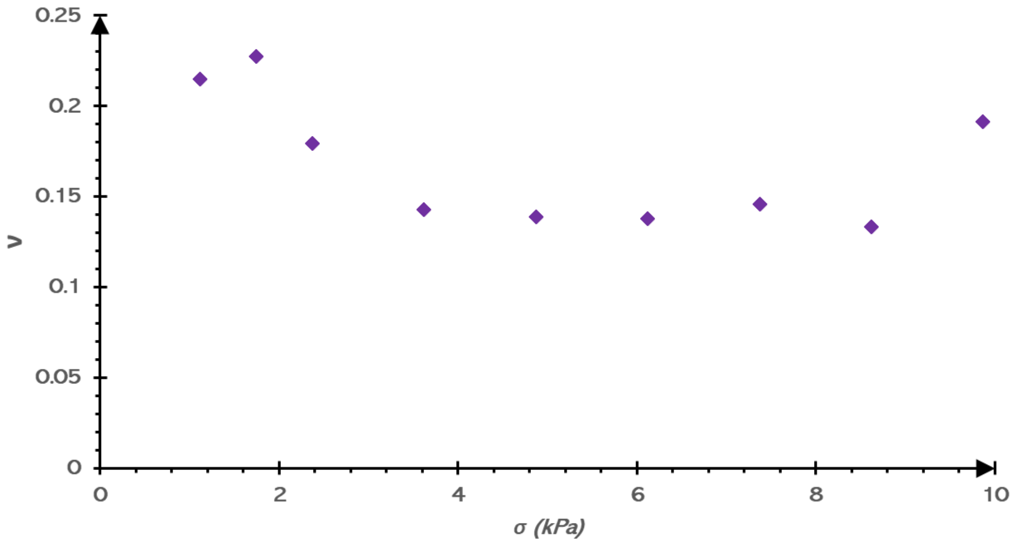

Figure 5-79. The use of the chosen interpretation criterion for both waves.

Comparison with Bender Element results

Finally, the obtained results are compared with the measurements presented in Chapter 4 using Bender Elements. As seen in Figure 5-80, the curve of the values obtained for Vp and Vs with the new setup presents a different slope in the initial segment of low stress. The new setup seems to measure values of V_p that are too high at lower stresses, and that increase too slowly with respect to applied stress. The same behaviour is observed for V_s.

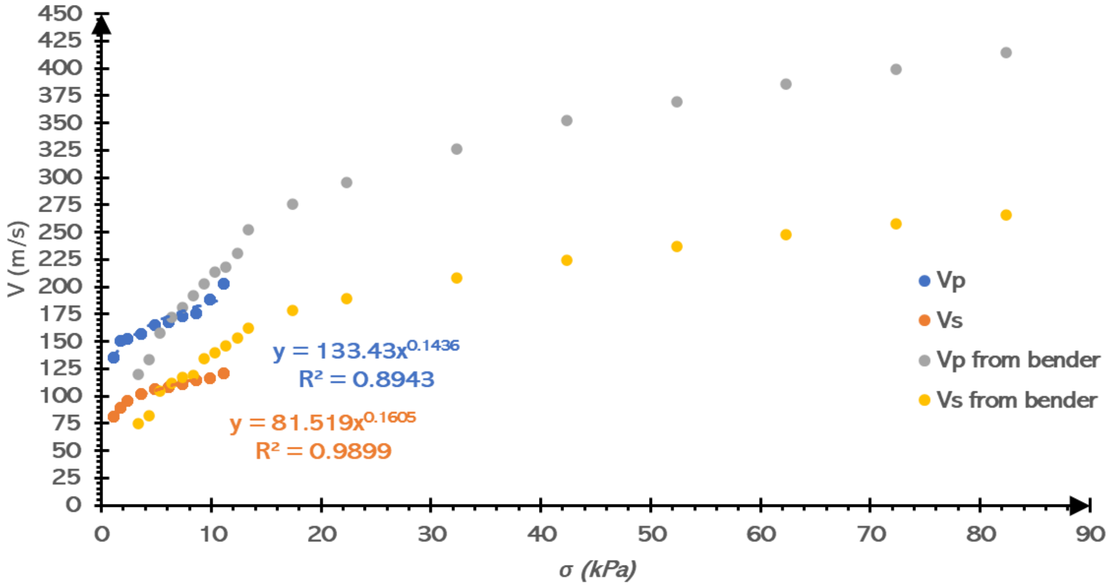

Figure 5-80. The use of the chosen interpretation criterion for both waves.

Figure 5-81 compares of the Poisson ratio of the new experiment with some of the Bender element results. It can be seen that both curves oscillate around a value of 0.15.

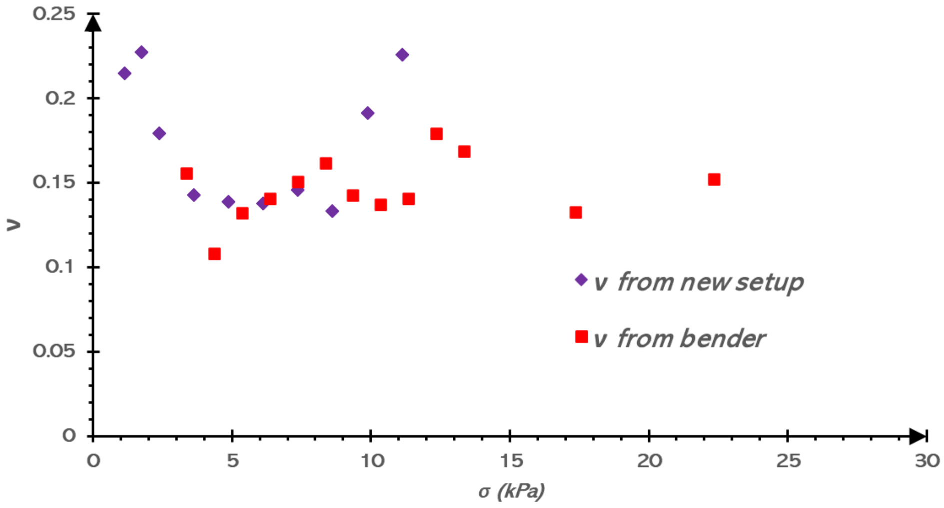

Figure 5-81. The use of the chosen interpretation criterion for both waves.

5.11. Conclusion

An experimental setup was developed at the Uniandes laboratory, conceived for coupled thermal conductivity and wave velocity measurements. The device allows work with extremely low-stress samples deposited in loose arrangements. Bender Elements were replaced by piezo actuators capable of generating a potent strike, producing mechanical P and S-waves that can traverse the soil sample and be recorded by uniaxial accelerometers placed directly facing the wave emitters.

The required adaptations were made to enable the recreation of most of the conditions of the atmosphere of Mars after the measurements of the InSight mission at Elysium Planitia. These include applying a vacuum to the experiment to reduce the atmospheric pressure to the very low values of 600-800pa (6-8 mbar) present on Mars and CO_2 saturation to substitute Earth's Nitrogen and Oxygen-rich air. A piston controlled by a pneumatic jack enables control of the material stress, which can be accurately monitored using a force cell. The temperature of the sample chamber was not recreated since other works showed no effect on the results.

Experiments consist of prolonged cooling cycles controlled by Peltier plates that impose a continuous boundary condition on the metallic walls of the samples. Several thermocouple sensors were carefully calibrated to monitor the process, and the obtained data is compared with the results of a numerical Finite Difference model, which accounts for heat conduction in the sample container, in which good care was taken to correctly impose the boundary conditions at the limits and material interfaces. Validation tests showed very good agreement between the model and the tests.

A testing program with four atmospheric pressure values (400, 600, 800 and 10000 Pa) near those present at the InSight site was then completed. The effect of sample stress was accounted for by testing conductivity at 5 different stresses between 0 and 10 kPa, and wave measurements were done at all these values plus 5 intermediate ones. Values of thermal conductivity of 0.08-0.14 W/mK were measured, observing an increasing dependency of conductivity $with$ pressure and actuating sample stress. These values are higher than other works by about 0.02 W/mK, but this can be attributed to the mineralogical differences in mineralogical composition models relating to these magnitudes proposed.

Square pulses with a length of 6 ms were used to produce P-waves and S-waves in the sample, which were recorded with both accelerometers. Very good reproducibility was obtained, acquiring 10 similar waves for every data point and observing similar waves in all 4 samples. It was verified that the waves were propagating through the soil and not the sample container, the signals were identified as a combination of those components, and advancements were made towards interpreting the travel times. Wave measurements were acquired for both normally and overconsolidated sample behaviour. Frequential analysis was performed, enabling the identification of the ranges associated with P and S waves and preliminary calibration for signal filtering of the acquired signals was proposed.

The comparison was made with the measured P and S wave velocities presented in the previous chapter using Bender Elements in the horizontal setup used to apply very low stresses on a loose sample of Fontainebleau sand. The stress ranges involved superpose since the bender element includes 3.75kPa to 10 kPa, whereas the work presented in this chapter spanned from 1.12 kPa to 10 kPa. The results obtained over this range from the wave velocity measurements were observed to be reasonably coherent with the measurements done using Bender Elements for both P and S waves and the computed Poisson ratio.

5.12. References

Halbert, D., & Parnell, J. (2022). Thermal conductivity of basalt between 225 and 290 K. Meteoritics and Planetary Science, 57(8), 1617–1626. https://doi.org/10.1111/maps.13829

Min, D. J., Shin, C., & Yoo, H. S. (2004). Free-surface boundary condition in finite-difference elastic wave modeling. Bulletin of the Seismological Society of America, 94(1), 237–250. https://doi.org/10.1785/0120020116

Nagihara, S., Ngo, P., & Grott, M. (2022). Thermal Properties of the Mojave Mars Regolith Simulant in Mars-Like Atmospheric Conditions. International Journal of Thermophysics, 43(7). https://doi.org/10.1007/s10765-022-03023-y

Vieira, A., Maranha, J. R., Lapa, J., & Figueiredo, A. (2019). Some aspects of measurement of sand thermal conductivity from laboratory tests. Proceedings of the XVII ECSMGE, September. https://doi.org/10.32075/17ECSMGE-2019-0541

Zhang, N., Yu, X., Pradhan, A., & Puppala, A. J. (2015). Effects of particle size and fines content on thermal conductivity of Quartz sands. Transportation Research Record, 2510, 36–43. https://doi.org/10.3141/2510-05

6. ATMOSPHERIC PRESSURE AND GROUND COMPLIANCE

“I always hope for the best. Experience, unfortunately, has taught me to expect the worst”.
Elim Garak, 2375(DS9)

This chapter differs from the previous ones since it focuses on numerical modelling rather than experimental activities. The chapter focuses on the surface displacement induced by atmospheric pressure variations, a phenomenon often encountered when exploring the field of seismic noise. The departing point in exploring this phenomenon is the original observation in seismology, from which the definition of a measurement known as ground compliance arises. The construction of a two-dimensional transient Finite Difference Model conceived to study the process is then explained, and the parameters necessary to apply it to a terrestrial context for validation are then explored. After exploring the effects of the key variables in the model, the validated approach is used to study the case of the ‘observed’ dust-devil’ events at the Mars Insight Landing site. The section is finally concluded with some comments elaborating on the pertinence of this work for the atmospheric-induced noise for seismological observations in both contexts.

6.1. The atmosphere of Mars

The properties of the Martian atmosphere have been characterised in detail (Petropoulos, 1989) and (Bardera et al., 2020) based on data acquired during the landing descent of both Viking 1 and Viking 2 probes. Wind velocity, pressure, and temperature profiles were corrected and compared here to each other, and the values at Earth's sea level are presented for comparison. As seen in Figure 6-3, Mars has a very light atmosphere compared to Earth (which at sea level has a density of 1.293 kg/m^3, in comparison to 0.02kg/m^3 on the Mars surface), with a different composition observed by the Viking 1 and 2 measurements. The pressure is also very low at about 600 Pa compared to 101 325 Pa and even lower at altitudes, as seen in Figure 6-1.

The temperatures on Mars are very low, with the highest values by the Viking probes at ground level being lower than -30 °C and lower than -170 °C at altitude, as seen in Figure 6-2. However, temperatures on Earth can reach these surface values in winter at high latitudes. Finally the Mars dynamic viscosity is $9.81 \times 10^{-6}\ N \cdot s/\mathrm{m}^2$ at the surface (see Figure 6-4), considerably lower than that of the Earth at $1.79 \times 10^{-5}\ N \cdot s/\mathrm{m}^2$. CO_2 is the main component of this atmosphere, making up about 95%. The evolution of the atmosphere was also studied based on observation of the solar arrays (Lorenz et al., 2020). Martian atmosphere presents variations at the surface level in terms of pressure and temperature, in the order of 0.5 Pa and 55K over a day, respectively (Petropoulos, 1989).

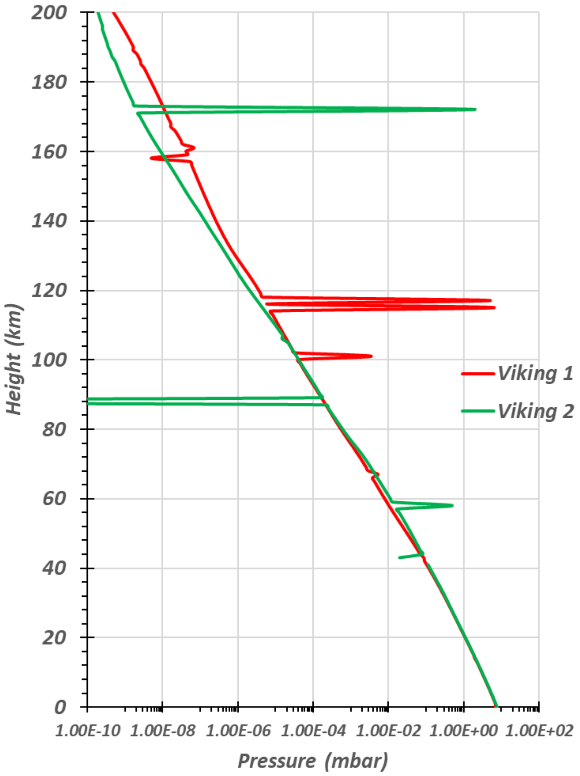

Figure 6-1. Atmospheric pressure of Mars after Viking descent data.

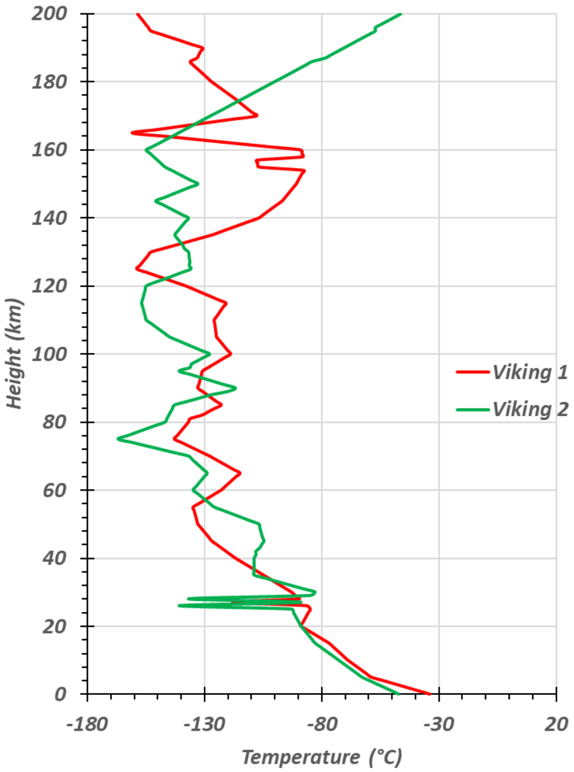

Figure 6-2. Atmospheric temperature of Mars after Viking descent data.

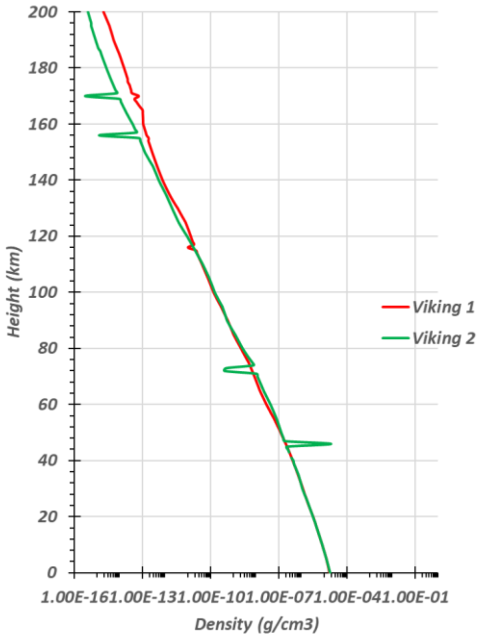

Figure 6-3. Atmospheric density of Mars after Viking descent data.

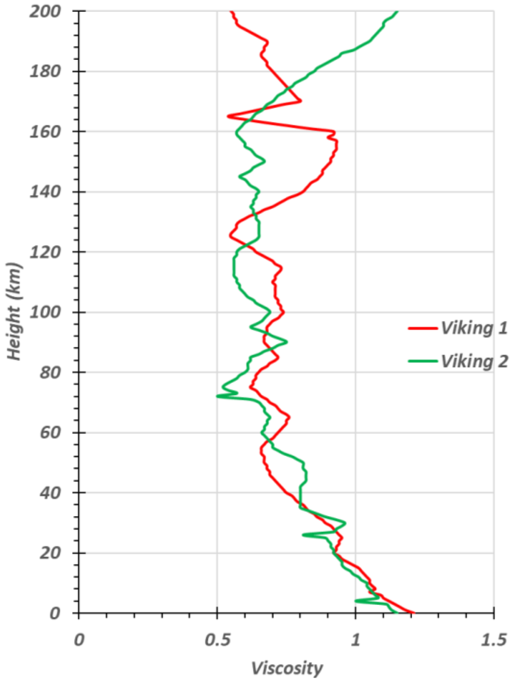

Figure 6-4. Atmospheric viscosity of Mars after Viking descent data.

6.2. Assessment of the compressibility of sand deposits by coupling seismic and meteorological measurements. (Article 5: Manuscript in process)

B. Caicedo[1], J. P. Castillo Betancourt[1,2], P. Delage[2] et.al

1 Ecole des Ponts ParisTech, lab. Navier-CERMES, CNRS, UGE, Marne la Vallée, France.

2 Universidad de los Andes, Bogota, Colombia.

Fluctuations in the atmospheric pressure of the surface induce ground surface displacements that may be detectable via the utilisation of instruments that are accurate enough and consequently constitute a source of seismic noise worth studying to identify when interpreting the signals obtained from such measurements adequately. The measurement known as ground compliance allows quantifying the effect on the surface displacement, considering the contribution emerging from these atmospheric variations in time. While several models and approaches have been employed to study this phenomenon, most of them have neglected the effect of pore pressure on soil strain. This particular point can be approached from the perspective of soil mechanics using effective stresses. Evaluating these strains allows determining whether soil porosity constitutes an adequate way to quantify the contribution of pore pressure on these pressure variations and their effect on surface displacements. The model was validated for Earth conditions; then, the NASA Mars Insight landing site case was evaluated. Previous works available on ground compliance are thus reinforced when the effect resulting from material porosity is accounted for.

Introduction

The first observation that variations in atmospheric pressure can affect the noise levels present in seismic measurements in some conditions can be found in the work of Sorrells (Sorrells et al., 1971). In that work, observations comparing the seismic noise of measurements conducted on the surface, where they would be affected by the atmospheric pressure fluctuations, with those obtained in a cave lower into the same rock mass, allow assessing the mechanical properties of the shallow layers of a deposit. Several scenarios were also evaluated, considering a calm period, a windy period, and the moment a seismic wave propagated through the rock. Buoyancy was discarded, and consequently, the source of the remaining noise was determined to be caused by the slight variations in the atmospheric pressure (Sorrells et al., 1971). However, other observations also address this problem of earth's atmosphere fluctuations and their effects (Beauduin et al., 1996, Crawford et al., 1991).

On Mars, the effect of atmospheric fluctuations on surface deformations has been studied from the point of view of seismology for the 2019 NASA Insight Lander (Banerdt et al., 2018), which has been able to measure and study the behaviour of the surface material (Martian regolith) via the monitoring of events referred to as ‘dust-devils’. To accomplish this, the measure known as compliance has played a role of the utmost importance; the effects of the atmospheric phenomena have been recorded in the highly accurate Seismic Experiment for Interior Structure

(SEIS) instrument (Lognonné et al., 2019), and values for the compliance have been established for several of the dust-devil events (Kenda et al., 2020). It is also worth mentioning that these works have used their results to try to determine elastic values for the surface regolith below SEIS.

However, compliance works usually consider the surface material as an impervious rock, so the fact that the porosity aspect of the medium is most often not accounted for, but in the case of granular deposits, their compressibility depends on the change in effective stress and approach that differs from the one coming from the seismology perspective. This research aims to establish how this pressure variation affects the surface settlement of the ground, considering effective stresses.

Calculations performed for the InSight case (Kenda et al., 2020, Garcia et al., 2020) were based on a model formulated in the frequency domain. However, when considering the effect of pore pressure soil's strain, the emerging coupled problem is more accessible from a time domain formulation. The model proposed here is based on the model developed by (Scott & Ko, 1968), which was initially conceived to study the effect of the gasses involved during the landing process of a rocket on the lunar surface.

This document presents the fundamentals and considerations behind a numerical model using the finite difference method (FDM) developed to study the effect of surface atmospheric pressure variation on ground surface displacement. The model considers the effect of the barometric pressure and its variations as it infiltrates a granular porous material. This porous nature is the case for the soils encountered on the surface of Earth, but also for those materials on the surface of other terrestrial planets, Mars included.

In the first part of this chapter, the developed model for ground compliance is presented. Then, this measurement is studied in terms of how the variation of the atmospheric stresses affects compliance, emphasising the behaviour of the pore pressure directly; the effect of the main variables involved is evaluated. The case study for this first section is the scenario of the work conducted by Sorrells et al., (1971) in his original work. In the second part, the specific conditions of the InSight landing site are used to select the appropriate value for the key variables and evaluate the situation at Elysium Planitia.

Part A: Ground compliance model in effective stress

The current study considers the case of porous materials and, specifically, their behaviour while in a dry state. This last consideration implies that the effective stress, in the absence of water pressure, is to be defined as the result of subtracting the gas pressure P from the total stress on the soil.

It is also relevant to consider that the material is behaving on a small strain and, thus, is still in the elastic regime. Therefore, elastic computation of the strain is employed.

The following paragraphs describe succinctly the model for ground compliance. Appendix A presents further details on the temporal and spatial discretisation of the problem.

Variation of total stress due to change in atmospheric pressure

The first consideration in the model is the description of the variations of total stress acting on the porous media resulting from the evolution of a passing surface wave.

The proposed model conceives the surface pressure variations as a sinusoidal wave with infinite depth outside the plane of study. The parameters of this wave, such as amplitude, wavelength, and velocity, may be adjusted to the desired values according to the environment and conditions.

The infinite sinusoidal pressure wave as seen in Figure 6-5 is composed by a juxtaposition of vertical straight-line load in plane strains. Therefore, at an instant t, on a specific point where surface displacement or acceleration is being measured, the wave is defined by the following expression:

$$P_g(x,t) = P_g^m + a_P cos\left[2\pi\left(f_w t - \frac{x}{\lambda_w}\right)\right] \qquad (1)$$

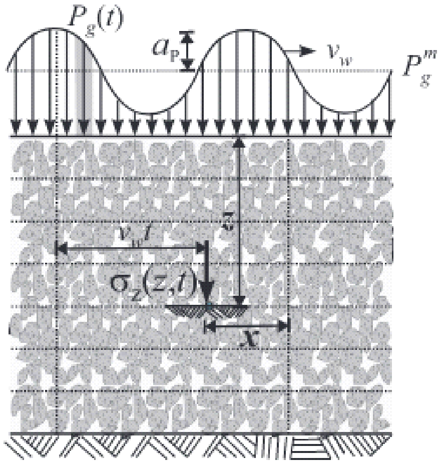

Figure 6-5 Vertical stress below the ground surface due to a pressure wave.

Where P_g is the gas pressure at a time t and position x; P_g^m is the mean atmospheric pressure, and its fluctuations are added by a wave with amplitude a_P, frequency f_w, and wavelength λ_w given by v_w/f_w. The passage of this wave induces normal and shear stress increments into the soil that are calculated using the Boussinesq solution considering a series of thin strips (Braja, 2011) with infinite depth (2D plane strains), given by the equation:

$$\Delta\sigma_z = \frac{q_x}{\pi} \cdot [\alpha + sin\alpha \cdot cos(\alpha + 2\beta)] \qquad (2)$$

Where $\Delta\sigma_Z$ is the increment in vertical stress, q_x is the surface load per unit of length, and α and β are the angles shown in Figure 6-6.

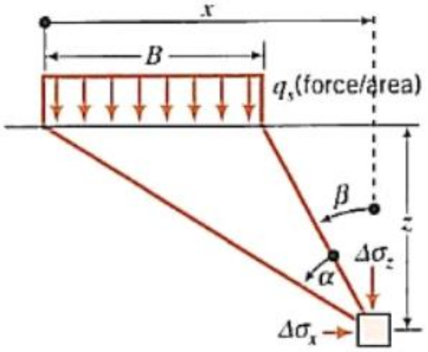

Figure 6-6 Layout of the Boussinesq solution for the stress increment induced by a strip load (Braja, 2011).

The remaining components for the horizontal and shear stresses increment may be calculated as follows:

$$\Delta\sigma_x = \frac{q_x}{\pi} \cdot [\alpha - sin\alpha \cdot cos(\alpha + 2\beta)] \qquad (3)$$

$$\Delta\sigma_y = \frac{2}{\pi} \cdot (\beta \cdot \nu) \qquad (4)$$

$$\Delta\tau_{zx} = \frac{q_x}{\pi} \cdot [sin\alpha \cdot cos(\alpha + 2\beta)] \qquad (5)$$

Where $\Delta\sigma_z$ represents the total stress increment, and the position of the angles α and β can be observed in Figure 6-6. Note that the horizontal component in the normal direction to the studied plane is obtained via the utilisation of the Poisson's ratio ν.

To account for the infinite strips, integration along the direction x of each strip whose loas is $q_x = P_g\ dx$ leads to:

$$\sigma_v(z,t) = \int_{\infty}^{\infty} \frac{\left(P_g^m + a_P \cos[2\pi(f_w t + x/\lambda_w)]\right) \cdot [\alpha + sin\alpha \cdot cos(\alpha + 2\beta)]}{\pi} dx \qquad (6)$$

At each instant, this expression is evaluated numerically, obtaining the total stress increment resulting from the wave.

Model for the diffusion of a compressible fluid into porous media

The flow of the gas into a porous material is governed by the diffusion equation, as presented in the work of Wu (Wu et al., 1998). The corresponding expression is:

$$\phi \frac{\partial(\rho_g)}{\partial t} = -\nabla \cdot \left(\rho_g v_g\right) \qquad (7)$$

Where t is the time, ϕ is the material porosity,ρ_g is the density of the gas, and v_g is Darcy's gas velocity.

As phenomenological relationships, the model uses the real gas law, the elastic compression law proposed by Mesri (Mesri & Vardhanabhuti, 2009), and the real gas law (Böttcher et al, 2012). Gass mass conservation and phenomenological relationships lead to the following expression for the evolution of gas pressure over time. Appendix A presents the derivation of this expression.

$$\frac{\partial P_g}{\partial t} = \frac{(1+e)M}{(M+P_g e)} \nabla \cdot \left(\frac{k_g P_g}{\mu_g T} \nabla P_g \right) + \frac{P_g e}{M+P_g e} \cdot \frac{\partial \sigma_T}{\partial t} \quad (8)$$

This differential equation can be solved numerically via Finite Differences in a transient one-dimensional domain (1D) of the line below a point over which the wave passes. A MATLAB script was implemented to evaluate the proposed FEM model in different scenarios. Note that while the equation is solved in a 1D domain, the calculation of the total stress due to the passage of the surface wave is computed in a 2D domain (integrating the increment induced by every segment on which the wave is discretised, as seen in Figure 6-5). Table 6-1 presents the parameters involved in the model. Some of these parameters are independent of the planetary environment and mechanical state variables.

Table 6-1. Parameters involved in the model.

Symbol	Parameter name	Role
E	Youngs modulus	Material parameter
ν	Poisson ratio	Material parameter
k	Permeability	Material parameter
ρ	Density	Material parameter
ϕ	Porosity	Material parameter
μ	Viscosity	Gas parameter

Elastic parameters (ν and E) enable computing the strains resulting from the induced effective stress, as already explained. Another parameter is the soil density ρ, which defines the initial material unit weight used to determine the initial stress condition; it also is related to soil porosity ϕ, which is necessary to model the compressing behaviour of the soil. Finally, the material permeability k is the most important parameter since it governs the gas infiltration into each soil layer, which induces variations in the effective stress used to calculate compliance.

The scenarios modelled include incompressible soil layers, such as rock layers, which are too stiff to be affected by the variations of effective stress induced by atmospheric pressure fluctuations. A bottom stiff layer can be placed on a model and serve as a boundary condition. These stiff rock materials have very high values of Youngs modulus. Thus, it is considered that E values for such layers are not dependent on the planetary location of any of the considered scenarios but rather on the material present at each location up to the depth of interest.

On the contrary, the softer materials, such as the regolith and soils on the earth's surface, may be affected by the effective stress variations due to atmospheric pressure fluctuations. Their values of E are much lower than the rock layers described previously, and in consequence, they must be carefully selected for each scenario. The strains, however, are very small, and the material can be described with a single elastic modulus E.

For the case of Mars, where the surface material is a very loose deposit, the work presented in previous chapters indicates that a value of 20 MPa can be adequate for materials at the very low densities present on Mars.

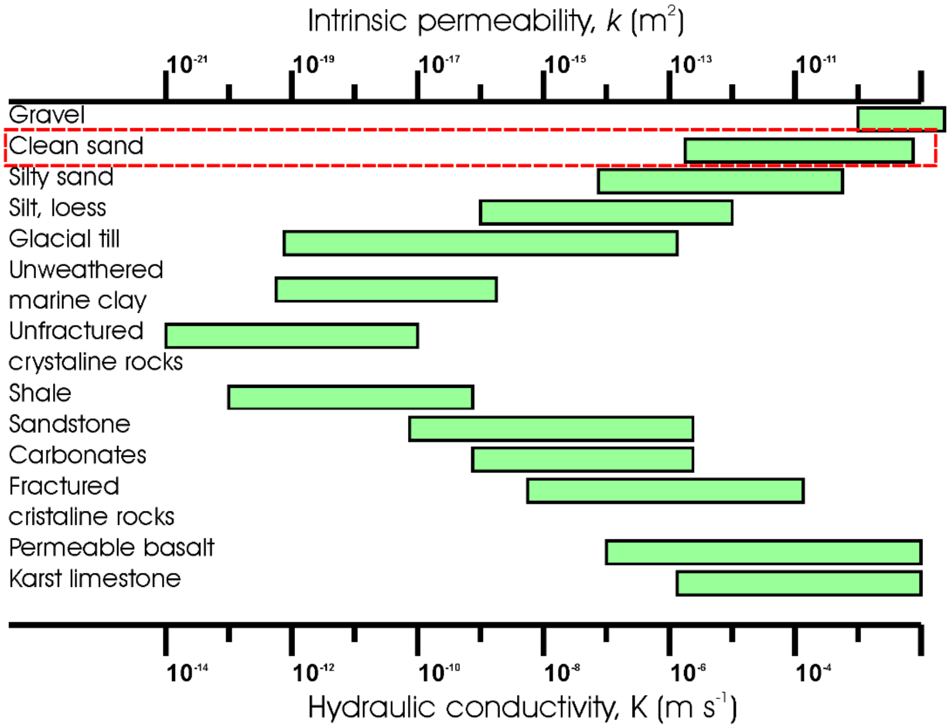

Figure 6-7. Values of intrinsic permeability for several materials (data from Berhane, 2006).

The value of the intrinsic permeability κ is not dependent on the planetary environment since it has been observed to be heavily dependent on material grain size (Mahmoodlu et. Al., 2018). Since it is highly sensitive to mean particle size, it is evaluated over a wide range of values around the expected range for each type of material (which can be seen in Figure 6-7). Permeability (Côté, 2011) and hydraulic conductivity can be measured with experiments and simulations or estimated from other properties (Jarvis, 2002; Wells, 2006). The effect of particle shape may be relevant here, too.

On the contrary, the values for air viscosity depend on each situation. The kinematic viscosity μ of the gas occupying the material depends on the temperature. In the terrestrial case, this would be air, while carbon dioxide gas is present in the Martian case. The different parameter values for each scenario must then be selected, and Sutherland's Law was chosen for this purpose. This expression holds from -170°C to 750°C (Ellis et al., 2010). Since Mars is colder than the Earth and temperatures as low as -170 °C are only seen in the higher levels of the atmosphere as seen in Viking 1 and 2 data (Petropoulos, 1989), the expression holds valid in this context. This relationship enables accounting for the present gas via constants. It describes the variation of the viscosity value at different temperatures, thus allowing the model to account for both variables simultaneously. The expression for the law is:

$$\mu(T) = \mu_0 \left(\frac{T}{T_0}\right)^{3/2} \left(\frac{T_0+S}{T+S}\right) \qquad (10)$$

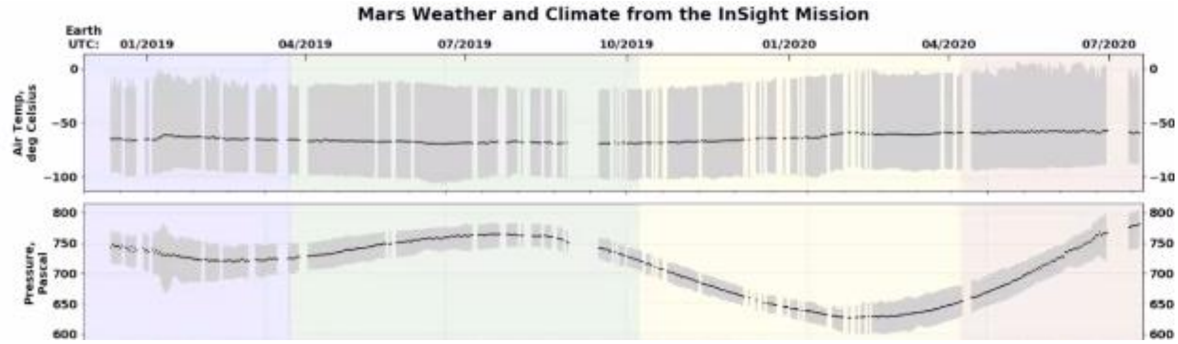

Figure 6-8. Mars InsSight data for atmospheric pressure for two years. (Image credit: NASA JPL, n.d.).

Where μ is the dynamic viscosity in $[N \cdot s]/[m^2]$ or $[Pa \cdot s]$, μ_0 is the dynamic viscosity of the gas at a reference temperature T_0 of 273, T is the temperature for the calculation and S is a constant known as Sutherlands temperature, with values of 110.4 K for air and 222 K for the CO2 which accounts for over 96% of the composition of the air on Mars. The results for the cases of Mars and Earth in a range of -200 °C to 300 °C are plotted on Figure 6-9.

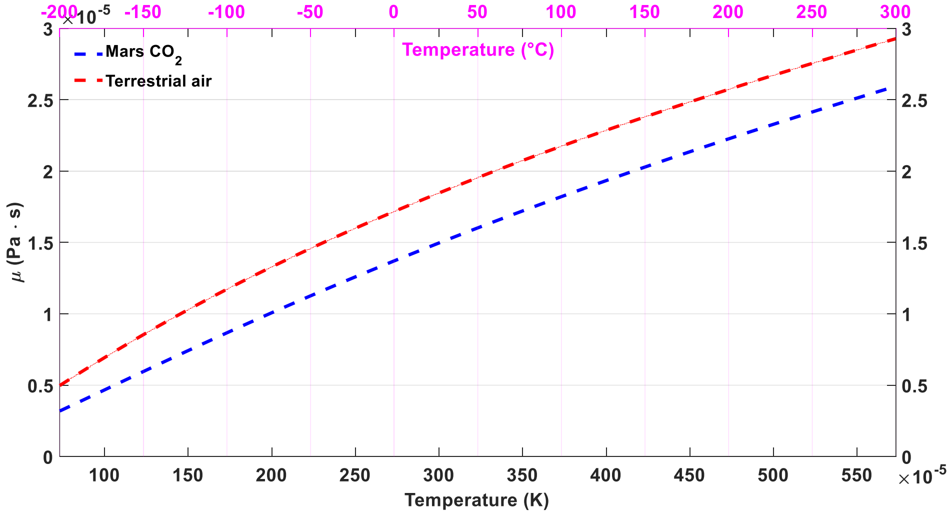

Figure 6-9. Kinematic Viscosity dependence on Temperature after Sutherland law.

Taking Earth's temperature at 20°C and the temperature at the Mars Insight site as -70°C (which is the mean value recorded on Mars APSS weather data through an entire year, as seen in Figure 6-8) and applying these expressions to these scenarios yields a value of 9.817 x 10^{-6} $Pa \cdot s$ for Mars Insight and of 1.8 x 10^{-5} $Pa \cdot s$ for terrestrial conditions.

Part B: Analysis of compliance, effective and total stress. Case of Earth.

In this first step, the problem is evaluated under conditions that recreate the scenario of the original Sorrell's work. The passage of a periodic wave is evaluated under the conditions displayed in Figure 6-10 to achieve this. A wide range of 12 frequencies/periods was evaluated to determine the effect of the wave characteristics on the results (observed in the Sorrells results to be of some significance). The parameters for the model layers were derived from the original Sorrells report, summarising this information in Table 6-2.

Table 6-2. Material parameters adapted for the model.

Layer	Depth	Density	S wave velocity	P wave velocity	ν
Layer 1	0-100 m	1994.63 kg/m^3	462.44 m/s	1374.22 m/s	0.43
Layer 2	100–1000 m	2174.87 kg/m^3	2532.95 m/s	4337.52 m/s	0.24

The layout described in the report consists of a very rigid rock top below a less stiff material, and E was estimated to be 4 GPa and 41 GPa for these layers, respectively. Since no information has been provided on a layer below the bottom rock, and the measurements of Sorrells were taken at a depth of 183m, it was decided to include a stiff impermeable rock at the bottom of the model to act as a boundary condition.

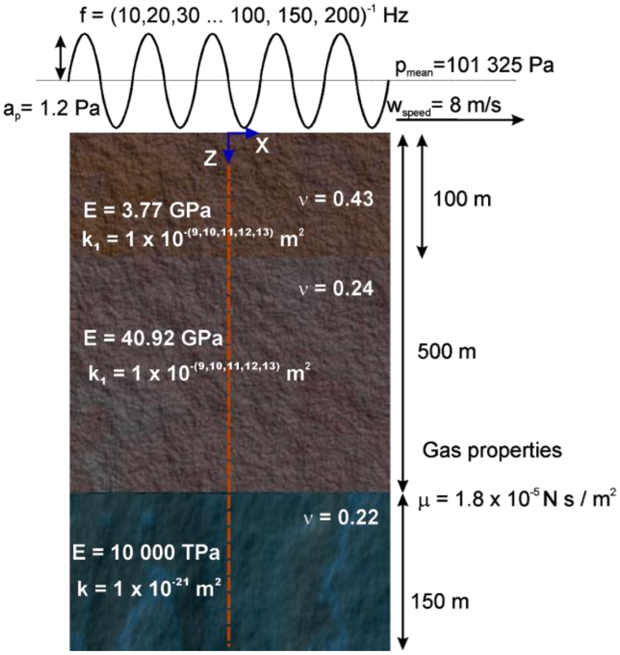

Figure 6-10. Conditions for the Sorrells scenario, under the passage of a periodic wave.

The chosen value for the intrinsic permeability was expected to play an essential role in the pore pressure propagation in the studied medium. It was observed that this could reach the extent of a determined set of model conditions (i.e., depth, density, Pressure value) being an unsuitable choice due to numerical instability occurring when a too-shallow layer is evaluated under too permeable conditions (higher κ values). A range of permeabilities spanning from $1\text{x}10^{-9}$ m^2 to $1\text{x}10^{-13}$ m^2 was evaluated for this effect.

Boundary conditions

Since a one-dimensional domain is being used to solve the problem, the relevant boundary conditions for the problem must be specified on the surface and at the bottom of the model. The upmost layer is under the direct action of the passing wave, and thus $P(z = 0, t) = P(t)$. The lower boundary is also considered impermeable and infinitely rigid compared to the modulus imposed upon the first layer of the domain.

Initial conditions

The initial pressure value at all nodes inside the domain is set to the atmospheric pressure of 101 325 Pa for this scenario.

Effect on compliance of gas diffusion

The results obtained applying the proposed model to the terrestrial case are now presented. The MATLAB script of the model stores the necessary information for 5-time instants distributed uniformly throughout the calculation and then displays plots of the results of interest. These results allow us to appreciate step-by-step calculation of the effective stress and the strain it induces, and these calculation results are now presented in order.

First, Figure 6-11 displays the total stress increment, showing how the value oscillates around the mean value of 0; it also shows that stress increments are induced well beyond the depth of 600 m, showing that calculating only the top 183m to the depth of Sorrells measurement would not be sufficient. It can also be appreciated that higher periods result in deeper propagation of the induced total stresses. This result is independent of the material's permeability since this simply results from calculating the stress increments along the length of the wave and adding them.

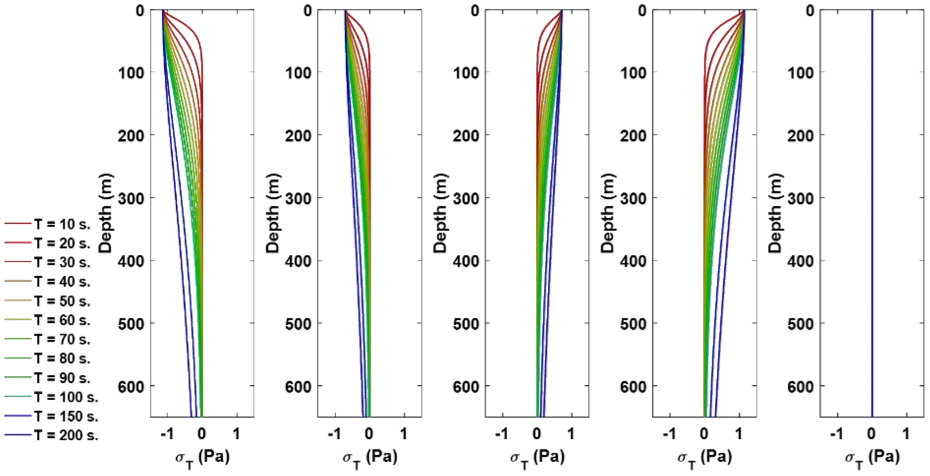

Figure 6-11 Increments of the total stress for the evaluated values of T.

Next Figure 6-12, Figure 6-13 and Figure 6-14 show the pore pressure for the minimum, maximum and intermediate values of permeability used. The highest value is 1x10^{-9} m^2, which induces significant gas infiltration into the porous up to depths of around 10-90 m. By contrast, the lowest value of 1x10^{-13} m^2 barely varies the pore pressure over the first meter. Meanwhile, the intermediate value of 1x10^{-11} m^2 results in effects over the first 5m layer. These results are relevant since they show the depths at which effective stress will be affected, which determine where strain occurs. Since pore pressure does not vary on the second layer (below 100m), only the elastic parameters of the first layer will affect the results when the permeability varies.

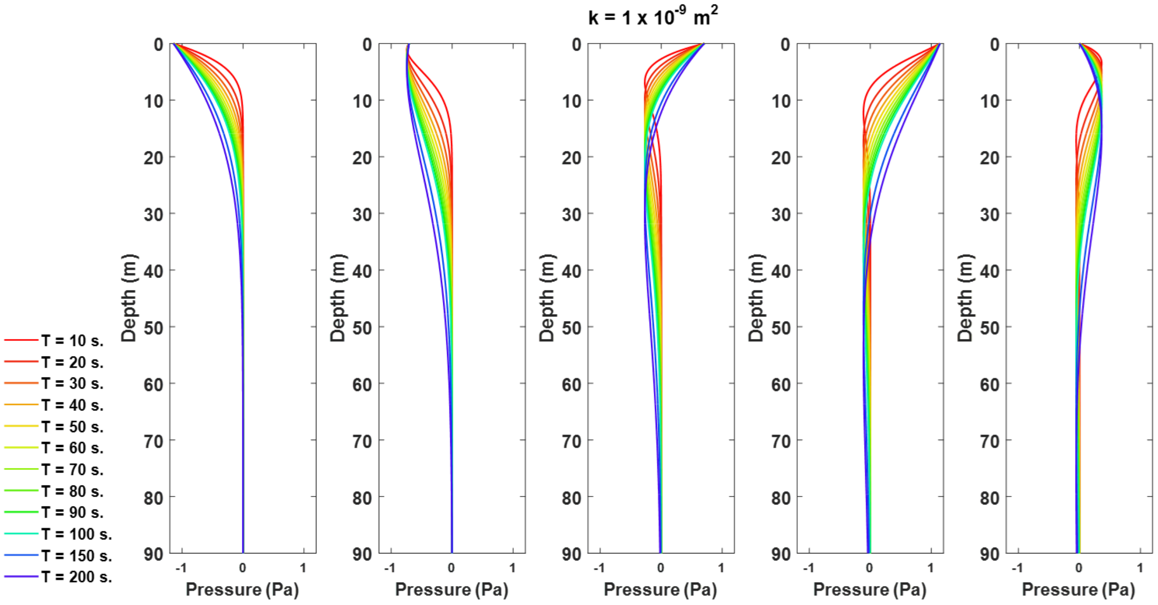

Figure 6-12 The pressure penetrates up to around 60 meters into the soil under the considered conditions and the highest utilised permeability value.

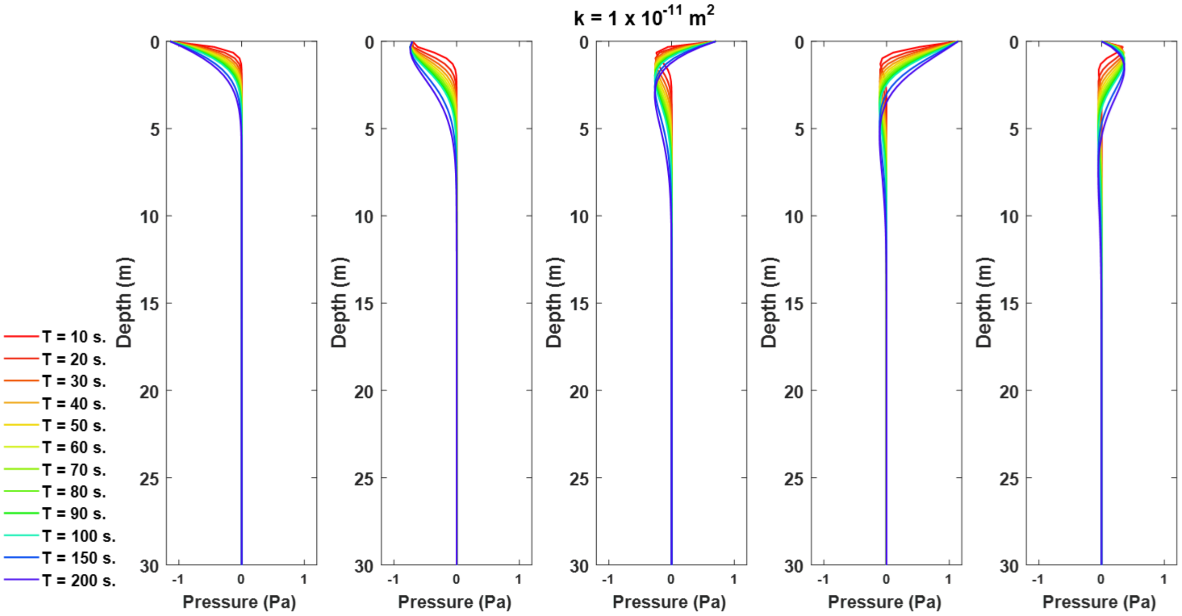

Figure 6-13. The pressure penetrates up to around 8 meters into the soil under the considered conditions and an intermediate selected permeability value.

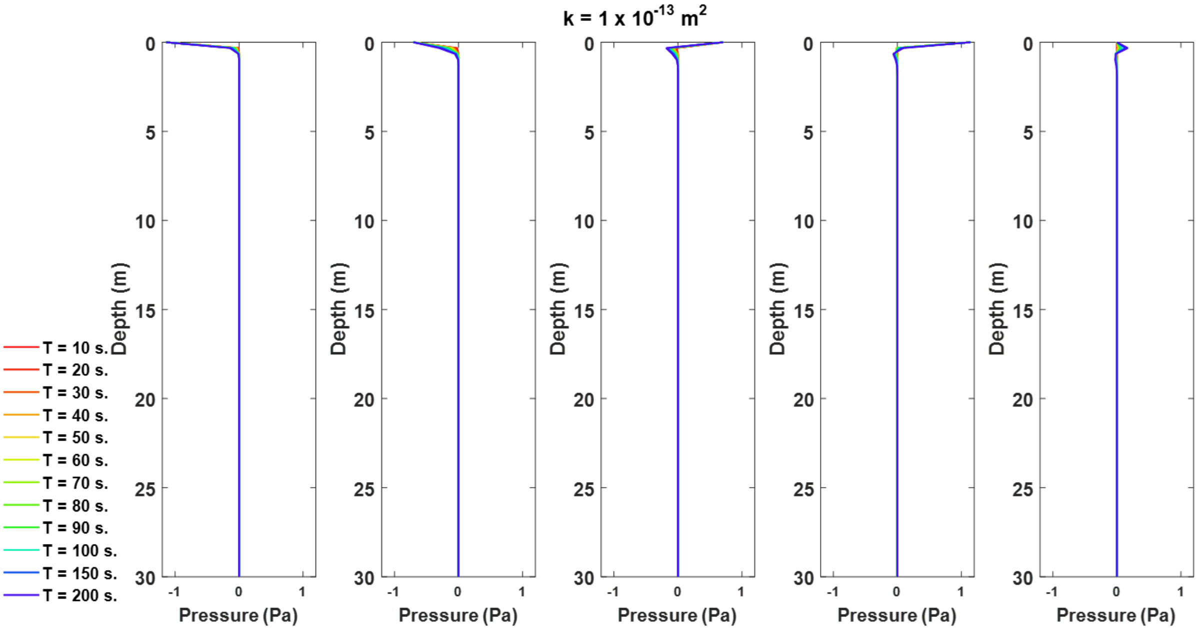

Figure 6-14. The pressure penetrates up to around 2 meters into the soil under the considered conditions and the lowest utilised permeability value.

Figure 6-12, Figure 6-13 and Figure 6-14 also show the significant effect of the period. A higher period results in deeper penetration of the gas into the layer. This can be seen in Figure 6-15 and Figure 6-16, which display the lowest and highest values of the period, respectively. With the lowest period of 10s, even the most permeable material only perceives pressure increments up to 20 m. In contrast, for the highest period of 200 s, some effect exists even at 60m. It can also be seen in both of these figures that only materials with permeability values above 1x10^{-10} m^2 will show a significant effect at depths greater than 10 m.

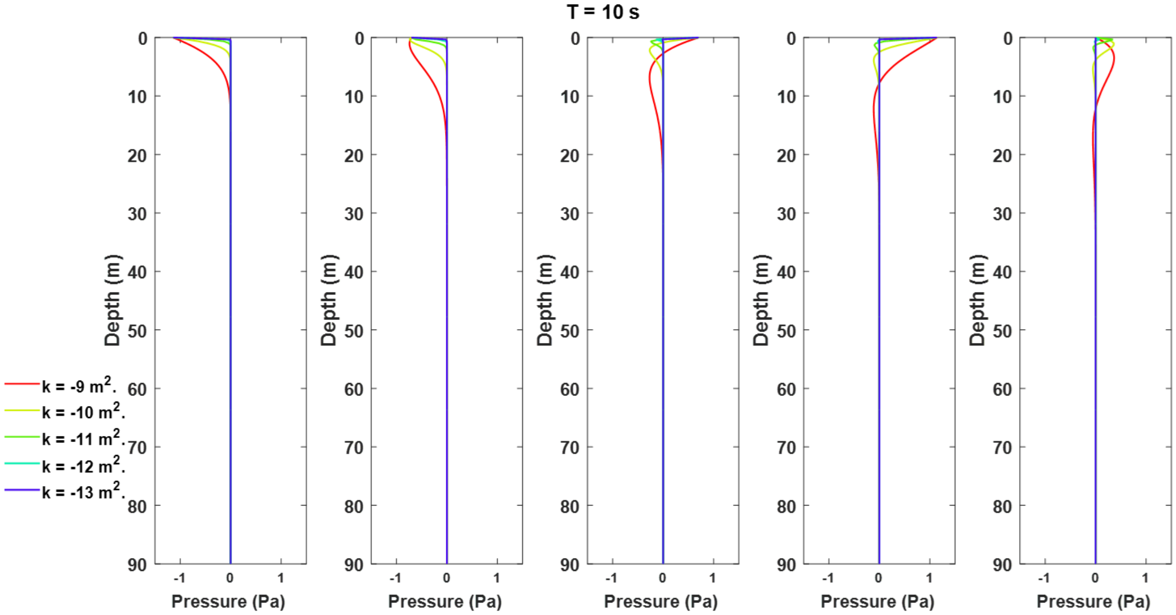

Figure 6-15. Effect of the permeability on material pore pressure for the lowest period of 10 seconds.

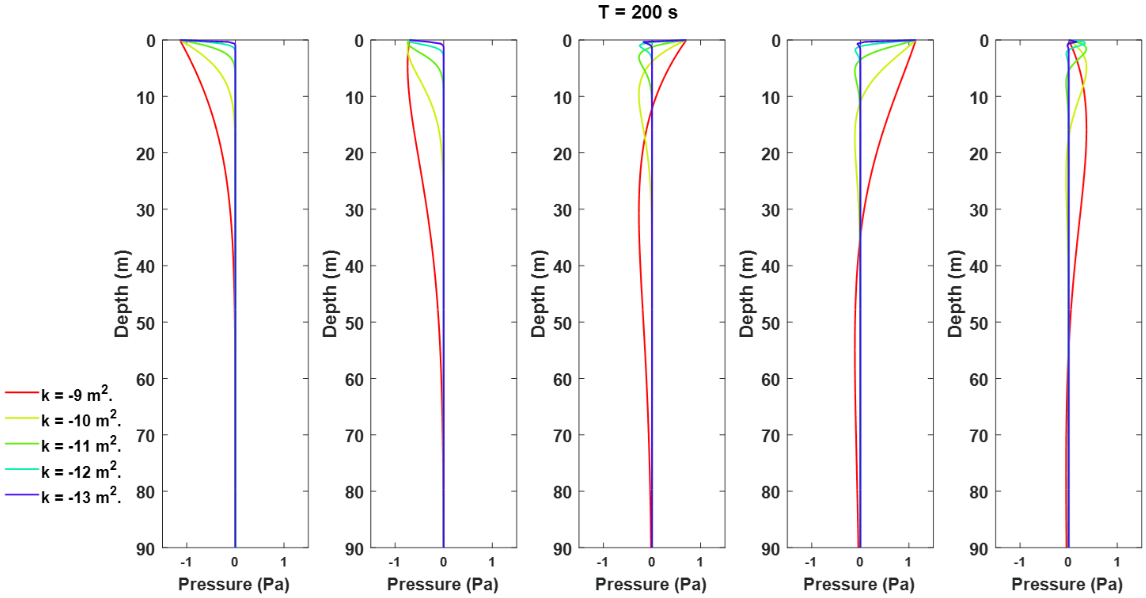

Figure 6-16. Effect of the permeability on material pore pressure for the highest period of 200 seconds.

The following result calculation is the effective stress, which results from subtracting the pore pressure from the total stress. The associated results are shown in Figure 6-17 and Figure 6-18 for the lowest period (10s) and highest (200s) period again. The effective stress changes are limited to the first material layer (100m deep) for the lower period. In contrast, the effect only becomes slight for the highest period value when approaching 650m of depth. This means the model has sufficient depth to study the considered frequency range.

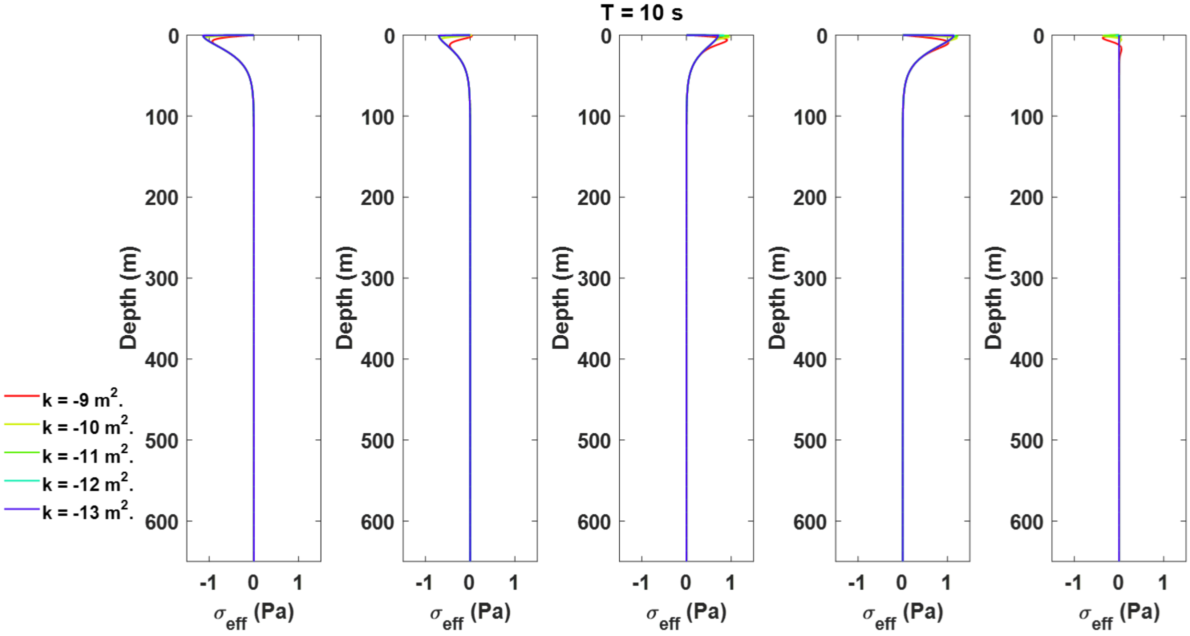

Figure 6-17. Effective stress profiles for the lowest period case presented for the evaluated intrinsic permeability, for the lowest period value of 10 seconds.

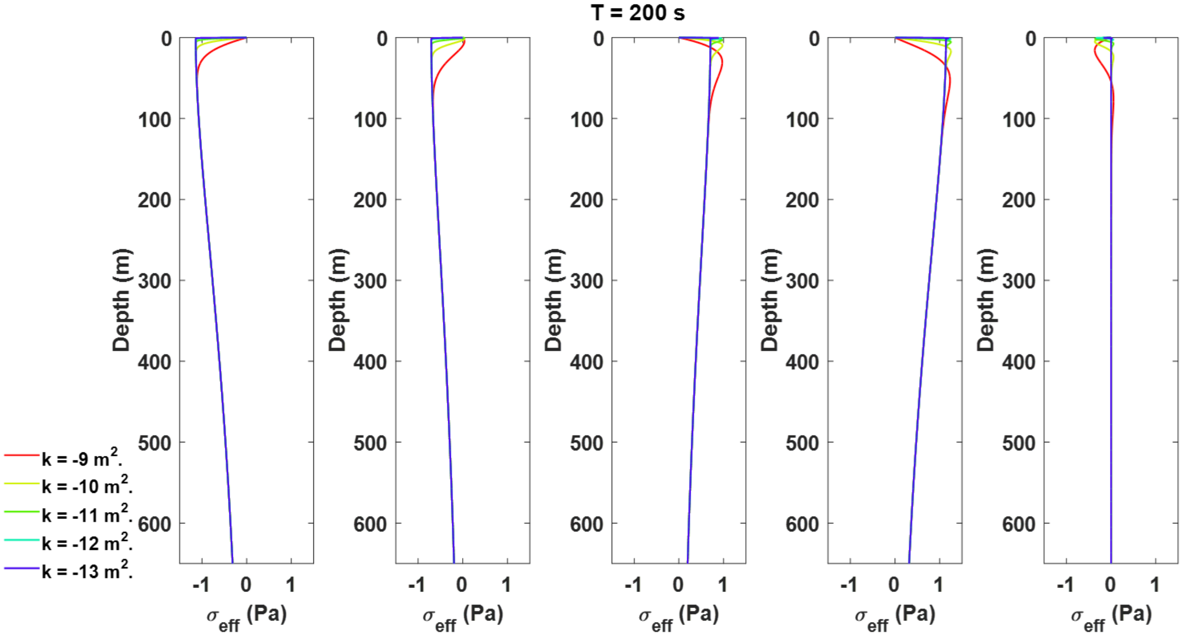

Figure 6-18. Effective stress profiles for the lowest period case presented for the evaluated intrinsic permeability, for the lowest period value of 10 seconds.

Finally, these effective stresses can be used to calculate deformations. The results are shown in Figure 6-19 and Figure 6-20. Both figures show that the second layer located below 100 m, being very stiff, is only slightly deformed. Strain becomes 0 at the 500m, where the bottom rock starts. The surface layer in contrast, is slightly deformed over the first meters for the 10 s case (Figure 6-19) and more significantly deformed for the 200 s case (Figure 6-20).

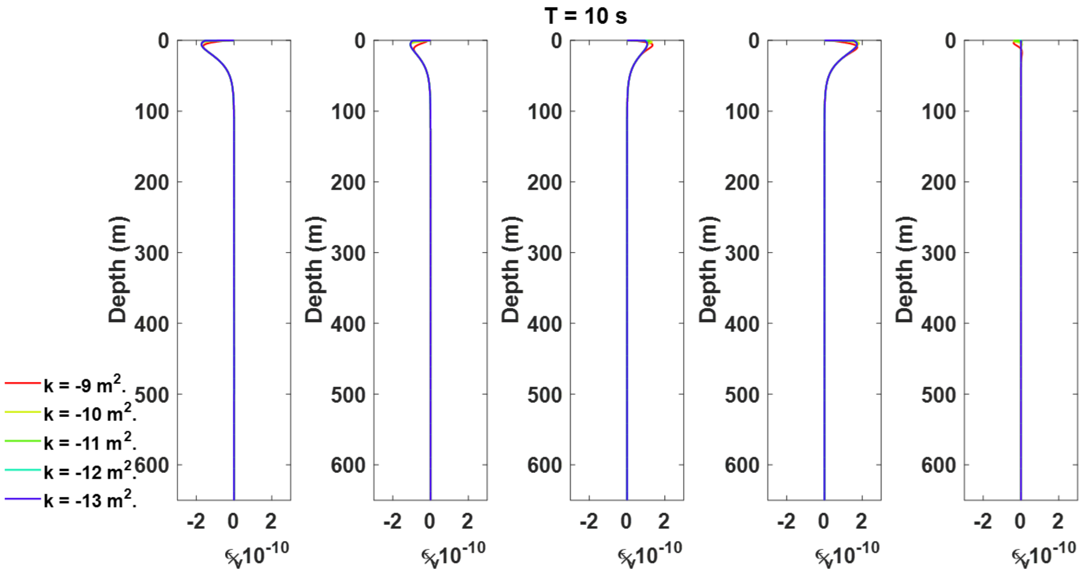

Figure 6-19. Vertical strain profiles for the lowest period case presented for the evaluated intrinsic permeability, for the lowest period value of 10 seconds.

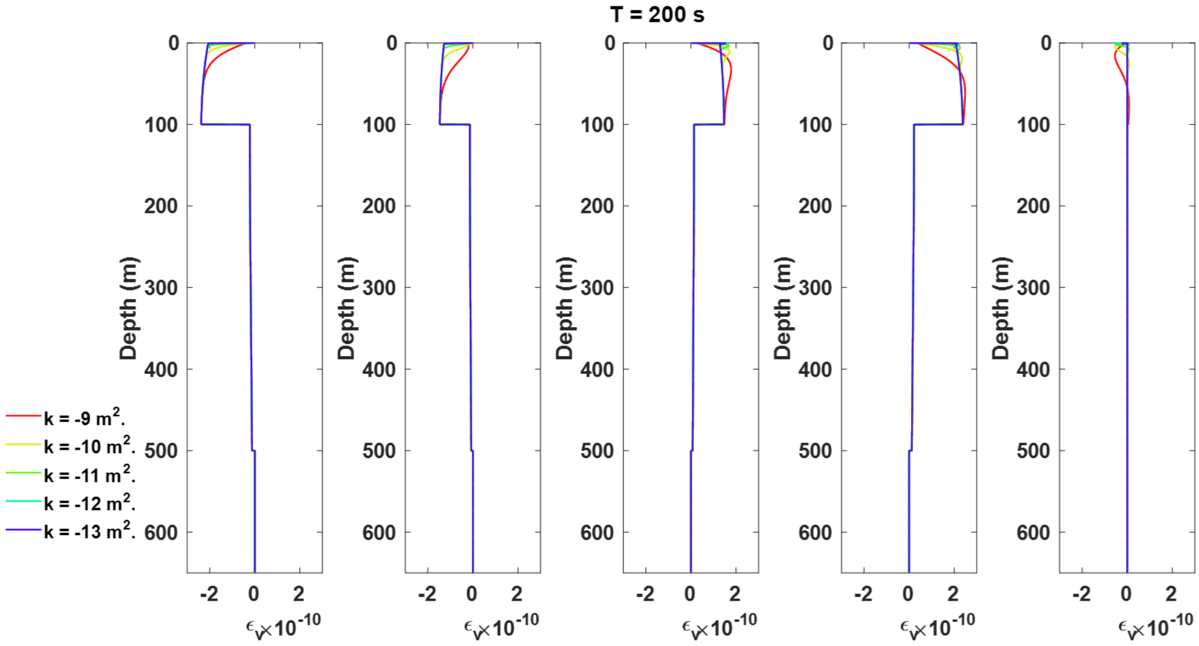

Figure 6-20. Vertical strain profiles for the lowest period case presented for the evaluated intrinsic permeability, for the highest period value of 200 seconds.

It also appears that the effect of the wave period is significantly more substantial than that of the permeability value. The loading process can be appreciated for the chosen value periods in the cycles presented in Figure 6-21 and Figure 6-22, making it possible to arrive at these appreciations somewhat more easily.

It can be observed in Figure 6-21a that while the order of magnitude of the maximum values for both extreme values of permeability coincide with those in Figure 6-21b, the shape of the cycle is more elliptical. The results of 1x10^{-13} m^2 resemble a straight line since it is not far from doing the calculation with total stress, as the pore pressure barely infiltrates the soil.

In contrast, Figure 6-22 shows that the maximum value attained for the extreme values of the period differs by an entire order of magnitude, hence confirming the appreciation that the effect of the period is more significant than that of the permeability for the considered scenario.

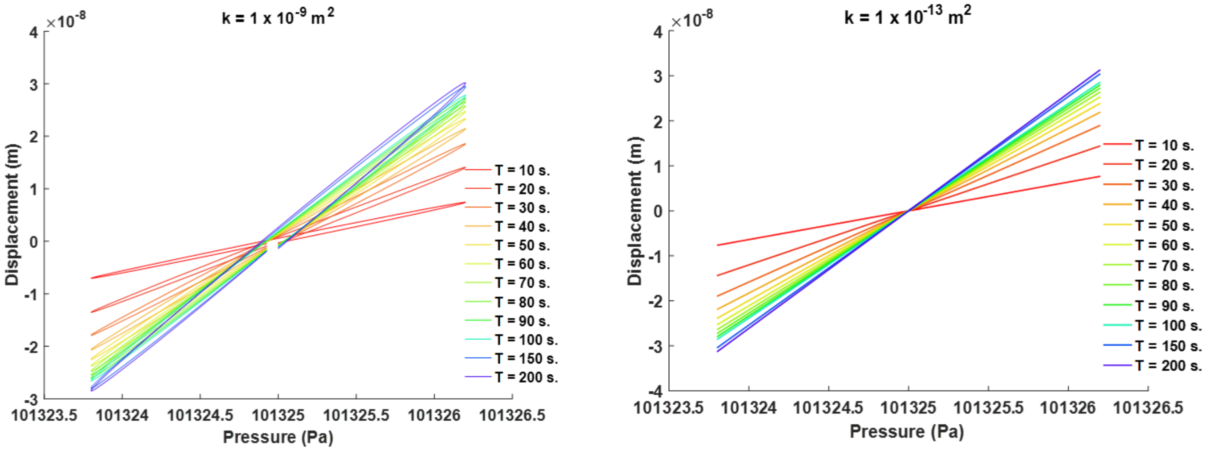

Figure 6-21. Compliance cycles for the lowest and highest values of permeability evaluated.

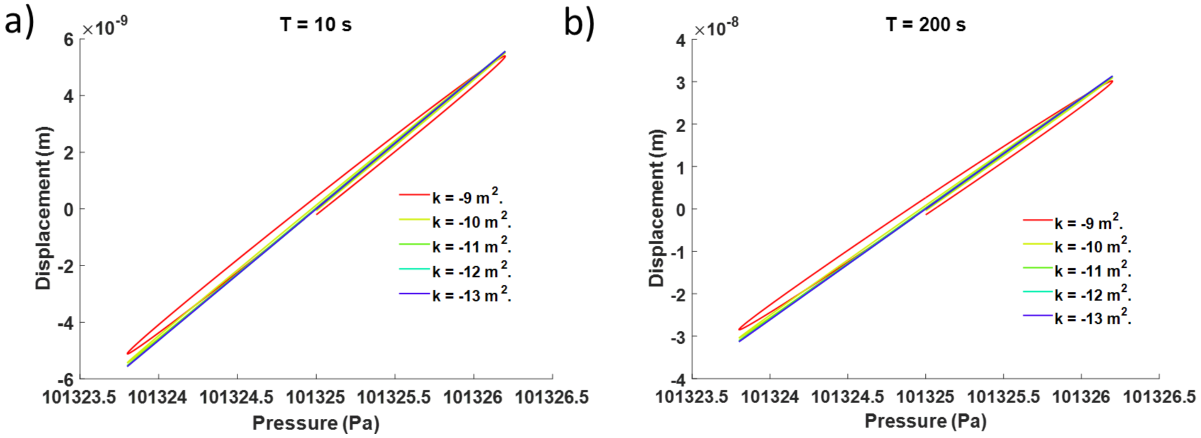

Figure 6-22. Compliance cycles for the lowest and highest values of period evaluated.

In these cycles it can already be appreciated that the effect of period is significantly more relevant than that of material permeability. The slope for the cycles in figure Figure 6-21 varies considerably, while in figure Figure 6-22, no slope variation is apparent. However, the thickness of the ellipsis described by each cycle can vary, suggesting the appearance of some potentially interesting hysterical response.

A global summary of the results is presented in Figure 6-23a and b, where the increasing tendency of compliance with the period with respect to the period can be appreciated. It can also be observed that the permeability effect is of reduced significance. In part b of the figure, it can be appreciated that the variation is in the order of 3 to 4% for the highest permeability value.

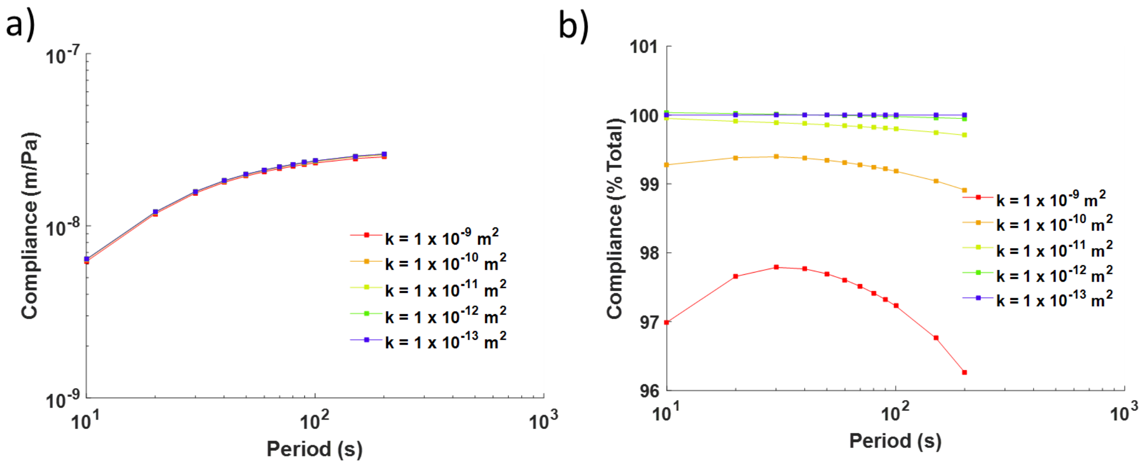

Figure 6-23. Global summary of the terrestrial scenario for the compliance model.

Finally, the comparison with the original Sorrells experimental data with a 95% confidence interval and Sorrells's prediction with an elastic calculation is displayed in Figure 6-24.

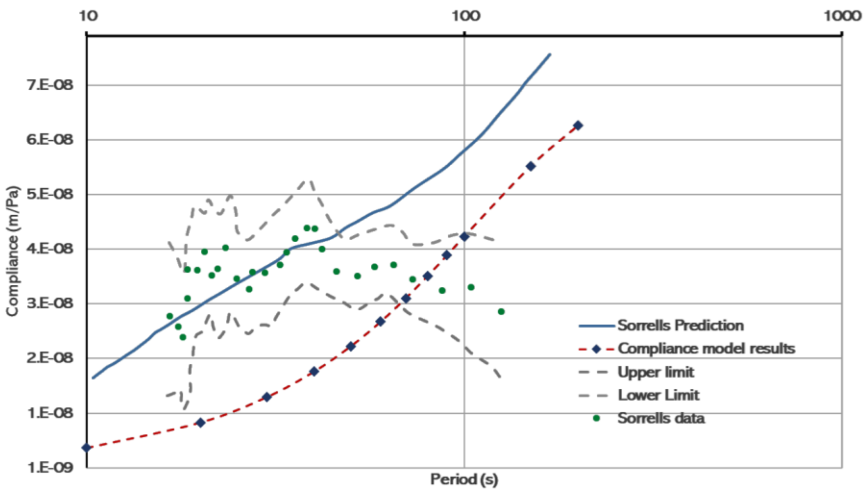

Figure 6-24. Comparison of the results with Sorrells data.

A similar tendency is observed in the attained results, with some offset in the value resulting in a model better suited for predictions in the higher periods contrasting with the better correspondence of the Sorrells model for the lower period range. The model can thus be considered adequate and a valuable complement to the existing tools provided by the original author.

Part C: Application of the ground compliance model to Mars Insight landing site

The second scenario (see Figure 6-25) is modelled after the Mars InSight landing site and seeks to recreate the situation under the lander at Elysium Planitia (Garcia et. al., 2020); it is hoped that this model may be used to contribute to the ongoing and already completed studies around the observed dust-devil events, by incorporating data directly from the APSS TWINS sensors.

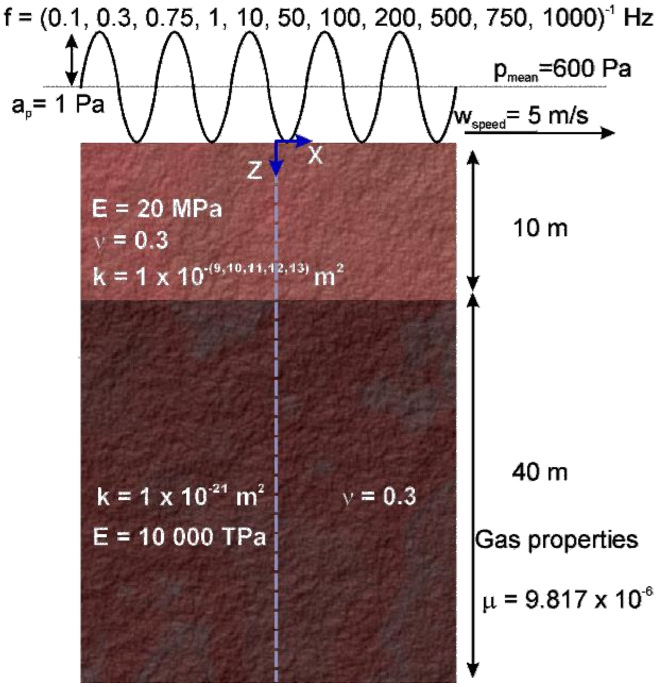

Figure 6-25. Model parameters used for the preliminary evaluation of the Mars scenario.

This preliminary calculation was done again with a sinusoidal wave. Notice that in this case, the 1Pa fluctuations are more representative in contrast to the case of the Earth.

As seen in Figure 6-26, gas penetration concerns the first 2-4 meters of material for the highest permeability values and the longest period considered. This time however, the material is much more compressible with a value of E = 20 MPa.

Results also become less trivial as seen in Figure 6-27, where a monotonic compliance increase with the period is no longer the case (as in the terrestrial scenario). Finally, Figure 6-28 shows that in this scenario the effect of material permeability can be much more substantial, being as significant as 20% for the most permeable materials.

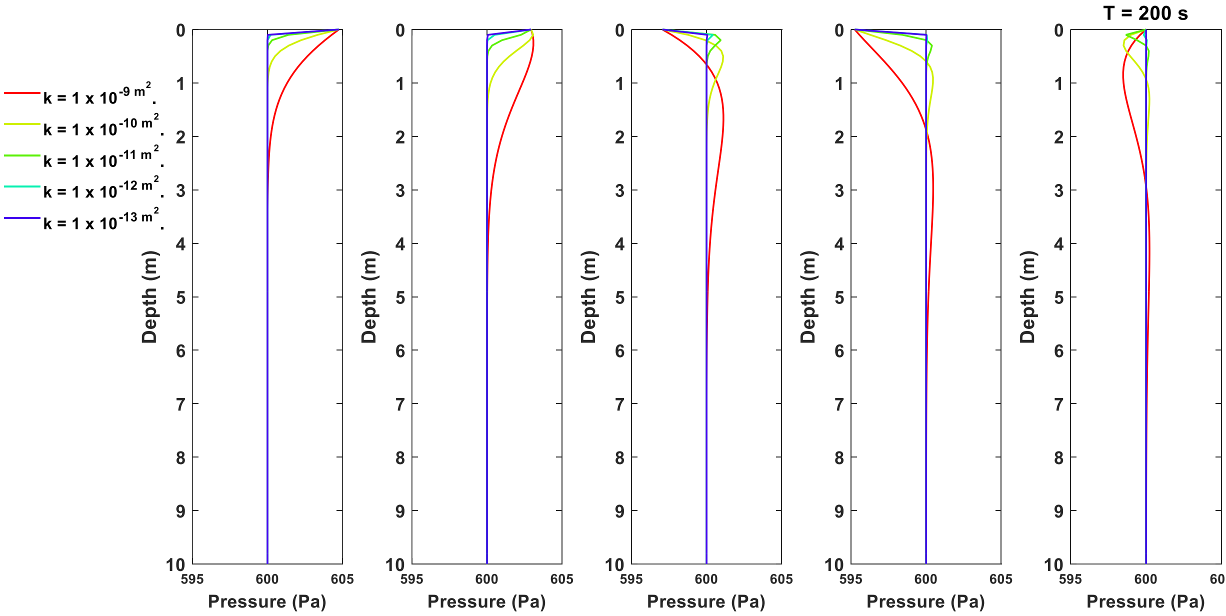

Figure 6-26. Pore pressure in the material for different permeabilities with the simplified Mars scenario.

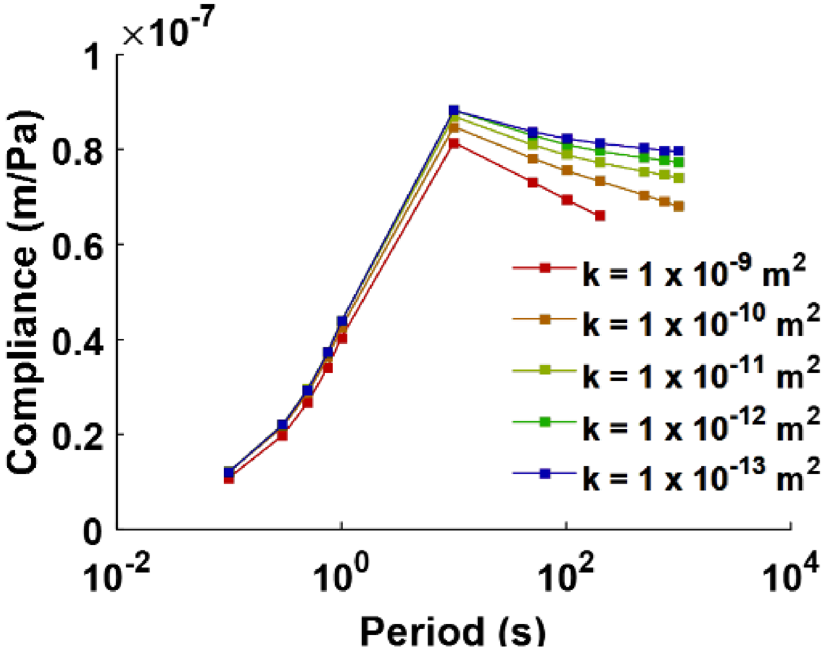

Figure 6-27. Compliance results for the Mars scenario.

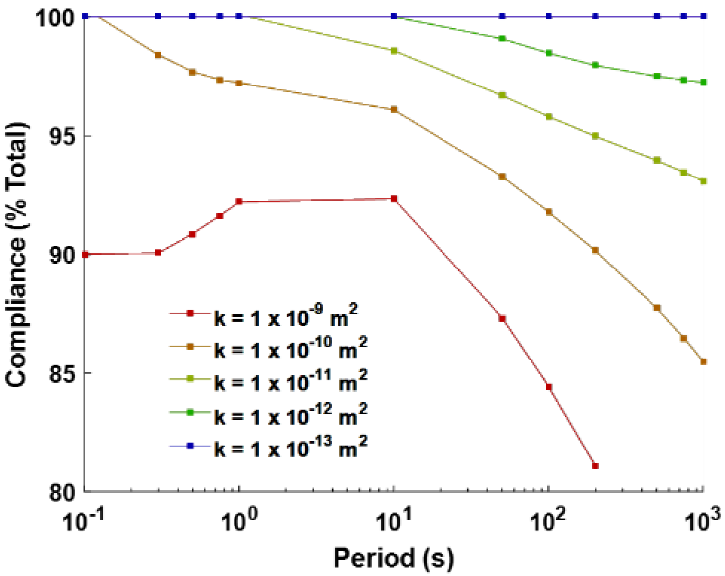

Figure 6-28. Compliance results for the Mars scenario as a percentage of a total stress calculation.

Ongoing work concerns the permeability's effect on the material's damping properties utilising the calculation results, and prospects include application for the landing site of Mars InSight at the Elysium Planitia. The model is hoped to be used in conjunction with actual APSS sensor data instead of the sinusoidal function presented here.

Conclusions

Atmospheric pressure fluctuations can induce surface displacement and are detectable with instruments that are accurate enough. This phenomenon was first observed in the 1970s and is a component of interest when analysing seismic noise. While the case has already been addressed for the case of the Mars InSight landing site, the assumption of the material being treated as a non-porous elastic material may have some effect on the results. Consequently, a model was prepared where the soil is taken as a porous compressible material.

The model is formulated in the time domain and solved with finite differences. Atmospheric pressure is modelled as a passing harmonic wave, which induces total stress increments into the material as the gas infiltrates the permeable material, varying the pore pressure. Then, a soil column is analysed, and its behaviour is calculated based on the effective stress increments it incurs. The equations necessary to derive the model and to implement it in finite differences were developed (see annexe) and solved in MATLAB.

Two scenarios were evaluated, one on Earth and a simplified version of the Mars scenario. The key variables explored were the material permeability and the period of the wave. The trajectory for the lowest permeability materials was perfectly reversible; this is expected since using the lowest permeability value resembles a calculation carried out with only total stresses and means that an appropriate range of permeability values was assessed. In materials with permeability values as low as $1\text{x}10^{-13}$ m^2, it was observed that the gas permeates less than 2 m in all cases considered; in contrast, for the highest values of $1\text{x}10^{-9}$ m^2, the effects were observed to reach over 20 m in depth.

Hysteretical behaviour was observed for the cases of higher material permeability, indicating an effect of the material permeability, estimated to be as high as 3-4% on the compliance value obtained in the most extreme cases of the Sorrells scenario. Preliminary calculations indicate that this effect may be more relevant in the Martian scenario, where they are more considerable with respect to the much lower atmospheric pressure.

Although material permeability plays a role in ground compliance, its effect appears to be much less significant than the wave period's. Using actual APSS data from the weather sensors present at InSight may also be an exciting prospect since signals with a more variable frequency content may result in more valuable results.

References

Banerdt, W. B., Folkner, W. M., Dehant, V., Le Maistre, S., Yseboodt, M., Rivoldini, A., Van Hoolst, T., Asmar, S. W., & Golombek, M. P. (2018). The InSight mission. *Space Science Reviews*, *214*(5).

Bardera, R., Sor, S., & García Margariño, A. (2020). Aerodynamics of Mars 2020 Rover Wind Sensors. In *Mars Exploration* (Vol. 1, Issue 1, p. 13). IntechOpen.

Böttcher, N., Singh, A. K., Kolditz, O., & Liedl, R. (2012). Non-isothermal, compressible gas flow for the simulation of an enhanced gas recovery application. *Journal of Computational and Applied Mathematics*, *236*(18), 4933–4943. https://doi.org/10.1016/j.cam.2011.11.013

Cho, G.-C., Dodds, J., & Santamarina, J. C. (2006). Particle Shape Effects on Packing Density, Stiffness, and Strength: Natural and Crushed Sands. *Journal of Geotechnical and Geoenvironmental Engineering*, *132*(5), 591–602. https://doi.org/10.1061/(asce)1090-0241(2006)132:5(591)

Côté, J., Fillion, M. H., & Konrad, J. M. (2011). Intrinsic permeability of materials ranging from sand to rock-fill using natural air convection tests. *Canadian Geotechnical Journal*, *48*(5), 679–690. https://doi.org/10.1139/t10-097

Delyukov, A., & Didyk, L. (1999). The effects of extra-low-frequency atmospheric pressure oscillations on human mental activity. *International Journal of Biometeorology*, *43*(1), 31–37. https://doi.org/10.1007/s004840050113

Fayon, L., Knapmeyer-Endrun, B., Lognonné, P., Bierwirth, M., Kramer, A., Delage, P., Karakostas, F., Kedar, S., Murdoch, N., Garcia, R. F., Verdier, N., Tillier, S., Pike, W. T., Hurst, K., Schmelzbach, C., & Banerdt, W. B. (2018). A Numerical Model of the SEIS Leveling System Transfer Matrix and Resonances: Application to SEIS Rotational Seismology and Dynamic Ground Interaction. In *Space Science Reviews* (Vol. 214, Issue 8). Springer Nature B.V. https://doi.org/10.1007/s11214-018-0555-9

Jarvis, N. J., Zavattaro, L., Rajkai, K., Reynolds, W. D., Olsen, P. A., McGechan, M., Mecke, M., Mohanty, B., Leeds-Harrison, P. B., & Jacques, D. (2002). Indirect estimation of near-saturated hydraulic conductivity from readily available soil information. *Geoderma*, *108*(1–2), 1–17. https://doi.org/10.1016/S0016-7061(01)00154-9

Kenda, B., Drilleau, M., Garcia, R. F., Kawamura, T., Murdoch, N., Compaire, N., Lognonné, P., Spiga, A., Widmer-Schnidrig, R., Delage, P., Ansan, V., Vrettos, C., Rodriguez, S., Banerdt, W. B., Banfield, D., Antonangeli, D., Christensen, U., Mimoun, D., Mocquet, A., & Spohn, T. (2020). Subsurface Structure at the InSight Landing Site From Compliance Measurements by Seismic and Meteorological Experiments. *Journal of Geophysical Research: Planets*, *125*(6), 1–30. https://doi.org/10.1029/2020JE006387

Lorenz, R. D., Lemmon, M. T., Maki, J., Banfield, D., Spiga, A., Charalambous, C., Barrett, E., Herman, J. A., White, B. T., Pasco, S., & Banerdt, W. B. (2020). Scientific Observations With the InSight Solar Arrays: Dust, Clouds, and Eclipses on Mars. *Earth and Space Science*, *7*(5), 1–28. https://doi.org/10.1029/2019EA000992

Mahmoodlu, M. G., van Genuchten, M. T., Sweijen, T., & Raoof, A. (2018). Unsaturated hydraulic properties of heterogeneously packed sands: A pore-scale computational study. *Journal of Hydrology*, *565*(July), 570–580. https://doi.org/10.1016/j.jhydrol.2018.07.060

Mesri, G., & Vardhanabhuti, B. (2009). Compression of granular materials. *Canadian Geotechnical Journal*, *46*(4), 369–392. https://doi.org/10.1139/T08-123

Shen, Y., Zhu, Y., Liu, H., Li, A., & Ge, H. (2018). Macro-meso effects of gradation and particle morphology on the compressibility characteristics of calcareous sand. *Bulletin of Engineering Geology and the Environment*, *77*(3), 1047–1055. https://doi.org/10.1007/s10064-017-1157-6

Wells, T., Fityus, S., Smith, D. W., & Moe, H. (2006). The indirect estimation of saturated hydraulic conductivity of soils, using measurements of gas permeability. I. Laboratory testing with dry granular soils. *Australian Journal of Soil Research*, *44*(7), 719–725. https://doi.org/10.1071/SR06037

Zheng, J., Hryciw, R. D., & Ventola, A. (2017). Compressibility of Sands of Various Geologic Origins at Pre-crushing Stress Levels. *Geotechnical and Geological Engineering*, *35*(5), 2037–2051. https://doi.org/10.1007/s10706-017-0225-9

Appendix A: Demonstration of the compliance model

This appendix contains a detailed demonstration of the procedure to derive the compliance model used in this work.

The starting expression is the diffusion equation as presented by Wu et al. (1998) for a gas in porous media:

$$\phi \frac{\partial(\mathrm{P}_g)}{\partial t} = -\nabla \cdot \left(\rho_g v_g\right) \qquad \text{(A1)}$$

Where t is the time, ϕ is the material porosity, ρ_g is the density of gas, P_g is the gas pressure, and v_g is the Darcy's velocity of the gas.

The density of the gas can be assumed to be constant at this scale, and the density of the gas is given by $\rho_g = m_g / \phi_s$. In a porous medium whose porosity is ϕ_s , the mass of gas in an elementary volume is:

$$m_g = \rho_g \phi_s \qquad \text{(A2)}$$

Therefore, allowing the original expression to be rewritten as:

$$\frac{\partial m_g}{\partial t} = -\nabla \cdot \left(\rho_g v_g\right) \qquad \text{(A3)}$$

where t is the time, m_g is the mass of gas, ρ_g its density, and v_g is the Darcy's velocity of the gas. This velocity is defined as:

$$v_g = -\frac{k_g}{\mu_g}\left(\nabla P_g - \rho g\right) \qquad \text{(A4)}$$

where k_g is the gas-phase permeability, μ_g and P_g correspond to the viscosity and the pressure of the gas respectively, and g is gravity. The latter is an effect that may be considered as negligible, given the low weight of gasses even on Earth (which is further decreased in Mars by a lighter atmosphere and a lower gravity). The expression may then be simplified to:

$$v_g = -\frac{k_g}{\mu_g}\left(\nabla P_g\right) \qquad \text{(A5)}$$

Furthermore, the ideal gas law allows relating the temperature, the density and the pressure of gas as follows:

$$\rho_g = \frac{M_g P_g}{RT} \qquad \text{(A6)}$$

where M_g is the molecular weight of the gas, R the universal gas constant; and T the temperature.

However, when considering a real gas, the compressibility depends on its state equation. For real gases (Böttcher et al., 2012) proposed to use a compressibility factor Z into the equation of ideal gasses, this coefficient describes the deviation of the gas behavior from an ideal gas. Therefore, the density of a gas becomes:

$$\rho_g = \frac{M_g P_g}{ZRT} \qquad \text{(A7)}$$

So, it becomes possible to rewrite the original expression into:

$$\frac{\partial m_g}{\partial t} = \frac{M_g}{ZR} \nabla \cdot \left(\frac{k_g P_g}{\mu_g T} \nabla P_g \right) \qquad \text{(A8)}$$

Moreover, when considering compressible soil, the derivative with respect to time (left side in Equation A7 becomes:

$$\frac{\partial m_g}{\partial t} = \frac{\partial}{\partial t} \left(\frac{M_g P_g \phi_s}{ZRT} \right) \qquad \text{(A9)}$$

Now consider Equations A2 relating mass and density, and also A7 which relates the variables of real gases. Taking the derivative of the product with respect to time of the variables P_g and ϕ_s.

$$\frac{\partial m_g}{\partial t} = \frac{M_g P_g}{ZRT} \frac{\partial \phi_s}{\partial t} + \frac{M_g \phi_s}{ZRT} \frac{\partial P_g}{\partial t} \qquad \text{(A10)}$$

The partial derivative $\phi_s = e/(1+e)$ of the porosity regarding the void ratio is:

$$\frac{\partial \phi_s}{\partial e} = \frac{1}{(1+e)^2} \qquad \text{(A11)}$$

So, since $\phi_s = f(e)$, chain rule is applied:

$$\partial \phi_s = \frac{1}{(1+e)^2} \partial e \qquad \text{(A12)}$$

$$\frac{\partial \phi_s}{\partial t} = \frac{1}{(1+e)^2} \frac{\partial e}{\partial t} \qquad \text{(A13)}$$

Now, the chain rule is applied again, including the derivative of the void ratio as a function of the effective vertical stress:

$$\frac{\partial \phi_s}{\partial t} = \frac{1}{(1+e)^2} \cdot \frac{\partial e}{\partial \sigma'_v} \cdot \frac{\partial \sigma'_v}{\partial t} \qquad \text{(A14)}$$

Moreover, the relationship between the void ratio as of Mesri (Mesri & Vardhanabhuti, 2009, 2009) of the porous material and the gas pressure is:

$$\frac{\partial e}{\partial \sigma'_v} = -\left(\frac{1+e}{M} \right) \qquad \text{(A15)}$$

So after replacing A12:

$$\frac{\partial \phi_s}{\partial t} = -\frac{1}{(1+e)^2} \cdot \left(\frac{1+e}{M} \right) \cdot \frac{\partial \sigma'_v}{\partial t} \qquad \text{(A16)}$$

To consider this last factor, one makes use of the definition for effective stress:

$$\sigma' = \sigma_T - P_g \qquad \text{(A17)}$$

After deriving it with respect to time:

$$\frac{\partial \sigma'_v}{\partial t} = \frac{\partial \sigma_{vT}}{\partial t} - \frac{\partial P_g}{\partial t} \qquad \text{(A18)}$$

Thus, the first term on the addition of equation A10, becomes:

$$\frac{M_g P_g}{ZRT}\frac{\partial \phi_s}{\partial t} = -\frac{M_g P_g}{MZRT(1+e)} \cdot \left(\frac{\partial \sigma_{vT}}{\partial t} - \frac{\partial P_g}{\partial t}\right) \qquad \text{(A19)}$$

After replacing $\phi_s = e/(1+e)$ and rearranging the terms, the full equation takes the form:

$$\frac{\partial m_g}{\partial t} = \frac{M_g}{ZRT(1+e)}\frac{\partial P_g}{\partial t} - \frac{M_g P_g e}{MZRT(1+e)} \cdot \left(\frac{\partial \sigma_{vT}}{\partial t} - \frac{\partial P_g}{\partial t}\right) \qquad \text{(A20)}$$

Factorising:

$$\frac{\partial m_g}{\partial t} = -\frac{M_g P_g}{MZRT(1+e)} \cdot \frac{\partial \sigma_{vT}}{\partial t} + \frac{M_g M + M_g P_g e}{MZRT(1+e)}\frac{\partial P_g}{\partial t} \qquad \text{(A21)}$$

Which can be rewritten to a simplified form:

$$\frac{\partial m_g}{\partial t} = c_1 \cdot \frac{\partial \sigma_T}{\partial t} + \cdot\, c_2 \frac{\partial P_g}{\partial t} \qquad \text{(A22)}$$

Where

$$c_1 = -\frac{M_g P_g e}{ZRT(1+e)M} \qquad \text{(A23)}$$

And

$$c_2 = \frac{M_g\left(M + P_g e\right)}{ZRT(1+e)M} \qquad \text{(A24)}$$

It is convenient to evaluate:

$$\frac{c_1}{c_2} = \frac{-\frac{M_g P_g e}{ZRT(1+e)M}}{\frac{M_g\left(M + P_g e\right)}{ZRT(1+e)M}} \qquad \text{(A25)}$$

Resulting in:

$$\frac{c_1}{c_2} = -\frac{P_g e}{M + P_g e} \qquad \text{(A26)}$$

Back to the original expression:

$$\frac{\partial m_g}{\partial t} = \frac{M_g}{ZR}\nabla \cdot \left(\frac{k_g P_g}{\mu_g T}\nabla P_g\right) \qquad \text{(A27)}$$

And replacing:

$$c_1 \cdot \frac{\partial \sigma_T}{\partial t} + c_2 \cdot \frac{\partial P_g}{\partial t} = \frac{M_g}{ZRT}\nabla \cdot \left(\frac{k_g P_g}{\mu_g}\nabla P_g\right) \qquad \text{(A28)}$$

Solving for the variable interest:

$$c_2 \cdot \frac{\partial P_g}{\partial t} = \frac{M_g}{ZRT} \nabla \cdot \left(\frac{k_g P_g}{\mu_g} \nabla P_g \right) - c_1 \cdot \frac{\partial \sigma_T}{\partial t} \tag{A29}$$

Dividing both sides of the equations by c_2

$$\frac{\partial P_g}{\partial t} = \frac{M_g}{c_2 ZRT} \nabla \cdot \left(\frac{k_g P_g}{\mu_g} \nabla P_g \right) - \frac{c_1}{c_2} \cdot \frac{\partial \sigma_T}{\partial t} \tag{A30}$$

Evaluating this first term:

$$\frac{M_g}{c_2 ZRT} = \frac{M_g}{\frac{M_g (M + P_g e)}{ZRT(1+e)M} ZRT} \tag{A31}$$

Resulting in:

$$\frac{M_g}{c_2 ZRT} = \frac{(1+e)M}{(M + P_g e)} \tag{A32}$$

So after substituting on A27 and A28, the final expression becomes:

$$\frac{\partial P_g}{\partial t} = \frac{(1+e)M}{(M + P_g e)} \nabla \cdot \left(\frac{k_g P_g}{\mu_g} \nabla P_g \right) + \frac{P_g e}{M + P_g e} \cdot \frac{\partial \sigma_T}{\partial t} \tag{A33}$$

Discretisation of the model on the spatial domain

The meaning of the space discretisation is transforming the right side of equation A33, which applies to a continuum, into a set of linear equations that applies to the discrete domain made by the set of nodes of a grid.

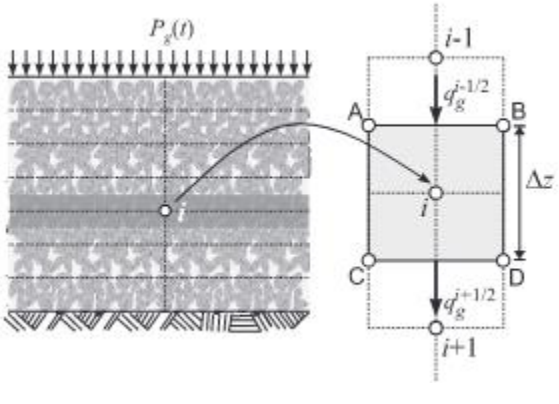

Figure 6-29: Schematic description of the space discretisation for gas flow.

Figure 6-29 exemplifies how a grid allows the space discretization, then, for a node i, transforming the the right side of Equation A33 in discrete form requires the following steps:

First, it is possible to calculate the flow of gas, denoted q_g, in each face of the element of the grid (i, j) as follows:

Flow through the face AB of Figure $Q_{AB} = q_g^{i-1/2}$

Flow through the face CD of Figure $Q_{CD} = q_g^{i+1/2}$

Afterwards, considering isothermal conditions, it is possible to use Darcy's equation to find out the flux of gas q_g as:

$$q_g^{i-1/2} = \rho_g^{i-1/2} \left(\frac{k_g}{\mu_g}\right)^{i-1/2} \frac{P_{g(i-1)} - P_{g(i)}}{\Delta z} \qquad \text{(A34)}$$

$$q_g^{i+1/2} = \rho_g^{i+1/2} \left(\frac{k_g}{\mu_g}\right)^{i+1/2} \frac{P_{g(i)} - P_{g(i+1)}}{\Delta z} \qquad \text{(A35)}$$

where $\left(\frac{k_g}{\mu_g}\right)^{i-1/2}$ represents the mean gas permeability between points i and $i-1$. This mean conductivity can be evaluated using the solution for permeability when two materials are in series:

$$\left(\frac{2\mu_g}{k_g}\right)^{i-1/2} = \left(\frac{\mu_g}{k_g}\right)^{i-1} + \left(\frac{\mu_g}{k_g}\right)^{i} \qquad \text{(A36)}$$

As well, the gas density $\rho_g^{i-1/2}$ is the mean density between points i and $i-1$. Densities in each point are related to pressure through the equation of perfect gases, and after all the simplifications made to the mass balance equation, the only term remaining in Equation A33 is the gas pressure. Therefore, involving the mean density in the flux of gas is equivalent to including the mean gas pressure as follows:

$$q_g^{i-1/2} = \frac{P_{g(i-1)} + P_{g(i)}}{2} \left(\frac{k_g}{\mu_g}\right)^{i-1/2} \frac{P_{g(i-1)} - P_{g(i)}}{\Delta z} \qquad \text{(A36)}$$

$$q_g^{i+1/2} = \frac{P_{g(i+1)} + P_{g(i)}}{2} \left(\frac{k_g}{\mu_g}\right)^{i+1/2} \frac{P_{g(i)} - P_{g(i+1)}}{\Delta z} \qquad \text{(A38)}$$

Leading to:

$$q_g^{i-1/2} = \left(\frac{k_g}{\mu_g}\right)^{i-1/2} \frac{P_{g(i-1)}^2 - P_{g(i)}^2}{2\Delta z} \qquad \text{(A39)}$$

$$q_g^{i+1/2} = \left(\frac{k_g}{\mu_g}\right)^{i+1/2} \frac{P_{g(i)}^2 - P_{g(i+1)}^2}{2\Delta z} \qquad \text{(A40)}$$

Subsequently, since the divergence represents the net flux per unit volume, then the divergence of q_g in a discrete form is:

$$\nabla \cdot q_g \approx \frac{Q_{AB} - Q_{CD}}{\Delta z} \qquad \text{(A41)}$$

After all, the divergence of the gas flow is:

$$\nabla \cdot q_g \approx \left(\frac{k_g}{\mu_g}\right)^{i-1/2} \frac{1}{2\Delta z^2} P_{g(i-1)}^2 + \left(\frac{k_g}{\mu_g}\right)^{i+1/2} \frac{1}{2\Delta z^2} P_{g(i+1)}^2 - P_{g(i)}^2 \left[\left(\frac{k_g}{\mu_g}\right)^{i-1/2} \frac{1}{2\Delta z^2} - \left(\frac{k_g}{\mu_g}\right)^{i+1/2} \frac{1}{2\Delta z^2}\right] \qquad \text{(A42)}$$

Which can be rewritten as:

$$\nabla \cdot q_g \approx \frac{1}{2\Delta z^2}\left(\left(\frac{k_g}{\mu_g}\right)^{i-1/2} P_{g(i-1)}^2 + \left(\frac{k_g}{\mu_g}\right)^{i+1/2} P_{g(i+1)}^2 - P_{g(i)}^2 \left[\left(\frac{k_g}{\mu_g}\right)^{i-1/2} - \left(\frac{k_g}{\mu_g}\right)^{i+1/2}\right]\right) \qquad \text{(A43)}$$

Back to the expression that is being discretised:

$$\frac{\partial P_g}{\partial t} = \frac{(1+e)M}{(M+P_g e)} \nabla \cdot \left(\frac{k_g P_g}{\mu_g} \nabla P_g\right) + \frac{P_g e}{M+P_g e} \cdot \frac{\partial \sigma_T}{\partial t} \qquad \text{(A44)}$$

The obtained expression for the flow is to take the place of the term in parenthesis:

$$\frac{\partial P_g}{\partial t} = \frac{(1+e)M}{(M+P_g e)} \nabla \cdot q_g + \frac{P_g e}{M+P_g e} \cdot \frac{\partial \sigma_T}{\partial t} \qquad \text{(A45)}$$

Moreover, the variables in this expression are to be evaluated at the point of interest i, resulting in the following:

$$\frac{\partial P_{g(i)}}{\partial t} = \frac{(1+e_i)M_i}{(M_i+P_{g(i)} e_i)} \nabla \cdot q_{g(i)} + \frac{P_{g(i)} e_i}{M_i+P_{g(i)} e_i} \cdot \frac{\partial \sigma_{T(i)}}{\partial t} \qquad \text{(A46)}$$

Discretization of the model on the temporal domain

The left hand of A33 represents the evolution of the pressure time. Discretized in time this side of the equation becomes:

$$\frac{\partial P_{g(i)}}{\partial t} \approx \frac{P_{g(i)}^{t+\Delta t} - P_{g(i)}^{t}}{\Delta t} \qquad \text{(A47)}$$

where Δt is the time lapse of discretization. Similarly, it is necessary to approach the term of the vertical stress evolution over time:

$$\frac{\partial \sigma_{T(i)}}{\partial t} \approx \frac{\sigma_{T(i)}^{t+\Delta t} - \sigma_{T(i)}^{t}}{\Delta t} \qquad \text{(A48)}$$

These 2 replacements result in:

$$\frac{P_{g(i)}^{t+\Delta t} - P_{g(i)}^{t}}{\Delta t} = \frac{(1+e_i^t)M_i^t}{\left(M_i^t+P_{g(i)}^t e_i^t\right)} \nabla \cdot q_{g(i)} + \frac{P_{g(i)}^t e_i^t}{M_i^t+P_{g(i)}^t e_i^t} \cdot \left(\frac{\sigma_{T(i)}^{t+\Delta t} - \sigma_{T(i)}^{t}}{\Delta t}\right) \qquad \text{(A49)}$$

Which is solved for the variable for interest:

$$P_{g(i)}^{t+\Delta t} = \frac{(1+e_i^t)M_i^t \Delta t}{\left(M_i^t+P_{g(i)}^t e_i^t\right)} \nabla \cdot q_{g(i)} + \frac{P_{g(i)}^t e_i^t \Delta t}{M_i^t+P_{g(i)}^t e_i^t} \cdot \left(\frac{\sigma_{T(i)}^{t+\Delta t} - \sigma_{T(i)}^{t}}{\Delta t}\right) + P_{g(i)}^t \qquad \text{(A50)}$$

Numerical solution using the explicit FDM.

Cancelling:

$$P_{g(i)}^{t+\Delta t} = \frac{(1+e_i^t)M_i^t\Delta t}{\left(M_i^t+P_{g(i)}^t e_i^t\right)}\nabla\cdot q_{g(i)} + \frac{P_{g(i)}^t e_i^t\left(\sigma_{T(i)}^{t+\Delta t}-\sigma_{T(i)}^t\right)}{M_i^t+P_{g(i)}^t e_i^t} + P_{g(i)}^t \tag{A51}$$

Replacing the expression for the flux, the final obtained equation becomes:

$$P_{g(i)}^{t+\Delta t} = \frac{(1+e_i^t)M_i^t\Delta t}{\left(M_i^t+P_{g(i)}^t e_i^t\right)}\cdot\left(\frac{1}{2\Delta z^2}\left(\left(\frac{k_g}{\mu_g}\right)^{i-1/2}P_{g(i-1)}^2+\left(\frac{k_g}{\mu_g}\right)^{i+1/2}P_{g(i+1)}^2-P_{g(i)}^2\left[\left(\frac{k_g}{\mu_g}\right)^{i-1/2}-\left(\frac{k_g}{\mu_g}\right)^{i+1/2}\right]\right)\right)+\frac{P_{g(i)}^t e_i^t\left(\sigma_{T(i)}^{t+\Delta t}-\sigma_{T(i)}^t\right)}{M_i^t+P_{g(i)}^t e_i^t}+P_{g(i)}^t \tag{A52}$$

And simplifying again:

$$P_{g(i)}^{t+\Delta t} = \frac{(1+e_i^t)M_i^t\Delta t}{\left(M_i^t+P_{g(i)}^t e_i^t\right)}\cdot\left(\left(\frac{k_g}{\mu_g}\right)^{i-1/2}P_{g(i-1)}^2+\left(\frac{k_g}{\mu_g}\right)^{i+1/2}P_{g(i+1)}^2-P_{g(i)}^2\left[\left(\frac{k_g}{\mu_g}\right)^{i-1/2}-\left(\frac{k_g}{\mu_g}\right)^{i+1/2}\right]\right)+\frac{P_{g(i)}^t e_i^t\left(\sigma_{T(i)}^{t+\Delta t}-\sigma_{T(i)}^t\right)}{M_i^t+P_{g(i)}^t e_i^t}+P_{g(i)}^t \tag{A53}$$

LESSONS LEARNED FROM INSIGHT

The Mars InSight mission was successful, acquiring and processing over 4 years of data, far surpassing the projected 1-year lifespan. It provided quite unique geological insights into the red planet, concerning its interior structure and formation history. The SEIS instrument, as the first of its type to be deployed outside of Earth, was key to achieve this. Along the important SEIS contribution, significant results were obtained from the other two main instruments RISE and HP3, as well as from the auxiliary instruments and cameras.

SEIS accomplished significant milestones for the study of Mars seismicity. The seismic activity recorded included numerous events (over 1300 events were registered processed and catalogued), particularly the 12 class A events with large and proper enough signals to trace their origin back to the formation known as Cerberus fossae (Stähler et al., 2022), where marginal activity of magma remains at depths of 30-50 km. The detected activity included a very large event (magnitude 5) on May the 4th, 2022, and another very large one (magnitude 4.2) on August 25, 2021. Impacts were also detected, particularly a very large impact on Amazonis Planitia that took place in December 24th of 2021, melting ice layers on the surface near the equator. This was a remarkable achievement, given how unlikely it was to have such a large impact during the relatively limited timespan of the mission. This impact generated surface waves transmitted through the planetary crust, helping its characterisation. Additionally, some of the seismic activity detected by SEIS resulted from smaller meteor impacts, such as the one that took place on 5 September 2021, which was the first event to be confirmed as an impact (Garcia et al., 2022).

The high sensibility of SEIS not only enabled to acquire signals from impacts on the planet, but also to record effects as subtle as the passage of the Phobos moon above Elysium Planitia. This effect (known as the Phobos tide), which was slightly delayed but visible on the SEIS data, also provided relevant scientific results (Pou et al., 2022a and 2022b). Studying this phenomena was also key to assess the size and state of the planet's core, resulting in a planet core size estimated to 1820+/-80 km (Pou et al., 2022b), similar to the liquid core size estimated from radio tracking of 1835+/-55 km obtained from the RISE instrument (Le Maistre et al., 2023). These contributions also suggested an entirely liquid core, in contrast to previous ideas, another key contribution of the mission.

SEIS data showed periodical spikes, known as glitches, that were not anticipated from pre-mission testing. Glitches are attributed to step-like dilations inside the instrument components due to thermal variations (Scholz et al., 2022). Some tilt also had a mechanical origin, such as that induced by the passage of dust devils, that could be observed on both VBB and SP data (Murdoch et al., 2017).

Besides the successful geophysical results gained on the structure of the planet, the InSight mission on Mars also provided rich output in the field of meteorology (Kenda et al., 2020), spatial imagery, and even on the evolution of the magnetic field from the onboard magnetometer (Johnson et al., 2020, Mittelholz et al., 2023a, 2023b). The magnetometer founded the remnants of an ancient magnetic field larger than expected, and monitored continuous fluctuations attributed to solar wind interaction with the thin atmosphere of Mars.

The effects of dust devils on the seismometer data (Kenda et al., 2020, Murdoch et al., 2017) were analysed in details, together with the seismic noise resulting from changes in atmospheric conditions. This was repeatedly observed through the contrast between quiet nights, with little seismic noise, in contrast to very active days, with convective vortices, noise generated by the interactions between the wind and the lander, and the large thermal cooling-heating cycle and other vortices that induced ground deformation at surface (Stutzmann et al., 2021).

The HP3 hammering to penetrate the Martian soil did not attain the desired 5 m depth (Spohn et al., 2022a). Nevertheless, the HP3 provided valuable lessons, since it became clear that despite its penetration power, it was too light to penetrate the surface of a too stiff material (Spohn et al., 2022b). The hammering process resulted in small seismic signals that were detected by SEIS and analysed to determine the wave velocities of the surface layer (Brinkman et al. 2022). The HP3 also provided interesting data on the thermal conductivity at the surface (Grott et al. 2022, Spohn et al., 2022a). These data were coherent with lab estimation provided by Nagihara et al. (2022), and also with the results presented in this work.

The properties of the surface material at the landing site were better known (Delage et al, 2022a). Interesting data were also obtained from the arm activities, including digging trenches, pushing down on the surface and measuring the SEIS tilt (Golombek et al., 2023, Marteau et al., 2023). The grain size distribution of the surface regolith was also better assessed by observing the effect of wind transportation during the pouring carried out with the robotic arm to cover the SEIS tether (Verdier et al, 2023).

GENERAL CONCLUSIONS

This thesis was focused on the study of the regolith at the Mars InSight mission site from the perspective of soil mechanics. It was conducted within this international project, collaborating to the goals of the Near Surface Working Group (NSWG) of the InSight Science Team, dedicated to investigating the properties of first 15 meters of regolith at the landing site. Within the frame of a joint supervision, the thesis has been conducted in the geotechnical laboratories of both Ecole des Ponts ParisTech (Navier- CERMES) and Universidad de los Andes in Bogota (GeoSI).

The experimental part of the work was devoted to the investigation of the thermo-mechanical behaviour of a sandy regolith simulant at very low stresses, in conjunction with the near surface regolith at the InSight landing site, with particular attention paid to the interaction between the SEIS seismometer and the ground. The Fontainebleau sand was selected as regolith simulant based on orbiter measurements of the thermal inertia and on the subrounded shape of its grains, an important feature in terms of mechanical response. Besides the SEIS ground interaction that was investigated on a novel device specially developed, other experimental investigations concerned the determination of wave velocities at surface (by extending the use of bender elements at low stress), another important feature for the analysis of the SEIS seismometer data. A specific device to investigate the coupling between wave and heat transfers under Mars atmospheric conditions was also developed. Due to the reduced gravity on Mars, all tests were conducted in a range of stresses smaller than those usually involved in standard geotechnical engineering (down to several kPa), and of low strains staying within the elastic domain.

Given the very loose density of the surface regolith at the Insight landing site, special attention was paid to the techniques of preparing loose samples (mass unit weight of 1400 – 1450 kg/m^3 corresponding to I_D around 6% for Fontainebleau sand). Beside the standard pluviation method used for preparing the cylindrical samples on which wave velocities were measured with bender elements, a specific investigation of the homogeneity of funnel deposited samples, used for investigating the SEIS/ground interaction, was carried out by using X-ray microtomography. It appeared that this commonly used method is less satisfactory than the standard pluviation one, with some heterogeneity observed at the sample bottom, whereas the homogeneity at the sample surface, where the interaction was studied, was better.

The device initially used at CERMES for the design of the SEIS feet was improved to achieve more accurate measurements of the parameters governing the SEIS/ground interaction. This was made possible by increasing the device stiffness (for better displacement measurements), by adopting a more accurate force gauge and by insulating the system from mechanical and thermal perturbations, resulting in temperature changes smaller than 0.5° within the device. The accuracy was good enough to demonstrate that only two-three sand grains were affected by the foot penetration (around 600 μm) under the 10 N force corresponding to the SEIS force supported by a SEIS foot. Negligible load cycle hysteresis illustrated a fairly good reversible elastic response. Interestingly, the Young modulus value (around 20 MPa) derived from these interaction measurements at low strains (10^{-6}) are comparable to those derived from wave velocities measurements. Note that the in-situ wave velocities carried out by analysing by SEIS the waves resulting from the hammering sessions of the HP^3 self-penetrating probe also provided comparable values, in spite of the difference in nature of the true surface layer, mainly made up of a loose cohesive sandy regolith with pebbles embedded.

The measurement of simultaneous compression and shear wave velocities by bender elements was extended to stress as low as 1.75 kPa by using a horizontal triaxial sample submitted to vacuum, with careful estimation of gravity and membrane effects. Wave analysis was carried out by using a specifically developed software. In a standard fashion, the results were fitted with a power law, with however slightly different power values for V_p and V_s, showing that the elastic assumption was perhaps not fully valid. The measurement of wave velocities also enabled determining the Poisson ratio, found equal to 0.15 with more variability at low stresses (< 5 kPa) and, perhaps, a tendency to decrease at very low stresses. Further investigation is obviously needed in this stress range, that if of particular importance for the surface deposits in planets and other celestial bodies of smaller size (comets, asteroids).

A theoretical model based on the mechanics of contacts was developed to better account for the effects on wave velocities of the local rugosity at the inter-grains contacts, suspected to become more influential at very low stresses. Atomic Force Microscope observations supported the characterisation of grain rugosity, and the effects of inter-grain slippage were also considered in the estimation of the Poisson ratio through wave velocities. The model satisfactorily predicted the change in wave velocities with stress, with perhaps a need of further improvement in the very low stress range (< 5 kPa), where it seems that a linear trend is observed.

A novel experimental device for the coupled measurements of thermal conductivity and wave velocities in loose sand was designed, set up and used. Low stress conditions are ensured by using a sand sample deposited in a parallelepiped container on which a low stress can be applied by using a piston. Wave velocities along the container length were measured by using piezo-actuators and accelerometers, preferred to bender elements at very low stresses. Thermal conductivity measurements were carried out by using Peltier plate actuators placed on both faces of the container, generating a one-dimensional heat flux along its length. Martian atmosphere conditions were ensured by using CO_2 as pore gas, with a pressure controlled between 600 and 1000 Pa by a special vacuum pump. Thermal tests carried out on Fontainebleau sand confirmed the significant effect of gas pressure on the thermal conductivity, with data reasonably comparable to the (scarce) literature values, showing an increase in conductivity with gas pressure. A combined effect of stress on thermal conductivity was also evidenced, probably for first time in Martian atmospheric and stress conditions, with an increase in conductivity with stress. Compared to the thermal conductivity directly measured at the InSight landing site surface (0.01 W/mK under 600 Pa, Grott et al. 2022), our data (0.05 - 0.1 W/mK) are larger, probably because of the higher conductivity of the quartz grains of Fontainebleau sand, compared to the basaltic mineralogical composition of the Martian InSight regolith.

Note that the wave measurements were less successful. Data analysis still deserve more attention with, probably, a need of improving the device, that could be useful for future missions on planets and other celestial bodies, in which thermal surface properties are easier to get from orbiter observations.

Finally, a numerical model was formulated to account for the effects of changes in atmospheric pressure on the vertical displacements of the surface. These data give access to the ground compliance and provide a value of the elastic properties at surface. The changes in atmospheric pressure, that are measured by the InSight weather station, are particularly sudden when dust devils pass close to the lander, and their effects are accurately detected by the SEIS seismometer. These calculations were done to extend the original Sorrels approach, in which atmospheric pressure changes are applied as a change in total stress (as if the surface was impervious). We accounted for the penetration of gas in the porous surface medium, allowing for a more relevant effective stress approach. In a first approach, two scenarios were evaluated, showing that this effect might account for a 5-15% difference in the estimation of ground compliance and surface elastic parameters. Further refinement accounting for the true profile detected at the InSight landing site is now necessary, but it has been showed that the permeable nature of the surface has to be accounted for in proper compliance estimation.

Globally, the various experimental, theoretical and numerical contributions of this thesis show how innovative approaches in soil mechanics may help analysing the surface properties in planetary missions. The approaches developed here may be extended to other missions on Mars, but also on the Moon where conditions are different, with no atmosphere at all and quite angular regolith grains, and probable significant consequences on the thermo-mechanical response of the surface regolith. Extending the performance of our device for the coupled analysis of waves and heat transfers seems particularly relevant, since it would allow improving the estimation of mechanical surface properties by thermal measurements, easier to conduct from orbiter measurements. Besides planets, these developments may also be useful for the extreme cases of small celestial bodies, known to be covered by granular angular material and submitted to extremely low gravity, a quite challenging condition for further soil testing and analysing.

PERSPECTIVES

The results of this work show that existing knowledge of soil mechanics enables exploration of the thermal and mechanical behaviour of the surface regolith of other planets by exploring the novel range of very low stresses. Samples of varied sizes and geometries can be prepared at very loose density levels using simple methodologies for different experiments aimed to measure stiffnesses, thermal conductivities and other properties. Numerical calculations and theoretical tools also can be used to interpret such data and further complement the findings to better interpret the results.

This novel domain of low stress soil mechanics remains relatively unexplored and presents interesting prospects for the field of extra-terrestrial geotechnics. One of the clearest prospects is the application of the experiments conceived and used in this work to other environments, such as the Moon or the landing sites for other future Mars missions. Other developments include the consideration of other characteristics of the soil for regolith analogue choice, such as the inclusion of less uniform gradation (to account for the effects of the pebbles observed at the landing site which may be displaced by the landing exhaust gases), and the use of analogues with some degree or cohesion for cases where it is adequate. Exploring more complex aspects of the material such as anisotropy, or considering the plastic behaviour present at higher stresses is also an interesting prospect.

A concrete application shall be the exploration of support structures of instrumentation to be placed in contact with the lunar surface. The regolith present there is subjected to vacuum and thus results from different formation conditions due to the complete absence of atmosphere. Nevertheless, the experimental setup used during the foot-regolith interaction work can be used with some modifications. The glitches observed on SEIS data were unexpected in all previous work, and should be carefully considered for future design. They are attributed in general to small thermal cycles inducing dilation of the metallic components of the instruments. It was observed that very small displacements in the scale of micrometers occured (though large in comparison to what SEIS is capable of detecting), which can be related to the rugosity of the metallic components of the SEIS foot design. This can be better evaluated in future works. A setup that induces somewhat greater stresses on the surface material may be worth considering (considering stronger manual installation in comparison to the very careful robotic arm), while also ensuring proper contact with the surface below and proper restrictions to potential lateral movement.

The materials encountered on the landing site have also shown to be quite complex. Use of clayeous material to study the rare clay deposits that have been encountered in Mars may also be possible. Partial inclusions of finer or coarser material into some simulants may pose an interesting prospect.

Another potential experimental prospect is the use of experimental setups in reduced gravity environments. Alternatively, the reduced gravities present on these extraterrestrial objects mean that terrestrial gravity could be used as a geotechnical centrifuge, and making adequate use of scale laws, such models can be sized to induce stress similarity conditions since Earth gravity is from 3 to several times larger than the one encountered on these sites.

LIST OF PUBLICATIONS

Journals (Published)

- The interaction between the SEIS seismometer of the InSight Martian mission and a regolith simulant. P. Delage, **Castillo-Betancourt J.P.**, Caicedo Hormaza B, Karakostas F, De Laure E., Lognonné P., Antonangeli D., Banerdt B. *Géotechnique* (2022). 2.
- Chaparro-Lopez M.J., **Castillo-Betancourt J.P.**, Cabrera M., Caicedo B., Delage P., Lognonné P., and Banerdt B., "Dynamic Mechanical Analysis Test for Evaluating Loose Sands on a Wide Strain Range—Application to the InSight Mission on Mars," Geotechnical Testing Journal. https://doi.org/10.1520/GTJ20230381.
- **Castillo-Betancourt J.P**., Delage P., Caicedo B., Lognonné P., Banerdt W. B. (2023). Wave Velocities and Poisson Ratio in a Loose Sandy Martian Regolith Simulant Under Low Stresses. Part 1: Laboratory Investigation. *Journal of Geophysical Research: Planets*. https://doi.org/10.1029/2023JE007988
- Caicedo B., **Castillo-Betancourt J.P.**, Delage P., Lognonné P., Banerdt W. B. (2023). Wave Velocities and Poisson Ratio in a Loose Sandy Martian Regolith Simulant Under Low Stresses. Part 2: Theoretical analysis. *Journal of Geophysical Research: Planet*. https://doi.org/10.1029/2023JE008008

Journals (Minor revisions)

- Caicedo B., Chaparro M.J, **Castillo-Betancourt J.P.**, Cabrera M.A., Delage P., Lognonné P., Banerdt B. (2023). A micromechanical model for estimating the shear modulus and damping ratio of loose sands under low stresses. application to a Mars regolith simulant. *Géotechnique*. GEOT-2023-244.
- Delage P., Caicedo B., Golombek M. P., Spohn T., Schmelzbach C., Brinkman N., Marteau E., Murdoch N., Warner N., Ansan V., Banerdt W. B., **Castillo-Betancourt J. P.**, Edme P., Gomez A., Grott M., Hurst K., Lemmon M., Lognonné P., Piqueux S., Robertsson J., Sollberger D., Stähler S., Verdier N., Vrettos C., Williams N. R.. Investigating the Martian soil at the InSight landing site. *Soils and Rocks*. SR-0050-2023

International Conferences

- Delage P., Marteau E., Vrettos C., Golombek M.P., Ansan V., Banerdt W. B., Grott M., Hurst K., Lognonné P., Murdoch N., Piqueux S., Schmelbach C., Spohn T., Warner N., Widmer-Schnidrig R., Brinkman N., Caicedo-Hormaza B., **Castillo-Betancourt J.P.**,

Edme P., Kedar S., Lange L., Lemmon M., Mueller N., Onodera K., Robertsson J., Sollberger D., Stähler S., Verdier N., Williams N.R. 2022. The mechanical properties of the Martian soil at the InSight landing site. Special Lecture, *Proc. 20th Int. Conf. on Soil Mechanics and Geotechnical Engineering*, Sydney, Australia, May 2022. Available on https://hal.science/hal-03706564/.

REFERENCES

Abiss, C. P. (1981). Shear wave measurements of the Elasticity of the Ground. Géotechnique, 31(1), 91–104.

Alshibli, K. A., & Hasan, A. (2008). Spatial variation of void ratio and shear band thickness in sand using X-ray computed tomography. Geotechnique, 58(4), 249–257. https://doi.org/10.1680/geot.2008.58.4.249

Allen, C. C., Jager, K. M., Morris, R. V., Lindstrom, D. J., Lindstrom, M. M., & Lockwood, J. P. (1998). JSC MARS-1: A Martian Soil Simulant. Space and Robotics.

Andria-Ntoanina, I. (2011). Caractérisation dynamique de sables de référence en laboratoire - Application à la réponse sismique de massifs sableux en centrifugeuse. [Thesis]. ENPC.

Archard, J. F. (1957). Fragmentation of Shell Cases Author (s): N . F . Mott Source : Proceedings of the Royal Society of London . Series A, Mathematical and Published by : Royal Society Stable URL : https://www.jstor.org/stable/97828. Proceedings of the Royal Society of London., 243(1233), 190–205.

Arulnathan, R., Boulanger, R. W., & Riemer, M. F. (1998). Analysis of Bender Element Tests. In Geotechnical Testing Journal, GTJODJ (Vol. 21, Issue 2).

Arvidson, R. E., Anderson, R. C., Bartlett, P., Bell, J. F., Blaney, D., Christensen, P. R., Chu, P., Crumpler, L., Davis, K., Ehlmann, B. L., Fergason, R., Golombek, M. P., Gorevan, S., Grant, J. A., Greeley, R., Guinness, E. A., Haldemann, A. F. C., Herkenhoff, K., Johnson, J., … Wilson, J. (2004). Localization and physical properties experiments conducted by Spirit at Gusev crater. Science, 305(5685), 821–824. https://doi.org/10.1126/science.1099922

Arvidson, R. E., J. Bibring, F. Poulet, S. W. Squyres, M. Wolff, and R. Morris (2004b), Coordinated Mars Exploration Rover and Mars Express OMEGA observations over Meridiani Planum, *Eos Trans. AGU*, 85(47), Fall Meet. Suppl., Abstract P24A-06.

Arvidson, Raymond E., Gooding, J. L., & Moore, H. J. (1989). The Martian surface as imaged, sampled, and analyzed by the Viking landers. Reviews of Geophysics, 27(1), 39–60. https://doi.org/10.1029/RG027i001p00039

Arvidson, Raymond E., Squyres, S. W., Anderson, R. C., Bell, J. F., Blaney, D., Brückner, J., Cabrol, N. A., Calvin, W. M., Carr, M. H., Christensen, P. R., Clark, B. C., Crumpler, L., Des Marais, D. J., de Souza, J. A., d'Uston, C., Economou, T., Farmer, J., Farrand, W. H., Folkner, W., … Yen, A. (2006). Overview of the Spirit Mars Exploration Rover Mission to Gusev Crater: Landing site to Backstay Rock in the Columbia Hills. Journal of Geophysical Research: Planets, 111(2), 1–22. https://doi.org/10.1029/2005JE002499

Asslan, M. (2009). An Experimental Study on the Initial Shear Stiffness in Granular Material under Controlled Multi-Phase Laboratory Conditions Milad Asslan An Experimental Study on the Initial Shear Stiffness in Granular Material under Controlled (Issue December). Bauhaus university Weimar.

Atkinson, J. H. (2000). Non-linear soil stiffness in routine design. Géotechnique.

Bachrach, R., Dvorkin, J., & Nur, A. M. (2000). Seismic velocities and Poisson's ratio of shallow unconsolidated sands. Geophysics, 65(2), 559–564. https://doi.org/10.1190/1.1444751

Bahrami, M., Yovanovich, M. M., & Culham, J. R. (2005). A compact model for spherical rough contacts. Journal of Tribology, 127(4), 884–889. https://doi.org/10.1115/1.2000982

Banerdt, W. B., Folkner, W. M., Dehant, V., Le Maistre, S., Yseboodt, M., Rivoldini, A., Van Hoolst, T., Asmar, S. W., & Golombek, M. P. (2018). The InSight mission. Space Science Reviews, 214(5).

Banerdt, W. B., Smrekar, S. E., Banfield, D., Giardini, D., Golombek, M., Johnson, C. L., Lognonné, P., Spiga, A., Spohn, T., Perrin, C., Stähler, S. C., Antonangeli, D., Asmar, S., Fillingim, M., Folkner, W., Garcia, R. F., Garvin, J., Grant, J., Grott, M., … Mclennan, S. M. (2020). *Initial results from the InSight mission on Mars*.

Banin, A. (1992). In H. H. Kieffer, B. M. Jakosky, C. W. Snyder, & M. S. Matthews (Eds.), Mars (pp. 594–625). University of Arizona Press.

Bardera, R., Sor, S., & García Margariño, A. (2020). Aerodynamics of Mars 2020 Rover Wind Sensors. In Mars Exploration (Vol. 1, Issue 1, p. 13). IntechOpen.

Bates, C. R. (1989). Dynamic soil property measurements during triaxial testing. Geotechnique, 39(4), 721–726. https://doi.org/10.1680/geot.1989.39.4.721

Bathurst, R. J., & Rothenburg, L. (1988). Note on a random isotropic granular material with negative poisson's ratio. International Journal of Engineering Science, 26(4), 373–383.

Baut, J., Researcher, I., Merle, D., & Hervet, S. (2003). Le gisement à vertébrés fossiles de Vayres-sur-Essonne une découverte importante pour l'histoire de la mer stampienne. *Cossmanniana, Hors-série*(April 2015), 37–38.

Belmokhtar, M., Delage, P., Ghabezloo, S., & Conil, N. (2018). Drained Triaxial Tests in Low-Permeability Shales: Application to the Callovo-Oxfordian Claystone. Rock Mechanics and Rock Engineering, 51(7), 1979–1993. https://doi.org/10.1007/s00603-018-1442-0

Benahmed, N. (2001). Comportement mécanique d'un sable sous cisaillement monotone et cyclique : application aux phénomènes de liquéfaction et de mobilité y clique. [Thesis]. ENPC.

Benedetto, H. Di, Delaporte, B., & Sauzéat, C. (2007). Three-Dimensional Linear Behavior of Bituminous Materials: Experiments and Modeling. International Journal of Geomechanics, 7(2), 149–157. https://doi.org/10.1061/(asce)1532-3641(2007)7:2(149)

Benedetto, H. Di, Sauzéat, C., & Sohm, J. (2009). Stiffness of bituminous mixtures using ultrasonic wave propagation. Road Materials and Pavement Design, 10(4), 789–814. https://doi.org/10.3166/rmpd.10.789-814

Binnig, G., Quate' ', C. F., Gi, E. L., & Gerber, C. (1986). Atomic Force Microscope. Physical Review Letters, 56(9), 1930–1934.

Bishop, A. W., & Wesley, L. D. (1975). A hydraulic triaxial apparatus for controlled stress path testing. Géotechnique, 25(4), 657–610.

Blanc, M., Di Benedetto, H., & Tiouajni, S. (2011). Deformation characteristics of dry hostun sand with principal stress axes rotation. Soils and Foundations, 51(4), 749–760. https://doi.org/10.3208/sandf.51.749

Borja, R. I., Song, X., Rechenmacher, A. L., Abedi, S., & Wu, W. (2013). Shear band in sand with spatially varying density. Journal of the Mechanics and Physics of Solids, 61(1), 219–234. https://doi.org/10.1016/j.jmps.2012.07.008

Böttcher, N., Singh, A. K., Kolditz, O., & Liedl, R. (2012). Non-isothermal, compressible gas flow for the simulation of an enhanced gas recovery application. Journal of Computational and Applied Mathematics, 236(18), 4933–4943. https://doi.org/10.1016/j.cam.2011.11.013

Boulanger, R. W., Arulnathan, R., Harder, L. F., Torres, R. A., & Driller, M. W. (1997). Dynamic Properties of Sherman Island Peat. Journal of Geotechnical and Geoenvironmental Engineering, 124(1), 12–20. https://doi.org/10.1061/(asce)1090-0241(1998)124:1(12)

Brignoli, E. G., Gotti, M., & Stokoe, K. H. (1996). Measurement of Shear Waves in Laboratory Specimens by Means of Piezoelectric Transducers. In Geotechnical Testing Journal, GTJODJ (Vol. 19, Issue 4).

Brinkman, N., Schmelzbach, C., Sollberger, D., Pierick, J. ten, Edme, P., Haag, T., Kedar, S., Hudson, T., Andersson, F., van Driel, M., Stähler, S., Nicollier, T., Robertsson, J., Giardini, D., Spohn, T., Krause, C., Grott, M., Knollenberg, J., Hurst, K., … Banerdt, W. B. (2022). In Situ Regolith Seismic Velocity Measurement at the InSight Landing Site on Mars. Journal of Geophysical Research: Planets, 127(10). https://doi.org/10.1029/2022JE007229

Brooks, R. A., & Di Chiro, G. (1976). Beam hardening in X-ray reconstructive tomography. Physics in Medicine and Biology, 21(3), 390–398. https://doi.org/10.1088/0031-9155/21/3/004

Butt, S., Antoine, J., Martin, P., Butt, S., Antoine, J., Martin, P., Butt, S. U., Antoine, J., & Martin, P. (2015). Simplified stiffness model for spherical rough contacts To cite this version : HAL Id : hal-02310407 Simplified stiffness model for spherical rough contacts. Tribology - Materials, Surfaces & Interfaces, 9(2), 63–70.

Cagliero, R., Barbato, G., Maizza, G., & Genta, G. (2015). Measurement of elastic modulus by instrumented indentation in the macro-range: Uncertainty evaluation. International Journal of Mechanical Sciences, 101–102, 161–169. https://doi.org/10.1016/j.ijmecsci.2015.07.030

Castillo-Betancourt Juan Pablo. (2023a). juan9715/MRA-Bender-Element-data: Bender data public repository release (Release) [Data set]. Zenodo. https://doi.org/10.5281/zenodo.8161970

Castillo- Betancourt Juan Pablo. (2023b). juan9715/WaveVelocitiesSoftwareAndSpreadsheet: Wave Velocities Data Release (v) [Data set]. Zenodo. https://doi.org/10.5281/zenodo.8415384

Cha, M., Asce, A. M., Santamarina, ; J Carlos, Asce, M., Kim, ; Hak-Sung, & Cho, G.-C. (2014). Small-Strain Stiffness, Shear-Wave Velocity, and Soil Compressibility. Journal of Geotechnical and Geoenvironmental Engineering. https://doi.org/10.1061/(ASCE)GT.1943

Chao-Fa, Z., Pinzón, G., Wiebicke, M., Andò, E., Niels, P. K., & Viggiani, G. (2017). Chao-Fa, Zhao Gustavo Pinzón. Computers and Geotechnics.

Chen, Y., Gélébart, L., Chateau, C., Bornert, M., King, A., Aimedieu, P., Sauder, C., Chen, Y., Gélébart, L., Chateau, C., Bornert, M., & King, A. (2017). Caractérisation des mécanismes d ' endommagement des tubes CVI-SiC / SiC par tomographie X To cite this version : HAL Id : hal-01598516 Caractérisation des mécanismes d ' endommagement des tubes CVI -SiC / SiC par tomographie X Characterization of damage .

Cho, G.-C., Dodds, J., & Santamarina, J. C. (2006). Particle Shape Effects on Packing Density, Stiffness, and Strength: Natural and Crushed Sands. Journal of Geotechnical and Geoenvironmental Engineering, 132(5), 591–602. https://doi.org/10.1061/(asce)1090-0241(2006)132:5(591)

CNES. (2018). INSIGHT. November 27. https://insight.cnes.fr/en/INSIGHT/index.htm

Combarieu, O. (1999). Caractérisation mécanique d 'un massif de sable compacté Cohérence des essais réalisés. *Bulletin des Laboratoires des Ponts Et Chaussées*, *mm*, 69–73.

Côté, J., Fillion, M. H., & Konrad, J. M. (2011). Intrinsic permeability of materials ranging from sand to rock-fill using natural air convection tests. Canadian Geotechnical Journal, 48(5), 679–690. https://doi.org/10.1139/t10-097

Cresswell, A., Barton, M. E., & Brown, R. (1999). Determining the maximum density of sands by pluviation. Geotechnical Testing Journal, 22(4), 324–328. https://doi.org/10.1520/gtj11245j

Dano, C., & Hicher, P.-Y. (2002a). Mesure du module de cisaillement de differents materiaux par la technique des bender elements. *Paramètres de Calcul Géotechnique*.

Darendeli, M. (2001). Development of a new family of normalized modulus reduction and material damping curves. http://www.kansai-airports.co.jp/en/efforts/our-tech/kix/sink/sink3.html

Delage, P., Betancourt, J. C., Hormaza, B. C., Karakostas, F., Laure, E. D. E., Lognonné, P., Antonangeli, D., & Banerdt, B. (2020). The interaction between the SEIS seismometer of the InSight Martian mission and a regolith simulant. Géotechnique.

Delage, P., Karakostas, F., Dhemaied, A., Belmokhtar, M., Lognonné, P., Golombek, M., De Laure, E., Hurst, K., Dupla, J. C., Kedar, S., Cui, Y. J., & Banerdt, B. (2017). An Investigation of the Mechanical Properties of Some Martian Regolith Simulants with Respect to the Surface Properties at the InSight Mission Landing Site. Space Science Reviews, 211(1–4), 191–213. https://doi.org/10.1007/s11214-017-0339-7

Delfosse-Ribay, E., Djeran-Maigre, I., Cabrillac, R., & Gouvenot, D. (2004). Shear modulus and damping ratio of grouted sand. *Soil Dynamics and Earthquake Engineering*, *24*(6), 461–471. https://doi.org/10.1016/j.soildyn.2004.02.004

Delyukov, A., & Didyk, L. (1999). The effects of extra-low-frequency atmospheric pressure oscillations on human mental activity. International Journal of Biometeorology, 43(1), 31–37. https://doi.org/10.1007/s004840050113

Dutta, T. T., Otsubo, M., Kuwano, R., & Sato, T. (2020). Estimating multidirectional stiffness of soils using planar piezoelectric transducers in a large triaxial apparatus. Soils and Foundations, 60(5), 1269–1286. https://doi.org/10.1016/j.sandf.2020.08.002

Duttine, A., Benedetto, H. Di, Bang, D. P. Van, & Ezaoui, A. (2007). Anisotropic small strain elastic properties of sands and mixture of sand-clay measured by dynamic and static methods. Soils and Foundations, 47(3), 457–472. https://doi.org/10.3208/sandf.47.457

Dyvik, R., and Madshus, C. 1985. Lab measurements of Gmax using bender ele- ments. In Proceedings of the Conference on the Advances in the Art of Test- ing Soil under Cyclic Conditions,.ASCE Geotechnical Engineering Division, New York. pp. 186–196

El Dine, B. S., Dupla, J. C., Frank, R., Canou, J., & Kazan, Y. (2010). Mechanical characterization of matrix coarse-grained soils with a large-sized triaxial device. *Canadian Geotechnical Journal*, *47*(4), 425–438. https://doi.org/10.1139/T09-113

Emam, S., Roux, J.-N., Canou, J., Corfdir, A., & Dupla, J.-C. (2005). Granular packings assembled by rain deposition: an experimental and numerical study. In T. & Francis (Ed.), Powders and Grains 2005, Two Volume Set (p. 4). CRC Press.

Fayon, L., Knapmeyer-Endrun, B., Lognonné, P., Bierwirth, M., Kramer, A., Delage, P., Karakostas, F., Kedar, S., Murdoch, N., Garcia, R. F., Verdier, N., Tillier, S., Pike, W. T., Hurst, K., Schmelzbach, C., & Banerdt, W. B. (2018). A Numerical Model of the SEIS Leveling System Transfer Matrix and Resonances: Application to SEIS Rotational Seismology and Dynamic Ground Interaction. In Space Science Reviews (Vol. 214, Issue 8). Springer Nature B.V. https://doi.org/10.1007/s11214-018-0555-9

Fernando, J., Schmidt, F., & Douté, S. (2016). Martian surface microtexture from orbital CRISM multi-angular observations: A new perspective for the characterization of the geological processes. Planetary and Space Science, 128, 30–51. https://doi.org/10.1016/j.pss.2016.05.005

Fernando, J., Schmidt, F., Pilorget, C., Pinet, P., Ceamanos, X., Douté, S., Daydou, Y., & Costard, F. (2015). Characterization and mapping of surface physical properties of Mars from CRISM multi-angular data: Application to Gusev Crater and Meridiani Planum. Icarus, 253, 271–295. https://doi.org/10.1016/j.icarus.2015.03.012

Fioravante, V. (2000). Anisotropy of small strain stiffness of ticino and kenya sands from seismic wave propagation measured in triaxial testing. Soils and Foundations, 40(4), 129–142. https://doi.org/10.3208/sandf.40.4_129

Flitti, A., Della, N., De Kock, T., Cnudde, V., & Verástegui-Flores, R. D. (2021). Effect of initial fabric on the undrained response of clean Chlef sand. European Journal of Environmental and Civil Engineering, 25(13), 2441–2456. https://doi.org/10.1080/19648189.2019.1631217

Folkner, W. M., Dehant, V., Le Maistre, S., Yseboodt, M., Rivoldini, A., Van Hoolst, T., Asmar, S. W., & Golombek, M. P. (2018). The Rotation and Interior Structure Experiment on the InSight Mission to Mars. *Space Science Reviews, 214*(5), 1–16. https://doi.org/10.1007/s11214-018-0530-5

Gade, V. K., & Dasaka, S. M. (2017). Assessment of Air Pluviation Using Stationary and Movable Pluviators. Journal of Materials in Civil Engineering, 29(5). https://doi.org/10.1061/(asce)mt.1943-5533.0001798

Garcia, R., Daubar, I., Beucler, É., Posiolova, L., Collins, G., Lognonné, P., Rolland, L., Xu, Z., Wójcicka, N., Garcia, R., Daubar, I., Beucler, É., Posiolova, L., & Collins, G. (2022). Newly formed craters on Mars located using seismic and acoustic wave data from InSight To cite this version : HAL Id : hal-03945839. Nature Geoscience, 15, 774–780.

Gaspar, N. (2010). A granular material with a negative Poisson's ratio. Mechanics of Materials, 42(7), 673–677. https://doi.org/10.1016/j.mechmat.2010.05.001

Georgiannou, V. N., Tsomokos, A., & Stavrou, K. (2008). Monotonie and cyclic behaviour of sand under torsional loading. Geotechnique, 58(2), 113–124. https://doi.org/10.1680/geot.2008.58.2.113

Giardini, D., Lognonné, P., Banerdt, W. B., Pike, W. T., Christensen, U., Ceylan, S., Clinton, J. F., van Driel, M., Stähler, S. C., Böse, M., Garcia, R. F., Khan, A., Panning, M., Perrin, C., Banfield, D., Beucler, E., Charalambous, C., Euchner, F., Horleston, A., … Yana, C. (2020). The seismicity of Mars. Nature Geoscience, 13(3), 205–212. https://doi.org/10.1038/s41561-020-0539-8

Goetz, W., Pike, W. T., Hviid, S. F., Madsen, M. B., Morris, R. V., Hecht, M. H., Staufer, U., Leer, K., Sykulska, H., Hemmig, E., Marshall, J., Morookian, J. M., Parrat, D., Vijendran, S., Bos, B. J., El Maarry, M. R., Keller, H. U., Kramm, R., Markiewicz, W. J., … Tanner, R. (2010a). Microscopy analysis of soils at the Phoenix landing site, Mars: Classification of soil particles and description of their optical and magnetic properties. Journal of Geophysical Research E: Planets, 115(8), 1–23. https://doi.org/10.1029/2009JE003437

Goetz, W., Pike, W. T., Hviid, S. F., Madsen, M. B., Morris, R. V., Hecht, M. H., Staufer, U., Leer, K., Sykulska, H., Hemmig, E., Marshall, J., Morookian, J. M., Parrat, D., Vijendran, S., Bos, B. J., El Maarry, M. R., Keller, H. U., Kramm, R., Markiewicz, W. J., … Tanner, R. (2010b). Microscopy analysis of soils at the Phoenix landing site, Mars: Classification of soil particles and description of their optical and magnetic properties. In Journal of Geophysical Research E: Planets (Vol. 115, Issue 8). Blackwell Publishing Ltd. https://doi.org/10.1029/2009JE003437

Golombek, M., Grott, M., Kargl, G., Andrade, J., Marshall, J., Warner, N., Teanby, N. A., Ansan, V., Hauber, E., Voigt, J., Lichtenheldt, R., Knapmeyer-Endrun, B., Daubar, I. J., Kipp, D., Muller, N., Lognonné, P., Schmelzbach, C., Banfield, D., Trebi-Ollennu, A., … Banerdt, W. B. (2018). Geology and Physical Properties Investigations by the InSight Lander. In *Space Science Reviews* (Vol. 214, Issue 5). Springer Netherlands. https://doi.org/10.1007/s11214-018-0512-7

Golombek, M., Hudson, T., Bailey, P., Balabanska, N., Marteau, E., Charalambous, C., Baker, M., Lemmon, M., White, B., Lorenz, R. D., Spohn, T., Maki, J., Kallemeyn, P., Garvin, J. B., Newman, C., Hurst, K., Murdoch, N., Williams, N., Banerdt, W. B., … Gabsi, T. (2023). Results from InSight Robotic Arm Activities. Space Science Reviews, 219(3). https://doi.org/10.1007/s11214-023-00964-0

Golombek, M., Kipp, D., Warner, N., Daubar, I. J., Fergason, R., Kirk, R. L., Beyer, R., Huertas, A., Piqueux, S., Putzig, N. E., Campbell, B. A., Morgan, G. A., Charalambous, C., Pike, W. T., Gwinner, K., Calef, F., Kass, D., Mischna, M., Ashley, J., … Banerdt, W. B. (2017). Selection of the InSight Landing Site. Space Science Reviews, 211(1–4), 5–95. https://doi.org/10.1007/s11214-016-0321-9

Golombek, M. P., Haldemann, A. F. C., Simpson, R. A., Fergason, R. L., Putzig, N. E., Arvidson, R. E., Bell, J. F., & Mellon, M. T. (2009). Martian surface properties from joint analysis of orbital, Earth-based, and surface observations. In The Martian Surface (Issue May). https://doi.org/10.1017/cbo9780511536076.022

Golombek, M. P., Huertas, A., Marlow, J., McGrane, B., Klein, C., Martinez, M., Arvidson, R. E., Heet, T., Barry, L., Seelos, K., Adams, D., Li, W., Matijevic, J. R., Parker, T., Sizemore, H. G., Mellon, M., McEwen, A. S., Tamppari, L. K., & Cheng, Y. (2009). Size-frequency distributions of rocks on the northern plains of Mars with special reference to Phoenix landing surfaces. *Journal of Geophysical Research: Planets*, *114*(3). https://doi.org/10.1029/2007JE003065

Golombek, M., Warner, N. H., Grant, J. A., Hauber, E., Ansan, V., Weitz, C. M., Williams, N., Charalambous, C., Wilson, S. A., DeMott, A., Kopp, M., Lethcoe-Wilson, H., Berger, L., Hausmann, R., Marteau, E., Vrettos, C., Trussell, A., Folkner, W., Le Maistre, S., … Banerdt, W. B. (2020). Geology of the InSight landing site on Mars. Nature Communications, 11(1). https://doi.org/10.1038/s41467-020-14679-1

Golombek, Matt P., Crumpler, L. S., Grant, J. A., Greeley, R., Cabrol, N. A., Parker, T. J., Rice, J. W., Ward, J. G., Arvidson, R. E., Moersch, J. E., Fergason, R. L., Christensen, P. R., Castaño, A., Castaño, R., Haldemann, A. F. C., Li, R., Bell, J. F., & Squyres, S. W. (2006). Geology of the Gusev cratered plains from the Spirit rover transverse. Journal of Geophysical Research: Planets, 111(2), 1–27. https://doi.org/10.1029/2005JE002503

Golombek, Matthew P., Grant, J. A., Crumpler, L. S., Greeley, R., Arvidson, R. E., Bell, J. F., Weitz, C. M., Sullivan, R. J., Christensen, P. R., Soderblom, L. A., & Squyres, S. W. (2006). Erosion rates at the Mars Exploration Rover landing sites and long-term climate change on Mars. Journal of Geophysical Research: Planets, 111(12), 1–14. https://doi.org/10.1029/2006JE002754

Greenwood, J. A., & Tripp, J. H. (1964). The elastic contact of rough spheres. Journal of Applied Mechanics, Transactions ASME, 34(1), 153–159. https://doi.org/10.1115/1.3607616

Greenwood, J. A., & Williamson, J. B. P. (1966). Contact of nominally flat surfaces. Proceedings of the Royal Society of London. Series A. Mathematical and Physical Sciences, 295(1442), 300–319. https://doi.org/10.1098/rspa.1966.0242

Grott, M., Piqueux, S., Spohn, T., Knollenberg, J., Krause, C., Marteau, E., Hudson, T. L., Forget, F., Lange, L., Müller, N., Golombek, M., Nagihara, S., Morgan, P., Murphy, J. P., Siegler, M., King, S. D., Banfield, D., Smrekar, S. E., & Banerdt, W. B. (2023). Seasonal Variations of Soil Thermal Conductivity at the InSight Landing Site. Geophysical Research Letters, 50(7). https://doi.org/10.1029/2023GL102975

Gu, X., Yang, J., Huang, M., & Gao, G. (2015). Bender element tests in dry and saturated sand: Signal interpretation and result comparison. Soils and Foundations, 55(5), 951–962. https://doi.org/10.1016/j.sandf.2015.09.002

Halbert, D., & Parnell, J. (2022). Thermal conductivity of basalt between 225 and 290 K. Meteoritics and Planetary Science, 57(8), 1617–1626. https://doi.org/10.1111/maps.13829

Hardin, B. 0. & Black, W. L. (1966). Sand stiffness under various triaxial stresses. J. Soil Mech. Fdns Div. Am. Sot. Civ. Engrs 92, SM2, 27-42.

Hardin, B. O., and Drnevich, V. P. (1972). “Shear modulus and damping in soils: Measurement and parameter effects.” J. Soil Mech. and Found. Div.

Hashin, Z., & Shtrikman, S. (1963). A variational approach to the theory of the elastic behaviour of multiphase materials. Journal of the Mechanics and Physics of Solids, 11(2), 127–140. https://doi.org/10.1016/0022-5096(63)90060-7

Haskin, L. A., Wang, A., Jolliff, B. L., McSween, H. Y., Clark, B. C., Des Marais, D. J., McLennan, S. M., Tosca, N. J., Hurowitz, J. A., Farmer, J. D., Yen, A., Squyres, S. W., Arvidson, R. E., Klingelhöfer, G., Schröder, C., De Souza, P. A., Ming, D. W., Gellert, R., Zipfel, J., … Soderblom, L. (2005). Water alteration of rocks and soils on Mars at the Spirit rover site in Gusev crater. Nature, 436(7047), 66–69. https://doi.org/10.1038/nature03640

Henkel, D. J., & Gilbert, G. D. (1952). The effect measured of the rubber membrane on the triaxial compression strength of clay samples. Géotechnique, 3(1), 20–29.

Hill, E., Mellin, M. J., Deane, B., Liu, Y., & Taylor, L. A. (2007). Apollo sample 70051 and high- and low-Ti lunar soil simulants MLS-1A and JSC-1A: Implications for future lunar exploration. *Journal of Geophysical Research: Planets*, *112*(2). https://doi.org/10.1029/2006JE002767

Hobiger, M., Hallo, M., Schmelzbach, C., Stähler, S. C., Fäh, D., Giardini, D., Golombek, M., Clinton, J., Dahmen, N., Zenhäusern, G., Knapmeyer-Endrun, B., Carrasco, S., Charalambous, C., Hurst, K., Kedar, S., & Banerdt, W. B. (2021). The shallow structure of Mars at the InSight landing site from inversion of ambient vibrations. Nature Communications, 12(1). https://doi.org/10.1038/s41467-021-26957-7

Hung Vu, Q. (2022). *Effect of fines content on hydro-thermal behaviour of sandy soil in the context of artificial ground freezing*. [Thesis]. ENPC.

Hurowitz, J. A., McLennan, S. M., Tosca, N. J., Arvidson, R. E., Michalski, J. R., Ming, D. W., Schröder, C., & Squyres, S. W. (2006). In situ and experimental evidence for acidic weathering of rocks and soils on Mars. Journal of Geophysical Research: Planets, 111(2), 1–16. https://doi.org/10.1029/2005JE002515

Jafri, N. J. S., Rahim, M. A. A., Bawadi, N. F., Zahid, M. Z. A. M., Ahmad, M. M., & Mansor, A. F. (2018). Determination of dry density ratio of compacted soils using sand replacement method. AIP Conference Proceedings, 2013(October). https://doi.org/10.1063/1.5054213

Jamiolkowski, M., Lancellotta, R., Di Torino, P., Carlo, D., & Presti, L. (1995). Remarks on the stiffness at small strains of six Italian clays. In P. D. B. of Geomaterials (Ed.), Pre-failure deformation of geomaterials (pp. 817–836). Pre-failure Deformation Behaviour of Geomaterials. https://www.researchgate.net/publication/306157192

Jarvis, N. J., Zavattaro, L., Rajkai, K., Reynolds, W. D., Olsen, P. A., McGechan, M., Mecke, M., Mohanty, B., Leeds-Harrison, P. B., & Jacques, D. (2002). Indirect estimation of near-saturated hydraulic conductivity from readily available soil information. Geoderma, 108(1–2), 1–17. https://doi.org/10.1016/S0016-7061(01)00154-9

Ji, S., Li, L., Motra, H. B., Wuttke, F., Sun, S., Michibayashi, K., & Salisbury, M. H. (2018). Poisson’s Ratio and Auxetic Properties of Natural Rocks. Journal of Geophysical Research: Solid Earth, 123(2), 1161–1185. https://doi.org/10.1002/2017JB014606

Johnson, C. L., Mittelholz, A., Langlais, B., Russell, C. T., Ansan, V., Banfield, D., Chi, P. J., Fillingim, M. O., Forget, F., & Haviland, H. F. (n.d.). Crustal and time-varying magnetic fields at the InSight landing site on Mars. Nature Geoscience, 2020(3), 199–204. https://doi.org/10.1038/s41561-020-0537-xï

Jovičić, V., & Vilhar, G. (2009). Measurement and interpretation of the small strain stiffness of boštanj silty sand. Acta Geotechnica Slovenica, 6(2), 57–75.

Karakostas, F., Delage, P., Laure, E. De, Dhemaied, A., Dupla, J. C., Tang, A. M., & Cui, Y. J. (2013). The geotechnical properties of some Mars regoliths simulants (Issue November).

Kenda, B., Drilleau, M., Garcia, R. F., Kawamura, T., Murdoch, N., Compaire, N., Lognonné, P., Spiga, A., Widmer-Schnidrig, R., Delage, P., Ansan, V., Vrettos, C., Rodriguez, S., Banerdt, W. B., Banfield, D., Antonangeli, D., Christensen, U., Mimoun, D., Mocquet, A., & Spohn, T. (2020). Subsurface Structure at the InSight Landing Site From Compliance Measurements by Seismic and Meteorological Experiments. Journal of Geophysical Research: Planets, 125(6), 1–30. https://doi.org/10.1029/2020JE006387

Khiatine, M., Reiffsteck, P., & Bahar, R. (2019a). Evaluation of Dynamic Soil Properties for Alluvial Plain of Bejaia Using Field Data and Laboratory Tests. Geotechnical and Geological Engineering, 37(6), 4707–4730. https://doi.org/10.1007/s10706-019-00933-x

Khiatine, M., Reiffsteck, P., & Bahar, R. (2019b). Evaluation of Dynamic Soil Properties for Alluvial Plain of Bejaia Using Field Data and Laboratory Tests. Geotechnical and Geological Engineering, 37(6), 4707–4730. https://doi.org/10.1007/s10706-019-00933-x

Kleinhans, M. G., Markies, H., De Vet, S. J., In't Veld, A. C., & Postema, F. N. (2011). Static and dynamic angles of repose in loose granular materials under reduced gravity. *Journal of Geophysical Research: Planets*, *116*(11). https://doi.org/10.1029/2011JE003865

Kodicherla, S. P. K., Gong, G., Fan, L., Moy, C. K. S., & He, J. (2018). Effects of preparation methods on inherent fabric anisotropy and packing density of reconstituted sand. Cogent Engineering, 5(1), 1–14. https://doi.org/10.1080/23311916.2018.1533363

Kolbuszewski, J. . (1984). International society for soil mechanics and foundation engineering. Geotextiles and Geomembranes, 1(2), 161–162. https://doi.org/10.1016/0266-1144(84)90012-8

Kumar, J., & Madhusudhan, B. N. (2010). Effect of relative density and confining pressure on Poisson ratio from bender and extender elements tests. Geotechnique, 60(7), 561–567. https://doi.org/10.1680/geot.9.T.003

Kuwano, R., & Jardine, R. J. (2007). A triaxial investigation of kinematic yielding in sand. Geotechnique, 57(7), 563–579. https://doi.org/10.1680/geot.2007.57.7.563

Kuwano, Reiko. (1999). A thesis submitted to the University of London (Imperial College of Science, Technology and Medicine) in partial fulfilment of the requirements for the degree of Doctor of Philosophy in the Faculty of Engineering: Vol. C (Issue March). Imperial College London.

Lane, J. E., Metzger, P., & Carlson, J. (2010). *Lunar Dust Particles Blown By Lander Engine Exhaust in Rarefied and Compressible Flow*.

Latham, G. (1970). Lunar Seismology. 52(1), 162–165.

Latham, G., Ewing, M., Press, F., & Sutton, G. (1969). The Apollo passive seismic experiment. Science, 165(3890), 241–250. https://doi.org/10.1126/science.165.3890.241

Latini, C., & Zania, V. (2017). Triaxial Tests in Fontainebleau Sand (Vol. 20).

Le Maistre, S., Rivoldini, A., Caldiero, A., Yseboodt, M., Baland, R.-M., Beuthe, M., Van Hoolst, T., Dehant, V., Folkner, W. M., & Buccino, D. (2023). Spin state and deep interior structure of Mars from InSight radio tracking. Nature, 619, 733–737. https://doi.org/10.1038/s41586-023-06150-0ï

Lee, J.-S., & Carlos Santamarina, J. (2006). Discussion "Measuring Shear Wave Velocity Using Bender Elements." Geotechnical Testing Journal, 28(5). www.astm.org

Lee, J.-S., & Santamarina, J. C. (2005). Bender Elements: Performance and Signal Interpretation. Journal of Geotechnical and Geoenvironmental Engineering, 131(9), 1063–1070. https://doi.org/10.1061/(asce)1090-0241(2005)131:9(1063)

Liu, K., Gu, D., Guo, M., & Sun, J. (2022). Effects of processing parameters on densification behavior, microstructure evolution and mechanical properties of W–Ti alloy fabricated by laser powder bed fusion. Materials Science and Engineering A, 829(October 2021), 142177. https://doi.org/10.1016/j.msea.2021.142177

Lognonné, P., Banerdt, W. B., Giardini, D., Pike, W. T., Christensen, U., Laudet, P., de Raucourt, S., Zweifel, P., Calcutt, S., Bierwirth, M., Hurst, K. J., Ijpelaan, F., Umland, J. W., Llorca-Cejudo, R., Larson, S. A., Garcia, R. F., Kedar, S., Knapmeyer-Endrun, B., Mimoun, D., … Wookey, J. (2019). SEIS: Insight's Seismic Experiment for Internal Structure of Mars. In *Space Science Reviews* (Vol. 215, Issue 1). The Author(s). https://doi.org/10.1007/s11214-018-0574-6

Lognonné, P., Banerdt, W. B., Pike, W. T., Giardini, D., Christensen, U., Garcia, R. F., Kawamura, T., Kedar, S., Knapmeyer-Endrun, B., Margerin, L., Nimmo, F., Panning, M., Tauzin, B., Scholz, J. R., Antonangeli, D., Barkaoui, S., Beucler, E., Bissig, F., Brinkman, N., … Zweifel, P. (2020). Constraints on the shallow elastic and anelastic structure of Mars from InSight seismic data. Nature Geoscience, 13(3), 213–220. https://doi.org/10.1038/s41561-020-0536-y

López-Retamales, S. (2022). *Development of a method to evaluate the risk of liquefaction of sands from a dynamic penetrometer test*. ENPC.

Lorenz, R. D., Lemmon, M. T., Maki, J., Banfield, D., Spiga, A., Charalambous, C., Barrett, E., Herman, J. A., White, B. T., Pasco, S., & Banerdt, W. B. (2020). Scientific Observations With the InSight Solar Arrays: Dust, Clouds, and Eclipses on Mars. Earth and Space Science, 7(5), 1–28. https://doi.org/10.1029/2019EA000992

M.L. Lings, & P. D. Greening. (2001). A novel bender/extender element for soil testing. Gétoechnique.

Mahmoodlu, M. G., van Genuchten, M. T., Sweijen, T., & Raoof, A. (2018). Unsaturated hydraulic properties of heterogeneously packed sands: A pore-scale computational study. Journal of Hydrology, 565(July), 570–580. https://doi.org/10.1016/j.jhydrol.2018.07.060

Majumdar, A., & Bhushan, B. (1991). Fractal Model of Elastic-Plastic Contact Between Rough Surfaces. Journal of Tribology, 113(1), 1–11. https://doi.org/10.11776/cjam.33.05.D068

Mckay, D. S., Carter, J. L., Boles, W. W., Allen, C. C., & Allton, J. H. (1994). JSC-1: A NEW LUNAR SOIL SIMULANT. *Engineering, Construction, and Operations in Space*, *4*, 857–866. http://ares.jsc.nasa.gov/HumanExplore/Exploration/EXLibrary/DOCS/EIC050.HTML

Mancuso, C., Simonelli, A. L. & Vinale, F. (1989). Numerical analysis of in situ S-wave measurements. Proc. 12th ICSMFE, Rio de Janeiro.

Mandal, S., Nicolas, M., & Pouliquen, O. (2019). Insights into the rheology of cohesive granular media. Proceedings of the National Academy of Sciences. https://doi.org/10.1073/pnas.1921778117/-/DCSupplemental.y

Marteau E, Golombek M, Vrettos C, Garvin JB, Williams NR (2021). Soil mechanical properties at the InSight landing site, Mars. In: 52nd Lunar and Planetary Science Conference, abstract #2067, Houston.

Marteau E, Golombek M, Vrettos C, Delage P, Williams NR, Ansan V (2022). Soil strength properties derived from scraping and dumping activities at the InSight landing site on Mars. In: 53rd Lunar and Planetary Science Conference. Abstract #1523, Houston.

Marteau, E., Wehage, K., Higa, S., Moreland, S., & Meirion-Griffith, G. (2023). Geotechnical assessment of terrain strength properties on Mars using the Perseverance rover's abrading bit. Journal of Terramechanics, 107, 13–22. https://doi.org/10.1016/j.jterra.2023.02.001

Marteau E, Golombek M, Delage P, Vrettos C, Hurst K, Gomez A et al. (2023a). Initial results from the Insight lander robotic arm soil mechanics experiments on Mars. 54th Lunar and Planetary Science Conference. Abstract #1597, Houston.

Massarsch, K. R. (2015). Determination of Shear Modulus of Soil from Static and Seismic Penetration Testing. Proceedings in Honour of Prof. A. Anagnostopoulos, December, 335–352. https://www.researchgate.net/publication/321937664_Determination_of_Shear_Modulus_of_Soil_from_Static_and_Seismic_Penetration_Testing

Mavko, G., Mukerji, T., & Dvorkin, J. (2009). The rock physics Handbook: Vol. Second Edition (C. U. PRESS (ed.); Second). Cambridge Press.

Mesri, G., & Vardhanabhuti, B. (2009). Compression of granular materials. Canadian Geotechnical Journal, 46(4), 369–392. https://doi.org/10.1139/T08-123

Min, D. J., Shin, C., & Yoo, H. S. (2004). Free-surface boundary condition in finite-difference elastic wave modeling. Bulletin of the Seismological Society of America, 94(1), 237–250. https://doi.org/10.1785/0120020116

Mindlin, R. D. (1949). Compliance of Elastic Bodies in Contact. Journal of Applied Mechanics, Transactions ASME, 16(3), 259–268. https://doi.org/10.1115/1.4009973

Miura, S., & Toki, S. (1982). A sample preparation method and its effec on static and cyclic deformation-strength properties of the sand. Japanese Society of Soil Mechanics and Foundation EngineeringJapanese Society of Soil Mechanics and Foundation Engineering, 22(1), 61–77. http://www.mendeley.com/research/geology-volcanic-history-eruptive-style-yakedake-volcano-group-central-japan/

Milushev, M., Süßer, M., & Wüchner, F. (2004). Investigation of two different types of displacement transducers in the cryogenic environment. *Cryogenics*, *44*(3), 197–201. https://doi.org/10.1016/j.cryogenics.2003.11.004

Mimoun, D., Murdoch, N., Lognonné, P., Hurst, K., Pike, W. T., Hurley, J., Nébut, T., & Banerdt, W. B. (2017). The Noise Model of the SEIS Seismometer of the InSight Mission to Mars. *Space Science Reviews*, *211*(1–4), 383–428. https://doi.org/10.1007/s11214-017-0409-x

Mittelholz, A., Johnson, C. L., Fillingim, M., Grimm, R. E., Joy, S., Thorne, S. N., & Banerdt, W. B. (2023). Mars' External Magnetic Field as Seen From the Surface With InSight. Journal of Geophysical Research: Planets, 128(1). https://doi.org/10.1029/2022JE007616

Mo, P. Q., Gao, F., Zhou, G., Li, R., Yan, K., & Chen, J. (2019). An experimental study on triaxial compression tests and cone penetration tests in planetary regolith simulant under low gravity fields. Journal of Testing and Evaluation, 47(3). https://doi.org/10.1520/JTE20180005

Mohsin, A. K. M., & Airey, D. W. (2005). Influence of cementation and density on Gmax for sand. 16th International Conference on Soil Mechanics and Geotechnical Engineering, 16(1), 413–416. https://doi.org/10.1016/0266-1144(84)90012-8

Morgan, P., Grott, M., Knapmeyer-Endrun, B., Golombek, M., Delage, P., Lognonné, P., Piqueux, S., Daubar, I., Murdoch, N., Charalambous, C., Pike, W. T., Müller, N., Hagermann, A., Siegler, M., Lichtenheldt, R., Teanby, N., & Kedar, S. (2018). A Pre-Landing Assessment of Regolith Properties at the InSight Landing Site. In Space Science Reviews (Vol. 214, Issue 6). https://doi.org/10.1007/s11214-018-0537-y

Murdoch, N., Kenda, B., Kawamura, T., Spiga, A., Lognonné, P., Mimoun, D., & Banerdt, W. B. (2017). Estimations of the Seismic Pressure Noise on Mars Determined from Large Eddy Simulations and Demonstration of Pressure Decorrelation Techniques for the Insight Mission. In Space Science Reviews (Vol. 211, Issues 1–4, pp. 457–483). Springer Netherlands. https://doi.org/10.1007/s11214-017-0343-y

Murillo, C. A. (2006). Caracterización geotécnica de estructuras multicapas en centrífuga empleando ondas de superficie. In Universidad de los Andes (Vol. 1999, Issue December).

Murillo, C. A., Thorel, L., & Caicedo, B. (2009). Spectral analysis of surface waves method to assess shear wave velocity within centrifuge models. Journal of Applied Geophysics, 68(2), 135–145. https://doi.org/10.1016/j.jappgeo.2008.10.007

Nagihara, S., Ngo, P., & Grott, M. (2022). Thermal Properties of the Mojave Mars Regolith Simulant in Mars-Like Atmospheric Conditions. International Journal of Thermophysics, 43(7). https://doi.org/10.1007/s10765-022-03023-y

Nakagawa, K., Soga, K., & Mitchell, J. K. (2001). Observation of Biot compressional wave of the second kind in granular soils. Géotechnique, 51(1), 85–89. https://doi.org/10.1680/geot.51.1.85.39355

Nakagawa, Koichi, Soga, K., & Mitchell, J. K. (1996). Wave Propagation in Soils. Journal of Geotechnical Engineering, 122(4), 302–308.

NASA/JPL. (2022). InSight's Seismogram of Big Martian Quake. May 09, 2022. https://mars.nasa.gov/resources/26731/insights-seismogram-of-big-martian-quake/

Newland, P. L., & Allely, B. H. (1959). Volume changes during undrained triaxial tests on saturated dilatant granular materials. Géotechnique, 9(4), 174–182.

Oda, M. (1972a). Initial fabrics and their relations to mechanical properties of granular material. Japanese Society of Soil Mechanics and Foundation Engineering, 12(1), 17–36. http://www.mendeley.com/research/geology-volcanic-history-eruptive-style-yakedake-volcano-group-central-japan/

Oda, M. (1972b). The mechanism of fabric changes during compressional deformation of sand. Japanese Society of Soil Mechanics and Foundation Engineering, 2(1), 17–36. http://www.mendeley.com/research/geology-volcanic-history-eruptive-style-yakedake-volcano-group-central-japan/

Ogino, T., Oikawa, T. M. H., & Takayuki, T. (2010). Frequency response characteristics of bender element test system identified by frequency-swept signal input-influence on accuracy of received waveform reconstruction. Soils and Foundations, 50(5).

Oztoprak, S., & Bolton, M. D. (2013). Stiffness of sands through a laboratory test database. Geotechnique, 63(1), 54–70. https://doi.org/10.1680/geot.10.P.078

Pan, L., Ehlmann, B. L., Carter, J., & Ernst, C. M. (2017). The stratigraphy and history of Mars' northern lowlands through mineralogy of impact craters: A comprehensive survey. Journal of Geophysical Research: Planets, 122(9), 1824–1854. https://doi.org/10.1002/2017JE005276

Panning, M. P., Beucler, É., Drilleau, M., Mocquet, A., Lognonné, P., & Banerdt, W. B. (2015). Verifying single-station seismic approaches using Earth-based data: Preparation for data return from the InSight mission to Mars. *Icarus*, *248*, 230–242. https://doi.org/10.1016/j.icarus.2014.10.035

Payan, M., Senetakis, K., Khoshghalb, A., & Khalili, N. (2017). Effect of Gradation and Particle Shape on Small-Strain Young's Modulus and Poisson's Ratio of Sands. International Journal of Geomechanics, 17(5), 04016120. https://doi.org/10.1061/(asce)gm.1943-5622.0000811

Pennington, D. S. (1999). The anisotropic small strain stiffness of Cambridge Gault clay by. In PhD. University of Bristol.

Persson, B. N. J. (2006). Contact mechanics for randomly rough surfaces B.N.J. Surface Science Reports 61, 61(201), 163–169. https://doi.org/10.1140/epje/e2006-00019-2

Peters, G. H., Abbey, W., Bearman, G. H., Mungas, G. S., Smith, J. A., Anderson, R. C., Douglas, S., & Beegle, L. W. (2008). Mojave Mars simulant-Characterization of a new geologic Mars analog. *Icarus*, *197*(2), 470–479. https://doi.org/10.1016/j.icarus.2008.05.004

Piqueux, S., & Christensen, P. R. (2009). A model of thermal conductivity for planetary soils: 2. Theory for cemented soils. *Journal of Geophysical Research: Planets*, *114*(9). https://doi.org/10.1029/2008JE003309

Posiolova, L. V., Lognonné, P., Banerdt, W. B., Clinton, J., Collins, G. S., Kawamura, T., Ceylan, S., Daubar, I. J., Fernando, B., Froment, M., Giardini, D., Malin, M. C., Miljković, K., Stähler, S. C., Xu, Z., Banks, M. E., Beucler, Cantor, B. A., Charalambous, C., … Zenhäusern, G. (2022). Largest recent impact craters on Mars: Orbital imaging and surface seismic co-investigation. Science, 378(6618), 412–417. https://doi.org/10.1126/science.abq7704

Pou, L., Nimmo, F., Lognonné, P., Mimoun, D., Garcia, R. F., Pinot, B., Rivoldini, A., Banfield, D., & Banerdt, W. B. (2021). Forward Modeling of the Phobos Tides and Applications to the First Martian Year of the InSight Mission. Earth and Space Science, 8(7). https://doi.org/10.1029/2021EA001669

Pou, L., Nimmo, F., Rivoldini, A., Khan, A., Bagheri, A., Gray, T., Samuel, H., Lognonné, P., Plesa, A.-C., & Gudkova, T. (2022). Tidal Constraints on the Martian Interior. Journal of Geophysical Research. Planets, 2022(11), 10. https://doi.org/10.1029/2022JE007291ï

Poulos & Davis. (1974). Elastic Solutions for Soil. CENTRE FOR GEOTECHNICAL RESEARCH, University Of Sidney. https://kupdf.net/download/elastic-solutions-for-soil-and-rock-mechanics-by-poulos-and-davis-pdf_59050e7edc0d600765959eac_pdf

Presley, M. A., & Christensen, P. R. (1997). Thermal conductivity measurements of particulate materials 2. Results. *Journal of Geophysical Research: Planets*, *102*(E3), 6551–6566. https://doi.org/10.1029/96JE03303

Saadi, F. Al, Wolf, K.-H., & Kruijsdijk, C. van. (2017). Characterization of Fontainebleau Sandstone: Quartz Overgrowth and its Impact on Pore-Throat Framework. Journal of Petroleum & Environmental Biotechnology, 08(03). https://doi.org/10.4172/2157-7463.1000328

Sanchez-Salinero, I., Roesset, J. M., & Stokoe, K. H. (1986). Analytical studies of body wave propagation and attenuation. TEXAS UNIV AT AUSTIN GEOTECHNICAL ENGINEERING CENTER, 290.

Santamarina, J. C., Klein, K. A., & Fam, M. A. (2001). Soils and waves (Wiley (ed.)).

Sauzeat, C., & Di Benedetto, H. (2015). Tridimensional linear viscoelastic behavior of bituminous materials. In Advances in Asphalt Materials: Road and Pavement Construction. Elsevier Ltd. https://doi.org/10.1016/B978-0-08-100269-8.00003-9

Schanz, T., & Vermeer, P. A. (1999). *Pre-failure Deformation Behaviour of Geomaterials*.

Scholz, J.-R., Widmer-Schnidrig, R., Davis, P., Lognonné, P., Pinot, B., Garcia, R. F., Hurst, K., Pou, L., Nimmo, F., Barkaoui, S., De Raucourt, S., Knapmeyer-Endrun, B., Knapmeyer, M., Orhand-Mainsant, G., Compaire, N., Cuvier, A., Beucler, É., Bonnin, M., Joshi, R., … Banerdt, W. B. (2022). Detection, Analysis, and Removal of Glitches From InSight's Seismic Data From Mars Detection, Analysis, and Removal of Glitches From InSight's Seismic Data From Mars Detection, Analysis, and Removal of Glitches From InSight's Seismic Data From Mars. Earth and Space Science, 2020(11), 10. https://doi.org/10.1029/2020ea001317ï

Schultheiss, P. J. (1981). Simultaneous measurement of P & S wave velocities during conventional laboratory soil testing procedures. Marine Geotechnology, 4(4), 343–367. https://doi.org/10.1080/10641198109379831

ScienceNASA. (2017). Discovery program. Discovery Program. https://www.nasa.gov/planetarymissions/discovery-program/

Scott, R. F., & Ko, H. Y. (1968). Transient rocket-engine gas flow in soil. AIAA Journal, 6(2), 258–264. https://doi.org/10.2514/3.4487

Seiferlin, K., Ehrenfreund, P., Garry, J., Gunderson, K., Hütter, E., Kargl, G., Maturilli, A., & Merrison, J. P. (2008). Simulating Martian regolith in the laboratory. Planetary and Space Science, 56(15), 2009–2025. https://doi.org/10.1016/j.pss.2008.09.017

SEIS-InSight. (2017). SEIS Instrument. Instruments. https://mars.nasa.gov/insight/spacecraft/instruments/seis/

Shen, Y., Zhu, Y., Liu, H., Li, A., & Ge, H. (2018). Macro-meso effects of gradation and particle morphology on the compressibility characteristics of calcareous sand. Bulletin of Engineering Geology and the Environment, 77(3), 1047–1055. https://doi.org/10.1007/s10064-017-1157-6

Shirley, D. J., & Hampton, L. D. (1978). Shear-wave measurements in laboratory sediments. The Journal of the Acoustical Society of America. http://acousticalsociety.org/content/terms.

Siddiquee, M. S. A., Islam, M. S., Tatsuoka, F., & Islam, M. K. (2018). An Anisotropic Model for Granular Material Based on Experiments. Geotechnical and Geological Engineering, 36(3), 1447–1462. https://doi.org/10.1007/s10706-017-0400-z

Sim, W. W., Aghakouchak, A., & Jardine, R. J. (2013). Cyclic triaxial tests to aid offshore pile analysis and design. Proceedings of the Institution of Civil Engineers: Geotechnical Engineering, 166(2), 111–121. https://doi.org/10.1680/geng.12.00056

Sneddon, I. N. (1965). The relation between load and penetration in the axisymmetric boussinesq problem for a punch of arbitrary profile. International Journal of Engineering Science, 3(1), 47–57. https://doi.org/10.1016/0020-7225(65)90019-4

Spencer, J. W., Cates, M. E., & Thompson, D. D. (1994). Frame moduli of unconsolidated sands and sandstones. Geophysics, 59(9), 1352–1361. https://doi.org/10.1190/1.1443694

Spohn, T., Grott, M., Smrekar, S. E., Knollenberg, J., Hudson, T. L., Krause, C., Müller, N., Jänchen, J., Börner, A., Wippermann, T., Krömer, O., Lichtenheldt, R., Wisniewski, L., Grygorczuk, J., Fittock, M., Rheershemius, S., Spröwitz, T., Kopp, E., Walter, I., … Banerdt, W. B. (2018). The Heat Flow and Physical Properties Package (HP3) for the InSight Mission. In *Space Science Reviews* (Vol. 214, Issue 5). The Author(s). https://doi.org/10.1007/s11214-018-0531-4

Spiga, A., Banfield, D., Teanby, N.A. *et al.* Atmospheric Science with InSight. *Space Sci Rev* **214**, 109 (2018). https://doi.org/10.1007/s11214-018-0543-0

Spohn, T., Hudson, T. L., Marteau, E., Golombek, M., Grott, M., Wippermann, T., Ali, K. S., Schmelzbach, C., Kedar, S., Hurst, K., Trebi-Ollennu, A., Ansan, V., Garvin, J., Knollenberg, J., Mueller, N., Piqeux, S., Lichtenheldt, R., Krause, C., Fantinati, C., … Banerdt, W. B. (2021). The InSight HP^3 Penetrator (Mole) on Mars: Soil Properties Derived From the Penetration Attempts and Related Activities. https://doi.org/10.1007/s11214-022-00941-z

Spohn, T., Hudson, T. L., Marteau, E., Golombek, M., Grott, M., Wippermann, T., Ali, K. S., Schmelzbach, C., Kedar, S., Hurst, K., Trebi-Ollennu, A., Ansan, V., Garvin, J., Knollenberg, J., Müller, N., Piqueux, S., Lichtenheldt, R., Krause, C., Fantinati, C., … Banerdt, W. B. (2022). The InSight HP3 Penetrator (Mole) on Mars: Soil Properties Derived from the Penetration Attempts and Related Activities. Space Science Reviews, 218(8). https://doi.org/10.1007/s11214-022-00941-z

Spohn, Tilman, Hudson, T. L., Witte, L., Wippermann, T., Wisniewski, L., Kedziora, B., Vrettos, C., Lorenz, R. D., Golombek, M., Lichtenheldt, R., Grott, M., Knollenberg, J., Krause, C., Fantinati, C., Nagihara, S., & Grygorczuk, J. (2022). The InSight-HP3 mole on Mars: Lessons learned from attempts to penetrate to depth in the Martian soil. Advances in Space Research, 69(8), 3140–3163. https://doi.org/10.1016/j.asr.2022.02.009

Stähler, S. C., Mittelholz, A., Perrin, C., Kawamura, T., Kim, D., Knapmeyer, M., Zenhäusern, G., Clinton, J., Giardini, D., Lognonné, P., & Banerdt, W. B. (2022). Tectonics of Cerberus Fossae unveiled by marsquakes. Nature Astronomy, 6(12), 1376–1386. https://doi.org/10.1038/s41550-022-01803-y

Stutzmann, E., Schimmel, M., Lognonné, P., Horleston, A., Ceylan, S., van Driel, M., Stahler, S., Banerdt, B., Calvet, M., Charalambous, C., Clinton, J., Drilleau, M., Fayon, L., Garcia, R. F., Giardini, D., Hurst, K., Jacob, A., Kawamura, T., Kenda, B., … Spiga, A. (2021). The Polarization of Ambient Noise on Mars. Journal of Geophysical Research: Planets, 126(1). https://doi.org/10.1029/2020JE006545

Suwal, L. P., & Kuwano, R. (2013). Statically and dynamically measured poisson's ratio of granular soils on triaxial laboratory specimens. Geotechnical Testing Journal, 36(4). https://doi.org/10.1520/GTJ20120108

Tabaroei, A., Abrishami, S., & Hosseininia, E. S. (2017). Comparison between Two Different Pluviation Setups of Sand Specimens. Journal of Materials in Civil Engineering, 29(10), 1–11. https://doi.org/10.1061/(asce)mt.1943-5533.0001985

Tatsuoka, F., Iwasaki, T., Fukushima, S., & Sudo, H. (1979). Cyclic undrained triaxial and torsional shear strength of sands for different sample preparation methods. Japanese Society of Soil Mechanics and Foundation Engineering, 19(1), 39–54. https://www.jstage.jst.go.jp/article/bpb1993/17/11/17_11_1460/_pdf/-char/ja

Tatsuoka, F., Ochi, K., Funjii, S., & Okamoto, M. (1986). Cyclic undrained triaxial and torsional shear strength of sands for different sample preparation methods. Japanese Society of Soil Mechanics and Foundation Engineering, 26(3), 23–41. http://www.mendeley.com/research/geology-volcanic-history-eruptive-style-yakedake-volcano-group-central-japan/

Tell, K., Dreißigacker, C., Tchapnda, A. C., Yu, P., & Sperl, M. (2020). Acoustic waves in granular packings at low confinement pressure. Review of Scientific Instruments, 91(3). https://doi.org/10.1063/1.5122848

Thiery, C. (2013). Tomographie à rayons X Tomographie à rayons X. Techniques de l'ingénieur. P950 V3 (2013) 1–30. https://doi.org/10.51257/a-v1-p950

Trebi-Ollennu, A., Kim, W., Ali, K., Khan, O., Sorice, C., Bailey, P., Umland, J., Bonitz, R., Ciarleglio, C., Knight, J., Haddad, N., Klein, K., Nowak, S., Klein, D., Onufer, N., Glazebrook, K., Kobeissi, B., Baez, E., Sarkissian, F., … Lin, J. (2018). InSight Mars Lander Robotics Instrument Deployment System. *Space Science Reviews*, *214*(5). https://doi.org/10.1007/s11214-018-0520-7

V. Jovičić, M. R. Coop, & M. Simić. (1996). Objective criteria for determining G max from bender element tests. Géotechnique.

Vaid, Y. P., Sivathayalan, S., & Stedman, D. (1999). Influence of Specimen-Reconstituting Method on the Undrained Response of Sand. Geotechnical Testing Journal, 22(3), 187–195. https://doi.org/10.1520/gtj11110j

Van Den Wildenberg, S., Van Hecke, M., & Jia, X. (2013). Evolution of granular packings by nonlinear acoustic waves. Epl, 101(1). https://doi.org/10.1209/0295-5075/101/14004

Van Den Wildenberg, Siet, Van Loo, R., & Van Hecke, M. (2013). Shock waves in weakly compressed granular media. Physical Review Letters, 111(21), 1–7. https://doi.org/10.1103/PhysRevLett.111.218003

Verdier, N., Ansan, V., Delage, P., Ali, K. S., Beucler, E., Charalambous, C., Constant, E., Spiga, A., Golombek, M., Marteau, E., Lapeyre, R., Gaudin, E., Yana, C., Hurst, K., Lognonné, P., & Banerdt, B. W. (2023). Using Wind Dispersion Effects During the InSight Tether Burial Activities to Better Constrain the Regolith Grain Size Distribution. Journal of Geophysical Research: Planets, 128(5). https://doi.org/10.1029/2022JE007707

Vieira, A., Maranha, J. R., Lapa, J., & Figueiredo, A. (2019). Some aspects of measurement of sand thermal conductivity from laboratory tests. Proceedings of the XVII ECSMGE, September. https://doi.org/10.32075/17ECSMGE-2019-0541

Viggiani, G., & Atkinson, J. H. (1995a). Interpretation of bender element tests. Geotechnique, 45(1), 149–154.

Viggiani, G., & Atkinson, J. H. (1995b). Stiffness of fine-grained soil at very small strains. Geotechnique, 45(2), 249–265.

Viggiani, G., & Atkinson, J. H. (1995c). Stiffness of fine-grained soil at very small strains. Geotechnique, 45(2), 249–265. https://doi.org/10.1680/geot.1995.45.2.249

Viggiani, G., & Atkinson, J. H. (1997). Interpretation of bender element tests. Geótechnique, 47(4), 873–877.

Walton, K. (1987). THE EFFECTIVE ELASTIC MODULI OF A RANDOM PACKING OF SPHERES. Journal of Public Health Dentistry, 35(2), 213–226. https://doi.org/10.1111/j.1752-7325.1991.tb02185.x

Wanatowski, D., & Chu, J. (2008). Effect of specimen preparation method on the stress-strain behavior of sand in plane-strain compression tests. Geotechnical Testing Journal, 31(4), 308–320. https://doi.org/10.1520/gtj101307

Wang, J., Zhang, F., & Yang, Z. (Joey). (2019). Anisotropy in small-strain shear modulus of permafrost at rising temperatures. Cold Regions Science and Technology, 160(January), 1–12. https://doi.org/10.1016/j.coldregions.2019.01.003

Wang, Y., Benahmed, N., Cui, Y. J., & Tang, A. M. (2017). A novel method for determining the small-strain shear modulus of soil using the bender elements technique. Canadian Geotechnical Journal, 54(2), 280–289. https://doi.org/10.1139/cgj-2016-0341

Warner, N. H., Golombek, M. P., Ansan, V., Marteau, E., Williams, N., Grant, J. A., Hauber, E., Weitz, C., Wilson, S., Piqueux, S., Mueller, N., Grott, M., Spohn, T., Pan, L., Schmelzbach, C., Daubar, I. J., Garvin, J., Charalambous, C., Baker, M., & Banks, M. (2022). In Situ and Orbital Stratigraphic Characterization of the InSight Landing Site—A Type Example of a Regolith-Covered Lava Plain on Mars. Journal of Geophysical Research: Planets, 127(4), 0–39. https://doi.org/10.1029/2022JE007232

Weiblen PW, & Gordon, K. (1988). Characteristics of a Simulant for Lunar Surface Materials. *Symposium on Lunar Bases and Space Activities in the 21st Century*, Paper No. LBS-88-213.

Wells, T., Fityus, S., Smith, D. W., & Moe, H. (2006). The indirect estimation of saturated hydraulic conductivity of soils, using measurements of gas permeability. I. Laboratory testing with dry granular soils. Australian Journal of Soil Research, 44(7), 719–725. https://doi.org/10.1071/SR06037

Witze, A. (2021). Mars's core has been measured - and it's surprisingly large. Nature, 591(7851), 514–515. https://doi.org/10.1038/d41586-021-00696-7

W.R. van Dijk (Ed.), Physics of Plant Environment, North Holland Publishing, Amsterdam (1963), pp. 210-235

Wu, Y. S., Pruess, K., & Persoff, P. (1998). Gas Flow in Porous Media with Klinkenberg Effects. Transport in Porous Media, 32(1), 117–137. https://doi.org/10.1023/A:1006535211684

Yamamuro, J. A., & Lade, P. V. (1997). Static liquefaction of very loose sands. Canadian Geotechnical Journal, 34(6), 905–917. https://doi.org/10.1139/t97-057

Yamamuro, J. A., & Wood, F. M. (2004). Effect of depositional method on the undrained behavior and microstructure of sand with silt. Soil Dynamics and Earthquake Engineering, 24(9–10), 751–760. https://doi.org/10.1016/j.soildyn.2004.06.004

Yimsiri, S., & Soga, K. (2003). Application of micromechanics model to study anisotropy of soils at small strains. Soils and Foundations, 42(5), 15–26. https://doi.org/10.3208/sandf.42.5

Youn, J. U., Choo, Y. W., & Kim, D. S. (2008). Measurement of small-strain shear modulus Gmax of dry and saturated sands by bender element, resonant column, and torsional shear tests. Canadian Geotechnical Journal, 45(10), 1426–1438. https://doi.org/10.1139/T08-069

Yu, W., Zeng, X., Li, X., Wei, G., & Fang, J. (2022). New Martian Dust Simulant JMDS-1 and Applications to Laboratory Thermal Conductivity Measurements. Earth and Space Science, 9(1), 1–15. https://doi.org/10.1029/2020EA001347

Zhang, N., Yu, X., Pradhan, A., & Puppala, A. J. (2015). Effects of particle size and fines content on thermal conductivity of Quartz sands. Transportation Research Record, 2510, 36–43. https://doi.org/10.3141/2510-05

Zheng, J., Hryciw, R. D., & Ventola, A. (2017). Compressibility of Sands of Various Geologic Origins at Pre-crushing Stress Levels. Geotechnical and Geological Engineering, 35(5), 2037–2051. https://doi.org/10.1007/s10706-017-0225-9

Zlatovic, S., & Ishihara, K. (1997). Normalized behavior of very loose non-plastic soils: effect of fabric. Soils and Foundations, 37(4), 47–56. http://www.mendeley.com/research/geology-volcanic-history-eruptive-style-yakedake-volcano-group-central-japan/

Zuiderveld, K. (1994). Contrast Limited Adaptive Histogram Equalization (CLAHE). In Academic Press. https://la.mathworks.com/matlabcentral/fileexchange/22182-contrast-limited-adaptive-histogram-equalization-clahe?s_tid=FX_rc2_behav

A. Appendix A: Wave velocity software

Seeking to enable the interpretation of the numerous waves acquired during the performed measurement experimental programs within a reasonable timeframe, a series of software tools were developed utilizing the built-in app construction tool *Guide* of the MATLAB computational environment. This chapter departs from the initial concept and main purpose of the tool, presenting and detailing the main and secondary versions of the tool up to its current state. Emphasis is placed upon the possibilities that the environment offers to aid the user implement the different methods for identification of wave departure and arrival times, as well as the computation of the wave velocities and the Poisson ratio. The interface components and functionality of the key versions are also presented in detail, as well as the software architecture and a utilization guide are provided; in general, the chapter intends to play the role of an advanced version of a user manual for the tool in question.

1.1. General concept and purpose of the tool

The idea for the tool originated from the necessity of processing numerous wave velocity n based on the existing time domain methods. Since the adequate interpretation of the data poses a key question, the idea was to design a User Interface that enabled the visualization of the acquired signals, and to identify the departure and arrival time instants for each wave.

Over the development process of the tool, the interface and even the general concept itself evolved as testing identified some defects and potential for improvement of the tool. Because of this, barely any resemblance is apparent between the initial version, consisting of a series of list selectors for automatically detected candidate points on a single wave, to the current version on which an entire program is displayed simultaneously, P and S waves analysed simultaneously and separate windows for Poisson ratio calculation and advanced functionality functions have been implemented.

1.2. Versions of the tool

As the idea for the tool evolved over its development, a series of versions were developed and tested. While a plethora of minor modifications took place, and a considerable number of versions existed, they can be grouped into three main stages of development.

Version 1.0

The first version of the program set out the general layout of the interface and the basic concept of the tool. In this version, a single group of either P or S waves were loaded along a txt file containing the associated stress values. Then, an automatic method (detailed in the next section) initialized a series of candidate points that were plotted along with the selected wave. The user was then able to utilize a series of list selectors to specify the departure and arrival times for up to three interpretation time-domain-based methods. The results were plotted in a curve for the user to see before exporting them to a txt file for further utilization. This first version remains adequate for when maximum accuracy is required for the determination of either a single or a few waves.

Version 2.0

The second version originated from the realization that the utilisation of list selectors to determine the key instants was not optimal for the interpretation of extensive experimental programs containing numerous signals. It also was observed that under some circumstances the automated identification of the candidate points of either departing or arriving times might malfunction. The utilization paradigm then switched to letting the automatic identification suggest initial values for both arrival and departure times for commonly utilised methods, and then having the user specify the rest of the points via manually clicking on a secondary visualization of the wave which would enable to do so accurately. This methodology was observed to be significantly better and enables to work within a single session with both P and S waves acquired during the same experimental program, as well as providing a useful visualization of the whole experimental program. Advanced persistency functionalities and the possibility of computing the Poisson ratio if desired were also added.

Version 3.0

The most recent version of the program emerged from observing that proper graphical visualization of the program could significantly aid into the interpretation of the acquired signals. It includes several modifications that enable parallel interpretation of the P and S wave signals acquired in similar conditions, particularly useful for the methods that take support in comparing both signal such as the Wang et. Al approach adopted during several stages of this work.

1.3. Software architecture of the tool

The basis for the tool is the input files. These are given in csv format and copied into the input folders created automatically by the program for every session. A txt file associating every data file to the value of the variable of interest (most often stress) exists in each input folder. It is used to create vectors where the departure and arrival times for every wave are stored, updated, and utilized for the calculation of wave travel times.

1.4. User interface of the tool

The user interface of the tool has been designed seeking to display the considerable amount of information of a full P wave and S wave experimental program in an easily comprehensible fashion. In this sense, the interface is structured into five main panels that are associated to the steps of the analysis process. The first panel enables for the selection of a group of data and displays the location of the chosen directory all through the session. This panel also contains a text box that enables to specify the length of the sample, to be utilised for the wave velocity computations. The button to read the files and redraw the results is also located on this panel.

The main panel contains the two graphs utilised to display the acquired waves, and the obtained velocities with the currently specified values for both departure and arrival times.

1.5. Utilization of the tool

Preparing the data

To begin, do not forget to set the desired value for sample length to be utilised in wave velocity computations; to do this, use the box available in the head panel for this purpose and push the “set length button”. The acquired waves must be organized into a folder containing two subfolders engulfing a series of files with the measured data. To utilize the tool, the acquired data, in form of csv files, is introduced into a folder divided into two subfolders containing the P Waves (ONDAS P) and another one containing the S waves (ONDAS S). In each folder, a txt file named DATOSX contains the stress values associated with each measurement.

To begin, push the button Browse on the first panel of the user interface. A window opens enabling to select the location of the folder containing the data to be analysed. Once the folder directory has been chosen, all the relevant files will be automatically copied to the current work location on a folder with the name Current session. If the data is properly loaded in, the button “Draw results” can now be pressed, and the selected data will be displayed in the graphic placed in the main panel. Additionally, a secondary figure window will display the same results, enabling the user access with full MATLAB figure functionality to interact with the results, which can be useful to rapidly zoom in or out, produce result figures, and other purposes. The lower panel will also display the graph for both the first P and S wave file found in the directory (considering alphanumerical order), and a series of coloured lines will display the result of the depart and arrival time initialization.

The second panel in the right contains two selector lists which have been updated to the filenames of every csv file found in each folder, and thus enable the user to select a desired P and S wave simultaneously for individual visualization and analysis. The buttons placed above the graph will then enable the user to initialize all the departure times, and to perform the minor adjustments if needed. Then, the lower panel displaying the active P and S wave can be used to use the button Initialize Departure times, to determine the departure times of up to 3 desired methods for n desired values; a small window will enable to specify the desired number of stress values to be manually adjusted, and then these times can be specified by clicking the graph near the desired value. The next step, and key activity for each session, is to determine the arrival times for each wave individually. The button Specify arrival time located in each panel for the P and S waves enables the user to accomplish this in a similar fashion, clicking 3 times for the 3 desired methods.

Further correction of initialization and arrival times can be performed with the other options from the interface. Since the specification of the arrival times for an abundant experimental program may become a considerably long task, advanced persistence functionalities have been implemented into the tool since its second version. By pushing the Save session button, all the necessary files to store the results and the analysis performed in the active session are created and stored into the "Last session" folder. This folder can be then used to continue the analysis in a later time simply by selecting it from the browser window displayed when pushing the button "Load Session". If the user so desires, the poisson ratio may be computed for any combination of the measurement methods employed simply by clicking the "Analyze results" button. The results are loaded here and may be written to a file using the Export Results button.

The output results create files containing the departure and arrival times specified for every method, so that wave velocity may be computed with a varying length if the user so desires.

1.6. The future of the tool

While the MATLAB guide tool considerably facilitated the development effort of this program, the requirement of having a MATLAB license to utilise the tool may hamper its extensiveness significantly. The idea then exists to develop a version of the tool on Python or other open-source code so that it may be accessible for free and potentially further utilized.

The MATLAB Guide-developed application (shown in Figure 8) enables both highly accurate and quick identification of both the departing and arrival times of the analysed waves, while enabling the user to consider simultaneously up to three methodologies for identifying the departing and arrival times.

Methodologies for travel time assessment are of special relevance when dealing with the identification of the S-wave, which is not trivial to identify in most of the cases. During the interpretation process, it was observed that simultaneous visualization of the waves recorded at different confining pressures in the same space can be of the utmost importance to achieve adequate identification of the first arrival in the signals; in the case of some measurements, the effects of the graphical scale at which the wave is displayed can also be of a high relevance for ensuring accurate locating of the points involved in travel time determination. This was often observed to be the case for the low stresses in both P and S wave signals. Proper signal visualization is also particularly important when making use of the finally chosen Wangs approach (choosing the S wave arrival with assistance from its appearance in a corresponding P signal) for the choice of the arrival time, since it becomes necessary to view P and S waves simultaneously on the same timescale to make adequate use of this approach.

The data is first read from csv files containing the registered waves and a txt with the utilised stress values. Once a set of data has been selected and visualized, the MATLAB based app allows for the identification of the relevant timestamps for the departure and arrival of the waves. For convenience, the tool allows the user to work simultaneously with up to 3 methods, as well as to visualize the results for the current set of signals and to export both a plot and a result file. For identification of the timestamps, a method was developed seeking to automatically identify the existing local maximum, minimum and zero values that make up the potential points of interest of the signal. This identification serves as an automatic initialization method, especially for the wave departure times. In order to achieve this, the following procedure is implemented.

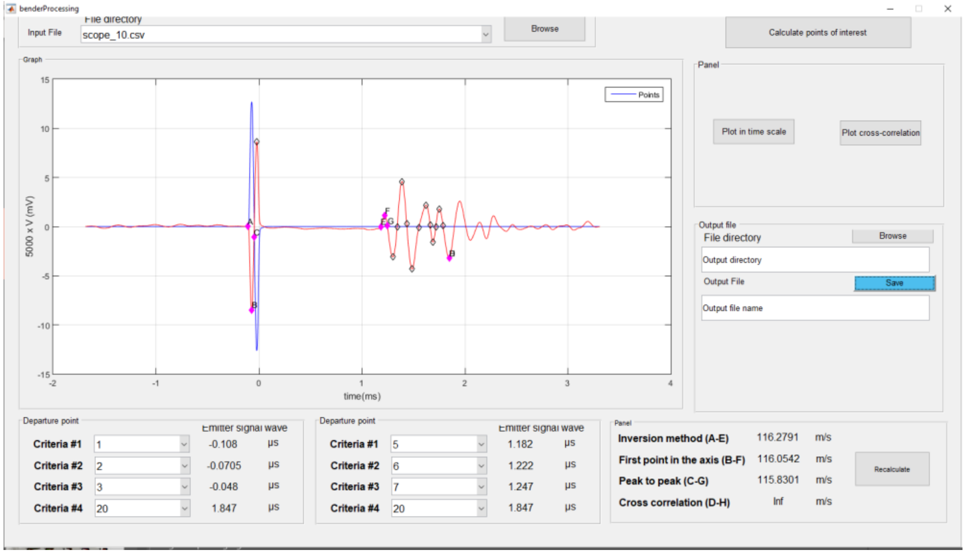

Input File: scope_10.csv

Departure point

		Emitter signal wave	
Criteria #1	1	-0.108	µs
Criteria #2	2	-0.0705	µs
Criteria #3	3	-0.048	µs
Criteria #4	20	1.847	µs

Departure point

		Emitter signal wave	
Criteria #1	5	1.182	µs
Criteria #2	6	1.222	µs
Criteria #3	7	1.247	µs
Criteria #4	20	1.847	µs

Panel

Inversion method (A-E)	116.2791	m/s
First point in the axis (B-F)	116.0542	m/s
Peak to peak (C-G)	115.8301	m/s
Cross correlation (D-H)	Inf	m/s

Figure A-1. Interface of the originally developed GUIDE tool for single wave data analysis.

Initially, a set of candidates for local maximum and minimums is established after evaluating the sign function of numerically calculated derivatives between every point in the signal and its surrounding neighbours. This procedure is a recursive method based on a parameter which was selected to determine an adequate number of points (seeking to not saturate the visual interface with too many choices of potential candidate points). After that, the search is widened from each of these candidate points by following the curve up to the previous existing inflection point (or the beginning of the signal should it be the case). A new candidate point is then proposed.

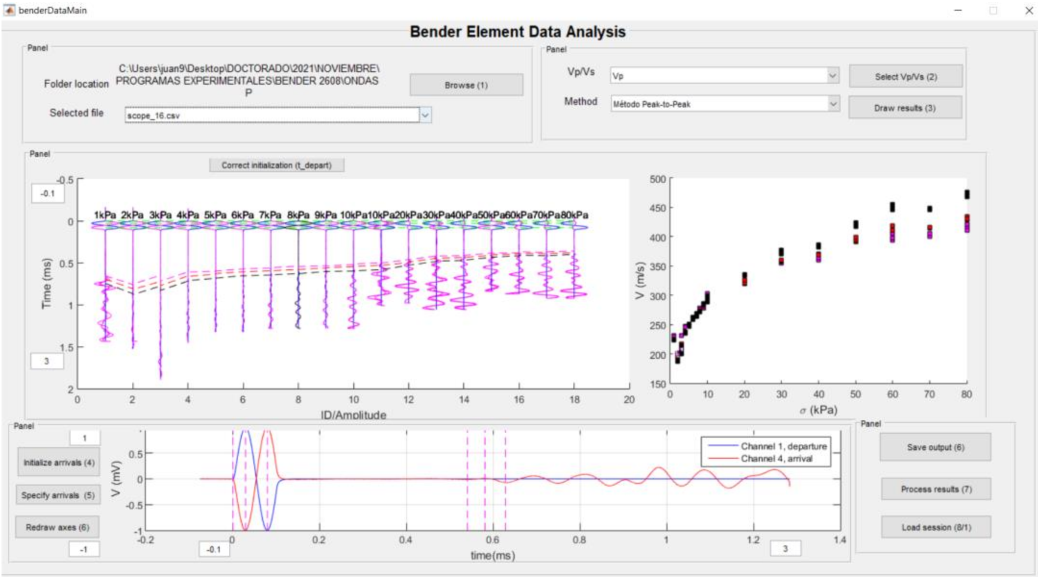
benderDataMain

Bender Element Data Analysis

Folder location: C:\Users\juan9\Desktop\DOCTORADO\2021\NOVIEMBRE\PROGRAMAS EXPERIMENTALES\BENDER 2608\ONDAS P

Selected file: scope_16.csv

Vp/Vs: Vp

Method: Método Peak-to-Peak

Figure A-2. Aspect of the second iteration of the result interpretation program.

After some work with the MATLAB application, a second version was developed, enabling simultaneous visualization of all the waves in a single experimental program as seen in Figure 9. Direct specification of arrival and depart was improved by enabling the user to specify them by clicking in a visual interface. Corrections of the automatically initialized values for departure and arrival times can be specified both separately and simultaneously for waves taken at the same stress value.

Another modification was then incorporated in the final version making it possible to directly visualize and compare corresponding P and S waves with the same timescale, which can be seen Figure 10. This was observed to be considerably more efficient, enabling accurate interpretation of the considerable of the data acquired using the criteria proposed by Wang; as seen in Figure 10, the points for the S wave arrival are chosen at the same location when the first negative peak with considerable amplitude appears in the matching P wave signal. The obtained travel times can then be exported for the chosen interpretation methods and are also utilised in the 'Process results' tool to compute the Poisson ratio. The wave velocities can also be visualized in the interface (see Figure 9) as they are displayed inside the program for a specified value of sample length.

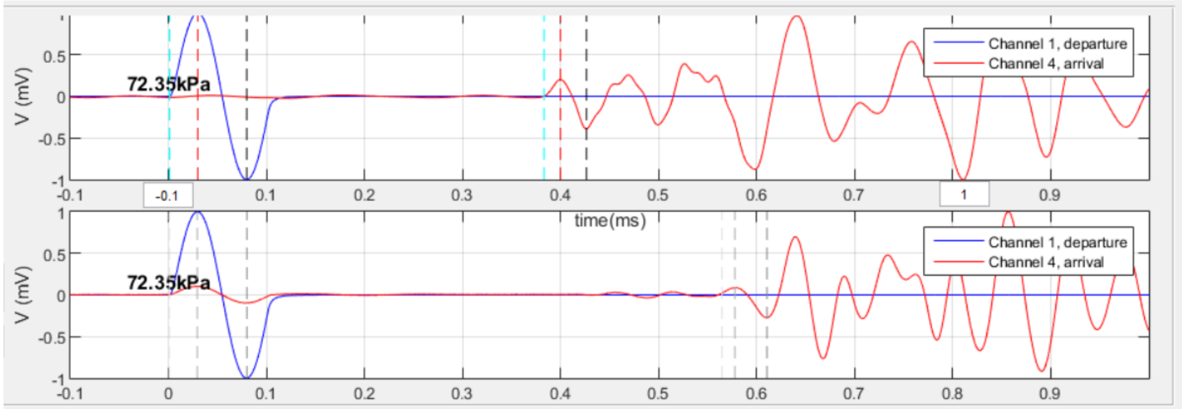

Figure A-3. Simultaneous visualization of the P and S waves using the result software.

An example of the waveforms acquired during one of the four experimental programs completed is now presented in Figure 11, along with lines marking the identified locations of the departure and arrival of the waves for the three utilized criteria. All the signals acquired at the same stress value are averaged to account for measurement variability and repeatability.

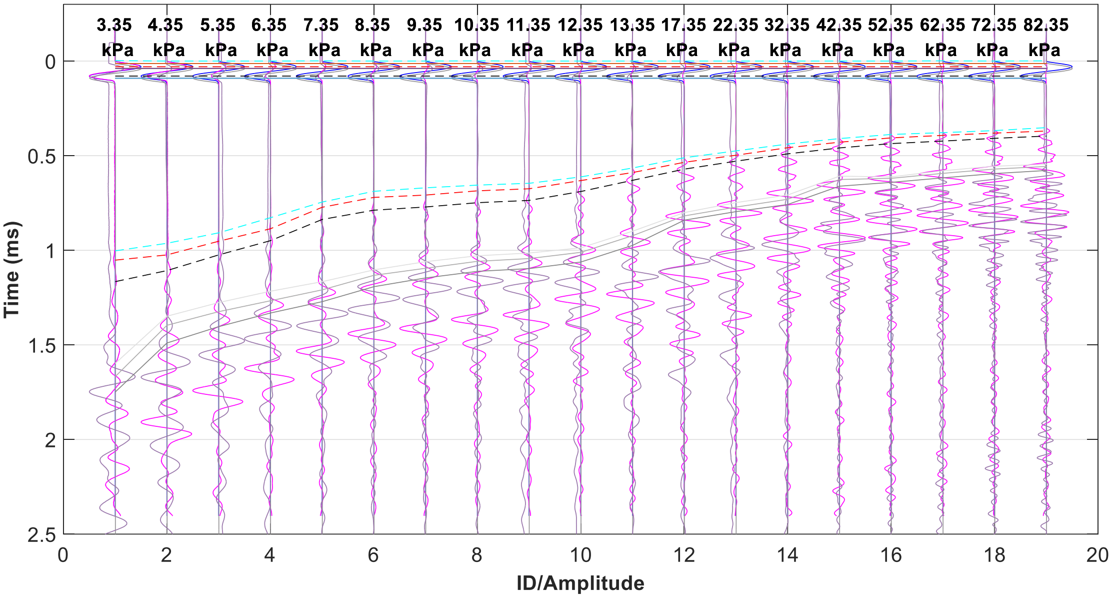

Figure A-4 Waves acquired during the 23/09 experimental program. Depart an arrival times are signaled both for P and S waves.

After trying several of these approaches, authors chose the common peak-to-peak method and the method proposed by (Wang et al., 2017) that chose the arrival time of the S-wave aided by a corresponding P-wave signal recorded at the same stress level in the sample. Once the travel time is determined, the velocity can be calculated dividing it with the travel distance L. This distance is not only the separation of the sample caps (corrected for every datapoint with the adequate measurements), but the length of the bender elements must also be subtracted so that the bender element tip-tip distance is utilised (Lee & Santamarina, 2005).

The obtained wave velocities are presented in Figure 12, showing that the expected trend of wave velocity increases due to the acting stress. The apparent continuity of the curves in all the Vp and V_s obtained curves seems to indicate the absence of any significant hysteretical effects occurring due to the unloading-reloading effect underwent by the sample.

B. Appendix B: Original expressions for the boundary condition

The proper boundary conditions were adopted following the equations developed by Dong-Joo Min et.Al, 2004. In this work the solution to the Elastic wave equation was bi-dimensional and formulated in the frequency domain. Although the formulation in the case of the code is three-dimensional and in the temporal domain, the same principle and notation is used for the equation notation.

The equation to solve was:

$$\omega^2 \rho u + \frac{\delta}{\delta x}\left[\lambda\left(\frac{\delta u}{\delta x} + \frac{\delta v}{\delta z}\right) + 2\mu \frac{\delta u}{\delta x}\right] + \frac{\delta}{\delta z}\left[\mu\left(\frac{\delta v}{\delta x} + \frac{\delta u}{\delta z}\right)\right] + f_x = 0$$

$$\omega^2 \rho v + \frac{\delta}{\delta z}\left[\lambda\left(\frac{\delta u}{\delta x} + \frac{\delta v}{\delta z}\right) + 2\mu \frac{\delta v}{\delta z}\right] + \frac{\delta}{\delta x}\left[\mu\left(\frac{\delta v}{\delta x} + \frac{\delta u}{\delta z}\right)\right] + f_z = 0$$

Where u and v are the Fourier-transformed displacements, λ and μ are the Lamé constants, and f are the vertical forces. The notation for the discretization can be seen in Figure B-1.

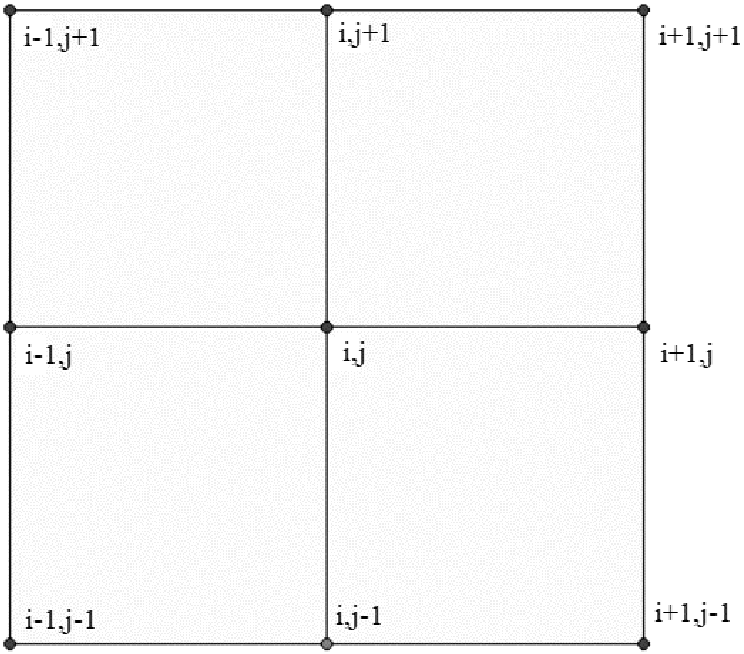

Figure B-1. Reference system for finite differences.

The formulation is based on applying the material properties in terms of cells rather than in terms of nodes at the boundary, much like it would be done in the finite element method. The material properties for the wave propagation problem are given the Lamé constants and the material density. Treating these properties at constants, the finite difference approximation for each term becomes:

$$\frac{\delta}{\delta x}\left(k\frac{\delta u}{\delta x}\right)=\frac{1}{\Delta x^2}\left[\frac{1}{2}(k_3+k_4)\left(u_{i+1,j}-u_{i,j}\right)-\frac{1}{2}(k_1+k_2)\left(u_{i,j}-u_{i-,j}\right)\right]$$

$$\frac{\delta}{\delta z}\left(k\frac{\delta u}{\delta z}\right)=\frac{1}{\Delta z^2}\left[\frac{1}{2}(k_2+k_4)\left(u_{i+1,j}-u_{i,j}\right)-\frac{1}{2}(k_1+k_3)\left(u_{i,j}-u_{i-,j}\right)\right]$$

$$\frac{\delta}{\delta x}\left(k\frac{\delta u}{\delta z}\right)=\frac{1}{\Delta x}\left[\left(k\frac{du}{dz}\right)_{i+1/2,j}-\left(k\frac{du}{dz}\right)_{i-1/2,j}\right]$$

$$\frac{\delta}{\delta z}\left(k\frac{\delta u}{\delta x}\right)=\frac{1}{\Delta \mathrm{z}}\left[\left(k\frac{du}{dx}\right)_{i,j+1/2}-\left(k\frac{du}{dx}\right)_{i,j-1/2}\right]$$

The local terms can be evaluated as:

$$\left(k\frac{du}{dz}\right)_{i+1/2,j}=\frac{1}{2}\left[k_3\left(\frac{du}{dz}\right)_3+k_4\left(\frac{du}{dz}\right)_4\right]$$

$$\left(k\frac{du}{dz}\right)_{i-1/2,j}=\frac{1}{2}\left[k_1\left(\frac{du}{dz}\right)_1+k_2\left(\frac{du}{dz}\right)_2\right]$$

$$\left(k\frac{du}{dx}\right)_{i,j+1/2}=\frac{1}{2}\left[k_2\left(\frac{du}{dx}\right)_2+k_4\left(\frac{du}{dx}\right)_4\right]$$

$$\left(k\frac{du}{dx}\right)_{i,j-1/2}=\frac{1}{2}\left[k_1\left(\frac{du}{dx}\right)_1+k_2\left(\frac{du}{dx}\right)_2\right]$$

With:

$$\left(\frac{du}{dx}\right)_1=\frac{1}{\Delta x}\left[\frac{1}{2}\left(u_{i,j-1}+u_{i,j}\right)-\frac{1}{2}\left(u_{i-1,j-1}+u_{i-1,j}\right)\right]$$

$$\left(\frac{du}{dx}\right)_2=\frac{1}{\Delta x}\left[\frac{1}{2}\left(u_{i,j+1}+u_{i,j}\right)-\frac{1}{2}\left(u_{i-1,j+1}+u_{i-1,j}\right)\right]$$

$$\left(\frac{du}{dx}\right)_3=\frac{1}{\Delta x}\left[\frac{1}{2}\left(u_{i+1,j-1}+u_{i+1,j}\right)-\frac{1}{2}\left(u_{i,j-1}+u_{i,j}\right)\right]$$

$$\left(\frac{du}{dx}\right)_4=\frac{1}{\Delta x}\left[\frac{1}{2}\left(u_{i+1,j+1}+u_{i+1,j}\right)-\frac{1}{2}\left(u_{i,j+1}+u_{i,j}\right)\right]$$

And in the other direction:

$$\left(\frac{du}{dz}\right)_1 = \frac{1}{\Delta z}\left[\frac{1}{2}\left(u_{i-1,j} + u_{i,j}\right) - \frac{1}{2}\left(u_{i-1,j-1} + u_{i-1,j-1}\right)\right]$$

$$\left(\frac{du}{dz}\right)_2 = \frac{1}{\Delta z}\left[\frac{1}{2}\left(u_{i-1,j+1} + u_{i,j+1}\right) - \frac{1}{2}\left(u_{i-1,j} + u_{i,j}\right)\right]$$

$$\left(\frac{du}{dz}\right)_3 = \frac{1}{\Delta z}\left[\frac{1}{2}\left(u_{i+1,j} + u_{i,j}\right) - \frac{1}{2}\left(u_{i+1-1,j-1} + u_{i-1,j-1}\right)\right]$$

$$\left(\frac{du}{dz}\right)_4 = \frac{1}{\Delta z}\left[\frac{1}{2}\left(u_{i+1,j+1} + u_{i+1,j}\right) - \frac{1}{2}\left(u_{i,j+1} + u_{i,j}\right)\right]$$

So, the term is evaluated as:

$$\begin{aligned}\frac{\delta}{\delta x}\left(k\frac{\delta u}{\delta z}\right) = {} & \frac{1}{4\Delta x\Delta z}\left[k_1 u_{i-1,j-1} + (k_1 - k_3)u_{i-1,j-1} - k_3 u_{i+1,j-1}\right] \\ & + \frac{1}{4\Delta x\Delta z}\left[(k_2 - k_1)u_{i-1,j} + (k_3 - k_1 + k_2 - k_4)u_{i,j} - k_3 u_{i1,j1} + (k_3\right. \\ & \left. - k_4)u_{i+1,j}\right] + \frac{1}{4\Delta x\Delta z}\left[-k_2 u_{i-1,j+1} + (k_4 - k_2)u_{i,j+1} + k_4 u_{i+1,j+1}\right]\end{aligned}$$

$$\begin{aligned}\frac{\delta}{\delta z}\left(k\frac{\delta u}{\delta x}\right) = {} & \frac{1}{4\Delta x\Delta z}\left[k_1 u_{i-1,j-1} + (k_1 - k_3)u_{i,j-1} - k_3 u_{i+1,j-1}\right] \\ & + \frac{1}{4\Delta x\Delta z}\left[(k_1 - k_2)u_{i-1,j} + (k_3 - k_1 + k_2 - k_4)u_{i-1,j-1} - k_3 u_{i1,j1} + (k_4\right. \\ & \left. - k_3)u_{i+1,j}\right] + \frac{1}{4\Delta x\Delta z}\left[-k_2 u_{i-1,j+1} + (k_2 - k_4)u_{i,j+1} + k_4 u_{i+1,j+1}\right]\end{aligned}$$

And for the case of the free surface terms:

$$\frac{\delta}{\delta x}\left(k\frac{\delta u}{\delta x}\right) = \frac{1}{\Delta x^2}\left[\frac{1}{2}k_4\left(u_{i+1,j} + u_{i,j}\right) - \frac{1}{2}k_2\left(u_{i,j} + u_{i-,j}\right)\right]$$

$$\frac{\delta}{\delta x}\left(k\frac{\delta u}{\delta z}\right) = \frac{1}{\Delta z^2}\left[\frac{1}{2}(k_2 + k_4)\left(u_{i,j+1} - u_{i,j}\right)\right]$$

$$\begin{aligned}\frac{\delta}{\delta x}\left(k\frac{\delta u}{\delta z}\right) = {} & \frac{1}{4\Delta x\Delta z}k_4(u_{i+1,j+1} + u_{i,j+1} - u_{i+1,j} - u_{i,j}) - \frac{1}{4\Delta x\Delta z}k_2(u_{i-1,j+1} + u_{i,j+1} \\ & - u_{i-1,j} - u_{i,j})\end{aligned}$$

$$\begin{aligned}\frac{\delta}{\delta z}\left(k\frac{\delta u}{\delta x}\right) = {} & \frac{1}{4\Delta x\Delta z}k_2(u_{i,j+1} + u_{i,j} - u_{i-1,j+1} - u_{i-1,j}) - \frac{1}{4\Delta x\Delta z}k_4(u_{i+1,j+1} + u_{i+1,j} \\ & - u_{i,j+1} - u_{i,j})\end{aligned}$$